

PROCEEDINGS OF

**The 56th Conference on
Simulation and Modelling
(SIMS 56)**

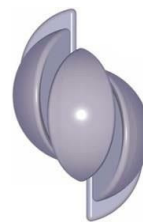
October, 7-9, 2015

Linköping University, Sweden



EDITORS: Lena Buffoni, Adrian Pop, and Bernhard Thiele

LIU LINKÖPING
UNIVERSITY



The conference is organized by Linköping University in cooperation with the Scandinavian Simulation Society (SIMS).

www.scansims.org

Proceedings of the 56th Conference on Simulation and Modelling (SIMS 56)
Linköping, Sweden, October 7-9, 2015

Editors:

Lena Buffoni, Adrian Pop, and Bernhard Thiele

Published by:

Scandinavian Simulation Society and Linköping University Electronic Press

ISBN: 978-91-7685-900-1

Series: Linköping Electronic Conference Proceedings, No 119

ISSN: 1650-3686

eISSN: 1650-3740

DOI: <http://dx.doi.org/10.3384/ecp15119>

Organized by:

Linköping University

Programming Environments Laboratory (PELAB)

Department of Computer and Information Science

SE-581 83 Linköping

Sweden

in co-operation with:

Scandinavian Simulation Society

c/o Esko Juuso, Department of Process and Environmental Engineering

P.O Box 4300

FIN-90014 University of Oulu

Finland

Conference location:

Linköping University

Campus Valla in Building B, Linköping

58183 Linköping

Sweden

Copyright © Scandinavian Simulation Society, 2015

WELCOME

The 56th Conference on Simulation and Modelling will be held in Linköping, Sweden. Linköping is one of Sweden's fastest growing cities. The population is constantly increasing and will soon surpass 150 000 inhabitants. It is currently Sweden's fifth largest city and a part of the expansive region Twin Cities of Sweden. Linköping has long been characterized by world-class high technology in the fields of aviation, IT and the environment. There is a strong force of innovation especially in Mjärdevi Science Park—one of Europe's leading technology parks, and at the highly ranked university, which stands for excellence and entrepreneurship.

SIMS is the Scandinavian Simulation Society with members from the five Nordic countries Denmark, Finland, Norway, Sweden and Iceland. The SIMS history goes back to 1959. The goal of SIMS is to further the science and practice of modeling and simulation in all application areas and be a Scandinavian forum for information interchange among modeling and simulation professionals and non-professionals in Denmark, Finland, Norway and Sweden as well as a channel for information exchange between the Scandinavian modeling and simulation community and the international modeling and simulation communities.

The ambition of the SIMS is to bring the field of modeling and simulation technology to a variety of application fields from energy extraction to building and automotive industries, resulting in more sustainable and ecological systems and reducing energy consumption and waste production. The scientific program includes technical sessions with submitted and invited papers and will cover broad aspects of simulation, modeling and optimization.

The focus of the conference is split evenly between papers on simulation and optimization in a variety of applied contexts spanning domains such as oil extraction, automotive and building industries and more methodological papers on tools and technologies for simulation and modeling.

This year we wanted to emphasize the importance of reducing the gap between state of the art methodologies and tools and industrial applications. To this end a number of invited talks, papers and tutorials were centered on tools and methodologies for successful modeling in an industrial context.

The format of the conference is somewhat changed compared to previous years. This year we have dedicated a half-day before the traditional two-day conference to tutorials, with 3 tutorials presenting state-of-the-art simulation tools.

Conference highlights:

- 4 Keynote speeches
- 40 papers in 2 parallel tracks
- 3 tutorials
- Electronic proceedings including all papers and some associated Modelica libraries and models

Finally, we want to acknowledge the support we received from the conference board and program committee as well as from the SIMS board. Special thanks to our colleagues at this year's organizers at Linköping University, especially to Åsa Kärrman, and Tina Malmström from Grand Travel Group. The support from the conference sponsors is gratefully acknowledged. Last but not least, thanks to all authors, keynote speakers, and presenters for their contributions to this conference.

We wish all participants an enjoyable and inspiring conference.

Linköping, September 1, 2015

Lena Buffoni, Adrian Pop and Bernhard Thiele

Tutorials:

This year the conference included three tutorials on simulation tools and environments with hands-on exercises.

Tutorial 1: *Principles of Object-Oriented Modeling and Simulation of Dynamic Systems with Modelica.*

Tutor: Dr. Lena Buffoni (Linköping University)

Tutorial 2: *FMI 2.0 Model Exchange, Cosimulation– Theory and Practice*

Tutor: MSc Adeel Asghar (Linköping University)

Tutorial 3: *Collaborative Modelling and Cosimulation using Crescendo: Tools and techniques for Designing Embedded Systems*

Tutor: Prof. Peter Gorm Larsen (Aarhus University, Denmark)

Invited talks:

SIMS 2015 had four invited talks on the state-of-the-art and future directions of simulation tools and methodology in the industrial context.

Keynote 1: *Accomplishing Ground Moving Innovations through Modeling, Simulation, and Optimal Control*

Presenter: Prof. Lars Eriksson, Linköping University, Sweden

Keynote 2: *INTO-CPS: An well-founded integrated tool chain for comprehensive Model-Based Design of Cyber-Physical Systems*

Presenter: Prof. Peter Gorm Larsen, Aarhus University, Denmark

Keynote 3: *Overview of Modeling, Simulation, Debugging, and Optimization with Modelica using OpenModelica*

Presenter: Prof. Peter Fritzson, Linköping University, Sweden

Keynote 4: *Virtual Engineering in the Automation Industry - How can we do better?*

Presenter: Dr. Mikelsons Lars, Bosch Rexroth, Germany

Program Committee

Program Chairs

Lena Buffoni, Linköping University

Adrian Pop, Linköping University

Bernhard Thiele, Linköping University

International Program Committee

Lena Buffoni, Linköping University, Sweden

Erik Dahlquist, Mälardalens Högskola, Sweden

Magnus Eek, SAAB, Sweden

Brian Elmegaard, DTU, Denmark

Lars Eriksson, Linköping University, Sweden

Alfredo Garro, UNICAL, Italy

Britt Halvorsen, Høgskolen i Telemark, Norway

Magnus Thor Jonsson, University of Iceland, Iceland

Kaj Juslin, VTT, Finland

Esko Juuso, University of Oulu, Finland

Tommi Karhela, VTT, Finland

Magnus Komperød, Nexans Norway AS, Norway

Bernt Lie, Høgskolen i Telemark, Norway

Mads Pagh Nielsen, Aalborg University, Denmark

Nikolaos Papakonstantinou, VTT, Finland

Adrian Pop, Linköping University, Sweden

Kim Sørensen, AAU, Denmark

Bernhard Thiele, Linköping University, Sweden

Conference Organization Team:

Lena Buffoni, Linköping University

Åsa Kärman, Linköping University

Adrian Pop, Linköping University

Bernhard Thiele, Linköping University

Contents

Session 3A: Session A	15
Effects of Pulsating Flow on Mass Flow Balance and Surge Margin in Parallel Turbocharged Engines .	15
Simulation of improved absorption configurations for CO ₂ capture	21
Optimal Operation of the Peat Drying Process in Steam Tube Dryers	31
Improving the Mathematical Formulas for Identification of Bitumen's Viscoelastic Properties at Large Shear Strains	43
Session 3B: Session B	55
Simulation as a Tool for Evaluating Biogas Purification Processes	55
Computational study of heavy oil production with inflow control devices	63
Process Simulation of Calcium Looping With Indirect Calciner Heat Transfer	71
Simulation of Simplified Model for Reaction Kinetics in Biomass Gasification	81
Session 4A: Session A	91
A Framework for Early and Approximate Uncertainty Quantification of Large System Simulation Models	91
Modelica Implementation and Software-to-Software Validation of Power System Component Models Commonly used by Nordic TSOs for Dynamic Simulations	105
Learning Modelica Models from Component Libraries	113
A Software Architecture for Simulation and Visualisation based on the Functional Mock-up Interface and Web Technologies	123
Session 4B: Session B	131
Nearwell simulations of a horizontal well in Atlanta Field - Brazil with AICV completion using OLGA/Rocx	131
Heat pump efficiencies simulated with Aspen HYSYS and Aspen Plus	141
Aspen Plus simulation of biomass gasification with known reaction kinetic	149
Near well simulation of extra heavy oil production using SAGD	157
Session 5A: Session A	169
Recursive dynamic modelling in changing operating conditions	169
Robust Simulation for Hybrid Systems: Chattering Bath Avoidance.	175
Job-Scheduling of Distributed Simulation-Based Optimization with Support for Multi-Level Parallelism	187
Validation Techniques Applied on the Saab Gripen Fighter Environmental Control System Model . . .	199
Session 5B: Session B	211
Integrated model of bioenergy and agriculture system	211
Modeling of the Energy Consumption within the Framework of the Energy Efficiency Management . .	229
Modeling for control of run-of-river power plant Grnvollfoss	237
Near Well CFD Simulation of SAGD Extra Heavy Oil Production	247
Session 9A: Session A	255
Gasification of biomass for production of syngas for biofuel	255
Temperature Effects in Anaerobic Digestion Modeling	261
Gasification of livestock manure	271
Modeling and simulation of Triclosan kinetics and distribution in humans using a PBPK model	279
Session 9B: Session B	289
Near well simulation and modelling of oil production from heavy oil reservoirs	289
Improved model for solar heating of buildings	299
Near well simulation of CO ₂ injection for Enhanced Oil Recovery (EOR)	309
The Kelvin-Voigt Model's Suitability to Explain the Viscoelastic Properties of Anticorrosion Bitumen at Large Shear Strain in Subsea Cables and Umbilicals	319

Session 10A: Session A	331
An optimization framework for tracking droplets in fire water spray images	331
Study of the effect of relative permeability and residual oil saturation on oil recovery	339
Simulation of CO ₂ -distribution in carbonate reservoir	347
Derivation of Arc Length of Helical Cable Element at Cable Bending, with Emphasize on Taylor Series	
Expansion of the Non-Integrable Infinitesimal Arc Length	357
Session 10B: Session B	369
Simulation of Transcritical Flow in Hydraulic Structures	369
Optimal Control of an EMU Using Dynamic Programming and Tractive Effort as the Control Variable	377
Multiphysics Numerical Modeling of a Fin and Tube Heat Exchanger	383
Numerical Investigation of Single-phase Fully Developed Heat Transfer and Pressure Loss in Spirally	
Corrugated Tubes	391

Contents

Session 3A: Session A	15
<i>Effects of Pulsating Flow on Mass Flow Balance and Surge Margin in Parallel Turbocharged Engines</i> .	15
<i>Simulation of improved absorption configurations for CO2 capture</i>	21
<i>Optimal Operation of the Peat Drying Process in Steam Tube Dryers</i>	31
<i>Improving the Mathematical Formulas for Identification of Bitumen's Viscoelastic Properties at Large Shear Strains</i>	43
Session 3B: Session B	55
<i>Simulation as a Tool for Evaluating Biogas Purification Processes</i>	55
<i>Computational study of heavy oil production with inflow control devices</i>	63
<i>Process Simulation of Calcium Looping With Indirect Calciner Heat Transfer</i>	71
<i>Simulation of Simplified Model for Reaction Kinetics in Biomass Gasification</i>	81
Session 4A: Session A	91
<i>A Framework for Early and Approximate Uncertainty Quantification of Large System Simulation Models</i> 91	
<i>Modelica Implementation and Software-to-Software Validation of Power System Component Models Commonly used by Nordic TSOs for Dynamic Simulations</i>	105
<i>Learning Modelica Models from Component Libraries</i>	113
<i>A Software Architecture for Simulation and Visualisation based on the Functional Mock-up Interface and Web Technologies</i>	123
Session 4B: Session B	131
<i>Nearwell simulations of a horizontal well in Atlanta Field - Brazil with AICV completion using OLGA/Rocx</i> 131	
<i>Heat pump efficiencies simulated with Aspen HYSYS and Aspen Plus</i>	141
<i>Aspen Plus simulation of biomass gasification with known reaction kinetic</i>	149
<i>Near well simulation of extra heavy oil production using SAGD</i>	157
Session 5A: Session A	169
<i>Recursive dynamic modelling in changing operating conditions</i>	169
<i>Robust Simulation for Hybrid Systems: Chattering Bath Avoidance.</i>	175
<i>Job-Scheduling of Distributed Simulation-Based Optimization with Support for Multi-Level Parallelism</i>	187
<i>Validation Techniques Applied on the Saab Gripen Fighter Environmental Control System Model</i>	199

Session 5B: Session B	211
<i>Integrated model of bioenergy and agriculture system</i>	211
<i>Modeling of the Energy Consumption within the Framework of the Energy Efficiency Management</i> ..	229
<i>Modeling for control of run-of-river power plant Grnvollfoss</i>	237
<i>Near Well CFD Simulation of SAGD Extra Heavy Oil Production</i>	247
Session 9A: Session A	255
<i>Gasification of biomass for production of syngas for biofuel</i>	255
<i>Temperature Effects in Anaerobic Digestion Modeling</i>	261
<i>Gasification of livestock manure</i>	271
<i>Modeling and simulation of Triclosan kinetics and distribution in humans using a PBPK model</i>	279
Session 9B: Session B	289
<i>Near well simulation and modelling of oil production from heavy oil reservoirs</i>	289
<i>Improved model for solar heating of buildings</i>	299
<i>Near well simulation of CO2 injection for Enhanced Oil Recovery (EOR)</i>	309
<i>The Kelvin-Voigt Model's Suitability to Explain the Viscoelastic Properties of Anticorrosion Bitumen at Large Shear Strain in Subsea Cables and Umbilicals</i>	319
Session 10A: Session A	331
<i>An optimization framework for tracking droplets in fire water spray images</i>	331
<i>Study of the effect of relative permeability and residual oil saturation on oil recovery</i>	339
<i>Simulation of CO2-distribution in carbonate reservoir</i>	347
<i>Derivation of Arc Length of Helical Cable Element at Cable Bending, with Emphasize on Taylor Series Expansion of the Non-Integrable Infinitesimal Arc Length</i>	357
Session 10B: Session B	369
<i>Simulation of Transcritical Flow in Hydraulic Structures</i>	369
<i>Optimal Control of an EMU Using Dynamic Programming and Tractive Effort as the Control Variable</i>	377
<i>Multiphysics Numerical Modeling of a Fin and Tube Heat Exchanger</i>	383
<i>Numerical Investigation of Single-phase Fully Developed Heat Transfer and Pressure Loss in Spirally Corrugated Tubes</i>	391

Author Index

Adhikari, Umesh	255	Nordin, Peter	187
Agu, Cornelius	81, 369	Ohenoja, Markku	55
Aljarbouh, Ayman	175	Ölvander, Johan	91
Andreassen, Monica	279	Pavlova, Yuliia	229
Aromada, Solomon Aforkoghene	21	Pfeiffer, Carlos F.	31
Bakke, Rune	261	Provan, Gregory	113
Baudette, Maxime	105	Røngaard Clausen, Lasse	211
Bergland, Wenche	261	Rondeel, Wilhelm	229
Bohlin, Markus	377	Rosen, Victor	31
Braun, Robert	187	Schaathun, Hans Georg	123
Caillaud, Benoit	175	Sharma, Roshan	31, 237, 279
Chathurangani, L.B.J.	309	Sigurjonsson, Hafthor Ægir	211
Condra, Thomas	383, 391	Singh, Shobhana	383
Da Silva, Katia Aparecida	131	Sorsa, Aki	55
Dahlquist, Erik	377	Sørensen, Kim	383, 391
Dinamarca, Carlos	261	Thapa, Rajan	81
Dirven, Hubert	279	Thapa, Rajan K.	149
Ediriweera, Mahesh	339	Thomasson, Andreas	15
Eek, Magnus	91, 199	Tirados, Irene Yuste	141
Eikeland, Marianne S.	149, 255, 271	Tokheim, Lars-Andre	71
Elmegaard, Brian	211	Vanfretti, Luigi	105
Elseth, Geir	369	Vytvytskyi, Liubomyr	237
Eriksson, Lars	15	Wallin, Fredrik	377
Furuvik, Nora C.I	347	Wijeratne, D.I. Erandi N.	63
Gavel, Hampus	199	Zhang, Houxiang	123
Ghaviha, Nima	377	Zhang, Mengjia	105
Granstrøm, Ingunn	237		
Guandang, Kou	157		
Hällqvist, Robert	199		
Halvorsen, Britt	81, 289		
Halvorsen, Britt M.	63, 131, 149, 157, 247, 255, 271, 309, 339, 347		
Hatledal, Lars Ivar	123		
Haugen, Hildegunn.H.	271		
Hærvig, Jakob	391		
Husøy, Trine	279		
Øi, Lars	21		
Øi, Lars Erik	71, 141		
Jayarathna, Chameera	71		
Juuso, Esko	169		
Kahawalage, Amila Chandra	247		
Karlén, Johan	91		
Komperød, Magnus	43, 319, 357		
Kotsar, Oleg	229		
Krus, Petter	187		
Kulakovskiy, Leonid	31		
Lavenius, Jan	105		
Lie, Bernt	31, 237, 279, 299, 369		
Lind, Ingela	199		
Lundberg, Joachim	331		
Løvlund, Stig	105		
Lysaker, Ola Marius	331		
Maharjan, Samee	279		
Malagalage, Anjana	289		
Mathiesen, Vidar	247		
Mathisen, Anette	71		

Effects of Pulsating Flow on Mass Flow Balance and Surge Margin in Parallel Turbocharged Engines

Andreas Thomasson¹ Lars Eriksson¹

¹Department of Electrical Engineering, Linköping University, Sweden, {andreast, larer}@isy.liu.se

Abstract

The paper extends a mean value model of a parallel turbocharged internal combustion engine with a crank angle resolved cylinder model. The result is a 0D engine model that includes the pulsating flow from the intake and exhaust valves. The model captures variations in turbo speed and pressure, and therefore variations in the compressor operating point, during an engine cycle. The model is used to study the effect of the pulsating flow on mass flow balance and surge margin in parallel turbocharged engines, where two compressors are connected to a common intake manifold. This configuration is harder to control compared to single turbocharged systems, since the compressors interact and can work against each other, resulting in co-surge. Even with equal average compressor speed and flow, the engine pulsations introduce an oscillation in the turbo speeds and mass flow over the engine cycle. This simulation study use the developed model to investigate how the engine pulsations affect the in cycle variation in compressor operating point and the sensitivity to co-surge. It also shows how a short circuit pipe between the two exhaust manifolds could increase surge margin at the expense of less available turbine energy.

Keywords: Engine modeling, Engine simulation, Compressor surge, Turbocharging

1 Introduction

Turbocharging is now days a common way to increase power density and reduce fuel consumption of internal combustion engines Emmenthal et al. (1979); Guzzella et al. (2000). To make further improvement and meet increasing demands, more advanced turbocharging concepts have been developed over the years (Petitjean et al., 2004; Galindo et al., 2009), that are now being put into production on a larger scale. One such concept that is used for V-type engines is to have two smaller, parallel turbochargers, where each turbine is feed by one of the two cylinder banks. This enables the turbines to be placed closer to the exhaust ports, reducing the size of the exhaust manifold and results in better utilization of the energy in the exhaust pulses Watson and Janota (1982).

Usually the two compressors are then connected to a common intake manifold, which is the configuration studied in this paper. This ensures that the intake pressure is equal for all cylinders, but introduces another balancing problem. If the two compressors does not produce equal flow, one compressor will be operating closer to the surge line than the other, and possibly go into surge even if the average operating point would be stable. When the surging compressor recovers it can then push the other compressor into surge, resulting in a mass flow oscillation between the two compressors that alternately go into surge. This phenomena has been investigated in Thomasson and Eriksson (2014), that also shows how the main behavior of the co-surge oscillation can be captured by a Mean Value Engine Model (MVEM), without considering in-cycle variations.

Due to the pulsations from the intake and exhaust valves, turbo speed and flow variations will occur during an engine cycle, even if the two compressors operates with equal average flow. To be able to capture these phenomena, and see how they can effect surge sensitivity, the MVEM is not sufficient. However the extension to a crank angle resolved 0D model requires only the cylinder model to be replaced. With that extension and the assumption that the MVEM submodels can be used in a quasi stationary pulsating flow, the in-cycle variations can be modeled.

1.1 Contributions

The paper integrates a crank angel resolved cylinder model in an existing MVEM. The resulting zero dimensional model is used to study the effect of cylinder pulsations on mass flow balance in parallel turbocharged V-engines. The effect of intake pulsations, exhaust pulsation and cylinder firing order is investigated separately, where the later is shown to have a very large impact on the in-cycle turbo speed variations for V8-engines. This is an important aspect when designing parallel turbocharge engines, as a too large compressor choice could otherwise make the system very sensitive to surge. The paper also shows how a short circuit pipe between the two exhaust manifolds could increase the surge margin, with the downside that a part of the available energy in the exhaust pulses are lost.

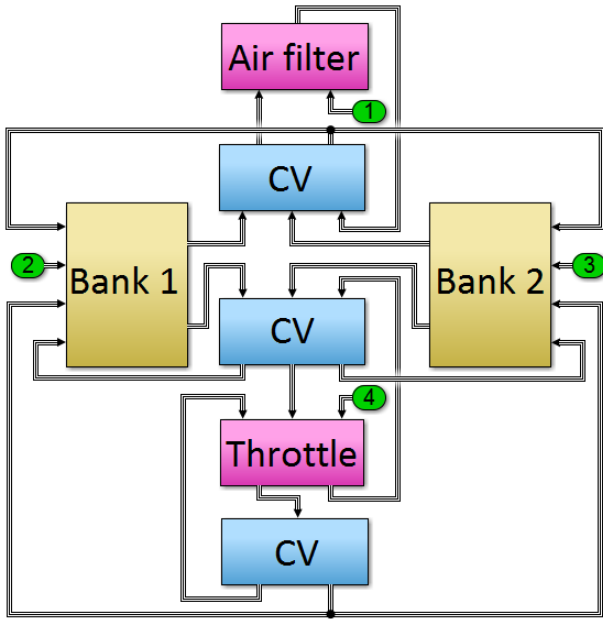


Figure 1. An overview of the simulink MVEM for the parallel turbocharged engine. Magenta colored blocks are restrictions (Air filter, Throttle), blue are control volumes (CV) and yellow blocks are collections of other blocks (Bank 1,2), in this case all doubled blocks: compressor, compressor CV, intercooler, cylinder bank, exhaust manifold CV, turbine, turbine CV and exhaust restriction.

2 Engine Model

A common approach in engine control is to work with Mean Value Engine Models (MVEM). These models are zero dimensional and does not resolve variations that occur during a cycle, which are instead averaged, resulting in very fast simulation models. These models started to develop in the late 80's and early 90's (Hendricks, 1989; Hendricks and Sorenson, 1990; Jensen et al., 1991), and soon started to be used for engine control, see for example Guzzella and Amstutz (1998). The starting point for the model in this investigation is a component based MVEM presented in Eriksson (2007), that has been arranged in a parallel turbocharged engine configuration outlined in Thomasson and Eriksson (2011, 2014). An overview of the model can be seen in Fig. 1.

2.1 Compressor Model

To capture the surge behavior in the compressor the Moore-Greitzer model is used Greitzer (1976, 1981); Hansen et al. (1981). It incorporates a state equation for the mass flow in the compressor

$$\frac{dW_c}{dt} = \frac{\pi D^2}{4L} (\hat{p}_{ac} - p_{ac}) \quad (1)$$

where \hat{p}_{ac} is the pressure build up after the compressor that is given by the compressor map as function of turbo speed and current compressor mass flow. To model the compressor speed lines and extrapolate the compressor

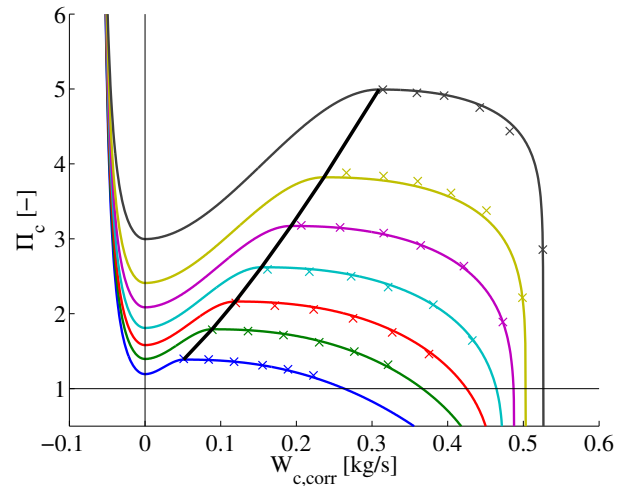


Figure 2. Model of the compressor speed lines together with the measured compressor map (crosses). The model is able to accurately capture the measured compressor map, offer interpolation in the map and extrapolation to the surge and choke region.

map to the surge region, the model presented in Leufvén and Eriksson (2013) is used, which has been shown to model compressor surge with good accuracy together with mean value engine models. The model fit to the measured compressor map and how the speed lines are extrapolated to the surge region are shown in Fig. 2.

2.1.1 Turbo shaft torque balance

The torque balance of the compressors are modeled with Newtons second law of motion for rotating systems, using the power balance between the turbine and the compressor with a viscous friction loss:

$$J_{tc} \frac{\omega_{tc}}{dt} = \frac{P_t}{\omega_{tc}} - \frac{P_c}{\omega_{tc}} - k_{fric} \omega_{tc} \quad (2)$$

The parameters are the compressor inertia, J_{tc} , the turbine power P_t , the compressor power P_c , the turbo speed, ω_{tc} , and the friction coefficient k_{fric} .

2.2 Model Extension to Valve Pulsations

To include the effect of pulsations from the intake and exhaust valves, the MVEM concept has to be abandoned to some extent. However since all components in the model are zero dimensional with filling and emptying dynamics, a first approach is to exchange only the engine block with a crank angle resolved model. The assumption that is made is that the submodels works approximately correct also under quasi-stationary conditions, with cyclic variations around the same mean value as in the MVEM. The new engine model needs to include restrictions to represent the intake and exhaust valves and variable size control volumes to represent the cylinders. Furthermore a model for the heat release from the combustion and heat losses in the cylinder have to be included.

2.2.1 Intake and Exhaust Valves

The intake and exhaust valves are modeled as compressible flow restrictions, with a crank angle dependent effective area. The valve flow area in this model is approximated with the lift times the circumference of the valve,

$$W = \frac{p_{us}}{\sqrt{RT_{us}}} A_{eff} \Psi(\Pi) \quad (3a)$$

$$A_{eff} = C_d L_v(\theta) D_v \pi \quad (3b)$$

where W is the mass flow, A_{eff} is the effective area, D_v is the valve diameter, L_v is the valve lift that depend on the valve profile and the crank angle, θ , and $\Pi = p_{ds}/p_{us}$ is the pressure ratio. The Ψ function is given by

$$\Psi(\Pi) = \begin{cases} \Pi^{1/\gamma} \left\{ \frac{2\gamma}{\gamma-1} \left[1 - \Pi^{\frac{\gamma-1}{\gamma}} \right] \right\}^{1/2} & \text{if } \Pi \geq \Pi_{crit} \\ \gamma^{1/2} \left(\frac{2\gamma}{\gamma+1} \right)^{\frac{\gamma+1}{2(\gamma-1)}} & \text{if } \Pi < \Pi_{crit} \end{cases} \quad (4)$$

where γ is the ratio of specific heats for the gas upstream of the valve. In general the flow area is a more complicated function of the valve and valve seat geometry, see for example Heywood (1988), but this is a good first approximation and enough to get reasonable flow pulsations in the intake and exhaust manifolds.

2.2.2 Cylinder Volume

The cylinder volume is treated a single-zone open system with four states, air mass, m_a , fuel mass, m_f , burned gas mass, m_b , and temperature, T . The mass balance for normal flow direction, from intake to cylinder and from cylinder to exhaust, is given by

$$\dot{m}_a = W_{ip}(1 - x_{b,im}) - W_{ep}x_a - W_{br}(A/F)_s \quad (5a)$$

$$\dot{m}_f = W_f - W_{br} \quad (5b)$$

$$\dot{m}_b = W_{ip}x_{b,im} - W_{ep}x_b + W_{br}(1 + (A/F)_s) \quad (5c)$$

where W_{ip} , W_{ep} and W_f is the intake, exhaust and fuel flow respectively, W_{br} is the fuel burn ratio and $(A/F)_s$ is the stoichiometric air/fuel ratio. The mass fractions are

$$x_a = \frac{m_a}{m_{tot}} \quad x_b = \frac{m_b}{m_{tot}} \quad x_f = \frac{m_f}{m_{tot}} \quad (6)$$

$$m_{tot} = m_a + m_b + m_f$$

where m_{tot} is the total cylinder mass in the cylinder and $x_{b,im}$ in (5) refer to the burned gas fraction in the intake manifold.

The equation for the temperature differential can be derived from the first law of thermodynamics. Under the assumption that the internal energy is only a function of temperature and that the gas mixture can be treated as an ideal gas the result is

$$\dot{T} = -\frac{(\gamma-1)RT}{V} + \frac{1}{c_v(T)m_{tot}} \times \dots \left(\dot{Q}_{hr} - \dot{Q}_{ht} - \sum_i (h_i(T_i) - u_i(T)) W_i \right) \quad (7)$$

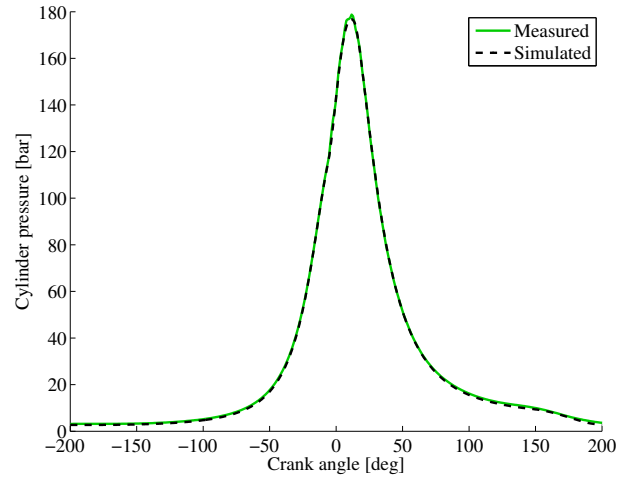


Figure 3. Measured and simulated cylinder pressure trace at 1400 rpm. The model can accurately capture the measured cylinder pressure trace.

where the subscript i indicate the i :th flow component. Three mass flows can occur in this model, gas mixture flowing through the intake and exhaust valves, and fuel flow to the cylinder volume.

2.2.3 Heat Release

To get the fuel burn ratio, a model presented in Chmela and Orthaber (1999) has been used for the heat release rate, \dot{Q}_{hr} . It is based on mixing controlled combustion and in addition to the instantaneous fuel mass in the cylinder considers both injection rate as well as the kinetic energy in the fuel spray. The fuel burn ratio are then calculated from the heat release rate using

$$\dot{Q}_{hr} = W_{br} q_{LHV} \quad (8)$$

where q_{LHV} is the lower heating value of the fuel.

2.2.4 Heat Transfer

The final component of the cylinder model is the heat transfer from the volume to the cylinder walls and piston. This is obtained by Newton's law of cooling

$$\dot{Q}_{ht} = h_c A (T - T_w) \quad (9)$$

where Woschni's heat transfer correlation (Woschni, 1967) is used for the instantaneous heat transfer coefficient, h_c .

2.3 Model Validation

The crank angle resolved cylinder model is validated by comparing the simulated cylinder pressure with measurements. A simulated and measured cylinder pressure trace at 1400 rpm can be seen in Fig. 3. The model is able to capture the cylinder pressure trace very well, and the resulting torque is within 2% of the measured value at this operating point. This accuracy is considered more than enough to get reasonably accurate exhaust pulsations which is the main purpose to introduce this submodel in this study.

3 Simulation Study

In this section the engine model outlined above is used to analyze how engine pulsations affect the mass flow balance in parallel turbocharged engines.

A steady state simulation of a parallel turbocharged V8 engine at 1400 rpm is shown in Fig. 4. The variations in intake side pressures are small, less than 1 %, but the instantaneous mass flow through each compressor varies a lot although the sum is almost constant. It should be emphasized that this is the modeled instantaneous mass flow based on the turbo speed, pressure ratio over the compressor and the compressor map, slightly low pass filtered by the gas inertia included in the Moore-Greitzer model. The shape of the mass flow oscillation is almost identical to the oscillation in compressor speed, indicating that the turbo speed variations is the main reason for mass flow variations. The amplitude of the turbo speed oscillation is around $\pm 1.7\%$ of the average turbo speed. This is larger than for a single turbocharged four cylinder engine, see for example Westin (2005) where a $\pm 0.4\%$ oscillation for a car sized turbo is shown. The main reason for this is the firing order, since the largest shift in turbo speed occurs when two cylinders fire in sequence on one bank. This effect is investigated further in Section 3.3.

3.1 Effect of intake pulsations

As the simulation shown in Fig. 4 shows, the intake side pulses are very small compared the exhaust, and could therefore be expected to have only a minor influence compared to other effects. The size of pulsations are largely influenced by the volumes on the intake side, and to confirm this hypothesis, the model was simulated with a significantly larger volumes on the intake side. Apart from low pass filtering the pressures on the intake side this has only a marginal effect on the turbo speed and instantaneous mass flow through the compressors. The result became almost identical in steady state compared to Fig. 4 and is not shown here. It is concluded that the pressure pulsations on the intake side has very little effect on the mass flow balance.

3.2 Effect of exhaust pulsations

To utilize as much as possible of the exhaust energy in the turbine, the exhaust manifold of turbocharged engines are usually small. This increases the available energy to the turbine but also introduces large cyclic variations in exhaust pressure. To see how large impact the exhaust pulsations have on the parallel turbocharged engine, the model is simulated with a ten times larger exhaust manifold. This low pass filters the pressure pulsations, and reduces the turbo speed oscillation significantly to approximately $\pm 0.6\%$, see Fig. 5. Another way to test the effect of pulsating turbine power is to increase the inertia of the turbocharger. This slows down the turbo dynamics, low pass filtering the speed oscillation without effecting the size of the exhaust

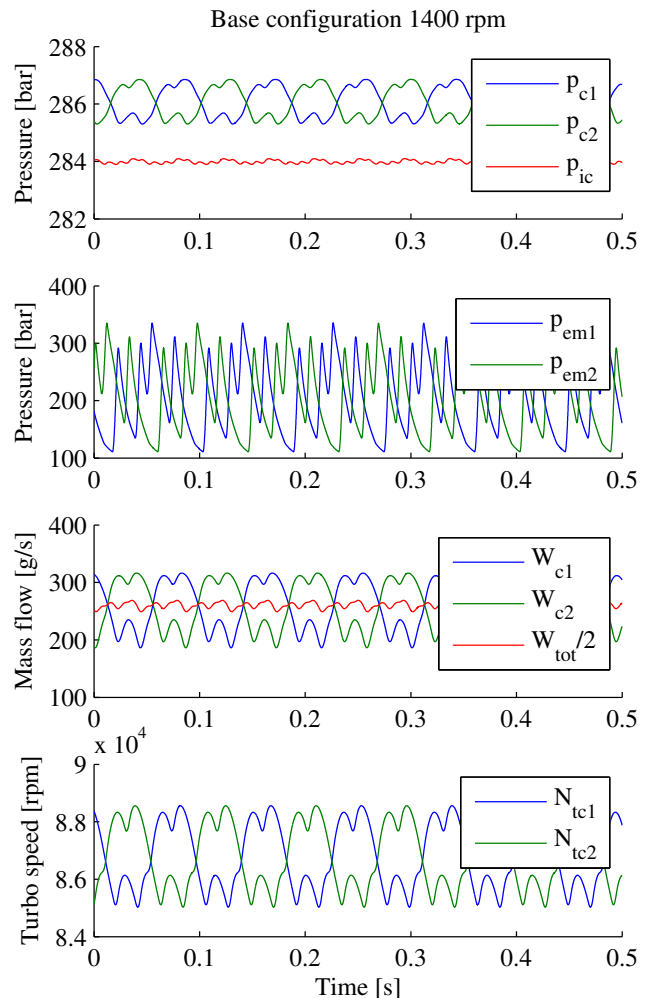


Figure 4. Simulation in a steady state operating point at 1400 rpm. The subscripts are c for compressor, ic for intercooler, em for exhaust manifold and tc for turbocharger. The intake pressure oscillations are small, however the instantaneous mass flow through the compressors pulsates shows large variations over the cycle.

pulses. Doubling the inertia has a similar effect on the turbo speed oscillation as the increased exhaust manifold simulation. It is clear that the major part of the oscillation in the instantaneous mass flow is due to the variations in turbo speed oscillation as a result of the exhaust pulses.

3.3 Effect of the firing order for V8 engines

As discussed earlier, the largest shift in speed between the turbochargers is when two cylinders fire sequentially on one bank. In V8 engines this is used to achieve second order balance, and therefore can not be changed in practice. However, the size of the effect is interesting to study in simulation to understand the limitation, and possibly find solutions. A simulation in the same operating point as previously, but with altered ignition order so that the two banks alternately fires one cylinder during the whole cycle, is shown in Fig. 6. With this firing order, the turbo speed variations are reduced to less than $\pm 0.6\%$, approximately a third compared to normal firing order for the V8 engine. For this reason a parallel turbocharged V8 engine should

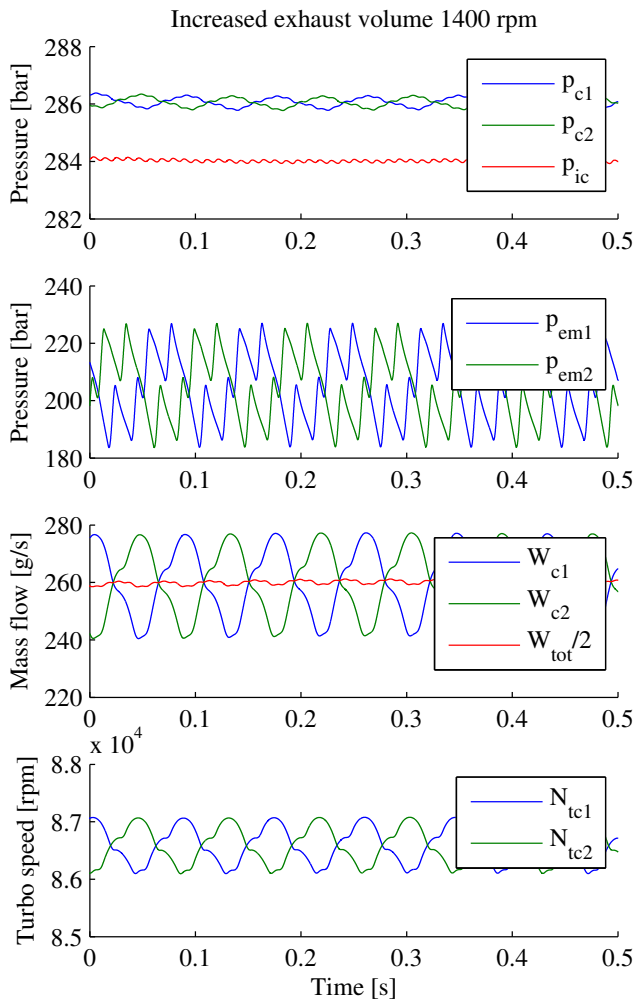


Figure 5. Simulation in a steady state operating point at 1400 rpm with increased exhaust manifold volume. This effectively reduces the pressure pulsation at the turbine inlet which reduce turbine speed and instantaneous mass flow oscillation. However it also reduces the available energy to the turbines which is not desirable.

be more sensitive to surge compared to a V6, when running low speed high torque operating points, where the compressor typically operates close to the surge line.

3.4 Impact on co-surge sensitivity

The cyclic variations in compressor speed results in large variations in compressor operating point. This is a consequence of the very flat characteristic of the speed lines immediately to the right of the surge line in the compressor map, see Fig. 2. Fig. 7 zooms in the compressor map around cyclic variations for the simulation in Fig. 4, which is shown by the blue line. The thin black dashed lines are compressor speed lines only 1000 rpm apart (85.5 krpm to 88.5 krpm). As evident, a very small change in compressor speed moves the operation point far in the mass flow direction for the compressor map. The green line show the corresponding variation for the simulation with altered ignition order from Fig. 6. The red line correspond a simulation with short-circuited exhaust manifolds - see Section 3.5.

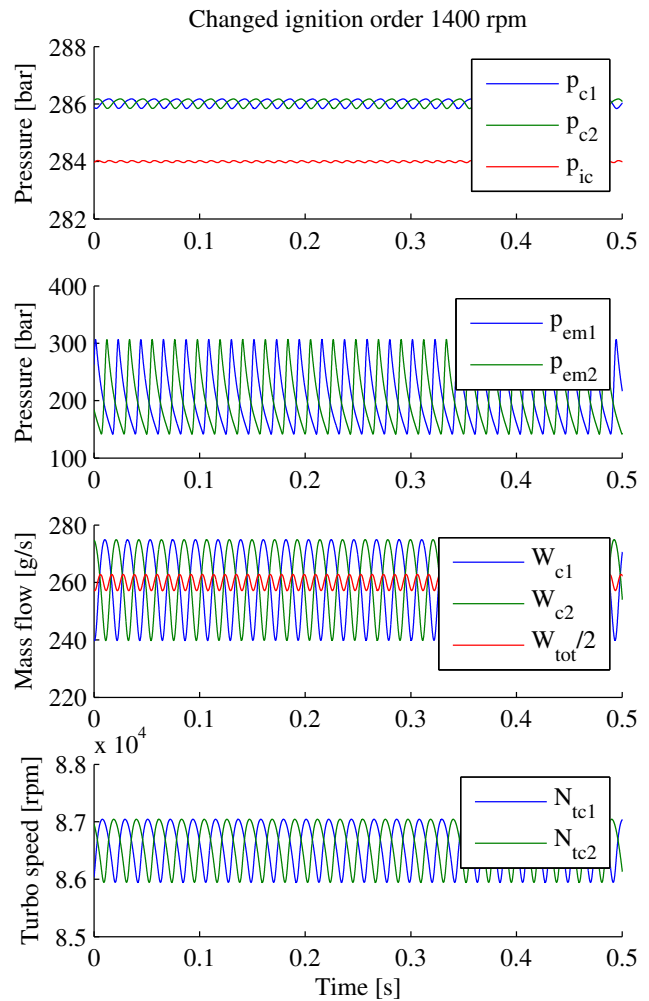


Figure 6. Simulation in a steady state operating point at 1400 rpm, with changed firing order so that each cylinder bank fires one cylinder every 180°. For this hypothetical situation the turbo speed oscillation is only about a third compared to the real firing order, and the same is true for the mass flow oscillation.

To quantify the difference in surge sensitivity, ramps in engine speed with fixed boost pressure reference was performed. The starting point was the fixed operating point in Fig. 4-6, at 1400 rpm. Then the engine speed was lowered until the model entered co-surge. For the base model this occurred around 1250 rpm, and for the changed ignition order around 1000 rpm, which is a significant difference. With increased exhaust manifold volume or double turbocharger inertia the system also enters surge slightly above 1000 rpm, but for that case with increased volume the available energy to the turbines were insufficient to keep the boost pressure at the same level.

3.5 Short-circuited exhaust manifolds

Since the large part of the turbo speed difference originates from the fact that the exhaust pulses alternately powers one of the turbines, one possible way to reduce this would be to short-circuit the exhaust manifolds. This transfers some of the exhaust energy from one bank to the other but has the downside that part of the exhaust pulse energy is lost. As an

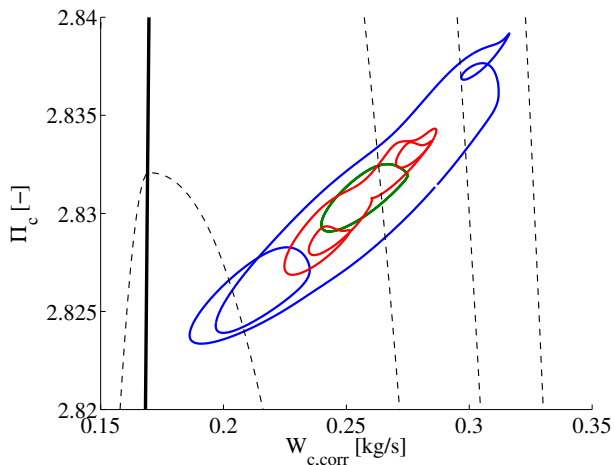


Figure 7. Compressor map zoomed in around cyclic operation for the simulation shown in Fig. 4. The blue and green lines corresponds to the compressor operation for simulations in Fig. 4 and Fig. 6 respectively. The red line shows the compressor operation with a short-circuit pipe between the exhaust manifolds.

example, with a 1 m long and 3 cm wide short-circuit pipe, modeled with two compressible restrictions and a control volume, the resulting compressor operation is shown by the red line Fig. 7. Doing the same engine speed ramp as in the previous section, the system enters surge around 1150 rpm, 100 rpm lower than the base configuration. Increasing the size of the pipe would trade available energy for more balanced turbo speeds. Adding controllable valves to the pipe could open for the possibility of utilizing the full pulse energy in operating points with more margin to the compressor surge line, and reducing the pulse energy in favor of more balanced operation closer to the surge limit.

4 Conclusions

The simulations study shows that the main source of cyclic variations in mass flow balance in parallel turbocharged engines is due to oscillations in turbo speed. This is mainly a result of exhaust pulsations, which has additional consequence for the V8 engine due to its firing order. Since two cylinders will fire in sequence once each engine cycle on each bank, the turbo speed oscillation will be larger compared to for example a similar sized four cylinder engine with a single turbocharger or a parallel turbocharged V6 engine where the cylinder on each bank fires with equal angle between them. For this reason parallel turbocharged V8 engines should be more sensitive to surge and require larger margin to the surge line compared to parallel turbocharged V6 engines. A way to reduce the cyclic variation is to short-circuit the exhaust manifolds. This reduces the surge sensitivity, but the trade off is a reduction in the available energy in the exhaust pulses.

References

Franz G. Chmela and Gerard C. Orthaber. Rate of Heat Release Prediction for Direct Injection Diesel Engines Based on Purely

Mixing Controlled Combustion. In *SAE World Congr.*, Techn. Paper 1999-01-0186, March 1999.

K.-D. Emmenthal, G. Hagermann, and W.-H. Hucho. Turbocharging small displacement spark ignited engines for improved fuel economy. In *SAE World Congr.*, Techn. Paper 790311, February 1979.

Lars Eriksson. Modeling and Control of Turbocharged SI and DI Engines. *Oil & Gas Science and Technology - Rev. IFP*, 62(4):523–538, 2007.

J. Galindo, H. Climent, C. Guardiola, and J. Domenech. Strategies for improving the mode transition in a sequential parallel turbocharged automotive diesel engine. *Int. J. of Automotive Technology*, 10(2):141–149, 2009.

E.M. Greitzer. Surge and rotating stall in axial flow compressors—Part I: Theoretical compression system model. *J. of Engineering for Power*, 98(2):190–198, April 1976.

E.M. Greitzer. The Stability of Pumping Systems. *J. of Fluids Engineering*, 103(1):193–242, June 1981.

L. Guzzella, U. Wenger, and R. Martin. IC-Engine Downsizing and Pressure-Wave Supercharging for Fuel Economy. *SAE World Congr.*, March 2000.

Lino Guzzella and Alois Amstutz. Control of Diesel Engines. *Control Systems*, 18(5):53–71, 1998.

K.E. Hansen, P. Jørgensen, and P.S. Larsen. Experimental and Theoretical Study of Surge in a Small Centrifugal Compressor. *J. of Fluids Engineering*, 103(3):391–395, 1981.

Elbert Hendricks. The Analysis of Mean Value Engine Models. In *SAE World Congr.*, Techn. Paper 890563, February 1989.

Elbert Hendricks and Spencer C. Sorenson. Mean value modelling of spark ignition engines. *SAE Trans. J. of Engines*, 99(3):1359–1373, 1990.

John B. Heywood. *Internal Combustion Engine Fundamentals*. McGraw-Hill series in mechanical engineering. McGraw-Hill, 1988. ISBN 0-07-100499-8.

J.-P. Jensen, A. F. Kristensen, S. C. Sorenson, N. Houbak, and E. Hendricks. Mean Value Modeling of a Small Turbocharged Diesel Engine. In *SAE World Congr.*, Techn. Paper 910070, February 1991.

Oskar Leufvén and Lars Eriksson. A Surge and Choke Capable Compressor Flow Model - Validation and Extrapolation Capability. *Control Engineering Practice*, 21(12):1871–1883, 2013.

Dominique Petitjean, Luciano Bernardini, Chris Middlemass, S. M. Shahed, and Ronald G. Hurley. Advanced Gasoline Engine Turbocharging Technology for Fuel Economy Improvements. In *SAE World Congr.*, Techn. Paper 2004-01-0988, March 2004.

Andreas Thomasson and Lars Eriksson. Modeling and Control of Co-Surge in Bi-Turbo Engines. In *Proc. of the IFAC World Congr.*, Milano, Italy, 2011.

Andreas Thomasson and Lars Eriksson. Co-Surge in Bi-Turbo Engines - Measurements, Analysis and Control. *Control Engineering Practice*, 32:113–122, November 2014.

N. Watson and M.S. Janota. *Turbocharging the Internal Combustion Engine*. The Macmillan Press Ltd, 1982. ISBN 0-333-24290-4.

Fredrik Westin. *Simulation of turbocharged SI-engines - with focus on the turbine*. PhD thesis, Royal Institute of Technology, May 2005.

G. Woschni. A Universally Applicable Equation for the Instantaneous Heat Transfer Coefficient in the Internal Combustion Engine. In *SAE World Congr.*, Techn. Paper 670931, February 1967.

Simulation of Improved Absorption Configurations for CO₂ Capture

Solomon Aforkoghene Aromada¹ Lars Erik Øi¹

¹Department of and Process, Energy and Environmental Technology, Telemark University College, Norway
lars.oi@hit.no

Abstract

The most well-known technology for post combustion CO₂ capture from exhaust gas is absorption in an amine-based solvent followed by desorption. The drawback of this method is the high heat consumption required for desorption. Reduction of the energy consumption can be achieved by using alternative configurations. In this work, the standard process, vapour recompression and vapour recompression combined with split-stream configurations have been simulated using Aspen HYSYS version 8.0 for 85% amine-based CO₂ removal in search for optimum process. Energy optimisation has also been performed by varying the most important parameters. This study shows that it is possible to reduce energy consumption with both the vapour recompression and the vapour recompression combined with split-stream processes. The vapour recompression process has been calculated to be the energy optimum alternative among the configurations investigated.

Keywords: CO₂, simulation, absorption, Aspen HYSYS, optimisation, MEA.

1 Introduction

Absorption of CO₂ in an amine based solvent like monoethanolamine (MEA) followed by desorption is the most standard technology for large scale post combustion CO₂ capture from exhaust gas. However, the high equivalent heat consumption requirement for desorption is an enormous challenge. Research efforts have been targeted at reducing the energy cost, usually referred to as “energy penalty”. According to (Rochelle, 2003), the energy requirement is estimated to be 15-30% of power plant output. (Le Moulec and Kanniche, 2011) calculated it to be about 25% loss of power output when coupled with compression.

The traditional approach for reducing energy consumption of amine-based absorption and stripping of CO₂ has been by the modification of process flow sheets. This work seeks to find an energy optimum process by simulation of alternative configuration energy demands and optimisation of such processes.

1.1 Literature on CO₂ absorption

Different ways exist for reduction of heat consumption in a CO₂ capture process using alternative configurations. In the case of high absorption pressures, (Kohl, 1997) presented some alternative

configurations in the reference book. (Polasek, 1982) also show a systematic overview of alternative flow schemes for CO₂ absorption at high pressures.

(Aroonwilas, 2006) have evaluated alternative CO₂ post combustion capture configurations. (Oyenekan and Rochelle, 2007) proposed different stripper configurations for energy reduction. (Cousins, Wardhaugh and Feron, 2011) evaluated four alternative configurations and compared their performance with a standard process configuration. (Cousins, Wardhaugh, and Feron, 2011) published a survey of 15 process flow sheet modifications for energy efficient CO₂ capture from flue gases using chemical absorption. (Le Moulec and Kanniche, 2011) also presented some flow sheet modifications with 8 minor modifications. (Fernandez, 2012) did cost estimation based on net present value from Aspen Plus simulations. (Karimi, Hillestad and Svendsen, 2011) have conducted process simulations with Unisim Design and Protreat and also evaluated the capital cost of the alternative configurations.

However, much work has not been published on calculations or simulations of alternative absorption configurations for CO₂ capture from flue gas (Øi et al., 2014; Øi and Shchuchenko, 2011).

At Telemark University College, (Øi and Vozniuk, 2010) have used Aspen HYSYS version 7.2 to evaluate and compare the split-stream scheme with the standard process. Different split-stream modifications and vapour recompression scheme were evaluated using Aspen HYSYS by (Øi and Shchuchenko, 2011). (Øi et al., 2014) did optimisation based only on absorber packing height and minimum approach temperature in the heat exchanger. (Øi and Kvam, 2014) also have evaluated and compared energy consumption of alternative configurations for CO₂ removal using Aspen HYSYS and Aspen Plus simulation programs. But their work did not cover energy optimisation as a function of absorber and desorber column height and minimum approach temperature in the heat exchanger. This paper presents simulations of different alternative process configurations and a more comprehensive optimisation of such processes towards the reduction of the energy requirements for amine based CO₂ absorption and desorption. The simulation program used is Aspen HYSYS version 8.0. And optimisation based on variation of the most important parameters is conducted.

2 Process description

The principles of the different alternative configurations are described in this section.

2.1 Standard process

Alternative configurations performances are mainly evaluated by comparison with the standard process as a reference configuration. It comprises of a simple absorber and desorber (stripper) with a reboiler and condenser, amine/amine heat exchanger, pumps and a cooler. CO₂ from an exhaust gas is absorbed in the absorption column with amine solvent (e.g. monoethanolamine-MEA). The CO₂-rich amine solution from the absorption column is then pumped through the lean/rich amine heat exchanger where it is heated before entering the stripper for regeneration. The regenerated (lean) amine is pumped back to the absorption column for re-use. It first flows through the amine/amine heat exchanger where it is used to heat up the rich stream and further cooled in the amine cooler. Figure 1 describes the principle of the standard amine-based CO₂ absorption-desorption process.

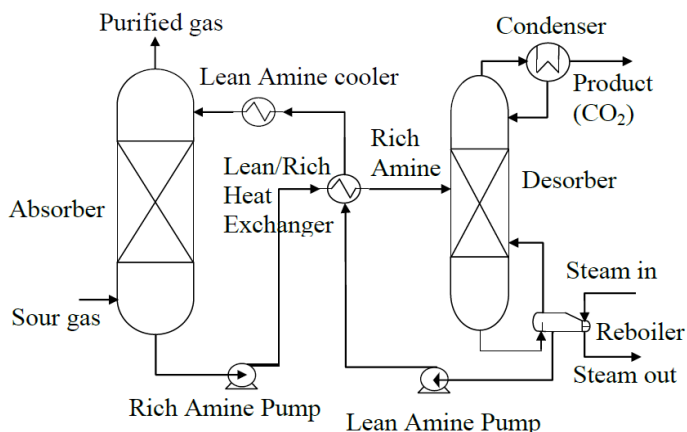


Figure 1. Principle of standard process

2.2 Vapour recompression process

The only difference between the vapour recompression and the standard process configurations is that the regenerated amine from the bottom of the stripper is flashed by creating a pressure drop using a valve. The resulting vapour is separated from the lean amine stream by the use of a gas/liquid separator. The vapour is then compressed and injected back to the desorber to aid the regeneration process. The result is an increase of the stripping vapour in the desorber but leaving the water balance of the system unaffected (Cousins et al., 2011). Figure 2 shows the principle of vapour recompression.

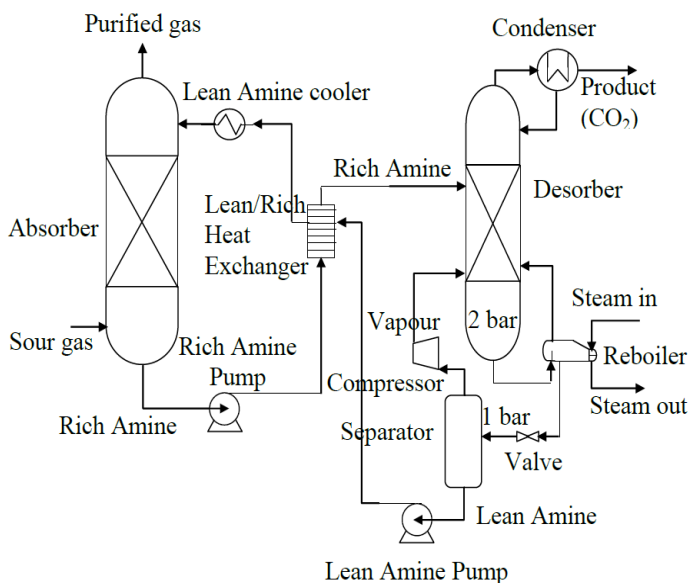


Figure 2. Principle of vapour recompression process

2.3 Vapour recompression process combined with split-stream process

This configuration combines both the vapour recompression process and split-stream process to harness the energy reduction benefit of both processes. In this process, the semi-lean amine can either be drawn from the middle or from the stream exiting the stripper before it is flashed for vapour recompression. Figure 3 describes vapour recompression combined with split-stream process with the semi-lean drawn from the bottom of the stripper.

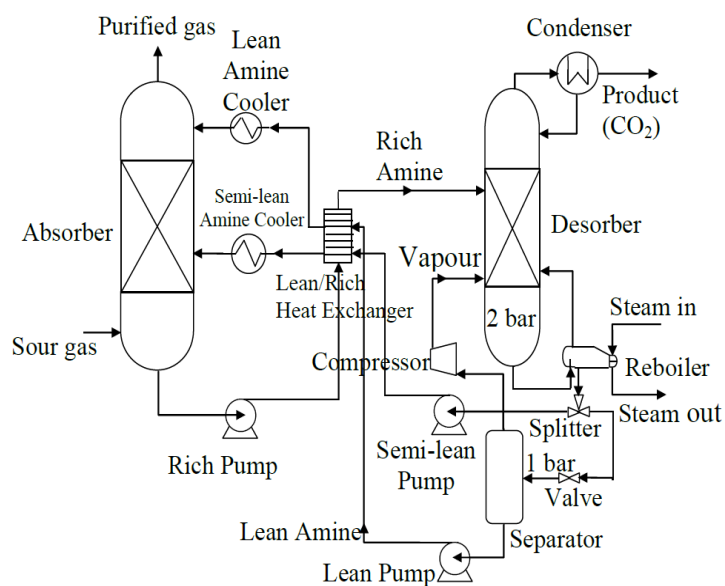


Figure 3. Principle of vapour recompression combined with split-stream process

3 Models

This section presents the most important models required for the simulations.

3.1 Equilibrium models

The available models in the Amine Property Package in Aspen HYSYS are the Kent-Eisenberg (Kent and Eisenberg, 1976) and Li-Mather (Li, 1996) vapour/liquid equilibrium models. “The models are quite complex” (Øi, 2007). Equilibrium of CO₂ concentration in the gas and liquid (absorbent) is described by the use of these models. Either of them can be selected with the Non-ideal vapour phase model for simulation.

3.2 Column models

Columns are usually modelled by the use of equilibrium stages. A plate/tray is evaluated by the assumption that the concentration of CO₂ in the gas and liquid leaving plate/tray are in equilibrium. A given packing height (e.g., 1m) can be modelled as an equilibrium stage. Murphree efficiency can be introduced to refine the equilibrium stage model and it is given as (Øi, 2007):

$$E_M = \frac{(y - y_{n-1})}{(y^* - y_{n-1})} \quad (1)$$

Where y is the mole fraction of CO₂ in the gas leaving the stage, y_{n-1} is the mole fraction of CO₂ leaving the stage below, and y^* is mole fraction of CO₂ in equilibrium with the liquid leaving the stage. In Aspen HYSYS, the user can specify the Murphree efficiency. Some references (Øi, 2007; Øi et al., 2014; Øi and Shchuchenko, 2011; Øi and Vozniuk, 2010) have used the values of 15% and 25%. Figure 4 illustrates the definition of Murphree efficiency.

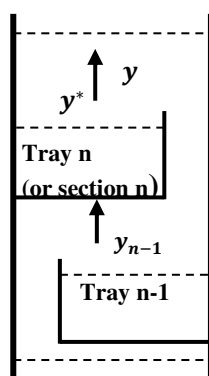


Figure 4. Illustration of of Murphree efficiency (Øi, 2007)

3.3 Column convergence

There is a default set of convergence criteria and a default set of calculation parameters in Aspen HYSYS. “Different calculation models are also available” (Øi, 2007). The default is the HYSIM Inside-Out algorithm. There is also the Modified HYSIM Inside-Out algorithm which usually enhances convergence in more complex process simulations. “A damping parameter for column iteration is adjustable and the damping can be specified as adaptive” (Øi, 2007).

4 Process specifications and simulations

This section has the specifications, results and discussion on the base case simulations.

4.1 Specifications and simulation of standard process for CO₂ capture

Simulation of a standard process for CO₂ capture with Aspen HYSYS V8.0 has been performed. The specifications used are presented in Table 1.

Table 1. Standard process simulation input specifications for 85% CO₂ removal

Parameter	Value
CO ₂ removal grade	85%
Inlet gas pressure	40°C
Inlet gas pressure	1.1 bar
Inlet gas molar flow rate	85540 kmol/h
CO ₂ in inlet gas	3.73%
Water in inlet gas	6.71%
Nitrogen in inlet gas	89.56%
Lean MEA temperature	40°C
Lean MEA pressure	1.01 bar
Lean MEA molar flow rate	116500 kmol/h
MEA content in Lean MEA	28.2 mass-%
CO ₂ in Lean MEA	5.3 mass-%
Number of stages in absorber	20
Murphree efficiency in absorber	0.15
Rich MEA pump pressure	2 bar
Rich MEA to desorber temperature	104.3°C
Number of stages in desorber	6 (2 + 4)
Murphree efficiency in desorber	1
Reflux ratio in desorber	0.3
Reboiler temperature	120°C
Lean MEA Pump pressure	4 bar
Minimum ΔT in Rich/Lean Heat Exchanger	10°C

The calculation method used is the same as in (Øi, 2007; Øi, 2012). These specifications are from a full scale Mongstad project from Gassnova. They are for 85% CO₂ absorption from a natural gas based power plant planned at Mongstad outside Bergen (Øi, 2007). Simulations have been performed using Amine Property Package with the Kent-Eisenberg equilibrium model (Kent and Eisenberg, 1976) and non-ideal vapour phase model. And the Li-Mather equilibrium model (Li, 1996) has also been used but for comparison purpose. Besides the optimisation calculations, all the simulations in this work have specifications of 20 absorber stages with a Murphree efficiency of 0.15 (Øi, 2012) and a minimum approach temperature of 10°C. The Aspen HYSYS flow diagram is given in Figure 5.

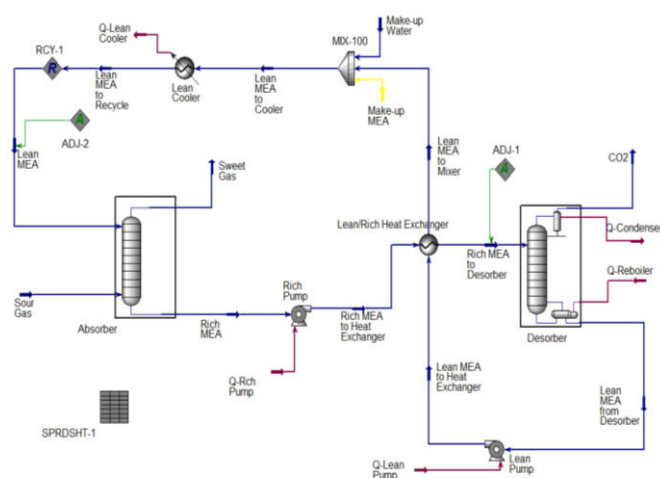


Figure 5. Aspen HYSYS flow sheet of standard process for CO₂ absorption-desorption in amine solution

The calculated heat consumptions are presented in Table 2. They are just slightly lower than other references (Cousins et al., 2011; Jordal et al., 2012; Karimi et al., 2011; Øi, 2007; Øi and Shchuchenko, 2011; Øi and Vozniuk, 2010). This is due to high number of absorber stages and in some cases the lower removal grade used. However, (Karimi et al., 2011; Øi et al., 2014; Øi and Kvam, 2014) calculated values less than the ones presented in this paper. This is as a result of the use of a lower minimum approach temperature in the amine/amine heat exchanger.

The simulation results of (Kothandaraman, 2010) for typical conditions are 4.30 MJ/kg CO₂ and 4.50 MJ/kg CO₂ with Aspen Plus equilibrium based model and rate-based model respectively. With Aspen Plus version 7.1 and 3 equilibrium stages in the absorber, 3.56 MJ/kg CO₂ was simulated by Fernandez et al. (Fernandez, 2012). 3.55 MJ/kg CO₂ and 3.61 MJ/kg CO₂ were calculated by Karimi et al. (Karimi et al., 2011) with 5°C and 10°C minimum approach temperature (ΔT_{\min}) respectively using Unisim. Unisim is a version of Aspen HYSYS and also has the same

Amine Property Packages as Aspen HYSYS with Kent-Eisenberg and Li-Mather vapour/liquid equilibrium models (Øi and Kvam, 2014).

4.2 Specifications and simulation of vapour recompression process for CO₂ capture

Simulation of 85% CO₂ removal has been performed using the vapour recompression principle as presented in Figure 2. The calculation method is similar to that in Section 4.1. The Aspen HYSYS flow diagram is presented in Figure 6. The lean amine flow rate that achieved 85% CO₂ removal is 106300kmol/h with CO₂ concentration of 5.08% (lean loading of 0.18 and rich loading is 0.35). The compressor's adiabatic efficiency is 75%.

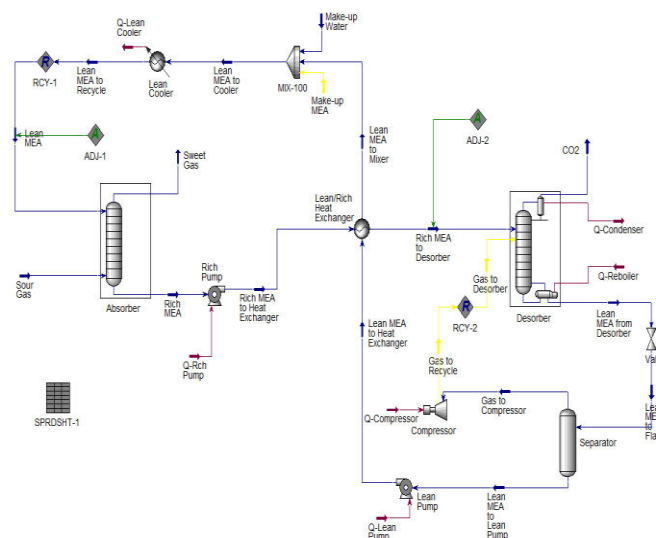


Figure 6. Aspen HYSYS flow sheet of vapour recompression process for CO₂ absorption-desorption in amine solution

The results of the vapour recompression simulation are given in Table 2. Energy savings of 0.37 MJ/kg CO₂ (10%) and 0.31 MJ/kg CO₂ (9%) with Kent-Eisenberg and Li-Mather models respectively were achieved. The equivalent heat consumption is calculated as the sum of the reboiler heat consumption and four times the compressor work. This is because it is assumed that about 25% efficiency can be obtained by converting the low pressure steam used by the reboiler to electricity by a steam turbine (Øi et al., 2014; Øi and Kvam, 2014). 1/0.28 and 1/0.23 were used by (Le Moulllec and Kanniche, 2011) and (Fernandez, 2012) respectively.

(Cousins et al., 2011) calculated a reboiler heat consumption of 3.04 MJ/kg CO₂ with a rate-based simulation program (program type not mentioned) and achieved a reboiler heat saving of 0.71 MJ/kg CO₂. In this paper, it is 0.82 MJ/kg CO₂ and 0.75 MJ/kg CO₂

with Kent-Eisenberg and Li-Mather models respectively. And (Fernandez, 2012) simulation results using Aspen Plus equilibrium model, with a flash pressure of 1.2 bar and desorber pressure of 1.8 bar, gave a reboiler duty of 3.03 MJ/kg CO₂ (this is almost equal to (Cousins et al., 2011) result) and equivalent heat consumption of 3.30 MJ/kg CO₂ removed. With a desorber pressure of 2.5 bar, (Le Moulec and Kanniche, 2011) calculated a lower reboiler heat consumption of 2.56 MJ/kg CO₂. This may likely be due to the difference of 0.5 bar pressure of the stripper between their work and this study. Using Unisim program, (Karimi et al., 2011) calculated a reboiler heat consumption of 2.72 MJ/kg CO₂ compared to 3.61 MJ/kg CO₂ of the standard process.

4.3 Specifications and simulation of vapour recompression combined with split-stream process for CO₂ capture

This is the most complex configuration among the three under consideration. The calculations are more challenging and more complicated. It involves three (3) recycle blocks. The calculation sequence and most of the specifications used in simulating this configuration are the same as the recompression process. The difference is that the regenerated amine stream is split into two at a ratio of 0.1 and 0.9 for the semi-lean and the lean amine streams respectively.

The semi-lean was sent to stage 8 of the absorber because it gives the best result (though negligible). The absorber liquid feeds are 10690 kmol/h (with CO₂-mass concentration of 5.35%) of the semi-lean flow and 96300 kmol/h (with CO₂-mass concentration of 5.05%) of the lean amine after make-up water and amine have been added to the stream at the mixer. The Aspen HYSYS process flow diagram (PFD) is shown Figure 7.

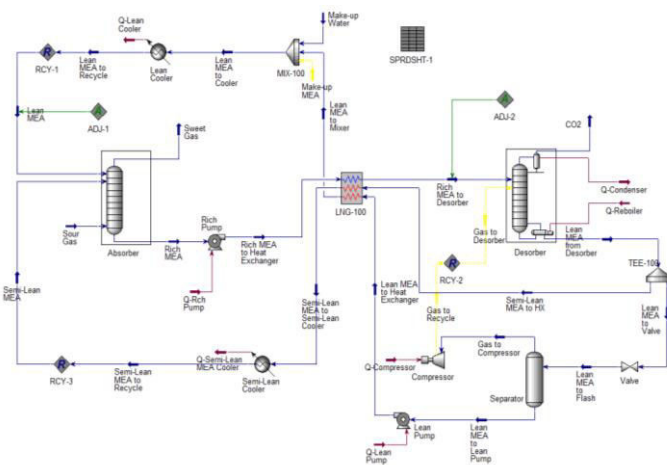


Figure 7. Aspen HYSYS flow sheet of vapour recompression process+split-stream for CO₂ capture.

The equivalent heat consumption is calculated as in the case of vapour recompression. The Kent-Eisenberg and Li-Mather vapour/liquid equilibrium models results are presented in Table 2. These results show that the energy savings in CO₂ removal with this configuration are 0.34 MJ/kg CO₂ (9%) and 0.29 MJ/kg CO₂ (8%) using the Kent-Eisenberg and the Li-Mather models respectively. However, the equivalent heat consumption is still 0.03 MJ/kg CO₂ higher than the result achieved with the vapour recompression configuration.

(Øi et al., 2014) calculated 3.02 MJ/kg CO₂ with Aspen HYSYS as the equivalent heat consumption with 20 absorber stages and semi-lean stream sent to stage 14 of the absorber. Murphree efficiency of 0.15 was specified for the absorber. This value was lower because a 5°C was specified as the minimum approach temperature for their simulation. (Øi and Kvam, 2014) calculated 3.12 MJ/kg CO₂ and 3.03 MJ/kg CO₂ with Aspen HYSYS Kent-Eisenberg and Li-Mather equilibrium models respectively. These values are also lower than the results achieved in this study because they simulated with a lower ΔT_{\min} of 5°C. With 24 absorber stages and the semi-lean stream sent to stage 13, (Øi and Shchuchenko, 2011) calculated a reboiler heat consumption of 2.45 MJ/kg CO₂ and 2.59 MJ/kg CO₂ as reboiler heat with split-streams from the bottom and middle of the reboiler respectively. In this paper and the other references mentioned, it has been shown that combining the vapour recompression with the split-stream processes cannot achieve lower equivalent heat consumption as the vapour recompression in spite of the advantage of the reduced compressor work.

4.4 Calculation strategy and sequence

The simulation strategy was based on earlier Aspen HYSYS simulations by (Øi, 2007) and (Kvam, 2013).

The compositions, flow rates, temperatures and pressures of the flue gas and lean amine solution flowing as feeds into the absorber were first specified. Then the absorption column was calculated. Subsequently, the rich pump was calculated followed by the rich side of the lean/rich heat exchanger and then the desorber. After the desorber, in the case of the vapour recompression combined with split-stream process, the split was executed at the ratio of 1 to 9 for the semi-lean and lean streams respectively. Then the resulting lean amine stream was flashed and vapour/liquid separation done. By the aid of an ADJUST block, the temperature of the rich amine stream to the desorber was adjusted such that the specified minimum approach temperature (ΔT_{\min}) in the heat exchanger was achieved. The lean pump, vapour compressor and coolers were then calculated. The compositions of both the lean and semi-lean streams were checked (in RECYCLE blocks) against

the specified feeds compositions to the absorber (particularly CO₂-concentration) to ensure convergence. Whenever it was difficult to reach convergence, it was expedient to check if the material balance of water and amine are fulfilled if not the required make-up water and amine were manually inputted. Then the specified CO₂ removal efficiency of 85% was achieved by adjusting (with the aid of an ADJUST block) the lean amine flow rate. The Modified HYSYM Inside-Out solver with adaptive damping was used to calculate the columns because better convergence is achieved.

In the case of vapour recompression combined with split-stream, the semi-lean stream column feed stage was optimised such that the column stage that gave the lowest heat consumption was selected.

4.5 Comparison of the energy consumption of alternative configurations

The summary of the simulation results of the three configurations are presented in Table 2. Significant energy savings were calculated for vapour recompression and vapour recompression combined with split-stream with both the Kent-Eisenberg and Li-Mather models respectively. The vapour recompression simulations recorded the lowest energy consumption with both Kent-Eisenberg and Li-Mather. The vapour recompression process has the highest rich loading in both simulations with Kent-Eisenberg and Li-Mather models. The vapour recompression combined with split-stream has the lowest rich loading with Kent-Eisenberg model while it is the standard process in the case of Li-Mather.

5 Energy optimisation

In this section, the energy consumption is calculated under varying conditions to seek for the optimum conditions. All simulations were done with Kent-Eisenberg equilibrium model.

5.1 Equivalent heat consumption as a function of absorber packing height

The vapour recompression and vapour recompression combined with split-stream were optimised by varying different process units (equipment) parameters to achieve a better energy saving with the Kent-Eisenberg model.

Both configurations could not yield significant result by increasing the number of absorber stages more than 20. The vapour recompression process simulations diverge with 24 absorber stages and above. While simulations with vapour recompression combined with split-stream diverge with 23 absorber stages and above.

5.2 Equivalent heat consumption as a function of desorber packing height

Varying the number of desorber stages from 6-20, the vapour recompression optimum heat consumption of 3.18 MJ/kg CO₂ (1% < standard case) was achieved with 9 stages. While it was 3.21 MJ/kg CO₂ (about 2% < standard case) with 10 stages for the vapour recompression combined with split-stream configuration. Optimisation of the conventional desorber number of stages might be new as no literature was found to compare results with. It is necessary to make economic evaluation of increasing the number of desorber stages to confirm if it is worthwhile. The results are shown in Figure 8.

Table 2. Summary of simulation results for CO₂ absorption and desorption using Kent-Eisenberg and Li-Mather models

Process configuration	Equilibrium model	Rich loading	Reboiler heat	Compressor work	Equivalent heat	Energy savings	Relative energy savings
							[MJ/kg CO ₂]
Base case		0.4783	3.600		3.600	0	0
Vapour recompression	Kent-Eisenberg	0.4792	2.785	0.1105	3.227	0.373	10
Vapour recompression + split-stream		0.4778	2.859	0.1003	3.260	0.340	9
Base case		0.4758	3.516		3.516	0	0
Vapour recompression	Li-Mather	0.4774	2.767	0.1105	3.209	0.307	9
Vapour recompression + split-stream		0.4769	2.826	0.0997	3.225	0.291	8

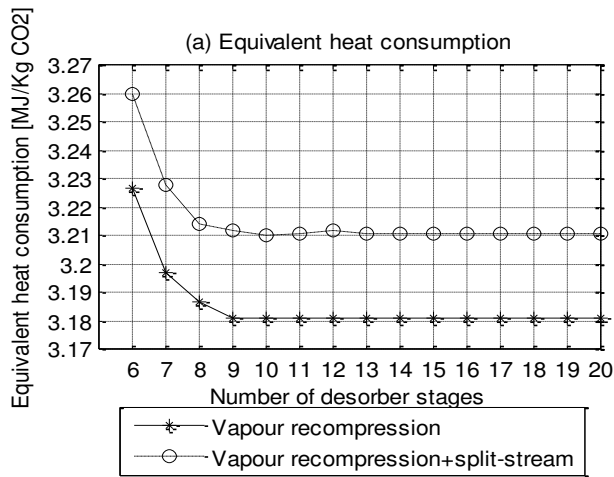


Figure 8. Equivalent heat consumption as a function of number of desorber stages

5.3 Equivalent heat consumption as a function of flash pressure (P_{flash})

Optimum energy consumption of 3.21 MJ/kg CO₂ (0.5%) was achieved at a flash pressure of 1.2 bar and 3.25 MJ/kg CO₂ (0.4%) at 1.1-1.2 bar with the vapour recompression and vapour recompression combined with split-stream respectively. (Kvam, 2013) achieved optimum flash pressures at 1.01-1.2 bar and 1.01 bar with the vapour recompression and vapour recompression combined with split-stream respectively. (Le Moullec and Kanniche, 2011) achieved optimum at around 1.25 bar for the vapour recompression process with 2.5 bar stripper pressure. (Karimi et al., 2011) stated about 1.12-1.17 bar as the optimum flash pressure. And it may be between 1.1 to 1.2 bar for the vapour recompression combined with split-stream configuration. Flash pressure optimisation results are given in Figure 9.

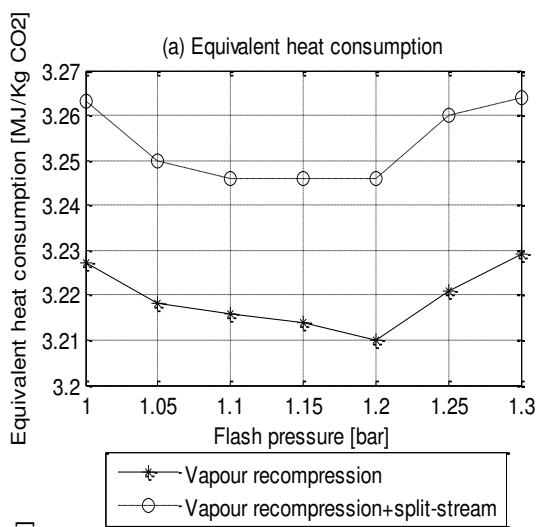


Figure 9. Equivalent heat consumption as a function of flash pressure.

5.4 Equivalent heat consumption as a function of minimum approach temperature (ΔT_{min})

According to (Øi, 2012), the suggested reasonable minimum approach temperatures (ΔT_{min}) in literatures are between 5 and 20°C. In this paper ΔT_{min} was varied from 10 to 3°C to reduce the energy consumption. The major objective here is to compare heat consumption values at 10 and 5°C. The results are displayed in Figure 10. The equivalent heat consumption decreased almost linearly from 10 to 3°C. 0.23 MJ/kg CO₂ (7%) and 0.23 MJ/kg CO₂ (7%) of heat consumption were saved in the case of vapour recompression and vapour recompression combined with split-stream configurations respectively. Karimi et al. (2011) calculated a reboiler heat reduction from 2.72 to 2.60 MJ/kg CO₂ (about 5%). But (Tobiesen, 2005) argued that reduction of ΔT_{min} will not result in reduction of the reboiler heat. However, in this work, the energy saving is significant.

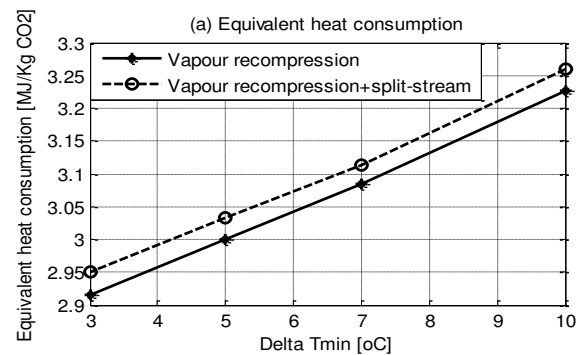


Figure 10. Equivalent heat consumption as a function of minimum approach temperature

5.5 Selection of optimum configuration and operation conditions

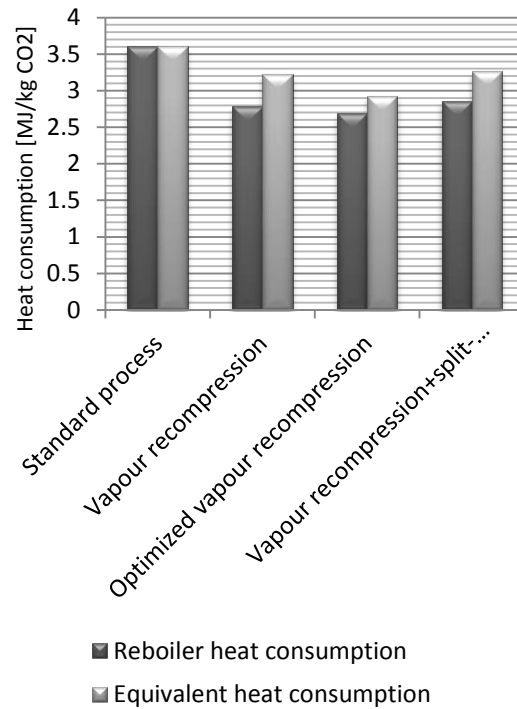
Based on the optimisation of the four process parameters in subsection 5.1-5.4 above, the vapour recompression achieved lower heat consumption in all cases; therefore it is a more reasonable option. **Table 3** presents the selected optimum and reasonable values from the four process parameters. ΔT_{min} of 5°C has been chosen as the most reasonable option because the heat exchange area required for 3°C is much larger than 5°C.

Table 3. Energy optimum specifications using Kent-Eisenberg model

Specification	Value	Reason
Number of absorber stages	20	No remarkable improvement after 20 stages
Number of desorber stages	9	Optimum
Valve outlet pressure [bar]	1.2	Optimum
ΔT_{\min} [°C]	5	Lowest energy (Øi, 2012)

5.6 Comparison of optimum configuration with the three standard process configurations

Table 4 and Figure 11 summarize the results of this study. The optimised vapour recompression process achieved the highest energy savings. This is 19% and 9% of the standard process and the ordinary vapour recompression equivalent heat consumptions respectively. Considering only reboiler heat consumption, it is 25% energy savings over the base case process.

**Figure 11.** Comparison of optimum configuration with other three standard process configurations**Table 4.** Comparison of optimum configuration with the three standard process configurations

Process configuration	Rich loading	Reboiler heat	Compressor work	Equivalent heat	Energy savings	Relative energy savings
Base case	0.4783	3.600	-	3.600	0	0
Vapour recompression	0.4792	2.785	0.1105	3.227	0.373	10
Energy optimised vapour recompression	0.4792	2.684	0.0609	2.927	0.673	19
Vapour recompression+split-stream	0.4778	2.859	0.1003	3.260	0.340	9

(Karimi et al., 2011) calculations with Unisim Design and ProTreat show about 28% energy savings with the vapour recompression processing using ΔT_{\min} of 5°C over the base case with ΔT_{\min} of 10°C. Therefore, optimizing the vapour recompression process may significantly result in energy requirements of an amine based CO₂ capture plant.

5.7 Accuracy

The calculated results change slightly with reference to initial values when simulating with the same specifications. In the case of the CO₂ removal grade, the accuracy is usually $\pm 0.05\%$ (absolute). And in the case of equivalent heat consumption, it is just a few per cent (%), usually within ± 0.006 MJ/kg CO₂ (absolute). The uncertainty with equilibrium is most likely higher.

6 Conclusion

Simulation and optimisation of an amine-based CO₂ removal process from an exhaust gas from natural gas power plant have been performed in the quest for an energy optimum process. The process configurations investigated are the standard process, vapour recompression process and the vapour recompression combined with split-stream process.

This study shows that it is possible to reduce energy consumption with both the vapour recompression and the vapour recompression combined with split-stream. The vapour recompression configuration shows the lowest energy consumption from simulations. Optimisation of parameters like number of desorber stages, flash pressure and minimum approach temperature is important to achieve a better energy saving.

The vapour recompression process with 20 absorber stages, 9 desorber stages, 1.2 bar flashing pressure and ΔT_{\min} of 5°C is found to be the optimum alternative. It achieves 19% energy saving compared to the standard process. The authors are currently investigating for the cost optimum process when considering investment.

References

- Aroonwilas, A., Veawab, A. (2006). *Cost structure and performance of CO₂ capture unit using split-stream cycle*. Paper presented at the 8th International Conference on Greenhouse Gas Control Technologies (GHGT-8), Trondheim, Norway.
- Cousins, A., Wardhaugh, L. T., & Feron, P. H. M. (2011). Preliminary analysis of process flow sheet modifications for energy efficient CO₂ capture from flue gases using chemical absorption. *Chemical Engineering Research and Design*, 89(8), 1237-1251. doi: <http://dx.doi.org/10.1016/j.cherd.2011.02.008>
- Cousins, A., Wardhaugh, L. T., & Feron, P. H. M. (2011). A survey of process flow sheet modifications for energy efficient CO₂ capture from flue gases using chemical absorption. *International Journal of Greenhouse Gas Control*, 5(4), 605-619. doi: <http://dx.doi.org/10.1016/j.ijggc.2011.01.002>
- Fernandez, E. S., Bergsma, E.J., de Miguel Mercader, F., Goetheer, E.L.V., Vlucht, T.J.H. (2012). Optimisation of lean vapour compression LVC as an OPTION for post-combustion CO₂ capture: Net present value maximisation. *International Journal of Greenhouse Gas Control*, 11, 114-121. doi: <http://dx.doi.org/10.1016/j.ijggc.2012.09.007>
- Jordal, K., Ystad, P.A.M., Anantharaman, R., Chikukwa, A., Bolland, O. (2012). Design-point and part-load considerations for natural gas combined cycle plants with post combustion capture. *International Journal of Greenhouse Gas Control*, 11, 271-282.
- Karimi, M., Hillestad, M., & Svendsen, H. F. (2011). Capital costs and energy considerations of different alternative stripper configurations for post combustion CO₂ capture. *Chemical Engineering Research and Design*, 89(8), 1229-1236. doi: <http://dx.doi.org/10.1016/j.cherd.2011.03.005>
- Kent, R. L., Eisenberg, B. (1976). Better data for amine treating. *Hydrocarbon processing*, 55(No.2), 87-90.
- Kohl, A., Nielsen, R. (1997). *Gas Purification* (5th ed. ed.). Houston, Texas: Gulf Publications.
- Kothandaraman, A. (2010). *Capture by chemical absorption: a solvent comparison study*. (PhD PhD Thesis), Massachusetts Institute of Technology, Boston.
- Kvam, S. H. P. (2013). *Vapour recompression in absorption and desorption process for CO₂ capture*. (Master of Science), Telemark University College, Porsgrunn, Norway.
- Le Moulllec, Y., & Kanniche, M. (2011). Screening of flowsheet modifications for an efficient monoethanolamine (MEA) based post-combustion CO₂ capture. *International Journal of Greenhouse Gas Control*, 5(4), 727-740. doi: <http://dx.doi.org/10.1016/j.ijggc.2011.03.004>
- Li, Y.-G., and Mather, A. (1996). Correlation and prediction of the solubility of CO₂ and H₂S in aqueous solutions of triethanolamine. *Ind. Eng. Chem. Res.*, 35 (12), 4804-4809.
- Øi, L. E. (2007). *Aspen HYSYS simulation of CO₂ removal by amine absorption a gas based power plant*. Paper presented at the The 48th Scandinavian Conference on Simulation and Modelling (SIMS2007) Göteborg, Sweden.
- Øi, L. E. (2012). *Removal of CO₂ from exhaust gas*. (PhD Thesis), Telemark University College, Porsgrunn. (TUC 3: 2012)
- Øi, L. E., Bråthen, T., Berg, C., Brekne, S. K., Flatin, M., Johnsen, R., Thomassen, E. (2014). Optimization of Configurations for Amine based CO₂ Absorption Using Aspen HYSYS. *Energy Procedia*, 51(0), 224-233. doi: <http://dx.doi.org/10.1016/j.egypro.2014.07.026>
- Øi, L. E., & Kvam, S. H. P. (2014). Comparison of Energy Consumption for Different CO₂ Absorption Configurations Using Different Simulation Tools. *Energy Procedia*, 63(0), 1186-1195. doi: <http://dx.doi.org/10.1016/j.egypro.2014.11.128>
- Øi, L. E., Shchuchenko, V. (2011). *Simulation of energy reduction in CO₂ absorption using split-stream configurations*. Paper presented at the 4th International Scientific Conference on Energy and Climate Change, Athens.
- Øi, L. E., Vozniuk, I.O. (2010). Optimizing CO₂ absorption using split-stream configuration. *Process and Technologies for a Sustainable Energy, Ischia*.
- Oyekan, B. A., & Rochelle, G. T. (2007). Alternative stripper configurations for CO₂ capture by aqueous amines. *AIChE Journal*, 53(12), 3144-3154. doi: 10.1002/aic.11316
- Polasek, J. C., Bullin, J.A., Donnelly, S.T. (1982). *Alternative flow schemes to reduce capital and operation costs of amine sweetening units*. Paper presented at the Proceedings, AIChE Spring National Meeting, AIChE, New York.
- Rochelle, G. T. (2003). *Innovative Stripper Configurations to Reduce the Energy Cost of CO₂ Capture* Paper presented at the Second Annual Carbon Sequestration Conference, Alexandria, VA.
- Tobiesen, F. A., Svendsen, H.F, Hoff, K.A. (2005). Desorber energy consumption amine based absorption plant. *International Journal of Green Energy*, 2, 201-215.

Optimal Operation of the Peat Drying Process in Steam Tube Dryers

Leonid Kulakovskiy¹ Victor Rosen¹ Roshan Sharma² Carlos Pfeiffer² Bernt Lie²

¹NTUU “Kyiv Polytechnic Institute” Borshchagivska 115, P.O. Box 311, Kyiv, Ukraine
kulakowsky.leonid@yandex.ua

²Telemark University College, Kjølnes ring 56, P.O. Box 203, N-3901 Porsgrunn, Norway
{roshan.sharma, carlos.pfeiffer, bernt.lie}@hit.no

Abstract

Ukraine is an energy-dependent country and directing its efforts into economical use of its own energy resources. One relevant available energy source is peat briquette. During its production it is necessary not only to improve the quality of briquettes, but also to reduce the total expenses of energy required for their production, particularly in the drying process. For this, a mathematical model of peat drying is developed using the GMDH (Group Method of Data Handle). Next, with measured disturbances, optimal input variables for the drying process are found using mathematical optimization and ANN (artificial neural network). To avoid fast changing of the operational conditions while avoiding over drying or under drying of the peat, the operational conditions are classified into a number of classes. Finally, an iterative procedure for changing the input parameters from the past values to new values is introduced to ensure improved quality and energy efficiency.

Keywords: Group Method of Data Handling, peat drying, energy efficient process, regimes map, steam tube dryer

1 Introduction

A high increase in the price for Russian gas and further reducing of its consumption in the Ukrainian energy sector requires Ukraine to find other energy resources. One of the solutions is to use peat briquettes instead of gas because the price of 1 GJ net energy produced from peat briquette is less than half the price of that of gas.

Some of the advantages of using peat briquettes over other fuels in Ukraine are (Hnyeushev, 2008):

1. high calorific value, 16-18 MJ/kg,
2. environmentally safe fuel during combustion,
3. considerable reserves of peat in Ukraine,
4. after peat extraction, the bogs can be re-cultivated and transferred to the domestic uses.

One of the most important processes of peat briquettes production that determines its quality and is the most

energy-intensive on the peat plant, is the process of drying peat. There is a lack of information and mathematical description associated with drying peat in steam tube dryers. Precise description of factors such as adjustment of fuel and air ratio during combustion and many significant perturbations that affect the process, are not readily available. This will lead to the production of poor quality peat, increases the cost of drying the peat and may give rise to emergency situations during the peat production.

For the development of methods for improving the operation of the drying process in the steam tube dryers, several investigations as described in (Korol' and Lishtvan, 2008) have been performed. Mathematical description, simulation and optimization of the production of peat briquettes and the drying process can be found in (Bohatov, 1976; Naumovich, 1984; Gatih and Genshaft, 1980). Research into the modelling and control of a rotary dryer have been carried out by (Yliniemi, 1999; Forsman and Slätteke, 2002; Slätteke and Åström, 2005).

A mathematical model of a physical system can be used for identification of the system, forecasting, and for optimization and control. For complex systems, various methods can be used for system identification and they have been studied actively in recent years. Among them the identification method known as Group Method of Data Handling (GMDH) — developed by A.I. Ivakhnenko, is well known (Ivakhnenko, 1970). The conceptual basis for the structure of the GMDH is based on heuristic self-organization, and the resulting polynomial equation obtained from its identification procedures is dependent on the Kolmogorov-Gabor polynomial. The development of the algorithm of GMDH that provide robust linear and nonlinear polynomial regression models can be found in (Aksyonova and Tetko, 2003). An inductive method that permits the choice of a model with least error and least bias and self-organizing data mining has been studied by (Ivakhnenko and Rogov, 2005).

In Section 2, the peat drying process, its basic conditions and disadvantages in the Ukrainian briquette plants

is described. Basic physical and mechanical properties of peat, the operational conditions of the drying process that affect the quality of dry peat, and the indicators for energy consumption are described. The feasibility of using the Group Method of Data Handling for creating a mathematical model of drying peat and the use of neural networks for determining the optimal input variables of the peat drying is shown with a brief description of the basic of GMDH. In section 3, the development of a mathematical model of the peat drying process by using the experimental data obtained from the industrial plant is discussed. The implementation of the model and the selection of structure and parameters of the neural network that allows to find the best energy saving parameters of the drying process is described. This forms the main feature of classifying and recognizing the industrial situations that is described in section 4. In section 5 the procedure of finding the optimal operational value for varying measurements is discussed. In section 6 and 7 discussions and conclusions of the approaches used for optimal operation of the drying process are given, respectively.

2 System description

Optimum drying regimes provide the most effective operations of dryers that satisfy modern requirements: quality of produced products, the minimum cost price (thermal and electrical energy consumption) and fire safety. The process of peat drying should be carried out with the aim of reducing costs for heat and electricity. The cost of electricity consist of the cost for electricity consumption by the electric drive of drum dryers, the electric drive of blowers (which determines the amount of air that passes through the dryer), and the electric drive of bootable units of dryer (auger and boot sleeves). Thermal energy is consumed as a heat carrier (saturated vapor) to heat the peat inside the dryer. As for the quality of peat, characteristics such as bulk density of peat and its temperature should be considered.

The main purpose of drying the peat is to produce dried peat with necessary moisture regardless of the fluctuations in the moisture content of the peat that enters into the dryer. According to various investigations the quality of peat depends on the duration and conditions of drying, temperature, primary moisture variation, average moisture content and the maximum particle size of the peat (Kulakovskiy and Rosen, 2013a).

A functional block diagram describing the process of drying the peat in the steam tube dryer is shown in Figure 1.

Variables Y_1, Y_2, \dots, Y_8 are the outputs of the system which should be optimized and controlled. The input variables that are manipulated to obtain the desired outputs are denoted by X_1, X_2, \dots, X_4 . The disturbances that act on the system are represented by F_1, F_2, \dots, F_8 . The description of the inputs, outputs and the disturbances are presented

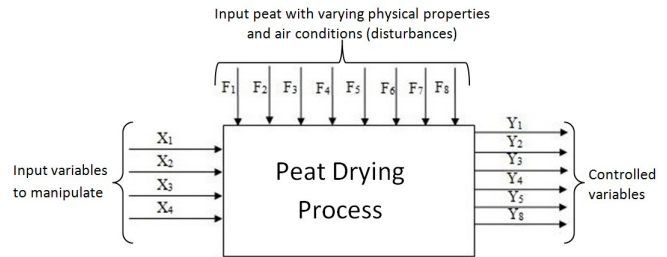


Figure 1. Functional description of peat drying process.

in Table 1. When the values of F_1, F_2, \dots, F_8 change, the outputs variables Y_1, Y_2, \dots, Y_8 will also change. To adjust the outputs to the desired values (quality and energy consumption), optimal values of inputs X_1, X_2, \dots, X_4 should be calculated and used.

Table 1. Description of variables and parameters in the peat drying process.

Var.	Description	Unit
X_1	auger rotational speed	<i>rev/min</i>
X_2	drum rotation speed	<i>rev/min</i>
X_3	steam temperature	$^{\circ}\text{C}$
X_4	fan flow rate	m^3/h
F_1	peat moisture	%
F_2	peat bulk density	kg/m^3
F_3	peat ash content	%
F_4	peat temperature	$^{\circ}\text{C}$
F_5	air temperature	$^{\circ}\text{C}$
F_6	peat flowability	$^{\circ}$
F_7	peat fractional composition	<i>mm</i>
F_8	peat moisture variation	%
Y_1	dried peat moisture content	%
Y_2	dried peat moisture variation	%
Y_3	dried peat temperature	$^{\circ}\text{C}$
Y_4	electrical energy consumption	<i>kWt</i>
Y_5	drying agent exit temperature	$^{\circ}\text{C}$
Y_8	thermal energy consumption	$\text{kJ}\cdot\text{h}\cdot 10^3$

Operation of the peat drying process with steam tube dryer is carried out according to a regimes map. Regimes map is a diagram of input variables and certain disturbances according for which the operator must set necessary regime of drying. A feature of the regimes map is that it helps to achieve the necessary moisture content and temperature of the dried peat in the drying process using input variables whose values depend on the characteristics of peat arriving at the plant. However, the operational regimes are not necessarily energy efficient, because the expediency of the adjustment of the drying process for a certain operational regime is not substantiated according to the influences due to disturbances in which the energy consumption for the drying would otherwise have been minimal (Hnyeushev, 2008). When using the regimes, there are often situations when briquettes are produced

with degraded quality. This is mainly due to the fact that the peat drying process in plants is continuous and a piece of peat remains in the drum dryer for about 15 minutes (from the moment it enters into the drum until the moment it is leaves to the conveyor that takes away the dried peat to the press). In every 25-40 minutes (depending on the workload of trolleys, screw speed, the time required to prepare peat at preparatory department etc.) a new trolley with peat to be dried enters into the dryer. The physical properties of these new peat can differ significantly from the peat in the previous trolleys. It is too complicated to determine the exact moment when the peat from the new trolley enters into the dryer: the time of incoming peat with different properties can only be determined approximately. In addition, when a new trolley with peat having different physical properties is charged into the dryer, the peat from previous trolley content may still be inside the dryer. If the input variables are quickly modified based on the regime maps for the new incoming peat trolley, the peat from the previous trolley (which is still inside the dryer) may be over/under dried and the quality of the peat may be poor (defective products).

In order to develop optimal operating regimes it is necessary to:

1. Collect information of peat drying regimes used in a real plant.
2. Develop a mathematical model of the drying process.
3. Optimize the values of the input variables for energy efficient performance and for necessary quality of dried peat.
4. Develop a procedure for implementing the optimal operational conditions for the peat drying process.

Getting accurate information for the construction of a mathematical model of peat drying is possible after planning and conducting the experiments of a peat drying process in a real dryer. During the investigation of a peat drying process with steam tube dryer, it was found that there are some features that can rise the playback error of some output functions. So at first, it is necessary to resolve the problem of features selection. For every model it is necessary to include input variables and parameters that have influence on the output variables. This allows to filter separate features and reduce the overall error of the model (because each feature has a measurement error and we find a model of optimal complexity in which the error is minimal). This task can easily be solved by Group Method of Data Handling. GMDH possesses an advantage when there is no (or almost no) *a priori* information about the structure and distribution of model parameters and when experimental data is extremely small (even when the number of the model parameters are smaller than the number of observations). (Ivakhnenko and Yurachkovskij).

The idea is to construct a model of optimal complexity based only on data, i.e. by knowing only simple input-output relations of the system; GMDH will construct a self-organizing model (a higher-order polynomial of the

input variables).

The GMDH approach for the construction of a mathematical model can be useful because (Ivakhnenko, 1970):

1. The optimal complexity of the model structure that is adequate to the level of noise in the data can be found. For real problems, with noisy or insufficient data, a simplified optimal model is more accurate.
2. It guarantees that the most accurate or unbiased models will be found, i.e. the method does not miss the best solution during exhaustive search (in the given class of functions).
3. Any non-linear functions or features, which can influence to the output variable can be used.
4. The method gets information directly from data and minimizes the influence of *a priori* assumptions about the model outputs.

Among the most well-known parametric algorithms are the combinatorial (COMBI) algorithm and the multiple iterative algorithm (MIA). The idea of all GMDH-type algorithms is to gradually generate complicated models and selecting a set of models that show a higher forecasting accuracy using data outside of the training set. These data outside of the training set are usually denoted a validation or testing set, and the top-ranked model is claimed to be optimally-complex.

The main idea of the COMBI algorithm is not miss any of the possible models (Ivakhnenko, 1971). Therefore, at each connection level, the COMBI algorithm:

1. covers all models;
2. conducts the selection of the best combinations of the variables.

The basic ideas of MIA is (Cheberkus and Ivakhnenko, 1980) to:

1. reduce the number of models considered in each row of the selection;
2. reduce the number of rows, and thus to accelerate the access to the best level of connection.

Therefore, for each row (in the MIA algorithm):

1. a fixed number of best transformation of a signals (each transformation of a signal is considered as a signal) is selected;
2. every combination of best variables creates a new signal in the transition to the next level.

For carrying out the identification it is possible to use an intelligent technology based on artificial immune systems (de Castro and Zuben, 1999), which allows to select the parameters of the mathematical model in accordance with the real signals. This approach is of particular relevance if the model has a large number of parameters.

According to Table 1, there are 15 design parameters in the model of the peat drying process and it is necessary to calculate 4 values of optimal input variables. For this reason development and installation of on-line optimization codes in programmable logic controllers (PLCs) for determining the optimal values of the input variables of the peat drying process will be more difficult than the hardware im-

plementation of neural networks in neurochips and neurosignal processors. Therefore, it is more appropriate to create a selection (data) for optimizing parameters and variables of the model under certain industrial operational situations for training, testing and construction of a neural network. For capturing the dynamics of the drying peat process, the most expedient action is to use a multilayer perceptron as a high-performance model after learning. A model with good extrapolation possibilities that allows to build functions of any complexity and is sensitive to an increase in the number of input actions, is important for building a multivariate model (Yurachkovskij and Zaentsev, 1987). A multilayer perceptron model that is trained by experimental data allows to realize "input-output" characteristics of the system. This means that when new values of perturbations appear in the drying process, the perceptron model allows to calculate the optimal control actions.

There are cases when input variables are found to change by a large value. For example, let us consider that the temperature of the steam should be increased from 100°C to 130°C according to optimal value of X_3 . This is done by burning an increased amount of peat for producing steam in the boilers. A significant amount of time is needed for changing the temperature (moving to the necessary operating conditions). It will be quite difficult to control the required amount of the peat needed for combustion in the boiler and the temperature of the drying agent (steam). To overcome major inconvenience in the operation of the drying process caused primarily by the inertia of the process, it is advisable to carry out a classification and recognition of industrial situations. It means that for a certain set of values of the disturbances acting on the system, a range of values of control actions or input variables for which the energy consumption is lowest and the quality of dried peat is satisfactory, is selected. This facilitates the task of adjusting the drying process, reduces the possibility of a quick change of the values of input variables in the process of drying and increases the intervals where the peat gets dried with the required quality.

3 Modeling of peat dryer

In order to develop mathematical dependencies of the changes in the target or output variables Y_j due to changes in the input variables X_i , active experiments were conducted. For conducting experiments, it is first necessary to plan the experiment.

For planning the experiment, regime maps of steam tube dryers are used. The experiments were carried out in the peat plant "Soyne" in Ukraine, where the inputs variables were changed in a well planned manner within the allowed range of the operation conditions. An increase in the moisture content of the incoming peat necessitates an increased temperature of the steam in the dryer or a reduced speed of the feeder (auger) (drying speed) or, in rare cases, redu-

cing the fan flow rate. The input variable X_3 interacts with X_2 . If the feeding rate of the peat in the dryer is increased, then with a constant temperature of the steam, the time that the peat stays in the dryer should be increased. However, with a constant drying time, the temperature of the heat carrier should be increased (Kulakovskiy and Rosen, 2013b).

The input variable X_4 in the peat plant is practically not regulated (although it is possible by using the electric drive present in the plant). The range within which employees can (in accordance with "Exploitation instructions") change the fan flow rate varies from 1370 to 1400 *rev/min*. This is due to the fact that in the existing regime maps this variable is ignored.

A plan of the active industrial experiments is shown in Table 2, where (-1) indicates the minimum, (+1) the maximum, and (0) indicates the average value of the input variables for certain values of the disturbances acting on the process.

Table 2. Plan of active experiments of drying in steam tube peat dryer.

Experiment	Input variables		
	X_1	X_2	X_3
1	0	0	0
2	+1	0	+1
3	+1	-1	0
4	-1	0	-1
5	-1	+1	0
6	0	+1	-1
7	0	-1	+1

Two series of industrial experiments using the plan of active experiments of drying with steam tube peat dryer (Table 2) were conducted. Results of the experiments are shown in Table 3.

It is necessary to relate the outputs Y_j to the inputs X_i . One possible way to model this relationship is to postulate an empirical model of type

$$Y_j^m = \sum_{k=1}^N \beta_{jk} \phi_k(X_1, \dots, X_4; F_1, \dots, F_8), \quad (1)$$

where β_{jk} is an unknown parameter (constant) while $\phi_k(\cdot)$ is a chosen set of basis functions. In the simplest case, $N=12$ and $k \in \{1, \dots, 4\}$: $\phi_k = X_k$, or $\phi_k = F_{k-4}$ —in other words, a linear model in the manipulatable inputs X_j and disturbances F_j .

The error of the model on the training set is the sum of the errors of the individual training vectors, root-mean-square error (RMS).

$$E = \sum_{j=0}^m (Y_j - d_j)^2, \quad (2)$$

where Y_j – output variable of learning vector; d_j – the corresponding target output value system.

Table 3. Experimental data set.

No.	F_1 [%]	F_2 [kg/m ³]	F_3 [%]	F_4 [°C]	F_5 [°C]	F_6 [°]	F_7 [mm]	F_8 [%]	X_1 [$\frac{rev}{min}$]	X_2 [$\frac{rev}{min}$]	X_3 [°C]	X_4 [m ³ /h]	Y_1 [%]	Y_2 [%]	Y_3 [°C]	Y_4 [kWt]	Y_5 [°C]	Y_8 [kJ]
1	43.6	417	23	24.7	28	41.1	1.49	3.5	3.81	9.63	27.6	128	14.7	5	72.6	67.3	96.7	15685
2	42.6	385	22	26.6	28.5	41.4	1.58	5.82	3.76	9.58	27.58	129	17.9	7.2	70.4	66.61	102.8	16600
3	41.9	377	16.9	24.7	27	42.9	1.58	4.39	3.72	9.5	27.62	123	15.8	5.1	59.4	66.82	97.2	20500
4	41.4	341	17.1	27.6	27	42	1.74	3.49	3.7	9.4	27.8	124	14.7	8.5	57.2	67.17	94.8	19920
5	40.9	305	16.8	28	26	43.8	1.66	2.53	3.71	9.32	27.8	119	14	4.2	55	66.68	93.7	22010
6	41.2	333	16.1	26.1	26	43.7	1.54	2.66	3.73	9.33	27.84	126	14.6	3.1	58.9	66.93	96	20800
7	45.4	358	15.5	26.6	26	43.9	1.61	1.95	3.77	9.3	27.84	112	16.1	4.6	55	66.83	88.5	22600
8	44.9	367	15.3	24.7	25	43.5	1.45	2.69	3.77	9.1	28.16	118	17.6	6.1	57.2	68.89	91.5	21435
9	45.2	369	15.7	26.1	25	43.3	1.44	2.52	3.7	10.1	28.02	117	16.4	4.8	60.5	73.82	91	19835
10	45	399	15.9	27.1	25.5	41.4	1.52	2.12	4.1	10	28	124	16.3	4.9	63.8	75.03	96.5	20390
11	45.1	407	16	28	26	40.5	1.6	1.67	4.03	10.1	27.9	128	17.1	5.1	63.3	73.27	100	28015
12	42.9	425	15.9	26.6	26	39	1.54	2.09	3.2	8.7	27.94	130	16.6	2.9	61.6	65.37	103.1	16930
13	47.1	376	18	28	25.5	43.4	1.55	4.19	4.3	10	27.82	132	19.8	6.2	63.8	71.29	102.5	15585
14	43.5	372	17.1	26.4	26.2	42.3	1.56	3.01	3.8	9.4	27.53	119	17.6	6.1	60.1	68.45	98.7	15105

Table 4. Values of Root-mean-square (RMS) error of objective functions.

learning algorithm	Objective function					
	Y_1	Y_2	Y_3	Y_4	Y_5	Y_8
COMBI	0.053298	0.057419	0.062413	0.054312	0.038591	0.065312
MIA	0.013399	0.019476	0.044706	0.043124	0.036048	0.048965

The value of the root-mean square error of the peat drying process for outputs using COMBI and MIA algorithms are shown in Table 4. As an example, the models for calculating the output Y_8 (thermal energy consumption) created with MIA and COMBI algorithms are presented in Figure 2 and Figure 3 respectively.

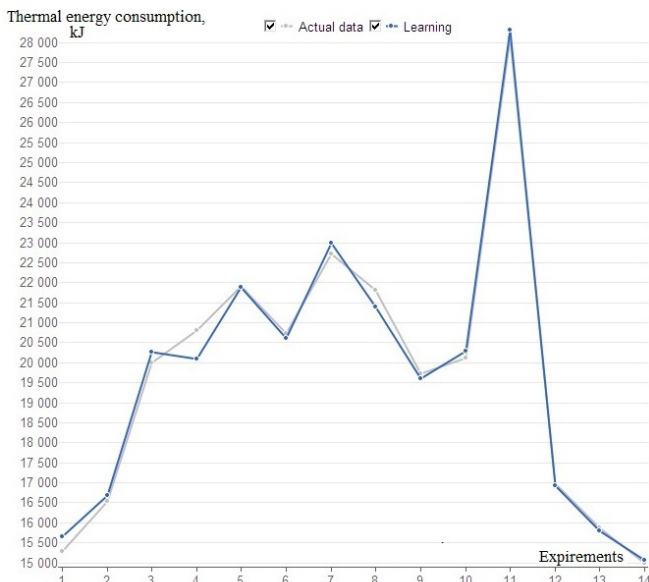


Figure 2. Graph of comparison of experimental data and model prediction of heat consumption (Y_8) using MIA GMDH algorithm.

From the plots of these figures and values of RMS error in Table 4 it can be concluded that the model con-

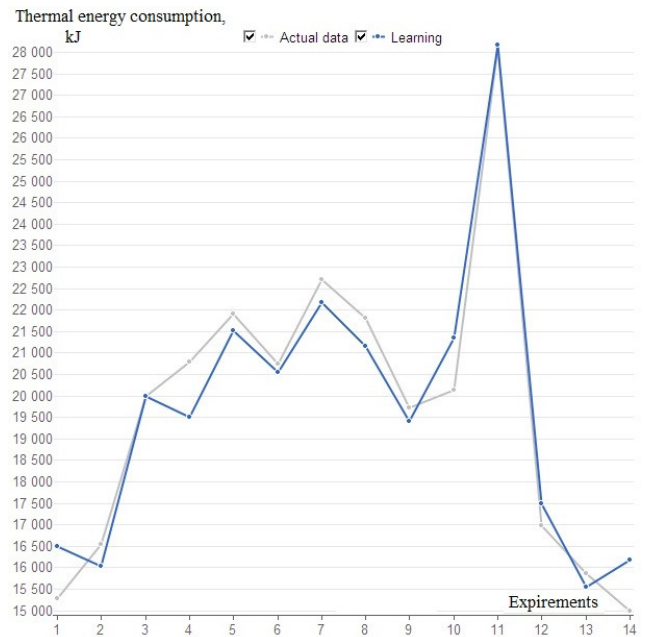


Figure 3. Graph of comparison of experimental data and model prediction of heat consumption (Y_8) using COMBI GMDH algorithm.

structed using GMDH with combinatorial algorithm has much higher RMS error than with MIA GMDH algorithm. The execution time of the COMBI algorithm is more than 3 times larger than that of the MIA algorithm because at each stage the best models that satisfy the necessary criteria are selected.

The main purpose of the work in this paper is to reduce the energy consumption for drying peat and to produce dried peat of required quality from the steam tube dryer. In other words, we consider two output functions to be minimized — consumption of heat and electricity. To solve the problem of the multi criteria which has two objective functions, the concessions method is applied (Gavrilov and Podinovskij, 1975). In order to minimize the energy consumption for the drying process, it is necessary to determine the amount of heat (in kJ) required for drying the peat at various physical properties. For this the required pressure and temperature of the saturated vapour (source of heat) should be determined. The minimum required values of the heat energy consumption for a series of experiments can be denoted by the symbol Z_k .

According to the factor analysis conducted in (Altuhov and Kulakovskiy, 2014) and the technical documentation of the peat briquette plant "Soyne":

1. the moisture content of dried peat (Y_1) should not exceed 20%,
2. differences in moisture content of the dried peat samples (Y_2) less than 6%,
3. temperature of the drying agent at the exit of the dryer (Y_5) should not exceed 120°C,
4. steam temperature (X_3) should not exceed 150°C,
5. temperature of dried peat (Y_3) should be in the range 30°C to 90°C,
6. speed of feeder/auger (X_1) — between 3 and 7 rev/min,
7. the frequency of rotation of the drum dryers (X_2) should be between 5 and 12 rev/min,
8. the air flow through the dryer (X_4) should not be more than $40 \cdot 10^3 \text{ m}^3/\text{h}$.

So, the conditions for minimizing the energy consumption of drying process in the peat steam dryer to obtain required qualitative characteristics of the dried peat and to maintain the safety of the briquettes production, the following objective function with constraints is considered. The models were obtained by using the GMDH method:

minimize

$$Y_4 = -315.781 - 0,2288F_1 + 0.0193F_2 + 1.004F_7 - 0,0624F_8 + 0.4966X_1 + 0,7834X_2 + 11.4723X_4 \quad (3)$$

subject to

$$0.6146F_1 - 0.4517F_3 + 0.6422F_4 + 0.4832F_5 - 0.2333F_6 - 10.26F_7 + 1.186F_8 + 1.57X_1 - 1.693X_2 \leq 20 \quad (4)$$

$$64,21 + 1.571F_1 - 0.1532F_2 - 2.137F_4 - 3.06F_7 + 17.09F_8 + 1,084F_{12} + 1.124X_1 + 1.679X_2 + 2.356X_4 \leq 64 \quad (5)$$

$$30 \leq 608,2 + 1.235F_1 - 0.1552F_2 + 2.823F_5 - 4.354F_7 - 59.09F_8 + 7.84X_1 - 13.29X_4 \leq 80 \quad (6)$$

$$-1,148F_1 - 0.1294F_2 + 1.961F_4 - 1.502F_5 + 1.074F_6 + 1.78F_8 - 1.782X_2 + 0.4177X_3 \leq 120 \quad (7)$$

$$-364.4F_4 - 1022F_6 + 4107X_1 - 105X_3 + 2417X_4 = Z_k \quad (8)$$

$$3 \leq X_1 \leq 7 \quad (9)$$

$$5 \leq X_2 \leq 12 \quad (10)$$

$$X_3 \leq 150 \quad (11)$$

$$X_4 \leq 40 \quad (12)$$

It is not always advisable to adjust the plant operation for maximum productivity because the production volumes for a certain period is dictated by market conditions, in particular the demand for products. The most effective way of regulating the productivity of a dryer is by regulating the amount of peat that fills the tube (speed of auger rotation), i.e. input variable X_1 . In addition, it is clear that the lowest electrical consumption will be during the minimum loading of the dryer and consequently during its lowest productivity. Therefore, in order to simplify further calculations and for considering the model's requirements, the possible values of the productivity must be divided into some levels of the auger rotational speed. For the "Soyne" peat plant where industrial experiments were carried out, it was divided into 3 levels — $X_{1min}=2.5 \text{ rev/min}$, $X_{1average}=3.5 \text{ rev/min}$, $X_{1max}=4.5 \text{ rev/min}$.

Let the optimal input values be denoted by X_k^* , where $k \in \{1,2,3,4\}$ denotes the k -th variables which corresponds to the optimal output value Y_k^* . With the known values of F_k it is possible to find inputs X_k^* , where now $k \in \{2,3,4\}$, such that the output Y_4 is minimized. For every new values of the disturbances F_1, \dots, F_8 , the optimization code must be re-run (e.g. using the simplex method) and new optimal value X_2^*, X_3^*, X_4^* should be calculated.

Because of a limited number of experiments, there are few data for getting good prediction models for calculating X_k^* . So synthetic data are created and used. Some of the disturbances F_k are correlated with each other. It is possible to find new values of the correlated disturbances using the Monte Carlo method (Vojtisek, 1999). From correlation analysis, it was found that parameter F_2 correlates with F_6 , F_3 with F_5 , F_3 with F_8 and F_7 with F_4 with a correlation coefficient of more than 50%. Some random numbers were used to compute the independent disturbances F_1, F_2, F_3, F_7 while the remaining disturbances were computed by using the correlation models and the Monte Carlo method.

By using an algorithm for searching the random values for the two factors, 86 observations were generated. In addition to 14 data series obtained from the experiments, a dataset of 100 inputs and 100 outputs for building a neural network was obtained.

The model that relates F_1, \dots, F_8 to optimal values of input variables X_k^* where $k \in \{2,3,4\}$ could have a

structure as,

$$X_j^{m*} = \sum_{k=1}^N \gamma_{jk} \varphi_k(F_1, \dots, F_8), \quad (13)$$

where γ_{jk} — is an unknown parameter (constant) and φ_k is the basis function, e.g. artificial neural network (ANN). For ANN, it is necessary to select and formulate a learning procedure of the neural networks. Input vectors for the neural network are the values of the eight disturbances $F_{1i}, F_{2i}, F_{3i}, F_{4i}, F_{5i}, F_{6i}, F_{7i}, F_{8i}$, and outputs of the ANN are the optimal values of the input variables $X_{2i}^*, X_{3i}^*, X_{4i}^*$, where i — denotes the number of samples (experiment and synthetic data).

The required number of hidden neurons and the activation function of hidden and output neurons were optimized by using automated strategies for creating neural network model in the Statistica Neural Network (Borovikov, 2008) package.

Using ANN, the three best models with the lowest Root mean square (RMS) error of the input variables were created (Table 5). According to Table 5, the network MLP 8-4-3 has the lowest training and test errors compared to other two neural networks. MLP 8-8-3 has the best training performance and MLP 8-15-3 has the best test performance and the smallest training and test errors.

Since the network MLP 8-15-3 has negligible amount of residuals and a good results on training performance this network is chosen.

4 Classification and recognition of industrial regimes

Using the experimental data, extended with synthetic data, we use a classification algorithm and classify the data into a number N_r of operational regimes. The production of dried peat is split into different classes with respect to the consumption of electrical energy in the process of drying peat under certain disturbances. A total of four classes are formed. Each class is formed by assigning a maximum, minimum and an average value of Y_4^* to the class. For each class there is a given range of the values of the input variables X_2^*, X_3^*, X_4^* , when X_k^* — is fixed to a known value as presented in Table 6.

To solve the problem of classifying the operational regimes, the training samples ($F_{1i}, \dots, F_{8i}, X_{2i}^*, X_{3i}^*, X_{4i}^*, Y_{4i}$) for $i=1, 2, \dots, N$ are needed to calculate unknown function $f(F_1, \dots, F_8, X_2, \dots, X_4)$, if $f(F_{1i}, \dots, F_{8i}, X_{2i}^*, X_{3i}^*, X_{4i}^*) = Y_{4i} \in K=1, 2, \dots, k$. The data set $F_{1i}, \dots, F_{8i}, X_{2i}^*, X_{3i}^*, X_{4i}^*$ is divided into $K=4$ classes, such that the k^{th} class represents the situation with input disturbances for which $f(F_{1i}, \dots, F_{8i}, X_{2i}^*, X_{3i}^*, X_{4i}^*) = K$. Then using discriminant analysis, new operating regimes can be recognized and assigned to the appropriate class. The aim of discriminant analysis is to develop methods for solving problems

Table 6. Classification of industrial regimes for $X_1=2.5$.

Value	X_2	X_3	X_4	Y_4	Class
minimum	7.42	119.00	26.1	43.54	1
maximum	9.3	139.00	26.65	49.67	1
average	8.19	126.00	26.4	47.08	1
minimum	8.31	113.67	26.6	50.05	2
maximum	9.5	127.67	26.83	52.94	2
average	8.89	119.21	26.73	51.77	2
minimum	8.97	104.67	26.82	53.1	3
maximum	9.8	133.26	26.94	54.17	3
average	9.16	118.3	26.89	53.73	3
minimum	9.10	95.55	27.02	55.01	4
maximum	9.70	118.43	27.60	60.30	4
average	9.43	107.65	27.26	57.64	4

of recognition (discrimination) of new objects by comparing the magnitude of their attributes with those clusters that are already created. Such a comparison allows us to classify new objects (situations) and include them in one group (class). The equation for canonical discriminant function can be written as (Mueller and Cozad, 1988):

$$S_{km} = u_0 + u_1 X_{2km} + u_2 X_{3km} + \dots + u_{11} F_{8km}, \quad (14)$$

where, S_{km} is the value (score) on the canonical discriminant function for case m in group k ; X_{ikm} is the value of input variable X_i for case m in group k , F_{ikm} is the value of disturbances F_i for case m in group k and u_i are coefficients which produce the desired characteristics of the function. Using the Mahalanobis distance (Jouan-Rimbaud and Maesschalck, 2000) for classification, a measure of the difference between two random vectors (X_i, X_{i+1}) with equal distributions is calculated as,

$$d(X_i, X_{i+1}) = \sqrt{(X_i - X_{i+1}) S^{-1} (X_i - X_{i+1})^T}, \quad (15)$$

with the probability that the sample belongs to data that is needed.

The Mahalanobis distance is the smallest distance for the class function to which the regimes belongs.

Since each sample is calculated using a *a priori* knowledge of the model variables, the probabilities are called posterior probabilities. Also, the accuracy of classification of industrial regimes is assessed using a classification matrix that indicates the percentage of classification accuracy of the regime to the required class.

As an example, the classification matrix that indicates the accuracy of classifying the production regime to the required class in the steam tube dryer for $X_1=2.5$ is shown in Table 7. P_1, P_2, P_3, P_4 are the amount of data set that belongs to class $K \in \{1, 2, 3, 4\}$. The results of the discriminant analysis of the peat drying regimes in the steam tube dryer showed that the data set which corresponds to a certain class, accurately belongs to a specific operational regime. The values of the coefficients for the classification

Table 5. The results of constructing the best neural networks for finding optimal parameters X_2, X_3, X_4 when $X_1=2.5$ using Statistica Neural Network package.

	Net. name	Training performance	Test performance	Validation performance	Training error	Test error	Validation error	Hidden activation	Output activation
1	MLP-8-4-3	0.6702	0.0337	0.82123	5.8844	1.85121	2.0113	Logistic	Logistic
2	MLP 8-8-3	0.9924	0.2589	0.84325	0.2769	6.38024	3.7267	Exponent.	Tanh
3	MLP 8-15-3	0.9899	0.3994	0.85092	0.1908	0.18109	4.0310	Logistic	Identity

Table 7. The classification matrix for indicating the accuracy of classifying the regimes for $X_1=2.5$.

Class	percent	$P_1=7$	$P_2=9$	$P_3=42$	$P_4=42$
1	100	7	0	0	0
1	100	0	9	0	0
3	97.619	0	0	41	1
4	100	0	0	0	42
Total	99	7	9	41	43

functions obtained from the results of discriminant analysis are presented in Table 8. The classification's functions

Table 8. Values of the coefficients u_i for $X_1=2.5$ obtained from the discriminant analysis.

Coeff.	$P_1=7$	$P_2=9$	$P_3=42$	$P_4=42$
u_0	-87196	-88996	-89339	-89273
u_1	3837.273	3676.194	3609.626	3607.79
u_2	349.0444	334.67	328.4349	328.0761
u_3	1640.103	1816.024	1877.824	1885.447
u_4	-682.357	-590.207	-573.424	-576.659
u_5	70.75283	66.05498	65.16128	65.2285
u_6	-347.997	-435.43	-440.25	-434.504
u_7	83.16267	130.5181	133.0582	128.128
u_8	530.0742	723.6801	733.9228	720.617
u_9	1302.379	1200.007	1187.654	1190.253
u_{10}	-3403.97	-5044.25	-5121.24	-5005.24
u_{11}	-664.441	-592.096	-578.54	-580.824

allow with sufficient accuracy to classify a sample to the required class.

5 Optimal operation of peat dryer

After classifying and recognizing industrial regimes it is necessary to develop an algorithm for operating the drying process of peat and to create a procedure for selecting input variables belonging to the relevant class. This is necessary to find a data set X_k^{**} which is the optimal value for a given value of disturbance F_k that would correspond to a certain class $\{X_k^{**}; F_k\} \in k_n$, where $n \in \{1, \dots, 4\}$. The algorithm for optimal operation of the peat drying

process in steam tube dryers given below:

- 1 Before starting the dryer, the physical properties of peat are defined ($N=1$, where N is the number of measurement perturbations; $F_{1i}, F_{2i}, F_{3i}, F_{4i}, F_{5i}, F_{6i}, F_{7i}, F_{8i}$, i — is the number of iteration of the algorithm for setting the optimal values of industrial regime parameters). Then the operator sets the required value of productivity by using the given value of input variable X_{1i} . Next, new optimal values $X_{2i}^*, X_{3i}^*, X_{4i}^*$ will be calculated using the neural network. These values must be set on the drying system. The nearest discriminant function which approximates the given industrial regime and therefore the class situation K_i^* , is defined by using discriminant analysis.
- 2 For the next measurements, $N=2$ ($F_{1i+1}, F_{2i+1}, F_{3i+1}, F_{4i+1}, F_{5i+1}, F_{6i+1}, F_{7i+1}, F_{8i+1}$), the optimum energy-efficient value of input variables ($X_{2i}^*, X_{3i}^*, X_{4i}^*$) are determined by using the neural network. After this, the class of production situation is determined using discriminant analysis. If the new class K_{i+1}^* lies in the same class as before (K_i^*), then no changes in the drying regime should be done. Thus the peat drying process is continues with values X_{2i}, X_{3i}, X_{4i} . If the new class K_{i+1} does not lie in the same class as before, then it is necessary to find new optimal values for the input variables. These values should belong to an appropriately defined new class of industrial regime.
- 3 At first, the value of X_{4i+1} must be set. This value should belong to a required class. Much of the electrical energy needed by the peat drying process is consumed by the fan. So we set the value of X_{4i+1} , which is closest to the area of the required class K_{i+1}^* ($X_{4,i+1} \in K_{i+1}^*$).
- 4 Change of value for X_{4i+1} leads to a change in the specific consumption of dry air ℓ . So it is necessary to determine a reasonable value of specific heat energy required to heat the drying agent due to change in the specific consumption of dry air ℓ . The specific consumption of heat for heating the drying agent (q_2 ,

kJ/kg of evaporated moisture) from the initial Θ_1 temperature to the final Θ_2 is written as,

$$q_2 = l \cdot c_{d.a} \cdot (\Theta_2 - \Theta_1), \quad (16)$$

where $c_{d.a}$ is a specific heat capacity of the drying agent; l is specific consumption of dry air required to evaporate 1 kg of water.

According to equation (16), it is necessary to define specific consumption of heat for heating the drying agent from the initial to the final temperature. Then according to equation (17) minimum acceptable values of specific consumption of heat for evaporation (q). Specific consumption of heat, which is removed from the peat (Hnyeushev, 2008), is written as

$$q = q_1 + q_2 + q_3 + q_4, \quad (17)$$

where q_1 is specific consumption of heat for evaporation of peat; q_3 is specific consumption of heat for heating the drying agent; q_4 is specific consumption of heat losses to the environment.

For calculating the minimum value of q for the peat drying process, it is necessary to know the variables $F_5, F_4, F_3, F_1, X_4, Y_1, Y_3, Y_5$. The values of disturbances are measured for each trolley. Variable X_4 has value corresponding to X_{4i+1} . The values of Y_1 is set to the maximal allowable; Y_5, Y_3 are minimally-acceptable levels of the requirements for the production of dried peat by the minimum value of q for the process of drying peat. The values must be such that they allow to obtain the dried peat with required quality and require fire safety of drying with a minimum value of q for the process of drying peat.

So for determining the minimum available value of specific consumption of heat per of water, which is removed from the peat (q_{\min}), the values $F_{1i+1}, F_{3i+1}, F_{4i+1}, F_{5i+1}, X_{4i+1}, Y_{1\max}=20\%, Y_{3\min}=30^\circ C, Y_{5\min}=90^\circ C$ are used. The minimum value of steam consumption (Y_8) for the industrial regime ($F_{1i+1}, F_{2i+1}, F_{3i+1}, F_{4i+1}, F_{5i+1}, F_{6i+1}, F_{7i+1}, F_{8i+1}, X_{2i}, X_{3i}, X_{4i+1}$) is found by the formula $Q=q \cdot W$ (where W is the dryer productivity on evaporated moisture kg/h).

- 5 From a mathematical model of heat consumption obtained using GMDH, the value of X_3 can be found as

$$X_3 = -3.47048F_4 - 9.73333F_6 + 39.11429X_1 + 23.01905X_4 - 0.00952Y_8 \quad (18)$$

So the optimal value of X_3 can be determined from the function of disturbances F_4, F_6, X_4, Y_8 that is determined previously ($F_{4i+1}, F_{6i+1}, X_{4i+1}, Y_8$).

- 6 The nearest discriminant function which approximates the given industrial regime ($F_{1i+1}, F_{2i+1}, F_{3i+1}, F_{4i+1}, F_{5i+1}, F_{6i+1}, F_{7i+1}, F_{8i+1}, X_{2i}, X_{3i+1}, X_{4i+1}$) is

set. Then a new class of the industrial regime K_{i+2} is defined. The class K_{i+2} must be compared with K_{i+1}^* . The value $X_{2i}, X_{3i+1}, X_{4i+1}$ must be set if class K_{i+2} corresponds to the class K_{i+1}^* . If not, the value of X_2 must be changed.

The value of input variable X_2 can be found by a mathematical relation $X_2=f(F_k; X_3^*, X_4^*)$ as,

$$X_2 = 18.0457 + 0.58F_3 + 0.1455F_4 + 0.1438F_8 - 0.1011X_3 \quad (19)$$

This function was found using algorithm MIA of GMDH. Thus, the new value X_{i+2} can be found.

- 7 Next, for industrial regime $\{F_{1i+1}, F_{2i+1}, F_{3i+1}, F_{4i+1}, F_{5i+1}, F_{6i+1}, F_{7i+1}, F_{8i+1}, X_{2i+1}, X_{3i+1}, X_{4i+1}\}$ the new meaning of class K_{i+2} is determined. If new class K_{i+2} meets the required class K_{i+1}^* , then the value of the input variables are the following: X_{2i+1}, X_{3i+1} and X_{4i+1} . If not, the algorithm of searching the energy-efficient values of input variables should be continued.
- 8 Then new value X_{4i+1} must be found. The change of value will be carried out with the relevant step from the average value of the necessary class (see Table 6). The change of the value of X_4 must not be very large. So it is possible to choose a small step, e.g. ± 0.001 .
- 9 Further, according to steps 4–8, the necessary values $X_{2i}^{**}, X_{3i}^{**}, X_{4i}^{**}$, that would meet the desired class K_{i+1}^* are determined.

This searching algorithm will smoothly change the operating condition of drying peat. The algorithm allows to obtain the dried peat in a certain acceptable range, it meets the fire safety of the drying process, and the process will take place in energy-saving drying regimes.

6 Discussion

The use of GMDH allows to solve the problem of features selection of the mathematical model. In particular, only 7 input parameters out of 12 that describe the peat drying process were included into the electrical energy consumption function. The linear model of drying peat was created using experimental data. In this model, an objective function for minimizing energy consumption of the drying process and fulfilling quality requirements of dried peat and fire safety was chosen. Then, optimization of the value of input variables was carried out. After that, the structure of neural networks were found. The training of neural networks was completed with the best quality of reproduction the data on training and testing samples of drying peat process models by optimal energy saving control variables. In this model the values of disturbance influences were considered as inputs, and optimal

energy efficient values of input variables were obtained as outputs. For neural networks, exponential basis function was chosen and for hidden layers, logistics functions were chosen. The classification of industrial regimes and discriminant analysis were conducted. Regimes were classified with respect to minimum electric energy consumption. So classification was carried out in situations with optimum energy saving regimes. Also for every class, the boundaries of adjustment of each input variables were determined. A discriminant function was found from the experimental and synthetic data. The discriminant function allowed to determine the required class situation of energy consumption with high accuracy. An iterative algorithm for searching the values of input variables with the least change was developed. Each of these values will belong to the appropriate class of industrial regime. Adjustment of the value of input variables according to the class of necessary regime allowed to reduce the impact of sudden changes in the conditions of the process of peat drying in the dryer. This reduces the probability of obtaining dried peat that does not satisfied the quality requirements. The procedure of finding and setting values of input variables allowed to move smoothly from one class of industrial regime to another. For further improvement it is necessary to develop a control system. Input variables of drying process in this system should be obtained by using the operation procedure of peat drying process. Thus, system may be represented as two procedures — procedure for adjustment of the heat energy consumption (consisting of airflow adjustment (X_4) and expenses of drying agent (X_3)), and procedure for adjustment of the drum rotational speed (X_2).

7 Conclusions

An optimal procedure for the operation of a drying peat process was developed. This procedure consist of defining the class of industrial regimes that depends on energy consumption, and selection of necessary values of input variables corresponding to a given class. The operation procedure allows to reduce the consumption of energy for 9% for production 1 ton of briquettes compare with operation according to the regime's map , and to obtain the required quality of dried peat. For further improvement it is necessary to develop an automatic control system to facilitate the implementation of operation of the drying process.

References

T. Aksyonova and I. Tetko. Robust polynomial neural networks in quantitative-structure activity relationship studies. *Systems Analysis Modelling Simulation*, 43(10):1331–1339, 2003.

E. Altuhov and L. Kulakovskiy. Formuvannya faktornogo polya dlya eksperimental'nikh dosldzhen' parovoi trubchatoi

susharki torfu [formation of factor field for experimental research in steam tube dryer peat]. *Vistnik NTUU "KP", seriya "Girnistvo"*, (24):88–95, 2014.

B. Bohatov. *Modelirovanie i optimizatsiya protsessov briketnogo proizvodstva [Simulation and optimization of briquette production processes]*. Moskva, Nedra, 1976.

V. Borovikov. *Nejronnye seti. Statistica Neural Networks [Neural networks. Statistica Neural Networks.]*. Moskva, Gornjachaja linija-Telekom, 2008.

V. Cheberkus and A. Ivakhnenko. Multilayer algorithm for self organization of long term predictions (illustrated by the example of the lake baikal ecological system). *Soviet Automatic Control*, 13(4):22–38, 1980.

L. N. de Castro and F. J. Von Zuben. *Artificial Immune Systems: Part I -Basic Theory and Applications*. Universidade Estadual de Campinas, Dezembro de, Tech., 1999.

K. Forsman and O. Slätteke. On identification and control tuning of cylinder dryers. *Proceedings Control Systems 2002*, pages 298–302, 2002.

M. Gatih and V. Genshaft. Matematicheskie modeli protsessa sushki i upravleniya sushilkoj tsemag [mathematical models of the drying process and control of tsemag dryer]. *Torfyaniya promyshlennost'*, 16(2):18–27, 1980.

V. Gavrilov and V. Podinovskij. *Optimizatsiya po posledovatel'no primenyaemym kriteriyam [Optimization of consistently applied criteria]*. Moskva, Sov. radio, 1975.

V. Hnyeushev. *Bryketuvannja torfu: Monografija, [Briquetting peat Monograph]*. NUWMNRU, Rivne, 2008.

A. Ivakhnenko. Polynomial theory of complex systems. *Systems, Man and Cybernetics, IEEE Transactions*, (5):364–378, 1971.

A. Ivakhnenko and A. Rogov. Inductive method permitting to choose model with least error and least bias allowing the solve interpolation tasks of artificial intelligence. *Systems Analysis Modelling Simulation*, 13(1):32–35, 2005.

A. Ivakhnenko and Yu. Yurachkovskij. *Modelirovanie Slozhnykh Sistem po Eksperimental'nym Dannym [Modeling of Complex System from Experimental Data]*.

G. Ivakhnenko. Heuristic self-organization in problems of engineering cybernetics. *Automatica*, 6(2):207–209, 1970.

D. Jouan-Rimbaud and R. De Maesschalck. The mahalanobis distance. *Chemom. Intellig. Lab. Syst.*, 50:1–18, 2000.

N. Korol' and I. Lishtvan. *Osnovnye svoystva torfa i metody ikh opredeleniya [The basic properties of peat and methods for their determination]*. Nauka i tehnika, Minsk, 2008.

L. Kulakovskiy and V. Rosen. Design the algorithm for constructing the field of factors of drying process of peat in the steam tube dryers. *POWER ENGINEERING: Economics, Technique, Ecology*, 3(34):64–70, 2013a.

- L. Kulakovskiy and V. Rosen. Planuvannya virobnychikh eksperimentv dlya bagatofaktornogo dosldzhennya tekhnologi sushnnya torfu v parovikh trubchatikh susharkakh" [planning of multivariate production experiments to study the technology of peat drying in steam tube dryer]. *Conference of Power and Control Systems*, (3):34–40, 2013b.
- R. Mueller and J. Cozad. Standardized discriminant coefficients: Which variance estimate is appropriate. *Journal of Educational and Behavioral Statistics*, 13(4):313–318, 1988.
- V. Naumovich. *Iskusstvennaya sushka torfa [Artificial drying of peat]*. Moskva, Nedra, 1984.
- Ola Slätteke and Karl Åström. Modeling of a steam heated rotating cylinder a grey-box. *American Control Conference 2005*, pages 1449–1454, 2005.
- A. Vojtishchek. *Osnovy metodov Monte-Karlo v algoritmakh i zadachakh. Chast' 5 [Basics of Monte Carlo in algorithms and tasks. Part V]*. Novosibirsk, izd-vo NGU, 1999.
- Leena Yliniemi. *Advanced control of a rotary dryer*. Department of Process Engineering, University of Oulu, 1999. ISBN 951-42-5280-2.
- Yu. Yurachkovskij and I. Zaentsev. *Modelirovanie Slozhnykh Sistem po Eksperimental'nym Dannym [Modeling of Complex System from Experimental Data]*. Moskva, Radio i Svyaz', 1987.

Improving the Mathematical Formulas for Identification of Bitumen's Viscoelastic Properties at Large Shear Strains

Magnus Komperød¹

¹Technological Analyses Centre, Nexans Norway AS, Norway, magnus.komperod@nexans.com

Abstract

Bitumen is used as anticorrosion to protect steel armor wires of subsea cables and umbilicals. Because bitumen's viscoelastic behavior influences the mechanical properties of cables, it is desirable to include bitumen in mechanical cable analyses. For this purpose, the author and his colleagues have in a previous scientific paper presented a newly developed laboratory instrument for identification of bitumen's viscoelastic properties. The present paper derives an improved mathematical model for how to establish bitumen's viscoelastic properties from the sensor measurements of the laboratory instrument. It is proved mathematically that the model of the previous paper and the model of the present paper give identical results when bitumen has shear modulus of small magnitude. The difference between the two models grows with increasing magnitude.

Keywords: Arctic Engineering; Bitumen; Complex Analysis; Cross Section Analysis; Large Shear Strain; Offshore Technology; Subsea Cable; Umbilical.

1 Introduction

Subsea power cables are essential for connecting power grids across seas, such as connecting the Scandinavian Peninsula, i.e. Norway and Sweden, to Finland and the Baltic countries in east, to Denmark and Germany in south, and to Britain in southwest.

For offshore oil and gas production, umbilicals are most important. Umbilicals are cable-like structures consisting of different types of elements, such as tubes for transportation of fluids and for running hydraulic equipment, as well as electric and fiber optic signal cables. Power umbilicals also include power phases for energizing subsea equipment, such as subsea compressors.

Both subsea cables and umbilicals often include helical armor wires, usually arranged in one to four armor layers located outside the other cable elements. The main purpose of the armor wires is to carry axial tension and thereby reduce the axial tension imposed on the other cable elements. Armor wires may also be used to tune the cables' and umbilicals' submerged-weight-to-diameter ra-

tio, where the submerged weight is the net force of gravity minus buoyancy. Figure 1 shows a subsea power cable with two layers of armor wires.



Figure 1. Subsea power cable. The two black arrows indicate the two layers of galvanized steel armor wires.

Armor wires are often made of galvanized steel, because this material has favorable mechanical properties, while being cost effective. However, as the cable is constantly submerged in seawater for decades, the galvanization may be insufficient corrosion protection for the steel wires. The viscoelastic material bitumen is commonly used as corrosion protection for the steel armor wires.

Olsen et al. (2014), Konradsen and Ouren (2014), Mullins et al. (2015), and Komperød et al. (2015) present efforts within identification of bitumen's viscoelastic properties for the purpose of including bitumen's behavior in cable analyses. Hedlund (2015) derives a model which describes how bitumen-coated armor wires influence the bending characteristics of subsea cables. A cable's bending characteristic describes the relationship between bending moment and bending curvature, which can be either static or dynamic. The model of Hedlund (2015) is based on the work of Mullins et al. (2015).

For many structures, for example steel tubes, the bending moment and the bending curvature are related through a real (non-complex) coefficient of proportionality, which is referred to as the structure's bending stiffness. However, for cables and umbilicals the bending characteristics may be nonlinear due to nonlinear materials, such as lead sheaths on power phases, and due to stick / slip behavior of helical elements as explained in Féret and Bournazel (1987) and in Caire (2014). Further, the bending characteristics may include dynamic behaviors due to viscoelastic materials, which is the case for cables and umbilicals with bitumen-coated armor wires.

The efforts of Olsen et al. (2014), Konradsen and Ouren (2014), Mullins et al. (2015), Komperød et al. (2015), and Hedlund (2015) are all based on the approach of identifying bitumen's viscoelastic properties in small-scale experiments, and then establishing the cables' and umbilicals' bending characteristics using first principle models. An alternative approach is to establish the bending characteristics directly from large-scale experiments on cables and umbilicals. The latter approach is considered in Maioli (2015), which presents interesting results on how the bending characteristic of a cable with bitumen-coated armor wires is influenced by bending curvature amplitude, bending curvature frequency, and the cable's temperature. Tarnowski (2015) also provides interesting considerations on identification of cables' dynamic bending characteristics through large-scale testing on cable segments.

Identification of materials' viscoelastic properties is widely covered in the literature. See (2001) provides an interesting survey on this topic. Olsen et al. (2014), as well as Konradsen and Ouren (2014), present identification of bitumen's viscoelastic properties based on rheometers. According to Konradsen and Ouren (2014), traditional low-strain rheometers typically operates in the shear strain range of 1% or less, while bitumen's shear strain in cables may be up to 500%. Hence, the viscoelastic properties established in low-strain rheometers may not be representative for bitumen's behavior in cables. Nexans Norway AS has therefore developed a laboratory instrument which is able to measure bitumen's viscoelastic properties at equally large shear strain as in real-life cables. This laboratory instrument is presented in Komperød et al. (2015).

In addition to the physical laboratory instrument, Komperød et al. (2015) also presents the mathematical derivation for how to calculate bitumen's viscoelastic properties from the logged measurements of the laboratory instrument. This derivation is based on a few assumptions and simplification that are valid for the temperature range of +5°C to +20°C, which is the temperature range considered in that publication. However, as bitumen's viscoelastic properties are highly temperature-dependent, one of this assumptions may become invalid for lower temperatures.

The contribution of the present paper is to improve the above mentioned mathematical derivation to also hold for bitumen at lower temperatures than +5°C. If the geometry

or the materials of the laboratory instrument are changed, the improvement may also be necessary for temperatures of +5°C and above. The improvement is explained in more detail in Section 4, after the basic principle of the instrument has been presented in Section 3.

2 Nomenclature

Table 1 presents the symbols used in this paper. Complex numbers are indicated with tilde, for example \tilde{G} . The variables \tilde{F} , \tilde{f} , \tilde{u} , \tilde{v} , $\tilde{\gamma}$, $\tilde{\epsilon}$, $\tilde{\sigma}$, and $\tilde{\tau}$ are phase vectors (phasors), i.e. complex number representations of variables changing with time in sinusoidal manners. The product EA is the rod's axial stiffness. The functions $\Re(\cdot)$ and $\Im(\cdot)$ return the real part and imaginary part, respectively, of their arguments.

3 Basic Principle of the Laboratory Instrument

This section explains briefly the basic principle of the laboratory instrument used to establish bitumen's viscoelastic properties at equally large shear strain as in subsea cables and umbilicals. For a more thorough explanation please refer to Komperød et al. (2015).

The laboratory instrument consists of a steel cylinder, a steel rod, a servomotor, and two sensors. The rod is inserted into the cylinder, and then axially and radially centered. Then the volume between the rod's outer surface and the cylinder's inner surface is filled with bitumen so that bitumen sticks to both surfaces. Figure 2 shows a side-view of the cylinder and the rod with bitumen.

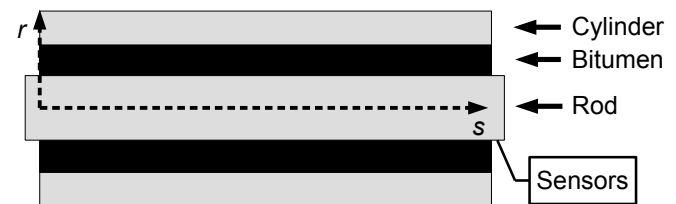


Figure 2. Basic principle of the laboratory instrument.

The servomotor moves the rod axially, i.e. in left / right direction of Figure 2, in a sinusoidal manner. The sensors measure the displacement of the rod and the axial force required to achieve this displacement. These measurements are logged as timeseries in a computer.

The dashed lines of Figure 2 show the coordinate system to be used in this paper. The s coordinate is a Cartesian coordinate that represents the length parameter of the cylinder. At the left end of the cylinder $s = 0$, while on the right end of the cylinder $s = L$, where L is the length of the cylinder. The r coordinate is the radial coordinate of a polar coordinate system oriented normal to the s -axis. In the center of the rod $r = 0$. At the inner radius of the

Table 1. Nomenclature.

A	Rod's cross section area [m ²], $A = \pi r_i^2$.
\tilde{c}_1, \tilde{c}_2	Solution constants of ODE Eq. 29 [N].
E	Rod's elastic modulus [Pa].
$\tilde{F}(s)$	Axial tension in rod [N].
$\tilde{f}(s)$	General function of s [m].
\tilde{G}	Complex shear modulus of bitumen [Pa].
G^*	$G^* = \tilde{G} $ [Pa].
G'	$G' = \Re(\tilde{G})$ [Pa].
G''	$G'' = \Im(\tilde{G})$ [Pa].
\tilde{H}	Defined in Eq. 40 [N/m].
j	Imaginary unit [-], $j^2 \stackrel{\text{def}}{=} -1$.
L	Length of cylinder [m].
\tilde{Q}	Defined in Eq. 24 [m ⁻¹].
\tilde{Q}_1, \tilde{Q}_2	Solutions of Eq. 24 w.r.t. \tilde{Q} [m ⁻¹].
Q'	$Q' = \Re(\tilde{Q}_1)$ [m ⁻¹].
Q''	$Q'' = \Im(\tilde{Q}_1)$ [m ⁻¹].
r	Radial coordinate [m].
r_i	Inner radius of bitumen layer [m].
r_o	Outer radius of bitumen layer [m].
s	Axial coordinate [m].
$\tilde{u}(r, s)$	Displacement of bitumen in direction parallel to rod's length [m].
$\tilde{v}(s)$	Axial displacement of rod [m].
$\tilde{\gamma}(r, s)$	Shear strain of bitumen [-].
$\tilde{\epsilon}(s)$	Axial strain of rod [-].
$\tilde{\sigma}(s)$	Axial stress of rod [Pa].
$\tilde{\tau}(r, s)$	Shear stress of bitumen [Pa].
φ	$\varphi = \arg(\tilde{G})$ [rad].

bitumen layer, i.e. the outer radius of the rod, $r = r_i$. At the outer radius of the bitumen layer, i.e. the inner radius of the cylinder, $r = r_o$.

The servomotor and the two sensors are located at the right end, i.e. at $s = L$. Hence, the sensors measures the force $F(L)$ and the displacement $v(L)$, respectively. The contribution of this paper is to derive how to identify bitumen's viscoelastic properties from the logged time series of these two sensors.

4 Assumptions and Simplifications

As stated in Section 1, the mathematical derivation of Komperød et al. (2015) is based on a few assumptions and simplification, of which one may not hold for bitumen at lower temperatures. The assumption that may not hold is to disregard the axial strain of the rod in Figure 2. That is: At higher temperatures, bitumen has a low shear stress amplitude to shear strain amplitude ratio, G^* . Then a certain displacement of the rod requires only a small force by the servomotor. However, at lower temperatures bitumen has a very large G^* . A large axial force is then required to achieve the same displacement.

Due to the steel rod's inherent material properties, the rod will be strained when being axially tensioned. Because the force of the servomotor, and hence the tension of the rod, are low at high temperatures, the strain of the rod can be neglected. However, at low temperatures the tension and the axial strain of the rod are high, hence, the axial strain should therefore be included in the mathematical derivation.

In other words: The contribution of the present paper is to improve the mathematical derivation of Komperød et al. (2015) to also include the effect of axial strain of the steel rod. This improvement may also be necessary subject to changes of the laboratory instrument's geometry or materials.

The mathematical derivation of the present paper is subject to the following assumptions and simplifications:

1. Bitumen's shear stress and shear strain are assumed to be related through a complex shear modulus, i.e. $\tilde{\tau} = \tilde{G}\tilde{\gamma}$. The modulus may be a function of the shear strain amplitude, the shear strain frequency, and the temperature of bitumen. Further, the phase shift of the modulus, φ , is assumed to be in the half-open interval $\varphi \in [0, \frac{\pi}{2})$.
2. The normal stress of bitumen in axial direction is neglected, because the force caused by this stress is neglectable compared to the axial force of the steel rod.
3. The force required to accelerate the rod and bitumen is disregarded, because this force is neglectable compared to the force required to strain bitumen.
4. The axial stress and axial strain of the steel rod are assumed to be related through a constant non-complex modulus, i.e. $\tilde{\sigma} = E\tilde{\epsilon}$.
5. The cylinder is assumed to be fixed and rigid; any strain in the cylinder is neglected.
6. The Poisson ratio effect is neglected for the cylinder, the rod, and bitumen.

5 Identification of Viscoelastic Properties from Sensor Measurements

This section derives how to identify bitumen's viscoelastic properties from the timeseries logged by the two sensors of the laboratory instrument. The sensors measure the axial force, $F(L)$, and the axial displacement, $v(L)$, at the end of the rod shown to the right in Figure 2.

The parameter to be identified is the complex shear modulus of bitumen, \tilde{G} . From \tilde{G} it is trivial to calculate the shear stress amplitude to shear strain amplitude ratio, G^* , the phase shift between shear stress and shear strain, φ , the storage modulus, G' , and the loss modulus, G'' , through the identity

$$\begin{aligned}\tilde{G} &= G^* e^{j\varphi} \\ &= G^* [\cos(\varphi) + j\sin(\varphi)] \\ &= G' + jG''.\end{aligned}\quad (1)$$

5.1 Equilibrium of a Rod Segment

Assume a rod segment of infinitesimal length ∂s . In one end of the segment the axial tension is $\tilde{F}(s)$ and in the other end the axial tension is $\tilde{F}(s) + \partial\tilde{F}(s)$. The circumferential surface of the rod sticks to bitumen giving a shear stress $\tilde{\tau}(r_i, s)$. This surface has an area of $2\pi r_i \partial s$. Hence, the shear force acting between bitumen and the rod over the segment length ∂s is $2\pi r_i \tilde{\tau}(r_i, s) \partial s$. This is illustrated in Figure 3.

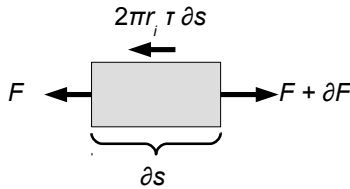


Figure 3. Forces acting on a rod segment of infinitesimal length ∂s .

By assumption 3 of Section 4, the force required to accelerate the rod and bitumen is neglectable. The following equilibrium is therefore stated

$$\tilde{F}(s) + \partial\tilde{F}(s) = \tilde{F}(s) + 2\pi r_i \tilde{\tau}(r_i, s) \partial s. \quad (2)$$

Cancelling and rewriting gives

$$\frac{\partial\tilde{F}(s)}{\partial s} = 2\pi r_i \tilde{\tau}(r_i, s). \quad (3)$$

The axial tension is related to the axial strain by $\tilde{F} = EA\tilde{\epsilon}$. Further, the axial strain is related to the axial displacement by $\tilde{\epsilon} = \frac{\partial\tilde{v}(s)}{\partial s}$. Hence, Eq. 3 can be rewritten to

$$EA \frac{\partial^2 \tilde{v}(s)}{\partial s^2} = 2\pi r_i \tilde{\tau}(r_i, s). \quad (4)$$

Bitumen's shear stress is related to the shear strain through the complex modulus, i.e. $\tilde{\tau}(r, s) = \tilde{G}\tilde{\gamma}(r, s)$. The shear strain is related to the displacement by $\tilde{\gamma}(r, s) = -\frac{\partial\tilde{u}(r, s)}{\partial r}$. Inserting into Eq. 4 gives

$$EA \frac{\partial^2 \tilde{v}(s)}{\partial s^2} = -2\pi r_i \tilde{G} \left. \frac{\partial\tilde{u}(r, s)}{\partial r} \right|_{r=r_i}. \quad (5)$$

5.2 Equilibrium of a Bitumen Segment

Consider a cylinder-shaped segment of bitumen with inner radius r , outer radius $r + \partial r$, and length ∂s . The shear force acting on the inner surface of the cylinder-shaped segment is $2\pi r \partial s \tilde{\tau}(r, s)$. The shear force acting on the outer surface is $2\pi[r + \partial r] \partial s [\tilde{\tau}(r, s) + \partial\tilde{\tau}(r, s)]$. By assumptions 2 and 3 of Section 4 the bitumen segment is in equilibrium by

$$2\pi r \partial s \tilde{\tau}(r, s) = 2\pi[r + \partial r] \partial s [\tilde{\tau}(r, s) + \partial\tilde{\tau}(r, s)]. \quad (6)$$

Canceling, simplifying, and disregarding the term $\partial r \partial\tilde{\tau}(r, s)$ gives

$$r \partial\tilde{\tau}(r, s) = -\partial r \tilde{\tau}(r, s), \quad (7)$$

$$r \tilde{G} \partial\tilde{\gamma}(r, s) = -\partial r \tilde{G} \tilde{\gamma}(r, s), \quad (8)$$

$$r \partial\tilde{\gamma}(r, s) = -\partial r \tilde{\gamma}(r, s), \quad (9)$$

$$-r \frac{\partial\tilde{\gamma}(r, s)}{\partial r} = \tilde{\gamma}(r, s), \quad (10)$$

$$-r \frac{\partial^2 \tilde{u}(r, s)}{\partial r^2} = \frac{\partial\tilde{u}(r, s)}{\partial r}. \quad (11)$$

In Eq. 8 it is used that $\tilde{\tau}(r, s) = \tilde{G}\tilde{\gamma}(r, s)$, and in Eq. 11 it is used that $\tilde{\gamma}(r, s) = -\frac{\partial\tilde{u}(r, s)}{\partial r}$.

5.3 Establishing an ODE

In this section an ordinary differential equation (ODE) is established based on the results from Sections 5.1 and 5.2.

Integrating Eq. 11 w.r.t. r gives

$$-\int r \frac{\partial^2 \tilde{u}(r, s)}{\partial r^2} \partial r = \int \frac{\partial\tilde{u}(r, s)}{\partial r} \partial r, \quad (12)$$

$$-\left[r \frac{\partial\tilde{u}(r, s)}{\partial r} - \int \frac{\partial\tilde{u}(r, s)}{\partial r} \partial r \right] = \int \frac{\partial\tilde{u}(r, s)}{\partial r} \partial r, \quad (13)$$

$$-r \frac{\partial\tilde{u}(r, s)}{\partial r} = \tilde{f}(s). \quad (14)$$

In Eq. 13 integration by parts is used for the left hand side of Eq. 12. The function $\tilde{f}(s)$ of Eq. 14 is the constant of integration, which is independent of r , but may be a function of s . Eq. 14 is an important result which states that the product $r \frac{\partial \tilde{u}(r,s)}{\partial r}$ is constant over the interval $r \in [r_i, r_o]$. Hence, Eq. 14 also holds for $r = r_i$. That is

$$-r_i \left. \frac{\partial \tilde{u}(r,s)}{\partial r} \right|_{r=r_i} = \tilde{f}(s). \quad (15)$$

Inserting Eq. 15 into Eq. 5 gives

$$EA \frac{d^2 \tilde{v}(s)}{ds^2} = 2\pi \tilde{G} \tilde{f}(s). \quad (16)$$

In Eq. 16 the partial derivatives of Eq. 5 are replaced by ordinary derivatives as there is no longer any dependency on r in the differential equation.

The next issue is to identify the unknown function $\tilde{f}(s)$. Eq. 14 can be rewritten to

$$\partial \tilde{u}(r,s) = -\tilde{f}(s) \frac{\partial r}{r}. \quad (17)$$

Integrating w.r.t. r with integration limits r_i and r_o gives

$$\int_{r=r_i}^{r=r_o} \partial \tilde{u}(r,s) = -\tilde{f}(s) \int_{r_i}^{r_o} \frac{\partial r}{r}, \quad (18)$$

$$\begin{aligned} \tilde{u}(r_o,s) - \tilde{u}(r_i,s) &= -\tilde{f}(s) [\ln(r_o) - \ln(r_i)] \\ &= -\tilde{f}(s) \ln \left(\frac{r_o}{r_i} \right). \end{aligned} \quad (19)$$

Bitumen sticks to the inner surface of the cylinder, which is fixed. Hence, $\tilde{u}(r_o,s) = 0$. Further, bitumen also sticks to the rod. Therefore, $\tilde{u}(r_i,s) = \tilde{v}(s)$. Eq. 19 then simplifies to

$$\tilde{v}(s) = \tilde{f}(s) \ln \left(\frac{r_o}{r_i} \right). \quad (20)$$

Rewriting gives

$$\tilde{f}(s) = \frac{\tilde{v}(s)}{\ln \left(\frac{r_o}{r_i} \right)}. \quad (21)$$

Then inserting Eq. 21 into Eq. 16

$$EA \frac{d^2 \tilde{v}(s)}{ds^2} = \frac{2\pi \tilde{G}}{\ln \left(\frac{r_o}{r_i} \right)} \tilde{v}(s), \quad (22)$$

$$\frac{d^2 \tilde{v}(s)}{ds^2} - \frac{2\pi \tilde{G}}{EA \ln \left(\frac{r_o}{r_i} \right)} \tilde{v}(s) = 0. \quad (23)$$

Eq. 23 is a second order, linear, homogeneous differential equation with constant coefficient written on standard form. However, note that the coefficient is complex.

To simplify the notation, the variable \tilde{Q} is introduced, which is defined implicitly as

$$\tilde{Q}^2 \stackrel{\text{def}}{=} \frac{2\pi \tilde{G}}{EA \ln \left(\frac{r_o}{r_i} \right)}. \quad (24)$$

Using \tilde{Q} , Eq. 23 becomes

$$\frac{d^2 \tilde{v}(s)}{ds^2} - \tilde{Q}^2 \tilde{v}(s) = 0. \quad (25)$$

Differentiating Eq. 25 w.r.t. s gives

$$\frac{d^3 \tilde{v}(s)}{ds^3} - \tilde{Q}^2 \frac{d\tilde{v}(s)}{ds} = 0, \quad (26)$$

$$\frac{d^2 \tilde{\epsilon}(s)}{ds^2} - \tilde{Q}^2 \tilde{\epsilon}(s) = 0, \quad (27)$$

$$EA \frac{d^2 \tilde{\epsilon}(s)}{ds^2} - EA \tilde{Q}^2 \tilde{\epsilon}(s) = 0, \quad (28)$$

$$\frac{d^2 \tilde{F}(s)}{ds^2} - \tilde{Q}^2 \tilde{F}(s) = 0. \quad (29)$$

In Eq. 27 it is used that $\tilde{\epsilon} = \frac{d\tilde{v}(s)}{ds}$, and in Eq. 29 it is used that $\tilde{F} = EA \tilde{\epsilon}$. It is trivial to verify that the solution of Eq. 29 is

$$\tilde{F}(s) = \tilde{c}_1 e^{\tilde{Q}s} + \tilde{c}_2 e^{-\tilde{Q}s}. \quad (30)$$

5.4 Boundary Conditions

The most common way to apply boundary conditions to an ODE on the form of Eq. 30 is to solve for \tilde{c}_1 and \tilde{c}_2 using two boundary conditions. However, the problem formulation of the present paper is somewhat different: The final goal is to identify \tilde{G} from timeseries logged by the sensors presented in Section 3. As \tilde{G} can easily be found from known \tilde{Q} using Eq. 24, goal is to identify \tilde{Q} .

The problem to be solved has three unknowns: \tilde{c}_1 , \tilde{c}_2 , and \tilde{Q} . There are also three boundary conditions available:

1. There is no force acting on the left side of the rod in Figure 2. Hence, $\tilde{F}(0) = 0$.
2. The force acting on the right side of the rod, $\tilde{F}(L)$, is known because it is logged from the force sensor.

3. The displacement of the right side of the rod, $\tilde{v}(L)$, is known because it is logged from the displacement sensor.

$$\tilde{H} = \frac{2\tilde{c}_1 \sinh(\tilde{Q}L)}{EA \frac{\cosh(\tilde{Q}L)}{\tilde{Q}}}, \quad (41)$$

Inserting boundary condition 1 into Eq. 30

$$\tilde{F}(0) = \tilde{c}_1 e^{\tilde{Q} \cdot 0} + \tilde{c}_2 e^{-\tilde{Q} \cdot 0}, \quad (31)$$

$$0 = \tilde{c}_1 \cdot 1 + \tilde{c}_2 \cdot 1, \quad (32)$$

$$\tilde{c}_2 = -\tilde{c}_1. \quad (33)$$

Then inserting Eq. 33 into Eq. 30

$$\begin{aligned} \tilde{F}(s) &= \tilde{c}_1 \left[e^{\tilde{Q}s} - e^{-\tilde{Q}s} \right] \\ &= 2\tilde{c}_1 \sinh(\tilde{Q}s). \end{aligned} \quad (34)$$

Differentiating Eq. 34 w.r.t. s gives

$$\frac{d\tilde{F}(s)}{ds} = 2\tilde{c}_1 \tilde{Q} \cosh(\tilde{Q}s), \quad (35)$$

$$EA \frac{d\tilde{\epsilon}(s)}{ds} = 2\tilde{c}_1 \tilde{Q} \cosh(\tilde{Q}s), \quad (36)$$

$$\frac{d^2 \tilde{v}(s)}{ds^2} = \frac{2\tilde{c}_1}{EA} \tilde{Q} \cosh(\tilde{Q}s), \quad (37)$$

where $\tilde{F} = EA \tilde{\epsilon}$ is used in Eq. 36, and $\tilde{\epsilon} = \frac{d\tilde{v}(s)}{ds}$ is used in Eq. 37. Inserting Eq. 25 into Eq. 37

$$\tilde{Q}^2 \tilde{v}(s) = \frac{2\tilde{c}_1}{EA} \tilde{Q} \cosh(\tilde{Q}s), \quad (38)$$

$$\tilde{v}(s) = \frac{2\tilde{c}_1 \cosh(\tilde{Q}s)}{EA \tilde{Q}}. \quad (39)$$

As explained in Section 3, the rod is moved in a sinusoidal manner by the servomotor. Hence, $\tilde{v}(L)$ is a sinusoidal signal. Further, according to Komperød et al. (2015), the signal of the measured force, $\tilde{F}(L)$, can be well approximated by a sinus curve of the same frequency as $\tilde{v}(L)$, but with different amplitude and different phase. It is then convenient to define the \tilde{H} as the complex ratio

$$\tilde{H} \stackrel{\text{def}}{=} \frac{\tilde{F}(L)}{\tilde{v}(L)}. \quad (40)$$

Hence, \tilde{H} is a complex number expressing the force amplitude to displacement amplitude ratio, and the phase shift between the force and the displacement. Komperød et al. (2015) explain how to find \tilde{H} from the logged measurement data.

Setting $s = L$ in Eqs. 34 and 39, and inserting these equations into Eq. 40 gives

$$\tilde{H} = EA \tilde{Q} \tanh(\tilde{Q}L). \quad (42)$$

Eq. 42 is the main result of this paper. This nonlinear equation in one complex variable relates \tilde{Q} to the measured force and measured displacement at the rod's right end in Figure 2. The non-complex parameters E , A , and L are known, while \tilde{H} can be established from the sensor measurements. When \tilde{Q} is identified, the viscoelastic properties of bitumen can easily be established through Eq. 24, and thereafter using Eq. 1.

As Eq. 42 is a complex equation, real part on both sides must be equal, and the imaginary part on both sides must be equal. Hence, Eq. 42 can be decomposed into two nonlinear equations

$$\Re(\tilde{H}) = \Re(EA \tilde{Q} \tanh(\tilde{Q}L)), \quad (43)$$

$$\Im(\tilde{H}) = \Im(EA \tilde{Q} \tanh(\tilde{Q}L)). \quad (44)$$

How to solve the nonlinear, complex Eq. 42 w.r.t. \tilde{Q} , or equivalently to solve Eqs. 43 and 44, using for example a numerical method, is beyond the scope of this paper.

The next two sections provide analytical approximations that are valid for small values of $|\tilde{Q}L|$, and for large values of $|\tilde{Q}L|$, respectively. Using these approximations, it is trivial to solve Eq. 42 analytically. The solutions based on the approximations give very useful information about the relationship between \tilde{Q} and \tilde{H} , which is of both theoretical and practical interest. Further, these solution may be good initial values for numerical solution of Eq. 42. Please note that there may be an interval between "small values" and "large values", where both approximations give inaccurate estimates of \tilde{Q} .

5.5 Approximation for Small Values of $|\tilde{Q}L|$

If $|\tilde{Q}L|$ is small, then $\tanh(\tilde{Q}L)$ can be approximated by a Maclaurin series expansion. The Maclaurin series of $\tanh(\tilde{z})$ is known to converge for $|\tilde{z}| < \frac{\pi}{2}$, where \tilde{z} is a complex number. The first order Maclaurin polynomial is

$$\tanh(\tilde{Q}L) \approx \tilde{Q}L. \quad (45)$$

Inserting Eq. 45 into Eq. 42

$$\begin{aligned} \tilde{H} &= EA \tilde{Q} \cdot \tilde{Q}L \\ &= EAL \tilde{Q}^2. \end{aligned} \quad (46)$$

That is

$$\tilde{Q}^2 = \frac{\tilde{H}}{EAL}. \quad (47)$$

5.6 Approximation for Large Values of $|\tilde{Q}L|$

The function $\tanh(\tilde{z})$ is by definition

$$\begin{aligned}\tanh(\tilde{z}) &\stackrel{\text{def}}{=} \frac{\sinh(\tilde{z})}{\cosh(\tilde{z})} \\ &= \frac{e^{\tilde{z}} - e^{-\tilde{z}}}{e^{\tilde{z}} + e^{-\tilde{z}}} \\ &= \frac{e^{\tilde{z}} - e^{-\tilde{z}}}{e^{\tilde{z}} + e^{-\tilde{z}}}\end{aligned}\quad (48)$$

The right hand side of Eq. 24 are real, except for the factor \tilde{G} . Hence,

$$\arg(\tilde{Q}^2) = \arg(\tilde{G}) \in \left[0, \frac{\pi}{2}\right), \quad (49)$$

$$\arg(\tilde{Q}_1) = \frac{1}{2} \arg(\tilde{G}) \in \left[0, \frac{\pi}{4}\right), \quad (50)$$

$$\arg(\tilde{Q}_2) = \frac{1}{2} \arg(\tilde{G}) + \pi \in \left[\pi, \frac{5\pi}{4}\right), \quad (51)$$

where \tilde{Q}_1 and \tilde{Q}_2 are the two solutions of Eq. 24. The interval of Eq. 49 follows from Assumption 1 of Section 4, while the other two intervals follow from the first one using the n th root of unity. Comparing Eq. 50 and Eq. 51 shows that

$$\tilde{Q}_2 = -\tilde{Q}_1, \quad (52)$$

because \tilde{Q}_1 and \tilde{Q}_2 have the same magnitude. Now using the notation

$$\tilde{Q}_1 = Q' + jQ'', \quad (53)$$

$$\tilde{Q}_2 = -Q' - jQ'', \quad (54)$$

where $Q', Q'' \in \mathbb{R}$, and $Q' > Q'' \geq 0$. Considering the limit of $\tanh(\tilde{Q}_1L)$ as $|\tilde{Q}_1| \rightarrow \infty$

$$\lim_{|\tilde{Q}_1| \rightarrow \infty} \tanh(\tilde{Q}_1L) \quad (55)$$

$$= \lim_{|\tilde{Q}_1| \cos(\arg(\tilde{Q}_1)) \rightarrow \infty} \tanh(\tilde{Q}_1L)$$

$$= \lim_{Q' \rightarrow \infty} \tanh(\tilde{Q}_1L)$$

$$= \lim_{Q' \rightarrow \infty} \frac{e^{\tilde{Q}_1L} - e^{-\tilde{Q}_1L}}{e^{\tilde{Q}_1L} + e^{-\tilde{Q}_1L}}$$

$$= \lim_{Q' \rightarrow \infty} \frac{e^{Q'L+jQ''L} - e^{-Q'L-jQ''L}}{e^{Q'L+jQ''L} + e^{-Q'L-jQ''L}}$$

$$= \lim_{Q' \rightarrow \infty} \frac{e^{Q'L}e^{jQ''L} - e^{-Q'L}e^{-jQ''L}}{e^{Q'L}e^{jQ''L} + e^{-Q'L}e^{-jQ''L}}$$

$$= \frac{\lim_{Q' \rightarrow \infty} e^{Q'L}e^{jQ''L} - \lim_{Q' \rightarrow \infty} e^{-Q'L}e^{-jQ''L}}{\lim_{Q' \rightarrow \infty} e^{Q'L}e^{jQ''L} + \lim_{Q' \rightarrow \infty} e^{-Q'L}e^{-jQ''L}}$$

$$= \frac{\lim_{Q' \rightarrow \infty} e^{Q'L}e^{jQ''L} - 0}{\lim_{Q' \rightarrow \infty} e^{Q'L}e^{jQ''L} + 0}$$

$$= 1.$$

Next, considering the limit of $\tanh(\tilde{Q}_2L)$ as $|\tilde{Q}_2| \rightarrow \infty$

$$\lim_{|\tilde{Q}_2| \rightarrow \infty} \tanh(\tilde{Q}_2L) \quad (56)$$

$$= \lim_{-|\tilde{Q}_2| \cos(\arg(\tilde{Q}_2)) \rightarrow \infty} \tanh(\tilde{Q}_2L)$$

$$= \lim_{-(-Q') \rightarrow \infty} \tanh(\tilde{Q}_2L)$$

$$= \lim_{Q' \rightarrow \infty} \tanh(\tilde{Q}_2L)$$

$$= \lim_{Q' \rightarrow \infty} \frac{e^{\tilde{Q}_2L} - e^{-\tilde{Q}_2L}}{e^{\tilde{Q}_2L} + e^{-\tilde{Q}_2L}}$$

$$= \lim_{Q' \rightarrow \infty} \frac{e^{-Q'L-jQ''L} - e^{Q'L+jQ''L}}{e^{-Q'L-jQ''L} + e^{Q'L+jQ''L}}$$

$$= \lim_{Q' \rightarrow \infty} \frac{e^{-Q'L}e^{-jQ''L} - e^{Q'L}e^{jQ''L}}{e^{-Q'L}e^{-jQ''L} + e^{Q'L}e^{jQ''L}}$$

$$= \frac{\lim_{Q' \rightarrow \infty} e^{-Q'L}e^{-jQ''L} - \lim_{Q' \rightarrow \infty} e^{Q'L}e^{jQ''L}}{\lim_{Q' \rightarrow \infty} e^{-Q'L}e^{-jQ''L} + \lim_{Q' \rightarrow \infty} e^{Q'L}e^{jQ''L}}$$

$$= \frac{0 - \lim_{Q' \rightarrow \infty} e^{Q'L}e^{jQ''L}}{0 + \lim_{Q' \rightarrow \infty} e^{Q'L}e^{jQ''L}}$$

$$= -1.$$

That is, when using the solution \tilde{Q}_1 of Eq. 24, then for large magnitude of \tilde{Q}_1L , Eq. 42 can be approximated by

6 Conformal Mapping

$$\begin{aligned}\tilde{H} &= EA \tilde{Q}_1 \cdot \lim_{|\tilde{Q}_1| \rightarrow \infty} \tanh(\tilde{Q}_1 L) \\ &= EA \tilde{Q}_1 \cdot 1 \\ &= EA \tilde{Q}_1.\end{aligned}\quad (57)$$

When using the solution \tilde{Q}_2 of Eq. 24, then the approximation for large $\tilde{Q}_2 L$ becomes

$$\begin{aligned}\tilde{H} &= EA \tilde{Q}_2 \cdot \lim_{|\tilde{Q}_2| \rightarrow \infty} \tanh(\tilde{Q}_2 L) \\ &= EA \tilde{Q}_2 \cdot (-1) \\ &= -EA \tilde{Q}_2.\end{aligned}\quad (58)$$

Inserting Eq. 52 into Eq. 58 gives

$$\tilde{H} = EA \tilde{Q}_1, \quad (59)$$

which is the same result as in Eq. 57. In other words: Both solutions of Eq. 24 yield the same approximation, i.e. Eq. 59. It is then trivial to solve for \tilde{Q}

$$\tilde{Q}_1 = \frac{\tilde{H}}{EA}, \quad (60)$$

$$\tilde{Q}_1^2 = \tilde{Q}_2^2 = \tilde{Q}^2 = \frac{\tilde{H}^2}{(EA)^2}, \quad (61)$$

which can be inserted into Eq. 24 to obtain \tilde{G} .

5.7 Summary

The problem that has been addressed is to identify \tilde{Q} from logged sensor measurements of the rod's axial displacement and axial force at the right end of the rod, see Figure 2. The complex number \tilde{H} expresses the force amplitude to displacement amplitude ratio, and the phase shift between the force and the displacement. The parameters E , A , L , r_i , and r_o are known.

When \tilde{H} has been established from timeseries of the sensor measurements, \tilde{Q} can be found from the complex, nonlinear Eq. 42, or from the nonlinear set of equations Eqs. 43 and 44. Small values of $|\tilde{Q}L|$ allow \tilde{Q} to be approximated by Eq. 47. Large values of $|\tilde{Q}L|$ allow \tilde{Q} to be approximated by Eq. 60. However, note that there may be an interval between "small values" and "large values" where both approximations are inaccurate. The approximations of Eq. 47 and Eq. 60 may be used as initial values when solving Eq. 42 numerically.

When \tilde{Q} has been identified, the viscoelastic properties of bitumen can be found through Eq. 24, followed by Eq. 1.

Although the function of Eq. 42 takes only one input parameter, \tilde{Q} , and gives one output, \tilde{H} , it is not possible to visualize the function in one (x, y) plot, because the input and the output have both a real part and an imaginary part each. Conformal mapping is an approach to visualize functions with complex inputs and outputs. Introductions to conformal mapping are given in books and other literatures on complex analysis, see for example Chapter 17 of Kreyszig (2011).

Conformal mapping of a function with one complex input and one complex output consists of two (x, y) plots: The input plot shows the real part of the input on the first axis (x -axis) and imaginary part of the input on the second axis (y -axis). The output plot shows the real part of the output on the first axis and imaginary part of the output on the second axis. In both plots it is drawn curves, often distinguished with different colors, line styles, or similar, such that a curve in the input plot represents a set of input values, and a corresponding curve in the output plot represents the corresponding set of output values. The plots may also include individual points, where one point in the output plot is the function evaluation of the corresponding point in the input plot.

6.1 Conformal Mapping of the Main Equation

The main result of this paper is Eq. 42, which can be rewritten to

$$\frac{\tilde{H}}{EA} = \tilde{Q} \tanh(\tilde{Q}L). \quad (62)$$

Figure 4 shows conformal mapping of Eq. 62. Each curve in the input plot represents a set of the input \tilde{Q} . The corresponding curve in the output plot, as distinguished by line color and line style, represents the corresponding set of the output $\frac{\tilde{H}}{EA}$. Also, each point marked by a circle or a square in the output plot is the function evaluation of the corresponding input in the input plot. In the input plot, each of the straight, solid lines with square markers corresponds to increasing magnitude of \tilde{Q} , while the argument is fixed. Each of the dashed lines with circle markers corresponds to fixed magnitude and variable argument.

Figure 4 shows that that for small $|\tilde{Q}|$ the output $\frac{\tilde{H}}{EA}$ has much larger argument than the input \tilde{Q} , i.e. the function $\frac{\tilde{H}}{EA} = \tilde{Q} \tanh(\tilde{Q}L)$ increases the argument, because the slopes of the solid curves are much steeper in the output plot than in the input plot for small $|\tilde{Q}|$. This can also be seen from the blue dashed curve with circle markers; this curve spans a larger angle in the output plot than in the input plot.

Further, Figure 4 shows that the the function $\frac{\tilde{H}}{EA} = \tilde{Q} \tanh(\tilde{Q}L)$ decreases the magnitude for small $|\tilde{Q}|$. This is seen from the fact that markers which are close to the

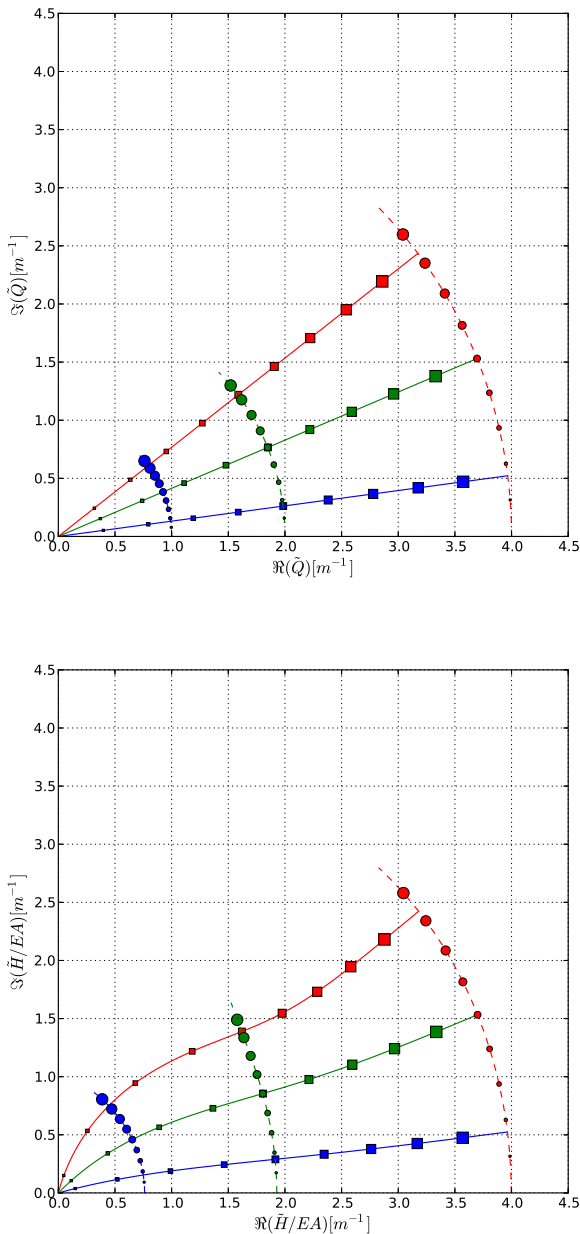


Figure 4. Conformal mapping of Eq. 62. The cylinder length is set to $L = 1.0$. The input plot (upper) shows the real part and the imaginary part of the input \tilde{Q} . The output plot (lower) shows the corresponding real part and imaginary part of the output $\frac{\tilde{H}}{EA}$. Please refer to the main text for further explanation.

origin in the input plot are even closer to the origin in the output plot.

The behavior of the function $\frac{\tilde{H}}{EA} = \tilde{Q} \tanh(\tilde{Q}L)$ as described in the previous two paragraphs is in accordance to the approximation for small values of $|\tilde{Q}L|$ presented in Section 5.5. Rewriting Eq. 47 gives

$$\frac{\tilde{H}}{EA} = \tilde{Q}^2 L, \quad (63)$$

which shows that the output corresponds to the input \tilde{Q} squared. From theory on complex numbers it is known that squaring a complex number is identical to squaring the magnitude and doubling the argument.

For larger values of $|\tilde{Q}|$, it is seen from Figure 4 that the output of the function $\frac{\tilde{H}}{EA} = \tilde{Q} \tanh(\tilde{Q}L)$ is near identical to the input. This is seen by observing that the larger square markers of any colors, as well as the red circular markers of any sizes, have nearly identical coordinates in the output plot as in the input plot. This behavior is also seen by the approximation of $\frac{\tilde{H}}{EA} = \tilde{Q} \tanh(\tilde{Q}L)$ for large $|\tilde{Q}L|$, which is derived in Section 5.6. The approximation is

$$\frac{\tilde{H}}{EA} = \tilde{Q}_1, \quad (64)$$

which states that the output is identical to the input for large $|\tilde{Q}L|$, provided that $\arg(\tilde{Q})$ obeys Eq. 50. (If $\arg(\tilde{Q})$ instead obeys Eq. 51, the output will be the negative of the input as follows from Eq. 58.)

6.2 Conformal Mapping of Approximations

The conformal mapping presented in Section 6.1 are in accordance to the approximations for small $|\tilde{Q}L|$ and for large $|\tilde{Q}L|$ as derived in Sections 5.5 and 5.6, respectively. The present section compares the two approximations, Eq. 63 and Eq. 64, with the main function, Eq. 62.

Figure 5 compares the main function and the approximations for small values of $|\tilde{Q}|$. Please read the figure caption for explanation of the figure. It is seen that Eq. 63 (dashed curves) follows Eq. 62 (solid curves) very closely for small values of $|\tilde{Q}|$ as the markers of same size and same color lie on top of each other. However, as $|\tilde{Q}|$ increases, the markers and the curves begin to deviate. Figure 5 shows that the approximation which is valid for large values of $|\tilde{Q}L|$, i.e. Eq. 64, performs very poorly for small values of $|\tilde{Q}|$.

Please note that it is not sufficiently to compare the slopes of the curves: Comparing the coordinates for markers of the same size and the same color shows that the markers of Eq. 64 are located farther from the origin than the corresponding markers of the other two equations. Hence, Eq. 64 significantly overestimates the magnitude of the output, $\frac{\tilde{H}}{EA}$.

Figure 6 shows the approximations Eq. 63 and Eq. 64 for large values of $|\tilde{Q}|$. The approximation for large values, i.e. Eq. 64 (dotted curves), approaches Eq. 62 (solid curves) as $|\tilde{Q}|$ increases. For the largest $|\tilde{Q}|$ shown in the figure, the markers of Eq. 62 and Eq. 64 lie on top of each other. In Figure 6, the approximation for small values of $|\tilde{Q}L|$, i.e. Eq. 63 (dashed curves), gives a poor approximation, except for the lowest values of $|\tilde{Q}|$.

From Figure 5 and Figure 6 it is concluded that Eq. 63 is a good approximation of Eq. 62 for small values of $|\tilde{Q}L|$,

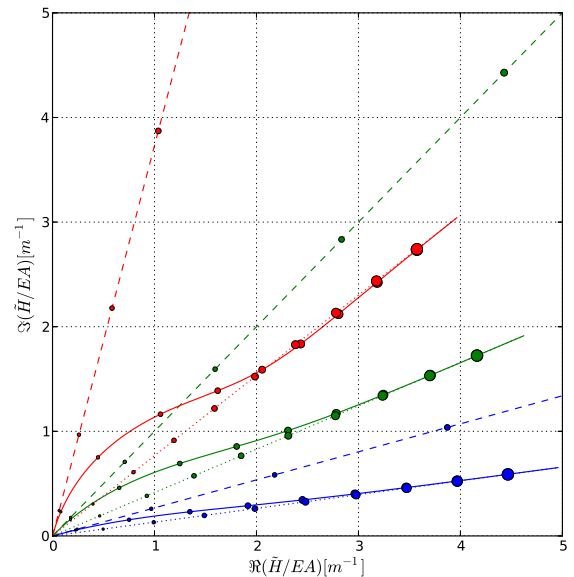
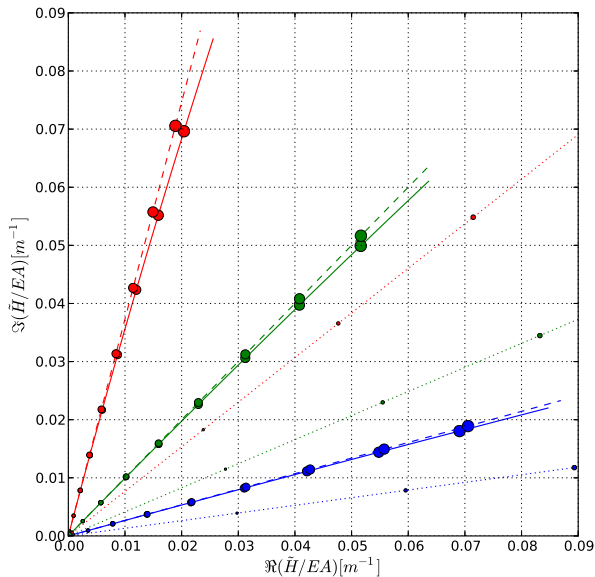
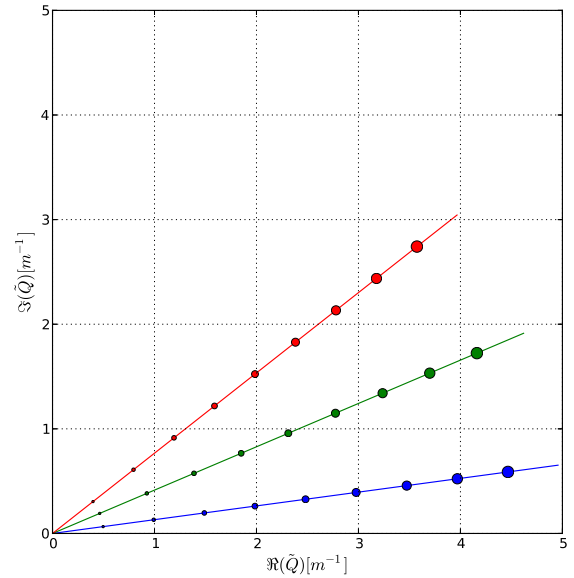
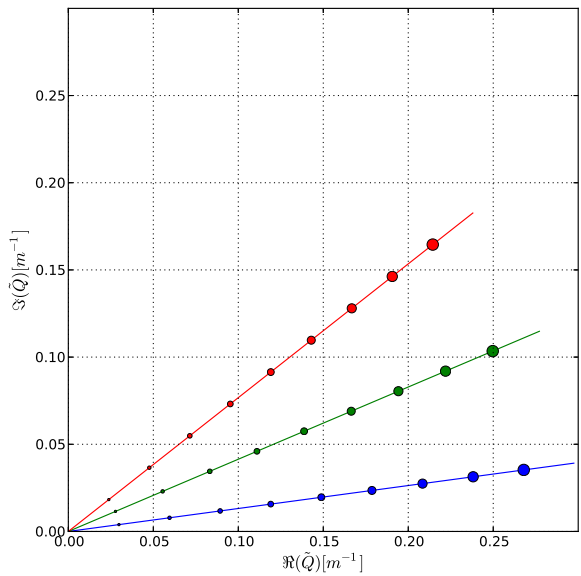


Figure 5. Conformal mapping for small values of $|\tilde{Q}|$ for the main function and the two approximations. The output plot (lower) shows the output of Eq. 62 (solid curves), Eq. 63 (dashed curves), and Eq. 64 (dotted curves). The input marked by red color in the input plot (upper) is used for all outputs marked by red color in the output plot, and similar for green color and blue color. The cylinder length is set to $L = 1.0$.

Figure 6. Conformal mapping for large values of $|\tilde{Q}|$ for the main function and the two approximations. The output plot (lower) shows the output of Eq. 62 (solid curves), Eq. 63 (dashed curves), and Eq. 64 (dotted curves). The input marked by red color in the input plot (upper) is used for all outputs marked by red color in the output plot, and similar for green color and blue color. The cylinder length is set to $L = 1.0$.

7 Practical Interpretations

while Eq. 64 is a good approximation for large values of $|\tilde{Q}L|$. However, as can be seen from Figure 6, there is a range between "small values" and "large values" where both approximations are inaccurate.

This section discusses the practical interpretations of the results derived in the present paper.

7.1 Comparison to Komperød et al. (2015)

Komperød et al. (2015) also derive how to identify the viscoelastic properties of bitumen based on timeseries of measured axial force and axial displacement of the rod in Figure 2. The main difference between the derivation of that paper and the present paper is that the former paper neglects axial strain in the rod, while the latter paper takes this effect into account. It is then of interest to compare the results of the two papers.

The derivation of Komperød et al. (2015) results in the following formula for identification of bitumen's viscoelastic properties

$$\tilde{G} = \frac{\ln\left(\frac{r_o}{r_i}\right)}{2\pi L} \tilde{H}. \quad (65)$$

The main result of the present paper is Eq. 42, which for small values of $|\tilde{Q}L|$ can be approximated by Eq. 46. Inserting Eq. 24 into Eq. 46 gives

$$\begin{aligned} \tilde{H} &= EAL \frac{2\pi\tilde{G}}{EA \ln\left(\frac{r_o}{r_i}\right)} \\ &= \frac{2\pi\tilde{G}L}{\ln\left(\frac{r_o}{r_i}\right)}. \end{aligned} \quad (66)$$

Solving Eq. 66 for \tilde{G} gives Eq. 65. Hence, the result derived in Komperød et al. (2015) yields the exact same identification of bitumen's viscoelastic properties as the approximation for small $|\tilde{Q}L|$ which is derived in Section 5.5. In other words: The result of Komperød et al. (2015) may be used for identification of bitumen's viscoelastic properties if and only if Eq. 46 is a good approximation of Eq. 42. It is then of interest to understand when this approximation is good. Eq. 46 can be rewritten to

$$\frac{\tilde{H}L}{EA} = (\tilde{Q}L)^2, \quad (67)$$

which gives

$$\tilde{Q}L = \pm \sqrt{\frac{\tilde{H}L}{EA}}. \quad (68)$$

Note that the right hand side of Eq. 68 can be calculated from logged timeseries of sensor measurements and known parameters. The approximation of Section 5.5 is based on a first order Maclaurin approximation of $\tanh(\tilde{Q}L)$, i.e.

$$\tanh(\tilde{Q}L) \approx \tilde{Q}L. \quad (69)$$

Hence, the accuracy of the result from Komperød et al. (2015) can be evaluated by calculating $\tilde{Q}L$ from Eq. 68, and then comparing the right hand side of Eq. 69 with the left hand side. If the difference is small, then the formula of Komperød et al. (2015) can be used to identify bitumen's viscoelastic properties, otherwise Eq. 42 of the present paper should be used. The analyst must then make a judgment of what is sufficiently small difference to use the result of Komperød et al. (2015).

From Eq. 65 it is seen that when the approximation of Eq. 69 is used, \tilde{G} and \tilde{H} are related through a real constant. Hence, bitumen's shear stress amplitude to shear strain amplitude ratio, G^* , is proportional to the rod's axial force amplitude to axial displacement amplitude ratio, $|\tilde{H}|$. Further, the phase shift between bitumen's shear stress and shear strain, φ , is equal to the phase shift between the rod's axial force and axial displacement, $\arg(\tilde{H})$.

Please note that the length of the cylinder, L , strongly influences whether the results from Komperød et al. (2015) can be used or not. For a given value of \tilde{Q} , the approximation of Eq. 69 is more accurate for a smaller value of L . In other words: Using a shorter cylinder is beneficial in the sense that the results of Komperød et al. (2015) can be used for lower bitumen temperatures. Increasing the rod's axial stiffness, EA , has the same desired effect: It is seen from Eq. 24 that increasing EA decreases $|\tilde{Q}|$. Increasing the ratio $\frac{r_o}{r_i}$ also has this benefit.

The rod's axial stiffness, EA , is not included in Eq. 65. However, EA is required in Eq. 68 for evaluating whether Eq. 65 can be used or not.

7.2 Behavior of Approximation for Large $|\tilde{Q}L|$

As derived in Section 5.6, the approximation of Eq. 60 and Eq. 61 is valid for large $|\tilde{Q}L|$. Inserting Eq. 24 into Eq. 61 gives

$$\frac{2\pi\tilde{G}}{EA \ln\left(\frac{r_o}{r_i}\right)} = \frac{\tilde{H}^2}{(EA)^2}, \quad (70)$$

$$\tilde{G} = \frac{\ln\left(\frac{r_o}{r_i}\right)}{2\pi EA} \tilde{H}^2. \quad (71)$$

That is, \tilde{G} is proportional to \tilde{H}^2 . This means that the identified bitumen shear stress amplitude to shear strain amplitude ratio, G^* , is proportional to the square of the rod's axial force amplitude to axial displacement amplitude ratio, $|\tilde{H}|$. Further, the identified phase shift between bitumen's shear stress and shear strain, φ , is twice the phase shift between the force and the displacement, $\arg(\tilde{H})$. This behavior is different from the behavior at low $|\tilde{Q}L|$ as explained in Section 7.1. However, this difference was expected from comparison of the dashed and dotted curves of Figures 5 and 6.

8 Further Work

The present paper derives an improvement in identification in bitumen's viscoelastic properties. When these properties are identified for a sufficient range of shear strain amplitude, shear strain frequency, and bitumen temperature, the properties will be included in first principle models of the mechanical properties of subsea cables and umbilicals.

9 Conclusion

This paper derives an improved mathematical model for how to identify bitumen's viscoelastic properties from the laboratory instrument illustrated in Figure 2. The improvement compared to the model of Komperød et al. (2015) is that the axial strain of the rod is included in the derivation. This improvement is important when identifying bitumen's viscoelastic properties at low temperatures.

The main result of the present paper is a nonlinear equation in one complex variable that relates bitumen's viscoelastic properties to the sensor measurements of the laboratory instrument. Under certain conditions, approximations of this equation can be used, which makes it trivial to obtain explicit expressions for bitumen's viscoelastic properties. The nonlinear equation, as well as the approximations, are illustrated using conformal mapping. The solutions based on the approximations can be used as initial values if solving the nonlinear equation numerically.

It is proved mathematically that one of the approximations is identical to the model of Komperød et al. (2015). It is also established a mathematical criterion for when this result can be used.

The final purpose of identifying bitumen's viscoelastic properties is to include these properties in models of subsea cables' and umbilicals' mechanical properties.

References

- M. Caire. Flexible riser bending hysteresis influence on bend stiffener response. In *Proceedings of the ASME 33rd International Conference on Ocean, Offshore and Arctic Engineering OMAE 2014*, 2014.
- J. J. Féret and C. L. Bournazel. Calculation of stresses and slip in structural layers of unbonded flexible pipes. *Journal of Offshore Mechanics and Arctic Engineering*, 109:263 – 269, 1987.
- J. Hedlund. Modelling of viscoelastic dynamic bending stiffness for VIV analysis of submarine cables. In *Proceedings of the 9th International Conference on Insulated Power Cables (Jicable '15)*, 2015.
- M. Komperød, B. Konradsen, and R. Slora. Viscoelastic large strain model of bitumen used for corrosion protection in subsea cables and umbilicals. In *Proceedings of the ASME 2015 34th International Conference on Ocean, Offshore and Arctic Engineering OMAE 2015*, 2015.
- B. Konradsen and S. V. Ouren. Modeling the effects of temperature and frequency on bitumen-coated helical cable elements. In *Proceedings of the 55th Conference on Simulation and Modelling (SIMS 2014) - Aalborg, Denmark*, 2014.
- E. Kreyszig. *Advanced engineering mathematics - 10th edition*. John Wiley & Sons, Inc., 2011.
- P. Maioli. Bending stiffness of submarine cables. In *Proceedings of the 9th International Conference on Insulated Power Cables (Jicable '15)*, 2015.
- J. Mullins, D. Morin, A. Tyrberg, C. Sonesson, and J. Ekh. Bitumen shear mechanics in a dynamic subsea electrical cable. In *Proceedings of the ASME 2015 34th International Conference on Ocean, Offshore and Arctic Engineering OMAE 2015*, 2015.
- E. Olsen, K. A. Hansen-Zahl, and S. Karlsen. Viscoelastic behaviour of bitumen in dynamic control umbilicals. In *Proceedings of the ASME 33rd International Conference on Ocean, Offshore and Arctic Engineering OMAE 2014*, 2014.
- H. See. Advances in measuring linear viscoelastic properties using novel deformation geometries and Fourier transform techniques. *Korea-Australia Rheology Journal*, 13(2):67–81, 2001.
- J. Tarnowski. Improved method of determining bending stiffness of underground cables. In *Proceedings of the 9th International Conference on Insulated Power Cables (Jicable '15)*, 2015.

Simulation as a Tool for Evaluating Biogas Purification Processes

Markku Ohenoja¹ Aki Sorsa¹

¹Control Engineering, Department of Technology, University of Oulu, Finland, `forename.lastname@oulu.fi`

Abstract

Biogas is an interesting fuel for the decentralized energy production as it can originate from many different sources. The purification of biogas to the point where it can also be used as a substitute for natural gas requires several purification steps. This paper focuses on the separation of carbon dioxide. A common solver using the discretized Gauss-Seidel method was applied for three different biogas purification process models describing MEA absorption, pressurized water scrubbing and multistage membrane separation. Simulations based on experimental designs were conducted in order to evaluate the applicability of those purification processes for different sources of biogas. The models used were rather simplified descriptions of the processes aimed to describe the directions of the changes in a general manner and to indicate the controllability of the processes.

Keywords: CO_2 separation, Steady-state mass balance, Discretized Gauss-Seidel method, Full factorial design

1 Introduction

The search for more efficient and environmentally friendly energy sources is a continuously treated topic in politics, marketing, business and, of course, in science. It is naive to expect that science finds one groundbreaking technique to decrease the dependency on fossil fuels. More probably a large number of feasible solutions for clean and efficient energy production will be used in parallel. This means that there would be a growing interest also on energy production in different scales. Biogas (biomethane) is a particularly interesting option: It can be collected as a landfill gas or be produced by anaerobic digestion from many different feed stocks regarded as a waste material, such as wastewater sludge, industrial by-products, manure and food residue. Biogas production is sizable and the product is storable and therefore it can be produced in various different locations and in many different scales. It also has a high number of possible end-users as it is suitable for transport fuel, heat production and combined heat and power production. Potentially, 50% of the present natural gas consumption in the EU could be replaced by biogas within the five next years (Wellinger et al. 2013).

The composition of biogas varies according to its source. It includes impurities among methane and thus

purification is needed in order to use biogas as a substitute for natural gas. The efficiency of this upgrading is significant to gain environmental benefits compared with fossil fuels. The purified biogas must have high enough methane content while the energy consumption must stay at low enough levels. This is a challenging task not only because of the number of impurities present but also because of the changes in inlet biogas composition. Furthermore, the planned way of usage may set tight requirements for the produced biogas.

Biogas purification may require a separation of large number of impurities including e.g. carbon dioxide, nitrogen, oxygen, hydrogen sulphide, ammonia and siloxanes (Wellinger et al. 2013). The purification process should therefore require a combination of methods such as absorption, adsorption, molecular sieves, membrane separation, condensation, cryogenics or ultrasonic separation. The purification steps needed depend on the composition of the inlet biogas and must be able to satisfy the criteria set for the produced gas. Designing such a purification scheme is a complex task where simulation offers valuable tools for evaluating and comparing different alternatives. However, the simulators must give realistic results and must be able to evaluate process performance and energy consumption in order to gain knowledge of proper processing schemes.

This paper concentrates on CO_2 separation where pressurized water scrubbing, chemical absorption, membrane separation and pressure swing adsorption are currently the most economically feasible methods. Mechanistic models of the three first purification processes are given in this paper. Also the energy consumption is approximated. Simulations using the discretized Gauss-Seidel solver are carried out with the models in order to evaluate their applicability for different sources of biogas. Through simulations, the sensitivity of the processes is evaluated to gain knowledge of the effects of certain disturbance and design variables on energy consumption and process behavior. The models used are rather simplified descriptions of the processes as they are expected to give the directions of the changes in a general manner and indicate the controllability of the processes. More detailed models are presented in literature. For example, (Scholz 2013) presents a membrane model incorporating a number of non-ideal effects and (Kucka et al. 2003) provide a rigorous rate-based model for

carbon capture with chemical absorption including tens of thousands of equations.

2 Modeling

Three processes for CO₂ bulk separation from biogas are considered: pressurized water scrubbing, chemical absorption with monoethanolamine (MEA) and membrane separation. The two former ones rely on the same model structure.

2.1 Absorption model

The absorption model incorporates the steady-state mass balance equations for the gas and liquid phase components that have a gradient along the absorption column height. In the gas phase, the mass transfer is negative as material is absorbed into the liquid phase. In liquid phase, there can be positive mass transfer due to absorption but also loss of material due to chemical reaction. The absorption rate N_i , [mol/m³·s] for component i can be written as:

$$N_i = K_i(C_{L,i}^{if} - C_{L,i}^{bulk}) \quad (1)$$

where K_i is the overall volumetric mass transfer coefficient (1/s), $C_{L,i}^{if}$ is the concentration (mol/m³) of component i at the vapor-liquid equilibrium (VLE) and $C_{L,i}^{bulk}$ is the concentration of component i at the bulk liquid. The equilibrium state (interface concentration) is approximated using Henry's law:

$$p_{G,i}^{if} = p_{G,i}^{bulk} = H_i C_{L,i}^{if} \quad (2)$$

where H_i is the Henry's law coefficient (Pa·m³/mol). The coefficients were taken from Greer (2008) and Mohebbi et al. (2012):

$$\begin{aligned} H_{CO_2}^{MEA} &= x_{MEA} \exp(170.7126 \\ &\quad - 8477.771/T_L \\ &\quad - 21.95743 \log(T_L) \\ &\quad + 0.005781T_L) \\ H_{CO_2}^{H_2O} &= x_{H_2O} \exp(89.452 - 2934.6/T_L \\ &\quad - 11.592 \log(T_L) \\ &\quad + 0.01644T_L) \\ H_{CH_4}^{H_2O} &= \exp(-7.037 + 0.1017T_L \\ &\quad - 0.0001426T_L^2 \\ &\quad + 100P/(83.15T_L)) \end{aligned} \quad (3)$$

The above-mentioned coefficients need to be divided by the total liquid concentration in order to get the SI-units Pa·m³/mol used in the model above-mentioned.

The overall volumetric mass transfer coefficient is an experimental constant that is related to the individual film mass transfer coefficients in the gas phase and liquid phase and the gas-liquid effective interfacial area. Here it is assumed that the overall mass transfer coefficient incorporates the specific interfacial area and that the coefficient is given in the form applicable to the concentration gradient. The chemical reaction has a positive effect on mass transfer and an enhancement

factor E is introduced to the mass transfer coefficient. The enhancement factor is the ratio between the mass transfer coefficient for chemical absorption and the mass transfer coefficient of physical absorption. The calculation of the enhancement factor requires the knowledge of chemical properties such as diffusivity and is also affected by the chemical reaction kinetics. In our case, the enhancement factor is assumed pre-known and constant throughout the column. The relationship between the enhancement factor and the mass transfer coefficients is given by:

$$K_{i,chemical} = E \cdot K_{i,physical} \quad (4)$$

It is assumed that the liquid phase is dilute i.e. no significant change in total liquid flow rate in the column take place. Also the inert gas molar flow rates are naturally constant. It is further assumed that all of the absorbed amount of component i reacts immediately in the chemical absorption. Therefore no accumulation occurs in the liquid phase for that component, i.e. $C_{L,i}^{bulk}$ is zero in chemical absorption. The balance equations in terms of molar flows (mol/s) for component i in gas phase $n_{G,i}$ and liquid phase $n_{L,i}$ can now be written as:

$$\begin{aligned} \frac{1}{A_c} \frac{dn_{G,i}}{dz} &= -N_i \\ \frac{1}{A_c} \frac{dn_{L,i}}{dz} &= \alpha_{ji} N_i \end{aligned} \quad (5)$$

where A_c is the cross-sectional area of the column, α is the stoichiometric factor of the reaction in chemical absorption and z is the distance from the bottom of the column.

2.2 Membrane model

The gas separation membrane model consists of steady-state mass balance equations for the retentate (feed) and permeate sides. The mass transfer is described with the solution-diffusion model. It is assumed that the system is isothermic and there is no pressure gradient along the membrane length. It is further assumed that there are no interactions between the permeance of different components in the system. The molar flux through the membrane N_i , [mol/m²·s] can be described as:

$$N_i = Q_i(p_{R,i} - p_{P,i}) \quad (6)$$

where Q_i , [mol/m²·h·bar] is the permeance of component i and $p_{R,i}$ and $p_{P,i}$ are the partial pressures of component i in the retentate side and permeate side, respectively. The mass transfer exchange area A in the membrane is equal to the surface area of the membrane multiplied by the number of fibers nof in the membrane system given by:

$$A = nof \cdot 2\pi r \cdot L = nof \cdot \pi d \cdot L \quad (7)$$

where r and d are the radius and the diameter of a single fiber and L is the length of the fiber. The discretized mass balance in terms of molar flows of component i in the retentate and permeate side can be written as:

$$\begin{aligned} \frac{dn_{R,i}}{dz} &= -N_i A = \text{nof} \cdot Q_i (p_{P,i} - p_{R,i}) \cdot \pi d \\ \frac{dn_{P,i}}{dz} &= N_i A = \text{nof} \cdot Q_i (p_{R,i} - p_{P,i}) \cdot \pi d \end{aligned} \quad (8)$$

The membrane is assumed to be operated in counter-current mode that usually is preferred as it increases the driving force. The model uses the permeance values given in $\text{mol}/\text{m}^2 \cdot \text{h} \cdot \text{bar}$. However, the permeances are often given in different units, such as GPU or $\text{m}^3/\text{m}^2 \cdot \text{h} \cdot \text{bar}$. Therefore, the following equations need to be applied:

$$\begin{aligned} Q_i[\text{m}_{STP}^3/\text{m}^2 \cdot \text{h} \cdot \text{bar}] &= 2.7 \cdot 10^{-3} Q_i[\text{GPU}] \\ Q_i[\text{mol}/\text{m}^2 \cdot \text{h} \cdot \text{bar}] &= \frac{P_{STP}}{T_{STP} R} Q_i[\text{m}_{STP}^3/\text{m}^2 \cdot \text{h} \cdot \text{bar}] \end{aligned} \quad (9)$$

where $P_{STP} = 1 \cdot 10^5 \text{ Pa}$, $T_{STP} = 273.15 \text{ K}$ and $R = 8.314 \text{ Pa} \cdot \text{m}^3/\text{mol} \cdot \text{K}$.

The multistage membrane system modelled has two stages with permeate recycling from the second membrane stage to the feed. First, the second membrane molar flows are solved and the results are iterated until they meet the molar flows leaving the first membrane.

2.3 Numerical algorithm

The discretized model equations were solved with a finite difference Gauss-Seidel method (Makaruk & Harasek, 2009). In this method, the half-step and full-step operations are calculated for each discrete point and the gradients are extrapolated using a relaxation factor. The results are then iterated until a pre-defined convergence criterion is fulfilled (or maximum number of iterations are performed). Hence the numerical algorithm has three adjustable parameters: the number of discrete elements, a relaxation factor and a convergence criterion.

2.4 Energy requirement calculations

In order to estimate the energy consumption of the modelled separation processes, models for the energy consumption of a compressor, a pump and a reboiler are presented. The energy consumption of water scrubbing is dependent on the amount of washing liquid pumped, whereas the energy consumption of chemical absorption mainly depends on the reboiler duty required in the regeneration stage. The energy consumption of membrane process is related to the operation pressure of the system. In all processes, additional compression may be required to bring the purified gas to pre-required system pressure.

The compressor model uses the compressor shaft power equation given in (Hall 2012). A motor efficiency of 0.75 is assumed. The pump model is the equation used for the recirculation pump of an absorption column in (Scholz 2013). The simulations assume an overall efficiency of 0.75. The reboiler model adopted from (Scholz 2013) assumes that the heat duty is proportional to the mass flow of absorbed component entering the desorption stage and the heat of reverse reaction

between the absorbed component and MEA. The molar flow of MEA was estimated from the consumption of MEA in the process.

2.5 Model validation

The models were validated against several literature results. The validation results, however, are not presented here in detail due to limited space.

The membrane model was validated against a two-component system described in (Scholz 2013), a three-component system presented in (Harlacher et al. 2012), a three-component system taken from (Makaruk & Harasek 2009) and a multistage membrane system described in (Makaruk et al. 2010). In general, all the results were reproduced with good accuracy taking into account that our model does not incorporate a pressure drop and there were some uncertainties in the simulation parameters.

The absorption model was used to represent the results from pressurized water scrubbing in (Nock et al. 2014), chemical absorption of CO_2 with MEA in (Khan et al. 2011) and (Kasikamphaiboon et al. 2013) and chemical absorption of CO_2 with AMP in (Gabrielsen et al. 2006). The validation showed that the absorption column model applied provides results with an adequate agreement to the results presented in literature both in physical absorption and chemical absorption. There were some discrepancies in the concentration profiles along the column height, but the outlet concentrations were in a good agreement. Naturally the assumptions of constant temperature and pressure along the column height restricts the accuracy of the simulation results.

The simple energy consumption calculations produce the same order of energy consumption for the three processes as in (Ferreira et al. 2014). The comparison showed, however, that both the energy consumption of water scrubbing and chemical absorption are underestimated in our simulations.

3 Results and discussion

Two simulation campaigns following experimental designs were conducted. The first one incorporated selected process design and operational parameters. The second one tested the sensitivity of solver parameters. Matlab[®] was used to perform the simulations.

3.1 Process parameters

The aim of the experimental design and simulations was to demonstrate the sensitivity of some process parameters to the operation of different biogas purification processes. A biogas upgrading plant with a nominal feed flow of $1000 \text{ m}^3/\text{h}$ and a target methane purity $>95 \%$ were assumed. A full factorial design (Diamond 1981) with two levels for five parameters was executed, producing a total amount of 32 experiments. The experimental design was applied for each of the three upgrading processes. The nominal simulation

parameters and the manipulated variables (MV) are listed in Table 1 and Table 2, respectively. For the absorption processes, the high levels for liquid flow rate and gas flow rate are 15 % higher than the nominal ones. For the chemical absorption, MEA concentration was altered instead of operation pressure. For the multistage membrane separation, membrane selectivity and area ratio were manipulated instead of operation temperature and liquid flow rate.

The output variables observed were biomethane production rate (PR), methane purity (MP) and specific energy consumption (SEC) with respect to treated biogas. In addition, a performance index presented in (Nock et al. 2014) was used:

$$PI = \frac{1 - \frac{y_{CH_4}^{out}}{y_{CH_4}^{in}}}{1 - \frac{y_{CH_4}^{out}}{100}} \quad (10)$$

where $y_{CH_4}^{out}$ and $y_{CH_4}^{in}$ are gas molar fractions of CH₄ in outlet and inlet, respectively.

Figures 1-3 show the most important findings in a boxplot graphs. In a boxplot graph, the red line inside the box represents the median value of the output

variable (indicated in the y-axis) during the experiments with the level of the manipulated variable indicated in the x-axis. There is a statistically significant difference (with 95 % confidence) between the two levels of manipulated variable in the experimental design if notches around the two median values do not overlap.

For the water scrubbing (Figure 1), manipulated variables causing statistically significant changes in the output variables are feed flow rate, temperature and liquid flow rate. The increment in the liquid flow rate increases the specific energy consumption. This can be expected as more water requires more pumping. Decreasing the temperature has a positive effect on the performance index and methane purity. This phenomenon is due to higher solubility in low temperatures. Increasing the feed flow rate decreases the performance index and methane purity. However, it also decreases the specific energy consumption and naturally increases the production rate. The performance index and methane purity decrease since the increment in feed flow causes that the area of the mass transfer and the liquid flow with respect to the gas flow decrease. Among the tested manipulated variables, three combinations resulted in methane purity less than 95 %.

Table 1. Simulation parameters.

	WATER SCRUBBING	CHEMICAL ABSORPTION	MEMBRANE SEPARATION
Column/fiber height/length, L	11.0 m	8.1 m	0.38 m
Column/fiber diameter, d	1.06 m	0.355 m	0.000398 m
Gas flow, V_G	1000 m ³ /h	1000 m ³ /h	1000 m ³ /h
CO₂ fraction, y_{CO2}	0.4	0.4	0.4
Liquid flow, V_L	145 m ³ /h	7.8 m ³ /h	Number of fibers 3000000
MEA/AMP concentration, C_{L,i}	n.a.	5000 mol/m ³	Area ratio 10
Operation temperature, T	25 °C	25 °C	25 °C
Operation pressure, P	9 bar	1 bar	10 bar
Final pressure	16 bar	16 bar	16 bar
Mass transfer coefficient of CO₂, K_{CO2}	0.0627 1/s	0.0627 1/s	Permeance of CO₂, Q_{CO2} 11.89 mol/m ² /h/bar
Mass transfer coefficient of CH₄, K_{CH4}	0.0609 1/s	n.a.	Permeance of CH₄, Q_{CH4} 0.24 mol/m ² /h/bar
Enhancement factor, E	1	150	n.a.
Compressor/pump efficiency	0.75	0.75	0.75
Discrete points, NoD	100	100	200
Relaxation factor, RF	0.4	0.05	0.4
Convergence criterion, CC	10 ⁻⁵	10 ⁻⁹	10 ⁻⁵

Table 2. Manipulated variables in experimental design.

	WATER SCRUBBING	CHEMICAL ABSORPTION	MEMBRANE SEPARATION
MV1	Feed flow (m ³ /h) 1=1000, 2=1150	Feed flow (m ³ /h) 1=1000, 2=1150	Feed flow (m ³ /h) 1=1000, 2=1150
MV2	CO ₂ feed mole fraction 1=0.35, 2=0.40	CO ₂ feed mole fraction 1=0.35, 2=0.40	CO ₂ feed mole fraction 1=0.35, 2=0.40
MV3	Operation pressure 1=9 bar, 2=10 bar	MEA concentration 1=4.5, 2=5 kmol/m ³	Operation pressure 1=10 bar, 2=12 bar
MV4	Operation temperature 1=20 °C, 2=25 °C	Operation temperature 1=20 °C, 2=25 °C	Membrane selectivity 1=40, 2=50 (CO ₂ /CH ₄)
MV5	Liquid flow (m ³ /h) 1=145, 2=166.75	Liquid flow (m ³ /h) 1=7.8, 2=8.97	Membrane area ratio 1=1, 2=10 (A2/A1)

In chemical absorption (see Figure 2), feed flow rate, CO₂ molar fraction and MEA concentration causes statistically significant changes to the output variables. The performance index decreases strongly by increasing the feed flow rate, but changes observed in the methane purity are less sensitive to the feed flow rate. Naturally the production rate is also affected by the feed flow rate. The CO₂ molar fraction has a strong effect on the specific energy consumption. This is due to the required reboiler duty that increases as the amount of CO₂ in the feed stream increases and more MEA need to be regenerated. The 15 % degradation in the MEA concentration has a similar effect on the performance index and methane purity than the 15 % increment in the feed flow rate. This can also be seen from the relative changes listed in Table 4. In chemical absorption, too low methane purity was observed in ten trials.

The membrane separation process shows sensitivity between the studied levels for operation pressure, feed flow rate and area ratio (Figure 3). Increasing the pressure increases the performance index and methane purity, increment in the feed flow rate increases the production rate and degradation of area ratio lowers the specific energy consumption considerably. The observations regarding operation pressure and feed flow rate are quite obvious. The last observation needs to be considered more closely. Increasing the area ratio while keeping the total membrane area constant means that the area of the first membrane decreases and the area of the second membrane increases. This leads to a situation where gas is mostly separated at the second stage. In the process structure used, permeate of the second stage is recycled to the first stage feed. Hence the total feed of the first stage membrane, as well as the amount of gas to be compressed into operation pressure, increases significantly. The results presented in (Makaruk et al. 2010) show the same effect, but also that the specific

compression power only increases when the area ratio is higher than 1. For the area ratios less than one (i.e. first stage membrane area is larger than second stage), the compression power remains constant. Notice that in (Makaruk et al. 2010), the specific compression power is calculated with respect to produced gas. Here the calculation was made with respect to treated biogas. There were two experiments, where the required methane purity was not achieved.

When only the feed conditions are considered, i.e. the changes in feed flow rate and CO₂ feed fraction, the membrane separation shows no sensitivity (if the production rate is neglected). Based on these observations, membrane separation might be suitable for processes with a varying feed flow and CO₂ feed fraction. In chemical absorption, the CO₂ feed fraction has a strong effect on specific energy consumption. The performance index and methane purity decrease as the feed flow rate increases. The results suggest that chemical absorption would be recommended for processes with a homogeneous feed flow rate and CO₂ feed fraction. Water scrubbing shows no statistically significant sensitivity to the CO₂ feed fraction. Therefore it might be suitable for biogas feed with varying feed CO₂ content. The simulations however show that some combination of parameters results in methane purity under 95 %. The 15 % change in the feed flow rate is seen in all recorder parameters, but the performance index and methane purity remain at a tolerable level. For the higher feed flow, the variation in the results is considerably higher. The specific energy consumption decreases as the feed flow rate increases. However, the comparison of literature data and simulated energy consumption of water scrubbing suggested that the energy consumption is underestimated here.

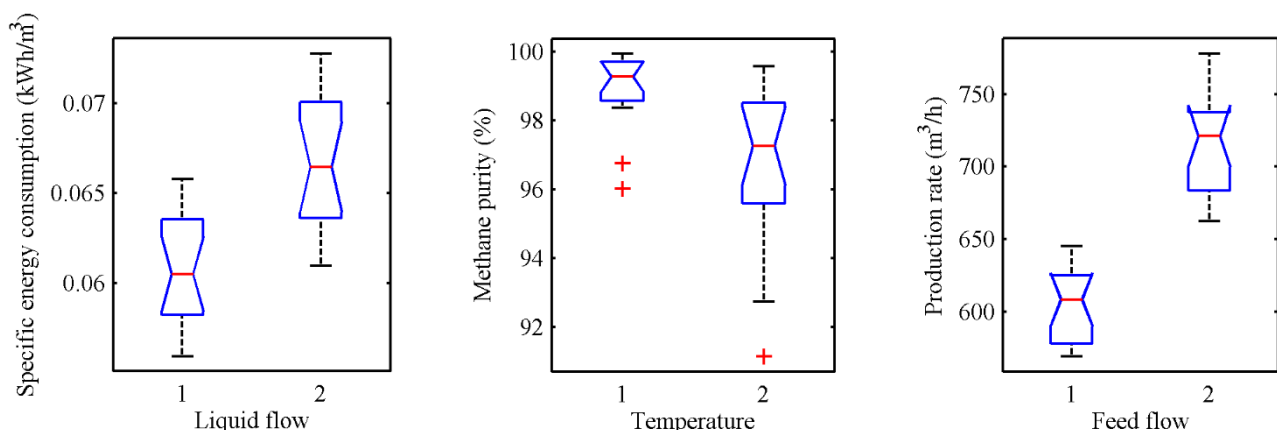


Figure 1. Selected boxplots from water scrubbing experiments.

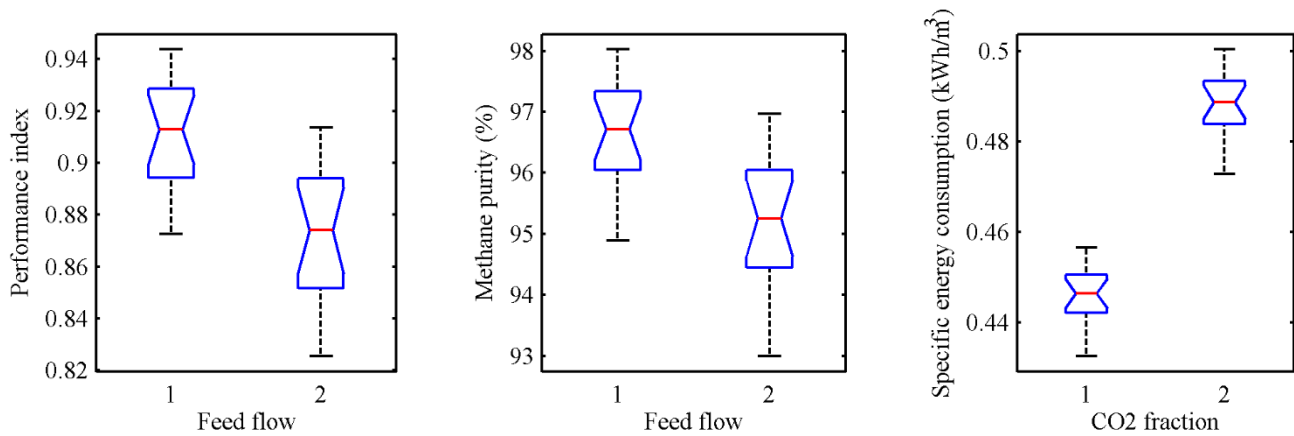


Figure 2. Selected boxplots from chemical absorption experiments.

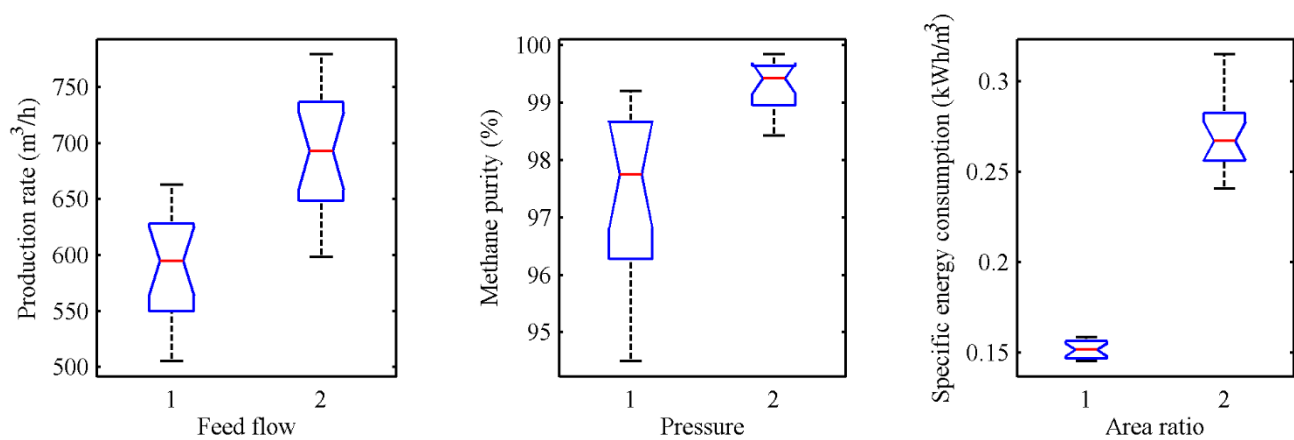


Figure 3. Selected boxplots from multistage membrane separation experiments.

Table 3. Manipulated solver parameter levels in experimental design.

	WATER SCRUBBING	CHEMICAL ABSORPTION	MEMBRANE SEPARATION
Number of discrete units (NoD)	1=75 2=100 3=150	1=75 2=100 3=150	1=150 2=200 3=300
Relaxation factor (RF)	1=0.3 2=0.4 3=0.5	1=0.04 2=0.05 3=0.06	1=0.3 2=0.4 3=0.5
Convergence criterion (CC)	1=5e-6 2=1e-5 3=5e-5	1=5e-10 2=1e-9 3=5e-9	1=5e-6 2=1e-5 3=5e-5

Table 4. Maximum relative change in the median during the experimental designs with respect to nominal results. The highlighted cells are the ones with statistically significant change.

		MV1	MV2	MV3	MV4	MV5	NoD	RF	CC
WS	PI	9.1 %	7.2 %	8.5 %	9.2 %	8.6 %	0.5 %	0 %	-0.1 %
	MP	3.5 %	2.9 %	3.3 %	3.5 %	3.3 %	0.2 %	0 %	-0 %
	PR	20.1 %	13.4 %	9.7 %	9.9 %	9.9 %	0.2 %	0 %	0 %
	SEC	8.1 %	4.6 %	5.9 %	3.7 %	8.1 %	0.1 %	0 %	0 %
CA	PI	-4.2 %	-2.4 %	-4.1 %	-3.8 %	-2.0 %	0 %	-7.3 %	0 %
	MP	-1.3 %	-0.9 %	-1.2 %	-1.1 %	0.4 %	0 %	-2.8 %	0 %
	PR	21.6 %	16.5 %	13.1 %	13.0 %	12.1 %	0 %	2.8 %	0 %
	SEC	-6.6 %	-9.6 %	-6.6 %	-6.5 %	-5.9 %	0 %	-3.2 %	0 %
MS	PI	2.7 %	2.2 %	3.2 %	2.2 %	2.4 %	-0.1 %	0.2 %	0 %
	MP	2.2 %	1.7 %	2.4 %	1.8 %	2.3 %	-0.1 %	0 %	0 %
	PR	13.0 %	7.8 %	6.1 %	5.0 %	10.4 %	0.1 %	-0 %	0 %
	SEC	-27.1 %	-27.1 %	-27.7 %	-27.5 %	-44.7 %	0.1 %	0.1 %	0 %

3.2 Solver parameters

The sensitivity of the results to the solver parameters was also tested. A full factorial design with three levels for the three adjustable parameters was simulated. The parameter levels are presented in Table 3. In Table 4, the results from both the process parameter experiments and the solver parameter experiments are listed as a maximum relative change in the median during the simulations. The results presented in Table 4 show that the relative changes in the observed output variables due to changes in the solver parameters are considerably lower with respect to changes caused by the manipulation of process parameters. The only exception is the relaxation factor in chemical absorption. These results suggest that the numerical algorithm is applicable to solving these type of problems once suitable solver parameters are found. The optimization of the solver parameters might only be necessary if the minimization of the CPU time is of interest.

4 Conclusions

Three potential CO₂ separation processes for biogas purification were modelled. Model parameters were scaled for 1000 m³/h biogas treatment and simulation campaign following an experimental design was conducted in order to see the sensitivity of the process behavior for some process disturbances and design parameters. The results show that the 15 % increment in the feed flow rate does not solely produce intolerable methane purity (<95 %) in any of the processes, indicating that each process retain some level of controllability. Multistage membrane separation and pressurized water scrubbing seem preferable for processes with varying biogas feed flow and CO₂ feed fraction. On the opposite, chemical absorption with MEA show more sensitivity to those parameters and is therefore more suitable for processes with rather constant feed conditions. The performance of the numerical algorithm was found to be good as the results did not show intolerable sensitivity to the parameters of the numerical algorithm.

Acknowledgements

This research was conducted during SmartH₂/CH₄-Oulu research project. ERDF(EAKR) and TEKES are gratefully thanked for enabling the project.

References

Diamond, W. *Practical experimental designs for engineers and scientists*, Van Nostrand Reinhold, New York, 1981, 0-534-97992-0.

Ferreira A., Ribeiro A., Kulaç S., Rodrigues A. (2014) Methane purification by adsorptive processes in MIL-53(AI), *Chemical Engineering Science*, 124, 79-95. doi:10.1016/j.ces.2014.06.014.

Gabrielsen J., Michelsen M., Stenby E., Kontogeorgis G. (2006) Modeling of CO₂ absorber using an AMP solution, *AIChE Journal*, 52(10), 3443-3451. doi:10.1002/aic.10963.

Greer T. 2008, *Modeling and simulation of post combustion CO₂ capturing*, M.Sc thesis, Telemark University College, Porsgrunn, Norway.

Hall S. (2012) *Branan's rules of thumb for chemical engineers*, 5th ed., Butterworth-Heinemann 2012, 978-0-12-387785-7.

Harlacher T., Scholz M., Melin T., Wessling M. (2012) Optimizing argon recovery: membrane separation of carbon monoxide at high concentrations via the water gas shift, *Industrial & Engineering Chemistry Research*, 51(38), 12463-12470. doi:10.1021/ie301485q.

Kasikamphaiboon P., Chungsiriporn J., Bunyakan C., Wiyaratn W. (2013) Simultaneous removal of CO₂ and H₂S using MEA solution in a packed bed column absorber for biogas upgrading, *Songklanakarinn Journal of Science and Technology*, 35(6), 683-591.

Khan F.M., Krishnamoorthi V., Mahmud T. (2011) Modelling reactive absorption of CO₂ in packed columns for post-combustion carbon capture applications, *Chemical Engineering Research and Design*, 89(9), 1600-1608. doi:10.1016/j.cherd.2010.09.020.

Kucka L., Müller I., Kenig E.Y., Górak A. (2003) On the modelling and simulation of sour gas absorption by aqueous amine solutions, *Chemical Engineering Science*, 58(16), 3571-3578. doi:10.1016/S0009-2509(03)00255-0.

Makaruk A., Harasek M., (2009) Numerical algorithm for modelling multicomponent multipermeator systems, *Journal of Membrane Science*, 344, 258-265. doi:10.1016/j.memsci.2009.08.013.

Makaruk A., Miltner M., Harasek M. (2010) Membrane biogas upgrading processes for the production of natural gas substitute, *Separation and Purification Technology*, 74(1), 83-92. doi:10.1016/j.seppur.2010.05.010.

Mohebbi V., Naderifar A., Behbahani R.M., Moshfeghian M. (2012) Determination of Henry's law constant of light hydrocarbon gases at low temperatures, *The Journal of Chemical Thermodynamics*, 51, 8-11. doi:10.1016/j.jct.2012.02.014.

Nock W., Walker M., Kapoor R., Heaven S. (2014) Modeling the Water Scrubbing Process and Energy Requirements for CO₂ Capture to Upgrade Biogas to Biomethane, *Industrial & Engineering Chemistry Research*, 53(32), 12783-12792. doi: 10.1021/ie501280p.

Scholz M. (2013) *Membrane based biogas upgrading processes*, Ph.D. dissertation, RWTH Aachen University, 2013.

Wellinger A., Murphy J., Baxter D. (eds.) *The Biogas Handbook: Science, Production and Applications*, Woodhead Publishing Limited 2013, 978-0-85709-498-8.

Computational Study of Heavy Oil Production with Inflow Control Devices

D.I Erandi N. Wijeratne Britt M. Halvorsen

Department of Process, Energy and Environmental Technology, Telemark University College,
N-3901 Porsgrunn, Norway,
erandinw@yahoo.com britt.halvorsen@hit.no

Abstract

Recovery of heavy oil is associated with challenges in terms of early water or gas breakthrough caused by the fingering phenomenon. This study is related to Californian heavy oil production and includes 2D simulations of heavy oil in horizontal wells with autonomous inflow control devices (AICDs). Simulations have been performed to study reservoir flow, annular flow and flow through the AICDs into the production pipe using ANSYS/Fluent as the Computational Fluid Dynamics (CFD) software. A model for heavy oil production has been developed and validated against experimental data in literature. Before breakthrough the results are quite realistic which can be theoretically justified. Higher pressure drop is observed near the well bore (or across AICD) as the finger growth takes place. According to the simulated results, oil production is highly affected by fingering behaviour, since it results early water breakthrough.

Keywords: Heavy oil reservoirs, fingering phenomenon, water breakthrough, oil production, CFD, multiphase flow

1 Introduction

Petroleum resources are one of the major drives of the industrial development. The petroleum industry uses various technologies to increase the recovery from the existing reservoirs and enhance the well performance. The importance of heavy oil production has increased due to the decrease in the large conventional oil reservoirs. Heavy oil represents a massive world resource more than twice the size of global reserves of light or conventional oil (Safwat, 2007). There are huge, well-known resources of heavy oil, extra-heavy oil, and bitumen in Canada, Venezuela, Russia, USA and many other countries (Clark, 2007). Recovery of heavy oil is a challenging task. Formation of finger-like patterns at the water-oil interface causes early water breakthrough, which affects the oil recovery.

The production trend of heavy and light oil in California is shown in Figure 1 (Annual report of the state oil and gas supervisor, 2008).

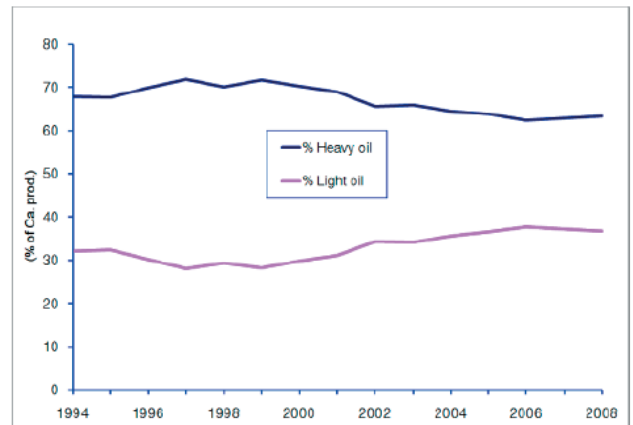


Figure 1. Heavy and light oil production in California (Annual report of the state oil and gas supervisor, 2008).

In addition to having large volumes of oil in place (OOIP), the typical California heavy oil reservoirs have favorable reservoir properties as shown in Table 1. This combination of abundant large heavy oil accumulations plus favorable reservoir properties led to California becoming the leader in U.S. heavy oil production. Challenges to the heavy oil industry include improving technology to increase the oil recovery in unusual reservoir matrices such as for example naturally fractured shales (Hanzlik, 1998).

Table 1. OOIP Weighted Median Values of California Heavy Oil Properties (Hanzlik, 1998).

Property	Value	Unit
Viscosity	100 - 10,000	cP
Porosity	0.30	-
Permeability	1400	mD
API Gravity	10 - 20	^o
Thickness	200	feet
Depth	2500	feet

A major challenge in oil production is to increase the ability to recover the oil that is in fact present in the reservoir. Estimates show that although the oil is localized and mobile, more than 50 percent of the oil is

remaining in the reservoir after shut down. Therefore there are strong incentives for developing technologies that can contribute in increasing the oil production and recovery. In order to increase oil production and recovery it is of great importance to obtain maximum reservoir contact (MRC) and prevent the negative effects of early gas or water breakthrough. Long horizontal wells and/or multi-lateral wells are used to obtain maximum reservoir contact and the use of horizontal drilling technology in oil exploration, development and production operations has grown rapidly over past years.

Horizontal wells are used in reservoirs where early gas or water breakthrough is a problem. They are used in high permeability heavy oil reservoirs, in low permeability gas reservoirs to increase the drainage volume, in reservoirs using thermal methods for oil recovery, in reservoirs with thin oil column and in reservoirs where water flooding is used (Joshi, 1994).

The concept of Inflow Control Device (ICD) was introduced in early 90s by Statoil researchers who observed that incremental increases in the length of horizontal wells did not create proportionately larger production rates. Further investigations revealed that this was due to the heel-toe effect (Daneshy, 2010). Different types of Inflow Control Devices are developed to delay early breakthrough by restricting the flow (Fernandes, 2009, Al-Khelaiwi, 2007). ICDs are designed to give a more uniform oil production along the horizontal well. The total oil recovery increases significantly with use of ICDs, but ICDs neither choke nor close for undesired fluids like water and gas after breakthrough has occurred.

Improvement of ICDs, Autonomous Inflow Control Devices (AICDs), are developed and the main advantage of AICDs compared to ICDs are that they choke for water and gas after breakthrough. AICDs can therefore be classified as 'smart' devices that are capable of changing their response depending on the properties of the inflowing fluid. Different types of AICDs are developed and the different principles are described in literature (Mathiesen et al., 2011; Halvorsen et al., 2012; Least et al., 2012; Aakre et al., 2013).

The objective of this paper is to make a transient computational study of fluid flow in the reservoir, fingering behavior and multiphase flow in pipe and annulus of a horizontal well with autonomous inflow control and packers. The study is related to California heavy oil reservoirs. The work focuses only on the AICD developed by Statoil ((Mathiesen et al., 2011; Halvorsen et al., 2012), and a function describing the functionality of this type of AICD is used in the simulations.

2 Computational study of annular flow and flow through AICDs

Computational studies of heavy oil production with water drive are performed. The simulations have been performed using ANSYS/Fluent as the Computational Fluid Dynamics (CFD) software (*ANSYS FLUENT 12.0 User's Guide*, 2009). Preliminary studies are performed and a model for heavy oil production has been developed and validated against experimental data (Wijerathne & Halvorsen, 2015). Volume of Fluid (VOF) is used as the multiphase model. The VOF model can be used to model two or more immiscible fluids by solving a single set of equations and tracking the volume fraction of each of the fluids throughout the domain. The tracking of the interface(s) between the phases is accomplished by the solution of a continuity equation for the volume fraction of one (or more) of the phases. Geo-Reconstruct is used as the VOF Scheme. This is assumed to be the most accurate interface tracking scheme, and is recommended for most transient VOF calculations. The displaced fluid is as the primary phase and displacing fluid is defined as the secondary phase. The effect of surface tension along the interface between two phases is included by defining the surface tension coefficient. Porous region is specified with the viscous resistance under cell zone conditions. Since the flow rate through the porous media is very low (laminar flow), Ergun equation can be simplified as:

$$\frac{\Delta p}{l} \approx \frac{V\mu}{\alpha} \quad (1)$$

V is average velocity of flow of the fluid [m/s], α is permeability of the porous medium [m²], μ is viscosity of the fluid [Pas], Δp is pressure drop across the porous bed [Pa] and l is thickness of the bed [m]. The viscous resistance coefficient ($1/\alpha$) is defined and the inertial resistance (the turbulent component) is set to be zero. PISO (Pressure Implicit with Splitting of Operators) scheme is used as the Pressure-Velocity Coupling method, the body-force-weighted scheme as pressure discretisation scheme and second order upwind method as momentum discretization scheme.

This study covers the two-dimensional transient simulation of reservoir flow, annular flow and flow through the AICDs into the production pipe. In order to study the annular flow the geometry of the reservoir is selected according to the Figure 2. The pipe length is taken as two sections of length 12.4 m each. The well is completed with two AICDs in each section. The geometry, dimensions and boundary conditions are shown in Figure 2. The AICDs to the left and right side in the figure are called AICD 1 and AICD 2 respectively.

The numerical grid is drawn using GAMBIT. The AICDs and reservoir zones are named separately as two porous sections in GAMBIT and the properties of the porous sections are specified in ANSYS/Fluent. The

created mesh is shown in Figure 3. The concentration of control volumes near the pipe is high. The sizes of the

cells near the pipe and in the rest of the reservoir are 0.05x0.01 m² and 0.05x0.05 m² respectively.

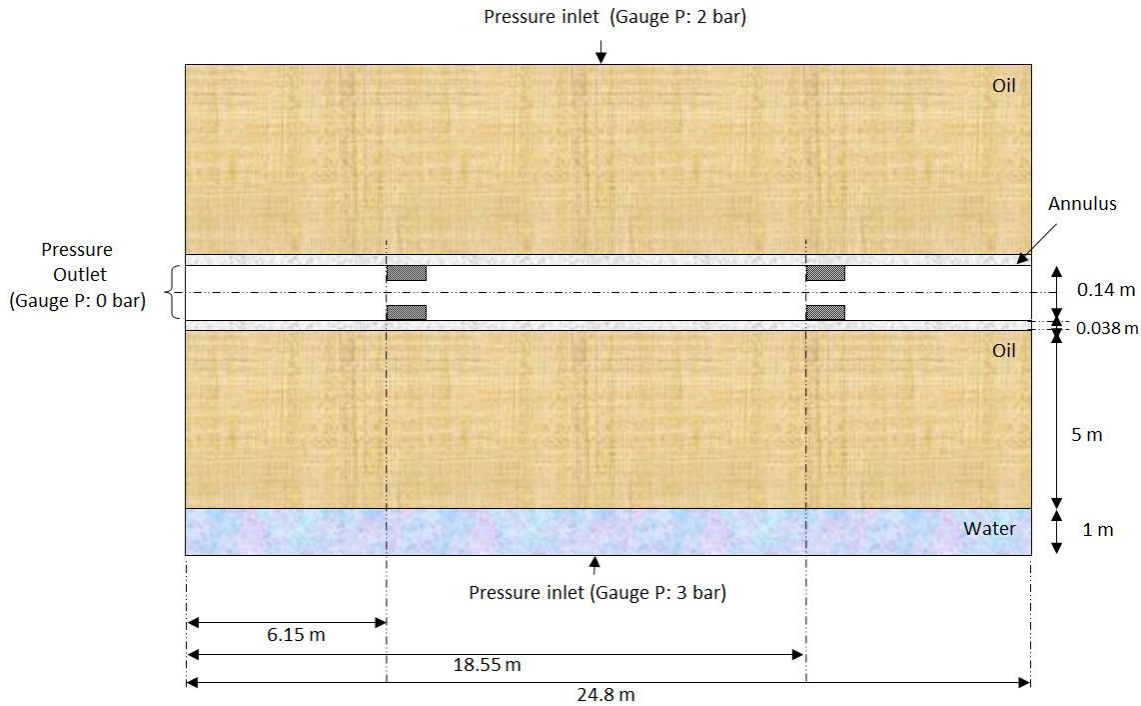


Figure 2. Geometry with the reservoir, production pipe, annulus, AICDs and boundary conditions.

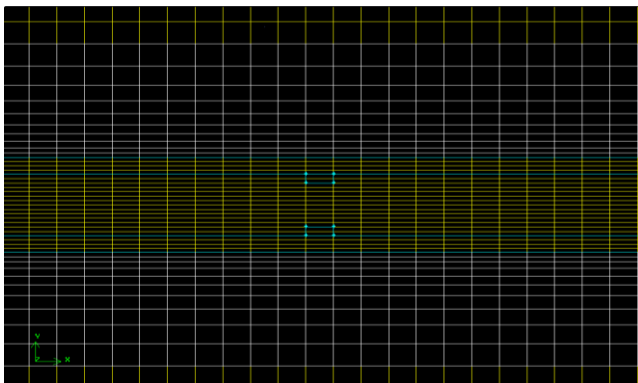


Figure 3. Enlarged view of mesh near the AICD.

2.1 ANSYS/Fluent Model

The reservoir properties used in the simulation are given in Table 2. The AICDs are modeled as porous regions and a power law model is describing the functionality of the valves according to Equation 2. The pressure-flow rate characteristics of the AICD is defined as below (Mathiesen et al., 2011):

$$dP = f(\rho, \mu) \cdot a_{AICD} \cdot q^x \quad (2)$$

dP is the differential pressure across the AICD, $f(\rho, \mu)$ is an analytic function of the mixture density and viscosity, a_{AICD} is a user-input 'strength' parameter, q is

a local volumetric mixture flow rate [m³/day] and x is a user-input constant.

Table 2. Reservoir and fluid properties.

Property Description	Property Value
Distance from the wellbore to the oil-water interface [m]	5.0
Water-oil interfacial tension [mN/m]	25
Width of drainage area [m]	10 x 2
Height of oil layer [m]	10
Height of water layer [m]	1.0
Wellbore diameter [m]	0.22
Length of one horizontal section [m]	12.4
Rock porosity [-]	0.3
Reservoir pressure [bar]	30
Well bore pressure [bar]	27
Water viscosity [cP]	0.5
Water density [kg/m ³]	1000
Oil viscosity [cP]	300
Oil density [kg/m ³]	920
Rock permeability [D]	3.0

The function $f(\rho, \mu)$ is presented in Equation 3.

$$f(\rho, \mu) = \left[\frac{\rho_{mix}^2}{\rho_{cal}} \right] \left[\frac{\mu_{cal}}{\mu_{mix}} \right]^y \quad (3)$$

ρ_{cal} and μ_{cal} are the calibration density and viscosity, properties of water typically, and y is a user-input constant. This implies that the pressure drop across AICD depends on a combination of the fluid properties and design variables. Constants used for the AICD valve function in this study are tuned based on data presented by Statoil (Mathiesen, 2011; Halvorsen, 2012) and are not exact. In the ANSYS Porous model (Flow Through Porous Media, 2007), the differential pressure per length is expressed as:

$$\frac{dP}{l} = C_0 |v|^{C_1} \quad (4)$$

Based on the tuned differential pressure calculated from Equation 2, the constants C_0 and C_1 for oil water and gas are estimated and used in the simulations. Figure 4 shows the theoretical performance curves for oil water and gas through the AICD. The curves show that the flow rate as a function of drawdown is much higher for viscous oil (300 cP) than for water and gas. This shows that the AICD is capable of choking for water and gas. The boundary conditions are set as shown in Figure 2. The numerical values of the boundary conditions are presented in Table 2.

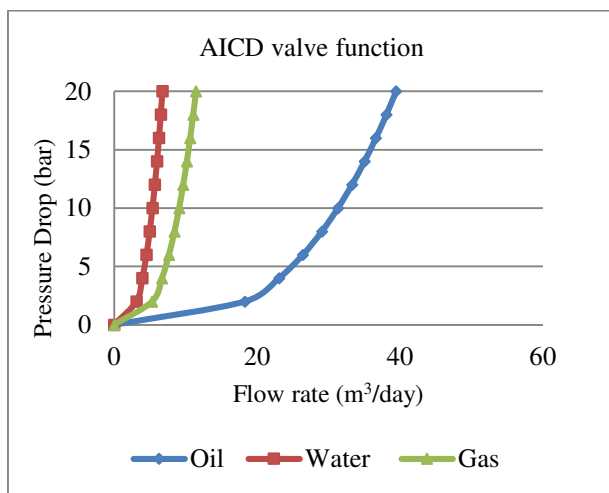


Figure 4. AICD valve function for oil, water and gas flow.

3 Results and Discussion

The velocity of the water/oil contact (WOC) just before any instability occurs is shown in Figure 5. The average velocity of the WOC is 7.07×10^{-7} m/s. The critical velocity U_C above which instabilities occur is calculated from:

$$U_C = \left(\frac{\rho_1 - \rho_2}{\mu_1 - \mu_2} \right) gK \quad (5)$$

K is the permeability, ρ the density and μ the viscosity. The critical velocity, U_C is calculated based on the fluid

properties and the permeability presented in Table 2. The critical velocity is 7.75×10^{-9} m/s (upwards). The average WOC velocity is higher than the critical velocity above which instabilities occurs, and this states that finger formation in the reservoir can be expected. Figure 6 shows the phase distribution, static pressure distribution and velocity vectors near the AICDs after short time of production, before the breakthrough. Initial fingering can be observed (a), the pressure decreases gradually towards the well (b) and the velocity profile has the direction towards the AICD in the annulus, and a typical laminar velocity profile in the pipeline (c). Figure 7 shows the pressure profile along the Y axis (vertical direction) through AICD 1 and 2 before breakthrough. The two curves have identical shape.

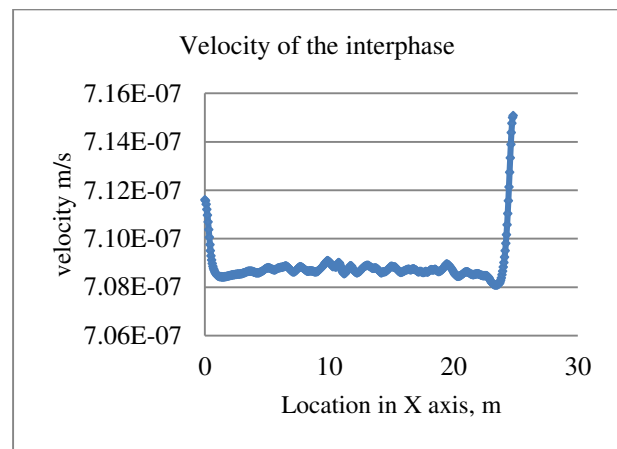


Figure 5. Velocity of WOC before fingers are formed

Figure 8a shows the contours of oil volume fraction at the time of breakthrough to the annular region and Figure 8b shows a closer view near the breakthrough location. Breakthrough to the annular region occurs after about 10.4 days. The effective interface is parallel to the production pipe, due to the negligible pressure drop in the short pipe. The long fingers at the two ends may not reflect the actual scenario, since these fingers are formed due to the high velocities observed in Figure 5.

There are few dominant fingers which have outstripped the adjacent fingers. They have mushroomed as a result of the lateral pressure gradients existing near the end of these fingers. The subsequent development of this mushrooming continues until the breakthrough to the annular space takes place. Between the water fingers, areas of residual oil are left without being influenced by the water flooding.

The resultant fingering pattern of the simulation shows the tendency of disintegrating the viscous fingers into bubbles. Some experimental data from literature showed that the tips of the fingers are spreading while the tails of the fingers are narrowing. The less viscous fluid has high velocities in these narrowing regions, which can ultimately cause the formation of a separated island of the less viscous fluid. This can also be due to interface tension

forces which try to minimize the surface area to achieve stability.

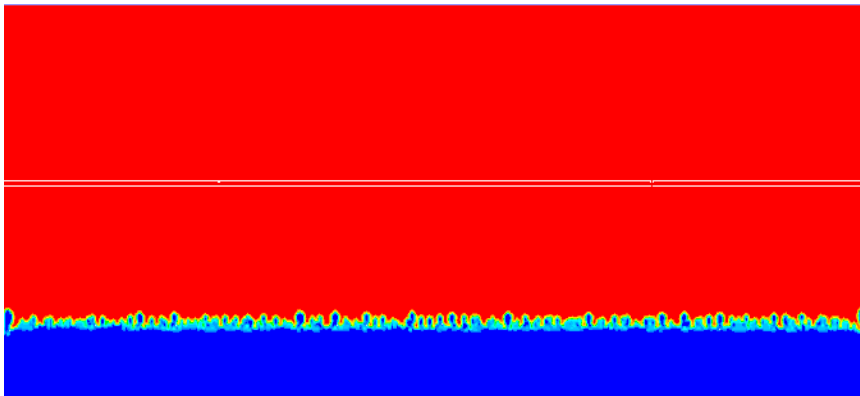


Figure 6(a). Phase distribution after short time of production. Blue indicates water and red indicates oil.

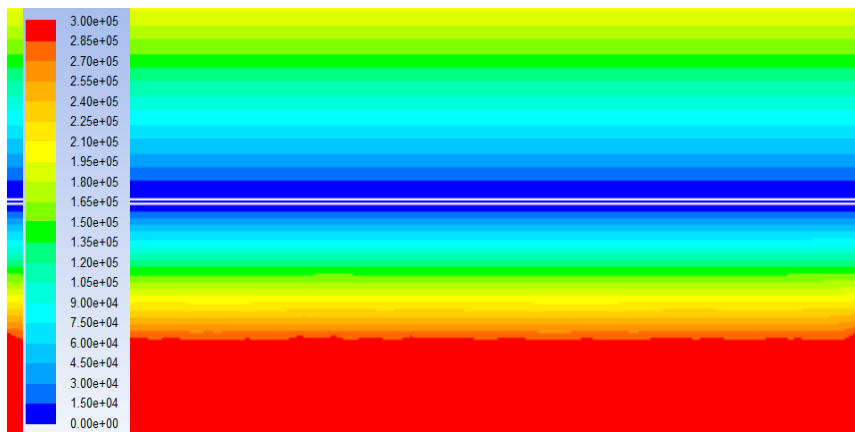


Figure 6(b). Static Pressure distribution after short time of production. Red is 3 bar gauge pressure and blue is 0 bar gauge pressure related to the well.

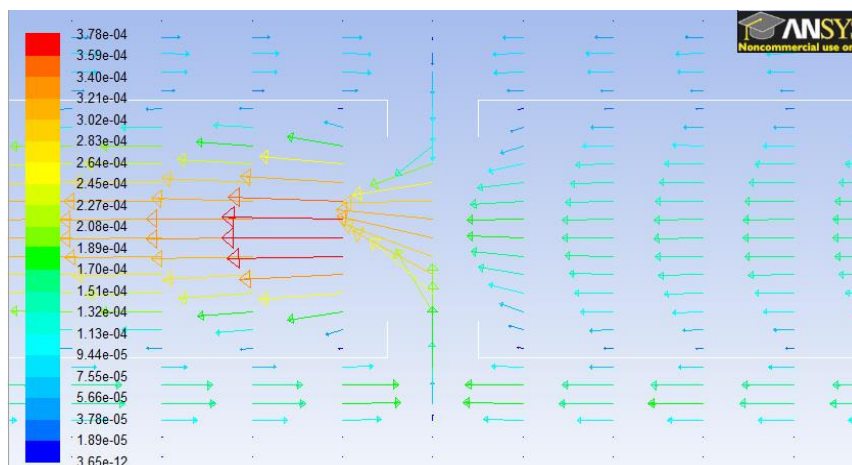


Figure 6(c) Velocity vectors near AICD after short time of production. The red arrows indicates higher velocity and the blue lower velocity. Range: $3.66 \cdot 10^{-12}$ to $3.76 \cdot 10^{-4}$ m/s.

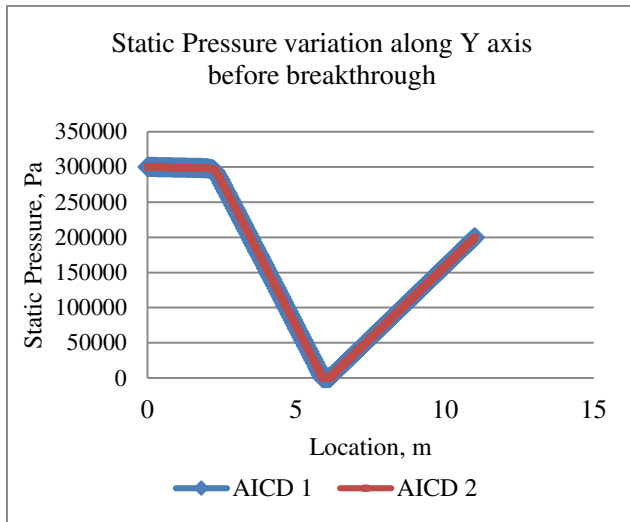


Figure 7. Static Pressure variation along the y axis through AICD 1 and 2 after short time of production (before breakthrough).

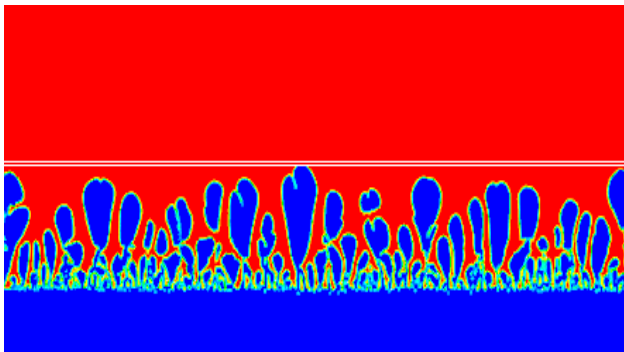


Figure 8(a). Phase distribution at the breakthrough. Blue and red represents water and oil respectively.

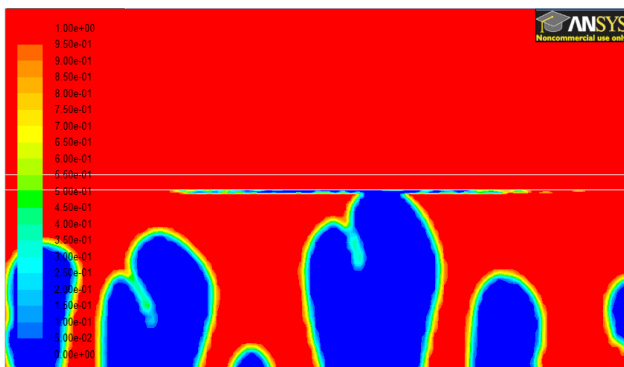


Figure 8(b). Closer view of finger at the breakthrough.

An additional simulation with a very fine numerical grid was carried out on a smaller part of the reservoir in order to check the grid size dependency on the fingering pattern. The resultant fingering pattern is shown in Figure 9. The fingers have better clear cut edges than the fingers observed in Figure 8. The fingers do not seem to disintegrate into bubbles, but narrowing points in the tail of the fingers are observed. The fingering pattern can be more complex under real reservoir

conditions due to heterogeneities of the rock, wetting and non-wetting characteristics of oil and water, initial and residual saturation conditions, the open pore volume available for flow and depletion of initial

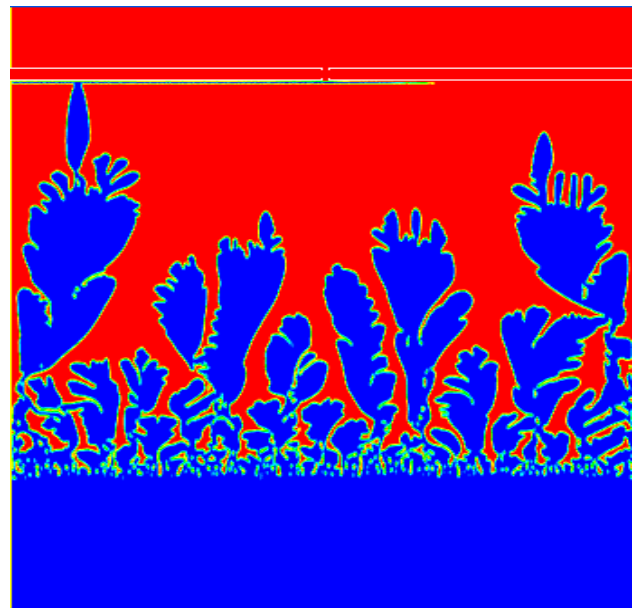


Figure 9. Fingering pattern caused by a very fine grid. Blue and red represents water and oil respectively.

reservoir conditions as production proceeds.

Figure 10 shows the contours of static pressure at the breakthrough. As the fingers develop towards the production pipe, the inlet pressure (colored in red) also develops in the same direction. At breakthrough, the pressure in the finger becomes approximately same as the pressure of the annular region.

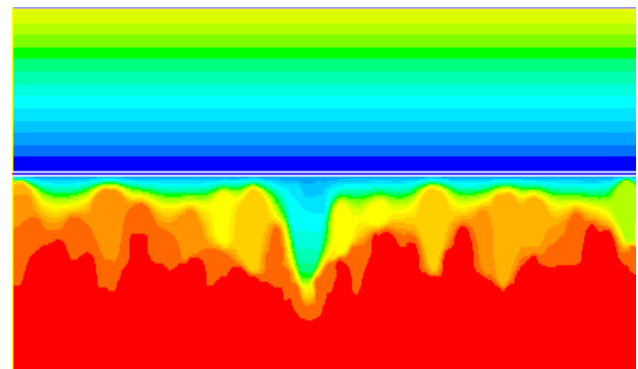


Figure 10. Static pressure distribution at the breakthrough. Pressure gauge range from 0bar (blue) to 3 bar (red).

Figure 11 shows the static pressure variation as a function of vertical position in the reservoir at breakthrough. It is clearly seen that the pressure gradient is very steep near the well bore due to the low pressure drop of water fingering through the reservoir. Comparing Figure 7 (static pressure before after short time of production) with the static pressure at breakthrough, it can be seen that the static pressure profile has changed significantly. This indicates that large

amounts of water can be produced in the breakthrough zone if inflow control is not used to restrict the flow. The change in static pressure profile only occurs below the well where the water layer approaches the pipe.

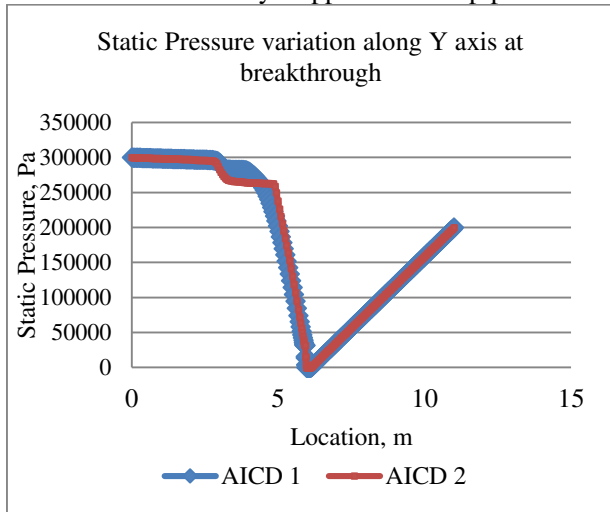


Figure 11. Static Pressure variation along Y axis through AICD 1 and 2 at breakthrough.

After the breakthrough, the simulation was run with maximum time step size 3-4 seconds and with Courant Number equals 70. Breakthrough to the pipe occurs after 10.5 days of production. Breakthrough occurs through the AICD 1 (water side). There is no flow restriction in the annular region compared to through the porous media. Figure 12 shows the breakthrough to the pipe via AICD 1. The white circles show the location of AICDs. The breakthrough occurs after short time through AICD 2 as well due to the unrestricted flow through the annulus.

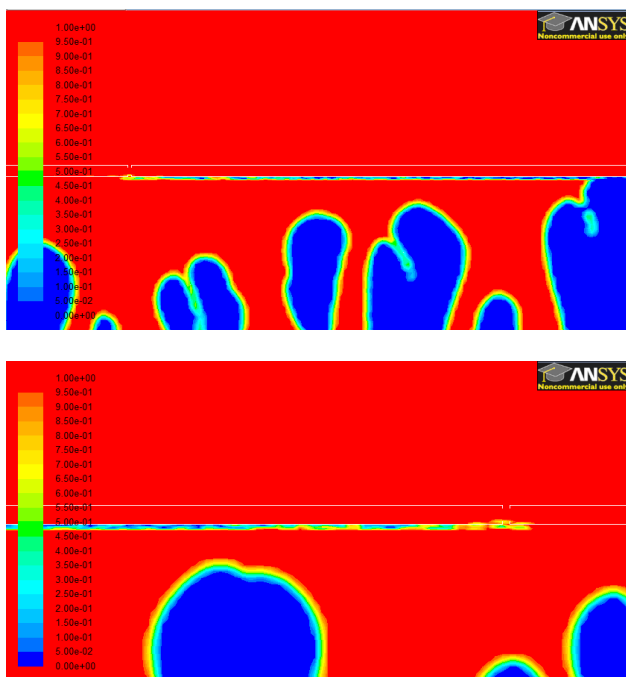


Figure 12. Breakthrough to the pipe via AICD1 (upper) and AICD2 (lower).

According to Figure 12, it is clear that packers in the annulus between the AICDs can delay the breakthrough through AICD 2. Figure 13 shows the volumetric flow rate of oil and water at the outlet of the well.

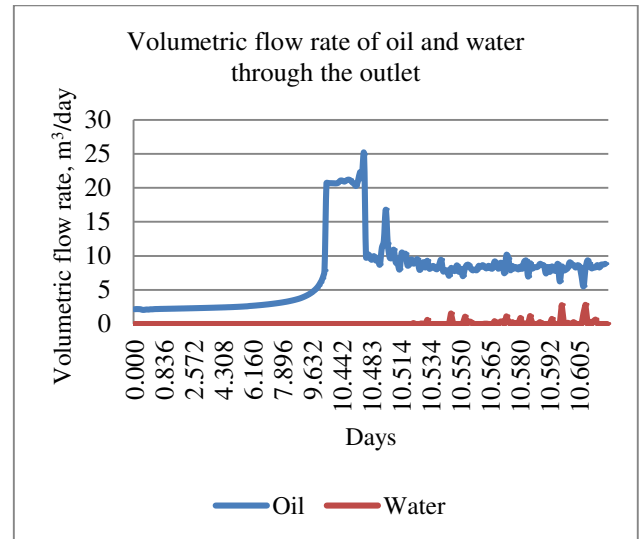


Figure 13. Volumetric flow rate of oil and water through the outlet.

The oil flow rate increases significantly before breakthrough, and decreases again after breakthrough occurs and the AICDs choke the flow into the well. The irregular peaks in the water flow rate imply that water has started to flow. After the breakthrough, the oil flow rate is still higher than before breakthrough. This is due to the increase drawdown and the high flow rate of oil into the well in a period before the breakthrough. Due to two-dimensional simulations, the AICDs in the upper wall of the pipeline are not influenced by the water flow in the annulus, and are still producing oil without any restrictions. Both oil and water flow rates are expected to decrease slowly after some time until oil is again surrounding the AICDs.

The two-dimensional computational study has shown that the fingering phenomenon occurs in heavy oil reservoirs with water drive. The simulations have also predicted the early breakthrough of water to the annulus and the well and the functionality of the AICD. The AICDs restricted the flow at water breakthrough, which indicated that the modelling of the AICD in Fluent agreed well with the expected functionality of the AICD. However, to investigate the potential of increased oil recovery with AICD, a much longer well with several AICDs and packers to isolate the breakthrough zones has to be simulated. The total picture of the production of heavy oil with water drive can only be obtained by using three-dimensional simulation.

4 Conclusion

Recovery of heavy oil is associated with difficulties in terms of early water or gas breakthrough caused by the fingering phenomenon. This study is related to Californian heavy oil production and includes 2D simulations of heavy oil with viscosity 300 cP in horizontal wells with autonomous inflow control devices (AICDs). The simulations have been performed to study reservoir flow, annular flow and flow through the AICDs into the production pipe using ANSYS/Fluent as the Computational Fluid Dynamics (CFD) software. Volume of Fluid (VOF) is used as the multiphase model. Preliminary studies are performed and a model for heavy oil production has been developed and validated against experimental data found in literature.

Before the breakthrough, the analysis of data gives quite realistic results which can be theoretically justified. The simulations clearly stated the fingering phenomenon and the effect on breakthrough and oil production. The simulation time after the breakthrough is very short due to multiphase flow in pipeline, which leads to instabilities. Higher pressure drop is observed near the well bore (or across AICD) as the finger growth takes place. Simulation of two pipe sections in a homogeneous reservoir does not reflect the function of AICDs adequately. This is due to negligible frictional pressure drop in the pipe which breakthrough at approximately the same time in the two sections. This study has detected/identified/proven the formation of fingering in heavy oil reservoir with water drive and according to the simulated results, oil production is highly affected by fingering behavior, since it enables the early water breakthrough while most of the oil is left unproduced. However, further simulations are needed to study the effect of inflow control devices. Further simulations should also involve packers to isolate the breakthrough zones.

References

- H. Aakre, B. Halvorsen, B. Werswick, V. Mathiesen, Smart well with autonomous inflow control valve technology, in: SPE Middle East Oil and Gas Show and Exhibition, 2013.
- F. Al-Khelaiwi, D. Davies, Inflow control devices: Application and value quantification of a developing technology, in: International Oil Conference and Exhibition, 2007.
- B. Clark, Heavy oil, extra-heavy oil and bitumen, Tech. rep., National Petroleum Council (2007).
- C. D. of Conservation, Annual report of the state oil and gas supervisor, Tech. rep., California Department of Conservation, Division of Oil, Gas and Geothermal Resources (2008).
- A. Daneshy, Icd design: Revisiting objectives and techniques, in: SPE Asia Pacific Oil and Gas Conference and Exhibition, 2010.
- P. Fernandes, Z. Li, D. Zhu, Understanding the roles of inflow-control devices in optimizing horizontal-well performance, in: SPE Annual Technical Conference and Exhibition, 2009.
- M. Halvorsen, O. Naevdal, G. Elseth, Increased oil production by autonomous inflow control with rcp valves, in: SPE Annual Technical Conference and Exhibition, 2012.
- E. Hanzlik, Status of heavy oil and tar sand resources in the United States, Tech. rep., UNITAR Center for Heavy Crude and Tar Sands (1998).
- Incorporation, F., *ANSYS FLUENT 12.0 User's Guide*, 2009.
- Incorporation, F., *Flow Through Porous Media*. 2007.
- S. Joshi, Horizontal wells: Successes and failures, *Journal of Canadian Petroleum Technology* 33(1994).
- B. Least, S. Greci, R. Burkey, A. Utford, A. Wilema., Autonomous icd single phase testing, in: SPE Annual Technical Conference and Exhibition, 2012.
- V. Mathiesen, H. Aakre, B. Werswick, G. Elseth, The autonomous rcp valve - new technology for inflow control in horizontal wells, in: SPE Annual Technical Conference and Exhibition, 2011.
- D. Mud, Horizontal well development of agravity drainage reservoir, in: SPE Western Regional Meeting, 1996.
- M. Safwat, Challenges of heavy oil production, OAPEC - IFP Seminar, 2007.
- D.I.Erandi N. Wijerathne, Britt M. Halvorsen, Computational study of fingering phenomenon in heavy oil reservoir with water drive, *Fuel* 158, 2015.

Process Simulation of Calcium Looping with Indirect Calciner Heat Transfer

Chameera K. Jayarathna^{1,2}, Anette Mathisen², Lars Erik Øi¹, Lars-André Tokheim¹

¹Telemark University College, Faculty of Technology, Porsgrunn, Norway

²Tel-Tek, Research Institute, Porsgrunn, Norway

Abstract

In calcium looping (CaL), calcium oxide (CaO) is used as a sorbent for carbon dioxide (CO₂). The CO₂ reacts with CaO to produce calcium carbonate (CaCO₃) in a carbonator. The CaCO₃ is then sent to another reactor, a calciner, where the CaCO₃ is calcined, producing CaO (which is returned to the carbonator for another cycle) and more or less pure CO₂, which is removed from the system. Conventional CaL with direct heat transfer using oxy-combustion has an unwanted energy penalty. However, if the heat could be transferred indirectly to the calciner, the energy penalty associated with oxy-combustion could be avoided. In this work, Aspen Plus is used to simulate the CaL process with indirect heat transfer. The results confirm that such a scheme could give an energy penalty lower than for example amine scrubbing or oxy-combustion.

Keywords: Aspen Plus, CO₂ capture, energy penalty

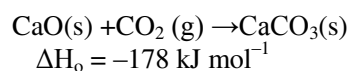
1. Introduction

Removal of carbon dioxide (CO₂) from gas streams has been a crucial unit operation for many decades to avoid corrosion and also to improve the calorific value of gas streams. More recently CO₂ reduction has become an urgent need due to the greenhouse effect. The average temperature of the earth's atmosphere and ocean is rising continuously. During the last 100 years, the average surface temperature has increased about 0.8°C (Choices, 2011). Scientists working on the topic agree that the major cause of the global warming is greenhouse gases emitted due to human activities. Deforestation and burning of fossil fuels are the two main reasons. According to Robinson et al. (Robinson et al., 2007), the total industrial CO₂ production, primarily from burning coal, oil and natural gas and the production of cement, is about 8Gt carbon per

year, as reported in 2007. In the last decade, scientific research and knowledge on climate change have progressed considerably and many political efforts have been made to reach worldwide agreement to the Kyoto treaty (UNFCCC, 1998).

The most mature technology for capturing CO₂ is using amine-based CO₂ solvents to absorb CO₂ from the exhaust gas. However, other concepts may be more attractive from an energy penalty point of view. Using a solid sorbent at high temperature is a concept which is now being widely considered as an alternative. Development of more advanced solid sorbents is a continuous process, but a challenge is the high sorbent production cost. CO₂ capture from flue gas by calcium looping (CaL) may be an attractive alternative due to the cheap and readily available sorbent (limestone). The calcium looping process, first brought up by Shimizu et al. (Shimizu et al., 1999), is regarded as one of the potential technologies.

In the CaL process, calcium oxide (CaO) is used as a regenerable solid sorbent to react with CO₂. Due to the formation of calcium carbonate in the process, it is also called carbonate looping (Lasheras et al., 2011), or carbonate cycling. Many of the CaL concepts described in the literature (Chang et al., 2013; Kremer et al., 2013; Ströhle et al., 2014; Dieter et al., 2014; Alstom, 2012; Hatzilyberis, 2011; Junk et al., 2013; Junk et al., 2012; Hoeflberger and Karl, 2013) are based on fluidized bed (FB) technology. In CaL, calcium oxide (CaO) reacts with CO₂ to form calcium carbonate (CaCO₃) in a fluidized bed reactor (carbonator) at a temperature around 650°C, in an exothermic reaction (Bennaceur, 2008):



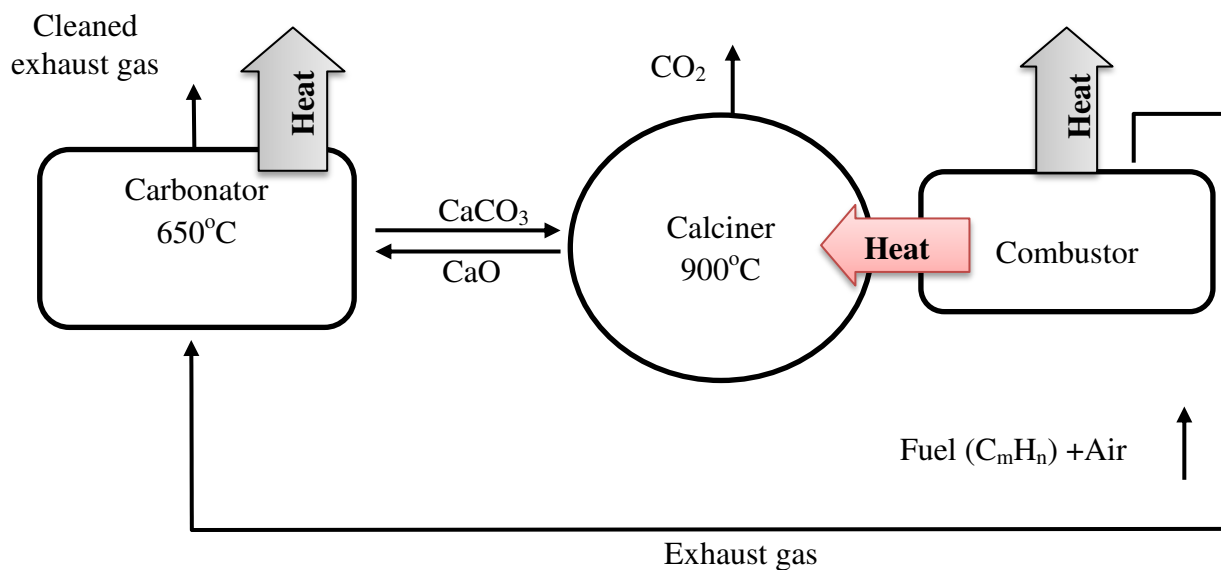


Figure 1. Calcium looping cycle with indirect heat transfer between combustor and calciner

The CaCO₃ is separated from the cleaned exhaust gas by a gas/solid separator. The cleaned exhaust gas exiting from the carbonator can be released to the atmosphere.

In a second reactor, the calciner, the reverse reaction happens, i.e. CaCO₃ decomposes into CaO and CO₂ at a temperature close to 900 C. This is an endothermic process, so a significant flow of thermal energy must be supplied to the calciner for the reaction to occur. The regenerated CaO is separated from the CO₂ in a gas/solid separator and recycled back to the carbonator.

In conventional CaL the heat is transferred directly by oxy-combustion in the calciner; pure oxygen is required as the oxidizer to avoid diluting CO₂ with nitrogen. Even though most of the thermal energy supplied in the calciner can be recuperated in the carbonator, the oxy-combustion gives an unwanted energy penalty of the CaL technology due to the Air Separation Unit (ASU) which is a key component in the system when it comes to the oxy-combustion.

However, if the heat could be transferred indirectly to the calciner, then the energy penalty associated with oxy-combustion could be avoided, and this would make CaL a much more attractive alternative for the thermal power industry. Since this concept requires extensive integration between the combustor and the calciner, it can be called Fully Integrated Calcium Looping (FICaL). The low energy penalty of CaL with indirect calciner heat transfer is due to high-temperature integration between the CO₂ capture plant and the power plant. The basic idea is illustrated in Figure 1. The fact that the heat transfer takes place at a

temperature higher than the typical operational temperature of a coal fired power plant means that the energy penalty usually associated with CO₂ capture processes can be significantly reduced.

In this work a coal fired power plant with a FICaL-based CO₂ capture facility was simulated using Aspen Plus V8.6® software. Three different indirect heat transfer cases were simulated and analyzed. The aim was to determine the impact on the energy balance of the system for each case. The capacity of the power plant was 1890MW_{th}.

2. The simulated process

An overview of the simulated process is given in Figure 2. The three major process units are the calciner, the carbonator and the combustor (coal-fired boiler).

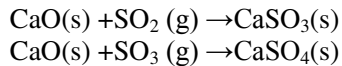
Basic coal combustion reactions occur in the combustor, generating CO₂, H₂O, SO₂ and other combustion products. The exhaust is cooled by the combustion air (which is preheated) and dedusted in a filter.

The CO₂ in the exhaust gas from the boiler reacts with CaO in the sorbent to form CaCO₃ in the carbonator in an exothermic reaction. The loaded sorbent (rich in CaCO₃) is separated from the exhaust gas in a cyclone, the clean exhaust gas is vented to the atmosphere via the ID fan and the loaded sorbent is transported to the calciner using steam as the transport medium.

In the calciner, the reverse endothermic reaction takes place with CO₂ and CaO as products. The gas (a mixture of CO₂ and steam) is separated from the CaO in a cyclone. The CO₂

and steam are then separated in a condenser and the water is preheated to produce steam again for reuse as a transport medium in the calciner. The lean sorbent (rich in CaO) is fed back into the carbonator for a new cycle, whereas CO₂ is pulled out of the system via another ID fan.

Desulfurization reactions take place at a relatively high temperature in the coal-fired boiler by adding CaCO₃ which is calcined in the combustor and reacts with SO₂ and SO₃ to form CaSO₃ and CaSO₄, respectively.



Fly ash from the boiler, possibly including some sulfates and sulfites (the part of the sulfates/sulfites not exiting with the bottom-ash), is separated from the boiler exhaust gas in a high-temperature filter.

The following assumptions are made for the reactions in the carbonator,

- 85% of the CO₂ is captured.
- 18% of the CaO in the lean sorbent reacts with CO₂ and is converted in to CaCO₃, mainly on the surface of the sorbent particles

(Baciocchi et al., 2009). The remaining 82% exists as an unreacted core not available for reactions due to diffusion limitations.

The energy required for the calcination reaction to occur is transferred indirectly via a tube wall separating the hot combustion gases and the gas/particle suspension in the calciner. Typically, this wall will be the sum of many tube walls, since a large heat transfer area is required. Here, it is assumed that the indirect heat transfer from the combustor to the calciner can be realized without considering material temperature constraints. One way of doing that could be by applying staged combustion, so that the combustion gas temperature is increased in steps in order to maintain the driving force (ΔT) for the heat transfer. This means that the simulations are based on the assumption that it is possible to transfer enough energy to capture 85% of the CO₂ generated in the boiler.

In principle, all the energy transferred from the boiler is released again in the carbonator, where it is further transferred to the steam cycle, giving no net loss of thermal energy.

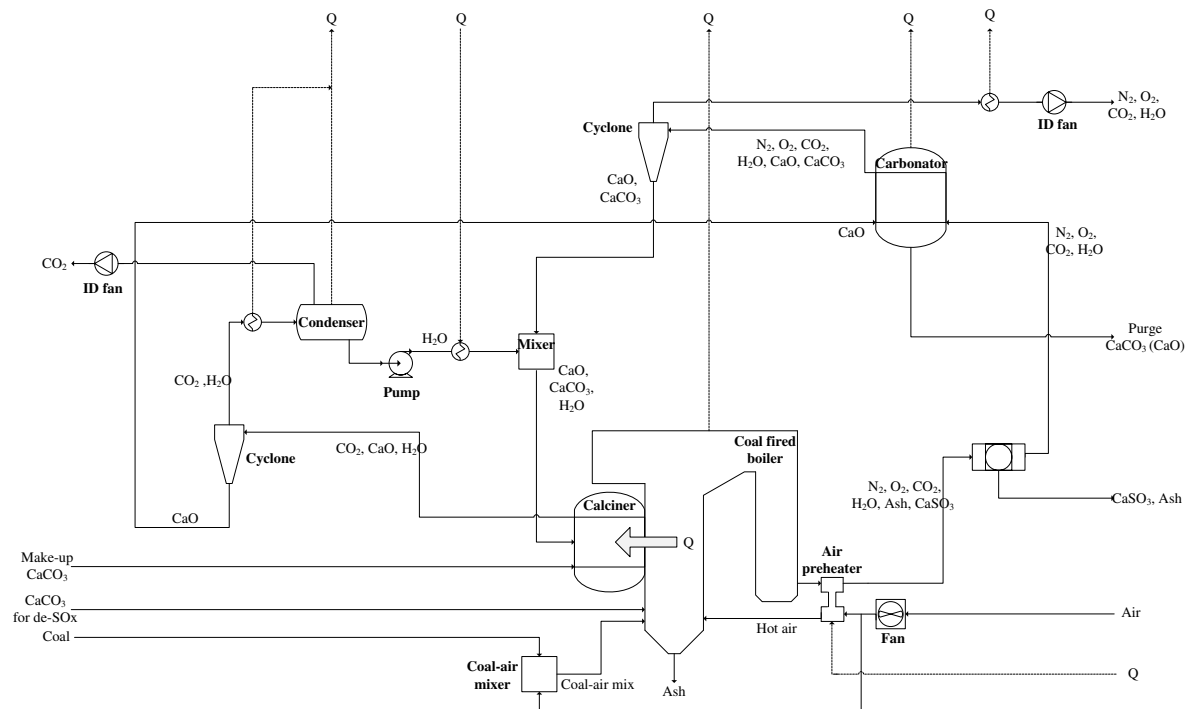


Figure 2. Process flow diagram based on heat transfer concept

3. Aspen Plus setup, input parameters and description

The flow sheet type was chosen with solids and a user defined unit package, allowing for the analysis and results presentation for solid-state input and output streams. The setup of the flow sheet involved assigning the MCINCPD stream class to the simulation. This allowed fluid streams (MIXED), conventional solid streams with Particle Size Distribution (CIPSD) and non-conventional solid streams with a certain Particle Size Distribution (NCPSD) to be specified. The process type was chosen as COMMON. The IDEAL base calculation method was selected for simplicity and thus phase equilibrium calculations were conducted using Raoult's Law, Henry's Law, ideal gas law, etc.

Coal was modelled as a non-conventional solid based on ultimate, proximate, and sulphur analyses as shown in **Table 1**. The enthalpy of coal is specified as a user defined value and the density is approximated based on IGT correlations (Aspen Technology, 2012) known as the DCOALIGT model in Aspen Plus. The Particle Size distribution (PSD) of coal was specified as a group of particles with size 25-350 μm .

Fluid streams were modelled using conventional components using thermophysical data stored in the Aspen Plus databanks. Therefore, no data input were required for these components. The components include: water (H_2O), oxygen (O_2), sulfur dioxide (SO_2), sulfur trioxide (SO_3), hydrogen (H_2), chlorine (Cl_2), hydrochloric acid (HCl), carbon monoxide (CO) and carbon dioxide (CO_2). Additionally, solid components were modelled using conventional solids which also have necessary thermophysical data stored in the databanks. The components include: calcium oxide (CaO), calcium carbonate (CaCO_3), calcium sulfite (CaSO_3), and calcium sulfate (CaSO_4). Input values for the Aspen Plus simulations are shown in Table 1. The air preheating temperature is kept as 650 $^\circ\text{C}$.

The Aspen Plus model contains all the main units in the process. The calculation sequence of the units is the same as the process flow. There are two main mass inputs to the process: coal and air to the combustor. In addition, CaCO_3 for de- SO_x is added. The two main outputs are the clean gas and the pure CO_2 , and in the addition the bottom ash and the fly ash exits from the system. The sorbent (CaO/CaCO_3) circulates internally in the system, between the calciner and the carbonator. Makeup and purge streams are not included in the model.

The required CaO mass flow to the carbonator is calculated in the Aspen Plus model based on the CO_2 concentration in the exhaust gas using an Aspen Plus Calculator Block. The required steam mass flow rate is calculated based on the solids mass flow to the calciner using another Calculator Block. The calciner and the carbonator were modelled as stoichiometric conversion reactors, however at temperatures not violating the thermodynamic constraints. Some key assumptions were applied to the simulations as shown below.

- The de-carbonation of CaCO_3 in the calciner is 100% efficient, leaving no uncalcined material in the lean sorbent exiting the calciner.
- The gas-solid separators are 100% efficient.
- The pressure drop over the carbonator, the calciner, the heat exchangers and gas/solid separators are 110, 150, 10 and 10mbar, respectively.

3.1. Case 1- Self-fluidization

In Case 1 (Figure 3) it is assumed that the CO_2 developed during calcination is sufficient for fluidization, hence no (or negligible amounts of) steam is used for fluidization. This means there is no need for the condenser, the pump or the water/steam pipelines that would otherwise make up the water/steam loop.

3.2. Case 2- Steam as the transport medium

In Case 2 (Figure 4) steam is used to fluidize and transport the sorbent particles in the calciner. The steam to CO_2 mass ratio at the calciner exit is 1:1. The required steam mass flow rate is calculated using a Calculator Block in Aspen Plus. This means that a water/steam loop system is required (there is a small increase in electrical energy consumption due to the condensate pump). Hence, the new features of this system are mixing of steam and particles, cooling of the steam/ CO_2 mixture, condensation of steam into water, separation of liquid H_2O and CO_2 , pressure increase of liquid H_2O , evaporation of water and reheating of steam. These process units are shown in the upper right area in Figure 4.

3.3. Case 3- Increased calciner pressure drop

In Case 3 the system is basically the same as in the reference case (Case 1), but the pressure drop over the calciner is increased to 300mbar. The consequence of this is an increased power consumption of the CO_2 fan and slightly higher heat transfer in the CO_2 cooling process.

Table 1. Input values used in the Aspen Plus simulations

<i>Parameter</i>	<i>Value</i>	<i>Unit</i>
Thermal power, full-scale	1890	MW _{th}
Fuel	Coal	-
Fuel heating value	27.7	MJ/kg
Feed rate of coal in to the combustor	68.2	kg/s
Excess air	15	wt%
<i>Fuel ultimate analysis:</i>		
C	71.7	wt%
H	3.9	wt%
O	5.9	wt%
S	1.2	wt%
N	1.7	wt%
Cl	0.1	wt%
Ash	14.3	wt%
Moisture	1.2	wt%
<i>Fuel proximate analysis:</i>		
Moisture	1.2	wt%
Volatiles	23.7	wt%
Fixed carbon	60.8	wt%
Ash	14.3	wt%
<i>Fuel sulfur:</i>		
Sulfate	0.15	wt%
Pyritic	0.90	wt%
Organic	0.15	wt%
<i>CaO PSD (μm)</i>		
<25	0	wt%
25-50	0.3	wt%
50-100	1.7	wt%
100-150	23.7	wt%
150-200	45.8	wt%
200-350	26.8	wt%
350-500	1.7	wt%
Maximum material temperature	1100	°C
Calcination temperature	max 900	°C
Carbonation temperature	650	°C

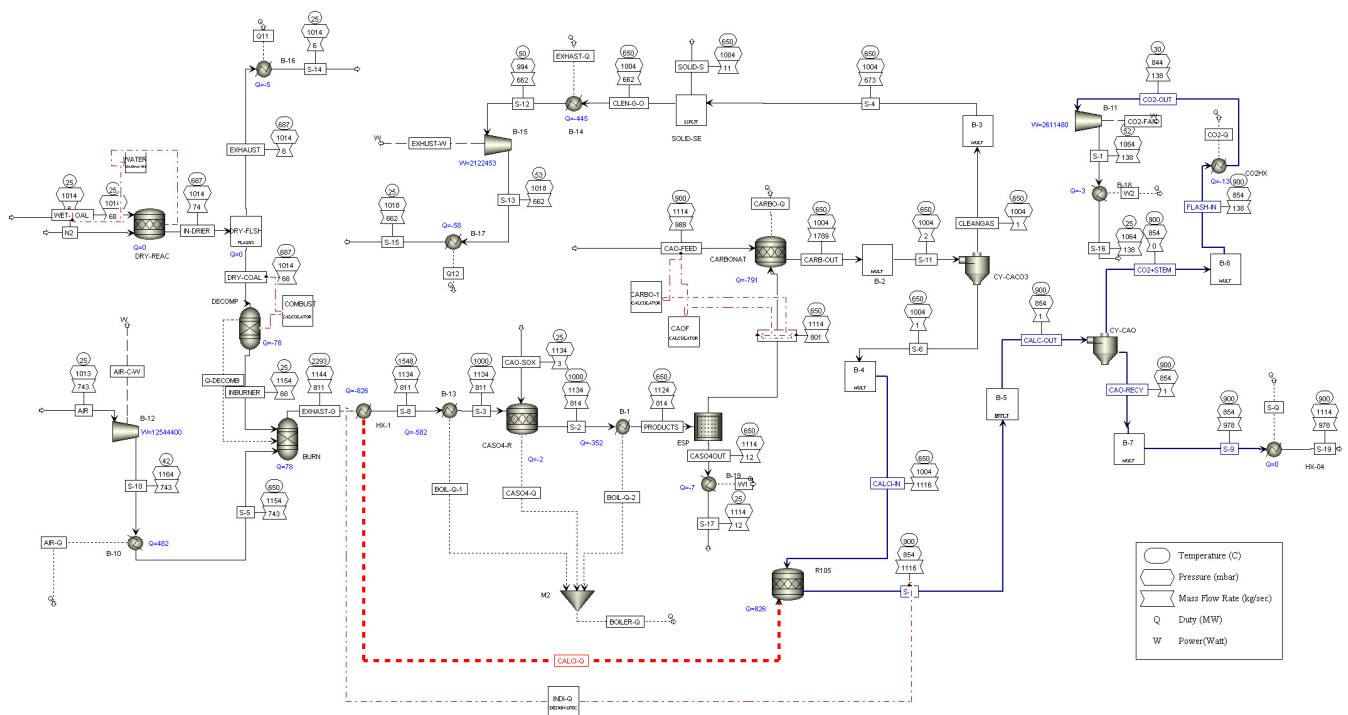


Figure 3. Aspen Plus flow diagram for Case 1

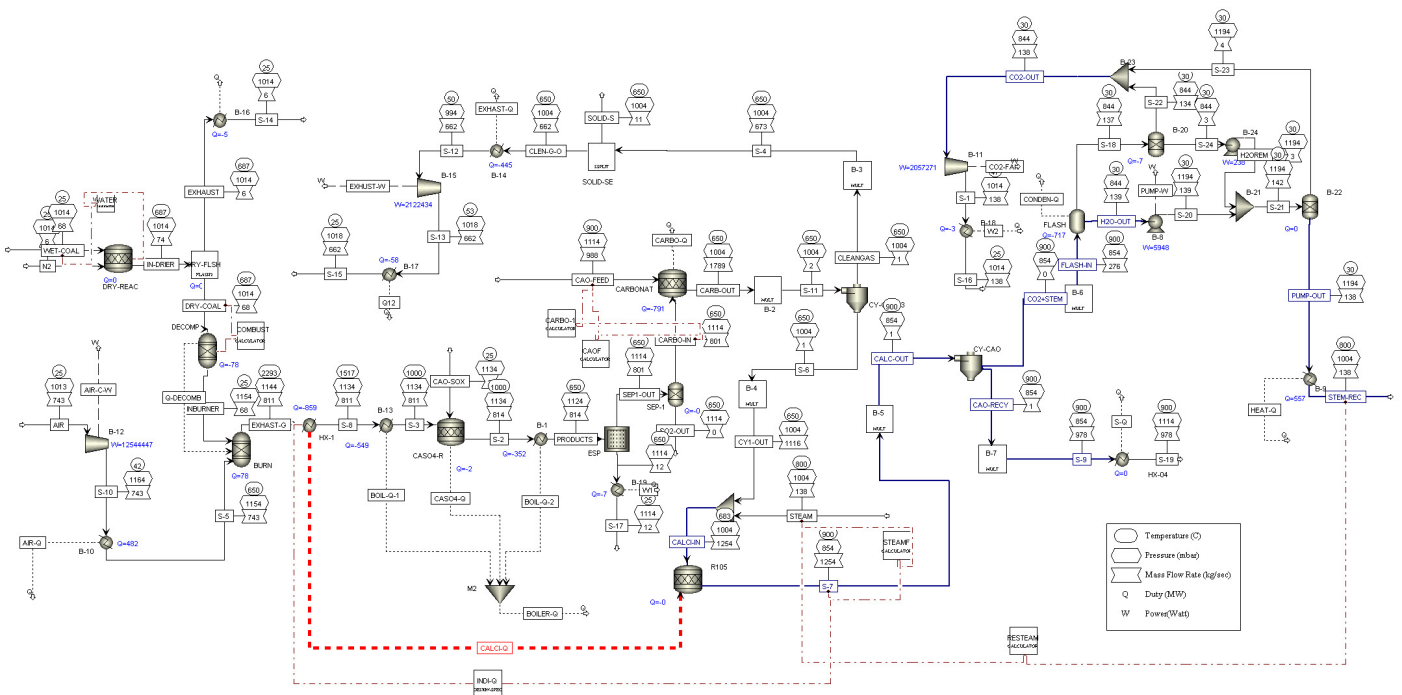


Figure 4. Aspen Plus flow diagram for Case 2

4. Energy penalty calculations

The material balance is given in the form of specified material streams between the equipment units in the Aspen Plus flowsheet. The energy balance is given in the form of energy streams (enthalpy streams of material streams, heat duties or electrical duties) into and out of the equipment units.

The energy penalty of the FICaL system ($\Delta\eta_{\text{penalty,FICaL}}$) can be defined as the difference in efficiency between the FICaL process (η_{FICaL}) and a reference process (η_{ref}) (in this case a coal-fired power plant without CO₂ capture):

$$\Delta\eta_{\text{penalty,FICaL}} = \eta_{\text{ref}} - \eta_{\text{FICaL}} \quad (4.1)$$

The efficiency of the reference plant and the FICaL plant can be calculated as the ratio of the net electrical power produced ($E_{\text{electric,ref}}$ or $E_{\text{electric,FICaL}}$, respectively) to the thermal energy input (Q_{input}), i.e. the coal combustion energy released):

$$\eta_{\text{ref}} = \frac{E_{\text{electric,ref}}}{Q_{\text{input}}} \quad (4.2)$$

$$\eta_{\text{FICaL}} = \frac{E_{\text{electric,FICaL}}}{Q_{\text{input}}} \quad (4.3)$$

The net produced electrical power of a FICaL process is found by subtracting the additional power of the FICaL system ($\Delta E_{\text{electric,FICaL}}$) from the net electrical power of the reference plant:

$$E_{\text{electric,FICaL}} = E_{\text{electric,ref}} - \Delta E_{\text{electric,FICaL}} \quad (4.4)$$

Neglecting any additional heat loss that might result from the FICaL system, the additional FICaL power consumption is mainly due to extra fan power ($E_{\text{fan,FICaL}} - E_{\text{fan,ref}}$), which in turn is due to increased pressure drop in the carbonator, calciner and cyclones.

$$\Delta E_{\text{electric,FICaL}} = E_{\text{fan,FICaL}} - E_{\text{fan,ref}} \quad (4.5)$$

The fan power of the reference plants ($E_{\text{fan,ref}}$) and the FICaL plant ($E_{\text{fan,FICaL}}$) may be estimated (assuming isothermal operation) as:

$$E_{\text{fan,ref}} = \frac{\dot{n}_{\text{ref}} R T_{\text{in,ref}}}{\eta_{\text{fan,ref}}} \ln \frac{p_{\text{out,ref}}}{p_{\text{in}}} \quad (4.6)$$

$$E_{\text{fan,FICaL}} = \frac{\dot{n}_{\text{FICaL}} R T_{\text{in,FICaL}}}{\eta_{\text{fan,FICaL}}} \ln \frac{p_{\text{out,FICaL}}}{p_{\text{in}}} \quad (4.7)$$

Here, \dot{n} is the gas flow rate [mol/s], R is the universal gas constant (8.314 J/mol · K), η_{fan} is the fan efficiency, T_{in} is the gas inlet temperature

[K], and p_{in} and p_{out} are pressure into and out of the fan [Pa].

The outlet pressure from the fan ($p_{\text{out,ref}}$) and ($p_{\text{out,FICaL}}$) will be the inlet pressure (p_{in}) plus the total pressure drop that has to be overcome in the process (Δp_{ref} and Δp_{FICaL}):

$$p_{\text{out,ref}} = p_{\text{in}} + \Delta p_{\text{ref}} \quad (4.8)$$

$$p_{\text{out,FICaL}} = p_{\text{in}} + \Delta p_{\text{FICaL}} \quad (4.9)$$

The total gas flow rate in the FICaL system is basically the same as in the reference plant although two fans (the CO₂ fan and the ID fan for the cleaned gas) are used instead of one fan (ID fan for the uncleaned exhaust gas). The inlet pressure is also the same and it should be a good assumption to use the same fan efficiencies and the same gas inlet temperature for two systems (with and without CO₂ capture).

By combining equations 4.1-4.9, the following, quite simple, equation for the energy penalty of the FICaL system is given:

$$\Delta\eta_{\text{penalty,FICaL}} = \frac{E_{\text{fan,FICaL}}}{Q} \left[1 - \frac{\ln\left(1 + \frac{\Delta p_{\text{ref}}}{p_{\text{in}}}\right)}{\ln\left(1 + \frac{\Delta p_{\text{FICaL}}}{p_{\text{in}}}\right)} \right] \quad (4.10)$$

5. Results and discussion

The energy balance, based on the Aspen Plus simulation results, is summarized in Table 2 for these cases. There is a relatively small balance error ($\approx 0.5\%$), which may be due to Aspen Plus iterative calculations. However, the error is sufficiently small that the numbers can be used to evaluate the concept.

A reasonable value for the total efficiency (produced electrical power / heat input from the coal feed) for a modern coal based power plant is 40%. With a thermal duty of 1890MW this gives a total electrical power of 756MW. The estimated energy penalty means that the FICaL plant will, in comparison, have an efficiency of 39.3-39.4%.

Inclusion of makeup and purge in the system (not accounted for above) will increase the energy penalty. Additional heat loss from the FICaL system is likely to occur due to higher surface area as a result of the extra equipment units, and this will also increase the energy penalty. This contribution is however not included here as its value is unknown. Also, auxiliary equipment potentially requiring some extra electrical energy is not included, but is not likely to be significant.

The pressure drop value of each unit (in particular the calciner and the carbonator) may later be determined more accurately, giving a more accurate energy penalty value.

Table 2. Energy balance (MW) for Case 1, 2 and 3

<i>Inputs</i>	<i>AP flowsheet reference</i>	<i>Case 1</i>	<i>Case 2</i>	<i>Case 3</i>
H ₂ O evaporation + heating	B-9*	0	557	0
Air preheating	B-10	482	482	482
Air fan	B-12	13	13	13
Exhaust gas fan	B-15	2	2	2
CO ₂ fan	B-11	3	2	5
Pump	B-8*	0	0	0
Sum inputs	-	499	1054	502
<i>Generation</i>				
Coal combustion	-	1890	1890	1890
SO _x unit	CASO4-R	2	2	2
Sum generation	-	1892	1892	1892
<i>Outputs</i>				
Cooling and condensation of H ₂ O/CO ₂	CO ₂ HX+ FLASH* + B-20* + B-18 + HX-04*	137	727	140
Boiler energy to steam cycle	B-1 + B-13	934	901	934
Carbonator energy to steam cycle	CARBONAT	791	791	791
Hot clean exhaust gas energy	EXHAUST-Q	445	445	445
Ash waste heat	B-19	7	7	7
Cold clean exhaust gas waste heat	B-17	58	58	58
Dryer heat recovery	B-16	5	5	5
CaO heat recovery	-	0	0	0
Sum outputs	-	2377	2934	2380
<i>Energy Penalty</i>				
Energy penalty (reduction in power plant efficiency)	-	0.6 %	0.6 %	0.7%

* Contained only in case 2

6. Conclusions

Aspen Plus has been used to simulate a CO₂ capture plant, fully integrated with a coal-fired power plant. Three different cases were studied and a simplified method was used to estimate the energy penalty. The estimated energy penalty is below 1 % in all cases.

With careful design considerations, the FICaL process is characterized by a very low energy penalty. Even if additional energy consuming effects are included, the FICaL process will likely have a competitive advantage over other technologies.

Acknowledgements

The authors acknowledge funding from Alstom and Gassnova via the FIRCC project (CLIMIT, 2014) and would like to thank Mr. Michael Balfe from Alstom Power, Germany, for his valuable discussions.

References

- Alstom. Fully Integrated Regenerative Carbonate Cycle (FIRCC), Pre-study description. *Alstom*, 2012.
- Aspen Technology. *Aspen Physical Property System*. Aspen Technology Inc., MA, USA, 2008.
- R. Baciocchi, G. Costa, A. Poletti and R. Pomi: Influence of particle size on the carbonation of stainless steel slag for CO₂ storage. *Energy Procedia*, 1:4859-4866, 2009.
- K.G. Bennaceur: *CO₂ capture and storage a key carbon abatement option* [Online]. Paris: OECD/IEA, 2008. Available: <http://www.sourceoecd.org/9789264041400>.
- M.H. Chang, C.M. Huang, W.H. Liu, W.C. Chen, J.Y. Cheng, W. Chen, T.W. WEN, S. Ouyang, C.H. Shen and H.W. HSU: Design and Experimental Investigation of Calcium Looping Process for 3-kWth and 1.9-MWth Facilities. *Chemical Engineering & Technology*, 36:1525-1532, 2013.

- A.S.C. Choices. Environmental Effects of Increased Atmospheric Carbon Dioxide. The National Academies Press, 15, 2011.
- CLIMIT. 226499 - Fully Integrated Regenerative Carbonate Cycle (FIRCC) - Pre study [Online]. Research Council of Norway, 2014. Available: <http://www.climit.no/en/projects/development-project/226499> [Accessed 26 May 2015].
- H. Dieter, A.R. Bidwe, G. Varela-Duelli, A. Charitos, C. Hawthorne and G. Scheffknecht: Development of the calcium looping CO₂ capture technology from lab to pilot scale at IFK, University of Stuttgart. *Fuel*, 127:23-37, 2014.
- K.S. Hatzilyberis: Design of an indirect heat rotary kiln gasifier. *Fuel Processing Technology*, 92:2429-2454, 2011.
- D. Hoeflberger and J. Karl. Self-Fluidization in an Indirectly Heated Calciner: *Chemical Engineering & Technology*, 36:1533-1538, 2013.
- M. Junk, M. Reitz, J. Ströhle and B. Epple. Thermodynamic evaluation and cold flow model testing of an indirectly heated carbonate looping process. *2nd International Conference on Chemical Looping*, Darmstadt, Germany, 2012.
- M. Junk, M. Reitz, J. Ströhle and B. Epple: Thermodynamic Evaluation and Cold Flow Model Testing of an Indirectly Heated Carbonate Looping Process. *Chemical Engineering & Technology*, 36:1479-1487, 2013.
- J. Kremer, A. Galloy, J. Ströhle and B. Epple: Continuous CO₂ Capture in a 1-MWth Carbonate Looping Pilot Plant. *Chemical Engineering & Technology*, 36:1518-1524, 2013.
- A. Lasheras, J. Ströhle, A. Galloy and B. Epple: Carbonate looping process simulation using a 1D fluidized bed model for the carbonator. *International Journal of Greenhouse Gas Control*, 5:686-693, 2011.
- A.B. Robinson, N.E. Robinson and W. Soon: Environmental Effects of Increased Atmospheric Carbon Dioxide. *Journal of American Physicians and Surgeons*, 12:79-90, 2007.
- T. Shimizu, T. Hiramata, H. Hosada, K. Kitano, M. Inagaki and K. Tejima: A Twin Fluid-Bed Reactor for Removal of CO₂ from Combustion Processes. *Chemical Engineering Research and Design*, 77:62-68, 1999.
- J. Ströhle, M. Junk, J. Kremer, A. Galloy and B. Epple: Carbonate looping experiments in a 1 MWth pilot plant and model validation. *Fuel*, 127:13-22, 2014.
- UNFCCC. Kyoto Protocol to the United Nations Framework Convention on Climate Change. *Review of European Community & International Environmental Law*, 7:214-217, 1998.

Simulation of Simplified Model for Kinetics of Biomass Gasification

Cornelius E. Agu¹ Rajan K. Thapa² Britt M. Halvorsen³

Department of Process, Energy and Environmental Technology, Telemark University College, Norway,
{cornelius.e.agu,rajan.k.thapa,britt.halvorsen}@hit.no

Abstract

Due to complexity in interactions between solid particles and between particles and carrier fluid, modeling of biomass gasification kinetics has been shown to be very challenging. Some commercial packages such as Barracuda VR describe the process using a complicated Eulerian-Lagrangian approach of modeling gas - solid multiphase flow. Since chemical reactions play the major role in the gasification process, this paper focuses on a simplified model that describes the influence of reaction kinetics on the process in a bubbling fluidized bed reactor with circulating bed material. The developed model assumes that the system is ideally mixed with a constant bed temperature. Two different set of reaction rate constants are applied to test the model, and their results are compared with that from Barracuda. The model is used to study the effect of steam-biomass ratio on char conversion, and the results show that the conversion of char increases with steam-to-biomass ratio. Sensitivity analysis shows that the output of the model strongly depends on temperature and slightly depends on the bed material particles size.

Keywords: Simplified Model, Biomass, Gasification, Fluidized Bed, Kinetics

1 Introduction

Biomass gasification process is a technology that has attracted the interest of many researchers recently. This is due to its potential as an alternative to fossil fuels that are major contributors to the environmental degradations. Aside being used as a fuel source for heat and power production, biomass gasification product, called syngas (a mixture of CO and H₂) can be used as a feedstock for chemical synthesis.

Gasification of biomass involves its partial combustion in the absence or limited amount of oxygen, mainly with a gasifying agent such as CO₂ or steam. In the gasification process, series of physical and chemical activities take place. The process usually begins with drying process, and then followed by pyrolysis. The pyrolysis process leads to breaking down of the biomass into solid matter (charcoal), gaseous mixture (mainly CO₂, CO, CH₄ and H₂) and liquid matter (tar). The main focus in biomass gasification process is to efficiently convert all the char constituent into gaseous product of the syngas by using either steam or CO₂.

Because of the complexities in particle-fluid and particle-particle interactions, modeling a complete set of biomass activities has been proven to be somewhat challenging. However, with introduction of appropriate assumptions, several attempts have been made with some successful results. Most of the existing models are centered around chemical kinetics, thermodynamics and transport of species in the reactor. Chemical kinetics play the largest role in the process since the conversion of char is mainly by chemical means. By inclusion of transport of mass, momentum and energy, the concentration gradient of the reacting species over the reaction chamber can be well captured.

The main objective of this paper is to study the reaction kinetic influences on the gasification process in bubbling fluidized bed reactor with circulating bed material. The bubbling fluidized bed reactor ensures a uniform heat distribution, and with a circulating bed material, a constant heat supply is maintained. The basic arrangement for such a system is shown in Figure 1.

Among several studies, (Lü et al, 2008; Fiaschi and Michelini, 2001) studied the gasification kinetics based on steady state 1-D model for two-phase systems distinguished by bubbling and emulsion phases. The studies consider the effects of hydrodynamics of the species in the reactor. (Farooq et al, 2013) uses CO₂ as a gasifying agent to study the influence of temperature and partial pressure on char conversion rate. (Xu et al, 2011) studied the conversion rate of char with a 1-D dynamic model that accounts for the effects of mass and heat transfer, and concluded that the char conversion depends on the exposed surface area and the micro-pore size of the particles in a fixed bed reactor.

In this work, char conversion rate with steam as the gasifying agent, and influences of steam-biomass ratio on the conversion rate in bubbling fluidized bed reactor with circulating bed material, are studied. A simplified model describing the concentration of each species over time is developed. The model accounts for mass fraction of char particles in the outflow of the bed material, and effective porosity of the total solid in the system. The proposed model excludes the influence of convective and diffusive transport of conserved properties. The model is used to investigate the influence of kinetics rate constants on reaction mechanism of the gasification process by comparing its results with those from a detailed 3-D model based on Barracuda VR. The model

sensitivities to temperature and bed material' particle size are also analyzed.

In the following sections, the governing equations are presented and a complete model for an ideally mixed reactor is developed. The model results based on two different reaction rate constants are compared for both variations in time and in steam-biomass ratio. Finally, some conclusions are drawn.

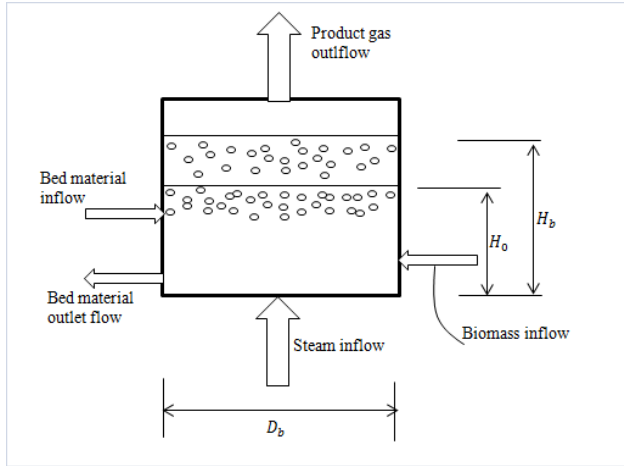
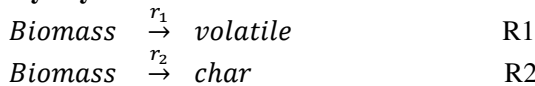


Figure 1. Bubbling Fluidized Bed Reactor with Circulating Bed Material.

2 Governing Equations

The model describing the gasification process in the reactor (Figure 1) is formulated based on a one-step pyrolysis process and the competitive reactions of gaseous species in both heterogeneous and homogeneous phases.

- **Pyrolysis**

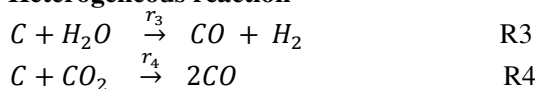


Here, the tar concentration is neglected. It is assumed that the product of complete pyrolysis contains 91% volatiles and 9% char by weight (Thapa et al, 2014). The only gases considered among the volatiles are CO_2 , CO and H_2 , and their compositions are given in Table 1 (Thapa et al, 2014).

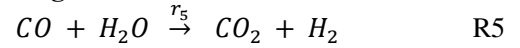
Table 1. Light Gases from Biomass Pyrolysis.

Volatile Component	Composition, v (wt%)
CH_4	0.1213
CO	0.6856
CO_2	0.1764
H_2	0.0167
H_2O	0.0

- **Heterogeneous reaction**



- **Homogeneous reaction**



2.1 Model Formulation

The following further assumptions are applicable in formulating the model.

- (1). Both the bed material and char particles have constant sizes.
- (2). The temperature of the reactor is constant and uniform across the reactor axis, which is achievable with constant particle sizes and sufficient bubbling effect of fluidization including homogeneity in the mixture.
- (3). There is no phase separation for the same species involving in both heterogeneous and homogeneous phase reactions.
- (4). The pyrolysis process is very fast, and all the biomass is converted into char and volatiles as it is being introduced into the reactor.

Applying a species mass balance for an ideally mixed system

$$\frac{dm}{dt} = \dot{m}_{in} - \dot{m}_{out} + \dot{m}_{gen}.$$

For biomass, $m = \rho_B V_b$, $\dot{m}_{out} = 0$ and $\dot{m}_{gen} = V_b R_B$, and these give

$$\frac{d\rho_B}{dt} = \frac{\dot{m}_{B,in}}{V_b} + R_B. \quad (1)$$

Here, ρ_B is the mass concentration of biomass in the reactor. V_b is the reaction volume and R_B is the rate of biomass pyrolysis described by reactions R1 and R2. $\dot{m}_{B,in}$ is mass flow rate of biomass into the reactor.

The reaction rate constants r_1 and r_2 in R1 and R2 respectively are given in Arrhenius form (Haseli et al, 2011)

$$r_i = A_i \exp\left(-\frac{E_i}{RT}\right); \quad i = 1, 2. \quad (2)$$

Here, T and R are temperature in Kelvin and gas constant in $\text{J}/(\text{mol}\cdot\text{K})$. The pre-exponential rate constant A and the activation energy E of the reactions according to (Fantozzi et al, 2007) are given as $1.44 \times 10^4 \text{ s}^{-1}$ and $88.6 \times 10^3 \text{ J/mol}$, respectively for R1, and $7.38 \times 10^5 \text{ s}^{-1}$ and $106.5 \times 10^3 \text{ J/mol}$, respectively for R2. R_B is given as

$$R_B = -(r_1 + r_2)\rho_B. \quad (3)$$

For the reactions R3-R5, the species concentrations are given in mol/m^3 . Equation (4) gives the general species balance in the reactor.

$$\begin{aligned} \frac{dc_j}{dt} &= \dot{C}_{j,in} - \dot{C}_{j,out} + R_j & (4) \\ j &= \text{C}, \text{H}_2\text{O}, \text{CO}_2, \text{CO}, \text{H}_2 \end{aligned}$$

For char, C particles

$$\dot{C}_{C,in} = w_{pc} r_2 \rho_B / M_C. \quad (5)$$

Here, w_{pc} is the weight fraction of char in the pyrolysis product and M_C is the molecular weight of carbon. The outflow concentration of char depends on circulation rate of the bed material. Assuming a homogenous mixture of char and bed material particles in the reactor,

$$\dot{C}_{C,out} = \frac{w_c \dot{m}_b}{V_b M_C}. \quad (6)$$

Here, w_c is the weight fraction of char in the solid mixture, and \dot{m}_b is mass circulation rate of the bed material. Based on a uniform distribution of solid particles in the reactor, the expression for w_c is derived and given by

$$w_c = \frac{M_C C_C}{(s_r - 1)(\bar{\rho}_C - M_C C_C) + \bar{\rho}_C}. \quad (7)$$

Here, $s_r = \bar{\rho}_b / \bar{\rho}_C$ is solid mass loading ratio, $\bar{\rho}_b = \varepsilon_b \rho_b$ is bulk density of the bed material, and $\bar{\rho}_C = \varepsilon_C \rho_C$ is bulk density of char. ρ_b and ρ_C are the densities of bed material and char, respectively, and their respective volume fractions are ε_b and ε_C .

Again, the effective volume fraction ε_s of the solid particles in the reactor is given by

$$\varepsilon_s = \varepsilon_b + \frac{M_C C_C}{\rho_C} (1 - \varepsilon_b / \varepsilon_C). \quad (8)$$

Since the amount of char decreases as the reaction goes, the total reaction volume decreases with char conversion. Assuming that circulation of the bed material is in steady state, the instantaneous reaction volume can be obtained from

$$V_b = \left(\frac{\varepsilon_s}{1 - \varepsilon_f} \right) \frac{V_0}{\left(1 - \frac{M_C C_C}{\bar{\rho}_C} \right)}. \quad (9)$$

Here, $V_0 = A_b H_0$ is the solid volume of bed material, with H_0 its solid height and $A_b = \pi D_b^2 / 4$ the reactor cross sectional area, where D_b is the bed diameter. ε_f is the average voidage of the bed under bubbling influence. It should be noted that because of lack of space, derivations of Eq. (7)-(9) are not part of this paper.

The decrease in char residue concentration due to its conversion is expressed as

$$R_C = -(r_3 + r_4). \quad (10)$$

For each of the gaseous species,

$$\begin{aligned} \dot{C}_{j,in} &= w_{pv} v_j r_1 \rho_B / M_j \\ j &= CO_2, CO, H_2. \end{aligned} \quad (11a)$$

For steam, H_2O

$$\dot{C}_{H_2O,in} = \frac{w_{pv} v_{H_2O} r_1 \rho_B}{M_{H_2O}} + \frac{\dot{m}_{steam}}{V_b M_{H_2O}}. \quad (11b)$$

Here, w_{pv} is the weight fraction of total volatile matters in the pyrolysis product and M_j is molecular weight of the j species. v_j is weight fraction of the species in the volatiles after pyrolysis. \dot{m}_{steam} is steam mass flow rate into the reactor.

The decrease in concentration of each species due to gas product outflow from the reactor depends on concentration of the species at exit of the reactor, and on the fluidization velocity. Assuming ideal gas behaviour, and that the gas outlet is subjected to atmospheric pressure,

$$\dot{C}_{j,out} = \left(C_j - \frac{x_j P_0}{RT} \right) \frac{\dot{V}_g}{V_b} \quad (12)$$

$$x_j = C_j / \sum C_j. \quad (13)$$

x_j is the mole fraction of species j in the gas phase mixture and P_0 is the atmospheric pressure. The reciprocal of $\frac{\dot{V}_g}{V_b}$ defines the reaction residence time. The gas volumetric flow rate \dot{V}_g is given by

$$\dot{V}_g = A_b (u_0 - u_{mf}). \quad (14)$$

Here, $u_0 = \frac{\dot{m}_{steam}}{f A_b \rho_{steam}}$ is superficial gas velocity of the approaching gasifying agent (steam) and u_{mf} is the minimum fluidization velocity. u_{mf} can be obtained from Eq. (15) (Radmanesh et al, 2006). f is a reduction factor of the bed cross sectional area which ensures high fluidization velocity. In this work, a value of 0.2 is used.

$$u_{mf} = \frac{\mu_g}{d_p \rho_g} \sqrt{(27.2^2 + 0.0408 Ar)} - 27.2 \quad (15a)$$

$$Ar = \frac{d_p^3 \rho_g (\rho_s - \rho_g) g}{\mu_g^2} \quad (15b)$$

Here, μ_g and ρ_g are gas mixture viscosity and density, respectively. d_p is solid particle diameter, and g is acceleration due to gravity.

The gas mixture density can be obtained from Eq. (16). The viscosity of gas mixture is given by Eq. (17) (Herning and Zipperer, 1936), in which μ_j is the individual species viscosity.

$$\rho_g = \frac{1}{1 - \varepsilon_s} \sum C_j \sum (x_j M_j) \quad (16)$$

$$\mu_g = \frac{\sum (\mu_j x_j \sqrt{M_j})}{\sum (x_j \sqrt{M_j})} \quad (17)$$

The average bed voidage at bubbling fluidization can be obtained from

$$\varepsilon_f = \delta + (1 - \delta)\varepsilon_{mf}. \quad (18)$$

The minimum fluidization voidage ε_{mf} is given by Eq. (19) and the bubble fraction in the bed δ can be obtained from Eq. (20).

$$\frac{1}{\phi_s \varepsilon_{mf}^3} \approx 14 \quad (19)$$

$$\delta = \frac{u_0 - u_{mf}}{u_b} \quad (20)$$

Here, u_b is the bubble rise velocity, which can be obtained by

$$u_b = u_0 - u_{mf} + 0.711\sqrt{gD_b}. \quad (21)$$

D_b is the average bubble diameter over the bed, and can be obtained by

$$D_b = \frac{0.30(u_0 - u_{mf})^{0.4} H_b^{0.8}}{g^{0.2}}. \quad (22)$$

H_b is the initial bed height. The overall generation rates of the species, assuming forward reactions as given in R3 - R5 are

$$R_{H_2O} = -(r_3 + r_5) \quad (23a)$$

$$R_{CO_2} = -r_4 + r_5 \quad (23b)$$

$$R_{CO} = r_3 + 2r_4 - r_5 \quad (23c)$$

$$R_{H_2} = r_3 + r_5. \quad (23d)$$

2.2 Reaction Rate Constants

The success of every chemical kinetic model depends on rate constants of the reactions. Several models for reaction rate constants are published in the literature. Since the main objective of this paper is to investigate the influence of reaction rate constants on biomass gasification, two set of models used in (Xie et al, 2012) and (Braun et al, 1981) are utilized, and their results are compared. The rate constants given for the pyrolysis process are applied in both cases. Table 2 gives a summary of these models as applied in each of the cases. The rate constants are expressed in mol/(m³.s).

The models in Case 1 account for reversibility, and for influence of char residue in the heterogeneous reactions R3 and R4. In addition to effects of char residue in the heterogeneous reactions, Case 2 takes into account the porosity of total solid particles in the homogeneous reaction. The generation rates of the species in Case 1 are given by

$$R_C = (r_{3r} + r_{4r}) - (r_{3f} + r_{4f}) \quad (24a)$$

$$R_{H_2O} = r_{3r} - (r_{3f} + r_5) \quad (24b)$$

$$R_{CO_2} = (r_{4r} + r_5) - r_{4f} \quad (24c)$$

$$R_{CO} = (r_{3f} + 2r_{4f}) - (r_{3r} + 2r_{4r} + r_5) \quad (24d)$$

$$R_{H_2} = (r_{3f} + r_5) - r_{3r} \quad (24e)$$

m_s in Case 1 model is the mass of a single carbon particle, and it is modeled as in Eq. (25).

$$\frac{dm_s}{dt} = (1 - \varepsilon_C) \frac{M_C}{\rho_C} m_s \frac{dC_C}{dt} \quad (25)$$

Based on the ideal gas behaviour, Eq. (26) gives the pressure, P in the reactor.

$$P = RT \sum C_j \quad (26)$$

$$j = H_2O, CO_2, CO, H_2$$

2.3 Char Conversion Factor

Char conversion factor, X_C describes the progress and efficiency of biomass gasification process. X_C given by Eq. (27), expresses how much of char is converted relative to its original concentration in the reactor.

$$X_C = \frac{C_{C,0} - C_C}{C_{C,0}} \quad (27)$$

Here, $C_{C,0}$ is the initial char concentration.

2.4 Initial Conditions

Assuming that the bed is initially filled with hot bed material and product of biomass pyrolysis (char and volatiles), the initial concentration of species in the reactor are obtained as follows.

$$C_{C,0} = \varepsilon_C \frac{V_C \rho_C}{V_b M_C} \quad (28)$$

The volume ratio, $\frac{V_C}{V_b}$ can be obtained from Eq. (29)

$$\frac{V_C}{V_b} = 1 - \left(\frac{w_{pc}}{r_m} S_r + 1 \right)^{-1} \quad (29)$$

Here, r_m is the solid mass mixing ratio of bed material to biomass.

For each of gas species, assuming the pressure in the reactor is initially atmospheric,

$$C_{j,0} = \frac{x_{j,0} P_0}{RT} (1 - \varepsilon_{s,0}) \quad (30a)$$

$$x_{j,0} = \frac{v_j}{M_j} / \sum \left(\frac{v_j}{M_j} \right) \quad (30b)$$

$m_{s,0} = \frac{\pi}{6} d_c^3 \rho_C$, where d_c is the diameter of single char particle. $\rho_{B,0} = 0$.

Table 2. Kinetic Rate Constants for Biomass Gasification Reaction

Reactions	Case 1 (Xie et al, 2012)	Case 2 (Braun et al, 1981)
R3	$r_{3f} = 1.272m_s T \exp\left(-\frac{22645}{T}\right) C_{H_2O}$ $r_{3r} = 1.044 \times 10^{-4} m_s T^2 \exp\left(-\frac{6319}{T} - 17.29\right) C_{H_2} C_{CO}$	$r_3 = \frac{k_1 P_{H_2O} C_C^2}{1 + k_2 P_{H_2} + k_3 P_{H_2O} C_{C,0}}$ $k_1 = 1.25 \times 10^5 \exp\left(-\frac{28000}{T}\right)$ $k_2 = 3.26 \times 10^{-4}$ $k_3 = 0.313 \exp\left(-\frac{10120}{T}\right)$
R4	$r_{4f} = 1.272m_s T \exp\left(-\frac{22645}{T}\right) C_{CO_2}$ $r_{4r} = 1.044 \times 10^{-4} m_s T^2 \exp\left(-\frac{2363}{T} - 20.92\right) C_{CO}^2$	$r_4 = \frac{k_4 C_C}{1 + \frac{x_{CO}}{k_{c4} x_{CO_2}}}$ $k_4 = 3.6 \times 10^5 \exp\left(-\frac{20130}{T}\right)$ $k_{c4} = 4.15 \times 10^3 \exp\left(-\frac{11420}{T}\right)$
R5	$r_5 = 2.78 \times 10^3 \exp\left(-\frac{1510}{T}\right) [C_{CO} C_{H_2O} - C_{CO_2} C_{H_2} / k_{c3}]$ $k_{c3} = 0.0265 \exp\left(\frac{3968}{T}\right)$	$r_5 = k_5 \left(x_{CO} x_{H_2O} - \frac{x_{CO_2} x_{H_2}}{k_{c5}}\right) \left(\frac{P}{RT}\right)^2 \varepsilon_f$ $k_5 = 377 \exp\left(-\frac{7300}{T}\right)$ $k_{c5} = 0.017 \exp\left(\frac{4400}{T}\right)$

3 Results and Discussion

The parameters used in this work are given in Table 3, where the variable, S_{br} is the steam-to-biomass ratio. The simulation is based on constant solid mass mixing ratio r_m .

3.1 Comparison with Barracuda Results

The gas-particle flow in the reactor is simulated in three dimensions using the commercial solver Barracuda VR 15. The Computational Particle Fluid Dynamic model is based on the Eulerian-Lagrangian approach of modeling gas-solid multiphase flow (Snider and Banerjee, 2010). The approach treats solid phase as discrete elements. The motion of individual particle is tracked using Newton's law. The particle-particle, particle-wall and fluid-particle interactions are taken into account (Boyalakuntla, 2003). The approach makes it possible to solve the gas-particle system with a wide range of particle size distribution (Amsden et al, 1989).

The evolution of mole fractions of the gas composition in the reactor based on the developed simplified (ideally mixed) model and based on the Barracuda (3D) model are compared in Figures 2 and 3, for a steam-biomass ratio of 0.6. The Barracuda result is obtained by simulating the 3D model in a reactor of 2 m high including the freeboard space under the same cond-

itions as given in Table 2. The 3D model results shown are the composition of the gaseous product just at the top of the bed.

Figure 2 shows that Case 1 model seems to show little or no conversion. Except water, all other compositions show decreasing trend with time, which differ widely from the 3D model results. On the other hand, Figure 3 shows that Case 2 model gives a similar

Table 2. Parameters for Model Computation.

Parameters	Values	Units
d_b	0.5	mm
d_c	2.0	mm
ε_b	0.6	-
ε_c	0.3	-
H_0	0.40	m
D_b	0.55	m
T	1100	K
P_0	1.01	bar
r_m	40	-
ρ_b	2960	kg/m ³
ρ_c	200	kg/m ³
ρ_{steam}	0.204	kg/m ³
\dot{m}_{steam}	4.0x10-3	kg/s
$\dot{m}_{B,in}$	$\frac{\dot{m}_{steam}}{S_{br}}$	kg/s
\dot{m}_b	$r_m \dot{m}_{B,in}$	kg/s

trend to Barracuda and predicts except H_2 , compositions of CO_2 , CO and H_2O closer to the 3D model. The high discrepancy in the mole fraction of H_2 (Case 2) could be due to non-inclusion of CH_4 in the simplified model simulation, which was considered in the 3D model. Because of similarities in the result trends, the proposed model can be used to study the effect of variables such as steam-biomass ratio that influence the gasification process.

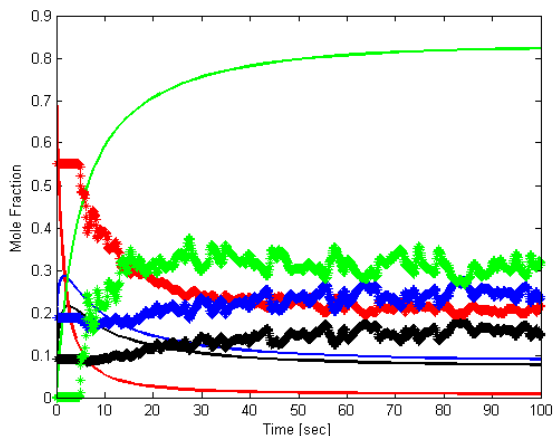


Figure 2. Comparison with 3D Model for Case 1.
Green = H_2O , Blue = H_2 , Red = CO , Black = CO_2
Ideally mixed: Solid lines; 3D model: Saw-toothed

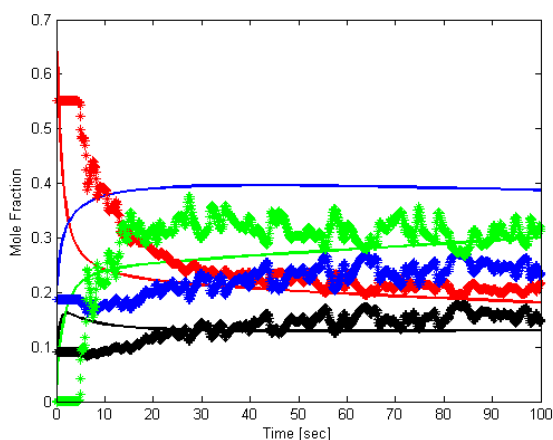


Figure 3. Comparison with 3D model for Case 2.
Green = H_2O , Blue = H_2 , Red = CO , Black = CO_2
Ideally mixed: Solid lines; 3D model: Saw-toothed

3.2 Conversion versus Time

Using the parameters in Table 3 and steam to biomass ratio of 0.25, the model developed in this paper is simulated using MATLAB ode solver. Figure 4 compares the char conversion factor obtained from both models in Case 1 and Case 2. The Case 1 result shows that less than 10% conversion can be achieved in 10 minutes. In Case 2, the result shows an appreciable increase in conversion factor, giving over 45% conversion at the end of 10 minutes. Figure 5(a) shows that the concentration of unconverted water in the

system is higher in Case 1 than in Case 2, and this confirms why the difference in the conversion factor obtained in the two cases.

Figures 5(b-d) show the evolution of concentration of CO_2 , CO and H_2 , respectively for both cases. Both cases show similar trends in CO_2 concentration, but Case 2 gives higher values over time. It can be seen from the results that the concentrations of CO_2 , CO and H_2 in Case 1 remain the same after 1 minute. This indicates that the product gas is mainly from pyrolysis process with little or none from gasification process. The corresponding concentrations in Case 2 are higher over time, possibly due to higher char conversion and more activities in the water gas shift reaction (R5). The slight decrease in H_2 in this case after attaining maximum concentration may be due to a decrease in char residue and retardation in water gas shift reaction due to decreasing CO concentration within this period as shown in Figure 5(c).

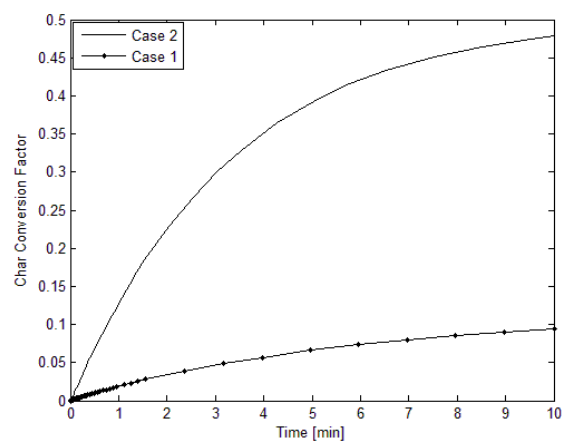


Figure 4. Evolution of Char Conversion Factor.

3.3 Conversion versus Steam-to-Biomass Ratio

The effect of steam-biomass ratio, S_{br} is represented by the results in Figures (6-8). The results for each S_{br} correspond to the values at the 10th minute. Figure 6 compares the trend of char conversion with steam-biomass ratio for both cases. The result trends from both cases are exactly opposite. Case 1 show a decreasing conversion factor as steam-biomass ratio increases. However, in Case 2, X_C increases as S_{br} increases. The increasing value of conversion factor in Case 2 can be attributed to the reduction in amount of biomass into the reactor since higher S_{br} indicates lower biomass flow rate.

Comparing Figures 7 and 8 (variation of mole fractions of the product gas composition with S_{br}), it can be seen that both have similar trend. Both show decrease in amount of CO_2 , CO and H_2 and increase in amount of water, but Case 2 gives higher values for CO_2 , CO and H_2 , and lower values for H_2O due to higher conversions. The decrease in the gas compositions may be due to less contribution from pyrolysis as S_{br} increases.

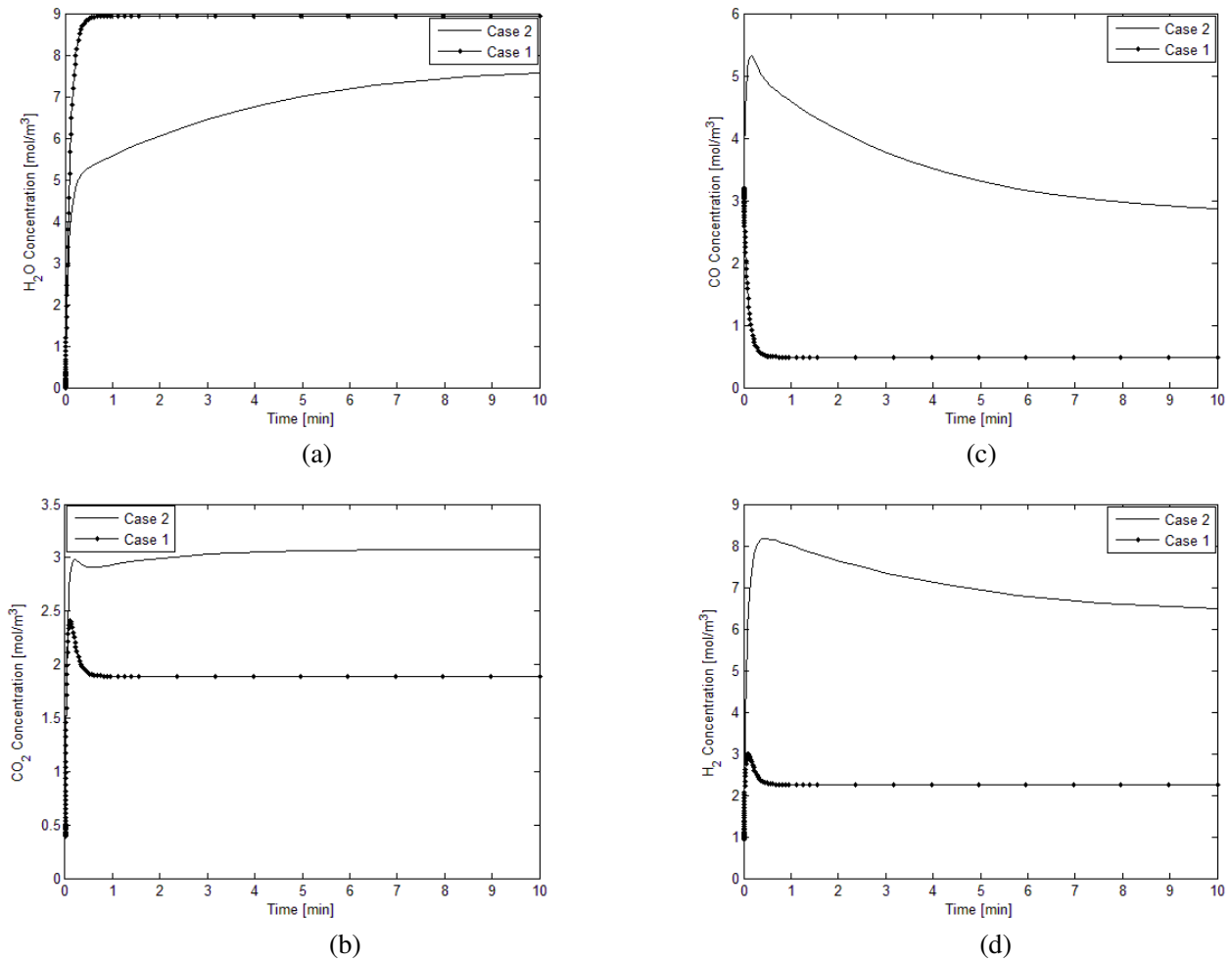


Figure 5 (a-d). Evolution of Product

Gas Concentration.

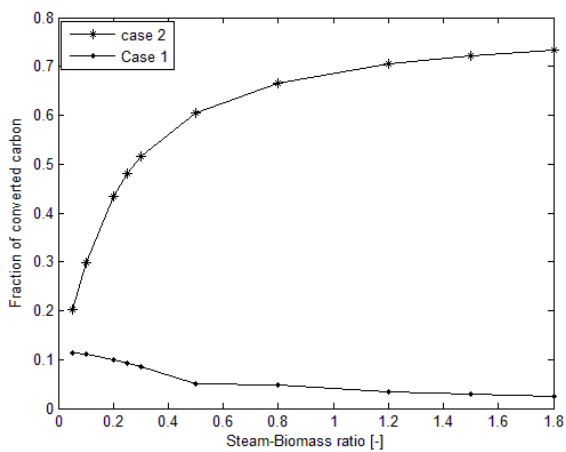


Figure 6. Effect of Steam-Biomass Ratio on Char.

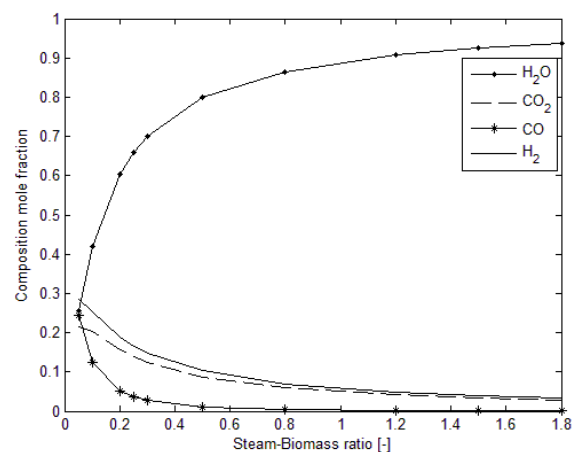


Figure 7. Effect of Steam-Biomass Ratio on Product Composition (Case 1).

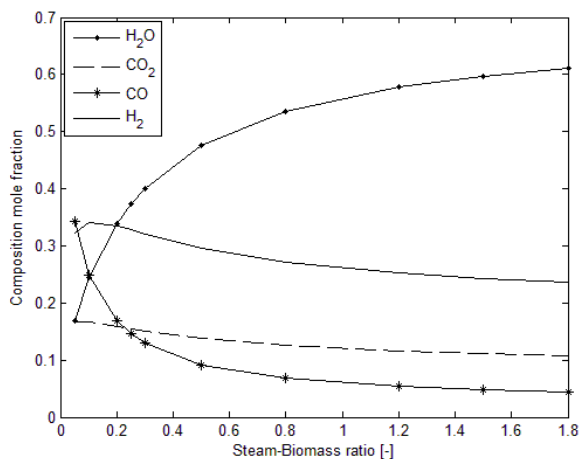


Figure 8. Effect of Steam-Biomass Ratio on Product Composition (Case 2).

3.4 Model Sensitivity

There are certain parameters of the model that are not certainly correct based on the simplified assumptions. Such parameters include temperature distribution and particle sizes of the bed material and char. The results obtained from the simplified model are based on the average bed material' particle diameter and on the mean reaction temperature. Sensitivity of the model to deviation of these parameters from the mean values, and to uncertainty in the parameter measurement, is analyzed here. The sensitivity measures the relative change in any output of the model due to relative change in any parameter of the model as expressed in Eq. (31).

$$S = \frac{\left(\frac{\Delta X}{X_0}\right)}{\left(\frac{\Delta Y}{Y_0}\right)} \quad (31)$$

Here, S is the sensitivity, X_0 and Y_0 are the model output and parameter, respectively, at the operating point. ΔY is the deviation of the parameter from the operating point and ΔX is the corresponding deviation of the model output.

Figures 9 and 10 show the relative change in char conversion factor, and in CO and H₂ concentrations, due to relative change in temperature and bed material' particle diameter, respectively, based on Case 2 model. From Figure 9, the sensitivity of the model in response to temperature change is 6.82 for char conversion, 7.27 for CO and 2.07 for H₂. This implies that for every 1% change in temperature, keeping other parameters constant, the char conversion increases by 6.82%, and CO and H₂ concentrations increase by 7.27% and 2.07%, respectively. The result in Figure 10 suggests that output of the model decreases for any increase in the bed material' particle size, keeping other parameters constant. The sensitivity to change in the material particle size is very low, giving 0.015%, 0.040% and 0.016% decrease in char conversion, CO and H₂

concentrations, respectively, for every 1% increase in the particle size.

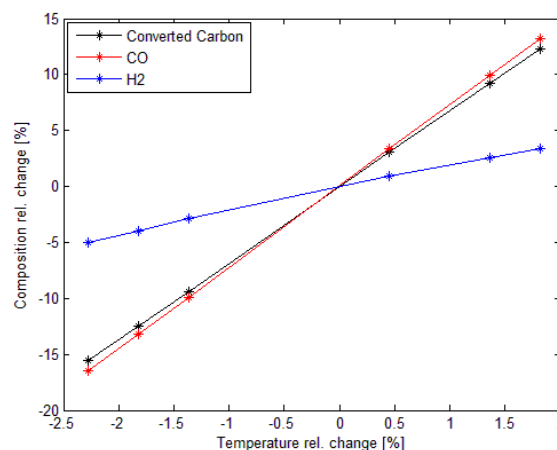


Figure 9. Model Response to Temperature Deviations.

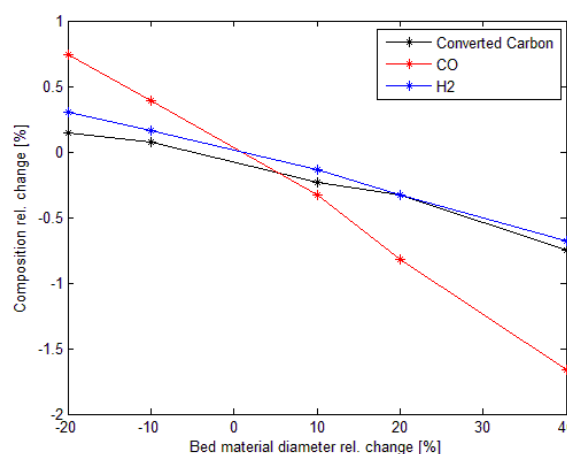


Figure 10. Model Response to Deviation of Bed Material' Particle Diameter.

4 Conclusions

In this paper, a model for predicting the kinetics of biomass gasification in a constant temperature bubbling fluidized bed reactor with circulating bed material is developed. In developing the model, effects of convection and diffusion of species in the reaction zone are neglected, and ideal mixing condition is assumed. The influence of bed material circulation on char residue reduction and the total reaction volume change due to char conversion and bubbling of the bed are captured. Two kinetics rate constants (Case 1 and Case2) are used to test the model and their results show that conversion of char and composition of the product gas depend on the kinetic rate constants. Case 2 model gives results closer to a 3D model based on Barracuda VR. The sensitivity analysis shows that the output of the model strongly depends on temperature and slightly depends on the bed material particles size.

The proposed model forms a basis for further work to develop a more detailed model that takes into account,

diffusion and convection of the reacting species as well as the dynamic of temperature.

References

- A. Farooq, M. Ghauri, M. H. Jaffery, and K. Shahzad (2013): Modeling of Biomass Gasification with CO₂ as Gasifying Agent. *Journal of Sci. Int. (Lahore)*, 25(3): 497-500, 2013.
- A.A. Amsden, P.J. O'Rourke, and T.D. Butler (1989): A Computer Program for Chemically Reactive Flows with Sprays. *Los Alamos National Laboratory*, 1989.
- D. Fiaschi, and M. Michellini (2001): A Two-Phase One-Dimensional Biomass Gasification Kinetics Model. *Journal of Biomass and Bioenergy*, 21: 121-132, 2001.
- D. Snider, and S. Banerjee (2010): Heterogeneous Gas Chemistry in the CPFD Eulerian-Lagrangian numerical scheme (ozone decomposition). *Journal of Powder*, 199(1): 100-106, 2010.
- D.S. Boyalakuntla (2003): Simulation of Granular and Gas-Solid Flows Using Discrete Element. *Department of Mechanical Engineering, Carnegie Mellon University*, pp.74, 2003.
- F. Fantozzi, S. Colatoni, P. Bartocci, and U. Desider (2007): Rotary Kiln Slow Pyrolysis for Syngas and Char Production from Biomass and Waste - Part II: Introducing Product Yields in the Energy Balance. *Journal of Engineering for Gas Turbines and Power*, 129: 908-913, 2007.
doi:10.1115/1.2720539.
- F. Hering, and L. Zipperer (1936): Calculation of the Viscosity of Technical Gas Mixtures from Viscosity of the Individual Gases. *Gas-Und Wasserfach*, 79: 69-73, 1936.
- J. Xie, W. Zhong, B. Jin, Y. Shao, and H. Liu (2012). Simulation on Gasification of Forestry Residues in Fluidized Beds by Eulerian-Lagrangian Approach. *Journal of Bioresource Technology*, 121: 36-46, 2012.
doi:10.1016/j.biotech.2012.06.080.
- P. Lü, X. Kong, C. Wu, Z. Yuan, L. Ma, and J. Chang (2008): Modeling and Simulation of Biomass Air-Steam Gasification in a Fluidized Bed. *Journal of Chem. Eng. China*, 2(2): 209-213, 2008.
doi:10.1007/s11705-008-0039-7
- Q. Xu, S. Pang, and T. Levi (2011): Reaction Kinetics and Producer Gas Compositions of Steam Gasification of Coal and Biomass Blend Char, Part 2: Mathematical Modelling and Model Validation. *Journal of Chemical Engineering Science*, 66: 2232-2240, 2011.
doi:10.1016/j.ces.2011.02.054.
- R. Radmanesh, J. Chaouki, and C. Guy (2006): Biomass Gasification in a Bubbling Fluidized Bed Reactor: Experiments and Modeling. *Journal of American Institute of Chemical Engineers*, 52(12): 4258-4272, 2006.
doi:10.1002/aic.11020.
- R.K. Thapa, C. Pfeifer, and B.M. Halvorsen (2014): Modeling of Reaction Kinetics in Bubbling Fluidized Bed Biomass Gasification Reactor. *Internal Journal of Energy and Environment*, 5(1): 35-44, 2014.
- R.L. Braun, R.G. Mallon, and H.Y. Sohn (1981): Analysis of Multiple Gas-Solid Reactions during the Gasification of Char in Oil Shale Blocks. *InProc. 14th Oil Shale Symposium*, Colorado School of Mines Press, Golden, Colo, pp. 289-300, 1981.
- Y. Haseli, J.A.V Oijen, and L.P.H. de Goey (2011): A Detailed One-Dimensional Model of Combustion of a Woody Biomass Particle. *Journal of Bioresource Technology*, 102, 9772-9782, 2011.
doi:10.1016/j.biotech.2011.07.075.

Notations

A	Cross sectional area [m ²]
A	Pre-exponential factor [s ⁻¹]
C	Molar density/concentration [mol/m ³]
\dot{C}	Mole density flow rate [mol/(m ³ .s)]
D	Reactor diameter [m]
d	Particle diameter [m]
E	Activation energy [J/mole]
g	Gravitational acceleration [m/s ²]
H	Height [m]
k	Reaction rate coefficient
M	Molecular weight [kg/kmol]
m	Mass [kg]
\dot{m}	Mass Flow rate [kg/s]
P	Pressure [Pa]
R	Gas constant [J/(mol.K)]
R	Net rate constant [kg/(m ³ .s)]/[mol/(m ³ .s)]
r	Rate constant [kg/(m ³ .s) or [mol/(m ³ .s)]
r_m	Mass mixing ratio
S_r	Solid bulk density ratio
S_{br}	Steam-biomass ratio
T	Temperature [K]
t	Time [s]
u	Velocity [m/s]
V	Volume [m ³]
v	Weight fraction reference to gas phase
\dot{V}	Volume flow rate [m ³ /s]
w	Weight fraction reference to solid phase
X	Conversion factor
ε	Volume fraction
ρ	Mass density/concentration [kg/m ³]
$\bar{\rho}$	Bulk density [kg/m ³]
Subscripts	
B	Biomass
b	Bed
C	Char
i	Number index
j	Any species
0	Initial/fixed position

A Framework for Early and Approximate Uncertainty Quantification of Large System Simulation Models

Magnus Eek¹, Johan Karlén¹, and Johan Ölvander²

¹*Saab Aeronautics, Linköping, Sweden, {magnus.eek, johan.karlen}@saabgroup.com*

²*Machine Design, IEI, Linköping University, Linköping, Sweden, johan.olvander@liu.se*

Abstract

Uncertainty Quantification (UQ) is vital to ensure credibility in simulation results and to justify model-based design decisions – especially in early development phases when system level measurement data for traditional model validation purposes are scarce. Central UQ challenges in industrial applications are computational cost and availability of information and resources for uncertainty characterization. In an attempt to meet these challenges, this paper proposes a framework for early and approximate UQ intended for large simulation models of dynamical systems. A Modelica simulation model of an aircraft environmental control system including a liquid cooling circuit is used to evaluate the industrial applicability of the proposed framework.

Keywords: Uncertainty quantification, aleatory uncertainty, epistemic uncertainty, model validation, aircraft system simulation models, Modelica

1 Introduction

In early phases of aircraft system design, a common situation is that only a simulation model of the system to be developed is available. That is, no physical test rig of the system exists, implying that no system level measurement data for model validation purposes are available. Nevertheless, for taking justified design decisions, an approximate estimation of the uncertainties in the simulation results is needed. Historically, this situation often ends up with a subjective experience-based assessment of simulation results uncertainty. The usefulness of subjective experience-based assessments should not be underestimated, but a more rational response to the need for well-founded estimations of uncertainties would be to apply a structured method for Uncertainty Quantification (UQ). UQ is here understood as the process of identifying, quantifying, and assessing the impact of uncertainty sources embedded along the

development and usage of simulation models. A case study carried out at Saab Aeronautics revealed a large gap between this part of industry and academia regarding the application of UQ (Eek, Kharrazi, Gavel and Ölvander, 2015). There are several reasons why UQ is not widely applied in aircraft system design; one is the always tight project budgets and time schedules and another the fact that many engineers working with Modeling and Simulation (M&S) are not aware of structured methods for UQ or do not know where to begin.

An overview of UQ methods in an industrial context together with a discussion on how model size and information availability affect the complexity of a UQ effort is provided by de Rocquigny, Devictor and Tarantola (2008). The UQ community, with substantial activity in high-consequence areas like nuclear power and climate, but also Computational Fluid Dynamics (CFD) in general, has come far but many techniques found in the literature seem to be suited for fast executing models or models with only a few uncertain parameters. This is rarely the case in M&S of aircraft vehicle systems, and a central challenge to enable UQ is therefore to reduce the dimensionality of the problem, i.e. to reduce the number of uncertain parameters that need to be considered. Another challenge is to find a suitable level of detail when performing UQ. That is, to simplify the UQ as far as possible without affecting the UQ results in such a way that they become irrelevant. In the work presented in this paper, a simulation model of a cooling system in the Saab Gripen fighter is used as the experimental frame for development and evaluation of an approximate and computationally relatively cheap UQ method.

The outline of the paper is as follows. First, the industrial application example is described, followed by an introduction to an established method for UQ. A few methods to reduce the computational cost as well as the engineering workload of UQ are then elaborated. This is followed by a proposal for a framework for early

and approximate UQ, together with experimental results. A discussion and conclusions are presented in the final section.

2 Industrial Application Example

Air supply, cabin pressurization, and avionics cooling are basic requirements for most aircraft, usually facilitated by an Environmental Control System (ECS) taking engine bleed air which is conditioned (decreased in pressure and temperature and dried) prior to distribution. For the Saab Gripen E fighter, a setup with two ECS is under consideration; a Primary ECS (P-ECS) and a Secondary ECS (S-ECS). The main task of the P-ECS is to provide conditioned air for cooling of

the avionics equipment, cabin thermal control and pressurization, pressurization of the fuel and anti-g systems, and to provide conditioned air to the On-Board Oxygen Generating System (OBOGS). Via a liquid cooling system, hereinafter referred to as Liquid Loop (LL), the S-ECS facilitates cooling of tactical systems. A more detailed description of the Saab Gripen ECS including system schematics is given by (Carlsson, Andersson, Gavel and Ölvander, 2012a).

To support system design and to estimate cooling performance, simulation models of the systems are developed and integrated into a total S-ECS model as shown in the schematic description in Figure 1.

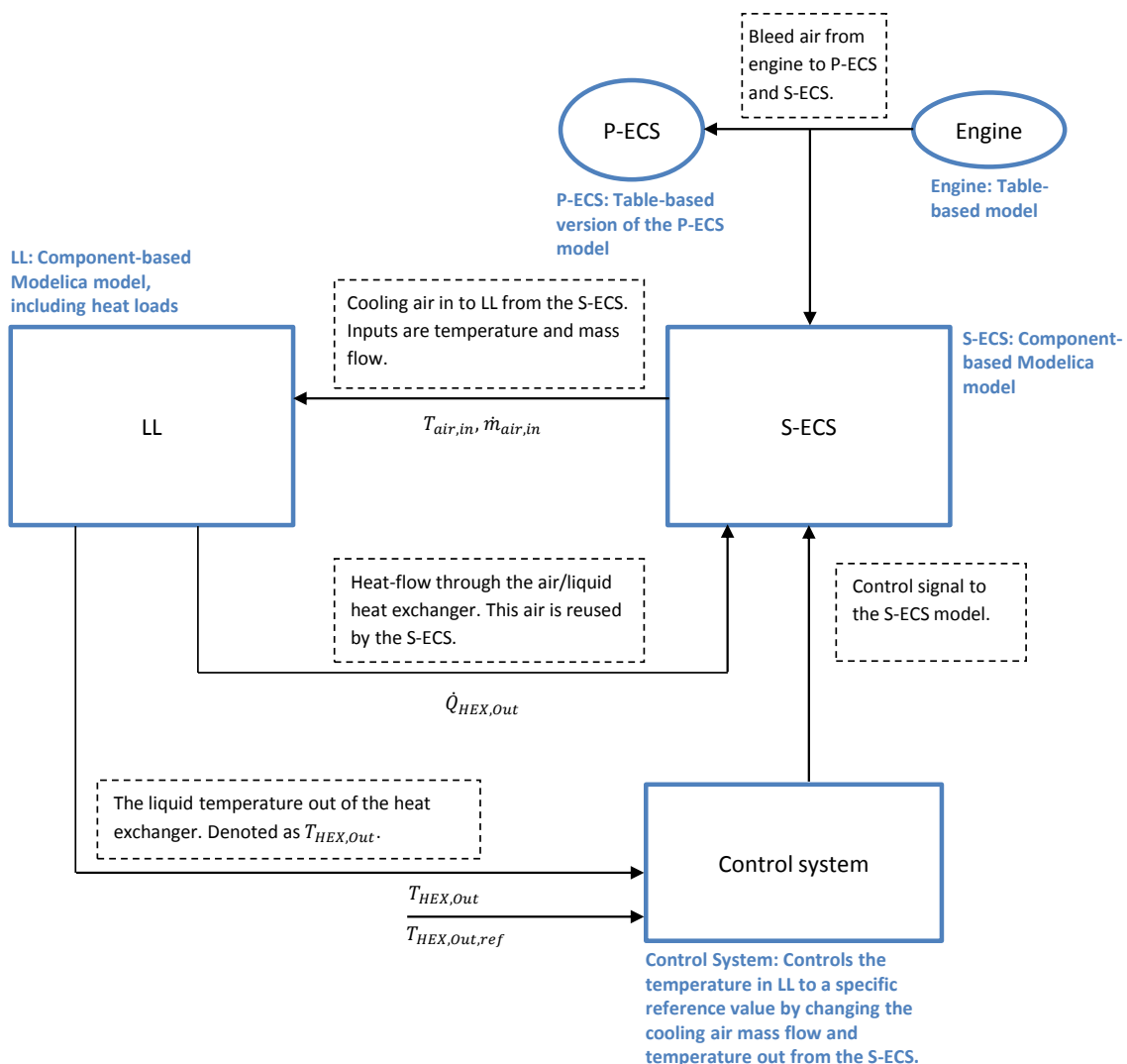


Figure 1. Schematic description of the total S-ECS simulation model.

The simulation model described above is used to estimate cooling performance, both in steady-state operation at specific points in the flight envelope and for full-length flight missions including transient conditions. The simulation

models are developed in the equation-based object-oriented language Modelica¹, using the

¹ <https://modelica.org/>

Dymola tool². Normally, simulation and analysis of results are performed directly in Dymola, but in the development of the UQ method presented in this paper, scripting and post-processing are done in MATLAB³, see Figure 2.

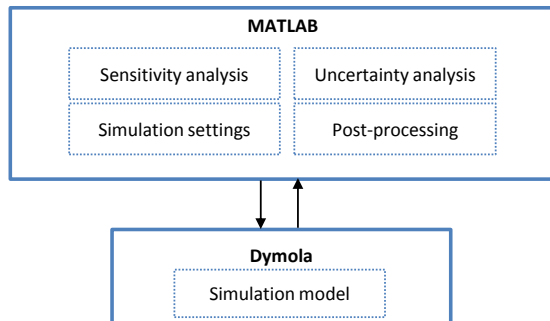


Figure 2. Simulation environment used for development and testing of UQ method.

3 Theoretical Background

Roy and Oberkampf (2011) describe a comprehensive framework for UQ where uncertainties are extensively propagated through a simulation model in order to obtain a detailed uncertainty response. This framework is generally considered to give a well-founded UQ and consists of six steps, as described below.

1. Identify all sources of uncertainty
2. Characterize uncertainties
3. Estimate the uncertainty due to numerical approximations
4. Propagate input uncertainties through the model
5. Estimate model form uncertainty
6. Estimate total uncertainty

The uncertainties can be divided into three categories in order to simplify and structure the identification process. These are input uncertainties, numerical approximations, and model form uncertainties. The input uncertainties can for example stem from model input signals, model parameters, boundary conditions, or initial conditions.

In the first step of the UQ framework proposed by Roy and Oberkampf (2011), all inputs and parameters in a simulation model should be considered as uncertain unless there is strong evidence that their uncertainty does not affect the system response.

In the second step, uncertainties are generally categorized into two different types,

either epistemic or aleatory (Helton, 1996, Helton and Davis, 2003, Oberkampf and Roy, 2012). Epistemic or reducible uncertainties are normally characterized with an interval, a minimum and maximum value, with no probability assigned to possible values. Epistemic uncertainties can be said to derive from lack of knowledge. Aleatory or irreducible uncertainties are stochastic uncertainties that are generally characterized with a Probability Density Function (PDF) or its corresponding Cumulative Distribution Function (CDF). Uncertainties characterized as aleatory therefore contain more information than epistemic ones. Mixed epistemic and aleatory uncertainty may be represented by an imprecise PDF, which here refers to when the parameters of the PDF, for example the mean and standard deviation, are given as intervals or PDFs themselves.

In the third step, the numerical uncertainties due to the solver are estimated. Numerical approximations can be treated as epistemic and added to the system response uncertainty.

When the identification and characterization have been done, the input uncertainties are propagated through the simulation model using a sampling technique. The idea of the sampling is to repeatedly take a random set of uncertainties and simulate the model. These simulations will give response deviations and hence the simulation results' uncertainty due to input uncertainties is obtained. Sampling techniques commonly used in industrial applications are Monte Carlo Sampling (MCS) and Latin Hypercube Sampling (LHS). The latter is a stratified sampling technique in which the range of each uncertain variable is divided into l intervals with equal probability. Only one value is drawn from each interval, but in a random order. This method ensures that all intervals of the uncertain variable are represented, but not more than once. This is in contrast to brute force MCS that is totally random with no guarantee of representing the entire variability of the uncertainties (Saltelli, Ratto, Andres, Campolongo, Cariboni, Gatelli et al., 2008).

Roy and Oberkampf (2011) suggest that each combination of the epistemic uncertainties is propagated with LHS in an outer loop while all the aleatory uncertainties are propagated with MCS in an inner loop. For m epistemic uncertainties, the recommended number of LHS intervals is m^3 . The number of simulations needed in order to propagate input uncertainties can then be calculated as

² <http://www.3ds.com/products-services/catia/products/dymola>

³ www.mathworks.com/products/matlab/

$$n = m^3 \cdot s \quad (1)$$

where n is the total number of simulations needed, m is the number of epistemic uncertainties, and s is the number of MCS samples of the aleatory uncertainties.

When the propagation of input uncertainties has been done, it is time to estimate the model form uncertainties. These stem from the selected model structure and assumptions and approximations of underlying equations made when developing the model. These uncertainties can be identified and characterized by comparing the simulation results with experimental measurement data in a probabilistic manner.

The total uncertainty in the simulation response consists of uncertainties due to inputs, numerical approximations, and model form. Roy and Oberkampf (2011) describe how these uncertainties can be combined to form a *probability box* for the system response (also known as a *p-box*), which is an interval-valued CDF.

4 Methods for Reduction of UQ Workload and Computational Cost

In the following subsections, a few methods to reduce the engineering workload as well as the computational cost required for UQ are proposed and described in the context of the industrial application example from section 2.

Some important conditions, which have great impact on the time needed for the UQ, both in terms of engineering workload and computational cost, can be stated:

- Limitations in the availability of information required for uncertainty characterization.
- Computational expense of the simulation model.
- The dimensionality of the UQ problem, i.e. the number of uncertainties.
- Number of nominal simulations required. For example, a model-based performance evaluation of a system to be developed may require a large number of nominal simulations, which in turn should be evaluated in terms of UQ.

The above combination of characteristics restricts the choice of UQ method. In early system development phases, the availability of information required for characterization of uncertainties is typically very limited.

Additionally, in early phases the system to be developed may not be completely defined and sometimes several possible system layouts are simulated. Thus, for UQ to be considered in early phases, the computational cost of UQ has to be kept as low as possible.

The comprehensive framework described in section 3 is mathematically stringent but requires many simulations when the number of epistemic uncertainties is large. A simulation of one single stationary operational point using the total model of the Gripen E, shown in Figure 1, takes about 20 minutes to run and can therefore be considered computationally expensive. To estimate the stationary cooling performance of the complete flight envelop (spanned by altitude and Mach number), typically about 60 points are needed. The computational cost combined with the high number of identified uncertainties (over 200 in the LL model alone) makes the UQ method described in Chapter 3 unfeasible. It is therefore of great importance to reduce the computational cost in order to enable a UQ.

4.1 Approximate Characterization of Uncertainties

To mitigate the problem of computational cost, one possibility is to consider a simplified characterization of the uncertainties in order to get rid of the inner sampling loop. A simplification of the characterization would decrease the accuracy of the UQ, but could in practical situations be necessary in order to enable a UQ. This simplification could be made by assuming all uncertainties to be epistemic or by assigning the epistemic uncertainties a uniform probability distribution (Carlsson, Steinkellner, Gavel and Ölvander, 2013). Both these alternatives are described in the two following subsections.

Generating surrogate models of the different sub-models seen in Figure 1 was initially considered. Both grey-box and neural-network approaches were considered. However, a surrogate model with the possibility to describe the liquid temperature over time in the total simulation model accurately, with all required inputs such as heat loads, altitude, speed, g-loads, thrust, climate (humidity and air temperature) and the model uncertainties on top of this, was considered to be too complex and time-consuming to derive. In addition, early attempts to create a surrogate model of only the LL model of the Gripen E, sufficiently representative for use in UQ, have shown that this is also a challenging task. At this stage, the research was directed towards the methods described in the following subsections.

4.1.1 Approximate characterization using uniform distributions

Approximating all uncertainties using uniform distributions is a significant simplification that can be pragmatically justified with the argument that a uniform PDF, with respect to the width of the resulting output distribution, is the most conservative distribution available. Thus, in an approximate UQ context, a uniform PDF may be seen as a compromise between a normal distribution and a fully epistemic interval.

An evaluation of this approach was made with a less computationally expensive simulation

model of the liquid loop (LL) in the Gripen Demo test aircraft. This model is similar to the LL model of Gripen E in terms of modeling technique, but far less complex. All the identified uncertainties (25) were approximately characterized with a uniform distribution and were sampled with 350 LHS through the simulation model for one flight mission. The simulation results were then plotted against measurement data with an estimated experimental uncertainty. The result can be seen in Figure 3 where the black lines represent the LHS.

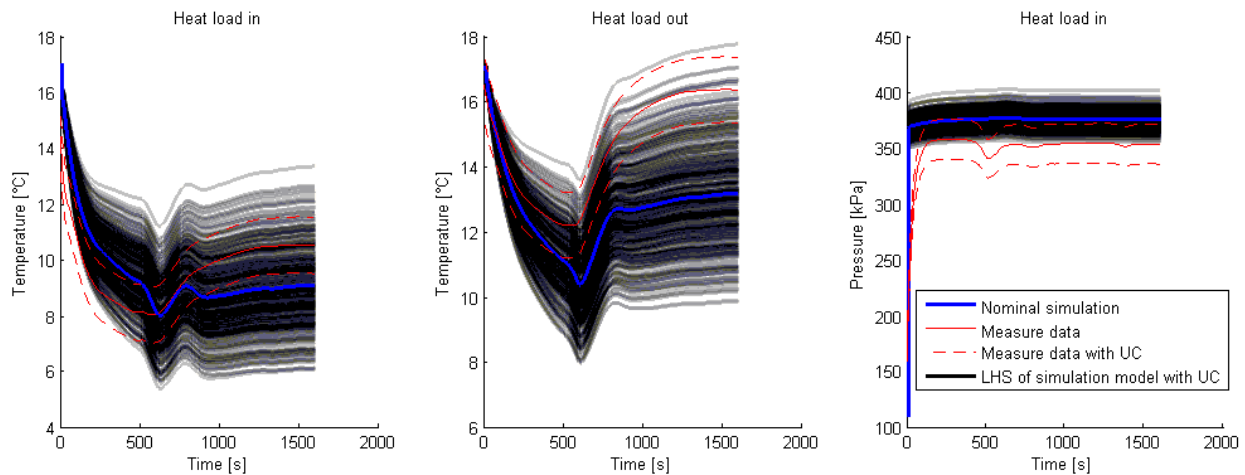


Figure 3. Propagation of the identified uncertainties (25 uncertainties) with 350 LHS through the Gripen Demo simulation model, compared to measurement data of the system.

From Figure 3 it can be seen that using the simplified characterization, the measured temperatures are captured within the range of simulation results. However, regarding the pressure level at the heat load inlet port, the identified and approximately characterized uncertainties do not produce simulation results that fully overlap the experimental data from flight testing. It should be noted that the nominal simulation results differ from the nominal measurement data both near steady-state (in the end of the simulation) and in the qualitative dynamic behaviour. This may be due to both simulation and experimental uncertainty, which both may be larger than estimated.

The method of approximating the uncertainty characterization using uniform distributions may be a suitable alternative for some applications. However, for the total S-ECS simulation model shown in Figure 1 this simplification is still not sufficient in terms of computational efficiency.

4.1.2 Approximate characterization using intervals

A method that can significantly reduce the number of simulations needed in order to determine the output uncertainty is to approximate all uncertainties as epistemic and apply an interval-based minimum/maximum analysis. Since epistemic uncertainties give an epistemic output, one theoretically needs only two simulations in order to find the output interval. If it is possible to find the uncertainty settings which give the output interval, one can drastically reduce the number of simulations needed of the total simulation model.

An approach to find this upper and lower output response is to use constrained optimization (Carlsson, Gavel and Ölvander, 2012c). When applying an optimization approach to computationally expensive models, it is advantageous to utilize Response Surface Methodology (RSM) in which the output response to the input uncertainties are described by a response surface (Khuri and Mukhopadhyay, 2010). An optimization approach using RSM in order to find the

uncertainty parameter settings that result in a minimum/maximum response can be complex if the uncertainties change nonlinearly and have strong interactions (Swiler, Mayes and Paez, 2009).

The total simulation model shown in Figure 1 consists of several connected sub-models, which can be run much faster when simulated as standalones. This opens up for new possibilities for interval-based UQ using RSM. In this work, a linear response surface has been used to approximate the output dependency of the input uncertainties. To clarify, the response surface is not a surrogate model of the simulation model itself, but rather a surrogate model of the relation between input and output uncertainties, i.e. used as a sensitivity measure. In fact, this can be seen as a way of performing global Sensitivity Analysis (SA) (Saltelli and Annoni, 2010). The response for a simulation can be written as

$$y = y_{nom} + \sum_{i=1}^n \Delta x_i \beta_i \quad (2)$$

where Δx_i denotes a change in input i from its nominal value and β_i denotes a constant, y represents the output affected by uncertainties and y_{nom} represents the nominal output. The constants β_i can be estimated using least square estimation and tell us how the uncertainties affect the response and can therefore be used to find the uncertainty settings that give the minimum and maximum response. In this paper, LHS is used to provide the input data to the least square estimation of β_i .

This is where the structure of the simulation model is utilized. The sub-models can be simulated as standalones in order to derive a response surface. The estimated constants β_i in the response surface can be used to find the settings of the uncertainties that give the minimum and maximum cooling performance with respect to each specific sub-model. These uncertainty parameter settings are from here on referred to as *minimum/maximum output parameter setting*.

We have so far assumed a linear dependency between the input and output uncertainties (in this case, the output is the uncertainty of the cooling liquid temperature at the heat exchanger outlet). But can this assumption be justified? A small change in an uncertainty can be assumed to have a small impact on the temperature, and this change can therefore be considered as linear. This assumption can be examined by varying the uncertainties one-at-a-time (OAT) while studying the temperature response; a simple form of local SA as described by Saltelli et al. (2008). This was done for the Gripen Demo LL model which was simulated as a standalone. The model was simulated for 440 seconds, during which time the uncertainties were varied OAT 10 times over their intervals with LHS while the other uncertainties were fixed at their nominal values during the simulation. It can be seen from Figure 4 that the uncertainties seem to affect the liquid temperature out of the heat exchanger linearly.

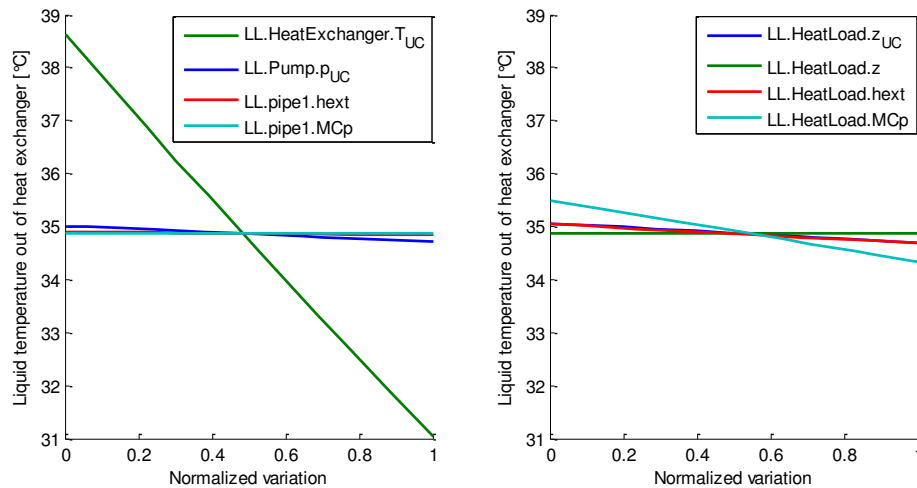


Figure 4. Graphs showing how the uncertainties affect the liquid temperature out of the heat exchanger when they are varied one-at-a-time 10 times over their intervals with LHS.

Such a study does not take interaction effects between uncertainties into consideration. It does, however, indicate that a linear approximation of how the uncertainties affect the response can be

justified. In order to examine whether interactions between the uncertainties have to be considered, one could compare the result when propagating uncertainties through the response

surface with an uncertainty propagation of the original model. This was done for the Gripen Demo LL model. A response surface according to equation (2) was derived with 26 simulations ($n = m + 1$). The uncertainties were then extensively propagated with MCS through the response surface and the resulting distribution of the heat exchanger outlet temperature was compared to the results of a MCS of the original model, see Figure 5. In this comparison, the uncertainties were characterized as uniform PDFs and propagated with 12000 MCS. The estimated β_i from the response surface were used to determine the min/max parameter output settings by examining the sign of β_i . These settings were then used to simulate the original model twice (with the minimum and maximum output parameter settings respectively), and the results can be seen as the green lines in Figure 5.

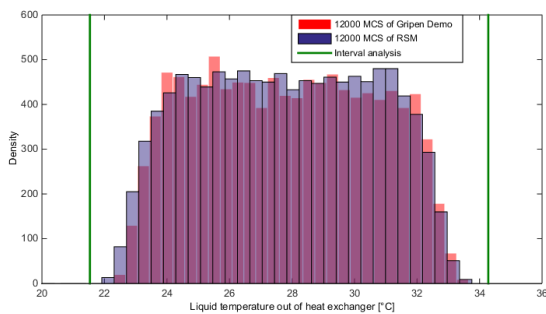


Figure 5. A comparison of the heat exchanger outlet temperature after 2000 seconds' simulation of the original Gripen Demo LL model (transparent red) and a linear response surface (transparent blue). The green lines are the results of the interval-based method. The purple area comes from the overlap of the blue and the red distribution.

Qualitatively, the linear response surface describes the output from the original Gripen Demo LL model relatively well. Figure 6 shows the time-series data obtained from two interval-based simulations and an extensive MCS respectively. Both Figure 5 and Figure 6 show that the results from the two interval-based simulations enclose the results from 12000 MCS, hence indicating that we have found the minimum/maximum output due to the identified uncertainties.

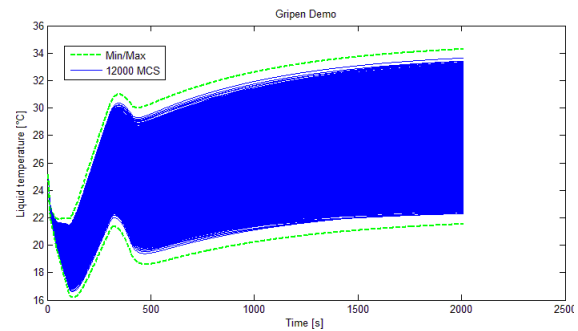


Figure 6. A comparison between 12000 MCS of the Gripen Demo LL model (blue) and two simulations of the same model using the minimum/maximum output parameter settings (red).

Another approach to find the min/max parameter output setting could be a local SA. However, by using the response surface one could use statistical methods as the coefficient of determination to examine the fit of the linear approximation and increase the credibility of the estimated min/max output parameter settings as described by Saltelli and Annoni (2010).

It is important to be aware that an epistemic approximation of all the uncertainties makes the UQ less informative since the information about aleatory uncertainties is lost. This might not be a problem if the uncertainties are epistemic or if the most significant uncertainties are epistemic. More about how to utilize SA in a UQ context is given in the following section.

4.2 Dimensionality Reduction of the UQ Problem

The credibility of the UQ relies on a good characterization of the uncertainties. According to Carlsson et al. (2013), the characterization workload for this type of simulation model can be extremely time-consuming. That characterization of uncertainties in general is time-consuming and expensive is also recognized by Saltelli et al. (2008) and Helton, Johnson, Sallaberry and Storlie (2006).

Treating all uncertainties as epistemic reduces the characterization workload, but the uncertainties still have to be assigned with well-founded intervals. The proposed characterization approach is to find the most important uncertainties, which affect the results the most, and devote the most resources to assigning these uncertainties with the most accurate intervals possible. The less important uncertainties with respect to the output of interest can be roughly assigned with “big enough intervals” or where justified ignored.

4.2.1 Reduction of uncertainties using SA

In combination with an initial rough uncertainty characterization, the importance of the uncertainties can be estimated using SA. Local SA using an OAT approach is easy to implement and has been proven to be suitable for complex 1-D simulation models of dynamical systems (Steinkellner, 2011). By comparing the sensitivity of a selected output with respect to each input uncertainty to the sum of the total sensitivity, a simple sensitivity metric can be calculated as

$$S_i = \frac{|y_{nom} - y(\theta_i)|}{\sum_{i=1}^n |y_{nom} - y(\theta_i)|} \quad (3)$$

where y_{nom} denotes is the nominal output, S_i is the sensitivity of the selected output to perturbations in the uncertain parameter θ_i , and n is the total number of uncertain parameters. The goal of this SA is to find the most influential uncertainties, which should be characterized more carefully, and to find insignificant uncertainties that can be safely ignored. This reduces the number of uncertainties, which is positive in terms of both computational cost and work effort related to detailed uncertainty characterization.

It should be noted that ignoring apparently insignificant uncertainties will make the uncertainty analysis less precise. Therefore, care has to be taken when setting a threshold for which uncertainties to ignore. A suitable threshold for this type of application could be to ignore the uncertainties that together account for less than 1% of the total sensitivity. This can be written as $\sum S_i < 1\%$ where the least significant uncertainties are added together. Such a threshold reduces the number of uncertainties for consideration from 259 to 39 for the Gripen E LL model, implying a significant reduction of the characterization workload.

As an alternative to the local SA OAT approach, a simple form of global SA may be carried out by using regression techniques, as described in section 4.1.2, equation (2).

4.2.2 Reduction of uncertainties using aggregation

In industrial applications, a major challenge when characterizing input uncertainties is lack of information. Obtaining credible information for uncertainty characterization may require extensive physical testing or development of alternative models of higher fidelity. Subject matter experts (SMEs) can be used, but in practice persons with relevant knowledge of a specific detail of an application may be very hard to find.

A method shown to be useful in the context of component-based 1-D system simulation models is to aggregate a number of input uncertainties into a smaller number of output uncertainties (Carlsson, Gavel and Ölvander, 2012b, Carlsson et al., 2012c). To clarify using an example of a pipe component, in which the differential pressure is calculated, the uncertain parameters (e.g. diameter, surface roughness, and pressure loss coefficients) are kept at their nominal values, and a new parameter is introduced to describe the total uncertainty of the differential pressure over the pipe. In this way, the number of uncertainties to be characterized and propagated is reduced. A nice feature of this method is that it can be used to describe not only input uncertainty but also model form uncertainty at component level.

5 Proposed Framework for Early and Approximate Uncertainty Quantification

Based on the comprehensive framework proposed by Roy and Oberkampf (2011), in combination with a number of methodological simplifications described in section 4, a method is proposed for early and approximate UQ applicable for large 1-D dynamic simulation models. The method consists of a number of steps as illustrated in Figure 7, and is briefly described in the subsections below. A prerequisite for carrying out a study according to the proposed workflow is that a main output of interest is defined and that a qualitative analysis is carried out of how each sub-model affects this output.

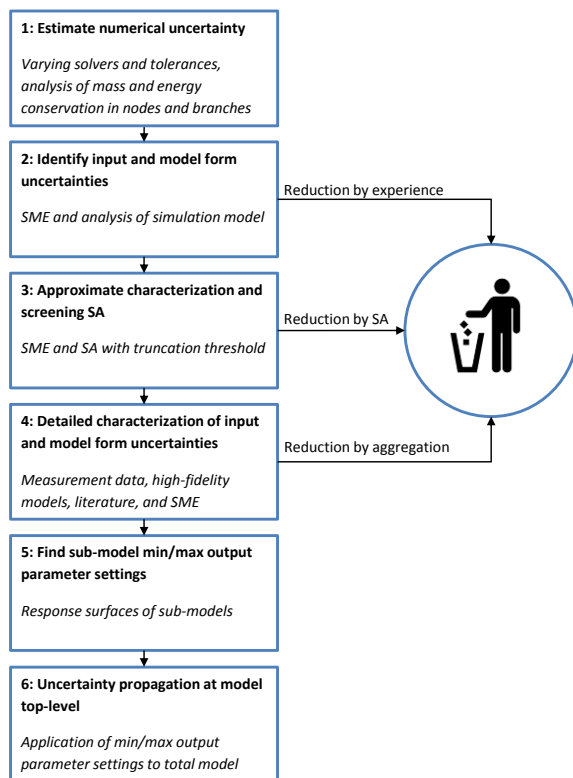


Figure 7. Proposed workflow of an approximate UQ for use in early system development phases, “SME” is an abbreviation of Subject Matter Expert. The number of uncertainties for consideration is reduced in three steps.

5.1 Estimate Numerical Uncertainty

To avoid unwanted effects of numerical uncertainty in later stages of the workflow, the numerical uncertainty is here estimated in the first step. In contrast to models of relatively high physical fidelity as often used in computational fluid dynamics (CFD) or computational solid mechanics (CSM), for 1-D simulation models of dynamical systems, the numerical uncertainty is typically insignificant. However, this has to be justified, which is the aim of the first step. This may be done by repeated simulations with varying solvers and solver tolerances, and by checking consistency of mass and energy conservation in nodes and branches of the model.

5.2 Identify Input and Model Form Uncertainties

In the second step, all uncertainty sources in addition to numerical uncertainty are identified. Regarding input uncertainty (uncertainties in for example input signals, parameters and boundary conditions), this is in accordance with the framework proposed by Roy and Oberkampf (2011). However, as the proposed approximate framework includes an estimation of model form

uncertainties by analysis at component or sub-model level rather than using measurement data from extensive repeated physical testing at system-level, there is a significant difference between the two frameworks. Estimation by analysis is less stringent but is the only applicable alternative found when extensive measurement data on system-level are not available – which is typically the case in early system development phases. For representation of model form uncertainty, the aggregation method described in section 4.2.2 may be used. Already at the second step, the number of uncertainties for later consideration can be reduced by experience.

5.3 Approximate Characterization and Screening SA

To further reduce the number of uncertainties, the third step includes an approximate experience-based characterization of the identified uncertainties in combination with a screening SA. Section 4.2.1 provides a simple example of how this can be done by the use of local SA. However, if global SA is applied and implemented with RSM, this step may be merged with step five below.

5.4 Detailed Characterization of Input and Model Form Uncertainties

The remaining uncertainties, and especially the ones found to be the most significant, are carefully characterized in step 4. To reduce the computational cost, all uncertainties are characterized using intervals. As shown in Figure 7, also this step may involve reduction of the number of uncertainties for consideration. A method that can be applied at this step is uncertainty aggregation as briefly described in section 4.2.2.

5.5 Find Sub-Model Min/Max Output Parameter Settings

With the characterization done, the minimum/maximum output parameter settings are found in step 5 using a linear response surface for each sub-model, as described in section 4.1.2. It should be noted that for some cases the minimum/maximum output parameter settings can be derived without applying RSM, e.g. for simpler sub-models or when there is significant experience of the specific sub-model.

5.6 Uncertainty Propagation at Model Top-Level

Finally, in step 6 the different minimum/maximum output parameter settings of the sub-models are

combined in order to obtain the resulting uncertainty of the total simulation model. For the industrial application example used in this paper, the minimum/maximum output parameter settings found are combined and two simulations for each operating point are carried out to obtain estimations of the best and worst cooling performance, respectively.

6 Results

To evaluate the industrial applicability of the proposed workflow for approximate UQ, it has been applied on the total S-ECS simulation model. The simulation models as well as the inputs used in the work described by this paper have been adjusted so as not to reveal confidential information about the systems and their performance. The outcome of interest from the simulations performed in this work is thus not the simulation results in themselves, but rather how the proposed UQ method performs on an industrial grade simulation model of a complex system.

The minimum/maximum output parameter settings for the Gripen E LL were found with a linear response surface by simulating the sub-model as a standalone. The inputs to the LL were the cooling air mass flow and temperature. The LL output of interest, affecting the cooling performance on a system level, was the liquid temperature out of the heat exchanger. An increase in the heat exchanger outlet temperature relative to the reference cooling temperature indicates deficient cooling performance. The inputs were the same throughout the different simulations when deriving the response surface. Only the uncertainties were changed between the different simulations using LHS and $1 + n$

samples, where $n = 259$ uncertainties (including all identified uncertainties). These uncertainty settings were then used when simulating the total simulation model.

Regarding identification and characterization as well as response surface generation, it should be noted that this study is limited to the uncertainties in the LL sub-model. Adding uncertainties from other sub-models will not increase the number of simulations needed of the total simulation model. The only increase in computational cost is related to finding the minimum/maximum output parameter settings using RSM also for the other sub-models (P-ECS, S-ECS, and Engine). The computational cost of adding uncertainties from other sub-models is therefore considered relatively low.

In the industrial application studied, a complicating factor is that the heat exchange with ambient air, and thereby the LL cooling performance, is affected by the actual flight case. Flying at low altitude in combination with high speed implies high skin temperature, which in turn heats up the components and the liquid in the LL. Similarly, the combination of high altitude and low speed cools the LL. These characteristics are visualized in Figure 8, which also shows the 25°C curve. It should be noted that the equipment bay temperatures, which directly affect the LL equipment, differ from the skin temperature, both in steady-state and transient conditions; however, this is accounted for in the LL model. To summarize the problem; when finding minimum/maximum output parameter settings for uncertain parameters related to the LL equipment heat exchange with ambient, the operational point in the flight envelope has to be considered.

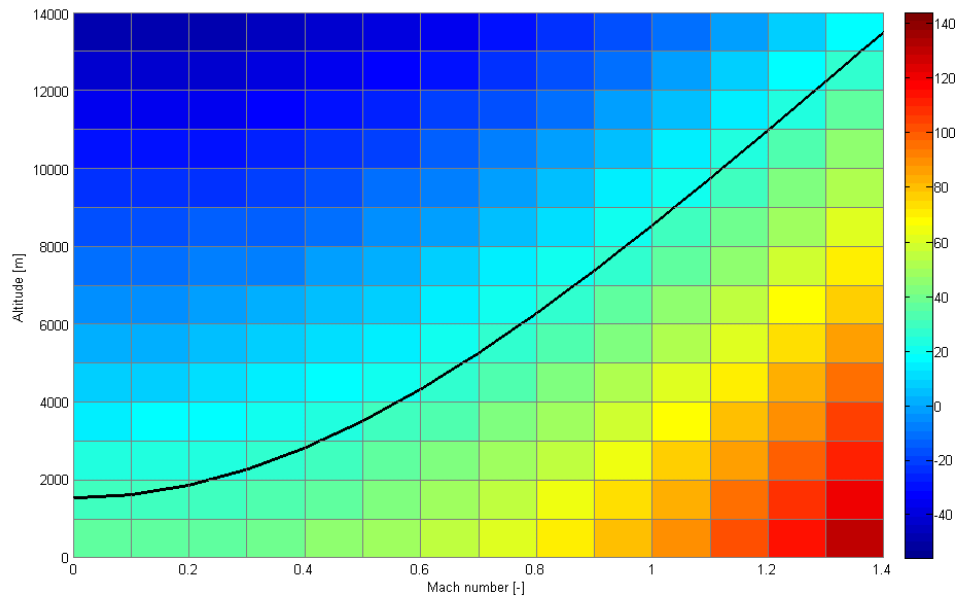


Figure 8. Flight envelope with colours representing skin temperature (recovery temperature) in [°C] for International Standard Atmosphere (ISA) + 20°C. The black curve indicates a temperature of 25°C, which is the assumed control reference temperature out of the LL heat exchanger.

6.1 Stationary cooling performance

The number of evaluated operating points in the flight envelope, where the aircraft altitude is plotted against the speed, was set to 59. Three simulations (minimum, nominal and maximum stationary cooling performance) at each evaluated operating point give a total of 177 simulations. The nominal simulations were utilized to attain the ambient air temperature. This temperature determines which combination of the minimum/maximum output parameters settings to use. In this study the stationary cooling performance is measured in terms of endurance time, i.e. the time in minutes that the system can keep the cooling liquid temperature out of the LL heat exchanger below a predefined temperature level in different points of the flight envelope. Simulating one stationary operating point with the total S-ECS simulation model takes approximately 20 minutes, giving a total simulation time of 59 hours. A typical performance plot for the nominal endurance time, without any uncertainty information, is shown in Figure 9.

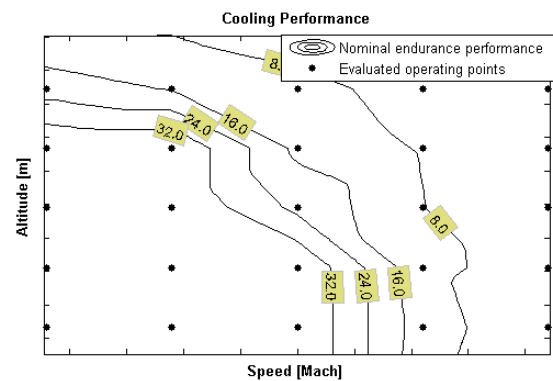


Figure 9. Nominal stationary cooling performance in terms of endurance time in minutes shown in square datatips. The dots are the evaluated operating points and the curves represent interpolated endurance time limits.

In the lower left corner of Figure 9, the nominal endurance time t_{nom} is unlimited with respect to cooling performance (in practical situations there are other limitations, such as available fuel). In the upper right corner of Figure 9, t_{nom} is zero. Figure 10 shows the same nominal data extended with the uncertainties resulting from the approximate UQ.

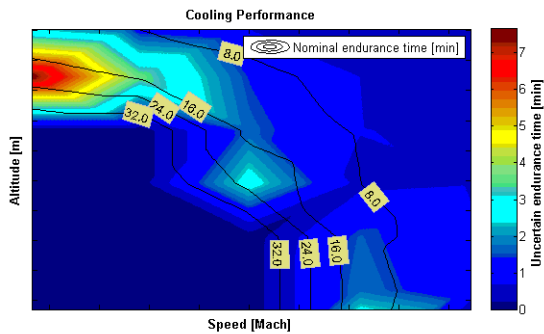


Figure 10. Nominal endurance time in minutes shown in square datatips. The estimated maximum uncertainty of the endurance time is represented by colours; dark blue for “no” uncertainty and dark red for an uncertainty of approximately 8 minutes.

As can be seen from Figure 10, the uncertainty of the endurance time is greatest in the limited region, i.e. where the nominal endurance time is $0 < t_{nom} < \infty$. The reason for this is that in the other parts of the flight envelope shown in Figure 10, the cooling performance of the system is either i) so high that

the S-ECS control system manages to keep the temperature at the set point value regardless of the uncertainties, or ii) so low that the endurance time is zero minutes regardless of the uncertainties.

6.2 Dynamic cooling performance

The nominal dynamic cooling performance for a complete flight mission of 50 minutes was simulated and the proposed approximate UQ framework was applied. Due to the fact that the cooling performance and its uncertainty is dependent on the actual flight case as described in Figure 8 (ambient temperatures heating or cooling the LL), four simulations in addition to the nominal simulation are needed for the approximate UQ.

To speed up the simulations to enable a comparison of the approximate UQ with an extensive LHS, the system was simulated with the less complex Gripen Demo LL model. The result can be seen in Figure 11.

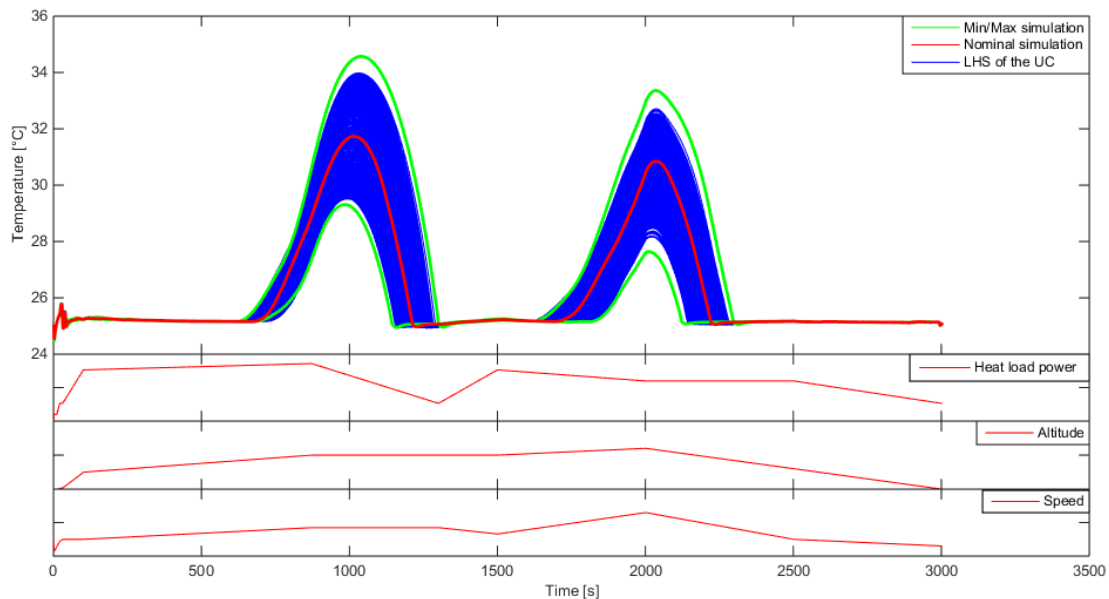


Figure 11. The liquid temperature out of the LL heat exchanger during a flight mission, where the heat loads and the aircraft altitude and speed change over time. The figure includes a comparison of the results from an extensive LHS (25 uncertainties sampled with 800 LH intervals) with the min/max results from the proposed approximate UQ framework.

As shown in Figure 11, the cooling performance is limited in two segments of the flight mission, with an increase in liquid temperature as a consequence. As expected, the min/max uncertainty resulting from the proposed approximated UQ framework encloses the results based on LHS.

7 Discussion and Conclusions

The proposed framework for approximate UQ significantly reduces both computational cost and engineering workload. In comparison with the framework proposed by Roy and Oberkampf (2011), this is at the expense of mathematical stringency as well as UQ accuracy. However, the proposed framework is intended for large system simulation models implying high computational

cost in combination with many uncertainties. In addition, users are often interested in performance predictions in several operational points, both in stationary and transient conditions. This makes computationally expensive UQ methods unfeasible.

Even though the challenge of computational cost is great, in an industrial context where information and resources are limited, the challenge of uncertainty characterization is even greater. This is especially true in early development phases, which is the focus of the proposed framework. Nevertheless, an approximate UQ is more worthwhile than no UQ.

To decrease the computational cost as well as the engineering workload required for uncertainty characterization, reducing the number of uncertainties for consideration is essential. In the proposed framework, the number of uncertainties for consideration is reduced by three means: i) experience, ii) aggregation, and iii) approximate characterization combined with sensitivity analysis.

The interval-based epistemic UQ approach was found to be suitable when analysing closed-loop systems, such as simulation models with a control system. For the industrial application studied it was seen that in many operational points, the uncertainties did not affect the ability of the S-ECS to control liquid temperature to the reference value since the available cooling power was more than enough in these operational points. In a UQ context, these simulations are unnecessary to evaluate with a more comprehensive propagation method, since the liquid temperature will always be close to the reference value. This implies that the most interesting simulations are those where the system starts to have deficient cooling performance.

If a more accurate but still computationally relatively cheap UQ is required to explicitly handle significant uncertainties characterized in detail as aleatory, the proposed framework can be extended; The proposed UQ framework can be used as described to find minimum/maximum output parameter settings for the epistemic uncertainties, and combined with sampling of the aleatory uncertainties. A probability box is thus derived without nested sampling. Instead of performing an extensive sampling of the aleatory uncertainties for each combination of epistemic uncertainties, the aleatory uncertainties are only sampled for the minimum and maximum output parameter settings, respectively.

Finally, it should be noted that if strong nonlinearities exist, the combination of the

minimum and maximum output parameter settings for the individual sub-models does not necessarily result in minimum and maximum response in the total simulation model. Such characteristics could possibly be detected by means of additional random samples at the model top level. Nevertheless, the execution of any UQ effort will benefit from extensive domain experience and system understanding.

Acknowledgements

The research leading to these results has received funding from Saab Aeronautics and the National Aviation Engineering Research Programme (NFFP) jointly driven by the Swedish Armed Forces, the Swedish Defence Materiel Administration (FMV), and the Swedish Governmental Agency for Innovation Systems (VINNOVA), (NFFP6 2013-01211).

References

- Carlsson, M., Andersson, H., Gavel, H., Ölvander, J., Methodology for Development and Validation of Multipurpose Simulation Models, *Proceedings of the 50th AIAA Aerospace Sciences Meeting*, Nashville, TN, USA, 2012a.
- Carlsson, M., Gavel, H., Ölvander, J., Evaluating Model Uncertainty Based on Probabilistic Analysis and Component Output Uncertainty Descriptions, *Proceedings of the ASME 2012 International Mechanical Engineering Congress & Exposition*, Houston, TX, USA, 2012b.
- Carlsson, M., Gavel, H., Ölvander, J., Utilizing Uncertainty Information in Early Model Validation, *Proceedings of the AIAA 2012 Modeling and Simulation Technologies Conference*, Minneapolis, MN, USA, 2012c.
- Carlsson, M., Steinkellner, S., Gavel, H., Ölvander, J., Enabling Uncertainty Quantification of Large Aircraft System Simulation Models, *Proceedings of the Council of European Aerospace Societies (CEAS) 2013 Conference*, Linköping, Sweden, 2013.
- de Rocquigny, E., Devictor, N., Tarantola, S., *Uncertainty in Industrial Practice: A Guide to Quantitative Uncertainty Management*, John Wiley and Sons, 2008.
- Eek, M., Kharrazi, S., Gavel, H., Ölvander, J., Study of Industrially Applied Methods for Verification, Validation & Uncertainty Quantification of Simulator Models, *International Journal of Modeling, Simulation, and Scientific Computing*, 2015.
- Helton, J.C., Probability, conditional probability and complementary cumulative distribution functions in performance assessment for radioactive waste

disposal, *Reliability Engineering & System Safety*, **54**(2–3): p. 145-163, 1996.

Helton, J.C., Davis, F.J., Latin hypercube sampling and the propagation of uncertainty in analyses of complex systems, *Reliability Engineering & System Safety*, **81**(1): p. 23-69, 2003.

Helton, J.C., Johnson, J.D., Sallaberry, C.J., Storlie, C.B., Survey of sampling-based methods for uncertainty and sensitivity analysis, *Reliability Engineering & System Safety*, **91**(10–11): p. 1175-1209, 2006.

Khuri, A.I., Mukhopadhyay, S., Response surface methodology, *Wiley Interdisciplinary Reviews: Computational Statistics*, **2**(2): p. 128-149, 2010.

Oberkampf, W.L., Roy, C.J., *Verification and Validation in Scientific Computing*, Cambridge University Press, Cambridge, UK, 2012.

Roy, C.J., Oberkampf, W.L., A comprehensive framework for verification, validation, and uncertainty quantification in scientific computing, *Computer Methods in Applied Mechanics and Engineering*, **200**(25–28): p. 2131-2144, 2011.

Saltelli, A., Annoni, P., How to avoid a perfunctory sensitivity analysis, *Environmental Modelling & Software*, **25**(12): p. 1508-1517, 2010.

Saltelli, A., Ratto, M., Andres, T., Campolongo, F., Cariboni, J., Gatelli, D., et al., *Global Sensitivity Analysis: The Primer*, John Wiley and Sons, 2008.

Steinkellner, S., *Aircraft Vehicle Systems Modeling and Simulation under Uncertainty*, Tekn. Lic. no 1497, Linköping University, Linköping, Sweden, 2011.

Swiler, L.P., Mayes, R.L., Paez, T.L., Epistemic uncertainty quantification tutorial, *Proceedings of the 27th Conference and Exposition on Structural Dynamics (IMAC XXVII)*, Orlando, FL, USA, 2009.

Modelica Implementation and Software-to-Software Validation of Power System Component Models Commonly used by Nordic TSOs for Dynamic Simulations

Mengjia Zhang¹ Maxime Baudette¹ Jan Lavenius¹ Stig Løvlund² Luigi Vanfretti^{1,2}

¹School of Electrical Engineering, KTH Royal Institute of Technology, Stockholm, Sweden {mengjia, baudette, janlav, luigiv}@kth.se

²Research and Development Division, Statnett SF, Oslo, Norway luigi.vanfretti@statnett.no

Abstract

Following the European Network of Transmission System Operators for Electricity (ENTSO-E) R&D Road Map, the *iTesla*¹ project aims to develop a common toolbox to support the future operation of the pan-European power grid. This toolbox was developed to allow unambiguous power system dynamic model exchange between simulation tools and performing simulations using Modelica models for Pan-European dynamic security assessment.

The work presented here comprises the development of Modelica classes for power grid components used by Nordic TSOs to model the Nordic synchronous grid. The performance of these Modelica models has been validated through different test cases implemented in both Power System Simulator for Engineering (PSS/E), as the reference domain-specific tool, and a Modelica simulation environment. The results from dynamic simulations with the presence of different perturbations have been compared to qualitatively and quantitatively the PSS/E results to validate the Modelica implementation, obtaining consistency simulation results between both tools. This paper describes the methodology used to develop and to perform model-to-model validation of the newly implemented Modelica models.

Keywords: Modelica, Simulation, Software validation, Power systems

1 Introduction

Ever since the 1970s (Schulz, 1975), a wide range of power system models has been developed to be used for different simulation analysis purposes. However, these models are tightly interlaced with the integration routine of particular software platforms. Therefore, the analysis of these models becomes solver- and implementation-

dependent, which results in difficulties for unambiguous model sharing, simulation, portability, maintenance and verification (Vanfretti et al., 2013).

This fact was an important design issue considered in the *iTesla* project. The *iTesla* toolbox was meant to offer multiple features for dynamic security assessment, based on extensive dynamic simulations of the power grid within different modules. To enable vendor-independent simulation and model consistency, the Modelica language was chosen for power system modeling and simulation in *iTesla*.

Statnett, the Norwegian TSO participated in *iTesla*. Statnett uses the Common Information Model (CIM) (IEC 61970-301, 2013) to specify the topology and parameters of their grid models and PSS/E (Siemens PTI Inc., 2005) for dynamic analysis. Statnett contributed to the *iTesla* by providing grid models and scenarios to test and validate the *iTesla* toolbox.

PSS/E is an integrated set of programs broadly used for power system transmission network steady-state and dynamic studies. Statnett has used it for several decades, gaining significant experience with grid models developed with PSS/E component models, making PSS/E a the software of choice for dynamic simulations. However, PSS/E internal models are integrated with its trapezoidal solver, in other words, the models can not be simulated by using different solvers or in other simulators. In addition, because the dynamic model has been developed over the course of many years, and because of its lack of portability, it is difficult to perform unambiguous model exchange and simulation using other tools. Thus, from the point of view of long-term model maintenance and portability, it is highly desirable to have the PSS/E models separated from the solver and implemented using a standardized modeling language to allow for model exchange between tools.

To guarantee dynamic model consistency against PSS/E and reassure Statnett's analysts that models implemented in Modelica would perform equally as in PSS/E (or better), a software-to-software validation approach was chosen for validation. To achieve this, different grid compo-

¹Innovative Tools for Electrical System Security within Large Areas; *iTesla* is a collaborative R&D project co-funded by the European commission 7th Framework Program. www.itesla-project.eu

ment models from PSS/E specified by Statnett were implemented in Modelica and validated against simulated response of the reference models obtained from PSS/E.

Modelica is a standardized non-proprietary, object-oriented, equation-based language (Modelica Association, 2014a), offering a great versatility to model complex physical systems. Different from modeling methods used in widely spread power system analysis tools, instead of using assignment declaration, the Modelica language provides a framework where models can be developed by explicitly declaring the equations containing all the models' dynamic. This facilitates the development of new models, maintaining existing ones, or even checking existing implementations.

Because Modelica is a standardized language, there is a broad range of modeling and simulation tools that are Modelica compliant, such as: OpenModelica, JModelica, Dymola, MapleSim, SimulationX, Mathematica, SystemModeler, etc. This facilitates unambiguous model and information exchange between tools offering different features. In addition, the Functional Mock-up Interface (FMI) standard (Modelica Association, 2014b) can be used to simulate exported Modelica code in other software which are widely used in today's industry such as MATLAB². The paper is organized as follows: Section 2 discussed the method for components model implementation by covering modeling procedures and showing two model examples. Section 3 introduces the validation process. Section 4 presents the results obtained from two sample validation tests. The last section gives general conclusions.

2 Model Development and Implementation

Seventeen of the component models are reported in this work, however, note that additional models are being implemented. The models include synchronous machines and their regulators, transformers, and composite load models. They are listed in Table 1.

The challenge of the implementation was to derive the dynamic equations for each model from the PSS/E documentation. Because the actual model equations are confined in PSS/E's source code and are not accessible to end-users, it is necessary to fully study the documentation of the software in order to understand the models and collect the correct equations to represent their dynamics. After collecting or deriving the equations (presumably used in PSS/E), there are mainly three steps towards modeling each components.

²The FMI Toolbox for MATLAB links FMI compliant models to the MATLAB/SIMULINK environment <http://www.modelon.com/products/fmi-toolbox-for-matlab/>.

Table 1. Developed Components

<i>Model type</i>	<i>Name / description</i>
Generator	GENROU, GENSAL, GENCLS
Transformers	2-winding & 3-winding with phase-shift and OLTC
Load model	ZIP load includes PSS/E's specified characteristics
FACTS devices	SVC (Static var compensator)
Exciter	IEEET1, IEEET2, SCR, EXST1, SEX, URST5T, ESST4B, ESAC2A
Governor	HYGOV, GAST, IEESGO, GGOV1
Stabilizer	IEEEST, STAB2A

2.1 Modeling steps

- 1. Define the input/output interface of the model.** There were two types of connector used, **Pwpin** and other single variable connectors (Bogodorova et al., 2013). **Pwpin** is a special type of connector which contains four real variables to express voltage and current phasors. Electrical components were connected by **Pwpin**.
- 2. Define model attributes.** Model attributes contain parameters, variables and equations. Other than the standard parameters given by model specifications, some auxiliary parameters should also be declared for initialization proposes.
- 3. Provide initial values for variables.** A power system model is commonly defined by equations (1-3)

$$\dot{\bar{x}} = f(\bar{x}_d, \bar{p}, \bar{u}) \quad (1)$$

$$0 = g(\bar{x}_{da}, \bar{p}, \bar{u}) \quad (2)$$

.....

$$0 = h(\bar{x}_{na}, \bar{p}, \bar{u}) \quad (3)$$

where, \bar{x}_d and \bar{x}_{da} are the vector of dynamic and algebraic state variable for dynamic components, respectively, while \bar{x}_{na} is the vector of algebraic variables of the network, e.g. $|\bar{V}|$ and $\angle \bar{V}$. \bar{p} is the vector of parameters of the model and \bar{u} defines a vector of inputs, such as perturbations to which the model can be subjected, e.g. ΔV_{ref} and ΔP_m .

Power system domain specific tools find \bar{x}_{na} by solving (3). The values obtained are used to solve for \bar{x}_d and \bar{x}_{da} , by setting (1) to zero. On the other hand, Modelica compilers attempt to solve for x by setting (1) to zero and simultaneously solving the resulting non-linear algebraic equations (1-3).

The difference in the solution approach needs to be carefully considered when implementing a typical power system model. Observe that due to the complexity of the power system model, it is common

that zero start values will cause singularity or convergence problems during the initialization process. Thus it is necessary to calculate the initial values explicitly. The calculations of these initial values are case dependent (i.e they are different for each model component).

These steps are explained in detail using two model examples in the following sections. They are a round rotor generator model and a three-winding transformer model.

2.2 Model example: Round rotor generator model (GENROU)

Every synchronous generator contains a rotor and a stator. The rotor of the GENROU model, shown on Fig. 1, is represented using two equivalent circuits per rotor axis and the armature fluxes are modeled as a function of the field voltage and the armature current (Schulz, 1975). Electric-magnetic saturation effects are represented by d- and q-axis mutual conductances, as a function of ψ'' . The block diagram of the rotor circuit is available in the PSS/E manual and in (Schulz, 1975).

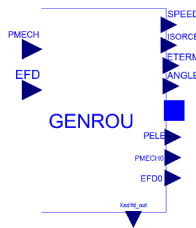


Figure 1. Genrou icon view

There is a need to use a change of coordinates because the dynamics of each synchronous machine is expressed in the rotor reference frame, thus to interface with the network, Park's transformation should be applied. The corresponding modelica implementation and complete equation set of the model is attached in Appendix, please refer to Schulz (1975) and Kundur et al. (1994) for the meaning of the symbols. Additional calculations should be performed in order to obtain the initial value of each state. Steady state operation is assumed during initialization, which means that there are not transient changes in the system. Thus, a power flow solution provides suitable initial values for \bar{x}_{na} by solving (3) for the power system.

The power flow solution was obtained using PSS/E and provided to the model explicitly. The procedure to provide initial guess value can be viewed as the chain in Fig. 2, which starts from the components connected to system bus such as generators, flexible AC transmission system (FACTS) devices, or loads until the last equipment in the chain. The initial values of each state and set points are calculated in a reverse manner considering that the generator should provide the power quantities at desired voltage

level according to power flow calculation³.

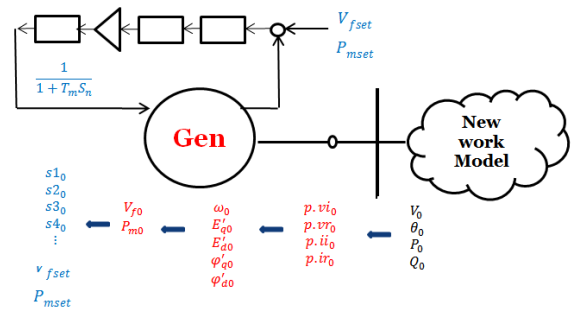


Figure 2. Procedure to provided initial guess values

In the case of initializing GENROU, the solution of the equations set was reduced to the solution of equation (4) in the rotor reference frame.

$$(X'_q - X''_q)i_{q0} + \psi''_{q0}K = 0 \quad (4)$$

where: $K = (1 + S_e |\psi''_0| \frac{X_q - X_l}{X_q - X_l})$

In order to take advantages of power flow and derived quantities (P_0, Q_0, I_0, V_0), it is necessary to express the equation above in the synchronous reference frame. In addition because changing the reference frame will not influence the magnitudes of the phasor, the value of ψ''_0 without saturation can be expressed in terms of voltage and current phasor at the generator bus (with the assumption that $X''_d = X''_q$). As a result, equation 4 can be written as:

$$\begin{aligned} -K|\psi''_0| \cos(\theta_{\psi''_0} - \delta_0) &= |I_{r0}|(X'_q - X''_q) \cos(\theta_{i0} - \delta_0) \\ j|\psi''_0| \angle \theta_{\psi''_0} &= |V_0| \angle \theta_{v0} + (R_a + jX''_q)|I_0| \angle \theta_{i0} \end{aligned}$$

from which the following initial guess value can be computed:

$$\delta_0 = \arctan\left(\frac{|I_0|(X'_q - X''_q) \cos(\delta_{\psi''_0} - \theta_{i0})}{|I_0|(X'_q - X''_q) \sin(\delta_{\psi''_0} - \theta_{i0}) - K|\psi''_0|}\right) + \delta_{\psi''_0}$$

where $\delta_{\psi''_0} = \theta_{\psi''_0} + \frac{\pi}{2}$. By substituting the value of δ_0 into the remaining equations, the initial values of all the states were obtained.

The initial values of states variables $\bar{x}_d, \bar{x}_{da}, \bar{x}_{na}$ can be specified with an equation through the initial equation construct or by setting the (fixed=true, start=x0) attribute when initializing variables (Fritzson, 2003). If nothing is specified, the default value would be zero and if (fixed=false) is set, the Modelica compiler will set a guess value. For parameters, setting (fixed=false) tells the compiler to implicitly compute them during initialization. At initialization, all the derivatives of the states (der(x)) and the parameters with (fixed=false) are treated as unknown variables. It is thus necessary to provide adequate initial values and initial equations to keep a balance between the number of unknown variables and equations.

³This is the typical method for initialization used in power system software, however, this method is used here only to provide initial "guess" values for Modelica to solve the initialization problem.

2.3 Model example: 3-winding Transformer with OLTC and phase-shifter

The three-winding transformer model is comprised by three two-winding transformer models with their secondary side interconnected, as shown on Fig. 3. Each two-winding transformer is equipped with both a phase-shifter and an on load tap-changer (OLTC) function. It is used to control the voltage magnitude of the user specified bus. Including the OLTC in a power system model results in a hybrid model. A hybrid model is comprised by continuous and discrete (and possibly event-driven) equations.

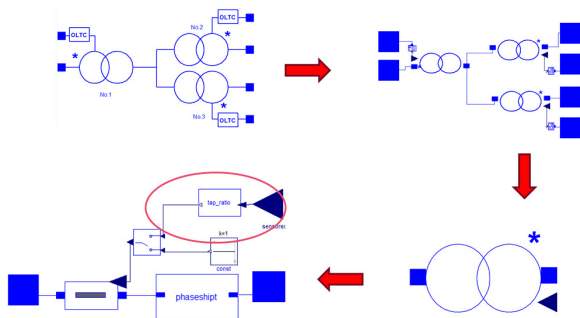


Figure 3. 3-winding transformer Icon and diagram view

The tapping logic of the OLTC is depicted in the block diagram in Fig. 4.

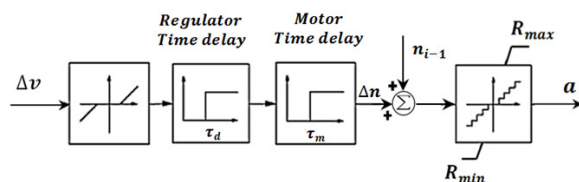


Figure 4. OLTC tapping logic block diagram

The corresponding Modelica code representation of this logic is listed in the Appendix. To keep the voltage at the controlled bus in the desired range, the OLTC adjusts the transformer turn ratio within the possible range in discrete steps. The model has internal delays to avoid unnecessary tapping actions.

A phase shifter is used to control active power flow by introducing a shift angle to both voltage and current phasors across the transformer. Ideally, there are no power losses due to the phase shifter. Hence, it is common practice to model the shift angle by introducing a variable impedance. However, in this work, a new method was adopted where the shift angle was introduced by modeling the receiving end phasor variables in a new axis which was separated from the sending end axis by the shift angle. The diagram is shown in Fig. 5. The receiving end phasor variables were obtained by applying Park's transformation to the sending end phasor variables.

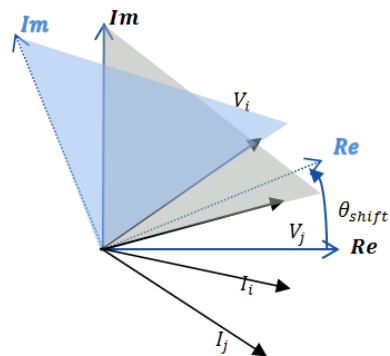


Figure 5. The diagram of phase shifter function

3 Software-to-Software Validation

The adopted software-to-software (SW-to-SW) validation approach consists in simulating an identical test system in both software environments and comparing simulation results qualitatively and quantitatively. For this approach to be successful, the solver chosen for the Modelica implementation should be equivalent to the PSS/E solver. The PSS/E documentation (Siemens PTI Inc., 2005) describes a trapezoidal integration method which corresponds to a second-order Runge-Kutta method, leading to the choice of "Rkfix2" for the simulations in Dymola (Dassault Systemes, 2015). A minimal difference between the two will guarantee the fidelity of the Modelica implementations. All of the models listed in Table 1 have been validated against PSS/E. To reduce the complexity of the validation procedure, identical small scale test systems were built in both Modelica and PSS/E for testing purposes.

Validation results of the components demonstrate both the correctness of the initialization and the transient behavior of the dynamic components under different disturbances. The validation tests were designed to activate each function inside the models and are, thus, case dependent. Different perturbations were applied to enable limiter and force the systems into a transient state after a few seconds from the simulation start.

In the sequel, the following sections briefly introduce the applied test scenarios and then go through the validation results of two of the test systems to prove the successful validation of the models.

3.1 Test system and validation scenarios

Validation tests are carried out using a simple system. In PSS/E it is not possible to test a controller (e.g exciter) without connecting it to a generator. Thus a single generator model was validated first and then each control system was validated using the validated generator. The basic scenarios used to study the transient performance of a generator and controllers are shown Fig. 6.

Most of the components were validated using the simple test system shown in Fig. 6. The perturbations intro-

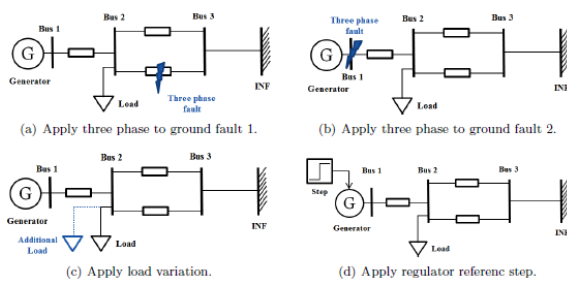


Figure 6. Test system and validation scenarios

duced were events such as three phase to ground faults, load variations and step changes applied to the regulators' set points. All of the perturbations were modeled in the same way in Modelica as they are in PSS/E.

3.2 Some Validation Results

The dynamic behavior of the power system a few seconds after a disturbance is driven by the stored energy in the rotors' inertias, transients in the field windings, and the controls of generators (Kundur et al., 1994). Therefore signals such as generator speed deviation, a bus voltage magnitude, and the injected active and reactive power P and Q of a generator are recorded and compared. When there exist regulators in the system, the output quantities of these devices are compared and analyzed. The applied perturbations are listed in Table 2. Results are shown in Fig. 7, where a comparison of the records of four state variables of the generator are presented. It shows that the behavior of the developed Modelica model matches perfectly with that of the PSS/E reference model in both steady state and transient conditions.

Table 2. Applied perturbations scenarios to validate the GENROU test system

Time	Changes Applied
0-2 s	Running under steady state
2 s	Vary the system load with constant P/Q ratio
2.15 s	Restore the original load
10 s	Apply a 3 phase fault to ground in the middle of one of the parallel lines
10.15 s	Clear the fault by tripping the line
20 s	Stop the simulation

Quantitative assessment as proposed in (Rogersten et al., 2014) is performed to measure the validity of a model response using numerical metrics. The assessment is carried out by calculating root mean square (RMS) of the difference between simulation outputs using the equation:

$$RMSE = \sqrt{\frac{1}{n} \sum_{i=1}^n (x_i - y_i)^2} \quad (5)$$

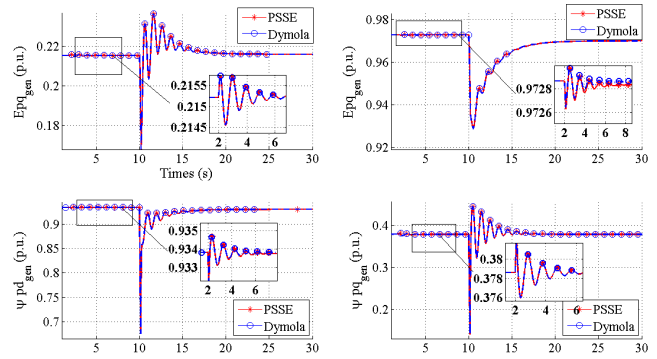


Figure 7. Validation results for the GENROU model

where x_i and y_i are the discrete measurement points at time t_i for software (a) and (b) respectively. The value is calculated on an interval of 2 s divided into total number of time steps in PSSE. In this case, the time step used is 0.001 s and the time interval included the period of pre-fault, fault, and post-faults such that the RMSE value reflects the response of the model against its reference. For example, for the test case shown in Fig. 8, there were seven changes applied and six variables were recorded to compute the RMSE values to validate the model quantitatively.

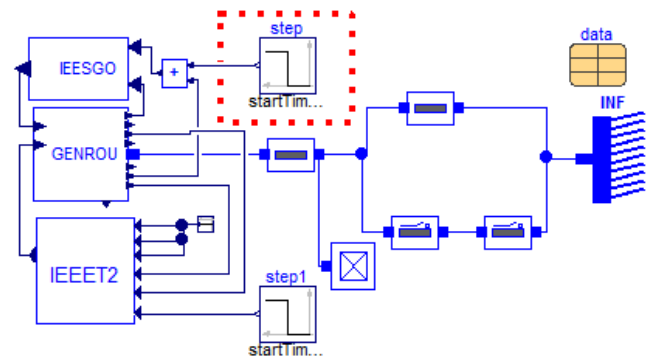


Figure 8. Test for GENROU, IEEESGO, IEEET2

For this case, all the perturbations scenario applied at 0.3 s and they are listed in Appendix Table 4. Results are shown in Appendix Table 5. This quantitative assessment has been carried out for each test case and the results show that the behavior of the developed Modelica model matches perfectly that of the PSS/E reference model in both steady state and transient conditions.

The test system used for the validation of the three winding transformer is shown in Fig. 9, where the remote and local loads were connected through a three-winding transformer. An infinite bus was connected to the primary side of the transformer, a local generation unit was connected to the secondary side and a composite load was connected to the tertiary side of the transformer. The local power plant was modeled using a GENROU model equipped with an IEEET1 exciter and a STAB2A stabilizer.

When the OLTC function of winding one is enabled, it

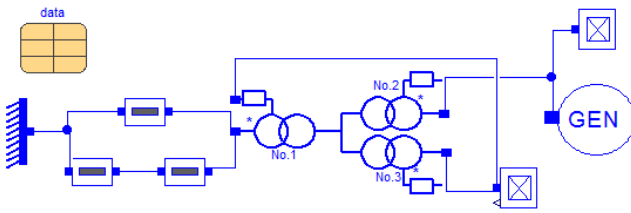


Figure 9. Test system for OLCT

controls the voltage at the load bus to stay within the desired range. The perturbations are designed to force the OLTC to activate following the logic shown in Fig. 4. They are listed in Table 3. The method to step Q in PSSE is not explained in the software documentation with sufficient detail, thus the value used in Q stepping in Dymola is not exactly the same as they are shown in Table 3. The actual value used in Dymola is obtained by trial-and-error to match the behavior in PSSE.

Table 3. Applied perturbations scenarios for OLTC validation

Time	Scenarios
0-20 s	Running under steady state
20 s-40 s	Increasing the Q load to 1.5 p.u.
40 s-80 s	Increasing the Q load to 2.2 p.u.
80 s-200 s	Increasing the Q load to 2.5 p.u.

The validation results are shown in Fig. 10 where the voltage magnitude at the three terminals of the transformer are compared. The comparison of Q stepping in both software is also shown in the figure. The small mismatch in the voltages are due to the differences in Q stepping. However, in this test, the aim is to verify the stepping logic of the OLTC instead of transient behavior, thus the results show that the Modelica OLTC model functions in the same way as the PSS/E reference model.

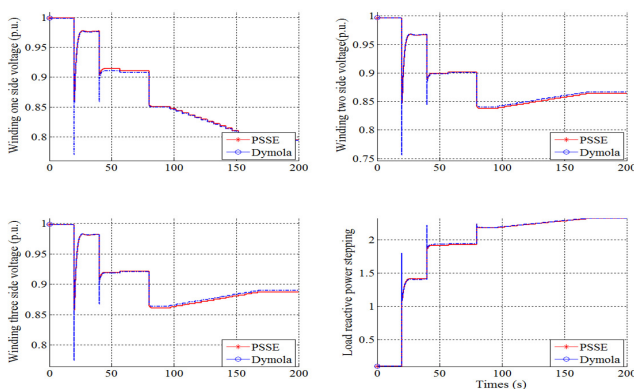


Figure 10. Validation results of OLCT

4 Conclusion

All the PSS/E component models specified by Statnett have been successfully implemented in Modelica. In addition, the developed models have been tested using OpenModelica and Dymola⁴. The validation results guarantee consistent simulation results among Openmodelica, Dymola, and PSS/E. This work can serve as a proof of the feasibility of using Modelica tools in power system for modeling and simulation as an alternative to PSS/E. This work also provides a proof of simulation capabilities of Modelica tools to handle power system problems in terms of the complex controls and initialization problems.

References

- Tetiana Bogodorova, Marc Sabate, Gladys Leon, Luigi Vanfretti, Milenko Halat, Jean-Baptiste Heyberger, and Patrick Panciatici. A modelica power system library for phasor time-domain simulation. In *2013 IEEE PES Innovative Smart Grid Technologies Europe (ISGT EUROPE)*, pages 1–5, 2013.
- Dassault Systemes. *Dymola*, 2015. <http://www.3ds.com/products-services/catia/products/dymola/>.
- Peter Fritzson. *Principles of object-oriented modeling and simulation with Modelica 2.1*. John Wiley & Sons, 2003.
- IEC 61970-301. *Energy management system application program interface (EMS-API) - Part 301: Common information model (CIM) base*, 2013.
- Prabha Kundur, Neal J Balu, and Mark G Lauby. *Power system stability and control*, volume 7. McGraw-hill New York, 1994.
- Modelica Association. *Modelica Language Specification*, 2014a. <https://modelica.org/documents>.
- Modelica Association. *FMI for Model Exchange and Co-Simulation Specification*, July 2014b. <https://www.fmi-standard.org/downloads>.
- R. Rogersten, L. Vanfretti, Wei Li, Lidong Zhang, and P. Mitra. A quantitative method for the assessment of vsc-hvdc controller simulations in emt tools. In *2014 IEEE PES Innovative Smart Grid Technologies Conference Europe (ISGT-Europe)*, pages 1–5, Oct 2014.
- Richard P. Schulz. Synchronous machine modeling. *IEEE publication* 75, 1975.
- Siemens PTI Inc. *PSSE User Manual v30.2*, Siemens Power Transmission & Distribution. Power Technologies International, 2005.
- L. Vanfretti, W. Li, T. Bogodorova, and P. Panciatici. Unambiguous power system dynamic modeling and simulation using Modelica tools. In *2013 IEEE PES General Meeting*, pages 21–25, 2013.

⁴OpenModelica results will be shown in future publication.

5 Appendix

5.1 Modelica OLTC logic

```

//Check difference between scheduled
// and measured voltage.
if u - Vmax > 0 then
  voltageDiff = -1;
elseif Vmin - u > 0 then
  voltageDiff = 1;
else
  voltageDiff = 0;
end if;
//Set resetRegulatorTimer
//if difference exists.
when ResetTimer then
  reinit(MotorTimer,0);
end when;
//Let timer run if we have
// a large enough difference
when voltageDiff<>0 and StartTimer then
  tapDirection=
  if RegulatorTimer<=0 then voltageDiff
  else pre(tapDirection);
end when;

when RegulatorTimer<=0 or
  RegulatorTimer>=1 then
  MotorEnabled = if RegulatorTimer>=1
  then true else false;
end when;

if RegulatorTimer<=0 then
  der(RegulatorTimer)= if (voltageDiff<>0)
  then 1/Td else 0;
  ResetTimer=false;
  StartTimer=true;

elseif RegulatorTimer>=1 then
  der(RegulatorTimer)=
  if (tapDirection==voltageDiff)
  then 0 else -1/Td;
  ResetTimer=true;
  StartTimer=false;

elseif RegulatorTimer<1 then
  der(RegulatorTimer) =
  if (tapDirection == voltageDiff)
  then 1/Td else -1/Td;
  ResetTimer=false;
  StartTimer=false;
else
  der(RegulatorTimer) = 0;
  ResetTimer=false;
  StartTimer=true;
end if;

if MotorEnabled and MotorTimer < 1 then
  der(MotorTimer)=1/TC;
elseif MotorEnabled then
  der(MotorTimer)=
  if (TSD)>0 then 1/(TSD) else 1/TC;
else
  der(MotorTimer)=0;
end if;

```

```

tapMoved = integer(MotorTimer);

when change(tapMoved) and tapMoved <>0
  and pre(MotorEnabled) then
  m = pre(m) + dtap * pre(tapDirection);
end when;

if m>=Rmax then
  y = Rmax;
elseif m<=Rmin then
  y = Rmin;
else
  y=m;
end if;

```

5.2 Dynamic equations of GENROU (Schulz (1975) and Kundur et al. (1994))

$$\begin{aligned} \dot{E}'_q &= \frac{1}{T'_{d0}}(E_{fd} - X_{ad}I_{fd}) \\ \dot{E}'_d &= \frac{1}{T'_{q0}}(-1)(X_{aq}I_{1q}) \\ \dot{\psi}_{kd} &= \frac{1}{T''_{d0}}(E'_q - \psi_{kd} - (X'_d - X_l)i_d) \\ \dot{\psi}_{kq} &= \frac{1}{T''_{q0}}(E'_d - \psi_{kq} + (X'_q - X_l)i_q) \\ X_{ad}I_{fd} &= \frac{(X'_d - X''_d)(X_d - X'_d)}{(X'_d - X_l)^2} [E'_q - \psi_{kd} - i_d(X'_d - X_l)] \\ &\quad + i_d(X_d - X'_d) + E'_q + S_e(|\psi''|)\psi''_d \\ X_{aq}I_{1q} &= \frac{(X'_q - X''_q)(X_q - X'_q)}{(X'_q - X_l)^2} [E'_d - \psi_{kq} + i_q(X'_q - X_l)] \\ &\quad - i_q(X_q - X'_q) + E'_d - S_e(|\psi''|)\frac{X_q - X_l}{X_d - X_l}\psi''_q \\ \psi''_d &= \frac{E'_q(X''_d - X_l) + \psi_{kd}(X'_d - X''_d)}{X'_d - X_l} \\ \psi''_q &= \frac{-E'_d(X''_q - X_l) - \psi_{kq}(X'_q - X''_q)}{X'_q - X_l} \\ |\psi''| &= \sqrt{(\psi''_d)^2 + (\psi''_q)^2} \\ \psi_d &= \psi''_d - X''_d i_d \\ \psi_q &= \psi''_q - X''_q i_q \\ 2H \frac{d\omega}{dt} &= T_m - T_e - D \frac{d\omega}{\omega} \\ \frac{d\delta}{dt} &= \omega_0 d\omega \\ T_e &= \psi_d i_q - \psi_q i_d \\ e_d &= -\psi_q - R_a i_d \\ e_q &= +\psi_d - R_a i_q \end{aligned}$$

$$\begin{bmatrix} V_r \\ V_i \end{bmatrix} = \begin{bmatrix} \sin(\delta) & \cos(\delta) \\ -\cos(\delta) & \sin(\delta) \end{bmatrix} \times \begin{bmatrix} e_d \\ e_q \end{bmatrix}$$

$$\begin{bmatrix} I_r \\ I_i \end{bmatrix} = - \begin{bmatrix} \sin(\delta) & \cos(\delta) \\ -\cos(\delta) & \sin(\delta) \end{bmatrix} \times \begin{bmatrix} i_d \\ i_q \end{bmatrix}$$

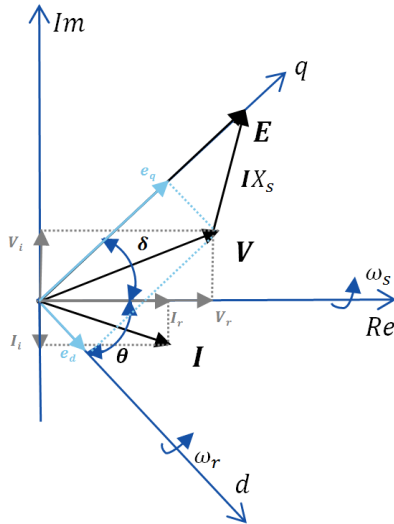


Figure 11. Synchronous and Rotor Coordinate

```
// swing equation
der(delta) = wbase * w;
der(w) = ((PMECH-D*w)/(w+1)-Te)/(2*H);
Te = PSId * iq - PSIk * id;
// transient voltage & flux
der(Epq) = (1 / Tpd0) * (EFD - XadIfd);
der(Epd) = (1 / Tpq0) * (-1) * XaqIiq;
der(PSIk) = (1 / Tppd0) *
(Epq-PSIk-(Xpd-Xl)*id);
der(PSIkq) = (1 / Tppq0) *
(Epd-PSIkq+(Xpq-Xl)*iq);
// flux linkage
PSId = PSId - (Xppd * id);
PSIk = PSIk - (Xppq * iq);
PSIdp = (Epq * K3d) + (PSIk * K4d);
PSIkq = (-Epd * K3q) - (PSIkq * K4q);
PSIp = sqrt(PSIdp^2 + PSIkq^2);
// saturation effect
XadIfd = (K1d*(Epq-PSIk-(Xpd-Xl)*id)
+ Epq + (id * (Xd - Xpd))
+ (Se(PSIp, s10, s12) * PSIdp);
XaqIiq = (K1q*(Epd-PSIkq+(Xpq-Xl)*iq)
+ Epd - (iq * (Xq - Xpq))
- (Se(PSIp, s10, s12) * PSIkq)
* (Xq - Xl) / (Xd - Xl));
```

5.3 Quantitative assessment

Table 4. Applied perturbations scenario to validate the system in Fig. 8

No.	Changed Applied
1	Three phase to ground fault ($Z=0.5 + 0.5j$ p.u.) in the middle of one parallel line at last for 0.5 sec
2	Three phase to ground fault ($Z=0.2 + 0.2j$ p.u.) at bus 2 last for 0.5 sec
3	Trip one parallel line
4	Step of Efd reference 0.01 p.u.
5	Step of Efd reference step -0.01 p.u.
6	Step of Pmech reference step -0.002 p.u.
7	Step of Pmech reference step 0.001 p.u.

Table 5. RMSE Calculations according to Equation(4)

	Genrou(Pelec)	Genrou(Qelec)	IEEET2(Efd)
1	5.6150e-13	1.4125e-11	5.8495e-11
2	4.9004e-13	3.1062e-13	6.1085e-13
3	4.3398e-14	1.2844e-18	7.3565e-13
4	3.9391e-14	3.1698e-16	7.7892e-13
5	4.7541e-14	5.5590e-15	4.2712e-13
6	2.9281e-14	7.9683e-15	3.9605e-13
7	1.0012e-14	5.1896e-15	6.4285e-13
	IEEESGO(Pmech)	Genrou(Speed)	Genrou(Vt)
1	1.6497e-14	3.3524e-15	2.5234e-12
2	4.6549e-16	1.4021e-17	1.6314e-14
3	1.7494e-18	3.3895e-19	1.4843e-17
4	1.0529e-15	1.5968e-20	9.1668e-15
5	2.6711e-16	1.7923e-19	6.5037e-16
6	1.6166e-16	5.3919e-20	9.4046e-16
7	6.1121e-16	1.5454e-17	3.6245e-16

Learning Modelica Models from Component Libraries

Gregory Provan¹ Alex Feldman²

¹Computer Science Department, University College Cork, Cork, Ireland, g.provan@cs.ucc.ie

²PARC Inc., Palo Alto, CA 94304, USA, afeldman@parc.com

Abstract

The Modelica language is one of the most important languages for representing a large class of systems, ranging from vehicles to climate control systems in buildings. Component libraries, containing components like valves, motors, pumps, etc., have been built to facilitate the construction of complex systems, but at present model construction and parameter estimation are entirely manual. We have developed software for automating the process of constructing models that optimise a range of metrics (e.g., model-simulation accuracy or diagnostics accuracy) to tailor models to a range of applications, such as diagnosis and control. We describe initial experimental results using a well-known dynamical benchmark model.

Keywords: Model Learning, Bayesian model selection

1 Introduction

Modelica is an important language for simulating a large class of systems, ranging from vehicles (Brückmann et al., 2009) to physiology (Mateják et al., 2014) and climate control systems in buildings (Plessis et al., 2014; Wetter et al., 2014). Given the increasing use of Modelica as a language for systems modeling, it is being applied to a range of applications beyond system simulation, such as embedded control, diagnosis, and prediction (Casella et al., 2008). For these other applications, the models must satisfy requirements beyond just simulation accuracy. Consider the case of control models: these models must balance model fidelity (to represent fundamental dynamics necessary for control system performance) with simplicity, since most advanced control design techniques, e.g., model-predictive control, start to become intractable for systems of order greater than about ten. Creating tractable control models requires simplifying traditional simulation models, deleting any behaviours that do not significantly affect the equilibrium values and/or the control-relevant system dynamics (Casella et al., 2008).

For simulation purposes, the key criterion for a Modelica simulation model is accuracy, i.e., how

closely does the model simulate the real system. In such cases, we can judge the quality of a Modelica model in terms of a criterion such as the mean squared error (MSE) measure, specified in terms of the difference between simulation output and data from the real system.

However, for applications like embedded control and diagnosis, other criteria are necessary. The computational complexity of evaluating the Modelica model is important, since inference involving control and diagnosis typically involves multiple simulations to determine an optimal system state. In addition, diagnostics accuracy may require different model properties than just simulation accuracy; for example, diagnosis involves computing whether the nominal simulation better matches the real data than a simulation of a failure behaviour, so we are comparing potentially multiple different simulation behaviours, rather than trying to make a single simulation as accurate as possible.

Component libraries, containing components like valves, motors, pumps, etc., have been built to facilitate the construction of complex systems. As useful as these libraries are, at present they have several deficiencies, including (1) model fidelity that may not be suitable for the application at hand, and (2) the fact that the component model construction and parameter estimation are entirely manual. It is well known that the models provided within Modelica component libraries, e.g., (Casella and Leva, 2003; Casella et al., 2006), are typically too detailed for control and diagnostics applications (Casella et al., 2008; Imsland et al., 2010). The models designed for control and diagnostics applications are referred to as reduced-order (RO) models (Antoulas et al., 2001) or balanced-complexity models (Elgsæter et al., 2012; Kittilsen et al., 2012).

The two approaches typically adopted for generating application-specific models are (a) reducing the order of a detailed simulation model (Antoulas et al., 2001), or (b) building the model from scratch (Kim et al., 2014; Provan, 2011). Approach (a) is challenging since model-reduction software is highly domain-specific and still requires further development

to achieve commercial applicability. Approach (b) is expensive, and does not make use of component libraries in which considerable time and effort have been directed.

We present an alternative approach for generating application-specific models that does not require the use of model-reduction software, but which can make use of model libraries, albeit a more generalized view of model libraries. We propose an approach that can use a model library containing component models of multiple levels of fidelity to generate a system-level model that optimizes a particular model metric. This approach has two key novel aspects. First, we define a metric for evaluating the fitness of a model for particular applications. Second, we describe a software tool that can apply the metric for generating application-specific models. We demonstrate our approach in the area of diagnostics for process-control systems.

In this article, we address the issue of matching component model fidelity to the application at hand. Most existing domain-specific libraries, e.g., the building energy library (Wetter et al., 2014), are built in a hierarchical fashion on top of lower-level libraries, in this case the Modelica hydraulic library (Casella et al., 2006; Tummescheit and Eborn, 1998). Since the hydraulic library is highly detailed, the building library inherits this level of fidelity. For applications like control and diagnostics, this level of detail may be unnecessary, and may limit the applicability of the generated code due to slow inference speeds.

We have been developing libraries with components that are described in multiple levels of fidelity. Variable-fidelity models have been used for many years for the systems optimization process in engineering design (Schmit and Farshi, 1974). However, typically each model is system-level, rather than component-based.

In this article, we describe an approach for developing a component library \mathcal{L} containing components described at multiple fidelity levels, e.g., as a non-linear system (high-fidelity model), linear system, or a qualitative system (low-fidelity model). Choosing the right component model for system simulation is a difficult task and requires a search in the space of all possible component-fidelity combinations.

We propose an automated method for computing a system model that optimizes a set of metrics (e.g., model-simulation accuracy or diagnostics accuracy) given a set of simulation scenarios. We describe initial experimental results showing the feasibility of this approach for diagnosis applications, using a tank benchmark to illustrate our approach.

2 Systems Model Specification

This section formalises the notion of model for two applications, simulation and diagnostics inference. As mentioned earlier, most uses of Modelica models are purely for simulation, but we will generalise that notion by defining a model that generates behaviours based on multiple modes, e.g., modes corresponding to normal behaviour, and modes corresponding to behaviour where a fault is present. For example, a valve can block flow when shut, but if it cannot close fully then it will not fully block flow when commanded shut. We first introduce the simulation and diagnosis tasks, and then define them more precisely.

2.1 Simulation and Diagnosis Tasks

We define a simulation task as follows.

Definition 1 (Simulation) *Given a model ϕ and initial conditions x_0 at t_0 , generate the behaviour of the system over an interval $[t_0, \tau]$.*

Standard Modelica simulation models have been extended for diagnostics purposes by many authors, e.g., (Åkerlund, 2001; de Kleer et al., 2013; Bäck, 2008). The extensions focus on enabling the model to generate multiple possible behaviours (corresponding to nominal and faulty component conditions) rather than the single behaviour for a simulation model.

We formalise a diagnosis model as follows. Assume that we have a system \mathcal{S} that can operate in a nominal state, ξ_N , or a faulty state, ξ_F , where Ξ is the set of possible states of \mathcal{S} . We further assume that we have a discrete vector of measurements, $\tilde{\mathbf{Y}} = \{\tilde{y}_1, \dots, \tilde{y}_n\}$ observed at times $t = \{1, \dots, n\}$ that summarizes the response of the system \mathcal{S} to control variables $\mathbf{U} = \{\mathbf{u}_1, \dots, \mathbf{u}_n\}$. Let $\mathbf{Y}_\phi = \{y_1, \dots, y_n\}$ denote the corresponding predictions from a dynamic (non-linear) model, ϕ , with parameter values θ : this can be represented by $\mathbf{Y}_\phi = \phi(x_0, \theta, \xi, \tilde{\mathbf{U}})$, where x_0 signifies the initial states of the system at t_0 .

Diagnostics takes as input anomalous data that disagrees with the system being in a nominal state, and isolates the fault causing the anomalous sensor readings. A range of definitions of diagnosis are possible, including the most likely diagnosis, all diagnoses, etc. We assume a fixed diagnosis task \mathcal{T} throughout this article, e.g., computing the most likely diagnosis, or a deterministic multiple-fault diagnosis. Diagnosis is significantly more complex than simulation, as we now show.

We specify a diagnosis model as follows:

Definition 2 (Diagnosis Model) *We characterise a Diagnosis Model ϕ using the tuple $\langle \mathbf{V}, \theta, \Xi, \mathcal{E} \rangle$, where*

- \mathbf{V} is a set of variables, consisting of variables denoting the system state (\mathbf{X}), control (\mathbf{U}), and observations (\mathbf{Y}).
- $\boldsymbol{\theta}$ is a set of parameters.
- Ξ is a set of system modes.
- \mathcal{E} is a set of equations, with a subset $E_\xi \subseteq \mathcal{E}$ for each mode $\xi \in \Xi$.

We assume that we can use a physics-based approach to hand-generate a set \mathcal{E} of equations to specify a model. Obtaining good diagnostics accuracy, given a fixed \mathcal{E} , entails estimating the parameters $\boldsymbol{\theta}$ to optimise that accuracy.

The classical definition of diagnosis is as a state estimation task, whose objective is to identify the system state that minimises a residual vector. We refer to this as *accuracy-based diagnosis*.

Definition 3 (Accuracy-Based Diagnosis)

$$\xi^* = \underset{\xi \in \Xi}{\operatorname{argmin}} \mathcal{R}(\tilde{\mathbf{Y}}, \mathbf{Y}_\phi), \quad (1)$$

where a residual vector $\mathcal{R}(\tilde{\mathbf{Y}}, \mathbf{Y}_\phi)$ measures the difference between the actual and model-simulated system behaviour. An example of a residual vector is the mean-squared-error (MSE).

Diagnostics inference (as well as control-based inference) require not just accuracy but also computational efficiency, especially in real-time applications. As a consequence, we need to generalise the accuracy-based diagnosis notion to incorporate inference efficiency as well as accuracy, using an inference complexity measure as $\mathcal{C}(\tilde{\mathbf{Y}}, \phi)$.

Definition 4 (Diagnosis Optimisation) A diagnosis task jointly minimises a function g that incorporates the accuracy (based on the residual function) and the inference complexity:

$$\xi^* = \underset{\xi \in \Xi}{\operatorname{argmin}} g(\mathcal{R}(\tilde{\mathbf{Y}}, \mathbf{Y}_\phi), \mathcal{C}(\tilde{\mathbf{Y}}, \phi)), \quad (2)$$

where g specifies a loss or penalty function that induces a non-negative real-valued penalty based on the lack of accuracy and computational cost.

Since this is a minimisation task, we typically need to run multiple simulations over the space of parameters and modes to compute ξ^* . We can abstract this process as performing model-inversion, i.e., computing some $\xi^* = \phi^{-1}(x_0, \boldsymbol{\theta}, \xi, \tilde{\mathbf{U}})$ that minimises $\mathcal{R}(\tilde{\mathbf{Y}}, \mathbf{Y}_\phi)$.

During this diagnostics inference task, a model ϕ can play two roles: (a) simulating a behaviour to estimate $\mathcal{R}(\tilde{\mathbf{Y}}, \mathbf{Y}_\phi)$; (b) enabling the computation of $\xi^* = \phi^{-1}(x_0, \boldsymbol{\theta}, \xi, \tilde{\mathbf{U}})$. It is clear that diagnostics inference requires a model that has good fidelity and is computationally efficient for performing these two roles.

In forward simulation, a model ϕ , with parameters $\boldsymbol{\theta}$, can generate multiple observations $\tilde{\mathbf{Y}} = \{\tilde{y}_1, \dots, \tilde{y}_n\}$. The diagnostics task involves performing the inverse operation on these observations. Our objective thus involves optimising the state estimation task over a future set of observations, $\tilde{\mathbf{Y}} = \{\tilde{\mathbf{Y}}_1, \dots, \tilde{\mathbf{Y}}_n\}$. Our model ϕ and inference algorithm \mathcal{A} have different performance based on $\tilde{\mathbf{Y}}_i, i = 1, \dots, n$: for example, (Feldman et al., 2008) shows that both inference-accuracy and -time vary based on the fault cardinality. As a consequence, to compute ξ^* we want to optimise the *mean* performance over future observations. This notion of *mean* performance optimisation has been characterised using the Bayesian model selection approach, which we examine in section 3.3.

2.2 Running Example: Three-Tank Benchmark

We now describe our running example, which is the well-known tank benchmark. We will first describe a tank component, and then connect three tanks in series to form a tank system.

2.2.1 Tank Component

A component consists of a set of interfaces (inputs and outputs), a set of functions to map inputs to outputs, and a set of parameters. We use a tank to illustrate this. A tank is a component that has an inflow of fluid (qIn), and a regulated outflow (qOut) through a hole at the bottom of the tank, which is controlled by a valve. The height h of liquid in the tank is governed by $h \propto (qIn - qOut)$.

A tank component has four interfaces (connectors in Modelica): *qIn* for input flow, *qOut* for output flow, *pressure* for providing pressure measurements, and *valve-control* for setting the position of the valve at the outlet of the tank.

Within Modelica, we assume that we will create connector classes as follows. First, we have a class *val* for reading the pressure level (Figure 1):

```
connector Measure "Measuring pressure"
  Real val(unit="m");
end Measure;
```

Figure 1. Modelica class for pressure level measurement

We create a class *ActSignal* for setting valve position, and a class *lflow* for the liquid flow at inlets and outlets.

The key equation regulating the behaviour of the tank is the mass balance equation, where the change in height of fluid is given by the difference in input and output flows (assuming constant pressure). Figure 2 shows the Modelica code for this component.

```

model Tank
  parameter Real A=1 "Ground area of tank in m2";
  parameter Real a=0.2 "Area of drain hole in m2";
  constant Real g=Modelica.Constants.g_n;
  Real h(start=0.0,unit="m") "Tank level";
  Real pressure(start=0.0,unit="Nm") "Pressure";
  Interfaces.Measure pressure "Connector, sensor
    reading pressure (Nm)";
  Interfaces.LiquidFlow qIn "Connector, flow (m3/s)
    through input valve";
  Interfaces.LiquidFlow qOut "Connector, flow (m3/s)
    through output valve";
  Interfaces.ActSignal valve-control "Connector,
    actuator controlling output flow";
equation
  der(h)=(qIn.lflow - qOut.lflow)/A;
  qOut.lflow = valve-control.ActSignal *
    sqrt(max(0,2*g*h))*a;
  pressure.val=pressure;
end Tank;
    
```

Figure 2. Modelica code for Tank component

Given this tank component, we can then generate a system with multiple tanks in series simply by connecting the output flow connector of one tank to the input flow connector of the succeeding tank.

2.2.2 Three-Tank System

In this paper, we use the three-tank system shown in Fig. 3 to illustrate our approach. The three tanks are denoted as T_1 , T_2 , and T_3 . Each tank has the same area $A_1 = A_2 = A_3$. For $i = 1, 2, 3$, tank T_i has height h_i , a pressure sensor p_i , and a valve V_i , $i = 1, 2, 3$ that controls the flow of liquid out of T_i . We assume that gravity $g = 10$ and the liquid has density $\rho = 1$.

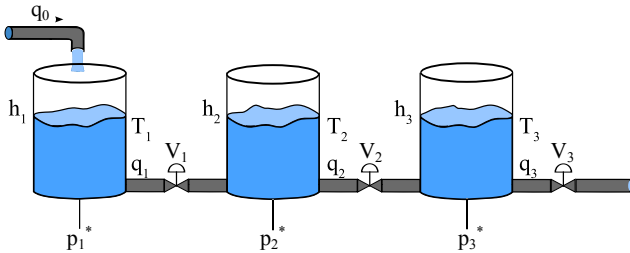


Figure 3. Diagram of the three-tank system.

Tank T_1 gets filled from a pipe, with measured flow q_0 . Using Torricelli's law, the model can be described by the following non-linear equations:

$$\frac{dh_1}{dt} = \frac{1}{A_1} \left[-\kappa_1 \sqrt{h_1 - h_2} + q_0 \right], \quad (3)$$

$$\frac{dh_2}{dt} = \frac{1}{A_2} \left[\kappa_1 \sqrt{h_1 - h_2} - \kappa_2 \sqrt{h_2 - h_3} \right], \quad (4)$$

$$\frac{dh_3}{dt} = \frac{1}{A_3} \left[\kappa_2 \sqrt{h_2 - h_3} - \kappa_3 \sqrt{h_3} \right]. \quad (5)$$

In eq. 3, the coefficient κ_1 denotes a parameter that

captures the product of the cross-sectional area of the tank A_1 , the area of the drainage hole, a gravity-based constant ($\sqrt{2g}$), and the friction/contraction factor of the hole. κ_2 and κ_3 can be defined analogously.

Finally, the pressure at the bottom of each tank is obtained from the height: $p_i = gh_i$, where i is the tank index ($i \in \{1, 2, 3\}$).

We emphasize the use of the κ_i , $i = 1, 2, 3$ because we will use these parameter-values as a means for "diagnosing" our system in term of changes in κ_i , $i = 1, 2, 3$. Consider a physical valve R_1 between T_1 and T_2 that constraints the flow between the two tanks. We can say that the valve changes proportionally the cross-sectional drainage area of q_1 and hence κ_1 . The diagnostic task will be to compute the true value of κ_1 , given p_1 , and from κ_1 we can compute the actual position of the valve R_1 .

We now characterise our nominal model in terms of Definition 2:

- variables \mathbf{V} consist of variables denoting the system state ($\mathbf{X} = \{h_1, h_2, h_3\}$), control ($\mathbf{U} = \{q_0, V_1, V_2, V_3\}$), and observations ($\mathbf{Y} = \{p_1, p_2, p_3\}$).
- $\boldsymbol{\theta} = \{\{A_1, A_2, A_3\}, \{\kappa_1, \kappa_2, \kappa_3\}\}$ is the set of parameters.
- Ξ consists of a single nominal mode.
- \mathcal{E} is a set of equations, given by equations 3 through 5.

Note that this model has a total of 6 parameters.

Fault Model In this article we focus on valve faults, where a valve can have a blockage or a leak. We model this class of faults by including in equations 3 to 5 an additive parameter β , which is applied to the parameter κ , i.e., as $\kappa_i(1 + \beta_i)$, $i = 1, 2, 3$, where $-1 \leq \beta_i \leq \frac{1}{\kappa_i} - 1$, $i = 1, 2, 3$. $\beta > 0$ corresponds to a leak, such that $\beta \in (0, 1/\kappa - 1]$; $\beta < 0$ corresponds to a blockage, such that $\beta \in [-1, 0)$. The fault equations allow faults for any combination of the valves $\{V_1, V_2, V_3\}$, resulting in system modes $\Xi = \{\xi_N, \xi_1, \xi_2, \xi_3, \xi_{12}, \xi_{13}, \xi_{23}, \xi_{123}\}$, where ξ_N is the nominal mode, and ξ is the mode where \cdot denotes the combination of valves (taken from a combination of $\{1, 2, 3\}$) which are faulty. This fault model has 9 parameters.

3 Modelling Metrics

This section describes the metrics that can be applied to estimate properties of a diagnosis model. We describe two types of metrics, dealing with accuracy (fidelity) and complexity.

Given a space Φ of possible models, we can define our model selection task as follows:

$$\phi^* = \underset{\phi \in \Phi}{\operatorname{argmin}} g_1(\tilde{\mathbf{Y}}, \mathbf{Y}_\phi) + g_2(\mathcal{C}(\tilde{\mathbf{Y}}, \phi)), \quad (6)$$

adopting the simplifying assumption that our loss function g is additively decomposable. We now briefly examine the accuracy (g_1) and complexity (g_2) metrics.

3.1 Model Accuracy

Model accuracy concerns the ability of a model to mimic a real system. Since model fidelity for a multi-mode approach varies depending on the mode, it is important to explicitly consider the *mean performance* of ϕ over the entire observation space \mathcal{Y} (the space of possible observations of the system). In this article simulation accuracy is defined using an expected residual:

Definition 5 (Expected Residual) *given a space $\mathcal{Y} = \{\tilde{\mathbf{Y}}_1, \dots, \tilde{\mathbf{Y}}_n\}$ of observations, the expected residual is the average over the n observations, e.g., as given by: $\bar{\mathcal{R}} = \frac{1}{n} \sum_{i=1}^n \mathcal{R}(\tilde{\mathbf{Y}}_i, \mathbf{Y}_\phi)$.*

Diagnostics accuracy is different, in that it involves computing the correct diagnosis without delays in fault isolation from the pair $(\tilde{\mathbf{Y}}, \mathbf{Y}_\phi)$. If we denote the tuple $(\boldsymbol{\omega}, t)$ as the correct diagnosis occurring at time t , and $(\hat{\boldsymbol{\omega}}, \hat{t})$ as the computed diagnosis identified at time \hat{t} , then our g_1 function must capture some difference measure for accuracy, e.g., $\|\hat{\boldsymbol{\omega}} - \boldsymbol{\omega}\|$, and some difference measure for isolation delays, e.g., $\|\hat{t} - t\|$. We can represent this abstractly as:

Definition 6 (Diagnosis Accuracy) *Given measures for isolation accuracy (g') and isolation delay (g''), diagnosis accuracy can be defined as*

$$g_1(\tilde{\mathbf{Y}}, \mathbf{Y}_\phi) = g'(\|\hat{\boldsymbol{\omega}} - \boldsymbol{\omega}\|) + g''(\|\hat{t} - t\|).$$

3.2 Model Complexity

At present, there is no commonly-accepted definition of model complexity, whether the model is used purely for simulation or if it is used for diagnostics or control. Defining the complexity of a model is inherently tricky, due to the number of factors involved.

Less complex models are often preferred either due to their low computational simulation costs (Keating et al., 2010), or to minimise model over-fitting given observed data (Pande et al., 2009; Schoups et al., 2008). Given the task of simulating a variable of interest conditioned by certain future values of input (control) variables, overfitting can lead to high uncertainty in creating accurate simulations. Overfitting is especially severe when we have limited observation variables for generating a model representing the underlying process dynamics. In contrast, models with low parameter dimensionality (i.e. fewer parameters) are considered less complex and hence are associated with low prediction uncertainty (Pande et al., 2014).

Several approaches have been used, based on issues like (a) number of variables (Kunz et al., 2006), (b) model structure (Provan and Wang, 2007), (c) number of free parameters (Pande et al., 2014), (d) number of parameters that the data can constrain (Spiegelhalter et al., 2002), (e) a notion of model weight (Du, 2014), or (f) *type* and *order* of equations for a non-linear dynamical model (Antoulas et al., 2001), where type corresponds to non-linear, linear, etc.; e.g., order for a non-linear model is such that a k -th order system has k -th derivatives in \mathcal{E} .

Factors that contribute to the true cost of a model include: (a) model-generation; (b) parameter estimation; and (c) simulation complexity, i.e., the computational expense (in terms of CPU-time and memory) needed to simulate the model given a set of initial conditions. Rather than try to formulate this notion in terms of the number of model variables or parameters, or a notion of model structural complexity, we specify model complexity in terms of a measure based on parameter estimation, and inference complexity, assuming a construction cost of zero.

A thorough analysis of model complexity will need to take into consideration the model equation class, since model complexity is class-specific. For example, for non-linear dynamical models, complexity is governed by the *type* and *order* of equations (Antoulas et al., 2001). In contrast, for linear dynamical models, which have only matrices and variables in equations (no derivatives), it is the order of the matrices that determines complexity. In this article, we assume that models are of appropriate complexity, and hence do not address Model order reduction techniques (Antoulas et al., 2001), which aim to generate lower-dimensional systems that trade off fidelity for reduced model complexity.

3.3 Bayesian Model Complexity

The Bayesian model complexity approach, which is based on the model likelihood, measures whether the increased “complexity” of a model with more parameters is justified by the data. The Bayesian approach chooses a model (and a model structure) from a set of competing models (from the set of corresponding model structures, respectively) such that the value of a Bayesian criterion is maximized (or prediction uncertainty in choosing a model structure is minimized).

The Bayesian approach addresses prediction uncertainty by specifying an appropriate likelihood function. In other words, it specifies the probability with which the observed values of a variable of interest are generated by a model. The marginal likelihood of a model structure, which represents a class of models capturing the same processes (and hence have the same parameter dimensionality), is obtained by integrating over the prior distribution of model parame-

ters; this measures the prediction uncertainty of the model structure (Vrugt and Robinson, 2007).

The idea is that by adding parameters to a model we obtain improvement in fit, but at the expense of making parameter estimates “worse” because we have less data (i.e., information) per parameter. In addition, the computations typically require more time. So the key question is how to identify how complex a model works best for a given problem.

In the statistics literature several decomposable approximations have been proposed. We now review the best-known methods. (Spiegelhalter et al., 2002) have proposed a well-known such decomposable framework, termed the Deviance Information Criterion (DIC), which measures the number of model parameters that the data can constrain.: $DIC = \bar{D} + p_D$, where \bar{D} is a measure of fit (expected deviance), and p_D is a complexity measure, the *effective* number of parameters. The Akaike Information Criterion (AIC) (Akaike, 1974, 1981) is another well-known measure: $AIC = \mathcal{L}(\hat{\theta}) + 2k$, where $\hat{\theta}$ is the Maximum Likelihood Estimate (MLE) of θ and k is the number of parameters.

Another computationally more tractable approach is the Bayesian Information Criterion (BIC) (Schwarz, 1978): $BIC = -2\mathcal{L}(\hat{\theta}) + k \log n$, where k is the number of *estimable* parameters, and n is the sample size (number of observations). BIC was developed as an approximation to the log marginal likelihood of a model, and therefore, the difference between two BIC estimates may be a good approximation to the natural log of the Bayes factor. Given equal priors for all competing models, choosing the model with the smallest BIC is equivalent to selecting the model with the maximum posterior probability. BIC assumes that the (parameters’) prior is the unit information prior (i.e., a multivariate normal prior with mean at the maximum likelihood estimate and variance equal to the expected information matrix for one observation).

(Wagenmakers, 2007) shows that one can convert the BIC measure to $BIC = n \log \frac{SSE}{SS_{total}} + k \log n$, where SSE is the sum of squares for the error term. In our experiments, we assume that the non-linear model is the “correct” model (or the null hypothesis H_0), and either the linear or qualitative models are the competing model (or alternative hypothesis H_1). Hence what we do is use BIC to compare the non-linear to each of the competing models.

4 Experimental Design

This section compares three tank benchmark models according to various model-selection measures. We adopt as our “correct” model the non-linear model.

We will examine the fidelity and complexity trade-offs of two simpler models over a selection of failure scenarios.

The diagnostic task will be to compute the fault state of the system, given an injected fault. This translates to different tasks given the different models.

non-linear model estimate the true value of κ_1 given p_1 , which corresponds to a most-likely failure mode assignment of one of (ξ_N, ξ_B, ξ_P) .

linear model estimate the true value of κ_1 given p_1 , which corresponds to a most-likely failure mode assignment of one of (ξ_N, ξ_B, ξ_P) .

qualitative model estimate the failure mode assignment of one of (ξ_N, ξ_B, ξ_P) .

4.1 Alternative Models

This section describes the two alternative models that we compare to the non-linear model, a linear and a qualitative model.

4.1.1 Linear Model

We compare the non-linear model with a linearised version. We can perform this linearised process in a variety of ways (Spanos, 1977). In this simple tank example, we can perform the linearisation directly through replacement of non-linear and linear operators, as shown below.

Nominal Model We can linearise the the non-linear 3-tank model by replacing the non-linear sub-function $\sqrt{h_i - h_j}$ with the linear sub-function $\gamma_{ij}(h_i - h_j)$, where γ_{ij} is a parameter (to be estimated) governing the flow between tanks i and j . The linear model has 4 parameters, $\gamma_{12}, \gamma_{21}, \gamma_{23}, \gamma_{32}$.

Fault Model The fault model introduces a parameter β_i associated with κ_i , i.e., we replace κ_i with $\kappa_i(1 + \beta_i)$, $i = 1, 2, 3$, where $-1 \leq \beta_i \leq \frac{1}{\kappa_i} - 1$, $i = 1, 2, 3$. This model has 7 parameters, adding parameters $\beta_1, \beta_2, \beta_3$.

4.1.2 Qualitative Model

Nominal Model For the model we replace the non-linear sub-function $\sqrt{h_i - h_j}$ with the qualitative sub-function $M^+(h_i - h_j)$, where M^+ is the set of reasonable functions f such that $f' > 0$ on the interior of its domain (Kuipers and Åström, 1994).

The tank-heights are constrained to be non-negative, as are the parameters κ_i . As a consequence, we can discretize the h_i to take on values $\{+, 0\}$, which means that $M^+(h_i - h_j)$ can take on values $\{+, 0, -\}$. The domain for $\frac{dh_1}{dt}$ must be $\{+, 0, -\}$, since

POSITION first generates a model where T_1 is non-linear, T_2 is non-linear, and T_3 is non-linear. In the second call NEXTMODELCOMPOSITION changes T_1 from non-linear to linear. Depending on the implementation of NEXTMODELCOMPOSITION the next candidate can be either T_1 and T_2 non-linear while T_3 linear or T_1 non-linear, T_2 linear, and T_3 non-linear.

The greedy search approach guarantees that Algorithm 1 will terminate with $O(n)$ model evaluations, but at the cost of optimality. Optimality is also limited by the “quality” of the component models and the set of test cases used for testing the metrics.

6 Experimental Results

This section describes our experimental results, summarising the data first and then discussing the implications of the results.

6.1 Model Comparisons

We have empirically compared the diagnostics performance of several multi-tank models. In our first set of experiments, we ran a simulation over 500 seconds, and induced a fault (valve V_1 at 50%) after 250 s. The model combinations involved a non-linear (NL) model, a model (denoted M) with tank T_1 being linear (and other tanks non-linear), a fully linear model (denoted L), and a Qualitative model (denoted Q).

To compute a measure of diagnostics error (or loss), we use the difference between the true fault (which is known for each simulation) and the computed fault. We denote the true fault existing at time t using the pair (ω, t) ; the computed fault at time t is denoted using the pair $(\hat{\omega}, \hat{t})$. The inference system that we use, LNG, computes an uncertainty measure associated with each computed fault, denoted $P(\hat{\omega})$. Hence, we define a measure of diagnostics error over a time window $[0, T]$ using

$$\gamma_1^D = \sum_{t=0}^T \sum_{\xi \in \Xi} |P(\hat{\omega}) - \omega|, \quad (7)$$

where Ξ is the set of failure modes for the model.

Our second metric covers the fault latency, i.e., how quickly the model identifies the true fault (ω, t) :

$$\gamma_3 = t - \hat{t}. \quad (8)$$

Table 1 summarises our results. The first columns compare the number of parameters for the different models, followed by comparisons of the error (γ_1) and the CPU-time (γ_3). The data show that the error (γ_1) does not grow very much as we increase model size, but it increases as we decrease model fidelity from non-linear through to qualitative models. In contrast,

the CPU-time (a) increases as we increase model size, and (b) is proportional to model fidelity, i.e., it and decreases as we decrease model fidelity from non-linear through to qualitative models.

Tanks		2	3	4
# Parameters	NL	7	9	11
	M	6	8	10
	L	5	7	9
	Q	2	3	4
γ_1	NL	242	242	242
	M	997	1076	1192
	L	1236	1288	1342
	Q	3859	3994	4261
γ_3	NL	10.59	23.7	39.5
	M	8.52	17.96	34.6
	L	6.11	10.57	32.0
	Q	4.64	7.31	26.4

Table 1. Data for 2-, 3-, and 4-tank models using Non-linear (NL), Mixed (M), Linear (L) and Qualitative (Q) representations

In a second set of experiments, we focused on multiple model types for a 3-tank system, with simulations running over 50s. The model combinations involved a non-linear (NL) model, a model with tank 3 linear (and other tanks non-linear), a model with tanks 2 and 3 linear and tank 1 non-linear, a fully linear model, and a qualitative model. Table 2 summarises our results.

The data show that, as model fidelity decreases, the error γ_1 increases significantly and the inference times γ_3 decrease modestly. If we examine the outputs from AIC_c , we see that the best model is the mixed model (T_3 -linear). BIC indicates the qualitative model as the best; it is worth noting that BIC typically will choose the simplest model.

	γ_1	γ_3	AIC_c	BIC
Non-Linear	0.97	23.7	29.45	43.7
T_3 -linear	3.12	17.96	26.77	42.9
T_2, T_3 -linear	21.96	13.21	31.12	39.56
Linear	77.43	10.57	35.76	37.55
Qualitative	304.41	9.74	43.01	29.13

Table 2. Data for 3-tank model, using Non-linear, Mixed, Linear and Qualitative representations, given a fault (valve V_1 at 50%) after 25 s

6.2 Discussion

Our results show that MBD is a complex task with several conflicting factors.

- The error γ_1 is inversely proportional to model fidelity, given a fixed diagnosis task.
- The error γ_1 increases with fault cardinality.
- The CPU-time γ_3 increases with model size (i.e., number of tanks).

We have shown how one can extend a set of information-theoretic metrics to combine these competing factors in diagnostics model selection. Further work is necessary to identify how best to extend the existing information-theoretic metrics to suit the needs of diagnostics inference.

It is important to note that we conducted experiments with un-calibrated models, and we have ignored the cost of calibration in this article. The literature suggests that linear models can be calibrated to achieve good performance, although performance inferior to that of calibrated non-linear models. This class of qualitative models does not possess calibration factors, so calibration will not improve their performance.

This article has introduced a framework that can be used to trade off the different factors in MBD. It is likely that the “best” model may be domain- and task-specific; further work is needed to answer this notion.

7 Conclusions

This article has presented a framework for generating Modelica models for a range of applications, such as simulation, control and diagnosis. Our approach can tailor the fidelity of the model to the application, using an application-specific metric for judging model “quality”. The metric aims to balance competing properties of models, e.g., fidelity and computational complexity.

We demonstrated our approach on the domain of model-based diagnosis (MBD). We have proposed some Bayesian metrics for MBD model evaluation, and conducted some preliminary experiments to show how these metrics may be applied. This work thus constitutes *a start* to a full analysis of model performance. Our intention is to initiate a more formal analysis of modeling and model evaluation, since there is no framework in existence for this task. Further, the experiments are only preliminary, and are meant to demonstrate how a framework can be applied to model comparison and evaluation.

Significant work remains to be done, on a range of fronts. In particular, a thorough empirical investigation is needed on diagnostics modeling. Second, the real-world utility of our proposed framework needs to be determined. Third, a theoretical study of the issues of mode-based parameter estimation and its use for MBD is necessary.

References

- Hirotsugu Akaike. A new look at the statistical model identification. *Automatic Control, IEEE Transactions on*, 19(6):716–723, 1974.
- Hirotsugu Akaike. Likelihood of a model and information criteria. *Journal of econometrics*, 16(1):3–14, 1981.
- Per Åkerlund. *Model-based diagnosis using MathModelica*. PhD thesis, Master’s thesis, Linköping University, SE-581 83 Linköping, 2001.
- AC Antoulas, DC Sorensen, and S Gugercin. A survey of model reduction methods for large-scale systems. *Contemporary mathematics*, 280:193–220, 2001.
- Olof Bäck. *Modelling for diagnosis in Modelica: implementation and analysis*. PhD thesis, Master’s thesis, Linköping University, SE-581 83 Linköping, 2008.
- H Brückmann, J Strenkert, U Keller, B Wiesner, and A Junghanns. Model-based development of a dual-clutch transmission using rapid prototyping and sil. In *International VDI Congress Transmissions in Vehicles*, 2009.
- Francesco Casella and Alberto Leva. Modelica open library for power plant simulation: design and experimental validation. In *Proceedings of the 3rd international Modelica conference*, 2003.
- Francesco Casella, Martin Otter, Katrin Proelss, Christoph Richter, and Hubertus Tummescheit. The modelica fluid and media library for modeling of incompressible and compressible thermo-fluid pipe networks. In *Proceedings of the Modelica Conference*, pages 631–640, 2006.
- Francesco Casella, Filippo Donida, and Marco Lovera. Beyond simulation: Computer aided control system design using equation-based object oriented modelling for the next decade. In *2nd International Workshop on Equation-Based Object-Oriented Languages and Tools*, page 35, 2008.
- Johan de Kleer, Bill Janssen, Daniel G Bobrow, Tolga Kurtoglu, Bhaskar Saha, Nicholas R Moore, and Saravan Sutharshana. Fault augmented modelica models. In *The 24th International Workshop on Principles of Diagnosis*, pages 71–78, 2013.
- Jing Du. The “weight” of models and complexity. *Complexity*, 2014.
- S Elgsæter, Pal Kittilsen, and Svein Olav Hauger. Designing large-scale balanced-complexity models for online use. In *Proc. IFAC Workshop on Automatic Control in Offshore Oil and Gas Production, Trondheim, Norway*, pages 157–162, 2012.
- Alexander Feldman, Gregory M Provan, and Arjan JC van Gemund. Computing observation vectors for maximum fault min-cardinality diagnoses. In *AAAI*, pages 919–924, 2008.

- Alexander Feldman, Helena Vicente de Castro, Arjan van Gemund, and Gregory Provan. Model-based diagnostic decision-support system for satellites. In *Proceedings of the IEEE Aerospace Conference, Big Sky, Montana, USA*, pages 1–14, March 2013.
- Lars Imsland, Pal Kittilsen, and Tor S Schei. Model-based optimizing control and estimation using modelica model. *Modeling, Identification and Control*, 31(3): 107–121, 2010.
- Elizabeth H Keating, John Doherty, Jasper A Vrugt, and Qinjun Kang. Optimization and uncertainty assessment of strongly nonlinear groundwater models with high parameter dimensionality. *Water Resources Research*, 46(10), 2010.
- Eui-Jong Kim, Gilles Plessis, Jean-Luc Hubert, and Jean-Jacques Roux. Urban energy simulation: Simplification and reduction of building envelope models. *Energy and Buildings*, 84:193–202, 2014.
- Pål Kittilsen, Svein Olav Hauger, and Stein O Wasbø. Designing models for online use with modelica and fmi. In *Proceedings of the 9th International Modelica Conference. Munich, Germany*, pages 197–204, 2012.
- Benjamin Kuipers and Karl Åström. The composition and validation of heterogeneous control laws. *Automatica*, 30(2):233–249, 1994.
- Martin Kunz, Roberto Trotta, and David R Parkinson. Measuring the effective complexity of cosmological models. *Physical Review D*, 74(2):023503, 2006.
- Marek Mateják, Tomáš Kulhánek, Jan Šilar, Pavol Privitzer, Filip Ježek, and Jiří Kofránek. Physioblibrary-modelica library for physiology. In *10th International Modelica Conference*, pages 499–505. Linköping University Electronic Press Lund, Sweden, 2014.
- S Pande, L Arkesteijn, HHG Savenije, and LA Bastidas. Hydrological model parameter dimensionality is a weak measure of prediction uncertainty. *Natural Hazards and Earth System Sciences Discussions*, 11, 2014, 2014.
- Saket Pande, Mac McKee, and Luis A Bastidas. Complexity-based robust hydrologic prediction. *Water resources research*, 45(10), 2009.
- Gilles Plessis, Aurélie Kaemmerlen, and Amy Lindsay. Buildsyspro: a modelica library for modelling buildings and energy systems. In *Proceedings of the International Modelica Conference*, 2014.
- Gregory Provan. Generating reduced-order diagnosis models for hvac systems. In *Intl. Workshop on Principles of Diagnosis, Murnau, Germany*, 2011.
- Gregory M Provan and Jun Wang. Automated benchmark model generators for model-based diagnostic inference. In *IJCAI*, pages 513–518, 2007.
- Lucien A Schmit and B Farshi. Some approximation concepts for structural synthesis. *AIAA journal*, 12(5): 692–699, 1974.
- G Schoups, NC Van de Giesen, and HHG Savenije. Model complexity control for hydrologic prediction. *Water Resources Research*, 44(12), 2008.
- G. Schwarz. Estimating the dimension of a model. *Ann. Statist.*, 6:461–466, 1978.
- Pol D Spanos. *Linearization techniques for non-linear dynamical systems*. PhD thesis, California Institute of Technology, 1977.
- David J Spiegelhalter, Nicola G Best, Bradley P Carlin, and Angelika Van Der Linde. Bayesian measures of model complexity and fit. *Journal of the Royal Statistical Society: Series B (Statistical Methodology)*, 64(4): 583–639, 2002.
- Hubertus Tummescheit and Jonas Eborn. Design of a thermo-hydraulic model library in modelica. In *12th European Simulation Multiconference*, 1998.
- Jasper A Vrugt and Bruce A Robinson. Treatment of uncertainty using ensemble methods: Comparison of sequential data assimilation and bayesian model averaging. *Water Resources Research*, 43(1), 2007.
- Eric-Jan Wagenmakers. A practical solution to the pervasive problems of p values. *Psychonomic bulletin & review*, 14(5):779–804, 2007.
- Michael Wetter, Wangda Zuo, Thierry S Nouidui, and Xiufeng Pang. Modelica buildings library. *Journal of Building Performance Simulation*, 7(4):253–270, 2014.

A Software Architecture for Simulation and Visualisation based on the Functional Mock-up Interface and Web Technologies

Lars Ivar Hatledal¹ Hans Georg Schaathun² Houxiang Zhang¹

¹Department of Maritime Technology and Operations, Aalesund University College, Norway,
{laht,hoz}@hials.no

²Department of Engineering and Natural Sciences, Aalesund University College, Norway, hasc@hials.no

Abstract

This paper presents a software architecture for a collaborative virtual environment (CVE) for simulation and visualisation based on the Functional Mock-up Interface (FMI) for co-simulation and web technologies. FMI has been chosen in order to have a standardised and independent interface to models created in different modelling tools.

The user interface has been implemented using web technologies, which enables a very high degree of flexibility. The Web Graphics Library (WebGL) is used for interactive 3D visualisations, enabling native cross-platform rendering directly in the browser without the need of installing any additional plug-ins. Employing the bi-directional communication capabilities of the WebSocket protocol, multiple users can interact with the same simulation models simultaneously.

A software prototype has been developed in order to demonstrate the applicability of the proposed architecture. As a case study, we have considered virtual prototyping of marine cranes, to illustrate the use on real world problems.

Keywords: Functional Mock-up Interface, WebGL, Virtual Prototyping, Web based Simulation

1 Introduction

Virtual prototyping is a hot topic in many industries. The construction of physical prototypes is costly and time consuming, but has traditionally been necessary to be able to test and evaluate new designs. As computer technology develops it becomes possible to make an increasing part of the necessary tests based on simulations. Modelling and simulation of components has been possible for some time, and good tools exist. Simulation of complex systems is harder, and in most cases it still depends on a costly and time consuming *ad hoc* integration of components. Virtual prototyping refers to a vision where models, or *virtual prototypes*, of complex systems can be developed, tested, and amended with a trial-and-error approach.

As the standards of the web has matured, a growing number of applications have been made accessible from a web browser. The latest version of the HTML standard, HTML5, has brought along new powerful developer Application Programming Interfaces (APIs), previously restricted to desktop applications. WebGL (Marrin, 2011), has made it possible to utilise the 3D rendering capabilities of the GPU from within the browser, without the use of plug-ins. Furthermore, the WebSocket standard (Fette and Melnikov, 2011) allows for low latency bi-directional communication between browsers and web servers.

FMI (Blochwitz et al., 2012) is an open and tool independent standard for model exchange and co-simulation of dynamic models. FMI is currently supported by 73 tools, which indicates a major impact on research and industry. In this architecture, FMI has been chosen in order to have a standardised and independent interface to simulation models created in different modelling tools. These FMI compliant models, called Functional Mock-up Units (FMUs), are distributed on the network and accessed using Remote Procedure Calls (RPC) in order to ensure scalability as the number of concurrent simulations increases. Modules that describes sub-systems (either in the form of FMUs or directly implemented in Java) can be assembled together in order to form more complete systems.

The user interface has been implemented using web technologies, which enables a very high degree of flexibility and low coupling. For instance, modifications to the underlying architecture can be applied without issuing software updates to clients. Furthermore, users can view and interact with live simulations just by opening a browser page. As all computations except rendering are done on a remote server, even less powerful devices such as tablets or smart-phones may interact with running simulations.

This paper is organised as follows. A review of related research work is given in Section 2. Section 3 outlines the software architecture for simulation and visualisation based on the functional mock-up interface and web technologies, while a case study is presented in Section 4. Finally, discussion and conclusion is given in Section 5.

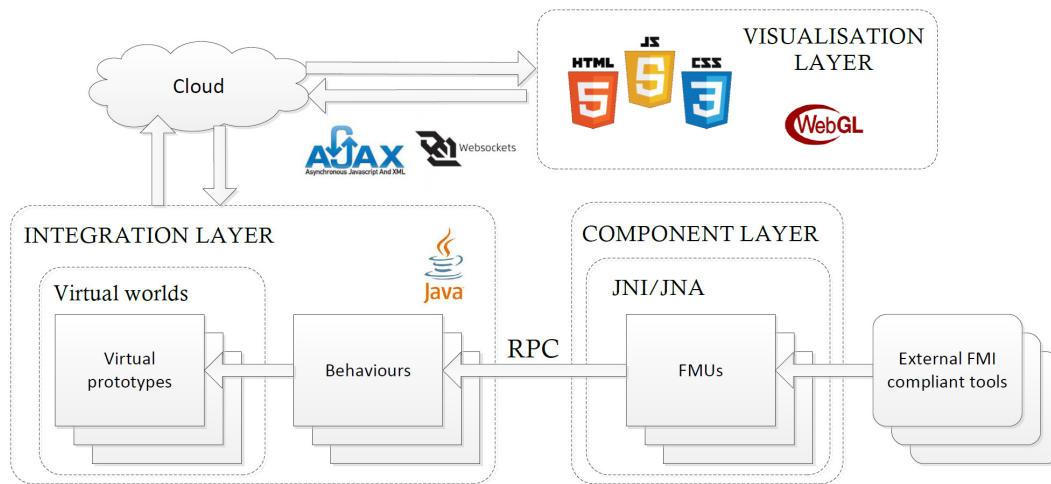


Figure 1. High level software architecture

2 Related work

Component-based simulations is a common topic in the literature, together with other approaches to modularising simulations. After the introduction of FMI, several authors have shown how to use it in modular simulations. A recent example is Neema et al. (2014), who used FMI for component models which were integrated using High-Level Architecture (HLA). Their system supports component models from a range of different modelling tools, in addition to FMI support.

Delafosse et al. (2012) discuss the use of simulation at every stage of the design and development, taking hybrid vehicles as a sample scenario. They start with a high-level model of the complete system, using generic components described by analytic models or lookup tables. When the components are developed later in the process, detailed behavioural models can be integrated into the original system model.

A comprehensive survey of web-based simulation is provided by Byrne et al. (2010). They define web-based simulation as any approach which uses the web browser to provide a user interface for the simulation. They classify different web-based simulation systems according to the role taken by the web browser. The simulation can be client-side, server-side, or hybrid. The latter runs the simulator on the server and the visualisation layer on the client, while the former run both in the web browser or both on the server, respectively. The web browser can also take other roles, such as providing access to a model repository or to documentation.

Several authors have applied WebGL to provide full 3D rendering in web-based simulations. A client-side approach is taken by McMullen et al. (2012), who implemented simulation of abstract models in JavaScript, with visualisation in WebGL for simulation. Pang et al. (2013) took a hybrid approach in a system for interactive e-learning environment for high performance buildings (HPB). They used using a single Functional Mock-

up Unit (FMU) as the simulation back-end running on the server.

Several authors have suggested to run simulations in a service oriented architecture (SoA). An early example is zu Eissen and Stein (2006) who proposed a method to simulate Modelica models as a Web Service. Their work is limited to non-distributed, single-user simulations. They used the YANOS simulator for Modelica and wrapped it in SOAP to provide the web service.

Wang and Zhang (2012) have developed a service-oriented and web-based framework for virtual prototyping in a distributed and collaborative environment. They focus on integration of different modelling tools, using High-Level Architecture (HLA) as part of the architecture. System-level modelling is explicitly out of scope. They also give a comprehensive historic overview, which is worth reading.

Zhang et al. (2010) take a model-driven approach to system-level modelling, and the development of a modular simulator. This means that some of the code needed to realise the simulator can be automatically generated from abstract models of the complete system. The works of Zhang et al. (2010) and Wang and Zhang (2012) are not directly applicable to virtual prototyping. They focus on the structured development of a simulator in a waterfall-approach. They do not discuss how domain experts can tinker with a virtual prototype in a trial and error fashion.

More recently, De Filippo et al. (2014) discuss a modular architecture for driving simulators. They give a historic overview of simulation in the automotive industry, discussing shortcomings of previous generations of simulators. Their own approach is called FDMU and is based on a Service-Oriented Architecture (SOA). The objective is similar to that of Distributed Interactive Simulation (DIS) and High-Level Architecture (HLA), but it is claimed that SOA gives looser coupling. SysML is adopted for wrapper design in FDMU. The FDMU set-up includes both a visualisation component and dedicated user interaction hardware.

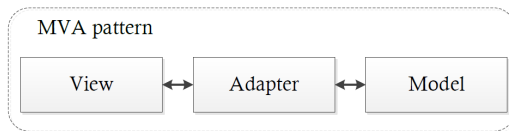


Figure 2. Model View Adapter pattern

3 Software architecture

Fig. 1 shows the high level architecture of the presented software architecture. It is based on the Model-View-Adapter (MVA) pattern and uses a centralised primary architecture (Pečiva, 2008). The MVA pattern is similar to the more well known Model-View-Controller (MVC) pattern, but differs by arranging the model, view and adapter linearly without any connections between the view and the model. This means that the view is completely decoupled from the model, such that the view and model can only interact via a mediating controller or adapter as seen in Fig. 2. As the model is oblivious to its presentation, the view/user interface can be implemented in any language/tool without modification of the underlying business logic. It should be noted that in the implemented MVA pattern, the model is oblivious to the adapter as well. In stead of implementing an observer pattern, the adapter reads the state of the model per request. The adapter is implementing the *singleton pattern*. In this way, as the views/user interfaces can only interact with the model through the adapter, it will know when a major user-initialised change has occurred. Allowing it to notify other clients if needed. The adopted MVA pattern is shown in Fig. 3.

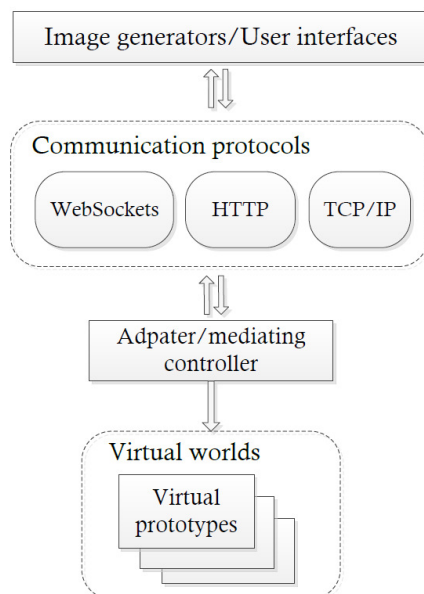


Figure 3. Adopted MVA pattern

3.1 Communication

Real-time communication between clients and the server is handled using the WebSocket protocol, while files are served using asynchronous JavaScript and XML (Ajax). The major benefit of utilising WebSockets, apart from the reduced latency, is the bi-directional communication capability. Before the introduction of WebSockets in HTML5, full-duplex transmissions between client and server was not straightforward. However, some methods for real-time data exchange based on HTTP has been available using *polling*, *long-polling* and *streaming* mechanisms. But these methods involve unnecessary HTTP request and response headers, which introduce latency, and the server itself cannot initiate a connection using the standard HTTP model (Loreto et al., 2011).

Google protocol buffers (Varda, 2008) are used to serialise data transmitted between the client and server. Protocol buffers have been chosen because of the language and platform neutral nature, the small overhead and the well defined message structure. In particular, messages sent using the protocol buffers are pre-defined inside files with a *.proto* extension. *Protobuf.js* (Wirtz, 2013) has been used in order to add support for protocol buffers in JavaScript, while support for C++, Java and Python, as well as some other languages, are bundled together with the protocol buffers.

An example protocol message is given in Listing 1. Actually, this message contains all the information needed to update the browser 3D visuals as the initial *Node* is the top-most node in the scene graph, and each child is also a *Node*. The optional geometry is only sent once if present, and contains the information necessary for rendering.

Listing 1. example .proto message

```
message Node {
  required int32 ID = 1;
  required string name = 2;
  required Vector3 worldPosition = 3;
  required Quaternion worldQuaternion = 4;
  repeated Node children = 5;
  optional Geometry geometry = 6;
}
```

3.2 Visualisation layer

The visualisation layer consists of a set of HTML5 web pages handling user input, displaying 3D visuals, 2D plots and other types of data presented according to users requirements. In order to preserve state when transitioning between different HTML pages during a user session, Java Server Pages (JSP) has been utilised, which allows variables to be serialised into Java beans.

WebGL is used to render the 3D visuals. In particular, WebGL is a cross-platform Javascript API for rendering 3D graphics inside of an HTML5 *<canvas>* ele-

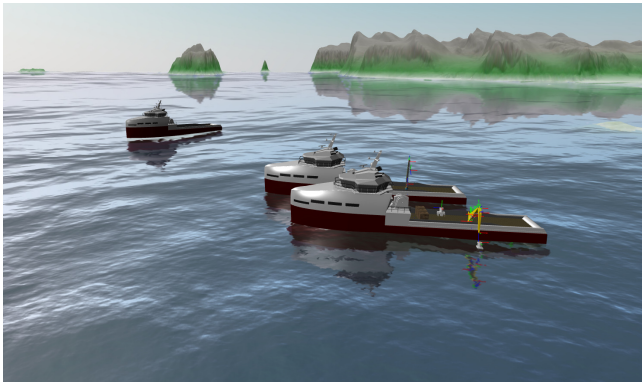


Figure 4. Virtual world rendered using WebGL

ment, without the use of plug-ins. WebGL is based on OpenGL ES 2.0, and Version 1.0 of the standard was released in 2011 and is today widely supported in modern browsers, both desktop and mobile versions. Fig. 4 shows a virtual world rendered in the browser using WebGL. The open-source Javascript library *three.js* (Cabello, 2010) has been used to simplify WebGL interaction. *Three.js* supports a number of common 3D formats such as Wavefront .OBJ, Standard Tessellation language (.STL) and Collada (.DAE) to name a few. The 3D models generated by the server side application are transmitted through the Web-Socket binary stream, while models available from a remote web server are loaded asynchronously through Ajax calls. However, due to cross-site HTTP requests being subject to restrictions for security reasons, a client-side request made from domain A to load a resource from domain B will be denied by web browsers. A simple way to bypass this restriction is to let domain A pass the request through a server-side resource, acting as a proxy, not bound by the same restrictions.

The plotting library, *CanvasJS*, has been used to simplify the creation of 2D plots, and a web page displaying real-time plots from a running simulation is shown in Fig. 5. Plotting works by having the client poll for updates at a regular interval. These updates contains the most current data at the time of the poll. Caching is done by the client in order to save bandwidth, and to let the view decide how many data points that should be visible.

3.2.1 Terrain

In some cases, the inclusion of real world terrain data can help create a more vivid and realistic simulation environment. Something which is especially true for training simulators. In this system, such data is specified as digital elevation models (DEMs). DEMs of the Norwegian mainland was released to the public in 2013 by the Norwegian Mapping Authority, with a resolution down to 10x10 meters. Using the Geospatial Data Abstraction Library (GDAL) (GDAL Development Team, 2015), the DEM files can be exported to a more lightweight and WebGL friendly format.

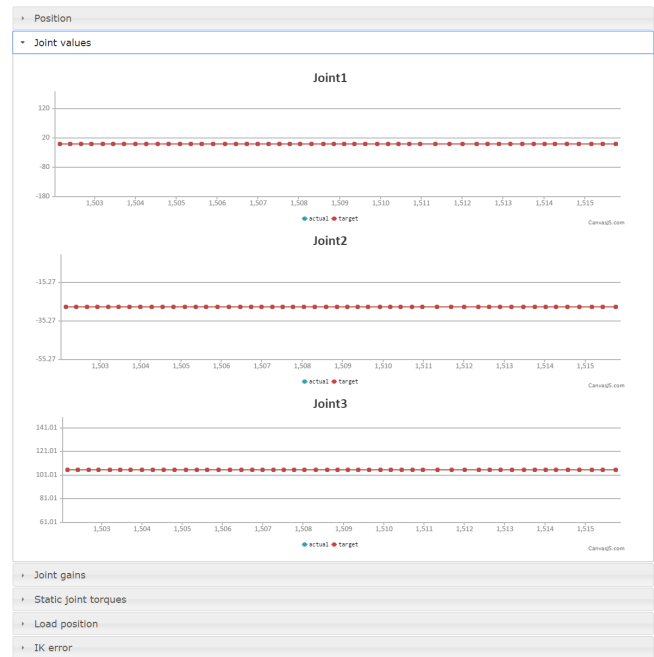


Figure 5. Real time plots available through the browser

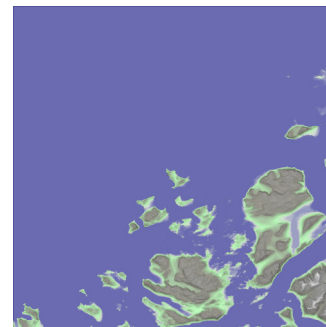


Figure 6. Terrain texture based on DEM data generated by combining hill-shade, hill-slope and color-relief textures

GDAL is also able to produce color-reliefs, hill-shade and hill-slope textures from the DEM source. These are combined into a single texture and mapped onto the terrain. An example of such a generated texture is given in Fig. 6.

3.2.2 Ocean Waves

Ocean waves are created by having the server and any connected clients implement the same wave equation. In this way, time is the only variable needed to be shared and is controlled by the server as seen in fig 7. The benefit of this approach is that views can set the height-map for an arbitrary sized mesh without increasing the load on the server. The server itself only needs to calculate the height-map around vessels and other floating objects.

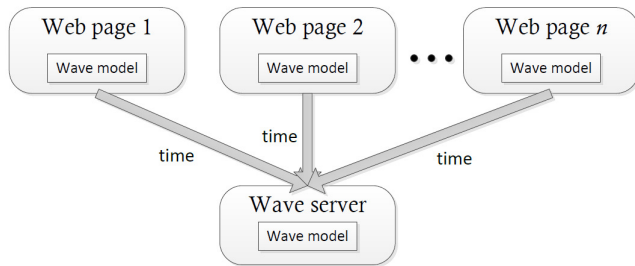


Figure 7. Wave generation principle

3.3 Integration Layer

The integration layer has been written using the Java Platform, Enterprise Edition (EE), which is built on top of the Java Standard Edition (SE) and provides the means for developing and running large-scale and scalable network applications. For instance the WebSocket and Servlet API's used to communicate with the web browsers are bundled with the EE API.

3.3.1 Virtual world

The virtual world, or collaborative virtual environment, is the simulated world in which the *virtual prototypes* exist. Simple objects such as crates etc. can also inhabit this world in order to increase realism, but are not necessarily important for the simulation in question. All objects in the same world are stepped forward using the same time step, such that a simulation may be slowed down or accelerated forward depending on the needs. The virtual world is managed by a scene graph in charge of managing the parent-child relationships and transformations of all the *nodes* in a scene. These nodes are arranged in a tree structure as shown in Fig. 8. A node can have zero or more children, but only one parent. Properties of the nodes include the local and world transformations along with an optional 3D representation. *Dual-quaternions* are used to represent these rigid-body transformations as they have been shown to be the most efficient and compact form of representing rotation and translation in a unified way (Kenwright, 2012).

Virtual worlds are generated by uploading configuration files to the server. These are written using the YAML data serialization format. YAML is similar to JavaScript Object Notation (JSON), but has additional features such as comments and anchors, and has been chosen because it is easy to parse, has a rich feature set and is easy to manually read/edit.

3.3.2 Virtual prototypes

The *Virtual prototypes* are the objects in the virtual world that users can interact with, edit, monitor etc. It could be a crane, winch system, propulsion system etc. In order for it to be a virtual prototype, one should be able to change

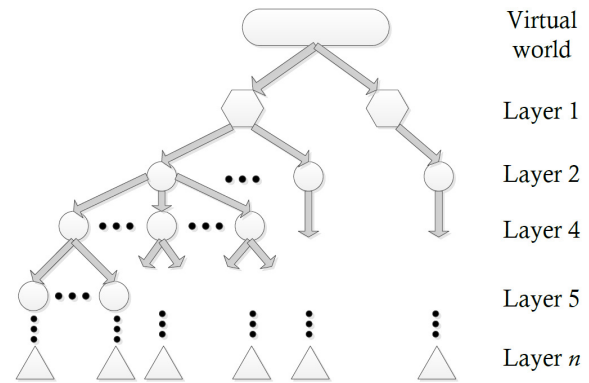


Figure 8. General scene graph layout

some physical property of the object in order to see how this change would affect its performance.

3.3.3 Behaviours

Behaviours alters the state of a virtual prototype over time, and could encapsulate the functionality of zero or more FMUs from the *component layer*. Several behaviours can be attached to a virtual prototype in order to simulate the desired functionality.

3.4 Component Layer

Simulation models can be written in a number of different domain specific tools. Integration of models across these tools are not necessary straightforward, and success depends on the tools having support for the same mechanisms for sharing data.

The integration of simulation models created in various software tools is achieved through the use of the FMI standard, by letting tools export their models as FMUs implementing the *co-simulation* standard. Basically, an FMU is a compressed folder consisting of a combination of compiled C code, describing the model equations, and XML files specifying the variables used. The most notable difference between a *model-exchange* and *co-simulation* FMU is that the latter includes its own solver. The open source library *javaFMI* (javaFMI Development Team, 2013) is used to simplify interaction with the FMUs. In particular, *javaFMI* takes care of unzipping, parsing the attached XML and invoking the pre-compiled C code using Java Native Access (JNA).

Functionality from FMUs in this layer is accessed through RPC calls. In this way, available FMUs can be distributed and computed on some remote resource. Currently, Remote Method Invocation (RMI), which is built into the Java API, is used as the RPC mechanism. As FMUs are invoked remotely, the server hosting them and the client accessing them are not required to run on the same platform or share bitness. That is, an RPC request

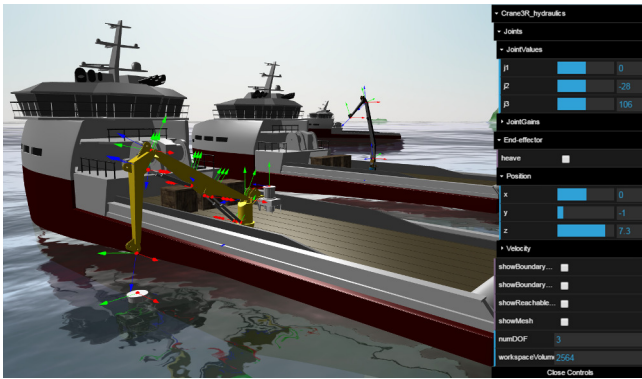


Figure 9. Controlling a crane in the virtual world

originating from a 64-bit windows program can take advantage of an FMU compiled as a 32-bit linux library.

4 Case Study

The presented software architecture has been used to implement a virtual prototyping system prototype for maritime crane design and operation (Yingguang et al., 2015). The crane kinematics and hydraulic properties are defined in a YAML document and uploaded to the server. In this prototype, dynamics has not been considered, but is planned to be added once a physics engine has been integrated. Links and joints are placed in the scene graph hierarchy by parsing the crane kinematics. The hydraulic properties are inputs to the FMUs making up the hydraulic system, which consists of a hydraulic motor for the base and hydraulic cylinders for the jib and boom. These were modelled using bond graphs in the modelling tool *20-sim* (Weustink et al., 1998). Multiple cranes can be defined in the same document, along with other world objects. In Fig. 9, two cranes have been defined. The widget visible to the right is used to interact with the cranes. Changes done to this widget are propagated to the server, which forwards the requested action to the crane model, and other users interacting with the same crane will have their widget updated accordingly. This particular widget uses Cascade Style Sheet (CSS) to overlay itself on-top of the WebGL *<canvas>*, but widgets could also be regular HTML pages. Additionally, real world terrain, multiple vessels and simple geometric entities have been included. Using the approach described in Hatledal et al. (2015), the workspace of the cranes are calculated and saved as a 3D model made accessible to the visualisation.

For a more elaborate description of the case study, refer to Yingguang et al. (2015).

5 Discussion and Conclusion

This paper presents a software architecture for simulation and visualisation based on FMI and web technologies.

FMI allows for the integration of simulation models from different domains tools, while the use of web technologies enables a highly flexible way of presenting data. Furthermore, as simulations are carried out server side, no software other than a browser is required to interact with them. As the simulations are centralised on a remote server, multiple user can interact with the same simulations for collaborative purposes.

A key feature of the architecture is that a user does not have to download the models with which he interacts. A proprietary behaviour model can just as well run on the servers of its owner, giving access only to the dynamic and observable variables. A 3D model would have to be downloaded to the client, but needs only to contain the data relevant for visualisation. Thus this is a potential solution to open for collaboration between secretive partners.

There are a number of immediate challenges. As the complexity and size of the world to simulate increases, manually editing the configuration document defining the virtual world becomes cumbersome and inefficient. To simplify this process, a visual editor should be implemented.

Our current focus is to integrate the system with a physics engine, to allow accurate simulation of physical and mechanical laws. After the initial submission of this paper we have made significant progress towards integration of *AgX Dynamics* from Algorix Simulation AB, which is highly suited for high fidelity maritime simulations. This will be discussed in future papers.

Acknowledgements

The contribution of Chu Yingguang, Deng Yuxiang and Filippo Sanfilippo is highly appreciated by the authors.

The project work of this paper is financially sponsored by a grant from the Norwegian National Research Foundation (Innovation Projects for the Industrial Sector MAROFF, ES486092).

References

- Torsten Blochwitz, Martin Otter, Johan Åkesson, Martin Arnold, Christoph Clauss, Hilding Elmquist, Markus Friedrich, Andreas Junghanns, Jakob Mauss, Dietmar Neumerkel, et al. Functional mockup interface 2.0: The standard for tool independent exchange of simulation models. In *9th International Modelica Conference*, 2012.
- James Byrne, Cathal Heavey, and P.J. Byrne. A review of web-based simulation and supporting tools. *Simulation Modelling Practice and Theory*, 18(3):253 – 276, 2010. ISSN 1569-190X. doi:<http://dx.doi.org/10.1016/j.simpat.2009.09.013>. URL <http://www.sciencedirect.com/science/article/pii/S1569190X0900149X>.
- Ricardo Cabello. Three.js. URL: <https://github.com/mrdoob/three.js>, 2010.

- F De Filippo, A Stork, H Schmedt, and F Bruno. A modular architecture for a driving simulator based on the FDMU approach. *International Journal on Interactive Design and Manufacturing (IJIDeM)*, 8(2):139–150, 2014.
- Vincent Delafosse, Scott Stanton, Takayuki Sekisue, and Jun-sik Yun. A methodology to use simulation at every stage of a hybrid vehicle design. In *IEEE Vehicle Power and Propulsion Conference*, October 2012.
- Ian Fette and Alexey Melnikov. The websocket protocol. 2011.
- GDAL Development Team. *GDAL - Geospatial Data Abstraction Library, Version 1.11.2*. Open Source Geospatial Foundation, 2015.
- Lars I Hatledal, Filippo Sanfilippo, and Zhang Houxiang. A voxel-based numerical method for computing and visualising the workspace of offshore cranes. *ASME 34th International Conference on Ocean, Offshore and Arctic Engineering*, 2015.
- javaFMI Development Team. javafmi. URL: <https://bitbucket.org/siani/javafmi/wiki/Home>, 2013.
- Ben Kenwright. A beginners guide to dual-quaternions: what they are, how they work, and how to use them for 3d character hierarchies. 2012.
- Salvatore Loreto, P Saint-Andre, S Salsano, and G Wilkins. Known issues and best practices for the use of long polling and streaming in bidirectional http. *Internet Engineering Task Force, Request for Comments*, 6202(2070-1721):32, 2011.
- Chris Marrin. WebGL specification. *Khronos WebGL Working Group*, 2011.
- TH McMullen, KA Hawick, VD Preez, and B Pearce. Graphics on web platforms for complex systems modelling and simulation. In *Proc. International Conference on Computer Graphics and Virtual Reality (CGVR'12)*, pages 83–89, 2012.
- Himanshu Neema, Jesse Gohl, Zsolt Lattmann, Janos Sztpanovits, Gabor Karsai, Sandeep Neema, Ted Bapty, John Batteh, Hubertus Tummescheit, and Chandrasekar Sureshkumar. Model-based integration platform for fmi co-simulation and heterogeneous simulations of cyber-physical systems. In *10th International Modelica Conference*, pages 10–12, 2014.
- Xiufeng Pang, Raj Dye, Thierry S Nouidui, Michael Wetter, and Joe J Deringer. Linking interactive Modelica simulations to HTML5 using the functional mockup interface for the LearnHPB platform. August 2013.
- Jan Pečiva. A summary of active transactions in collaborative virtual environments. In *Proceedings of the Annual Strathmore University ICT Conference 2008*, pages 1–1, 2008. URL http://www.fit.vutbr.cz/research/view_pub.php?id=8765.
- Kenton Varda. Protocol buffers: Googles data interchange format, 2008.
- Hongwei Wang and Heming Zhang. Using collaborative computing technologies to enable the sharing and integration of simulation services for product design. *Simulation Modelling Practice and Theory*, 27:47 – 64, 2012. ISSN 1569-190X. doi:<http://dx.doi.org/10.1016/j.simpat.2012.05.002>. URL <http://www.sciencedirect.com/science/article/pii/S1569190X12000664>.
- PBT Weustink, TJA De Vries, and PC Breedveld. Object-oriented modeling and simulation of mechatronic systems with 20-sim 3.0. *Mechatronics*, 98:873–787, 1998.
- D Wirtz. Protobuf.js. URL: <https://github.com/dcodeIO/ProtoBuf.js>, 2013.
- Chu Yingguang, Lars I Hatledal, Filippo Sanfilippo, Hans G Schaathun, Vilmar Æsøy, and Zhang Houxiang. Virtual prototyping system for maritime crane design and operation based on functional mock-up interface. *OCEANS: Discovering Sustainable Ocean Energy for a new World*, 2015.
- Heming Zhang, Hongwei Wang, David Chen, and Gregory Zacharewicz. A model-driven approach to multidisciplinary collaborative simulation for virtual product development. *Advanced Engineering Informatics*, 24(2):167–179, 2010.
- Sven Meyer zu Eissen and Benno Stein. Realization of web-based simulation services. *Computers in Industry*, 57(3):261 – 271, 2006. ISSN 0166-3615. doi:<http://dx.doi.org/10.1016/j.compind.2005.12.007>. URL <http://www.sciencedirect.com/science/article/pii/S0166361506000169>. Advanced Computer Support of Engineering and Service Processes of Virtual Enterprises Advanced Computer Support Special Issue.

Nearwell Simulation of a horizontal well in Atlanta Field in Brazil with AICV[®] completion using OLGARocx

K.A. Silva B.M. Halvorsen
Faculty of Technology, Telemark University College, Norway,
samsioray@hotmail.com, Britt.Halvorsen@hit.no

Abstract

Brazil has had special attention in the world oil scenario due its crescent findings in oil reservoirs. The horizontal drilling has being applied due to its higher recovery rate. The early water and/or gas breakthrough characteristic of the horizontal well can be avoided with a new inflow control technology, the Autonomous Inflow Control Valve (AICV[®]). AICV[®] are capable of closing for unwanted fluids and keep open for oil.

In this paper, a computational study of a heavy oil reservoir is modeled using Rocx coupled with OLGARocx, which simulated the well. The horizontal well is simulated with both AICV[®] (300 days) completion and openhole with gravel pack completion (200 days).

In the AICV[®] completion the valves closes first according to the highest permeability zone and then following the heel-to-toe effect.

The water breakthrough is delayed with AICV[®] completion, extending the lifetime of the well and reducing the costs related to oil/water separation.

Keywords: increased oil recovery, AICV, heavy oil, heterogeneous reservoir.

1 Introduction

Brazil has experienced a significant number of discoveries in oil and gas reserves. The discovery of high quality oil (about 30° API) in the pre-salt layer has led to the production level of 520.000 barrels of oil per day achieved in July 2014 based on 25 installed wells (Team, 2014). Although Brazil has extensive production in electric energy from hydropower and other sources, 48.5% comes from fossil fuels and most of that comes from heavy oil reservoirs. More than 90% of Brazil's oil production is offshore and in deep waters (EIA, 2014). The offshore fields are distributed at two main depths called the Post-salt and the Pre-salt layers. The post-salt layer is located in depth up to 2000m and the pre-salt layer in depth up to 7000m. Offshore post-salt layers have heavy oil (<20° API)

and pre-salt layers have oil quality higher than 30° API. Heavy oil has become an important resource with the decline in conventional oil reserves. However, the low mobility of the viscous oil makes it more difficult to be extracted. In the process of extracting oil from the reservoirs, much of the oil remains in the reservoir and the principal factor is the water and/or gas breakthrough that limits the recovery of the oil in place. To mitigate this low recovery factor, technologies such as it Inflow Control Devices and different methods for Improved Oil Recovery (IOR) and Enhanced Oil Recovery (EOR) (Carlson *et al*, 1992) have been developed.

In this work the efficiency of the AICV[®] was studied and simulated by using the OLGARocx software. The results were compared with the production in an openhole gravel pack completed well in Brazil. The AICV reduces the effect of early water breakthrough in heterogeneous and fractured reservoir in addition to reducing the heel-to-toe effect. The oil in the reservoir is considered as heavy oil with high viscosity. Drilling of horizontal wells has increased in the world due to the advantages regarding higher recovery factor. These types of wells are well suited for reservoirs with thin oil column due to the increased contact area between the reservoir and the well. The chosen well is located in the Santos basin, in the post-salt layer.

2 Atlanta Field

The Atlanta field is located in the Santos basin about 185 km from the coastline, as can be seen in **Figure** . The development area is 115,920 km² (ANP, 2009). The volume of oil in place is 1500 millions of barrels and the volume of recoverable oil is 260 millions of barrels which gives a recovery factor of only 17%. (QGEP, 2013). Santos has some oil in the post-salt layer and has the largest reservoirs in the pre-salt layer.

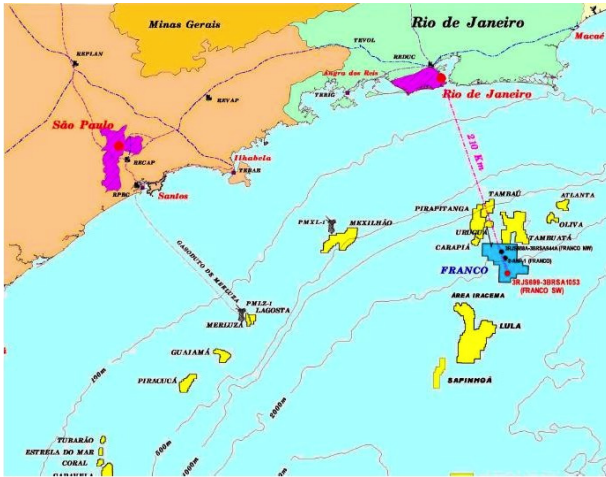


Figure 1: Localization of the Atlanta and Oliva Field. (QGEP, 2013)

The reservoir rock is Eocene turbiditic sandstone, which has a high porosity and high permeability. The sand is non-consolidated. The quality of the oil is 14° API and is considered as heavy oil. The reservoir characteristics are summarized in Table 1. The reservoir counts with an aquifer and high rock compressibility, and those characteristics will be the agents to the primary drive (Gaffney, 2014). The recovery mechanism is a combination of simple depletion (fluids expansion and porous media contraction) and water cap drive. **Table 2** shows the fluid and rock properties for the field.

Table 1: Reservoir Characteristics

Water depth	1550 m
Well depth	2316 m
Oil in place	210 millions of barrels
Recovery factor	17%
Rock compressibility	$8.7E^{-4}/\text{bar}$
Completion	Open-hole with Gravel packing
Start of production	2017

Table 2: Fluid and rock properties

Reservoir	Turbidity Sandstones
Porosity	36%
Thickness	115 m
Temperature	41° C
Oil Density	14° API
Viscosity	228 cP
GOR	7.5 m ³ /bbl
Pressure	239 bar
Permeability	5 D

The well considered in this study is the second one drilled in the Atlanta Field as a part of the Early Production System. Figure 2 shows the porosity map and the location of the well. A fracture at position 180 m from the vertical well 3-SHEL-8 has been considered. The length of the well is 650m and it has a slight inclination of 34 m in the pressure nod. The depth is 2300m. The reservoir is considered heterogeneous.

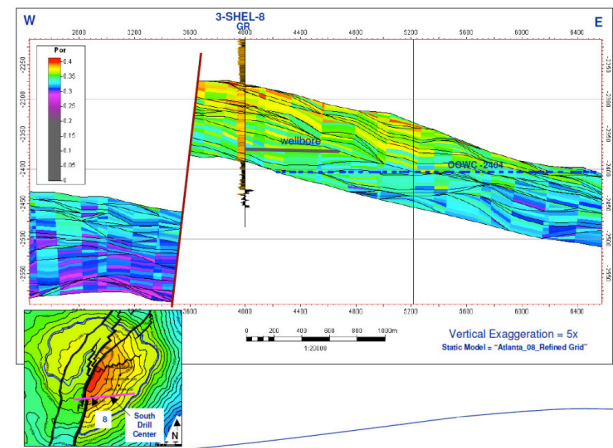


Figure 2: Porosity map and the location of the well. (QGEP, 2013)

Figure 3 shows a sketch of the well completion, which is open-hole with gravel-pack. The well includes an electrical submersible pump (ESP) to supplement low pressure and high frictional losses. The completion is consistent with sandstone rock with high porosity and high permeability and the gravel-pack prevents premature screen out and erosion.

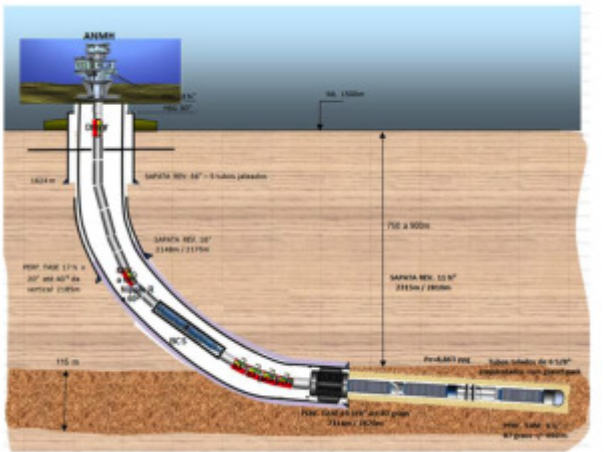


Figure 3: Sketch of the completion (QGEF, 2013)

3 Theory

3.1 Permeability

The permeability is the characteristic of the rock and indicates how easy the fluid flows between interconnected pores. The permeability is measured in Darcy (D) or milliDarcy (mD), and the higher the permeability is, the easier it is for the fluid to flow. Permeability can be expressed by Darcy's law:

$$Q = -\frac{kA \Delta p}{\mu L} \quad (1)$$

where Q is the flow rate, k is permeability measured in Darcy, A is the cross sectional area, Δp is the pressure drop across the length L and μ is the viscosity.

The permeability can be further specified as effective, absolute and relative. The effective permeability is the capacity of the rock to let one fluid flow in the present of others fluids. It is dependent of the reservoir fluid saturation and the wetting characteristics of the formation (Ahmed, 2006).

The relative permeability measures how one fluid can hinder the others when two or more fluids flow at same time through a porous media. The relative permeability $k_{r,i}$ is the ratio of permeability of one phase ($k_{e,i}$) related to the absolute permeability (k). It is a dimensionless measure of the effective permeability of that phase. The equation for the relative permeability is:

$$k_{r,i} = \frac{k_{e,i}}{k} \quad (2)$$

During the production of oil, the saturation of each phase changes. Accordingly, the effective and the relative permeability also change. To be able to simulate oil production correctly, the software uses as input the accurate correlation for the relative permeability versus saturation. The relative permeability curves can be inserted manually or the known correlations can be used. Corey correlation was used in this work.

3.2 Oil viscosity

The viscosity is the measure of the fluid internal resistance to flow. It is the most important fluid property influencing on the recovery factor. The temperature of the fluid influences the viscosity and it is directly proportional with the production costs.

The heterogeneous reservoir has zones with higher permeability, resulting in higher flow in these zones – the “highways”. This causes occurrence of water and/or gas conning in these zones – a fluid with lower viscosity runs faster and enter the high permeability zones, which leads to an early water and/or gas breakthrough, reducing the reservoir recovery and the well performance.

3.3 Horizontals wells

The horizontal well technology is widely used nowadays. Horizontal wells have superior production and recovery performance compared to conventional vertical wells (Porturas *et al*, 2009). Horizontal wells are commonly used to increase the production in reservoirs with thin oil column and for reservoirs with water and/or gas cap drive (Ahmed, 2006). By using horizontal wells in these cases, breakthrough of water and/or gas will be delayed due to the reduced drawdown. These types of wells improve the reservoir performance by increasing the contact area between reservoir and a long wellbore. Increased contact area results in increased production rate in reservoirs with heavy oil. Horizontal wells also open up for increased oil production in fractured reservoirs with low permeability and low porosity. The disadvantage in sandstone reservoirs is that the flow gets uneven leading to cresting/coning effects (Ferro, 2010). In carbonate reservoirs, the variations in the permeability and fractures can lead to water or gas coning. (Ferro, 2010)

One of the challenges related to long horizontal wells are the heel-to-toe effect. The heel-to-toe effect is a result of the pressure losses in the well due to friction.

During production, the drawdown (i.e. the differential pressure that drives fluids from the reservoir into the wellbore (Schlumberger, 2014)) changes differently along the well, causing uneven flow. In the toe the drawdown is low compared to the heel. Figure 4 shows the the differential pressures as a function of the distance from the heel.

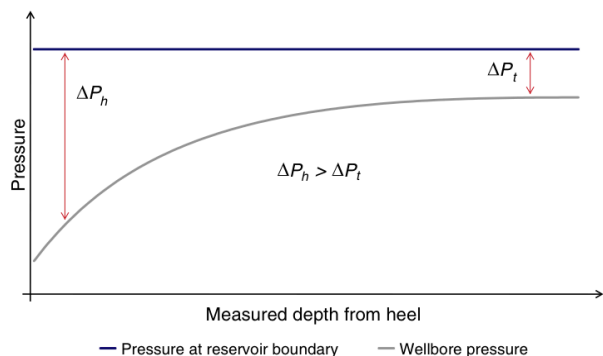


Figure 4: Heel-toe effect (Birchenco *et al.*, 2009)

The higher driving force in the heel causes early water and/or gas breakthrough to the wellbore. The water or gas coning occur due to the lower viscosity and higher mobility of these phases compared to the oil. Water coning is shown in the Figure 5.

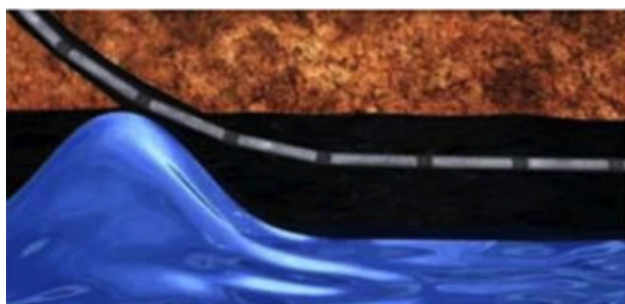


Figure 5: Water coning due to heel-to-toe effect. (AAPG, 2010)

The problems related to horizontal wells can be mitigated by varying the perforation density or by increasing the number of perforations in the toe to equalize the flow in the well extension. In addition flow restrictions as Inflow Control Devices (ICD), Inflow Control Valves (ICV), Autonomous Inflow Control Devices (AICD) and Autonomous Inflow Control Valves (AICV[®]) can be used. These devices works by restricting the flow according to its the position along the well. Inflow controllers can be passive or active. This work has focused on the Autonomous Inflow Control Valve, which is a suitable technology for the case of the Atlanta Field.

3.4 AICV[®]

Autonomous Inflow Control Valve is a technology developed for different oil qualities, from ultra light oil to extra heavy oil. The technology is the only one to the authors' knowledge that can autonomously stop the inflow of unwanted water and/or gas in a zone and reopens again when it feels oil. (Aakre *et al.*, 2015). With AICV[®], the flow of low viscous fluids (water and gas) to the well stops autonomously in the zones where breakthrough occurs. Meanwhile, oil keeps being produced in the other zones of the well. Wells with AICV-completion have the potential for optimum oil production and recovery. The AICV[®] works in a self-regulating way, without any control or surface connection. Implementation of AICV[®] allows for drilling of longer horizontal wells and the costs related to treatment of unwanted fluids produced together with the oil, will be significantly reduced. (Inflow Control, 2015). The valve works with a pilot flow through a laminar and a turbulent elements. The flow reacts differently in those elements, creating a pressure drop accordingly in the elements, identifying which fluid is running through the valve. Figure 6 shows picture and drawing of the AICV[®].

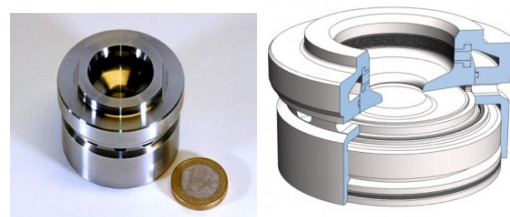


Figure 6. The AICV[®] (Aakre et al, 2015)

4 Simulations

Simulations with OLGA (wellbore) coupled with Rocx (reservoir) were performed to estimate the oil production using the actual completion (openhole with gravel packing) and AICV[®] completion. The grid chosen for the reservoir simulations is shown in Figure 7. The mesh is equally divided into grids in the x and z direction and a finer mesh towards the position of the wellbore is chosen in the y direction.

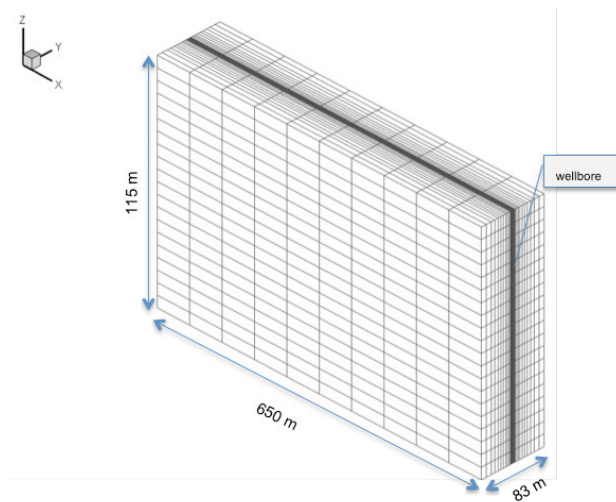


Figure 7 Reservoir section with grid and well position.

The Rocx software defines the near-well reservoir and OLGA uses the data from Rocx and simulates the flow in the wellbore. In the simulation the elements of the real completion as packers, choke devices, wellbore and inflow controllers are substituted by valves and PID controllers. The properties used in Rocx are listed in the Table .

Table 3: Reservoir and fluid properties

Properties	
Oil viscosity	228 cP
Pressure water drive	239.73 bar
Temperature	41°C
Oil specific gravity	0.866
Porosity	38%
Permeability	5 D
Permeability in the fracture	50 D
Wellbore pressure	220 bar

4.1 OLGA settings

OLGA is applied to simulate the multiphase flow in the wellbore. The settings and the layout for OLGA

were included according to the technology of the completion. In both cases the wellbore was divided in ten zones to locate the zone with highest permeability (fracture) and to facilitate the comparison between the two cases. The settings to OLGA/Rocx are given in Table 4.

Table 4: Settings in OLGA/Rocx

	Open-hole	AICV®
Extension	650 m	
Diameter	0.24 m	
Number of sections	10	20
Water cut	0.8	0.5
Drive pressure	20 bar	
Valve diameter	7 cm	2 cm

In the outlet node (pressure node) a PID controller was installed to choke the total production when the water cut exceeds 0.8. The oil flows by water drive mechanism to the well in the whole extension of the reservoir, as can be seen in Figure 8. Ten nearwell oil sources distributed uniformly along the well were defined as the input from the reservoir (defined in Rocx) to the wellbore (defined in OLGA. Figure 9 shows the layout used in OLGA.

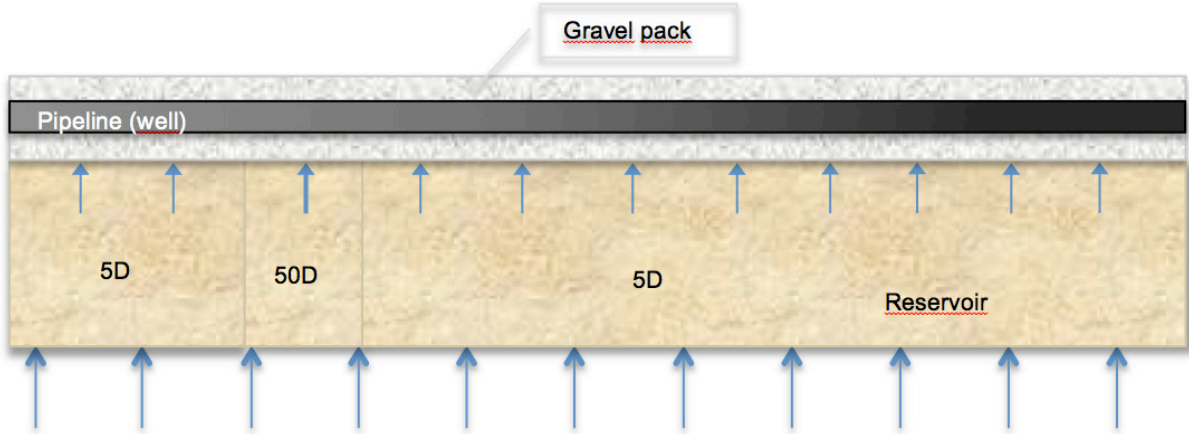


Figure 8: Section of the reservoir and the pipeline for the Openhole completion

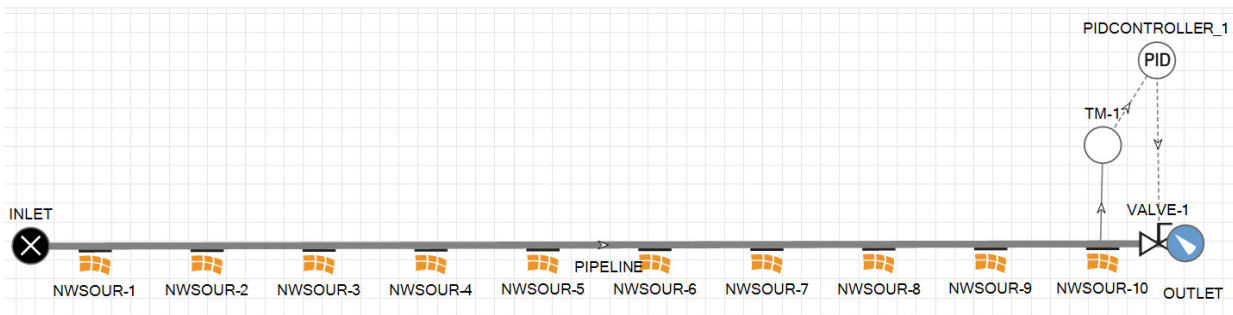


Figure 9: System layout for openhole completion.

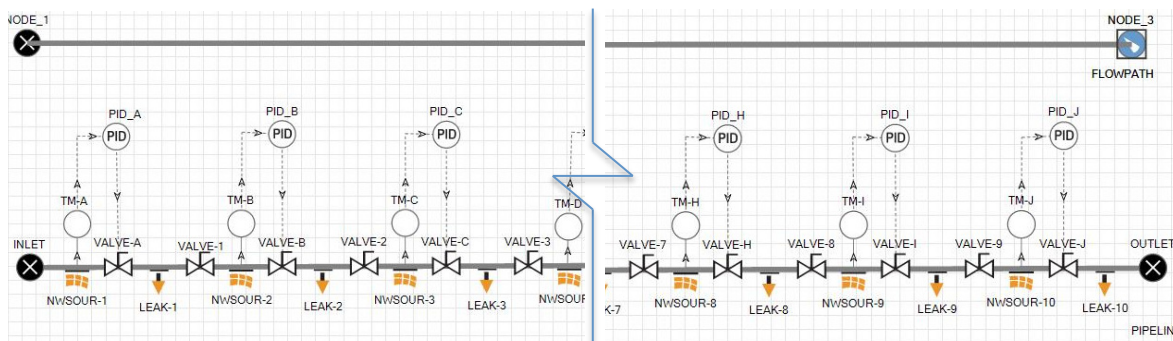


Figure 10: System Layout for AICV[®] completion

4.2 AICV[®] completion

In order to simulate a more complex system, OLGA needs a pipeline to simulate the annulus and a flowpath to simulate the well. This configuration is presented in Figure 10. The case with AICV[®] completion was made by dividing the well into twenty sections to locate the elements. Valves 1, 2, 3, 4, 5, 6, 7, 8, and 9 are closed and located in the odd sections. These valves act like

packers which isolate the different zones from each other. The valves A, B, C, D, E, F, G, H, I and J are the AICV[®]s and are located in the even sections. The mechanism of the AICV[®] is here presented by a transmitter with water cut as variable and a PID controller to activate the valve to close when the set point for the water cut is reached. The nearwell source illustrates the flow from the reservoir into the annulus and the leak illustrates the flow of the fluids from the

annulus into the well. Figure 10 shows the location of the elements. The distance between the AICV[®]'s is 65m. Figure 11 shows the division of the annulus

(pipeline) and reservoir into ten zones where the fracture (50D) is located in the third zone.

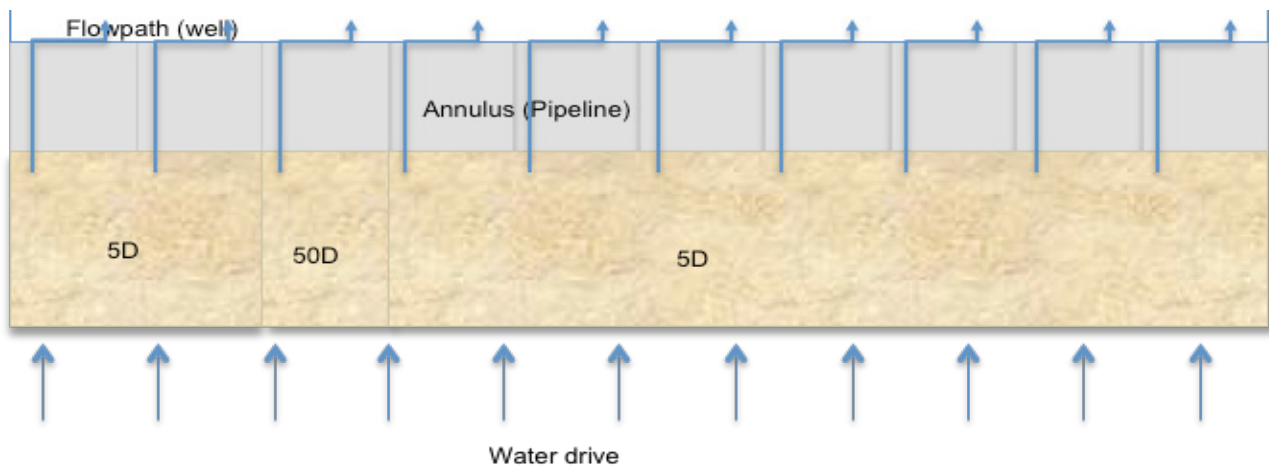


Figure 11: Section of the reservoir and the pipeline for the AICV completion

The set point for water cut was set to 50% for each of the zones. When the water cut set point is reached in a certain zone, the corresponding valve closes to 0.8% and the others remain open, producing oil until the set point value is reached. The opening of 0.8% corresponds to a minor flow which will flow through a closed AICV[®]. This minor flow is necessary to make it possible to identify which fluid is surrounding the valve, and thereby make the valve capable of opening again when it feels oil.

5 Results and discussion

The results of the computational study made to compare the performance of open-hole with gravel pack and AICV[®]-completion are presented. The goal of this study is to compare performance curves for the two cases and to show the potential improvement in oil recovery when AICV[®] completion is used. The simulations were performed for the period of 300 days for the AICV[®] well and 200 days for the open-hole well. Different time periods were used because those periods were illustrative for what happened in the two cases.

PID controllers were used together with valves to simulate the functionality of the AICV[®]'s. For the open-hole completion a PID controller was used in the outlet of the flowpath to ensure choking at high flow rates of water. Figure 12 shows a summary of the results with open-hole and AICV[®] completion. For the open-hole well the accumulated production of water is higher than the oil production after 128 days.

After that the production is choked, and at day 170, the accumulated oil production increases insignificantly whereas the accumulated water production is increasing with a significantly higher rate..

5.1 AICV[®]

The heel-to-toe effect was not the reason for the early water breakthrough in this case. The main contributor to the water coning was the “highway” from the fracture located in zone 3 in the reservoir. Figure 13 shows the closing time for the AICV[®] in the different positions. As can be seen, the AICV[®] in the high permeable zone (zone 3) closes after 40-50 days. Zone 2 and 4 (as presented in Figure 11) are influenced by the fracture in the neighboring zone (zone 3) and therefore the breakthrough occurs earlier at these locations than in the other zones with the same permeability. The AICV[®]'s in the remaining zones are closing following the heel-to-toe effect. Figure 13 also shows the volumetric flow rate of oil as a function of time. Initially the production rate is about 220 m³/day, and decreases to 60 m³/day as the valves are closing. It can be noticed that after 280 days all the valves are closed. If the simulation was performed for a longer period it is expected that the valves would open after encountering oil again.

5.2 Comparison of AICV[®] and Open-hole completion

Figure 12 shows oil and water production for a well with AICV completion compared to and openhole well. The dashed lines represent the openhole case and

the continuous lines represent the AICV[®] completion case. The blue and the green lines show the water and oil production respectively. After 170 days of

production in the openhole completion case, the water cut

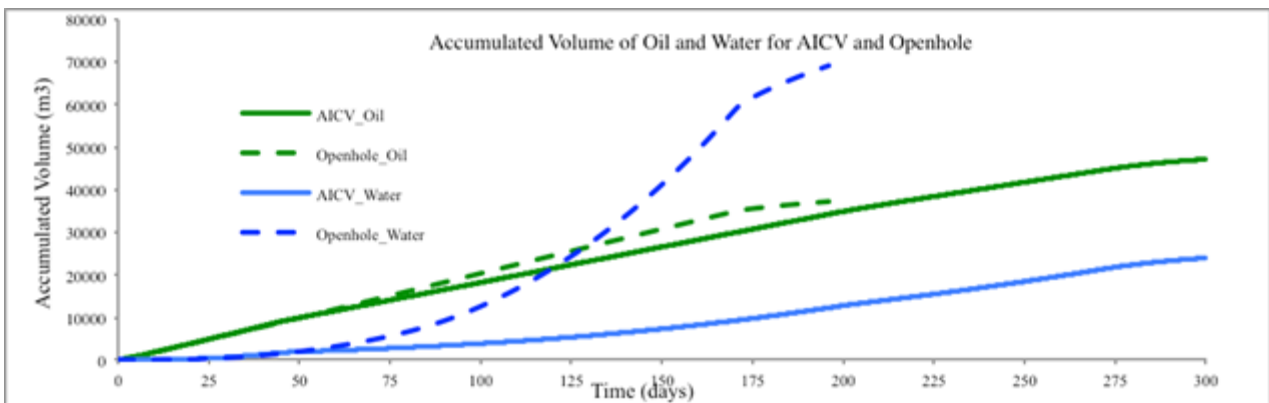


Figure 12: AICV[®] and Openhole: Accumulated oil and water

exceeds 70% and the valve starts to choke. The AICV[®]-completed well is still producing oil through 3 valves after 200 days. The result indicates that the lifetime of a well can be significantly extended when using AICV-completion. The accumulated oil is higher for the open-hole well until the production rate is choked

down. After that, the well is mainly producing water. The amount of water produced in AICV[®]-completed well is much lower, which will have a positive effect on the costs for separation in surface installation.

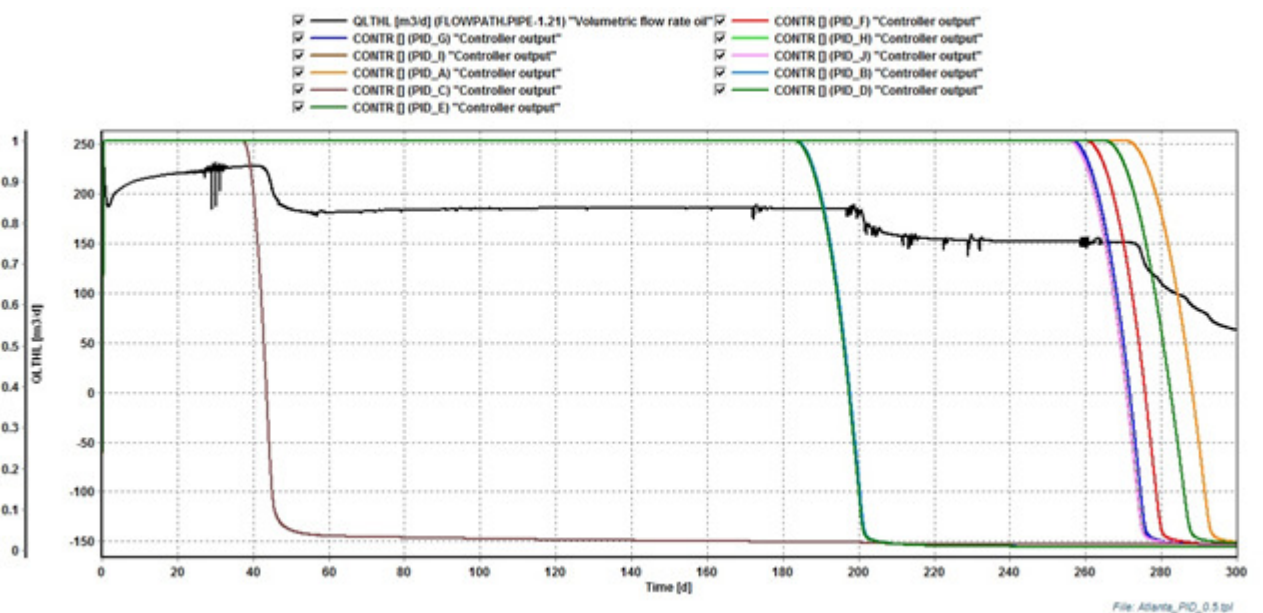


Figure 13: Volumetric oil rate and AICV[®] Closing sequence

6 Conclusion

The following concluding remarks are listed below.

- Brazil has a wide field to implement new technologies as AICV[®] especially in the pre-salt layer with thin oil column.
- Open-hole completion is well suited to sandstone, but suffer with early water and/or gas breakthrough due to fractures in the reservoir and/or uneven drawdown pressure along the reservoir characteristic for horizontal wells.
- The open-hole completion requires higher separation of the water from the oil on the surface

facilities. This result in requirement of larger separation installations and higher costs.

- The well with AICV® completion produces 45000m³ oil compared to 35000 m³ with open-hole until the valves close.
- The production of water is much higher for openhole: 70000 m³ against 20000 m³ for AICV®, a reduction of 71%.
- Increase of 28.5% in total oil production with the AICV® technology.
- The dependency of viscosity on relative permeability for heavy oil must be further studied.

7 Bibliographic references

- Aakre, H., Halvorsen, B., & Mathiesen, V. (2015). Autonomous Inflow Control Valve for Heavy and Extra-Heavy Oil. *Society of Petroleum Engineers*, 171141.
- AAPG. (2010). Completions with and without ICD. Retrieved 15 January, 2015, from <https://archives.aapg.org/europe/newsletters/2009/06jun/dryoil0609fig4.cfm>
- Ahmed, T. (2006). *Reservoir Engineering handbook* (Third ed. Vol. 1). United States of America: Elsevier Inc.
- ANP. (2009). *Sumario Executivo Externo do Campo de Atlanta: Contrato de Concessao*. ANP.
- Birchenco, V. M., Muradov, K. M., & Davies, D. R. (2009). Reduction of the horizontal well's heel-toe effect with inflow control devices. *Journal of Petroleum Science and Engineering*, 75(2010), 6.
- EIA, U. E. I. A. (2014). Brazil. Retrieved 03 december 2014, from <http://www.eia.gov/countries/country-data.cfm?fips=BR - pet>
- Ferro, S. G. (2010). *Modeling Inflow Control Devices in Gas Condensate Reservoirs with Reservoir Simulation*. (Master), Norwegian University of Science and Technology, Norway.
- Gaffney, C. A. (2014). Atlanta Statement of Reserves (Vol. 1, pp. 6). Rio de Janeiro.
- Jon, Carlson, Gurley, D., King, G., Price-Smith, V., & Waters, F. (1992, 1992). Sand Control: Why and How? *Oilfield Review*.
- Inflow Control. (2015). About the AICV® Technology. Retrieved January 2015, from <http://www.inflowcontrol.no>
- Porturas, F., Vela, I., Pazos, J., & Humbert, O. (2009, 2009). Lifting More dry Oil by Reducing Water Production with ICD's in Wells Drilled and Completed in Consolidated Reservoirs, Bloque 15, Ecuador. *American Association of Petroleum Geologists*, 4.
- QGEP, Q. G. E. e. P.-. (2013). Block BS-4: Atlanta Field - Early Production System (EPS). Rio de Janeiro: Queiroz Galvao.
- Schlumberger. (2014). Oilfield Glossary. Retrieved 19 January, 2015, from <http://www.glossary.oilfield.slb.com>
- Team, T. (2014). Petrobras' Prolific Pre-Salt Wells Now Pumping Half A Million Barrels Of Oil Per Day. *Forbes*.

Heat Pump Efficiencies simulated in Aspen HYSYS and Aspen Plus

Lars Erik Øi¹ Irene Yuste Tirados¹

¹Department of Process, Energy and Environmental Technology, Telemark University College, Norway
lars.oi@hit.no

Abstract

The efficiency of a heat pump system has been calculated for varying temperature conditions, refrigerants, simulation programs and thermodynamic models. Evaluated components are ammonia, the chlorofluorocarbons R-11, R-12, R-22 and propane. The equations of state Peng-Robinson (PR) and Soave-Redlich-Kwong (SRK) and the activity model Non-Random-Two-Liquid (NRTL) were used. COP values have been calculated to values between 3 and 9. Aspen Plus and Aspen HYSYS are evaluated to be powerful tools for heat pump calculations. The calculated differences between heat pump efficiencies with different components at different conditions are reasonable.

Keywords: Heat pump, Aspen HYSYS, Aspen Plus, PR, SRK, NRTL

1 Introduction

Heat pump technology provides an efficient and sustainable solution for both heating and cooling. A traditional heat pump can be defined as a mechanical compression cycle refrigeration system powered by mechanical energy or electricity. Traditional refrigerants used in heat pumps are ammonia and chlorinated or fluorinated hydrocarbons. Because many of the most used chlorofluorohydrocarbons (CFC's) are ozone-depleting components, development of more environmentally friendly refrigerants like pure hydrocarbons is important (EU, 2009). The efficiency of a heat pump is traditionally measured by the ratio of delivered heat at a high temperature divided by the electricity (or work) input. This is defined as the coefficient of performance (COP).

There are several simulation tools available for the simulation of heat pumps. Traditional process simulation tools like Aspen HYSYS or Aspen Plus are useful because they have data for several components inside the program, and many thermodynamic models like equations of states available. It is of interest to calculate the efficiency of a heat pump system when varying temperature conditions, refrigerants, simulation programs and thermodynamic models. There are few references to such comparisons in the open literature. An example of earlier work on simulation of heat pumps is Domanski and Didion (1985).

This work is based on the Master Thesis work of Irene Yuste Tirados (Tirados, 2015). The background information and the evaluation of the calculation results are extended compared to the content in the Master Thesis report.

2 Process Description

The circulation medium (refrigerant) alternates between different pressures and temperatures by the help of a compressor and an expansion valve between the temperatures 25 and 4, 27 and 2 or 27 and -20 °C. The lowest temperature is the evaporation temperature and the highest is the condensing temperature. The pressures are specified as the saturation pressures at the given temperatures. A simple diagram of the refrigeration circuit is shown in Figure 1.

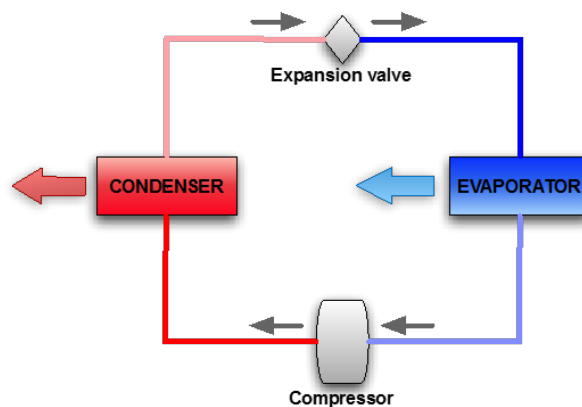


Figure 1. Simple diagram of a heat pump's mechanical compression cycle

In an air to air heat pump, taking heat from a cold environment to a warmer environment, the temperature profiles in the condensation unit and evaporating unit are typically as in Figure 2. The condensing and evaporating temperatures in the figure are 25 and 4 °C. The corresponding outside and outside air temperatures are 9 and 20 °C. In the condenser, the refrigerant coming from the compressor is normally warmer than the condensation temperature and the refrigerant must be cooled down to the condensation temperature in the first part of the condenser.

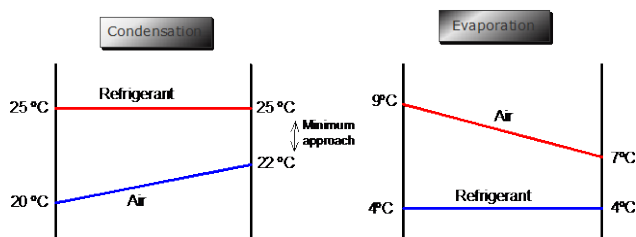


Figure 2. Temperature profiles in the evaporator and condenser for low difference temperature conditions.

The evaluated components are ammonia, R-11, R-12, R-22 and propane. The CFC components are not accepted as refrigerants in heat pumps any longer, but they are relevant because they have been used in many heat pump applications, and new refrigerant components will be compared against the CFC components. The explanations for the abbreviations for the different refrigerant components (the R-numbers) can be found e.g. in an EU report on ozone layer depletion (EU, 2009). The equations of state Peng-Robinson (PR) and Soave-Redlich-Kwong (SRK) and the activity model Non-Random-Two-Liquid (NRTL) were used in the process simulation programs Aspen HYSYS and Aspen Plus.

The coefficient of performance (COP) is an expression of the efficiency of a heat pump. The coefficient of performance for a heat pump is the ratio of the energy transferred for heating to the input energy used in the process.

$$COP = \frac{Q_C}{W}$$

$$W = Q_C - Q_E \quad (1)$$

In equation (1) Q_C is the heat output from the condenser, Q_E is the heat input from the evaporator and W is the power supplied to the compressor. If there is no heat loss the work added equals the difference between the heat output and the heat input.

In this work, it is assumed that the refrigerant loop operates at a specified condensation and evaporation temperature. Because pure components are used in this work, the evaporating and condensing pressures are the saturation pressures. The expansion valve is assumed to operate adiabatically and except of that it is assumed no pressure drops in the circulation loop. The compressor is assumed to have the default adiabatic efficiency of 0.75. A motor or motor efficiency is not included in the calculations, and if a motor efficiency should be included, this would reduce the COP slightly. Version 8.0 of Aspen Plus and Aspen HYSYS have been used.

3 Thermodynamic Models

3.1 General about Property Calculations

To calculate the temperature (T), pressure (P or p), specific volume (v), heat (Q) or work (W) for different conditions in process simulation programs like Aspen Plus and Aspen HYSYS, there are thermodynamic models, model parameters and calculation procedures available. In other tools for heat pump calculations, thermodynamic property data for the components are directly available as correlations in data banks. These data can be based on direct measurements or they can be based on thermodynamic models.

In the addition to the calculation of energy functions as enthalpy (H) and entropy (S), the key thermodynamic property calculation performed in a simulation is the phase equilibrium. Phase equilibrium is calculated using the fugacity (which is a measure of the tendency of a component to leave its phase). Equilibrium is achieved when the fugacity of the component is equal in all phases. In this work only pure components are treated, so φ_i is the fugacity of the actual component.

There are two common methods for representing the fugacity coefficients from the phase equilibrium relationship in terms of measurable state variables, the equation of state method and the activity coefficient method as explained in Smith et al. (2005).

Equation of state methods use the various equations of state from chemical engineering thermodynamics to calculate the equilibrium conditions. The two most familiar are PR (Peng and Robinson, 1976) and SRK or Soave-Redlich-Kwong (Soave, 1972). Both of them are cubic equations of state and they only need critical properties and ideal gas enthalpies for each component to calculate all the necessary thermodynamic properties for equilibrium calculations.

An activity coefficient method is a more empirical approach to calculate the equilibrium. This method uses various relationships to calculate the liquid phase activity coefficient and then the fugacity coefficient. A common activity model is NRTL or Non-Random Two Liquid (Renon and Prausnitz, 1968). In Aspen Plus ideal gas enthalpy and heat of vaporization correlations are used to calculate enthalpies. The NRTL model is the same in Aspen HYSYS and Aspen Plus as in the original paper. The results from an activity model are dependent on the parameter values for the components and enthalpy correlations. These parameter values may be different in different program versions.

3.2 General about Equations of State

Equation of states are often expressed by critical or reduced temperatures and pressures. The critical temperature (T_c) and pressure (P_c) for a pure component are component characteristics. Reduced properties (T_r and P_r) are defined as the property divided by the critical

property. R is the gas constant. The acentric factor ω is also a component characteristic which is defined in equation (2).

$$\omega = -1 - [\log_{10} P_r^{sat}]_{T_r=0,7} \quad (2)$$

A widely used equation of state is the SRK model (Soave, 1972). This model is described by equation (3) with a (the pressure correction parameter), b (the volume correction parameter), α and m defined below.

$$p = \frac{RT}{v-b} - \frac{a\alpha}{v(v+b)} \quad (3)$$

$$\left\{ a = \frac{0,42748R^2T_c^2}{p_c} \mid b = \frac{0,08664RT_c}{p_c} \right\}$$

$$\alpha = \left[1 + m \left(1 - T_r^{1/2} \right) \right]^2$$

$$m = 0.48508 + 1.55171\omega - 0.15613\omega^2$$

These coefficients in the m equation are from the original work of Soave and can be different in other versions.

A similar equation of state shown in equation (4) was developed by Peng & Robinson (1976) with more accurate liquid density predictions.

$$p = \frac{RT}{v-b} - \frac{a\alpha}{v(v+b)+b(v-b)} \quad (4)$$

$$\left\{ a = \frac{0,45724R^2T_c^2}{p_c} \mid b = \frac{0,07780RT_c}{p_c} \right\}$$

$$\alpha = \left[1 + m \left(1 - T_r^{1/2} \right) \right]^2$$

$$m = 0.37464 + 1.54226\omega - 0.26992\omega^2$$

The coefficients in the m equation are from the original work of Peng and Robinson.

There are numerous of other equation of state and activity coefficient models, and some of them are available in the Aspen HYSYS and Aspen Plus programs. The PR, SRK and NRTL models are used because they are well-known to be simple and efficient. There are some equations of state which are further developments of the SRK and PR equations of state. One variation is from Peneloux (1982) where a volume correction c is added to every volume in the SRK or PR equations. This is used in the SRK and PR versions in the program Aspen Plus.

In this work, the default parameter values from the Aspen HYSYS and Aspen Plus programs for the PR, SRK and NRTL models are used. There are some small differences between the two programs in the model equations and the parameter values.

3.3 Aspen HYSYS Property Documentation

The equations used in Aspen HYSYS are shown in equations (5) to (10). They are from the documentation of an earlier version of the Aspen HYSYS program (Hyprotech, 2003). This documentation is more complete than for the later versions. It is assumed that the equations used are the same also in Aspen HYSYS version 8.0. The equations include mole fractions (x_i values) and k_{ij} parameters (component interaction coefficients) which are not used in this work with only pure components.

SRK:

$$p = \frac{RT}{v-b} - \frac{a}{v(v+b)} \quad (5)$$

$$b = \sum_{i=1}^N x_i b_i, \quad b_i = \frac{0,08664RT_c}{p_c}$$

$$a = \sum_{i=1}^N \sum_{j=1}^N x_i x_j (a_i a_j)^{0,5} (1 - k_{ij})$$

$$a_i = a_{ci} \alpha_i, \quad a_{ci} = \frac{0,42748R^2T_c^2}{p_c}$$

$$\alpha_i = \left[1 + m_i \left(1 - T_r^{1/2} \right) \right]^2$$

$$m_i = 0,48 + 1,574\omega_i - 0,176\omega_i^2$$

PR:

$$p = \frac{RT}{v-b} - \frac{a}{v(v+b)+b(v-b)} \quad (6)$$

$$b = \sum_{i=1}^N x_i b_i, \quad b_i = \frac{0,077796RT_c}{p_c}$$

$$a = \sum_{i=1}^N \sum_{j=1}^N x_i x_j (a_i a_j)^{0,5} (1 - k_{ij})$$

$$a_i = a_{ci} \alpha_i, \quad a_{ci} = \frac{0,457235R^2T_c^2}{p_c}$$

$$\alpha_i = \left[1 + m_i \left(1 - T_r^{1/2} \right) \right]^2$$

$$m_i = 0,37464 + 1,54226\omega_i - 0,26992\omega_i^2$$

It can be noted that the m coefficients in equation (6) are equal to the original PR coefficients in equation (4). The coefficients in equation (5) are not equal to the original SRK coefficients in equation (3).

Enthalpy and entropy departure calculations

The principles for the numerical calculation of the enthalpy and entropy calculation (based on residual properties) can be found in Smith et al. (2005). These

numerical calculations (and also fugacity calculations) may be different in Aspen Plus and Aspen HYSYS.

The enthalpy and entropy departure calculations used in Aspen HYSYS are shown in equations (7) and (8). Z is the compression factor (defined by RT/Pv). Superscript ID is for ideal gas, and subscript 0 is a reference state.

$$\frac{H-H^{ID}}{RT} = Z - 1 - \frac{1}{RT} \int_{\infty}^v \left[T \left(\frac{\partial p}{\partial T} \right)_v - P \right] dv \quad (7)$$

$$\frac{S-S_0^{ID}}{T} = \ln Z - \ln \frac{P}{P^0} + \int^v \left[\frac{1}{R} \left(\frac{\partial p}{\partial T} \right)_v - \frac{1}{v} \right] dv \quad (8)$$

Fugacity coefficient

SRK:

$$\ln \phi_i = -\ln \left(Z - \frac{Pb}{RT} \right) + (Z-1) \frac{b_i}{b} - \dots \\ \dots - \frac{a}{bRT} \left[\frac{1}{a} (2\alpha_i^{0.5} \sum_{j=1}^N x_j a_j^{0.5} (1-k_{ij})) - \frac{b_i}{b} \right] \ln \left(1 + \frac{b}{v} \right) \quad (9)$$

PR:

$$\ln \phi_i = -\ln \left(Z - \frac{Pb}{RT} \right) - \frac{a}{2^{1.5} b RT} + (Z-1) \frac{b_i}{b} \cdot \dots \\ \dots \cdot \left[\frac{1}{a} (2\alpha_i^{0.5} \sum_{j=1}^N x_j a_j^{0.5} (1-k_{ij})) - \frac{b_i}{b} \right] \ln \left[\frac{V + (2^{0.5} + 1)b}{V - (2^{0.5} - 1)b} \right] \quad (10)$$

3.4 Aspen Plus Property Documentation

The equations used in Aspen Plus are shown in equation (11) to (14). The equations are taken from the documentation of an earlier version of the Aspen Plus program (Aspentech, 2001). As for Aspen HYSYS it is assumed that these are the equations used also for Aspen Plus version 8.0.

SRK:

$$p = \frac{RT}{v_m + c - b} - \frac{a}{(v_m + c)(v_m + c + b)} \quad (11) \\ b = \sum_{i=1}^N x_i b_i, \quad b_i = \frac{0,08664 RT_c}{p_c} \\ a = \sum_{i=1}^N \sum_{j=1}^N x_i x_j (a_i a_j)^{0.5} (1 - k_{ij}), \quad a_{ci} = \frac{\alpha_i 0,42747 R^2 T_c^2}{p_c} \\ \alpha_i = \left[1 + m_i \left(1 - T_r^{1/2} \right) \right]^2 \\ m_i = 0,48508 + 1,5517 \omega_i - 0,15613 \omega_i^2 \\ c = \sum_{i=1}^N x_i c_i, \quad c_i = 0,40768 \left(\frac{RT_c}{P_c} \right) (0,29441 - z_{RAi})$$

These versions of SRK and PR are not equal to the original versions. A volume translation concept and the c parameter introduced by Peneloux and Rauzy (1982) is used to improve the molar liquid volume calculated from the cubic equation of state.

PR:

$$p = \frac{RT}{(c+v_m)-b} - \frac{a}{(v_m+c)(v_m+c+b)+b(v_m+c-b)} \quad (12) \\ b = \sum_{i=1}^N x_i b_i, \quad b_i = \frac{0,07780 RT_c}{p_c} \\ a = \sum_{i=1}^N \sum_{j=1}^N x_i x_j (a_i a_j)^{0.5} (1 - k_{ij}) \\ a_i = a_{ci} \alpha_i, \quad a_{ci} = \frac{\alpha_i 0,45724 R^2 T_c^2}{p_c} \\ \alpha_i = \left[1 + m_i \left(1 - T_r^{1/2} \right) \right]^2 \\ m_i = 0,37464 + 1,54226 \omega_i - 0,26992 \omega_i^2 \\ c = \sum_{i=1}^N x_i c_i, \quad c_i = 0,40768 \left(\frac{RT_c}{P_c} \right) (0,29441 - z_{RAi})$$

Enthalpy and entropy departure calculations

The enthalpy and entropy departure calculations use the following equations (13) and (14). Subscript m is for mixture conditions and superscript ig is for ideal gas conditions.

$$(H_m - H_m^{ig}) = - \int_{\infty}^v \left(P - \frac{RT}{v} \right) dv - RT \ln \left(\frac{v}{v^{ig}} \right) + \dots \\ \dots + T(S_m - S_m^{ig}) + RT(Z_m - 1) \quad (13)$$

$$(S_m - S_m^{ig}) = - \int_{\infty}^v \left[\left(\frac{\partial p}{\partial T} \right)_v - \frac{R}{v} \right] dv + R \ln \left(\frac{v}{v^{ig}} \right) \quad (14)$$

4 Specifications and Calculation Principle

4.1 Specifications

When calculating the COP for a process as in Figure 1 in Aspen HYSYS or Aspen Plus, only a few specifications are necessary. A circulation flow must be specified, but can be specified arbitrarily as e.g. 1 kg/h. If it is assumed that the evaporation and condensing is at saturation conditions, the only necessary specifications

are the evaporating temperature and condensing temperature.

It is not necessary to calculate the conditions outside the refrigeration circuit to calculate the COP. The air amounts in Figure 2 can be calculated if all the air temperatures are specified. Including an efficiency loss in the compressor motor and including the power needed for air flow in Figure 2 would reduce the calculated COP values slightly.

4.2 Calculation Principle

The calculation starts with a pure component flow at the lowest (evaporating) temperature at saturated vapour conditions. Then the vapour is compressed with a default adiabatic efficiency to the pressure which gives condensation at the highest (condensing) pressure. The compressed gas is cooled in a condenser to saturated liquid. Then the liquid is expanded in an expansion valve at adiabatic conditions. The expanded gas/liquid mixture is heated in the evaporator to the original state of saturated vapour. The COP is calculated as the condenser heat divided by the power consumption in the compressor.

5 Results

The results are shown in Figures 3 to 7, one figure for each component. In all the figures the results are shown for 3 temperature differences using 3 models and 2 simulation tools.

All the models in both simulation programs show as expected a decrease in COP with increase in temperature difference for all the cases.

For some of the components, the deviations in COP are large for the same model in different programs. These differences are larger than expected.

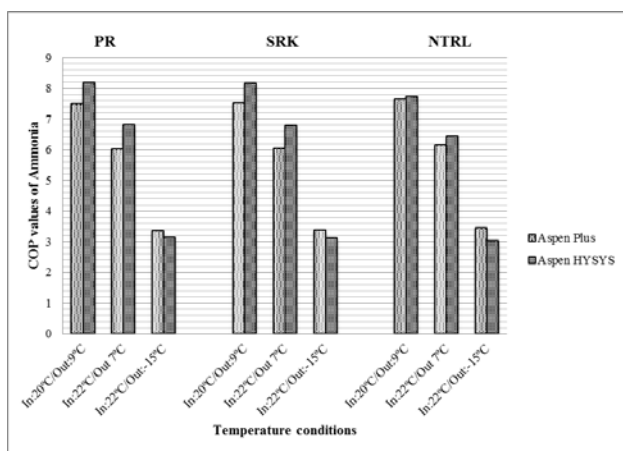


Figure 3. Calculated COP values for ammonia for different temperature conditions, programs and models.

Ammonia is the component with the highest COP (together with R-12) for the lowest temperature difference. As can be seen in Figure 3, all the models in Aspen Plus gave similar COP results for the lowest temperature difference, while Aspen HYSYS gave higher COP values (about 8.2) than Aspen Plus (about 7.5) when using the models PR and SRK.

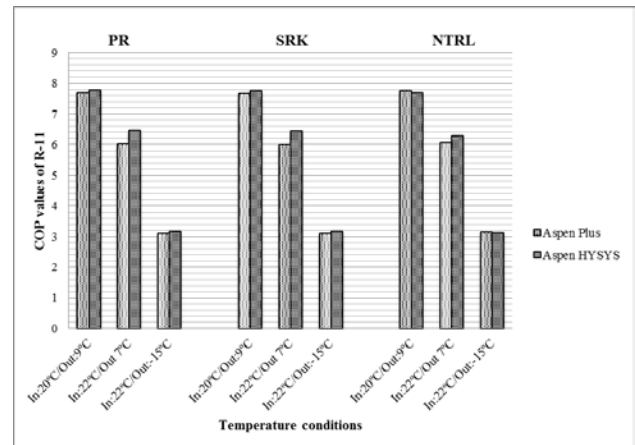


Figure 4. Calculated COP values for R-11 for different temperature conditions, programs and models.

For R-11 there were very few deviations between the models, as seen in Figure 4, but there were slight deviations between COP values calculated with Aspen Plus and Aspen HYSYS. Aspen HYSYS calculated slightly higher COP values for most of the cases.

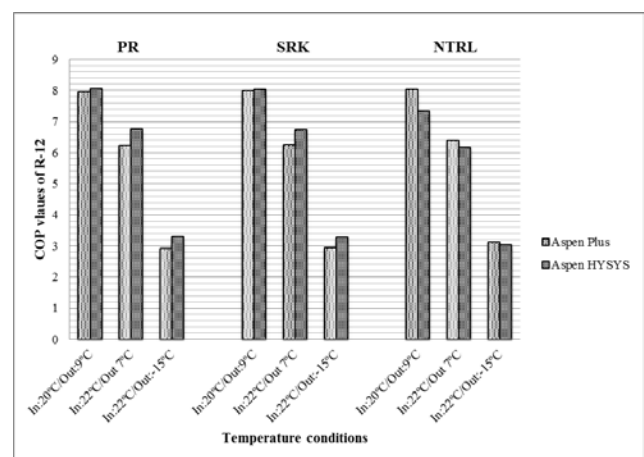


Figure 5. Calculated COP values for R-12 for different temperature conditions, programs and models.

R-12 (together with ammonia) gave the highest COP for the lowest temperature difference. For the low temperature difference, Aspen Plus and Aspen HYSYS gave very similar COP results close to 8.0 as seen in

Figure 5. Using NRTL, Aspen Plus gave 8.0, while Aspen HYSYS gave a lower value (7.5).

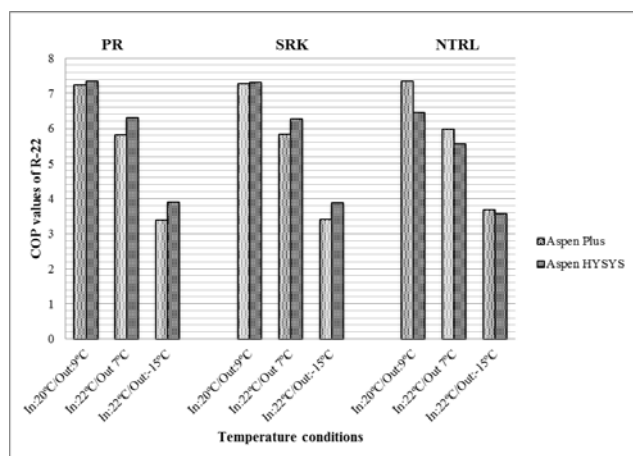


Figure 6. Calculated COP values for R-22 for different temperature conditions, programs and models.

R-22 gave the highest COP values for the highest temperature difference. For the high temperature difference, the COP results in Figure 6 were similar, all between 3.4 and 3.9. The largest deviations were between the simulation programs Aspen Plus and Aspen HYSYS for the PR and SRK models. For PR and SRK Aspen HYSYS calculated the highest COP values. When using the NRTL model, Aspen Plus calculated a slightly higher COP than Aspen HYSYS.

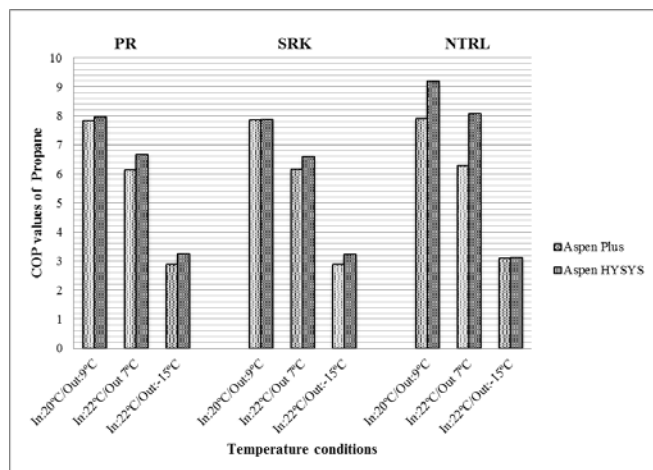


Figure 7. Calculated COP values for propane for different temperature conditions, programs and models.

The COP values in Figure 7 calculated with propane were only slightly less than for the more usual refrigerants. The COP value calculated with Aspen HYSYS using NRTL for the lowest temperature difference was very high (9.2), but all the other COP values for the same conditions was close to 8.0.

6 Discussion

The calculated absolute values (COP values) are probably high compared to actual values for heat pumps in operation. Including motor efficiency, heat losses and pressure drops would reduce the calculated COP values. It is however expected that the calculated differences are reasonable. The main purpose of this work is to evaluate these differences.

The models PR and SRK have obtained similar values as expected when calculated in the same simulation program. Both are equations of state using the same parameters, T_c , P_c and ω .

The model NRTL gave similar results in most of the cases compared to values obtained with PR and SRK, but there were some deviations. As NRTL is not an equation of state method, this difference could be reasonable.

Differences between Aspen Plus and Aspen HYSYS for the same model can be seen. For the PR model slightly higher values are calculated in Aspen HYSYS than in Aspen Plus. However, for the case of NRTL model there is not a clear trend in the deviations.

The explanation of deviations in PR and SRK is also difficult, but some differences in the equations of the models have been found which could be the reason for deviations.

The parameter values of the critical data (T_c , P_c and ω) were checked to be the same in Aspen Plus and Aspen HYSYS, so this cannot explain the differences. The coefficients in the m equations for SRK are slightly different from Aspen Plus to Aspen HYSYS. The coefficients are however equal for the PR equations, so this can not explain the difference in case of the PR equation.

The most clear difference between the Aspen HYSYS versions and Aspen Plus versions of SRK and PR is that the Aspen HYSYS versions are close to the original SRK and PR versions while the Aspen Plus versions use a volume correction as suggested by Peneloux (1982). These corrections influence the equation of state, the equations for calculation of enthalpy and entropy corrections and the calculation of the fugacity coefficients. This may explain the differences between COP values calculated by Aspen Plus and Aspen HYSYS.

In development of new refrigerants, one trend is to use a mixture of different components. The simulations in Aspen HYSYS and Aspen Plus in this work can be easily extended to multicomponent simulations. The uncertainty in the calculated COP values will probably be slightly higher due to higher uncertainty in the physical property calculation methods. When using the SRK and PR models, it is expected that the thermodynamic properties are calculated quite accurately also for mixtures. It is assumed that calculating heat pumps with a mixture of refrigerants using Aspen HYSYS or Aspen Plus with the SRK or PR

model will give reasonable results. A reasonable extension of this work is to evaluate the heat pump efficiency for different mixtures at different conditions.

7 Conclusion

COP values have been calculated to values between 3 and 9. The highest COP was calculated for the lowest temperature difference. The components giving the highest COP value between the temperatures 22 and 7 °C were ammonia and R-12, and R-22 gave the highest COP between -15 and 22 °C. Propane (which is not a CFC) gave slightly lower COP values than the other components.

The differences between the thermodynamic models and the different programs were normally low. However, some differences between Aspen Plus and Aspen HYSYS for the same model were calculated. The calculated deviations between the same models using different programs are difficult to explain. Different equations and model parameters in different programs may explain differences between the same models in different programs.

Aspen Plus and Aspen HYSYS are powerful tools for heat pump calculations. The calculated differences between heat pump efficiencies with different components at different conditions are thought to be reasonable.

Symbol List

Symbol	Description	Unit
a	Parameter in PR and SRK	[J·m ³ /mol ²]
b	Parameter in PR and SRK	[m ³ /mol]
c	Parameter in PR and SRK	[m ³ /mol]
G	Specific Gibbs Free Energy	[J/mol]
H	Specific enthalpy	[J/mol]
k	Binary parameter in PR and SRK	[-]
m	Parameter in PR and SRK	[-]
P, p	Pressure	[N/m ²]
Q	Heat	[J/s]
R	Gas constant	[J/(mol·K)]
S	Specific entropy	[J/(mol·K)]
T	Temperature	[K], [°C]
v	Molar volume	[m ³ /mol]
W	Work	[J/s]
x	Mole fraction	[-]
Z	Compressibility factor	[-]
α	Parameter in PR and SRK	[-]
φ	Fugacity coefficient	[-]
ω	Acentric factor	[-]

Subscripts/superscripts:

C	Condenser
c	Critical
E	Evaporator
i	General component
ID	Ideal
ig	ideal gas
j	General component
m	mixture
r	Reduced
sat	Saturated
0	Reference state

References

- AspenTech: Aspen Physical Property System 11.1, 2001.
- P.A. Domanski and D.A. Didion: Simulation of heat pump operating with nonazeotropic mixture. *ASHRAE Technical Data Bulletin*, 91(3):54, 1985.
- EU Parliament: Regulation (EC) No 1005/2009 on Substances that Deplete the Ozone Layer, 2009.
- Hyprotech: HYSYS Simulation Basis, 2003.
- A. Peneloux, E. Rauzy and R. Freze: A Consistent Correction for Redlich-Kwong-Soave Volumes. *Fluid Phase Equilibria*, 8:7-23, 1982.
- D.Y. Peng and D.B. Robinson: A New Two-Constant Equation of State. *Industrial and Engineering Chemistry Fundamentals*, 15(1):59-64, 1976.
- H. Renon and J.M. Prausnitz: Local compositions in Thermodynamic Excess Functions for Liquid Mixtures. *A.I.Ch.E. Journal*, 14(1):135-144, 1968.
- J.M. Smith, H.C. Van Ness and M.M. Abbott. *Introduction to Chemical Engineering Thermodynamics*, 7th ed., McGraw Hill, 2005.
- G. Soave: Equilibrium Constants from a Modified Redlich-Kwong Equation of State. *Chemical Engineering Science*, 27:1197-1203, 1972.
- I.Y. Tirados: Heat pump efficiencies simulated with Aspen HYSYS and Aspen Plus. *Master Thesis*, Telemark University College, 2015.

Aspen Plus Simulation of Biomass Gasification with known Reaction Kinetic

M.S. Eikeland¹ R.K. Thapa¹ B.M. Halvorsen¹

¹Department of Process, Energy and Environmental Technology, Telemark University College, Norway,

¹marianne.eikeland@hit.no

Abstract

The energy from biomass can be utilized through the thermochemical conversion processes of pyrolysis and gasification. The Aspen Plus simulation tool is applicable for simulation of the gasification processes.

The most common way is to simulate the gasification reactor using Gibbs reactor, which applies Gibbs free energy minimization to calculate equilibrium. The reactions in the gasification process are complex and by using the Gibbs reactor, it is not necessary to specify the stoichiometry or the reaction rates. However, reactions that describe the major conversion rates in a gasifier can be extracted from the literature. By using these reaction rates in Aspen Plus, it is possible to simulate the gasification process also by using a continuous stirred tank reactor (CSTR).

Comparison of the composition of produced gas based on simulation with Gibbs reactor and CSTR is performed. The influence of parameters like reactor temperature, residence time and steam flow rate are studied.

Keywords: gasification, Aspen Plus, reaction kinetic

1 Introduction

Biomass is an attractive source of energy. It is possible to utilize the energy through the thermo-chemical conversion processes of pyrolysis and gasification. In the pyrolysis process, the biomass is devolatilized by heat to char and volatiles. Depending on the feedstock, the volatiles include H₂O, H₂, N₂, O₂, CO₂, CO, CH₄, H₂S, NH₃, C₂H₆ and very low levels of unsaturated hydrocarbons like acetylenes, olefins, aromatics and tars (Basu, 2008). Char has after the pyrolysis a higher carbon concentration than the dry feedstock. The char is converted to gases by using gasification agents like air, oxygen, carbon dioxide or steam.

There are different types of reactors used for gasification. Fluidized bed reactors are the most popular amongst them because of their high heat and mass transfer rates that result in high rate of produced gas. Steam gasification of wood using a dual fluidized bed reactor is one of the promising technologies for biomass conversion (Wilk, 2010; Hofbauer *et al*, 2002; Thapa, 2014). The principle of dual fluidized bed gasification process is shown in Figure 1.

The reactor is divided into two separate zones: combustion and gasification. The combustion zone is a circulating fluidized bed reactor where the fluidizing gas is air. In the combustion zone, inert bed materials, such as olivine particles or quartz sand, are heated by burning of char. The heated bed material is then circulated to the gasification reactor. The purpose of the recirculation of bed material is to supply necessary heat for the endothermic gasification reaction in the gasification zone.

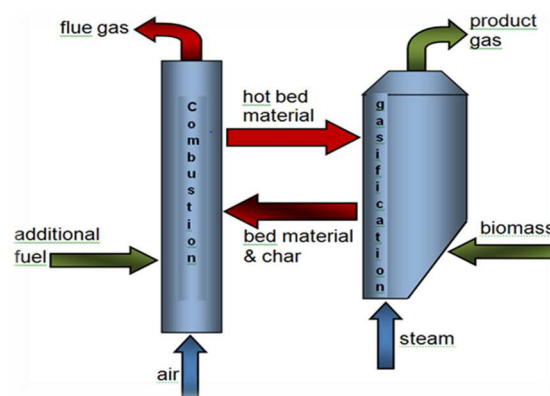


Figure 1. Principle of dual fluidized bed gasification technology (Thapa, 2014).

The gasification zone is a bubbling fluidized bed reactor for gasification of biomass. The fluidizing gas is high temperature steam. The biomass feed to the gasification reactor is mixed with hot bed materials. The biomass in the reactor is dried and devolatilized to produce volatile gases and solid char particles. The char particles react with steam to produce a mixture of combustible gases in addition to some CO₂ and water vapour. The technology is developed by researchers at Vienna University of Technology. The technology is demonstrated as a successful story in the example of the biomass CHP plant in Güssing, Austria (Hofbauer *et al*, 2002).

Despite the novelty of the technology, the efficiency of the technology needs to be increased in order to make it sustainable and competitive in the world energy market. It is believed that the thermo-chemical process in the gasification reactor is one of the major factors that can increase the performance of the gasification process

significantly. The thermo-chemical process in the reactor depends on a number of operating parameters as well as the design of the reactor. Experimental study of the thermo-chemical behaviour has been difficult due to high operating temperature in addition to time consumption and material costs related to the requirements of constructing hot models and pilot plants (Thapa, 2014).

The possibility to study the performance of the reactor by using simulation tools like Aspen Plus is valuable for a better understanding of the gasification process. A validated computational model could give an approximate answer to many factors effecting the efficiency of the plant.

Often, in literature, simulation models with Aspen Plus for gasification of biomass are performed in a Gibbs reactor where no reaction kinetics are applied (Doherty *et al.*, 2013; Nikoo, 2008; Mavukwana *et al.*, 2013). The Gibbs reactor uses Gibbs free energy minimization with phase splitting to calculate equilibrium. Gibbs reactor in Aspen Plus does not

require specified reaction stoichiometry (Aspentech, 2010). This reduces the complexity of the process by ignoring the reactions taking place in the gasification process.

Xie and Umeki (Xie *et al.*, 2013; and Umeki *et al.*, 2010) have published a set of chemical reactions and their reaction rate expression as given in Table 1. The set of equations describes the major conversion rates in a gasifier. The gasification process can be simulated in Aspen Plus by using a continuous stirred tank reactor (CSTR) and including the stoichiometric equations and the related reaction rates.

This work is focused on the analysis of the thermo-chemical process in the gasification reactor and the effect of implying the reaction kinetics in the Aspen Plus model of the process. The continuous stirred tank reactor and the Gibbs reactor are utilized as gasifiers to study the composition and the heating value of the produced gas. The aim is to develop a model, which gives a good approximation to the gasification reactor.

Table 1. Reaction kinetics for the major conversion rates in a gasifier reactor (Xie *et al.*, 2013 and Umeki *et al.*, 2010).

Reactions	Reaction rate
<u>Water-gas reaction:</u> $C(s) + H_2O \rightarrow CO + H_2$	$r = 1,272 * m_s * T * \exp\left(\frac{-22645}{T}\right) [H_2O]$
$CO + H_2 \rightarrow C(s) + H_2$	$r = 1,044 * 10^{-4} * m_s * T^2 * \exp\left(\frac{-6319}{T} - 17,29\right) [H_2][CO]$
<u>Boudouard reaction:</u> $C(s) + CO_2 \rightarrow 2 CO$	$r = 1,272 * m_s * T * \exp\left(\frac{-22645}{T}\right) [CO_2]$
$2 CO \rightarrow C(s) + CO_2$	$r = 1,044 * 10^{-4} * m_s * T^2 * \exp\left(\frac{-2363}{T} - 20,92\right) [CO]^2$
<u>Methanation reaction:</u> $0,5C(s) + H_2 \rightarrow 0,5 CH_4$	$r = 1,368 * 10^{-3} * m_s * T * \exp\left(\frac{-8078}{T} - 7,087\right) [H_2]$
$0,5 CH_4 \rightarrow 0,5C(s) + H_2$	$r = 0,151 * m_s * T^{0,5} * \exp\left(\frac{-13578}{T} - 0,372\right) [CH_4]^{0,5}$
<u>Water gas shift reaction:</u> $CO + H_2O \rightarrow CO_2 + H_2$	$r = 7,68 * 10^{10} * T * \exp\left(\frac{-36640}{T}\right) [CO]^{0,5} [H_2O]$
$CO_2 + H_2 \rightarrow CO + H_2O$	$r = 6,4 * 10^9 * T * \exp\left(\frac{-39260}{T}\right) [H_2]^{0,5} [CO_2]$
<u>Methane-reforming:</u> $CH_4 + H_2O \rightarrow CO + 3H_2$	$r = 3,1005 * \exp\left(\frac{-15000}{T}\right) [CH_4][H_2O]$
$CO + 3H_2 \rightarrow CH_4 + H_2O$	$r = 3,556 * 10^{-3} * T * \exp\left(\frac{-15000}{T}\right) [CO][H_2]^2$

2 Theory

The thermodynamic equilibrium model predicts the maximum achievable yield of a desired product from a reacting system (Li *et al.*, 2001; Basu, 2013). The reactants are left to react for an infinite of time and will reach the equilibrium yield. In practice, only a finite time is available for the reactant to react in the gasification reactor, so for practical purpose a kinetic

model must be used to predict the product composition after a certain time of reaction.

Thermodynamic equilibrium calculation is independent of the gasifier design and is convenient to use to study the influence of fuel and process parameters. Thermodynamic or chemical equilibrium may not be reached in the gasifier, but the simulations may provide reasonable prediction of the maximum achievable yield of the desired product. Minimization of Gibbs free energy (non-stoichiometric model) can be used to determine chemical equilibrium. The only input

needed is the elemental composition of the feed, which is known from its ultimate analysis (Basu, 2013).

In a kinetic model the gas yield and the product composition from a gasifier is determined after a finite time of reaction. Reaction rate and reactor residence time is included in the model. The kinetic rates determine how fast the reaction products are formed and whether the reactions are completed in the gasifier.

There are many chemical reactions taking place in a gasification reactor. For simplification, it is assumed that a set of reactions describes the major conversion rates in the reactor (Xie *et al.*, 2013). The solids are consumed and the particles shrinks by heterogeneous chemistry reactions of gasification and methanation. (Xie *et al.*, 2013). The reaction kinetics, given in Table 1, show that the water gas-shift reaction and methane-reforming reactions are rate determining for this set of reactions. The most common gas-solid reactions in the gasification zone are the Boudouard reaction, the water-gas reaction and the methanation reaction as described in Table 1. Typical temperature range in the gasification zone in a fluidized bed is 700-900 °C.

Table 2 gives the heats of reaction for the major conversion reactions in a gasifier (Moulijn *et al.*, 2013).

Table 2. Heats of reaction for the major conversion rates in a gasifier reactor (Moulijn *et al.*, 2013).

	$\Delta H^{\circ}_{800^{\circ}\text{C}}$ [kJ/mol]
$\text{C(s)} + \text{H}_2\text{O} \rightarrow \text{CO} + \text{H}_2$	136
$\text{C(s)} + \text{CO}_2 \rightarrow 2 \text{CO}$	173
$\text{C(s)} + 2\text{H}_2 \rightarrow \text{CH}_4$	-87
$\text{CO} + \text{H}_2\text{O} \rightarrow \text{CO}_2 + \text{H}_2$	-37
$\text{CH}_4 + \text{H}_2\text{O} \rightarrow \text{CO} + 3\text{H}_2$	228

The reaction with steam is highly endothermic. Also the reaction with carbon dioxide gasification is endothermic, while the methanation and the water gas shift reactions are exothermic.

3 Model description

Zanzi, 2002, reported the yield products obtained in rapid pyrolysis for wood, birch, as shown in Table 3. These data have been used to define the composition of the feed into the gasification reactor. Table 4 gives the composition of the gaseous products on a nitrogen and water free basis. The data in Table 3 and 4 are converted to weight fractions, where H_2 , CH_4 , CO and CO_2 are assumed to be gas yield, while the other components are added to tar. As an average component, C_3H_6 is used in the Aspen Plus simulation as tar component, and solid carbon is used as char.

Table 3. Yield of products obtained in rapid pyrolysis of birch (maf: moisture and ash free), (Zanzi, 2002).

Temperature °C	800
Gas Yield wt% maf	77.7
Tar yield wt% maf	1.1
Char yield wt% maf	7.2
Moisture wt%	14

Table 4. Composition of the gaseous products (vol %) on a nitrogen and water free basis in rapid pyrolysis at 800 °C (Zanzi, 2002).

Gas	vol%
H_2	16.8
CH_4	16.2
CO_2	8.3
CO	50.7
$\text{C}_2\text{H}_2, \text{C}_2\text{H}_4$	6.2
C_2H_6	0.3
Benzene	1.2
Other	0.3

The feed composition in Aspen Plus is specified as presented in Table 5. The feed temperature is 800°C and pressure is set to 1 bar.

Table 5. Mass fraction from birch wood used in Aspen plus simulation

Gas	Mixed substream [mass-frac]	CISolid substream [mass-frac]
CH_4	0.0969	0
CO	0.5307	0
CO_2	0.1365	0
H_2	0.0125	0
C	0	1
H_2O	0.1509	0
C_3H_6	0.0725	0

The following assumptions were made for the Aspen simulation:

- The system is isothermal and operates under steady state conditions.
- Operation at atmospheric pressure, pressure drops are neglected.
- Nitrogen, sulphur, chlorine and ash are neglected.
- Tar formation is not considered.
- Char is 100% carbon.
- Heat loss from the gasifier is neglected.

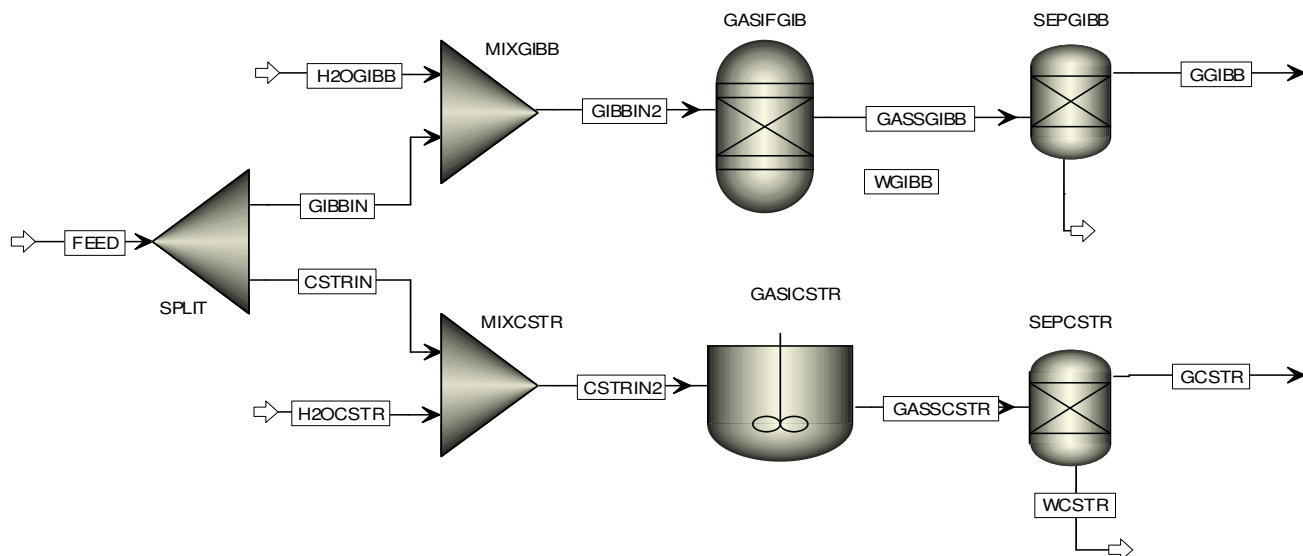


Figure 2. The Aspen Plus process flow sheet.

The stream class used in Aspen Plus is MIXCISLD and the property method used is Redlich-Kwong-Soave (RKS) cubic equation of state with Boston-Mathias alpha function (RKS-BM). The RKS-BM property method is recommended for gas processing, refinery, and petrochemical applications. The RKS-BM property method is used for nonpolar or mildly polar mixtures. Examples are hydrocarbons and light gases, such as carbon dioxide, hydrogen sulphide, and hydrogen. The RKS-BM property method is consistent in the critical region. The results have the lowest accuracy in the region near the mixture critical point (Aspentech, 2010).

3.1 Flow Sheet

The Aspen Plus flow sheet used in the simulation is presented in Figure 2. The feed composition is defined as described in Table 5.

The feed is split into two equal streams, which is directed to two different reactors: Gibbs reactor and CSTR. The flow is entering a mixer where the gasification agent, in this case steam, is added before entering the gasification reactor. After the reactor, water is removed to determine the gas composition on a dry basis.

For the Gibbs reactor, the reactions presented in Table 2 were specified in the reactor setup with a temperature approach of 0°C, meaning that the calculation is done at reactor temperature. For the CSTR the reactions stoichiometry and their reaction rates are defined in the reaction setup in Aspen Plus, and the residence time is defined in the reactor setup.

Information about the process parameters are given in Table 6. The parameters are based on the same dimensions used in the work of Thapa, 2014.

4 Reaction rates

Table 1 refers to the reaction rates given by Xie and Umeki (Xie *et al.*, 2013 and Umeki *et al.*, 2010). Chemical reactions are expressed by stoichiometric equations and reaction rates are described in terms of a power law format. The rate coefficients based on Arrhenius law are empirically fitted with measured data (Xie *et al.*, 2013).

Table 6. Process parameters used in Aspen Plus simulation (Thapa, 2014).

	Gibbs	CSTR
Feed in pr. reactor [kg/h]	112	112
Steam in pr. reactor [kg/h]	112	112
Volume reactor [m ³]		0,4752
Reactor temperature [°C]	850	850
Reactor pressure [bar]	1	1

The Arrhenius coefficient is expressed as:

$$k = A_0 m_s^{C1} T^{C2} \exp\left(-\frac{E}{RT} + E_0\right) \quad (1)$$

Where k is the chemical reaction rate coefficient, A_0 is the pre-exponential factor, E [J/mole] is the activation energy, E_0 is the activation energy constant, R [J/mole K] is the universal gas constant and $C1$ and $C2$ are constants. T [K] denotes the temperature and m_s [kg] is the solid mass of fixed carbon per volume (Xie *et al.*, 2013). In this work the following assumption is made:

$$m_s = M_{wc} * C(s) \quad (2)$$

where M_{wc} is the molecular weight of carbon [kg/kmol], and $C(s)$ is molar concentration of solid carbon [kmol/m³].

Aspen Plus provides a built-in power law expression for calculation of the rate of reaction. The general power law expression is:

$$\text{Kinetic factor} = k \left(\frac{T}{T_0}\right) \exp\left(-\frac{E}{R}\left(\frac{1}{T} - \frac{1}{T_0}\right)\right) \quad (3)$$

If the reference temperature T_0 [K] is not specified, Aspen Plus uses the reduced power law expression:

$$\text{Kinetic factor} = kT^n \exp\left(-\frac{E}{RT}\right) \quad (4)$$

5 Results and discussion

The results of the simulations are given in Table 8. The results are compared with typical composition of the produced gas from the biomass gasification plant in Güssing, Austria (Güssing Renewable Energy). The results from the gasification plant are based on wood chips.

Table 8. Results of the main components after gasification

	CSTR	Gibb	Experimental data (Güssing Renewable Energy)
Residence time [s]	1.7		
CH ₄ (vol % dry basis)	16.4	0.012	~10
CO (vol % dry basis)	44.1	25.8	~24
CO ₂ (vol % dry basis)	15.6	16.8	~23
H ₂ (vol % dry basis)	24.0	57.5	~44
LHV [MJ/m ³]	14.0	9.5	~13-15
Volume reactor [m ³]	0.48		
Gasification temperature [°C]	850	850	850

5.1 Steam flow

A sensitivity analysis of volume fraction (dry basis) composition in the produced gas as function of steam flow is performed in Aspen Plus. The results are presented in Figure 3. Both the CSTR and the Gibbs reactors show a decrease in CO concentration as a function of steam rate, but a steeper decrease is observed in the Gibbs reactor compared to the CSTR. CH₄ concentrations is also decreasing in both cases, but in the Gibbs reactor the concentration of CH₄ is approaching zero, while the methane concentration in the CSTR will be about 13 %. H₂ and CO₂ concentrations increase when the steam flow increases in both the cases. However, the H₂ concentration within

a Gibbs reactor can reach over 60 %, while the H₂ concentration with the same amount of water will be less than 30% in a CSTR. The CO₂ concentration will also be higher in a Gibbs reactor compared to the CSTR. The residence time in CSTR is 1.7 s, giving a finite time for the reactions to be completed.

An increase in the steam flowrate results in production of CO, CO₂ and H₂ related to the Le Chateliers principle. However, in the water gas shift reaction CO is consumed, thus CO₂ and H₂ will be the dominating products based on chemical equilibrium. For the kinetics, the water gas shift reaction has the dominating reaction rate and here CO will also be consumed. However, this reaction is exothermic and the reaction will therefore go to the left direction when the reaction temperature is high. This will imply that less CO is consumed when the kinetics are considered, and consequently less CO₂ and H₂ are produced.

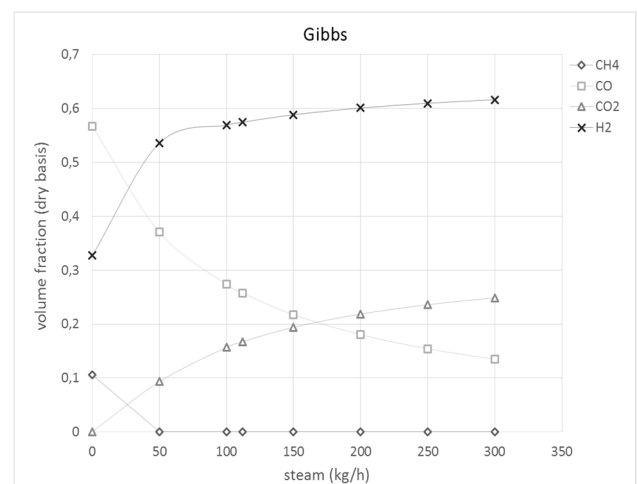
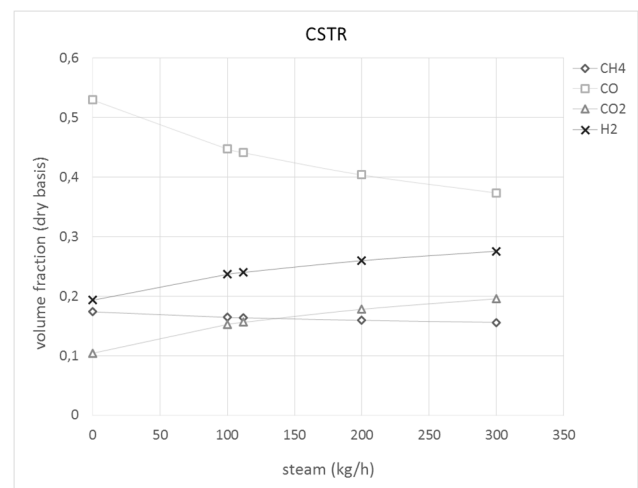


Figure 3. Steam (kg/h) as function of volume fraction (dry basis) of CH₄, CO, CO₂ and H₂ simulated by Aspen Plus for CSTR and Gibbs reactor. Reactor temperature 850°C.

5.2 Temperature

Variation of temperature in the gasification reactors will influence on the composition of the produced gas. Figure 4 shows the composition of the gas as a function of the temperature in the reactor.

The CO concentration increases in the Gibbs reactor, but decreases in CSTR when temperature increases. CH₄ decreases in both cases, but in a lesser degree in CSTR. CO₂ increases in the CSTR, but decreases in Gibbs. H₂ increases in CSTR, but in the Gibbs reactor H₂ increases with temperature up to 700°C and decreases slightly at higher temperatures. Also, notice that the change of composition in the CSTR is largest in the temperature interval of 800 -1000°C.

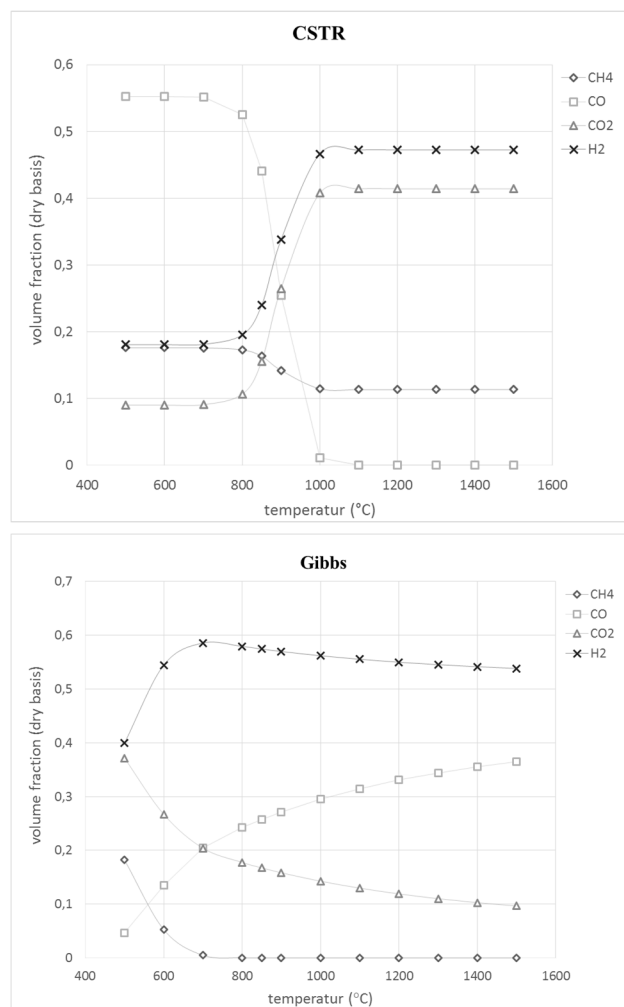


Figure 4. Temperature (°C) as function of volume fraction (dry basis) of CH₄, CO, CO₂ and H₂ simulated by Aspen Plus. Steam 112kg/h.

The differences in temperature profiles for the two reactors can be explained due to thermodynamics and kinetics. In a Gibbs reactor, where the thermodynamic or chemical equilibrium is reached, a temperature increase will favour the endothermic reactions. The

water-gas reaction, the Boudouard reaction and the methane-reforming reaction, all of them having a positive heat of reaction (Table 2), are endothermic reactions. These three sets of reactions will favour a production of CO and H₂ and consumption of methane.

The methanation and the water gas shift reactions are both exothermic. Increasing the temperature for these reactions will make the heat content of the system to increase. The system will then consume some of that heat by shifting the equilibrium to the left as described by Le Chateliers principle. This will lead to a reduction of the CO₂ and CH₄ concentrations. This describes the profiles that can be observed in the Gibbs reactor.

For the CSTR the temperature profiles are different due to the kinetics defined for the reactions. All of the reaction rates are temperature dependent in different extent. An increase in temperature gives a decrease in the exponential factor of the reaction rate expression. The water gas shift reaction has the dominating reaction rate implying a consumption of CO and production of CO₂ and H₂. It can also be observed that CH₄ is consumed in the methane reforming reaction to produce H₂ and CO.

Inflection point for all the reaction sets are typical at around 800°C and is the reason for the steep increase /decrease in concentrations around this temperature.

5.3 Residence time

Residence time or reactor volume will influence on the composition of produced gas from the gasifier. A longer residence time will give the reactions more time to reach equilibrium. To increase the residence time it is necessary to either increase the reactor volume or reduce the feed inlet flow to the reactor. Figure 5 gives the composition of produced gas at different residence times in CSTR.

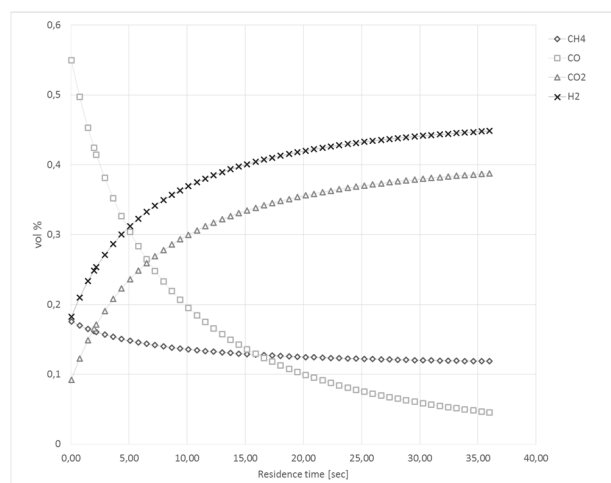


Figure 5. Residence time (s) as function of volume fraction (dry basis) of CH₄, CO, CO₂ and H₂ simulated by Aspen Plus. Steam flow 112 kg/h, temperature 850°C.

Increased residence gives a higher H₂ and CO₂ concentration, while CH₄ and CO concentrations decrease with residence time. A residence time of about 8 sec. gives a comparable gas composition to the experimental data from Güssing, with 14 vol% CH₄, 23 vol % CO, 28 vol % CO₂ and 35 vol% H₂.

6 Conclusion

Simulation of the gasification process in Aspen Plus is useful in studying the produced gas composition. The simulations using Gibbs reactor and CSTR as models for the fluidized gasification reactor show how the composition of the produced gas differs because of the different principles in the two methods. Gibbs reactor is based on minimizing free energy and chemical and thermodynamic equilibrium are reached. In the CSTR, it is necessary to define the reaction rates of the actual reactions taking place in the reactor. The kinetics will determine how fast the reaction is approaching and the residence time will determine whether the equilibrium conditions are obtained.

The product gas composition obtained from simulation of the gasification reactions using Gibb's reactor and CSTR are compared with data from the Güssing plant. The lower heating value of the product gas agree well for the three cases, but the gas compositions show some deviations. Sensitivity analysis for the product gas composition have been performed with respect to steam flow rate, reaction temperature and residence time. In both the Gibb's and CSTR reactor, the concentration of CO and CH₄ decreases whereas the concentration of CO₂ and H₂ increases with increasing steam flow rate. In both of the reactors, the concentration of CH₄ decreases with increasing temperature. In Gibb's reactor, CO concentration increases and CO₂ concentration decreases with increasing temperature. These results are opposite of the results obtained from the CSTR reactor. The concentration of H₂ and CO₂ increases while the concentration of CO and CH₄ decreases with increasing residence time in CSTR reactor.

The results from the simulation of the Gibbs reactor is based on calculations where the reactions reach thermodynamically and chemical equilibrium over an infinite of time. In a real process, the time of reactions is finite and the different reactions have different reaction rates. CSTR reactor will approach a more realistic description of the process. However, a further analysis of the simulation process is necessary to reach a good model for the gasification process compared to experimental data.

References

Aspen tech. Aspen Physical Property System, Physical Property Methods. *Version Number: V7.2*, July 2010.

- Basu Prabir. Biomass Gasification, Pyrolysis and Torrifaction, Practical Design and Theory. Second edition. *Academic Press*. 2013.
- Bolhar-Nordenkamp, M. and Hofbauer H. Gasification demonstration plants in Austria. IV. *International Slovak Biomass Forum*. 2004. Bratislava.
- Doherty W., Reynolds A., Kennedy D. Aspen Plus Simulation of Biomass Gasification in a Steam Blown Dual Fluidised Bed. Materials and processes for energy: communicating current research and technological developments. Méndez-Vilas (Ed.). *Formatex Research Centre*. 2013.
- Güssing Renewable Energy GmbH; GRE MULTIFUEL GASIFICATION <http://www.guessingrenewable.com>. 2014.
- Hofbauer, H., Rauch R., and Bosch K.. Biomass CHP Plant Güssing - A Success Story. *Expert Meeting on Pyrolysis and Gasification of Biomass and Waste*. 2002. Strasbourg, France.
- Li X., Grace J.R., Watkinson A.p., Lim C.J. Ergünderler A. Equilibrium modeling of gasification: a free energy minimization approach and its application to a circulating fluidized bed coal gasifier. *Fuel*, 80, pp. 195-207. 2001.
- Mavukwana A., Jalama K., Ntuli F., and Harding K. Simulation of Sugarcane Bagasse Gasification using Aspen Plus. *International Conference on Chemical and Environmental Engineering (ICCEE'2013)*. 2013. Johannesburg, South Africa.
- Nikoo M. B., Mahinpey N. Simulation of biomass gasification in fluidized bed reactor using ASPEN PLUS. *Biomass and Bioenergy*, volume 32, Issue 12, pp. 1245-1254. 2008.
- Moulijn J. A., Makkee M., van Diepen A. Chemical process technology *John Wiley & Sons*, pp. 143. 2013.
- Thapa R. K., Halvorsen B. M. Stepwise analysis of reactions and reacting flow in a dual fluidized bed gasification reactor. *Advances in Fluid Mechanics X*, Volume 82, WIT Transactions on Engineering Sciences. 2014.
- Umeki K., Yamamoto K., Namioka T., Yoshikawa K. High temperature steam-only gasification of woody biomass. *Applied Energy*, 87, pp. 791-798. 2010.
- Wilk V., Koppatz S., Pfeifer C., Hofbauer H. Gasification of residues and waste wood in a dual fluidised bed steam gasifier. *ICPS 10 Proceedings*. 2010.
- Xie J., Zhong W., Jin B., Shao Y., Huang Y. Eulerian-Lagrangian method for three-dimensional simulation of fluidized bed coal gasification. *Advanced Powder Technology*, 24, pp. 382-392. 2013.
- Zanzi, R., Sjoström K., and Bjornbom E. Rapid pyrolysis of agricultural residues at high temperature. *Biomass and Bioenergy*, 23, pp. 357-366. 2002

Near well simulation of extra-heavy oil production using SAGD

¹Kou Guandong ¹Britt Halvorsen

¹Department of Technology, Telemark University College, Norway

Abstract

Steam-Assisted Gravity Drainage (SAGD) is an enhanced oil recovery method. One challenge for SAGD process is that part of the injected steam flows directly into the production well without condensation, which causes energy loss and lower oil production rate. Autonomous Inflow Control Valves (AICVs) can shut off water and gas autonomously, and can therefore be useful in the SAGD process. The multiphase simulator OLGA in combination with the near well simulation tool ROCX are used for simulation of the application of AICVs in the SAGD process.

The result shows that AICVs are able to close for water (and thereby also for steam), and the closing time depends on controller set point of water cut. It is also observed that the production rate of water increases significantly after water breakthrough.

Keywords: SAGD, AICV, simulation, heavy oil, bitumen, reservoir, OLGA, ROCX, flow rate, permeability

1 Introduction

Nowadays, demand for heavy oil and bitumen is increasing, since conventional oil has limited amount and oscillating price. Thermal methods are often used for producing heavy oil, among them the Steam-Assisted Gravity Drainage (SAGD) process is one of the most widely used. The basic mechanism in SAGD is that heavy oil is heated up by injected steam from the injection well, and as a result the heavy oil becomes less viscous and mobile and can be produced from the production well. (Speight, 2013) Autonomous Inflow Control Valves (AICVs) can also be used in the SAGD process for production of heavy oil and bitumen, since it can shut off water and increase the oil recovery rate.

In this study, the theoretical background of heavy oil and common production methods are first introduced. Besides, a program for calculating required steam injection amount is developed in MATLAB. (mathworks, 2015) In addition, fundamental knowledge of AICV and the simulation software OLGA (Schlumberger) are briefly demonstrated. Moreover, the simulation of the SAGD process combined with AICVs are performed, with the result presented and discussed. Finally, limitations and prospects of this study are provided.

1.1 Heavy oil and bitumen

Heavy oil is characterized as an asphaltic, dense, viscous nature, and its asphaltene content, as defined by the U.S. Geological Survey (Meyer, 2003).

Although variously defined, the upper limit for heavy oil is 22° API gravity with a viscosity of 100 centipoise (cP) (Meyer, 2003). API gravity is short for “American Petroleum Institute’s gravity”, and is used as a standard to express the specific weight of oil. The equation for calculating the API gravity is shown in equation (1).

$$\text{API gravity} = \frac{141.5}{SG} - 131.5 \quad (1)$$

where SG stands for specific gravity of oil.

Based on this criterion, light oil and extra heavy oil are also explained respectively in the following. Oil with at least 22° API gravity and a viscosity less than 100 cP is known as conventional oil (Meyer, 2003). Extra heavy oil is the portion of heavy oil having an API gravity of less than 10°. In comparison with light oil, heavy or extra heavy oil cannot flow naturally and has to be heated or diluted to be pumped out.

Bitumen shares the attributes of heavy oil but is even more dense and viscous. Natural bitumen has a viscosity higher than 10,000 cP. Extra-heavy oil natural bitumen is also known as "oil sands". (Banerjee, 2012)

In Canada, bitumen is regarded as the crude obtained from oil sands. However, it should be noted that oil sands are often incorrectly called tar sands, since oil sand is neither tar nor sand. Tar is a residual product that remains after severe thermal cracking of heavy oil, rather than a raw material. Similarly, asphalt and pitch should not be confused with bitumen, because they are actually the residual products after processing of heavy oil or bitumen.

Heavy oil deposits are found in many places in the world with large varieties of types and sizes. Among them, the most explored and biggest reserves are Alberta in Canada, Alaska in the USA, and Orinoco belt in Venezuela. The deposits in Alberta contain very highly viscous hydrocarbons that make it fall into the category of bitumen. In comparison, deposits in Alaska and the Orinoco belt, by definition, belongs to the category of extra heavy oil. (Dusseault, 2001)

1.2 SAGD

SAGD is the abbreviation of Steam-Assisted Gravity Drainage, a thermal in-situ heavy oil recovery process.

The SAGD method was invented in the 1978 by Dr. Roger Butler, former holder of Endowed Chair of Petroleum Engineering at University of Calgary in Canada. By 1997, the Underground Test Facility (UTF) project successfully demonstrated that SAGD technology is commercially viable in the Athabasca Oil Sands.

There are several steps in a SAGD process. First, two parallel and horizontal wells are drilled into the oil reservoir, one a few meters above the other, as shown in **Figure 1**. Then, steam is injected into an injection well forming a cone-shaped steam chamber. As the steam chamber expands with time, new heavy oil or bitumen is heated and replaced by steam; the heated bitumen lowers in viscosity and flows downward along the steam chamber boundary into the production well by gravity. Finally, the mobile heavy oil is pumped to the surface through the lower production well. This method can improve heavy oil recovery by between 50% and 60% of the original oil in place (OOIP) and is therefore more efficient than most other thermal recovery methods. (Speight, 2013)

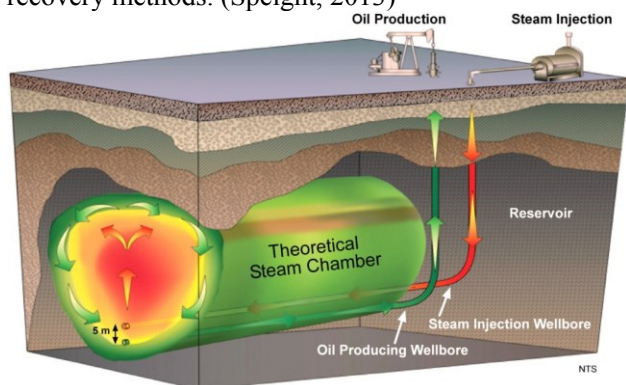


Figure 1. Sketch of SAGD process (Purkayastha)

The key benefits of the SAGD process are lower residual oil saturation (SOR), and high ultimate recovery. The issues of this technique relates to low initial oil rate, artificial lifting of heavy oil to the surface, horizontal well operation, and extrapolation of the process to reservoirs with low permeability, low pressure, or bottom water.

1.3 AICV

AICV is the abbreviation of Autonomous Inflow Control Valve. It is a technology that can shut off the gas and water autonomously and locally in the production well. It combines the advantages of passive inflow control device (ICD), Autonomous ICD (AICD) and inflow control valves (ICV) used in smart wells.

For most oil production fields, the draining mechanism is based on pressure support from gas and/or water, meaning that gas or water breakthrough will occur after a period of production. Production of oil has to be limited once a breakthrough expands along the horizontal well. Then, the production from the well has to be choked or stopped, although there is still oil left

along the wellbore. ICD and AICD have significantly increased oil production and recovery, however, neither of them is able to completely shut off unwanted gas and water production. The novel AICV technology is a major step for improving oil recovery.

The internal structure of an AICV is shown in **Figure 2**. When oil arrives to the inlet of an AICV, the valve is open and oil can flow from the annulus into the production flow path, as shown in **Figure 3**. In comparison, when less viscous as water and/or gas is reaching the AICV, it keeps closed, which can be seen in **Figure 4**.

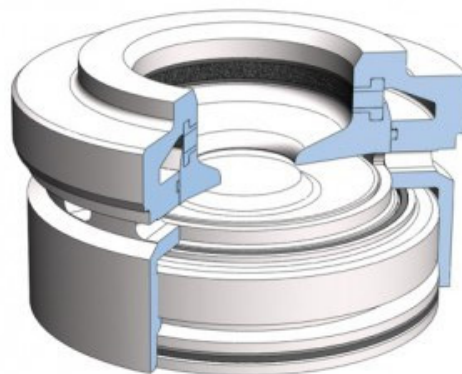


Figure 2. Internal structure of an AICV (InflowControl)

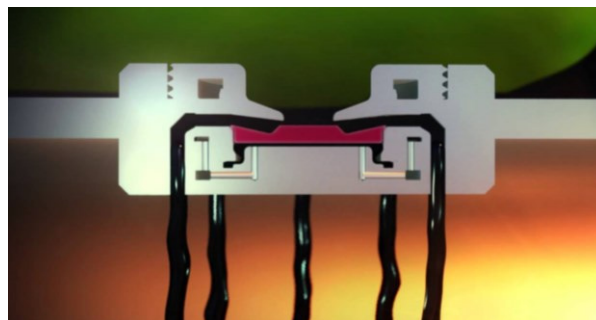


Figure 3. Cross-sectional view of AICV at open state (InflowControl)

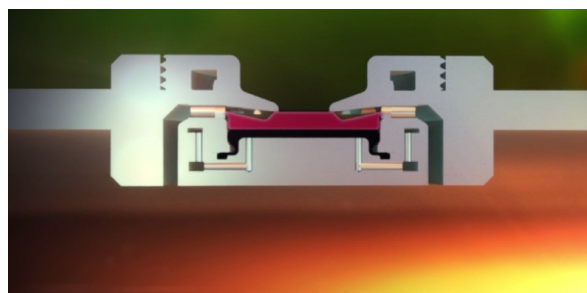


Figure 4. Cross-sectional view of AICV at closed state (InflowControl)

For high capacity wells, there is usually laminar flow (viscosity dependent) at the toe. As the cumulative flow increases towards the heel, as a result of friction at the wall of a long well, the flow becomes turbulent (density dependent). The flow rate versus pressure drop is highly non-linear and varies with the degree of depletion.

Pressure drop across the inflow control device is also an important parameter. The restriction has normally turbulent flow which is density dependent and non-linear. The equivalent laminar and turbulent flow restrictors in series can be seen in **Figure 5**.

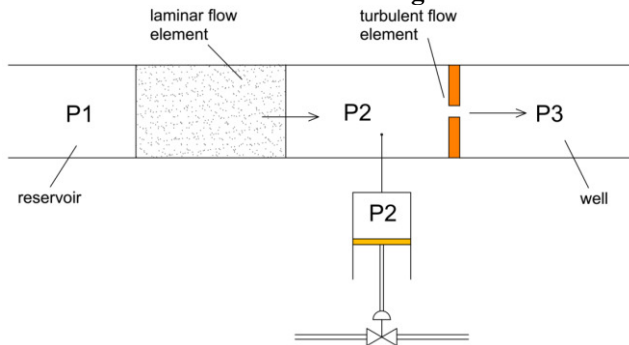


Figure 5. Laminar and Turbulent flow restrictors in series
Pressure drop across the laminar and turbulent flow restrictors can be calculated with formula (2) and (3).
For turbulent flow restrictor

$$\Delta p = p_2 - p_1 = C \cdot \frac{1}{2} \rho v^2 \propto \rho v^2 \quad (2)$$

For laminar flow restrictor

$$\Delta p = p_2 - p_1 = \frac{32\mu v L}{D^2} \propto \mu v \quad (3)$$

Based on these equations, the pressure profile along the laminar and turbulent flow restrictors is briefly plotted in **Figure 6**.

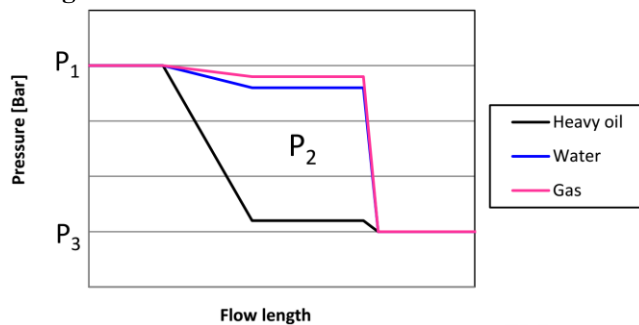


Figure 6. Pressure drop along flow length for three phases

Pressure difference between top and bottom sides of AICV is thus caused, depending on the viscosity of fluid flowing through the AICV. By designing different cross-sectional area of top and bottom surface, AICV can be tuned for their automatic opening and closing properties.

AICV can solve gas and water breakthrough problems during heavy oil production. In the SAGD process, steam breakthrough problem can also be avoided by AICV. In summary, AICV can stop unwanted fluid to the well completely; huge potential in oil recovery can be achieved with AICV; AICV gives a more uniform oil production along the well.

1.4 Simulation software

In the simulation study, OLGA, ROCX, MATLAB and Tecplot are used.

OLGA is the industry standard tool for transient simulation of multiphase petroleum production. It can be used for well networks, flow lines, pipelines, process equipment, covering the production system from bottom hole to the production system.

ROCX is a near-wellbore reservoir model that can be easily coupled to the OLGA simulator to perform integrated wellbore-reservoir transient simulations. ROCX is a three-dimensional model, capable of simulating three-phase flow in porous media. The OLGA-ROCX coupling is easy to build, robust and numerically stable. (Schlumberger)

MATLAB is used for generation of permeability data string in ROCX. (mathworks, 2015) Tecplot is used for viewing oil and water saturation profiles. (Tecplot)

2 Simulation settings

There are two main simulation cases, one with homogeneous reservoir and the other with heterogeneous reservoir. Simulation setting is mainly manipulated through Graphical User Interface (GUI) of OLGA, including flow diagrams, parameters and algorithm.

Before discussing other further content of this paper, it should be stated that one thermodynamic assumption is made. The SAGD process is already at thermal equilibrium once it is initialized, since transient state is not that important for most cases.

2.1 General Parameters

The general parameters are used in both homogeneous and heterogeneous reservoir simulations. The meaning of homogeneous reservoir is that the permeability of reservoir does not vary in space, although permeability values of x-y plane is different from that of z direction. For heterogeneous reservoir, permeability varies along x direction. In our case specifically, permeability is lower at all three directions on the left side of the packer (toe) than the right side of the packer (heel).

2.1.1 Reservoir gridding

Because the variations in the y-z plane are of more importance than in the x-direction, the y-z plane is divided into 31×20 grids. And since the depth of the reservoir is fixed as 20 m, all dz values are set as 1 m. In comparison, dy values varies with their distance to the production well: the closer the well, the smaller control volumes. This is because the relative importance of accuracy decreases with distance from the well. The dy grid length values are 1, 1, 1, 1.5, 1.5, 1.5, 2, 2, 2, 2.5, 2.5, 2.5, 2.5, 3, 3, with symmetry on the two sides of the well.

In the x direction, the number of grids depends on the number of applied AICVs. In this first case with homogeneous reservoir, there are 3 AICVs and thus $dx=3$ was set for that case. Notwithstanding, in the case with heterogeneous reservoir with 6 AICVs, dx was set as 6 accordingly.

2.1.2 Other reservoir settings

Porosity is defined as constant 0.3, without variation in space. In order to simplify the problem and reduce calculation time, compression of rock is neglected, and the rock thermal properties are turned off.

Permeability is an important parameter in this simulation study. For heterogeneous reservoir, there are 1860 grid cells, and the string of permeability values is generated in MATLAB and copied into ROCX.

The residual saturation for water, oil and gas are all assumed to be 0. This is because we are more interested in the performance of AICVs, and the simulation time is less than 200 days so the oil is not depleted.

Relative permeability of water and oil k_{rw} and k_{ro} are set as manual with the default values in ROCX.

Initial condition of reservoir is the same as the SAGD equilibrium state. Based on this, the boundary conditions for the reservoir are set as 120 °C and 125 bar.

2.1.3 Pipeline geometry and thermal properties

The production well consists of the outer annulus and the inner real flow path. The diameter of the annulus is 0.15 m, and 0.12 m for the pipeline. Absolute roughness of the pipeline is 5×10^{-5} m, as material is assumed as slightly corroded carbon steel. Each production zone, corresponding to one AICV, has a length of 20 m.

The mean heat transfer coefficient to the outer wall surface is 6.5 W/(m²K). Ambient temperature in the SAGD chamber is set as 120 °C, which is also the initial temperature of the wellbore and the reservoir liquids.

2.1.4 Feed liquid properties

Gas specific gravity is 0.64, i.e. 0.64 times of the density of air at 1 atm and 20 °C. Oil specific gravity is 0.85, i.e. 0.85 g/cm³ as calculated. Viscosity of oil is set as 100 cP, measured at 120 °C and 125 bar, assuming that the production is already in thermal equilibrium. The pressure and temperature value for this measurement is also used as boundary conditions of the production well and the reservoir.

2.1.5 Settings for simulated AICV

The diameter of simulated AICV is set as 0.01 m, which is close to the real diameter of a physical AICV. The discharge coefficient is 0.84, which is within the normal range of most valves. The model for the valve

is selected as HYDROVALVE, an OLGA choke model for determining pressure drop and flow rate over the choking range. Stroke time is 0, meaning negligible time for movement, and recovery tuning is 1 giving maximum recovery. The orifice geometry is assumed for the valve, so that there is no spatial extension and vena contracta appearing behind the valve. Moreover, it is also assumed that no slip occurs between gas and liquid.

Besides, the PID controller for the simulated AICV has maximum output signal 1 and minimum output signal 0.008, meaning that the valve can be completely open but not one hundred percent closed. Sample time is 60 s, with bias 0.1 and amplification -0.01; integral constant is set as 50 s.

2.1.6 Summary of general parameter settings

The general parameters for the simulation cases are summarized in **Table 1**.

Table 1. Fixed parameter settings for simulation

Section	Parameter	Unit	Value
Pipe	Diameter of annulus	m	0.15
	Diameter of inner flow path	m	0.12 m
	Roughness of pipe wall (both annulus and path)	m	5×10^{-5}
	Heat transfer coefficient from pipe wall to ambient	W/(m ² K)	6.5
	Section length for each production zone	m	20
Reservoir	Gridding of reservoir (nx × ny × nz)	[-]	3×31×20
	Initial oil saturation	[-]	1
	Thermodynamic equilibrium temperature	°C	120
	Thermodynamic equilibrium pressure	bar	125
	Specific gravity of gas	[-]	0.64
	Specific gravity of oil	[-]	0.85
	Porosity of reservoir	[-]	0.3
	Viscosity of oil (120 °C and 125 bar)	cP	100
AICV	Diameter of AICV	m	0.01
	Discharge coefficient	[-]	0.84
	minimum output	[-]	0.008
	Recovery tuning	[-]	1
	Stroke time	s	0
	PID controller integral constant	s	50
	PID controller bias	[-]	0.1
	PID controller amplification	[-]	-0.01
	Controller sample time	s	60
	Controller delay	s	0
Outlet	Pressure	Bar	100
	Temperature	°C	120
Leak	Diameter	m	0.12
	Discharge coefficient	[-]	0.84

2.2 Model and algorithm

2.2.1 Blackoil model

Blackoil modelling allows the user to make a compositional model with minimum input. Details about the fluid composition are not needed for a Blackoil simulation, and the only necessary data is specific gravity of gas and oil and the gas-oil ratio (GOR) at standard conditions. Compared to Compositional Tracking, the Blackoil model is faster in CPU cycles, and it treats shut-in cases more accurately than a standard PVT table option.

Water properties are calculated by the standard OLGA routines. The physical properties of gas and oil are calculated from correlations belonging to a specific blackoil model decided by the user. To find the properties at a specific position in a pipe, the correlations use the pressure, temperature specific gravities of gas, oil and water, as well as GOR at that position. If there are multiple feeds, the specific gravities and GOR are the averages taken over the constituting blackoils weighted by volume at standard conditions.

The Blackoil model is often used when limited specification about the production fluids are available, as during planning or design. Later when production is established, the actual values can be used, and possibly with the module's tuning mechanism to improve the match between observations and predictions made by OLGA.

Assumptions for blackoil model:

1. An oil component cannot exist as gas in the gas phase
2. Gas can dissolve in oil
3. Gas cannot dissolve in the water phase, and water cannot exist as steam in the gas phase

2.2.2 Second order scheme TVD method

Mass equations can be solved with two different schemes in OLGA: the first order upwind implicit scheme and the second order Total Variation Diminishing (TVD) scheme. The first order scheme is more robust and should be preferred in most situations, while the second order scheme has less numerical diffusion and therefore keeps holdup fronts better. (Schlumberger)

In the black-oil approach, one mass conservation equation per component in each of the three phases is solved. Also in this approach one pressure equation and one temperature equation (if requested) is solved. PVT data is in this case computed by the user selected black-oil GOR model. And this is also the calculation method in this simulation study.

TVD is short for total variation diminishing, and it is a property of discretization scheme used for solving hyperbolic partial differential equations. For example, in a hyperbolic PDE advection equation (4)

$$\frac{\partial u}{\partial t} + a \frac{\partial u}{\partial x} = 0 \quad (4)$$

The total variation (TV) is given by equation (5)

$$TV = \int \left| \frac{\partial u}{\partial x} \right| \quad (5)$$

Total variation (TV) for the discrete case is (6)

$$TV = \sum_j |u_{j+1} - u_j| \quad (6)$$

Total variation diminishing (TVD) is satisfied if equation (7) is validated.

$$TV(u^{n+1}) \leq TV(u^n) \quad (7)$$

2.2.3 Modeling of AICV

In Schlumberger OLGA, an AICV is represented by a transmitter of water cut (WC), a PID controller, a valve, and a leak, as shown in **Figure 7**.

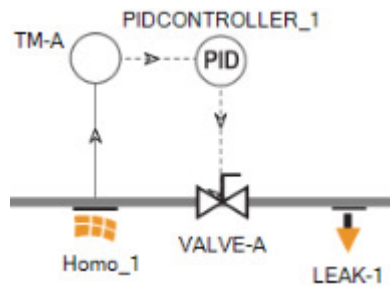


Figure 7. AICV model in OLGA graphical user interface

The transmitter (TM-A) measures the value of water cut in the annulus of production well, and send the value to the PID controller (PIDCONTROLLER_1). The PID controller controls the opening of the valve (VALVE-A), with the controller output calculated by equation (8).

Controller output for a PID controller

$$e(t) = K_p e(t) + K_i \int_0^t e(\tau) d\tau + K_d \frac{d}{dt} e(t) \quad (8)$$

Where:

K_p : Proportional gain

K_i : Integral gain

K_d : Deviation gain

e : Error = SP (setpoint) – PV (process variable)

t : Time or instantaneous time

τ : variable of integration; takes on values from time 0 to present time t .

The valve is completely open at the initial time, and only becomes closed when the water cut value in the annulus is higher than the setpoint. The leak (LEAK-1) in **Figure 7** connects the annulus of production well to the inner flow path. Ideally, the pressure drop through the leak is negligible. Relevant parameters of the simulated AICV can be found in section 2.1.5.

3 Simulation results

There are two simulation cases demonstrated. One is for homogeneous reservoir with three AICVs and the other is for heterogeneous reservoir with six AICVs.

3.1 Simulation of homogeneous reservoir

Main flow diagram of homogeneous reservoir is shown in **Figure 8**.

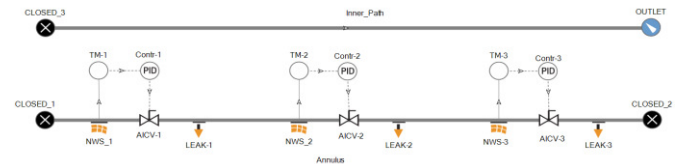


Figure 8. Flow diagram of simulation with homogeneous reservoir

There are three near-well sources, each of them connected to one AICV. The reservoir permeability is set as 2000 mD in the x and y direction and 200 mD at the z direction. Water Cut (WC) is used as set points for the controllers, and is defined as 0.3, 0.6 and 0.9 from left to the right respectively. The relevant results after 120 days of production are simulated and plotted.

3.1.1 Flow rate of oil and water in homogeneous reservoir simulation

Volumetric flow rates of oil and water at the outlet of the production well are plotted as a function of time and presented in **Figure 9**. It should be noticed that the valves cannot be completely closed, since the minimum opening of valves is set to be 0.008 as referred in section 2.1.6.

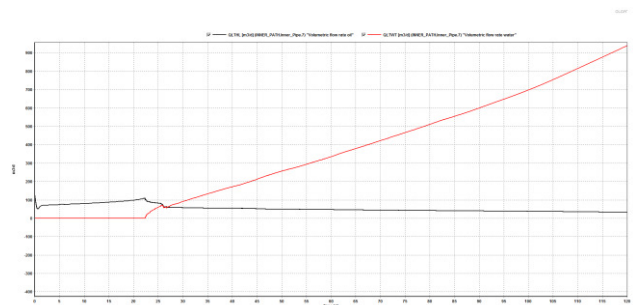


Figure 9. Volumetric flow rate of oil and water in homogeneous reservoir simulation

It can be observed that the water breakthrough takes place after 22 days of production, superseding the oil production rate at day 27, whereas the water production continues to increase rapidly with time. At the end time of the simulation, day 120, the water flow rate is 950 m³/d. In comparison, the oil production rate only slightly increases before day 22, and afterwards decreases slowly and continuously. The highest flow rate of oil is 100 m³/d at day 22; at the end time of simulation, this value is only 30 m³/d.

3.1.2 Controller signal of AICV in homogeneous reservoir simulation

Trend data of controller signals are plotted in **Figure 10**. Controller 1 (black line) starts to close at day 24 and is completely closed after day 26 days, controller 2 (blue line) starts to close after 30 days and becomes totally closed at day 35 and controller 3 (red line) closes at day 76 and at day 98 it is closed completely.

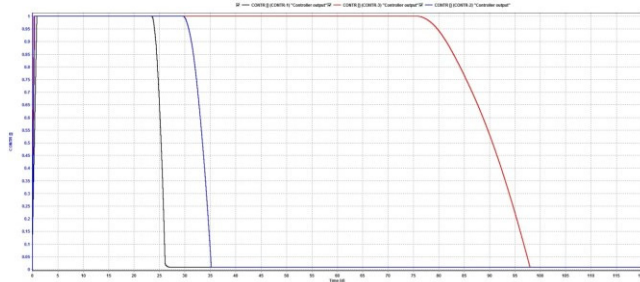


Figure 10. Controller output signal for homogeneous reservoir simulation

In order to make it easier to compare the descriptions of controller signal of the homogeneous reservoir, the results are summarized in **Table 2**.

Table 2. Controller signal of homogeneous reservoir simulation

Number of AICV	Color	Setpoint	Closing start day (d)	Fully close day (d)
1	black	0.3	24	26
2	blue	0.6	30	35
3	red	0.9	76	98

3.1.3 Oil saturation profile of homogeneous reservoir

Oil saturation profiles show the relative distribution of oil and water in the space of reservoirs at a specific time. Variation of oil saturation in y-z plane is of greater interest than along x direction.

The simulation results of oil saturation profiles can be viewed in Tecplot, a software package used in post-processing simulation results. (Tecplot) The oil saturation profiles after 15 days, 30 days, 60 days and 120 days of production are presented from **Figure 11** to **Figure 14**.

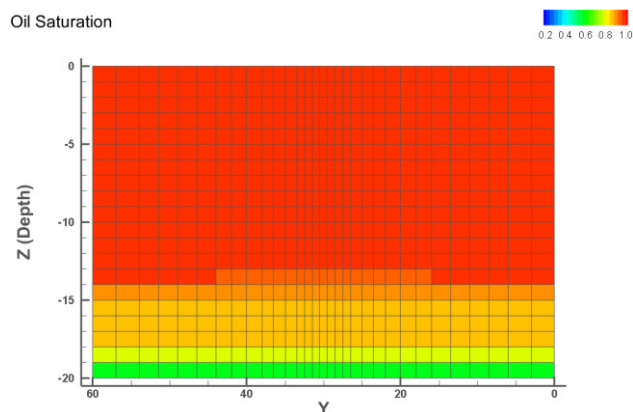


Figure 11. Oil saturation after 15 days of production in homogeneous reservoir

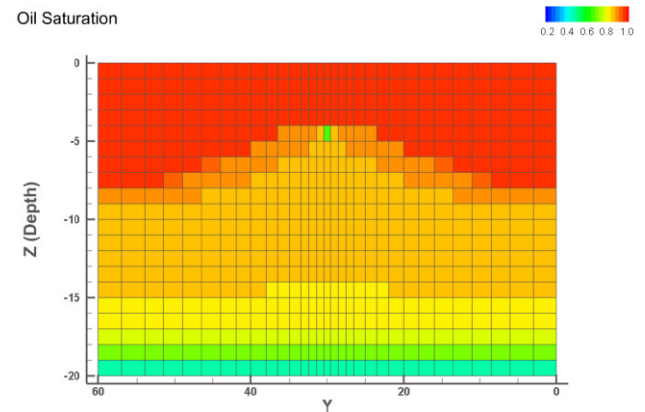


Figure 12. Oil saturation after 30 days of production in homogeneous reservoir

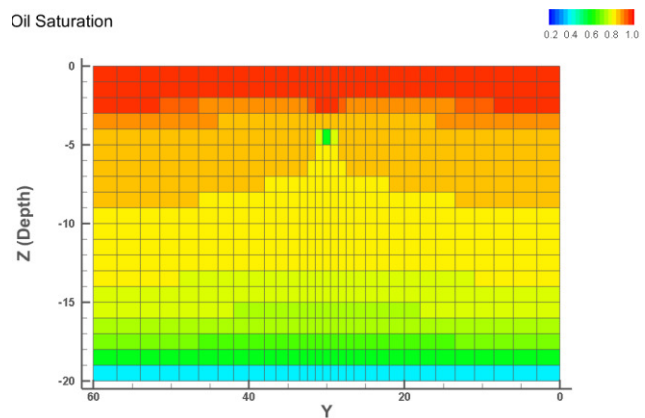


Figure 13. Oil saturation after 60 days of production in homogeneous reservoir

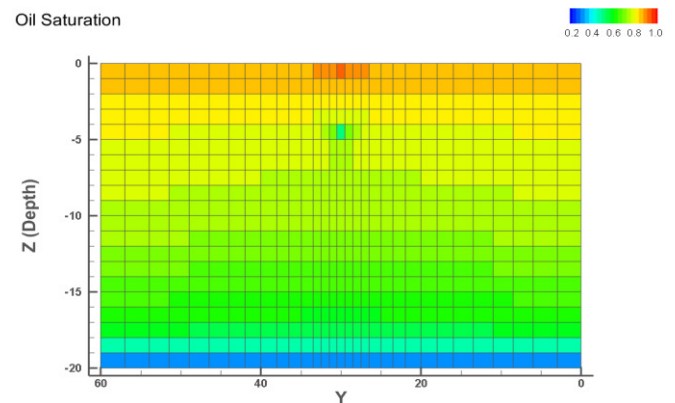


Figure 14. Oil saturation after 120 days of production in homogeneous reservoir

It can be seen the oil saturation in the reservoir decreases from the bottom and moves up to the production well with a cone shape (Figure 8 and 9). After the breakthrough of water to the well, the profile of oil saturation continues to increase and has two peaks at each side of the well (Figure 10 and 11).

3.2 Simulation of heterogeneous reservoir

The flow diagram of heterogeneous reservoir simulation is shown in **Figure 15**. In this case, there are two production regions, and 3 near-well sources in each region. The two regions are separated by a packer, included as a closed valve in the simulation setting. On the left side of the packer, the reservoir permeability is 2000 mD on x-y plane and 200 mD in z direction. In comparison, on the right side of the packer, the permeability is 5000 mD on x-y plane and 500 mD at z direction.

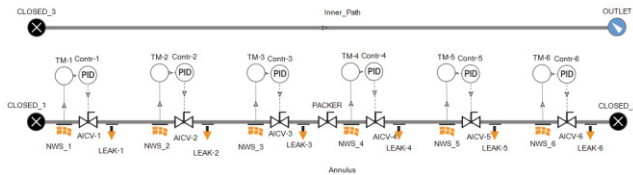


Figure 15. Flow diagram of Heterogeneous reservoir simulation

3.2.1 Volumetric flow rate of oil and water

The volumetric flow rates of oil and water production are plotted as presented in **Figure 16**.

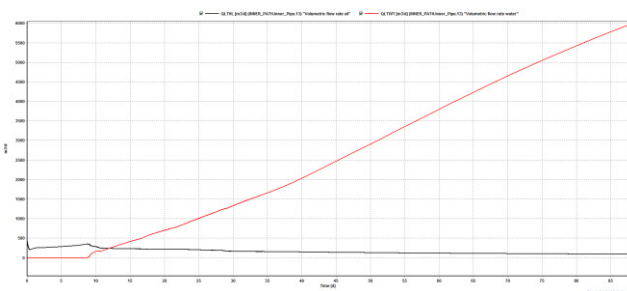


Figure 16. Volumetric flow rate of oil and water in homogeneous reservoir simulation

The water flow rate starts to increase rapidly from day 8, becomes higher than oil flow rate at day 12, and continues to increase with time afterwards. At the end day of the simulation, i.e. after 87 days, the volumetric water flow rate is close to 6000 m³/d.

However, the oil flow rate starts to decrease slowly after water breakthrough from 390 m³/d at day 8, to 90 m³/d at day 87.

3.2.2 Controller signal of heterogeneous reservoir

A plot of the six controllers' signal is given in **Figure 17**.

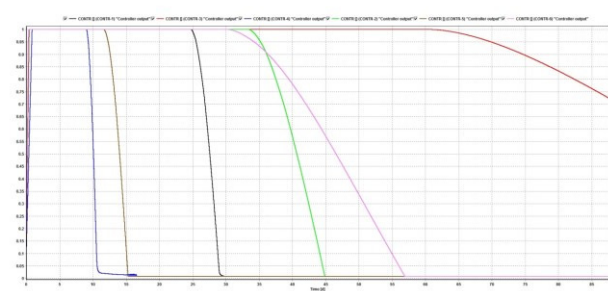


Figure 17. Controller output signal for heterogeneous reservoir simulation

The closing order of AICVs is No.4, No.5, No.1, No.6, No.2, and No.3, as shown in the figure. The last one, AICV No.3 is still in the process of closing at the end time of simulation (87 days). The summary of controller signals is listed in **Table 3**.

Table 3. Controller signal of heterogeneous reservoir simulation

Number of AICV	Color	Setpoint	Source x-y plane Permeability (mD)	Closing start (d)	Fully close (d)
1	black	0.3	2000	25	29
2	green	0.6	2000	34	45
3	yellow	0.9	2000	61	-
4	blue	0.3	5000	9	11
5	brown	0.6	5000	12	15
6	pink	0.9	5000	30	56

3.2.3 Oil saturation profile of heterogeneous reservoir

For the simulation of the heterogeneous reservoir, the oil saturation variance along the pipeline, x-direction, can be observed from **Figure 18** to **Figure 21**. For example, after 30 days of production, oil saturation at the well position is about 0.75 for both the production regions. However, the neighboring blocks for the low permeable region have clearly higher oil saturation than the high permeable region.

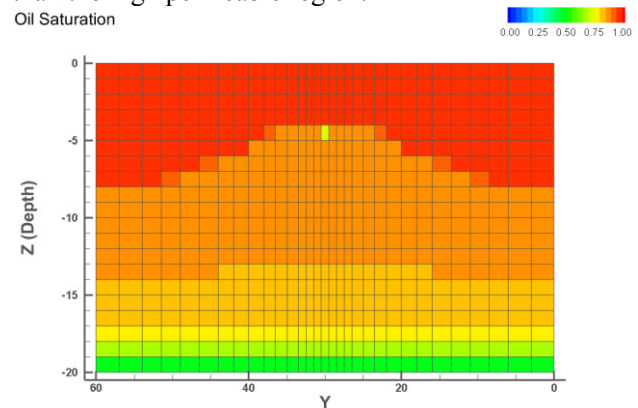


Figure 18. Oil saturation profile for I=1 in I-YZ plane after 30 days' production in heterogeneous reservoir

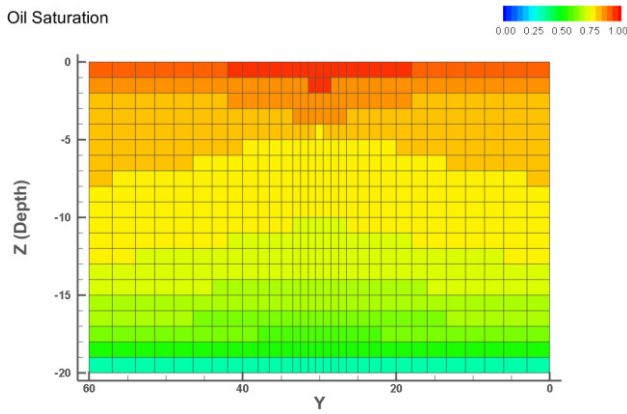


Figure 19. Oil saturation profile for I=6 in I-YZ plane after 30 days' production in heterogeneous reservoir

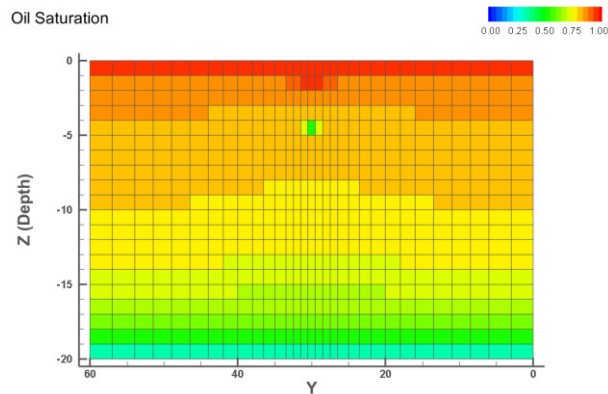


Figure 20. Oil saturation profile for I=1 in I-YZ plane after 120 days' production in heterogeneous reservoir

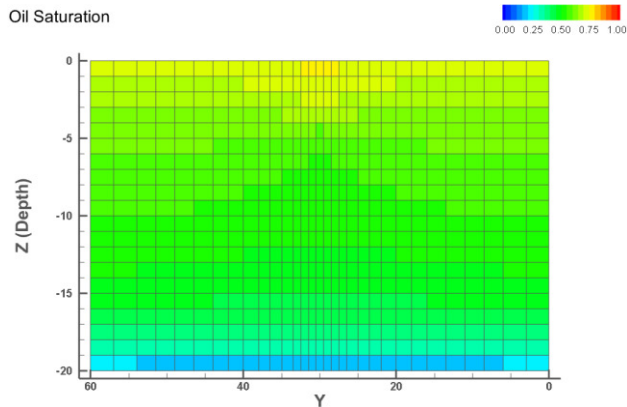


Figure 21. Oil saturation profile for I=6 in I-YZ plane after 120 days' production in heterogeneous reservoir

At the end of the simulation, 120 days, the oil saturation is around 0.5 at the location of the production well, as shown in and **Figure 20** and **Figure 21**. The oil saturation values for the neighboring blocks are still at least 0.75 in the low permeable region. But at high permeable regions, oil saturation values for the neighboring blocks are close to 0.5.

4 Discussion of results

4.1 High production rate of water

In the simulations of both the homogeneous and the heterogeneous reservoir, the volumetric flow rate of water supersedes the oil very soon after water breakthrough, and continues to increase until the end time of the simulation. This phenomenon is due to several reasons. First of all, the viscosity of water is much lower than the viscosity of oil at 125 bar and 120 °C. Secondly, during the production of oil, the oil saturation in the reservoir decreases while the water saturation increases. This causes the relative permeability of oil to decrease and relative permeability of water to increase.

Relative permeability is the ratio of the effective permeability of the actual phase to the absolute permeability. In other words, relative oil permeability is the ratio of effective permeability of oil to the absolute permeability of the reservoir, and similarly for the relative permeability of water.

The formula for calculating relative oil permeability and relative water permeability are given in equations (9) and (10).

Relative oil permeability

$$k_{ro} = \frac{k_{oil}}{k_{reservoir}} \quad (9)$$

Relative water permeability

$$k_{rw} = \frac{k_{water}}{k_{reservoir}} \quad (10)$$

In ROCX, there is a pre-defined series of relative permeability values of oil and water phase, and the plot of those data is shown in **Figure 22**. These values are valid for any arbitrary heavy oil reservoir, but are used in this study.

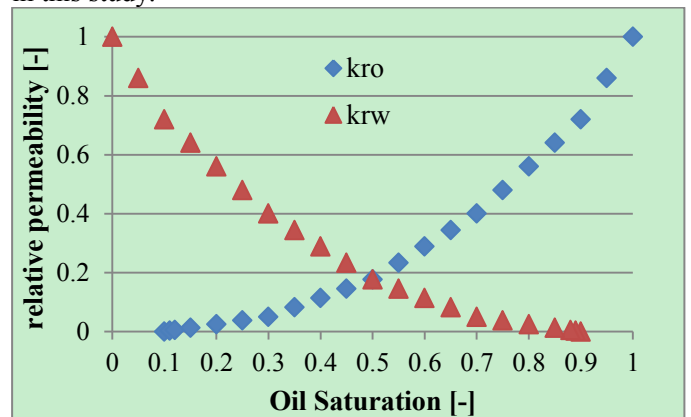


Figure 22. Relative permeability of oil and water over different oil saturation

Thus, the relative permeability values for oil and water at any oil saturation can be determined, either by direct reading or linear interpolation. In addition, Darcy's law can be used for calculating volumetric flow rate along a flow path.

Darcy's law for 1-dimensional flow is shown in equation (11).

$$Q = -\frac{kA}{\mu} \cdot \frac{dp}{dx} \quad (11)$$

Where Q is the discharge rate, k is the permeability, A is cross-sectional area of the flow, μ is dynamic viscosity, and $\frac{dp}{dx}$ is pressure gradient along the flow path. All these four parameters influence on the volumetric flow rate of the liquid mixture.

Viscosity of water is a function of temperature and pressure, mainly determined by temperature. Equation (12) shows the temperature dependency of water viscosity (Al-Shemmeri, 2012).

$$\mu(T) = 2.414 \times 10^{\left(\frac{247.8}{T-140}-5\right)} \quad (12)$$

where T has unit Kelvin and μ has unit $kg/(m \cdot s)$

Since the temperature of the SAGD chamber is 120 °C, the calculated dynamic viscosity of water is $2.30 \times 10^{-4} kg/(m \cdot s)$, or 2.30×10^{-7} cP. In comparison, the dynamic viscosity of heavy oil is assumed to be 100 cP, much larger than water.

For the near well mixture of oil and water, the only differences between oil and water are the viscosity and the effective permeability, i.e. cross-sectional area and pressure gradient are the same. Thus, the volumetric flow rate of the fluids can be compared by division. Since the relative permeability values of oil and water change with oil saturation, which varies with time, the values of oil saturation must be specified.

Mobility ratio is the ratio between water/oil volumetric flow rates. It depends on viscosity and permeability of water and oil phases.

Equation (13) Mobility ratio

$$\frac{Q_w}{Q_o} = \frac{\mu_o}{\mu_w} \cdot \frac{k_w}{k_o} \quad (13)$$

Mobility ratio can be calculated based on viscosity and relative permeability values of oil and water phase. Mobility ratios with oil saturation 0.2, 0.5 and 0.8 are listed in **Table 4**.

Table 4. Mobility ratio with different oil saturation values

Soil [-]	0.2	0.5	0.8
krw [-]	0.56	0.177	0.025
kro [-]	0.025	0.177	0.56
Mobility ratio [-]	9739	435	19.4

It is clear that the ratio between water and oil volumetric flow rate increases rapidly with the depletion of oil. As a result, in the initial period, the oil production rate is relatively high; however, when water breakthrough occurs, the water flow rate increases rapidly. The huge difference between volumetric flow rate of water and oil in the simulation can be understood, given the calculations above.

4.2 Controller signal of AICV

It can be observed that the closing performance of valves depends on both permeability of reservoir and set point of controllers, and the later one indicates the strength of the AICVs. Besides, the time it takes for the valves from the start of closing to they are fully closed also depends on those two factors.

The reason for the starting date of AICVs closing is easily understandable. The lower the setpoint, the earlier the setpoint of water cut is reached, since the oil saturation does not change much along the flow path. This can explain well the controller signal for the homogeneous reservoir.

According to the plot of the closing sequence in the heterogeneous reservoir, the other reason that influences the starting date of the closing is the permeability of the reservoir. It is obvious that the higher the permeability, the earlier the closing occurs. Controller 5, although with set point 0.5, even starts closing earlier than controller 1 with set point 0.2, due to the higher permeability.

Another interesting phenomenon is the time it takes for the AICVs to complete the closing progress. The PID controllers for the analogue AICVs have the same parameter settings, except for the setpoint. It can also be observed that the time span for closing the valves increases with increasing setpoint value, as reflected by the homogeneous reservoir simulation. Besides, the time span for the closing also decreases with reservoir permeability, which can be seen from heterogeneous reservoir simulation.

4.3 Oil saturation profile

The results of the oil saturation profile are reasonable and matches well with the controller signals.

Initially, only oil is present in the reservoir. As the production goes on, water comes from the bottom of the reservoir. Since the oil specific gravity is set as 0.85, and water at 120 °C and 125 bars has specific gravity 0.949 (peacesoftware: water density calculation), thus water is heavier and comes from the bottom.

In addition, the position of the production well in y-z plane is: $y=30$ (m) and $z = -5$ (m). As the production goes on, oil saturation nearest to the well drops firstly, and water continues to fill in the space of removed oil in the reservoir. The more oil produced the lower oil saturation, and the higher water flow rate. Till the time of water breakthrough, a cone-shaped oil saturation profile is formed.

From simulation of the heterogeneous reservoir, the lower permeable (2000 mD) region has larger difference of oil saturation near the production well. At the high permeable (5000 mD) region, neighboring blocks almost have the same oil saturation values as the well. Permeability plays an important role in oil

distribution in the reservoir during the production process.

4.4 Limitations of the study

4.4.1 Insufficient information of reservoir

In this study, a lot of simplifications and assumptions of the parameters of the reservoir are made, due to lack of detailed information for an exact reservoir. These details include geometry, porosity, permeability, relative permeability curves, initial oil and water saturation and fluid phase properties, etc. Among the assumptions and simplifications, there could be one or more that are not reasonable.

4.4.2 Implicit algorithm in OLGA

The mathematical approach in OLGA is implicit and the original program cannot be viewed or modified by users. Although the developers of OLGA programmed the software in a deliberate way, there are still some assumptions and simplifications behind. So, it is also possible that some options of simulation setting are not appropriate, causing imprecise or inaccurate result.

4.4.3 Macroscopic property of OLGA

OLGA is widely-used and powerful software, as discussed before, however, it is more suitable for macroscopic utilities rather than microscopic simulations. In this study specifically, although water cut can be calculated for each section of the pipeline, the exact place where the water is present cannot be approached. To clarify, the interface between water and oil in the annulus is not a perfect plane; oil can be accumulated in one spot for a period of time, meanwhile water is enriched in another spot. This is the case in which AICV shows its proficient ability in shutting down for water and allowing in for oil.

Even if the water cut is as high as 0.9, i.e. only 10% is oil in the annulus, oil can still be produced with high purity as long as at least one of the AICVs is covered by oil.

4.5 Prospective improvements

If more details of the reservoir are available, then practical parameters of the reservoir and the fluids can be used. With less assumptions and guesses, the simulation results can be more realistic. The most important parameters include but are not limited to permeability, porosity, relative permeability curve, initial oil and water saturation. All of these parameters can more or less influence the simulation result. Future study could focus on sensitivity analysis for quantifying results uncertainty.

5 Conclusion

In this study, simulations of the SAGD process are performed using the multiphase simulator OLGA in

combination with near well simulation tool ROCX. Since gas breakthrough causes energy loss and lower production rate in SAGD process, AICVs are often used to avoid this problem. In OLGA, a simulated AICV is built up by a normal valve combined with a water-cut transmitter and a PID controller. Controller signals of analogue AICVs have shown that the valves can shut down for water (and thereby also steam), and that the closing time of valves are dependent on WC setpoint of the PID controllers.

Simulations of both homogeneous and heterogeneous reservoirs have shown significant increase of water flow rate after breakthrough. Even when the AICVs are closing one by one and the oil flow rate begins to decrease; the water flow rate continues to increase. This is partly due to much lower viscosity of water compared to oil at high temperature. Another important reason is that water relative permeability increases with oil production. Calculations results show that the volumetric flow rate ratio between water and oil is 19.4 when oil saturation is 0.2, while this ratio changes to 9739 when oil saturation is 0.8.

Tecplot is used to view the results for individual reservoir blocks. The oil saturation profiles in Tecplot well indicate the water breakthrough time in both homogeneous and heterogeneous reservoirs. For the heterogeneous reservoir simulation, oil saturation profiles at regions with different permeability are compared. And it can be seen that the oil saturation has larger differences near the production well in the lower permeable region. This is also reasonable and can be explained by Darcy's law.

There are three main limitations of this simulation study: lack of detailed reservoir information, implicit algorithm, and macroscopic properties in OLGA. The prospect for improvement is to add detailed and practical parameters of a specific reservoir to OLGA and ROCX.

References

- Aakre, H. (2015). *Autonomous Inflow Control Valve for Heavy and Extra-Heavy Oil*. SPE International.
- Al-Shemmeri, T. (2012). *Engineering Fluid Mechanics*. Ventus Publishing ApS.
- Alvarez, Johannes, and Sungyun Han. (2013). *Current Overview of Cyclic Steam Injection*. Journal of Petroleum Science Research.
- Banerjee, D. K. (2012). *OIL SANDS, HEAVY OIL & BITUMEN*. Tulsa, Oklahoma: PennWell Corporation.
- Dusseault, M. (2001). *Comparing Venezuelan and Canadian heavy oil and tar sands*. Retrieved from South Portland: http://www.southportland.org/files/3713/9387/3165/Heavy_Oil_and_Tar_Sands.pdf

- Hoffman, B. Todd, and Anthony R. Kovscek. (2003). *Light-Oil Steamdrive in Fractured Low-Permeability Reservoirs*. SPE Western Regional/AAPG Pacific Section Joint Meeting.
- InflowControl. (n.d.). *AICV*. Retrieved from YouTube: <https://www.youtube.com/watch?v=E2g4hxGZP94>
- InflowControl. (n.d.). *AICV Technology*. Retrieved from InflowControl: <http://www.inflowcontrol.no/about-aicv/>
- International Energy Outlook 2010*. (2010). US. Energy Information Administration.
- Jørgensen, Ø. (2010). *Reservoir modelling of lithofacies scale heterogeneities within the middle McMurray formation*. Alberta, Canada.
- mathworks. (2015). *MATLAB*. Retrieved from <http://www.mathworks.com/products/matlab/>
- Meyer, R. F. (2003). *Heavy Oil and Natural Bitumen*. Retrieved from USGS: <http://pubs.usgs.gov/fs/fs070-03/fs070-03.html>
- peacesoftware: water density calculation*. (n.d.). Retrieved from peacesoftware: http://www.peacesoftware.de/einigewerte/calc_dampf.php5
- Polikar. (2000). *Fast-SAGD: half the wells and 30% less steam*. SPE/CIM International Conference on Horizontal Well Technology. Society of Petroleum Engineers.
- Purkayastha, S. N. (n.d.). *Control and optimization of steam injection for Steam-Assisted Gravity Drainage (SAGD)*. Retrieved from <http://people.ucalgary.ca/~spurkaya/research.html>
- Schlumberger. (n.d.). *OLGA Dynamic Multiphase Flow Simulator: User Manual*. Schlumberger.
- Schlumberger. (n.d.). *OLGA ROCX*. Retrieved from http://www.software.slb.com/store/_layouts/SLB/Pages/ProductDetailPage.aspx?pid=AROX-M1
- Schlumberger. (n.d.). *Schlumberger OLGA*. Retrieved from <http://www.software.slb.com/products/foundation/Pages/olga.aspx>
- Sheng, J. J. (2011). *Modern Chemical Enhanced Oil Recovery*. Burlington, USA: Gulf Professional Publishing.
- Speight, J. G. (2013). *Heavy oil production processes*. Waltham: Gulf Professional Publishing.
- Tecplot. (n.d.). *Tecplot*. Retrieved from <http://www.tecplot.com/>
- Torsæter, O. (2011). *Heavy oil reservoirs*. Retrieved from NASJONAL FORSKERSKOLE I PETROLEUMSFAG: <http://nfipweb.org/oneday2011/HeavyOiIntroNov11.pdf>
- Yves, A. (2011). *Heavy crude oils: an overview from geology to upgrading*. Ginoux, France: TECHNIP.

Recursive dynamic modelling in changing operating conditions

Esko K. Juuso

Control Engineering Group, Faculty of Technology, University of Oulu, Finland
esko.juuso@oulu.fi

Abstract

Changing operating condition may require updates for the dynamic models. Recursive updates are needed especially when sufficient information about the new situations is not available. In machine diagnostics and prognostics, the analysis starts from good conditions and new phenomena activated with time may considerably change the model. In biological wastewater treatment processes, the condition of the biomass drastically changes during the operation of the treatment process. Measurements based on the image analysis of the biomass condition is recently included. Recursive modelling is clearly needed in these situations. The usual approach is to modify the model equations. However, the interactions do not necessarily change if the meanings of the variables are modified. This paper keeps the model equations constant and modifies the non-linear scaling of the variables by extending the data-driven scaling to a recursive approach. The recursive methodology is tested in two applications: machine diagnostics and wastewater treatment.

Keywords: intelligent modelling, recursive statistical analysis, adaptive modelling, prognostics, transitions

1 Introduction

Changing operating conditions need to be taken into account in prognostics since new phenomena activate gradually with time. In the condition-based maintenance (CBM), the most obvious and widely used form of prognostics is to predict how much time is left before a failure occurs. The time left before observing a failure is usually called remaining useful life (RUL) (Jardine et al., 2006). It is even better if the maintenance actions are taken before the failure occurs, especially when a fault or a failure is catastrophic. Dynamic models include hazard functions and stochastic processes for the process states which activate with time. A time-dependent proportional hazard model (PHM) has a hazard function of the form

$$h(t) = h_0(t) \exp\left(\sum_{j=1}^n \eta_j x_j(t)\right) \quad (1)$$

where $h_0(t)$ is a baseline hazard function, $x_j(t)$, $j = 1, \dots, m$, are covariates which are functions of time and

$\eta_j(t)$, $j = 1, \dots, m$ are coefficients. The baseline hazard function $h_0(t)$ can be in non-parametric or parametric form, e.g. a Weibull hazard function, which is the hazard function of the Weibull distribution. The covariates $x_j(t)$, $j = 1, \dots, m$, can be any condition variables such as health indicators and features in condition monitoring. (Jardine et al., 2006)

In biological wastewater treatment in pulp and paper industry, a lot of process measurements are available, but measurement sets do not include sufficient information on the special features of the influent nor on the microbial composition of the sludge (Juuso, 2009a). Activated Sludge Models provide a basis for phenomenological modelling and can be linked to process expertise (Henze et al., 1987; Lindblom, 2003). Their use has been limited by complexity of the models. Hybrid models with a cascade approach are needed in biological wastewater treatment to cover different operating conditions. The condition of the biomass need to modelled as well (Juuso, 2009a).

Many variables are normally measured in a plant, but some of them are strongly cross-correlated. Data-based analysis is needed for variable selection (Teppola et al., 1997; Mujunen et al., 1998; Oliveira-Esquerre et al., 2002) and for detection of operating conditions has used in (Heikkinen et al., 2008b) to analyse specialised submodels. As the sludge settling properties have remarkable effects on the treatment results, the modelling of the diluted sludge volume index (DSVI) is important (Heikkinen et al., 2008b). Heikkinen et al. (2008a) used models for predicting the chemical oxygen demand (COD) of the effluent in an industrial activated sludge plant. Image analysis has been studied in (Tomperi et al., 2015) to find out dependencies to the process variables of the plant and to the quality of the treated wastewater.

The main idea of time series modelling is to fit the waveform data to a parametric time series model and extract features based on this parametric model, where the output at time t can depend on many signal values y from previous time instants. The amount of signals should be chosen according to the appropriate time delays (Ljung, 1999). Fuzzy and neural models are based on the same structures. The most common structure for the input-output models is the NARX /Nonlinear AutoRegressive

with eXogenous input model, where the input and output values are chosen according to appropriate system orders, as in the ARX model. The regressor vector consists of a finite number of past inputs and outputs (Babuška and Verbruggen, 2003). Another possibility is to use recurrent networks, e.g. Elman networks are two-layer feedforward networks, with the addition of a feedback connection from the output of the hidden layer to its input (Elman, 1990).

The basic form of the linguistic equation (LE) model is a static mapping in the same way as fuzzy set systems and neural networks, and therefore dynamic models will include several inputs and outputs originating from a single variable (Juuso, 2004). External dynamic models provide the dynamic behaviour, and LE models are developed for a defined sampling interval in the same way as in various identification approaches discussed in (Ljung, 1999). Nonlinear scaling reduces the number of input and output signals needed for the modelling of nonlinear systems. For the default LE model, all the degrees of the polynomials become very low:

$$Y(t) + a_1 Y(t-1) = b_1 U(t - n_k) + e(t) \quad (2)$$

for the scaled variables Y and U .

The nonlinear scaling maps from the operation area of the (sub)system, defined with feasible ranges, to the linguistic values represented inside a real-valued interval $[-2, 2]$. The feasible range is defined by a membership function, and membership functions for finer partitions can be generated from membership definitions (Juuso et al., 1993). The basic scaling approach presented in (Juuso, 2004) has been improved later: a new constraint handling was introduced in (Juuso, 2009b), and a new skewness based methodology was presented for signal processing in (Juuso and Lahdelma, 2010).

Recursive modelling can be done by including new model components as in (1) or by modifying the coefficients as is done in identification. The highly complex model structures, which are based on data fitting, can be difficult to understand. In LE models, the structure is kept compact, see (2), to keep process insight clear.

This paper combines compact model structures with the data-driven analysis of variable meanings and discusses results and requirements in two applications: machine diagnostics and wastewater treatment.

2 Nonlinear scaling

Scaling functions are monotonously increasing functions $x_j = f(X_j)$ where x_j is the variable and X_j the corresponding scaled variable. The function $f()$ consist of two second order polynomials, one for the negative values of X_j and one for the positive values, respectively. The corresponding inverse functions $x_j = f^{-1}(X_j)$ based on square root functions are used for scaling to the range $[-2, 2]$, denoted linguistification. In LE models, the results are scaled to the real values by using the function $f()$.

The parameters of the functions are extracted from measurements by using generalised norms and moments. The support area is defined by the minimum and maximum values of the variable, i.e. the support area is $[\min(x_j), \max(x_j)]$ for each variable $j, j = 1, \dots, m$. The central tendency value, c_j , divides the support area into two parts, and the core area is defined by the central tendency values of the lower and the upper part, $(c_l)_j$ and $(c_h)_j$, correspondingly. This means that the core area of the variable j defined by $[(c_l)_j, (c_h)_j]$ is within the support area.

2.1 Generalised norms

The corner points can be extracted from measurements with generalised norms defined by

$$\|\tau M_j^p\|_p = (\tau M_j^p)^{1/p} = \left[\frac{1}{N} \sum_{i=1}^N (x_j)_i^p \right]^{1/p}, \quad (3)$$

where $p \neq 0$, is calculated from N values of a sample, τ is the sample time. With a real-valued order $p \in \mathfrak{R}$ this norm can be used as a central tendency value if $\|\tau M_j^p\|_p \in \mathfrak{R}$, i.e. $x_j > 0$ when $p < 0$, and $x_j \geq 0$ when $p > 0$. For variables with only negative values, the norm is the opposite of the norm obtained for the absolute values. If a variable has both positive and negative values, each norm is an average of two norms where the data sets are made positive and negative by subtracting a value $x_L < \min((x_j))$ and a value $x_H > \max(x_j)$, respectively (Juuso, 2011). These norms generalise the earlier analysis based on arithmetic means or medians (Juuso, 2004).

The computation of the norms can be divided into the computation of equal sized sub-blocks, i.e. the norm for several samples can be obtained as the norm of the norms of the individual samples:

$$\|^{K_s} \tau M_j^p\|_p = \left\{ \frac{1}{K_s} \sum_{i=1}^{K_s} [(\tau M_j^p)_i]^{1/p} \right\}^{1/p} = \left[\frac{1}{K_s} \sum_{i=1}^{K_s} [(\tau M_j^p)_i]^{1/p} \right]^{1/p}, \quad (4)$$

where K_s is the number of samples $\{x_j\}_{i=1}^N$. In automation and data collection systems, the sub-blocks are normally used for arithmetic mean ($p = 1$).

2.2 Parameters

The generalised skewness γ_3^p is used when choosing appropriate methods for defining the central tendency. The central tendency value and the core area are based on the normalised moment

$$\gamma_k^p = \frac{1}{N \sigma_j^k} \sum_{i=1}^N [(x_j)_i - \|\tau M_j^p\|_p]^k \quad (5)$$

where k is a positive integer. The standard deviation σ_j , which is calculated about the origin, is used to obtain a dimensionless feature. (Juuso and Lahdelma, 2010) The

central tendency value is chosen by the point where the skewness changes from positive to negative, i.e. $\gamma_3^p = 0$. Then the data set is divided into two parts: a lower part and an upper part. The same analysis is done for these two data sets. The estimates for the corner points, $(c_l)_j$ and $(c_h)_j$, are the points where $\gamma_3^p = 0$ for the lower and upper data sets, respectively.

3 Recursive modelling

Recursive data analysis facilitates the adaptation of the functions to changing operating conditions, also the orders of the norms are re-analysed if needed. The existing scaling functions provide a basis for assessing the quality of the new data: outliers should be excluded, but the suspicious values may mean that the operating conditions are changing. In this research, the scaling functions are extended for analysing outliers and suspicious values to select data for the adaptive scaling. Different operating areas can be analysed from previous measurements with various clustering methods and the statistical process control (SPC) provides additional tools for detecting changes, anomalies and novelties in connection with the operation.

3.1 Data selection

Process data often contains outliers, which must be removed before generating the feasible area, because the procedure described above is sensitive to them. This is the idea in medians and trimmed means, which are used for the data samples containing outliers. A good estimate for the support area can be obtained with the generalised norms (3) with large negative and large positive orders since these features are less sensitive to the outliers than the minimum and maximum values. Discarding values at the high and low end can be used together with the generalised norms if there are obvious outliers. Trimming does not need to be the same for the low and high values.

Clear outliers need to be excluded in both the first analysis and the subsequent adaptation steps. In linear scaling, the z-score values outside the range $[-3, 3]$ are often considered as an indication of an outlier. This is a feasible solution for the normal distribution, but it is not optimal for steeper and wider distributions. The effect of the shape factor is presented in Figure 1.

For LE models, the scaled values X_j are in the range $[-2, 2]$ (Figure 2), and this is also the range for the monotonous increase if $\alpha_j^- = \alpha_j^+ = \frac{1}{3}$. The minimum and maximum points depend on the shape factors: the maximum point in the linguistic range

$$(X_j)_{max} = -\frac{b_j^+}{2\alpha_j^+} = \frac{3 - \alpha_j^+}{2(\alpha_j^+ - 1)}, \quad (6)$$

which goes to infinity when $\alpha_j^+ \rightarrow 1$, and the upper polynomial does not have any maximum point when $\alpha_j^+ > 1$.

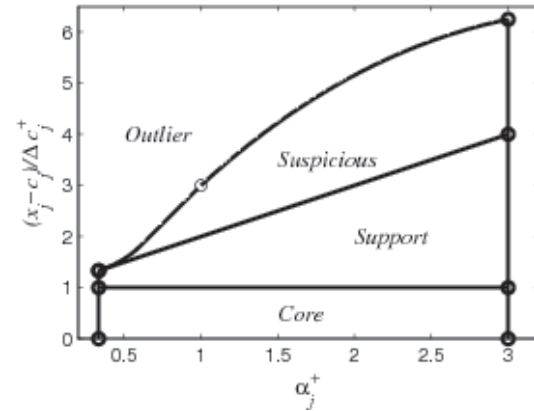


Figure 1. Relative score values for the core, support, suspicious and outlier areas as a function of the shape factor $\alpha_j^+ = 3$.

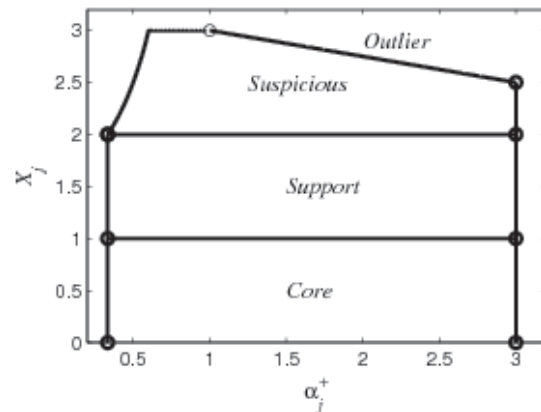


Figure 2. Scaled score values for the core, support, suspicious and outlier areas as a function of the shape factor $\alpha_j^+ = 3$.

3.2 Adaptation

The parameters of the nonlinear scaling functions can be recursively updated with (4) by including new equal sized sub-blocks in calculations. The number of samples K_s can be increasing or fixed with some forgetting, and weighting of the individual samples can be used in the analysis. If the definitions should cover all the operating areas, also suspicious values are included as extensions of the support area. In each adaptation step, the acceptable ranges of the shape factors α_j^- and α_j^+ are checked and corrected if needed. The orders $(p_l)_j$, $(p_0)_j$ and $(p_h)_j$ of the corresponding norms are re-analysed if the distribution is changing considerably with new measurements.

Since the search of these points is performed by using the order of the moment, the resulting orders $(p_l)_j$, $(p_0)_j$ and $(p_h)_j$ are good estimates when additional data sets are used. The norm values are recursively updated with (4), and a new search for the orders is done only if the values change considerably (Juuso, 2011).

Data values are classified with fuzzy logic to three categories: (1) extended area, (2) new operating area, or

(3) outliers. Decision is based on the difference of the feasibility areas of the recent data and the current definitions. Outliers were discussed in the previous section. High overlap supports the extension alternative. Lower and lower overlap proposes a new operating area. The approach goes smoothly and requires several new data points to change the parameters. The window of the short recent time period depends on the process. The decisions should be based on expert knowledge, especially when really drastic changes are detected.

3.3 LE Models

The same model, e.g. (2), is used all the time, even with same coefficients. The recursive adaptation is principally done by updating for the parameters of the scaling functions. The coefficients are updated in the second level, and naturally, it is also possible to include more equations if needed. The solution is more compact than repeated regression analysis to get the coefficients of the models. Naturally, the scaling approach can be enhanced with regression if needed.

4 Applications

The approach is aimed for processes where the online modelling is needed to adapt in new situations without sufficient information needed in predefined adaptation.

4.1 Prognostics

Remaining useful life (RUL) is a conditional random variable, which is estimated by using the current age and the past condition profile up to the current moment. The failure is assumed as a case where the fault defined by the condition variables reaches a predetermined level. The need for detailed prognostics could be detected by monitoring indices with SPC. The indication could be given when the index exceeds the warning level. (Lahdelma and Juuso, 2011)

Trend monitoring of vibration features is a more useful maintenance tool than a one-time survey of absolute magnitudes (Kaufman, 1975). Models have been presented for the increase of vibrations with the machine operation time, e.g. according to (Sankar and Xistris, 1972; Collacott, 1977) the increase is first linear and turns into exponential when 75 % of the machine life time is exceeded. However, the life time is not known as it varies from machine to machine. Degradation curves can be based on time series analysis where time series models are developed to trend the condition variables for failure prediction. A dynamic model can also be used. Heng et al. (2009) used a feedforward neural network.

Trends from two paper machines are analysed in (Lahdelma and Juuso, 2011). In the first case, the resonance of the press section resulted in a fast increase of the

root mean square velocity, v_{rms} . The machine speed was reduced 4 %, and a breakdown and an additional stoppage were avoided. The machine operated with reduced speed for two weeks, and the same or lower vibration level was kept for one week. In the second case, resin problems of a press roll in the felt washer were seen as a typical trend represented by

$$\ln \frac{v_{rms}(t)}{(v_{rms})_0} = b_0 + b_1 t + b_2 t^2, \quad (7)$$

where b_0 , b_1 and b_2 are constants. The velocity v_{rms} is growing with an accelerating speed (Figure 3). The models for the periods one and two are linear in a semilogarithmic scale, but the model for the whole data set requires the quadratic term.

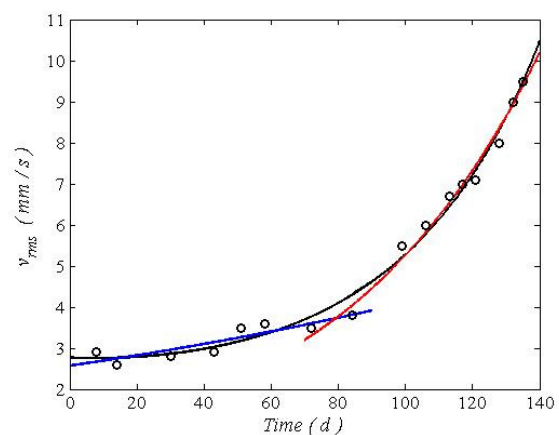


Figure 3. Exponential models v_{rms} (Lahdelma and Juuso, 2011).

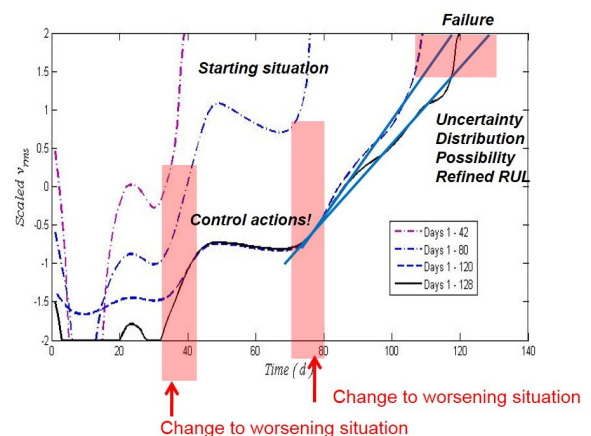


Figure 4. Recursive adaptation in prognostics.

In prognostics, the scaling functions are expanding when the new phenomena activate (Figure 4). The first models do not predict a failure: they are only used to detect the need for the update. Later, the LE models, which are in Figure 4 shown as lines, predict well the failure. In the beginning, the time window includes only good operation. Since the window is continuously increased, it contains the whole data only in the end.

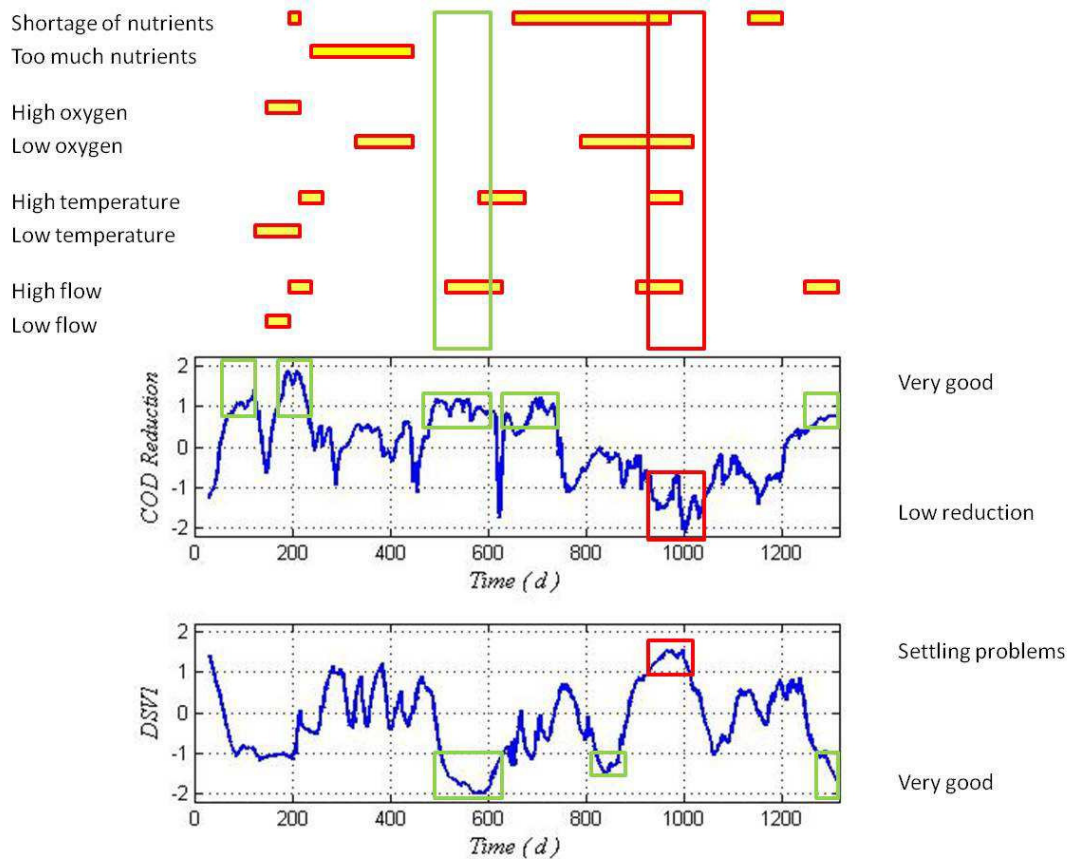


Figure 5. Treatment results of an activated sludge treatment plant: reduction of chemical oxygen demand (COD) and diluted sludge volume index (DSVI), see (Juuso, 2010).

In prognostics, the data points do not always cover the whole area of operation, e.g. only the close neighbourhood of the normal operation point may be covered, or we would like to extend the model of upper part later to the lower part. In fault diagnosis, only one part may be in use. In these cases, expert knowledge is used in extending the feasible range or selecting the methodologies.

4.2 Wastewater treatment

Biological water treatment depends strongly on the operating conditions. Load and nutrient levels should be balanced since both an exceptionally high load and excess nutrients cause problems. The operating conditions are modified by oxygen, temperature and flow. The worst case, which includes both low reduction and settling problems, arise when there multiple warnings and alarms (Figure 5). Correspondingly, good reduction and very good settling is achieved when there were very few warnings. As it takes some time to lose good conditions and recover from problematic conditions, the intelligent indices are useful for supervisory control.

In wastewater treatment, all the alternative decisions are feasible. Drastic changes take place, but they start with smooth changes (Figure 5). Strong transitions are especially seen in settling: different operating conditions are

seen in the parameters of the scaling functions of the measurements: temperature, oxygen, flow and nutrient feed. A moving window is suited for these applications to recursively update the parameters of the scaling functions. The coefficients and variables of the model are the same in all operating conditions. The new measurements reported in (Tomperi et al., 2015) are included in the analysis.

5 Conclusions

Changing operating condition can be handled by updating the scaling functions without specific information about the new situations. The recursive analysis operates well and the nature of the process can be taken into account. In machine diagnostics and prognostics, the scaling functions are expanded when new phenomena activate. In wastewater treatment, drastic changes require completely new parameters. The model equations are not changed.

Acknowledgment

This work was done within the research program “Measurement, Monitoring and Environmental Efficiency Assessment (MMEA)” funded by the TEKES (the Finnish Funding Agency for Technology and Innovation).

References

- R. Babuška and H. Verbruggen. Neuro-fuzzy methods for non-linear system identification. *Annual Reviews in Control*, 27(1):73–85, 2003.
- R. A. Collacott. *Mechanical Fault Diagnosis and Condition Monitoring*. Chapman and Hall, London, 1977.
- J. L. Elman. Finding structure in time. *Cognitive Science*, 14(2):179–211, 1990.
- M. Heikkinen, T. Heikkinen, and Y. Hiltunen. Modelling of activated sludge treatment process in a pulp mill using neural networks. In *The 6th International Conference on Computing, Communications and Control Technologies: CCCT 2008, Orlando, Florida, USA, June 29th - July 2nd 2008.*, page 6 pp. 2008a.
- M. Heikkinen, T. Latvala, E. Juuso, and Y. Hiltunen. SOM based modelling for an activated sludge treatment process. In *Tenth International Conference on Computer Modelling and Simulation, EUROSIM/UKSim, Cambridge, UK, April 13, 2008.*, pages 224–229. The Institute of Electrical and Electronics Engineers IEEE, 2008b. doi: 10.1109/UKSIM.2008.78.
- A. Heng, A. C. C. Tan, J. Mathew, N. Montgomery, D. Banjevic., and A. K. S. Jardine. ‘intelligent condition-based prediction of machinery reliability. *Mechanical Systems and Signal Processing*, 23(5):1600–1614, 2009.
- M. Henze, C. P. L. Grady Jr., W. Gujer, G. V. R. Marais, and T. Matsuo. Activated sludge model no. 1., IAWQ scientific and technical report no. 1. London, UK, 1987.
- A. K. S. Jardine, D. Lin, and D. Banjevic. A review on machinery diagnostics and prognostics implementing condition-based maintenance. *Mechanical Systems and Signal Processing*, 20(7):1483–1510, 2006.
- E. Juuso and S. Lahdelma. Intelligent scaling of features in fault diagnosis. In *7th International Conference on Condition Monitoring and Machinery Failure Prevention Technologies, CM 2010 - MFPT 2010, 22-24 June 2010, Stratford-upon-Avon, UK*, volume 2, pages 1358–1372, 2010. URL www.scopus.com.
- E. K. Juuso. Integration of intelligent systems in development of smart adaptive systems. *International Journal of Approximate Reasoning*, 35(3):307–337, 2004. doi: 10.1016/j.ijar.2003.08.008.
- E. K. Juuso. Hybrid models in dynamic simulation of a biological water treatment process. In J. Kunovský, P. Hanáček, F. Zboril, Al-Dabass, and A. Abraham, editors, *Proceedings First International Conference on Computational Intelligence, Modelling and Simulation, 7- 9 September 2009, Brno, Czech Republik*, pages 30–35. IEEE Computer Society, 2009a. doi: 10.1109/CSSim.2009.52.
- E. K. Juuso. Tuning of large-scale linguistic equation (LE) models with genetic algorithms. In M. Kolehmainen, editor, *Revised selected papers of the International Conference on Adaptive and Natural Computing Algorithms - ICANNGA 2009, Kuopio, Finland, Lecture Notes in Computer Science*, volume LNCS 5495, pages 161–170. Springer-Verlag, Heidelberg, 2009b. doi: 10.1007/978-3-642-04921-7_17.
- E. K. Juuso. Data-based development of dynamic models for biological wastewater treatment in pulp and paper industry. In *SIMS 2010 Proceedings, The 51st Conference on Modelling and Simulation, Oulu, 14-15 October, 2010*. 2010. 9 pp.
- E. K. Juuso. Recursive tuning of intelligent controllers of solar collector fields in changing operating conditions. In S. Bittani, A. Cenedese, and S. Zampieri, editors, *Proceedings of the 18th World Congress The International Federation of Automatic Control, Milano (Italy) August 28 - September 2, 2011*, pages 12282–12288. IFAC, 2011. doi: 10.3182/20110828-6-IT-1002.03621.
- E. K. Juuso, J.C. Bennavil, and M.G. Singh. Hybrid knowledge-based system for managerial decision making in uncertainty environment. In N. Piera Carreté and M. G. Singh, editors, *Qualitative Reasoning and Decision Technologies, Proceedings of the IMACS International Workshop on Qualitative Reasoning and Decision Technologies -QUARDET’93, Barcelona, June 16 - 18, 1993*, pages 234–243, Barcelona, 1993. CIMNE.
- A. B. Kaufman. ‘measure machine vibration – it can help you anticipate and prevent failures. *INSTRUMENTS & CONTROL SYSTEMS*, 48:50–62, 1975.
- S. Lahdelma and E. Juuso. Trend analysis in condition monitoring of process equipments. In *Proceedings of the 8th International Conference on Condition Monitoring and Machinery Failure Prevention Technologies, CM 2011 - MFPT 2011, 20-22 June 2011, Cardiff, UK*, volume 2, pages 904–913. Curran Associates, NY, USA, 2011. ISBN 978-1-61839-014-1.
- E. Lindblom. *Dynamic modelling of nutrient deficient wastewater treatment process. M.Sc. Thesis*. Lund University, Lund, Sweden, 2003. TEIE-5175.
- L. Ljung. *System Identification - Theory for the User*. Prentice Hall, Upper Saddle River, N.J., 2nd edition, 1999.
- S.-P. Mujunen, P. Minkkinen, P. Teppola, and R.-S. Wirkkala. Modeling of activated sludge plants treatment efficiency with PLSR: a process analytical case study. *Chemometrics and Intelligent Laboratory Systems*, 41(1):83–94, 1998.
- K. P. Oliveira-Esquerre, M. Mori, and R. E. Bruns. Simulation of an industrial wastewater treatment plant using artificial neural networks and principal component analysis. *Brazilian Journal of Chemical Engineering*, 19(4):365–370, 2002.
- T. S. Sankar and G. D. Xistris. Measure machine vibrations - It can help you anticipate and prevent failures. *Journal of Engineering for Industry*, 94:133–137, 1972.
- P. Teppola, S.-P. Mujunen, and P. Minkkinen. Partial least squares modeling of an activated sludge plant: A case study. *Chemometrics and Intelligent Laboratory Systems*, 38(2):197–208, 1997.
- J. Tomperi, E. Koivuranta, A. Kuokkanen, E. K. Juuso, and K. Leiviskä. Real-time optical monitoring of the wastewater treatment process. *Environmental Technology*, pages 1–8, 2015. doi:10.1080/09593330.2015.1069898.

Robust Simulation for Hybrid Systems: *Chattering Bath Avoidance*

Ayman ALJARBOUH¹ Benoit CAILLAUD¹

¹INRIA/IRISA Rennes, Campus de Beaulieu, 35042 Rennes Cedex, France,
{ayman.aljarbough,benoit.caillaud}@inria.fr

Abstract

The sliding mode approach is recognized as an efficient tool for treating the chattering behavior in hybrid systems. However, the amplitude of chattering, by its nature, is proportional to magnitude of discontinuous control. A possible scenario is that the solution trajectories may successively enter and exit as well as slide on switching manifolds of different dimensions. Naturally, this arises in dynamical systems and control applications whenever there are multiple discontinuous control variables. The main contribution of this paper is to provide a robust computational framework for the most general way to extend a flow map on the intersection of p intersected $(n - 1)$ -dimensional switching manifolds in at least p dimensions. We explore a new formulation to which we can define unique solutions for such particular behavior in hybrid systems and investigate its efficient computation/simulation. We illustrate the concepts with examples throughout the paper.

Keywords: Hybrid systems, Non-smooth dynamical systems, Discontinuity mappings, Chattering-free simulation, Numerical methods.

1 Introduction

Hybrid systems are heterogeneous dynamical systems exhibiting both continuous and discrete dynamics. Systems of this type arise naturally in control systems where the value of a control variable may jump or whenever the laws of physics are discontinuous. They are common in a wide variety of engineering applications dealing with multi-modal systems such like mechanical systems with impact phenomena, robotics, mechatronics, automotive industry, power systems, process control, as well as embedded computation where program codes interact with the physical world (Zhang et al., 2001; Cai et al., 2007). In such dynamical systems, the state variables are capable of evolving continuously (flowing) and/or evolving discontinuously (jumping) (Cai et al., 2007). The dynamical behavior characterized by interacting continuous variables and discrete switching logics can be captured by

a mathematical framework given in terms of time-driven continuous variable dynamics (usually described by differential or difference equations) and event-driven discrete logic dynamics (whose evolutions depend on “if-then-else” type of rules and may be described by automata) (Lin and Antsaklis, 2009).

Such interaction of continuous-time and discrete-time dynamics may lead to an infinitely fast and continuous switching between several dynamics, such behavior is called a *chattering* behavior (Zhang et al., 2008). This often occurs in the optimal control of continuous and hybrid systems. Chattering executions can be defined as solutions to the hybrid system having infinitely many discrete transitions in finite time. Such behavior can be intuitively thought of as *involving infinitely fast switching among different control actions or modes of operation*. Similar behavior appears in variable structure control systems and in relay control systems (Johansson et al., 2002). The numerical simulation of hybrid systems exhibiting a chattering behavior appears to come to a halt, since infinitely many transitions would need to be simulated. This requires high computational costs as small step-sizes are required to maintain the numerical precision. Chattering behavior has to be treated in an appropriate way to ensure that the numerical integration progress in a reasonable time. This has been investigated by means of different methods. In general, one may prevent the chattering in hybrid systems by inducing a smooth sliding motion on the switching manifold on which the chattering occurs (di Bernardo et al., 2008; Weiss et al., 2014; Guardia et al., 2011). While the infinitely fast switching between modes occurs, a smooth motion along the switching surface may emerge while eliminating the fast chattering. Differential inclusions (DIs) of the Filippov type (the so-called equivalent dynamics) can be used to define a regularized solution trajectory in a small neighborhood of the switching manifold on which the chattering occurs so that the average velocity of sliding on the surface can be determined (Filippov, 1988; Biák et al., 2013). Another approach (the so-called equivalent control) was proposed by Utkin (Utkin, 1992). However, the computation of the equivalent dynamics turns out to be difficult whenever the systems chat-

ters between more than two dynamics. One of the main properties of chattering behavior is that the solution trajectory may successively enter and exit as well as slide on switching manifolds of different dimensions. Problems with this type of sliding arise naturally in dynamical systems and control applications whenever there are multiple discontinuous control variables. Such multiple sliding behavior may be the origin of non-uniqueness of solution as an inescapable and important property of heterogeneous dynamical systems with discontinuous control variables. The main contribution of this paper is to provide an adequate technique to detect chattering “on the fly” in real-time simulation and compute its regularization beyond the infinitely fast mode switching. In particular, we present a robust and computationally efficient framework for the most general case of p intersected switching manifolds, as well as the extent of how unique solutions in such cases can be defined. A hierarchical application of convex combinations to form a differential inclusion on the intersection is employed. We provide a novel computational framework which treats non-smoothness in the trajectory of the state variables during the regularization of chattering by a smooth correction after each integration time-step. The paper is organized as follows: Section 2 provides preliminaries on the modeling of hybrid systems. Section 3 deals with the chattering behavior as well as the chattering on switching intersection. Section 4 presents a numerical approach to integrate the system dynamics while eliminating the fast switching. Finally, simulation results and conclusion of the study are given in Sections 5 and 6, respectively.

2 Modeling of Hybrid Systems

Definition 1: (Hybrid Automaton)

A hybrid automaton HA is a collection $HA = (Q, X, Init, f, I, E, G, R)$, where

1. Q , a finite set of discrete states $q \in Q$.
2. X , a finite set of continuous states variables $x_i \in X$.
3. $Init \subseteq Q \times X$, is a finite set of initial states.
4. $f : Q \times \mathbb{R}^n \rightarrow \mathbb{R}^n$, is a flow map, which describes, through a differential equation, the continuous evolution of the continuous state variable x .
5. $I : Q \Rightarrow \mathbb{R}^n$, assigns to each location $q \in Q$ an invariant map, which describes the conditions that the continuous state x has to satisfy at this mode.
6. $E \subset Q \times Q$, is a collection of discrete transitions, which identifies the pairs (q, q') such that a transition from the mode q to the mode q' is possible.
7. $G : E \Rightarrow \mathbb{R}^n$, assign to each $e = (q, q') \in E$ a guard to which the continuous state x must belong so that a transition from q to q' can occur.
8. $R : E \times \mathbb{R}^n \rightarrow \mathbb{R}^n$ assign to each $e = (q, q') \in E$ and $x \in X$ a reset map $R(e, x)$, which describes, for each $e = (q, q') \in E$, the value to which the continuous state $x \in \mathbb{R}^n$ is set during a transition from mode q to mode q' .

Definition 2: (The dynamics of a Hybrid Automaton)

As a hybrid system with explicitly shown modes, the continuous behavior in the hybrid automaton is modeled by a flow map $\dot{x} = f_q(x)$, while the discrete behavior is modeled by a jump map $\phi_q(x)$ (Cai et al., 2007). The conditions that permit flows and/or jumps are given by the flow set C and the jump set D , respectively, subsets of the state space. The dynamics of a hybrid automaton is given by

$$\mathcal{H} : \left\{ \begin{array}{l} \dot{x} = f_q(x) \quad x \in C_q \\ \left[\begin{array}{l} x^+ \\ q^+ \end{array} \right] \in \phi_q(x) \quad x \in D_q \end{array} \right\} \quad (1)$$

where

$$D_q = \bigcup_{e=(q,q') \in E} G(e); \quad C_q = I_q; \quad (2)$$

$$\phi_q(x) = \bigcup_{e=(q,q'); x \in G(e)} \left[\begin{array}{l} R(e, x) \\ q' \end{array} \right]; \quad (3)$$

$$C = \bigcup_{q \in Q} (C_q \times \{q\}); \quad D = \bigcup_{q \in Q} (D_q \times \{q\}) \quad (4)$$

The discrete transitions between modes are always guarded by zero-crossings of the guard functions, and continuous modes are always defined by a Boolean expression over discrete variables, which are piecewise constant in continuous time, this is to make sure that a mode change can only happen on discrete transitions. In general, there are three natural choices for the semantics of a zero-crossing $up(z)$ (Schrammel, 2012):

- “At-zero” : $z(x_{k-1}, t_{k-1}) \leq 0 \wedge z(x_k, t_k) \geq 0$
- “Contact” : $z(x_{k-1}, t_{k-1}) < 0 \wedge z(x_k, t_k) \geq 0$
- “Crossing” : $z(x_{k-1}, t_{k-1}) \leq 0 \wedge z(x_k, t_k) > 0$

Based on non-standard analysis, by the continuity of the event function z in the “Crossing” semantics we can deduce that $z(t) = 0$ is valid at the zero-crossing point in standard semantics: by standardizing $z(t) \leq 0 \wedge z(t + \partial) > 0$ we get $st(z(t)) = st(z(t + \partial)) = 0$, where ∂ is a non-standard infinitesimal (Benveniste et al., 2012). This gives an unambiguous meaning to hybrid systems even if they contain chattering behavior. In order to allow chattering in the standard semantics, the trajectories are allowed to actually go above zero, up to a constant $\varepsilon > 0$.

Definition 3: (Lie derivatives)

Assume the flow map f_q is analytic in its second argument, the Lie derivatives $L_{f_q}^k g_q : \mathbb{R}^n \rightarrow \mathbb{R}^n$ of a function

g_q , also analytic in its second argument, along f_q , for $k > 0$, is defined by:

$$\mathcal{L}_{f_q}^k g_q(x(t)) = \left(\frac{\partial \mathcal{L}_{f_q}^{k-1} g_q(x(t))}{\partial x(t)} \right) \cdot f_q(x(t)) \quad (5)$$

with

$$\mathcal{L}_{f_q}^0 g_q(x(t)) = g_q(x(t)) \quad (6)$$

Definition 4: (Pointwise relative degree)

We define the relative degree $n_q(x) : \mathbb{R}^n \rightarrow \mathbb{N}$ by:

$$n_q(x) = k \text{ if } \bigwedge_{j < k} \mathcal{L}_{f_q}^j g_q(x) = 0 \wedge \mathcal{L}_{f_q}^k g_q(x) \neq 0 \quad (7)$$

3 The Chattering Behavior

Physically, chattering behavior occurs if equal thresholds for the transition conditions of different modes are given and the system starts to oscillate around them. A specific issue is the existence of multiple sliding modes due to intersecting switching manifolds, that is, the chattering occurs on switching manifolds of different dimension, roughly speaking, the chattering set may belong to many $\mathbb{R}^{(n-r)}$ switching manifolds of the same system, where $r \in \{1, 2, \dots, n\}$. To illustrate this particular case, we study, in the following, a mechanical stick-slip system with dry Coulomb friction.

3.1 Case Study 1:

The non-smooth system to be investigated (Figure 1), consists of three blocks of masses m , M_1 , and M_2 , where only the block of mass m is connected to a fixed support by a linear spring of stiffness k and is under the action of a sinusoidal external force u generated by an actuator P ($u = A \sin(\omega t + \varphi)$). We denote x_m , x_{M_1} , and x_{M_2} to the position of the small mass m and the two inertial masses M_1 and M_2 , respectively. We denote \mathcal{F}_1 to the tangential contact force on the frictional interface between the small mass m and the inertial mass M_1 , and \mathcal{F}_2 to the tangential contact force on the frictional interface between the small mass m and the inertial mass M_2 . The friction between the inertial mass M_2 and the ground is neglected. The origin of the displacements x_m , x_{M_1} , and x_{M_2} is taken where the spring is un-stretched. The system's state space representation is given by

$$f(x) : \left\{ \begin{array}{l} \dot{x}_m = v_m \\ \dot{v}_m = \frac{1}{m}(u - kx_m - \mathcal{F}_1 - \mathcal{F}_2) \\ \dot{x}_{M_1} = v_{M_1} \\ \dot{v}_{M_1} = \frac{1}{M_1} \mathcal{F}_1 \\ \dot{x}_{M_2} = v_{M_2} \\ \dot{v}_{M_2} = \frac{1}{M_2} \mathcal{F}_2 \end{array} \right\} \quad (8)$$

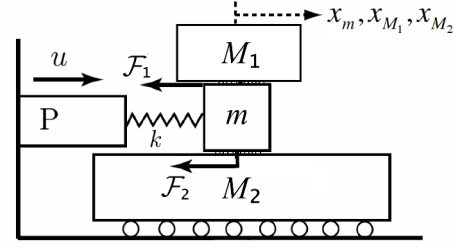


Figure 1. Schematic of the studied Stick-slip system.

where $x = [x_m \ v_m \ x_{M_1} \ v_{M_1} \ x_{M_2} \ v_{M_2}]^T$, and v_m , v_{M_1} , and v_{M_2} are the velocities of the small mass m and the inertial masses M_1 and M_2 , respectively. In modeling friction-induced vibration and noise problems, friction force is often treated phenomenologically, as a function of relative velocity between surfaces.

$$\mathcal{F}_1 = \left\{ \begin{array}{l} -F_{c_1} \text{ for } v_{r_1}(t) < 0 \\ F_{c_1} \text{ for } v_{r_1}(t) > 0 \end{array} \right\} \quad (9)$$

$$\mathcal{F}_2 = \left\{ \begin{array}{l} -F_{c_2} \text{ for } v_{r_2}(t) < 0 \\ F_{c_2} \text{ for } v_{r_2}(t) > 0 \end{array} \right\} \quad (10)$$

where F_{c_1} , F_{c_2} are the levels of the Coulomb friction, $v_{r_1} = v_m - v_{M_1}$ is the relative velocity related to the masses m and M_1 , and $v_{r_2} = v_m - v_{M_2}$ is the relative velocity related to the masses m and M_2 . In the physical system, for the frictional interface between the small mass m and the inertial mass M_1 , as long as the force acting at the interface (call it ρ_1) does not exceed the Coulomb friction level F_{c_1} , the two masses m and M_1 move together with $v_{r_1} = 0$. As soon as ρ_1 exceeds the Coulomb friction level, one mass slips over the other with $v_{r_1} \neq 0$. The slip is said to be positive ($Slip_1^+$) with a friction force $\mathcal{F}_1 = +F_{c_1}$ if $v_m > v_{M_1}$. The slip motion is said to be negative ($Slip_1^-$) with a friction force $\mathcal{F} = -F_{c_1}$ if $v_{M_1} > v_m$. The same applies for the interface between the masses m and M_2 .

Obviously, we have a hybrid system with four explicitly shown modes $Q = \{q_1, q_2, q_3, q_4\}$, where the four modes $q_1 = slip_1^+ slip_2^+$, $q_2 = slip_1^- slip_2^+$, $q_3 = slip_1^- slip_2^-$, and $q_4 = slip_1^+ slip_2^-$ are distinguished by negative and positive relative velocities v_{r_1} and v_{r_2} . The hybrid automaton of this system is given, in the form (2), by

$$\mathcal{H} : \left\{ \begin{array}{l} \dot{x} = f_q(x) \ x \in C_q \\ \left[\begin{array}{l} x^+ \\ q^+ \end{array} \right] \in \Phi_q(x) \ x \in D_q \end{array} \right\} \quad (11)$$

$$f_1(x) : \left\{ \begin{array}{l} \dot{x}_m = v_m \\ \dot{v}_m = \frac{1}{m}(u - kx_m(t) - F_{c_1} - F_{c_2}) \\ \dot{x}_{M_1} = v_{M_1} \\ \dot{v}_{M_1} = \frac{1}{M_1} F_{c_1} \\ \dot{x}_{M_2} = v_{M_2} \\ \dot{v}_{M_2} = \frac{1}{M_2} F_{c_2} \end{array} \right\} \quad (12)$$

$$f_2(x) : \left\{ \begin{array}{l} \dot{x}_m = v_m \\ \dot{v}_m = \frac{1}{m}(u - kx_m(t) + F_{c_1} - F_{c_2}) \\ \dot{x}_{M_1} = v_{M_1} \\ \dot{v}_{M_1} = \frac{-1}{M_1}F_{c_1} \\ \dot{x}_{M_2} = v_{M_2} \\ \dot{v}_{M_2} = \frac{1}{M_2}F_{c_2} \end{array} \right\} \quad (13)$$

$$f_3(x) : \left\{ \begin{array}{l} \dot{x}_m = v_m \\ \dot{v}_m = \frac{1}{m}(u - kx_m(t) + F_{c_1} + F_{c_2}) \\ \dot{x}_{M_1} = v_{M_1} \\ \dot{v}_{M_1} = \frac{-1}{M_1}F_{c_1} \\ \dot{x}_{M_2} = v_{M_2} \\ \dot{v}_{M_2} = \frac{-1}{M_2}F_{c_2} \end{array} \right\} \quad (14)$$

$$f_4(x) : \left\{ \begin{array}{l} \dot{x}_m = v_m \\ \dot{v}_m = \frac{1}{m}(u - kx_m(t) - F_{c_1} + F_{c_2}) \\ \dot{x}_{M_1} = v_{M_1} \\ \dot{v}_{M_1} = \frac{1}{M_1}F_{c_1} \\ \dot{x}_{M_2} = v_{M_2} \\ \dot{v}_{M_2} = \frac{-1}{M_2}F_{c_2} \end{array} \right\} \quad (15)$$

$$\phi_1(x) = \left\{ \begin{array}{l} (x, q_2) \text{ if } v_{r_1} = 0 \wedge v_{r_2} \geq 0 \\ (x, q_4) \text{ if } v_{r_1} \geq 0 \wedge v_{r_2} = 0 \end{array} \right\} \quad (16)$$

$$\phi_2(x) = \left\{ \begin{array}{l} (x, q_1) \text{ if } v_{r_1} = 0 \wedge v_{r_2} \geq 0 \\ (x, q_3) \text{ if } v_{r_1} \leq 0 \wedge v_{r_2} = 0 \end{array} \right\} \quad (17)$$

$$\phi_3(x) = \left\{ \begin{array}{l} (x, q_2) \text{ if } v_{r_1} \leq 0 \wedge v_{r_2} = 0 \\ (x, q_4) \text{ if } v_{r_1} = 0 \wedge v_{r_2} \leq 0 \end{array} \right\} \quad (18)$$

$$\phi_4(x) = \left\{ \begin{array}{l} (x, q_1) \text{ if } v_{r_1} \geq 0 \wedge v_{r_2} = 0 \\ (x, q_3) \text{ if } v_{r_1} = 0 \wedge v_{r_2} \leq 0 \end{array} \right\} \quad (19)$$

$$D_{q_1} = G(q_1, q_2) \cup G(q_1, q_4) \quad (20)$$

$$= \{(v_{r_1} = 0 \wedge v_{r_2} \geq 0) \cup (v_{r_1} \geq 0 \wedge v_{r_2} = 0)\}$$

$$D_{q_2} = G(q_2, q_1) \cup G(q_2, q_3) \quad (21)$$

$$= \{(v_{r_1} = 0 \wedge v_{r_2} \geq 0) \cup (v_{r_1} \leq 0 \wedge v_{r_2} = 0)\}$$

$$D_{q_3} = G(q_3, q_2) \cup G(q_3, q_4) \quad (22)$$

$$= \{(v_{r_1} \leq 0 \wedge v_{r_2} = 0) \cup (v_{r_1} = 0 \wedge v_{r_2} \leq 0)\}$$

$$D_{q_4} = G(q_4, q_1) \cup G(q_4, q_3) \quad (23)$$

$$= \{(v_{r_1} \geq 0 \wedge v_{r_2} = 0) \cup (v_{r_1} = 0 \wedge v_{r_2} \leq 0)\}$$

Clearly, the system is discontinuous on two hyper switching manifolds Γ_a and Γ_b characterized as zero sets of the switching functions $\gamma_a(x)$ and $\gamma_b(x)$, respectively:

$$\Gamma_a = \{x \in \mathbb{R}^6 : \gamma_a(x) \models v_{r_1}(t) = 0\} \quad (24)$$

$$\Gamma_b = \{x \in \mathbb{R}^6 : \gamma_b(x) \models v_{r_2}(t) = 0\} \quad (25)$$

We will assume that $\frac{\partial \gamma_a(x)}{\partial x} \neq 0$ for all $x \in \Gamma_a$ and $\frac{\partial \gamma_b(x)}{\partial x} \neq 0$ for all $x \in \Gamma_b$ so that the normal units $\perp_a(x)$ and $\perp_b(x)$ orthogonal to the tangent planes $T_x(\Gamma_a)$ and $T_x(\Gamma_b)$, respectively, are well defined (Filippov, 1988). Furthermore, we assume that $\perp_a(x)$ and $\perp_b(x)$ are linearly independent for all $x \in \Gamma_a \cap \Gamma_b$. In the neighborhood of the intersection

$\Delta = \Gamma_a \cap \Gamma_b$ (Figure 2), for the continuous time variables v_m, v_{M_1}, v_{M_2} , the \mathbb{R}^3 phase space consists of four open regions (the flow sets) C_i , for $i = 1, 2, 3, 4$, with the flow map vector fields $f_1(x), f_2(x), f_3(x)$, and $f_4(x)$. The curve Δ is a $\mathbb{R}^{(n-2)}$ switching manifold results from the intersection of two transversally intersected $\mathbb{R}^{(n-1)}$ manifolds and is given by $\Delta = \Gamma_a \cap \Gamma_b = \{x \in \mathbb{R}^n : v_{r_1} = 0 \wedge v_{r_2} = 0\}$. Clearly, the curve Δ belongs to the boundary of each one of discrete states q_1, q_2, q_3 , and q_4 . Furthermore, each two adjacent regions are separated by a hyper switching manifold defined by opposed zero crossings of the same switching function. Let Γ be the entire discontinuity re-

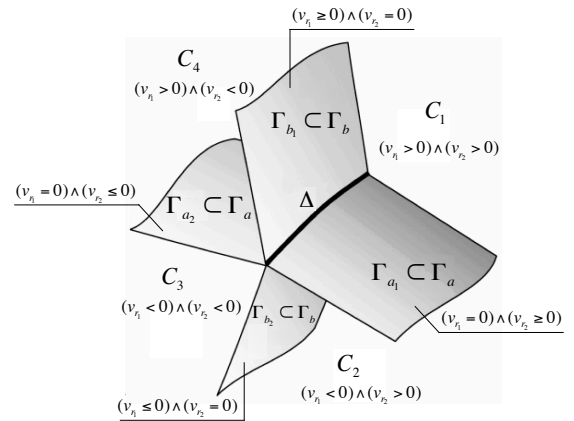


Figure 2. The switching intersection set in the \mathbb{R}^3 -dimensional phase space of the studied system.

gion in the phase space defined as the union of the two hyper switching manifolds Γ_a and Γ_b : $\Gamma = \Gamma_a \cup \Gamma_b$. A switching between the four different flow map's vector fields f_1, f_2, f_3 , and f_4 takes place in the neighborhood of the intersection Δ . A trajectory that crosses Γ transversally will switch instantaneously between the vector fields f_q without any specific form of flow map vector on Γ . The only alternative is that a trajectory exhibits an attractive chattering on Γ , which yields an attractive chattering: i) between q_1 and q_2 on $\Gamma_{a_1} \in \mathbb{R}^{(n-1)}$, ii) between q_3 and q_4 on $\Gamma_{a_2} \in \mathbb{R}^{(n-1)}$, iii) between q_1 and q_4 on $\Gamma_{b_1} \in \mathbb{R}^{(n-1)}$, iv) between q_2 and q_3 on $\Gamma_{b_2} \in \mathbb{R}^{(n-1)}$, v) as well as between the four discrete states q_1, q_2, q_3 , and q_4 on $\Delta \in \mathbb{R}^{(n-2)}$. On the intersection Δ , an infinite number of discrete transitions between the four modes is expected as long as for all $q \in Q$ the gradient of the continuous-time behavior according to the flow map's vector field f_q is directed into the intersection Δ , that is, in the neighborhood of the intersection the gradients direct behavior towards Δ so that upon each entering to a new mode an infinitesimal step causes another mode change. When simulating this system, in general, such behavior breaks down the numerical integration of the dynamics, as it does not progress in time, but chatters between modes.

3.2 Chattering in The Neighborhood of a Switching Intersection: where

We consider a hybrid automaton \mathcal{H} with a finite set of discrete states $q \in Q$ with transverse invariants (Morris, 2009) where the state space is split into different regions (flow sets $C_q \in \mathbb{R}^n$) by the intersection of p transversally intersected \mathbb{R}^{n-1} switching manifolds Γ_j defined as the zeros of a set of scalar functions $\gamma_j(x)$ for $j = 1, 2, \dots, p$,

$$\Gamma_j = \{x \in \mathbb{R}^n : \gamma_j(x) = 0 ; \quad j = 1, 2, \dots, p\} \quad (26)$$

The zero crossing in opposite directions defines the switching between two adjacent flow sets. All switching functions γ_j are assumed to be analytic in their second arguments so the normal unit vector \perp_j for each one of the intersected switching manifolds Γ_j is well defined. Moreover, the normal unit vectors are linearly independent for all the $\mathbb{R}^{(n-r)}$ intersections where $r \in \{2, 3, \dots, n\}$. The system phase space $C \subseteq \mathbb{R}^n$ is partitioned into 2^p open convex regions (sub-domains) $C_q \in \mathbb{R}^n$, $q = 1, \dots, 2^p$, and p switching manifold $\gamma_j(x) \in \mathbb{R}^{n-1}$, $j = 1, 2, \dots, p$. In the convex flow sets C_q , the solution trajectory flow is governed by different vector fields $f_q(x(t))$. Furthermore, it is assumed that the flow maps f_q are smooth in the state x for any open flow set adjacent to the flow set C_q and all f_q can be associated to the intersection.

In general, the disjoint 2^p regions flow sets can be characterized in a systematic way by defining a sign matrix Ψ of size $(p, 2^p)$ as following:

Let $W^{(k)} = (W_i)_{1,2^k}$ be an 1×2^k vector of values $W_i = 1, \forall i$, with $k = 1, \dots, p-1$.

1. The first row vector of the matrix Ψ : $V_1 = \Psi(1, :)$ consists of 2^{p-1} pairs of $(-W^{(1)}(1, 1), W^{(1)}(1, 2))$.

$$\Psi^{(1)} = \{-W^{(1)}(1, 1), W^{(1)}(1, 2)\}_{2^{p-1}} \quad (27)$$

2. The second row vector $V_2 = \Psi(2, :)$ consists of 2^{p-2} pairs of $(-W^{(1)}, W^{(1)})$.

$$\Psi^{(2)} = \{-W^{(1)}, W^{(1)}\}_{2^{p-2}} \quad (28)$$

3. The j^{th} row vector $V_j = \Psi(j, :)$ consists of 2^{p-j} pairs of $(-W^{(j-1)}, W^{(j-1)})$ for $j = 3, \dots, p$.

$$\Psi^{(j)} = \{-W^{(j-1)}, W^{(j-1)}\}_{2^{p-j}} \quad (29)$$

Each column vector defines the signs of the switching functions $\gamma_j(x)$ for a given flow set C_q . We use the multi-valued function $\alpha_j(x)$ such that the convex set is given for all $\Gamma_j|_{j=1,2,\dots,p}$ and $C_i|_{i=1,2,\dots,2^p}$ by:

$$\dot{x} \in \sum_{i=1}^{2^p} \left(\left(\prod_{j=1}^p \frac{1 + 2\Psi_{j,i} \cdot \alpha_j(x) - \Psi_{j,i}}{2} \right) \cdot f_i(x) \right) \quad (30)$$

$$\alpha_j(x) = \left\{ \begin{array}{ll} 1 & \text{for } \gamma_j(x) > 0 \\ [0, 1] & \text{for } \gamma_j(x) = 0 \\ 0 & \text{for } \gamma_j(x) < 0 \end{array} \right\} \quad (31)$$

$$\sum_{i=1}^{2^p} \left(\prod_{j=1}^p \frac{1 + 2\Psi_{j,i} \cdot \alpha_j - \Psi_{j,i}}{2} \right) = 1 \quad (32)$$

Equation (31) yields in

$$\dot{x} \in (1 - \alpha_j) \cdot \sum_{i=1}^{2^p} (R_1 \cdot f_i(x)) + \alpha_j \cdot \sum_{i=1}^{2^p} (R_2 \cdot f_i(x)) \quad (33)$$

$$R_1 = \prod_{k=1; k \neq j; \Psi_{k,i} = -1}^p \left(\frac{1 + 2\Psi_{k,i} \cdot \alpha_k - \Psi_{k,i}}{2} \right) \quad (34)$$

$$R_2 = \prod_{k=1; k \neq j; \Psi_{k,i} = 1}^p \left(\frac{1 + 2\Psi_{k,i} \cdot \alpha_k - \Psi_{k,i}}{2} \right) \quad (35)$$

We then define a matrix F of the normal projections $f_i^{\perp j}(x)$ for $j = 1, 2, \dots, p$ and $i = 1, 2, \dots, 2^p$ as

$$F = \begin{Bmatrix} f_1^{\perp 1}(x) & f_1^{\perp 2}(x) & \cdots & f_1^{\perp p}(x) \\ f_2^{\perp 1}(x) & f_2^{\perp 2}(x) & \cdots & f_2^{\perp p}(x) \\ \vdots & \vdots & \ddots & \vdots \\ \vdots & \vdots & \ddots & \vdots \\ f_{2^p}^{\perp 1}(x) & f_{2^p}^{\perp 2}(x) & \cdots & f_{2^p}^{\perp p}(x) \end{Bmatrix} \quad (36)$$

where

$$f_i^{\perp j}(x) = \mathcal{L}_{f_i} \gamma_j(x) = \left(\frac{\partial \gamma_j(x)}{\partial x} \right)^T \cdot f_i(x) \quad (37)$$

In agreement with the sign matrix Ψ , the attractive chattering on any $\mathbb{R}^{(n-r)}$ switching manifold for $r = 2, 3, \dots, n$ can be easily observed by checking the signs of the matrices F and Ψ .

Lemma 1:

The sufficient condition for having an attractive chattering on any switching intersection in the system's state space requires a nodal attractivity towards the intersection itself, for all the flow maps f_i in the \mathbb{R}^n regions C_i associated to this intersection. That is, the following constraint should be satisfied

$$\forall i, j : \text{sgn}(f_i^{\perp j}(x)) = -\text{sgn}(\Psi_{j,i}) \quad (38)$$

To keep the solution trajectory in a sliding motion on the intersection as long as the attractive chattering condition is satisfied we impose

$$\forall j = 1, 2, \dots, p : \sum_{i=1}^{2^p} \left(\prod_{j=1}^p \frac{1 + 2\Psi_{j,i} \cdot \alpha_j - \Psi_{j,i}}{2} \right) \cdot f_i^{\perp j}(x) = 0 \quad (39)$$

so that

$$\alpha_j = \frac{W_1}{W_1 - W_2} \quad (40)$$

$$W_1 = \sum_{i=1}^{2^p} \left(\prod_{k=1; k \neq j; \Psi_{k,i} = -1}^p \frac{1 + 2\Psi_{k,i} \cdot \alpha_k - \Psi_{k,i}}{2} \right) \cdot f_i^{\perp j} \quad (41)$$

$$W_2 = \sum_{i=1}^{2^p} \left(\prod_{k=1; k \neq j; \Psi_{k,i} = 1}^p \frac{1 + 2\Psi_{k,i} \cdot \alpha_k - \Psi_{k,i}}{2} \right) \cdot f_i^{\perp j} \quad (42)$$

For all $\alpha_k \in (0, 1)$, the product term in (42) (respectively (43)) takes always a value in $(0, 1)$ since it is always a product of $(1 - \alpha_k)$ (respectively α_k). It holds always that $W_1 > 0 \wedge W_2 < 0$ as long as an attractive chattering takes place at $x \in \left(\bigcup_{j=1}^p \Gamma_j \right) \cap C$, where C is the entire flow set in the system phase space.

This gives us a hypercube convex hull of sign coordinates $(\pm 1, \pm 1, \dots, \pm 1)$ with an edge of length 2 and \mathbb{R}^n volume 2^p . Therefore, a solution to the fixed point non-linear problem (40) exists. However, the uniqueness of the solution is not guaranteed. To deal with non-uniqueness on the intersection—on which the attractive chattering occurs—we propose to give an equivalent to the product term in (40) so that the sliding parameters are given in term of a rational function of coefficients κ_i :

$$\prod_{j=1}^p \frac{1 + 2\Psi_{j,i} \cdot \alpha_j - \Psi_{j,i}}{2} = \frac{\kappa_i}{\sum_{k=1}^{2^p} \kappa_k} \quad (43)$$

where

$$\kappa_i = \frac{\left(\prod_{l=1; l \neq i}^{2^p} (\Omega_l) \right)^{\frac{1}{2^p-1}}}{\left(\prod_{l=1; l \neq i}^{2^p} (\Omega_l) \right)^{\frac{1}{2^p-1}} - (\Omega_i)} \quad (44)$$

$$\Omega_i = [(b_i)_1 \ (b_i)_2 \ \dots \ (b_i)_p] \cdot \begin{bmatrix} \mathcal{L}_{f_i} \gamma_1(x) \\ \mathcal{L}_{f_i} \gamma_2(x) \\ \vdots \\ \mathcal{L}_{f_i} \gamma_p(x) \end{bmatrix} \quad (45)$$

$$\Omega_l = [(b_l)_1 \ (b_l)_2 \ \dots \ (b_l)_p] \cdot \begin{bmatrix} \mathcal{L}_{f_l} \gamma_1(x) \\ \mathcal{L}_{f_l} \gamma_2(x) \\ \vdots \\ \mathcal{L}_{f_l} \gamma_p(x) \end{bmatrix} \quad (46)$$

The vectors b_n for $n = i, l$ are given as sign permutations of coordinates $[\pm 1, \pm 1, \dots, \pm 1]^T$ under the constraint:

$$\text{sgn}(b_n)_j = \begin{cases} \text{sgn}(\mathcal{L}_{f_n} \gamma_j(x)) & \text{for } n = 1 \\ -\text{sgn}(\mathcal{L}_{f_n} \gamma_j(x)) & \text{for } n = 2, 3, \dots, 2^p \end{cases} \quad (47)$$

where $j = 1, 2, \dots, p$ and p is the number of the intersected $\mathbb{R}^{(n-1)}$ switching manifolds. This gives always $\Omega_1 > 0$ and $\Omega_n < 0$ for all $n \in \{2, 3, \dots, 2^p\}$ which is exactly what we want. Another advantage of using the signs constraint

in (48) is that $\kappa_j = 0$ for all $j \neq i$ when $\kappa_i = 1$ for a given index $i \in \{1, 2, \dots, 2^p\}$, this allows us to detect when a switching regime of different dimension has been reached by the solution trajectory, and then, to select the appropriate vector fields on this regime. Moreover, the parameter κ_i takes always a value $0 \leq \kappa_i \leq 1$ for $i = 1, 2, \dots, 2^p$, yields in $\sum_{i=1}^{2^p} \left(\frac{\kappa_i}{\sum_{k=1}^{2^p} \kappa_k} \right) = 1$, which is consistent with the approach of Filippov differential inclusion.

Case Study 1 Revisited:

With $A = u - kx_m$, the Lie derivatives of the switching functions $\gamma_a(x)$ and $\gamma_b(x)$ along the flow map vector fields f_1, f_2, f_3 , and f_4 are given by

$$f_1^{\perp a}(x) = \frac{1}{m} \cdot \left(A - \left(\frac{m+M_1}{M_1} \right) \cdot F_{c_1} - F_{c_2} \right) \quad (48)$$

$$f_1^{\perp b}(x) = \frac{1}{m} \cdot \left(A - F_{c_1} - \left(\frac{m+M_2}{M_2} \right) \cdot F_{c_2} \right) \quad (49)$$

$$f_2^{\perp a}(x) = \frac{1}{m} \cdot \left(A + \left(\frac{m+M_1}{M_1} \right) \cdot F_{c_1} - F_{c_2} \right) \quad (50)$$

$$f_2^{\perp b}(x) = \frac{1}{m} \cdot \left(A + F_{c_1} - \left(\frac{m+M_2}{M_2} \right) \cdot F_{c_2} \right) \quad (51)$$

$$f_3^{\perp a}(x) = \frac{1}{m} \cdot \left(A + \left(\frac{m+M_1}{M_1} \right) \cdot F_{c_1} + F_{c_2} \right) \quad (52)$$

$$f_3^{\perp b}(x) = \frac{1}{m} \cdot \left(A + F_{c_1} + \left(\frac{m+M_2}{M_2} \right) \cdot F_{c_2} \right) \quad (53)$$

$$f_4^{\perp a}(x) = \frac{1}{m} \cdot \left(A - \left(\frac{m+M_1}{M_1} \right) \cdot F_{c_1} + F_{c_2} \right) \quad (54)$$

$$f_4^{\perp b}(x) = \frac{1}{m} \cdot \left(A - F_{c_1} + \left(\frac{m+M_2}{M_2} \right) \cdot F_{c_2} \right) \quad (55)$$

We distinguish between the following cases:

- An infinitely fast back and forth switching between the discrete states q_1 and q_2 occurs on Γ_{a_1} if and only if $f_1^{\perp a}(x) < 0 \wedge f_2^{\perp a}(x) > 0$. This happens when $|(u - kx_m - F_{c_2})| < \left(\frac{m+M_1}{M_1} \right) \cdot F_{c_1}$. The resulting sliding vector field $f_{s_{a_1}}$ is:

$$f_{s_{a_1}} = \left\{ \begin{array}{l} v_m \\ \frac{1}{m+M_1}(u - kx_m - F_{c_2}) \\ v_{M_1} \\ \frac{1}{m+M_1}(u - kx_m - F_{c_2}) \\ v_{M_2} \\ \frac{1}{M_2}F_{c_2} \end{array} \right\} \quad (56)$$

- An infinitely fast back and forth switching between the discrete states q_3 and q_4 occurs on Γ_{a_2} if and only if $f_3^{\perp a}(x) < 0 \wedge f_4^{\perp a}(x) > 0$. This happens when

$|(u - kx_m + F_{c_2})| < (\frac{m+M_1}{M_1}) \cdot F_{c_1}$. The resulting sliding vector field $f_{s_{a_2}}$ is:

$$f_{s_{a_2}} = \left\{ \begin{array}{l} \frac{v_m}{m+M_1}(u - kx_m + F_{c_2}) \\ \frac{v_{M_1}}{m+M_1}(u - kx_m + F_{c_2}) \\ \frac{v_{M_2}}{m+M_1}F_{c_2} \\ \frac{-1}{M_2}F_{c_2} \end{array} \right\} \quad (57)$$

- An infinitely fast back and forth switching between the discrete states q_1 and q_4 occurs on Γ_{b_1} if and only if $f_1^{\perp b}(x) < 0 \wedge f_4^{\perp b}(x) > 0$. This happens when $|(u - kx_m - F_{c_1})| < (\frac{m+M_2}{M_2}) \cdot F_{c_2}$. The resulting sliding vector field $f_{s_{b_1}}$ is:

$$f_{s_{b_1}} = \left\{ \begin{array}{l} \frac{v_m}{m+M_2}(u - kx_m - F_{c_1}) \\ \frac{v_{M_1}}{m+M_2}F_{c_1} \\ \frac{v_{M_2}}{m+M_2}(u - kx_m - F_{c_1}) \\ \frac{-1}{M_1}F_{c_1} \end{array} \right\} \quad (58)$$

- An infinitely fast back and forth switching between the discrete states q_2 and q_3 occurs on Γ_{b_2} if and only if $f_2^{\perp b}(x) < 0 \wedge f_3^{\perp b}(x) > 0$. This happens when $|(u - kx_m + F_{c_1})| < (\frac{m+M_2}{M_2}) \cdot F_{c_2}$. The resulting sliding vector field $f_{s_{b_2}}$ is:

$$f_{s_{b_2}} = \left\{ \begin{array}{l} \frac{v_m}{m+M_2}(u - kx_m + F_{c_1}) \\ \frac{v_{M_1}}{m+M_2}F_{c_1} \\ \frac{-1}{M_1}F_{c_1} \\ \frac{v_{M_2}}{m+M_2}(u - kx_m + F_{c_1}) \end{array} \right\} \quad (59)$$

- An infinitely fast switching between q_1 , q_2 , q_3 , and q_4 takes place on the intersection Δ if and only if the following four conditions are satisfied

1. $(f_1^{\perp \Gamma_a} < 0) \wedge (f_2^{\perp \Gamma_a} > 0)$ which happens when $|(A - F_{c_2})| < (\frac{m+M_1}{M_1}) \cdot F_{c_1}$.
2. $(f_1^{\perp \Gamma_b} < 0) \wedge (f_4^{\perp \Gamma_b} > 0)$ which happens when $|(A - F_{c_1})| < (\frac{m+M_2}{M_2}) \cdot F_{c_2}$.
3. $(f_2^{\perp \Gamma_b} < 0) \wedge (f_3^{\perp \Gamma_b} > 0)$ which happens when $|(A + F_{c_1})| < (\frac{m+M_2}{M_2}) \cdot F_{c_2}$.
4. $(f_4^{\perp \Gamma_a} < 0) \wedge (f_3^{\perp \Gamma_a} > 0)$ which happens when $|(A + F_{c_2})| < (\frac{m+M_1}{M_1}) \cdot F_{c_1}$.

The resulting sliding vector field f_{s_Δ} is:

$$f_{s_\Delta} = \left\{ \begin{array}{l} \frac{v_m}{m+M_1+M_2}(u - kx_m) \\ \frac{v_{M_1}}{m+M_1+M_2}(u - kx_m) \\ \frac{v_{M_2}}{m+M_1+M_2}(u - kx_m) \end{array} \right\} \quad (60)$$

4 Numerical Approach:

The algorithm has to detect: (i) when a switching manifold of different dimension is reached, and (ii) whether the trajectory stays on or leaves the switching manifold. This has to be decided depending on the gradients of the continuous time behavior in the neighborhood of the current state. Let $\Gamma = \bigcup_{j=1}^p \Gamma_j$ be the entire discontinuity region. The algorithm has to perform the following tasks: (1) Robust integration outside the entire discontinuity region Γ ; (2) Accurate detection and location of the switch points x_m when the solution trajectory reaches Γ , this includes switching intersections for lower dimensions; (3) Check at $x_m \in \Gamma$ for the existence of a regular switching (transversality) as well as for the existence of an attractive chattering behavior (sliding motion); (4) Integration with a sliding mode on Γ ; (5) Decision of whether or not we should leave the sliding region. We would like to mention that our contribution is **independent** of using particular integration schemes. For discretizing the differential equations outside the discontinuity region Γ any explicit integration scheme can be used. In this work we have used the mid-point rule of explicit 2^{nd} order Runge-Kutta integration scheme (Butcher, 2008; Cellier and Kofman, 2006; Munz et al., 2011). At the end of each integration step we check whether the discontinuity region Γ has been reached or not. We distinguish the following cases:

1. If $\langle \gamma_j(x_i) \cdot \gamma_j(x_{i+1}) \rangle > 0$ for all $j = 1, 2, \dots, p$ where p is the number of the intersected $\mathbb{R}^{(n-1)}$ switching manifolds, then we continue integrating the system with the same flow map vector f_q .
2. If there exist $j \in \{1, 2, \dots, p\}$ such that $\langle \gamma_j(x_i) \cdot \gamma_j(x_{i+1}) \rangle < 0$, this indicates a zero crossing in the time interval $(t_i, t_i + \Delta t_i)$. In this case we have a continuous smooth switching function $\gamma_j(x_{i+1}(\sigma))$ taking opposed signs at $\sigma = 0$ and $\sigma = \Delta t_i$ and therefore there exist a zero at $\sigma_m \in (0, \Delta t_i)$ which defines the switch point $x_m = x_{i+1}(\sigma_m) \in \Gamma_j$.
3. The case in which we have $\langle \gamma_j(x_i) \cdot \gamma_j(x_{i+1}) \rangle < 0 \wedge \gamma_j(\sigma_m) = 0$ for all $j = 1, 2, \dots, k$ where $k \leq p$ and $\sigma_m \in (0, \Delta t_i)$ indicates that the solution trajectory has reached the intersection of $k \leq p$ of transversally intersected $\mathbb{R}^{(n-1)}$ hyper switching manifolds Γ_j .

In the last two cases, secant approach (Allen and Isaacson, 1998; Kaw and Kalu, 2008) is employed to find the root

σ_m of the switching function $\gamma_j(\sigma) = \gamma(x_{i+1}(\sigma))$. Once the switch point x_m has been located, the algorithm checks whether the switch point x_m is a transversality point (leads to cross Γ) or a chattering equilibrium (leads to slide on Γ) by checking the sign of the two matrices Ψ and F (Lemma 1). The proposed convexification (Equation 40, 44-48) is used to approximate the system dynamics when sliding on Γ . For the integration during the sliding any implicit integration scheme can be used. In this work we have used the midpoint rule of implicit Bathe time integration scheme (Bathe and Noh, 2012). To avoid any situation in which the intermediate stages values don't lie exactly on the sliding surface we use a projection formulation for convex sets together with semi-smooth Newton methods to project back to the sliding region the approximated stage values $x_{i+\frac{1}{2}}$ and x_{i+1} at $t_i + \frac{\Delta t_i}{2}$ and $t_i + \Delta t_i$, respectively. The objective of the projection formulation is to stabilize the solution during the sliding on Γ . Consider a point x^* close to the hyper switching manifold Γ , each one integration step of the projected Bathe scheme on the sliding manifold Γ_s then is given as

1. $x_{i+\frac{1}{2}}^* = x_i + \frac{\Delta t_i}{4} (f_s(x_i) + f_s(x_{i+\frac{1}{2}}))$
2. $x_{i+\frac{1}{2}} = \text{proj}(x_{i+\frac{1}{2}}^*)$
3. $x_{i+1}^* = -\frac{1}{3}x_i + \frac{4}{3}x_{i+\frac{1}{2}} + \frac{\Delta t_i}{3}f_s(x_{i+1})$
4. $x_{i+1} = \text{proj}(x_{i+1}^*)$

The projection point $x \in \Gamma$ to x^* : $x = P(x^*)$ is given by the solution of the projection function:

$$P: \min_{x \in \Gamma_s} u(x) : u(x) = \left(\frac{1}{2}(x^* - x)^T (x^* - x) \right) \quad (61)$$

where Γ_s is the sliding manifold. To find the projected value x we introduce a Lagrange multiplier λ and we need to find the root of the equation system

$$G(x, \lambda) = \begin{pmatrix} \frac{\partial u(x)}{\partial x} + \lambda \frac{\partial \gamma(x)}{\partial x} \\ \gamma(x) \end{pmatrix} \quad (62)$$

We use Newton iteration, by imposing the condition $G(x_{k+1}, \lambda_{k+1}) = 0$ and expand $G(x_{k+1}, \lambda_{k+1})$ in Taylor series neglecting the terms of order equal or greater than 2.

$$0 = G(x_k, \lambda_k) + \begin{pmatrix} x_{k+1} - x_k \\ \lambda_{k+1} - \lambda_k \end{pmatrix} \cdot G'(x_k, \lambda_k) \quad (63)$$

for $k \geq 0$ so that

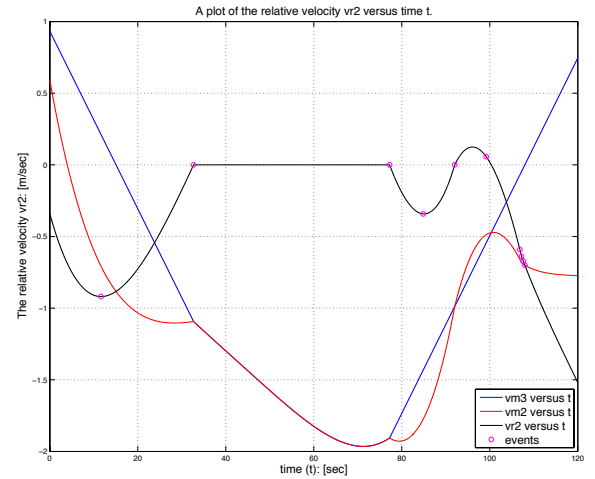
$$G'(x_k, \lambda_k) \cdot \begin{pmatrix} x_{k+1} - x_k \\ \lambda_{k+1} - \lambda_k \end{pmatrix} = -G(x_k, \lambda_k) \quad (64)$$

$$G'(x, \lambda) = \begin{bmatrix} I + \lambda \frac{\partial}{\partial x} \left(\frac{\partial \gamma(x)}{\partial x} \right) & \frac{\partial \gamma(x)}{\partial x} \\ \left(\frac{\partial \gamma(x)}{\partial x} \right) & 0 \end{bmatrix} \quad (65)$$

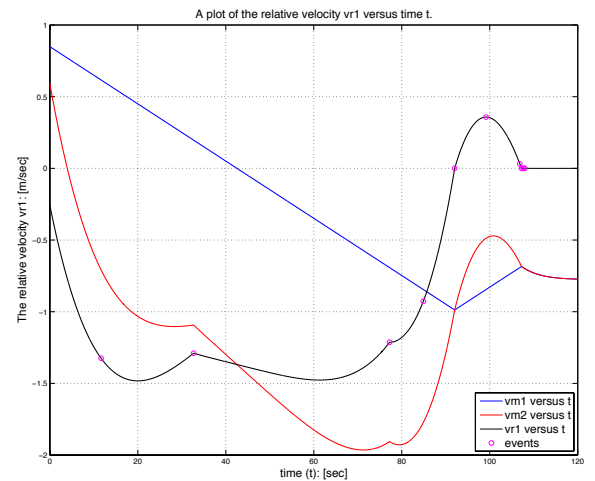
At the end of each integration step from t_i to $t_i + \Delta t_i$ while we integrate with the sliding vector f_s , we keep checking whether we have to keep sliding on Γ_s or leaving it, by checking the value of κ_i in (45).

5 Simulation Results:

As shown in Figure 3, the system in Case Study 1 was simulated for $m = M_1 = M_2 = 1[\text{kg}]$, $k = 0.88[\text{N} \cdot \text{m}^{-1}]$, $F_{c1} = 0.01996[\text{N}]$ $F_{c2} = 0.062[\text{N}]$, and $x_0 = [0.8295 \ 0.8491 \ 0.3725 \ 0.5932 \ 0.8726 \ 0.9335]^T$. The force u was simulated as a sine wave of frequency of $\omega = 0.073[\text{rad}/\text{sec}]$. The relative and absolute error tolerance used in the approximation were adjusted to $ATOL = RTOL = 10^{-8}$.



(a)



(b)

Figure 3. The sliding mode simulation of Example 2.4 with $m = M_1 = M_2 = 1[\text{kg}]$, $k = 0.88[\text{N} \cdot \text{m}^{-1}]$, $F_{c1} = 0.01996[\text{N}]$ $F_{c2} = 0.062[\text{N}]$, and $x_0 = [0.8295 \ 0.8491 \ 0.3725 \ 0.5932 \ 0.8726 \ 0.9335]^T$. In (a): The time evolution of the relative velocity v_{r2} . In (b): The time evolution of the velocities v_{r1} .

The sliding bifurcations depend on the effect of the external force u and the level of Coulomb friction. We can observe that, at the beginning of the simulation, the

execution of the hybrid automaton starts in the discrete state $q_3 = Slip_1^- Slip_2^-$, the system starts in a slip phase for the two frictional interfaces in the system; since the effect of the external force applied tangentially on the interface is lower than the level of Coulomb friction. At the time instant $t = 32.69 \text{ sec}$, two masses m and M_2 stick together and the solution trajectory start a sliding motion on the switching manifold Γ_{b_2} (see Figure 3 (a)) ensuring a chattering path avoidance between the discrete states $q_3 = Slip_1^- Slip_2^-$ and $q_2 = Slip_1^- Slip_2^+$. A smooth exit from the sliding motion on Γ_{b_2} into q_3 was detected at the time instant $t = 77.23 \text{ sec}$. A regular switching (transversality) from the discrete state $q_3 = Slip_1^- Slip_2^-$ to the discrete state $q_1 = Slip_1^+ Slip_2^+$ at the intersection $\Delta = \Gamma_a \cap \Gamma_b$ was detected at $t = 92.04 \text{ sec}$. At $t = 108 \text{ sec}$, two masses m and M_1 stick together and the solution trajectory start a sliding motion on the switching manifold Γ_{a_2} ensuring a chattering path avoidance between the discrete states $q_4 = Slip_1^+ Slip_2^-$ and $q_3 = Slip_1^- Slip_2^-$. During a simulation time of 120 seconds, 5 mode switches have been recorded.

Case Study 2:

Consider a mechanical system as depicted in Figure 4. The system consists of three blocks of masses m_1 , m_2 , and m_3 on a moving belt with constant velocity v_d . The three blocks are connected along a line by two linear springs of stiffness k_{12} and k_{23} , and connected to a fix support by to linear springs of stiffness k_1 , k_2 , and k_3 , respectively.

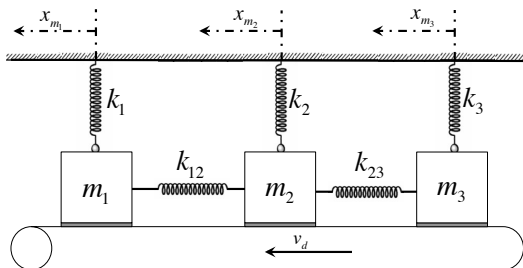


Figure 4. The schematic of the studied Mechanical stick-slip system with 3 blocks.

The equations of the system model in \mathbb{R}^6 are given by

$$f(x) : \left\{ \begin{array}{l} \dot{x}_{m_1}(t) = v_{m_1}(t) \\ \dot{v}_{m_1}(t) = \frac{1}{m_1}(u_1 - k_1 x_{m_1}(t) - \mathcal{F}_1) \\ \dot{x}_{m_2}(t) = v_{m_2}(t) \\ \dot{v}_{m_2}(t) = \frac{1}{m_2}(u_2 - k_2 x_{m_2}(t) - \mathcal{F}_2) \\ \dot{x}_{m_3}(t) = v_{m_3}(t) \\ \dot{v}_{m_3}(t) = \frac{1}{m_3}(u_3 - k_3 x_{m_3}(t) - \mathcal{F}_3) \end{array} \right\} \quad (66)$$

$$u_1 = k_{12}(x_{m_2} - x_{m_1}) + k_{13}(x_{m_3} - x_{m_1}) \quad (67)$$

$$u_2 = k_{12}(x_{m_1} - x_{m_2}) + k_{23}(x_{m_3} - x_{m_2}) \quad (68)$$

$$u_3 = k_{13}(x_{m_1} - x_{m_3}) + k_{23}(x_{m_2} - x_{m_3}) \quad (69)$$

We denote x_{m_1} , x_{m_2} , and x_{m_3} to the position of the masses m_1 , m_2 , and m_3 respectively, \mathcal{F}_1 , \mathcal{F}_2 , and \mathcal{F}_3 to the tangential contact force on the frictional interfaces between the moving belt and the three masses m_1 , m_2 , and m_3 respectively. The functional relationship between the friction force and the relative velocity on the three frictional interfaces between the moving belt and the blocks m_1 , m_2 , and m_3 is given by

$$\mathcal{F}_1 = \left\{ \begin{array}{l} F_{c_1} \text{ for } v_{m_1} > v_d \\ -F_{c_1} \text{ for } v_{m_1} < v_d \end{array} \right\} \quad (70)$$

$$\mathcal{F}_2 = \left\{ \begin{array}{l} F_{c_2} \text{ for } v_{m_2} > v_d \\ -F_{c_2} \text{ for } v_{m_2} < v_d \end{array} \right\} \quad (71)$$

$$\mathcal{F}_3 = \left\{ \begin{array}{l} F_{c_3} \text{ for } v_{m_3} > v_d \\ -F_{c_3} \text{ for } v_{m_3} < v_d \end{array} \right\} \quad (72)$$

where v_{m_1} , v_{m_2} , and v_{m_3} are the velocities of m_1, m_2 , and m_3 respectively. F_{c_1} , F_{c_2} , and F_{c_3} are the levels of the coulomb friction. Physically, for each one of the three frictional interfaces in the system, as long as the force acting at the interface (call it ρ_j) does not exceed the Coulomb friction level F_{c_j} , the moving belt and the mass m_j move together with $v_{r_j} = 0$ where $j = 1, 2, 3$. As soon as ρ_j exceeds the Coulomb friction level, the mass m_j slips over the belt with $v_{r_j} \neq 0$. The slip is said to be positive ($Slip_j^+$) with a friction force $\mathcal{F}_j = +F_{c_j}$, i.e. the mass m_j slips on the belt, if $v_j > v_d$. The slip motion is said to be negative ($Slip_j^-$) with a friction force $\mathcal{F} = -F_{c_j}$, if $v_j < v_d$. Obviously the system is discontinuous on three hyper switching manifolds Γ_a , Γ_b , and Γ_c characterized as zero sets of the switching functions $\gamma_a(x)$, $\gamma_b(x)$, and $\gamma_c(x)$ respectively

$$\Gamma_a = \{x \in \mathbb{R}^n : \gamma_a(x) \mid v_{m_1}(t) = v_d(t)\} \quad (73)$$

$$\Gamma_b = \{x \in \mathbb{R}^n : \gamma_b(x) \mid v_{m_2}(t) = v_d(t)\} \quad (74)$$

$$\Gamma_c = \{x \in \mathbb{R}^n : \gamma_c(x) \mid v_{m_3}(t) = v_d(t)\} \quad (75)$$

The system was simulated for the data set: $m_1 = m_2 = m_3 = 1[\text{kg}]$, $F_{c_1} = 0.14[\text{N}]$, $F_{c_2} = 0.13[\text{N}]$, $F_{c_3} = 0.12[\text{N}]$, $k_1 = k_2 = k_3 = k_{12} = k_{13} = k_{23} = 0.01[\text{N} \cdot \text{m}^{-1}]$, $v_d = 0.5\text{m/sec}$ and $x_0 = [4.7799 \ 0.2797 \ 4.0038 \ 1.7144 \ 1.2922 \ 4.1263]^T$. The external force u was simulated as a sine wave of frequency of $\omega = 0.24[\text{rad/sec}]$. The relative and absolute error tolerance used in the approximation were adjusted to $ATOL = RTOL = 10^{-8}$.

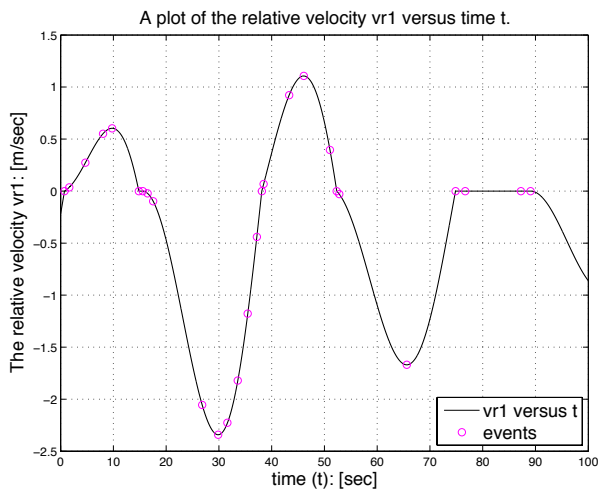
The simulation results for simulation time adjusted to 100 seconds are shown in Figure 5. At the beginning of the simulation, the execution of the hybrid automaton starts in the discrete state $q_1 = Slip_1^+ Slip_2^+ Slip_3^+$ (i.e. the system starts in a slip phase), since the effect of the external force applied tangentially on the frictional interface is greater than the level of Coulomb friction, for the three frictional interfaces in the system. Both m_1 and m_2 stick with the moving belt in the time interval from $t = 74.84\text{sec}$ to $t = 89.07\text{sec}$ and the solution

trajectory start a sliding motion on the intersection $\Gamma_a \cap \Gamma_b = \{x \in \mathbb{R}^6 : v_{m_1} = v_{m_2} = v_d\}$. At the time instant $t = 76.69\text{sec}$ the solution passes through the intersection of the three transversally intersected switching manifolds $\Gamma_a \cap \Gamma_b \cap \Gamma_c = \{x \in \mathbb{R}^6 : v_{m_1} = v_{m_2} = v_{m_3} = v_d\}$ switching from a sliding on the intersection $\Gamma_a \cap \Gamma_b$ in the positive direction of the switching manifold Γ_c into sliding on the intersection $\Gamma_a \cap \Gamma_b$ in the negative direction of Γ_c providing a chattering bath avoidance between the flow sets associated to these intersections. During a simulation time of 100 seconds, 16 mode switches as well as 12 tangential crossings have been recorded.

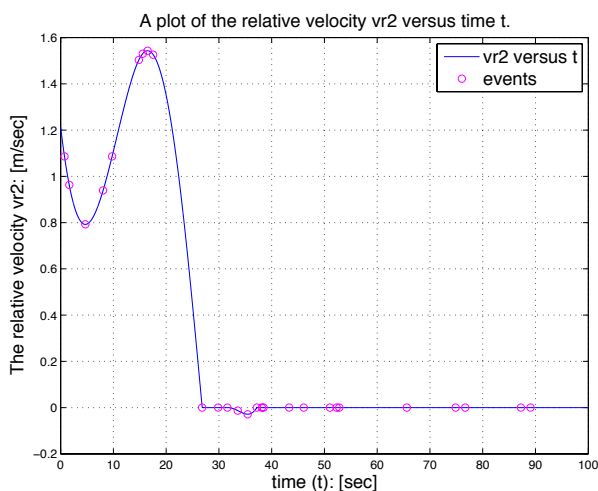
6 Conclusions

In this paper we presented a new approach for the robust and stable numerical simulation of hybrid systems with chattering behavior, characterized either by infinite fast control actions or by discontinuous laws of physics. We have proposed a technique to detect chattering behavior “on the fly” in real-time simulation. Necessary and sufficient conditions driving to chattering behavior are explicitly introduced, and the treatment of chattering behavior during the numerical simulation using so-called sliding mode simulation is studied. A simulation algorithm is proposed that guarantees a robust treatment of chattering behavior. Its purpose is to organize mode switching and to allow sliding mode simulation each time the necessary and sufficient condition for chattering is satisfied. A novel computational framework which treats automatically any non-smoothness in the trajectory of the state variables during the regularization of the chattering path by a smooth correction after each integration time-step was also provided. The main objective of the computational algorithm is to switch between the transversality modes and the sliding modes simulation automatically as well as integrating each particular state appropriately and localize the structural changes in the system in an accurate way. Our approach is based on mixing compile-time transformations of hybrid programs (generating what is necessary to compute the smooth equivalent dynamics), the decision at runtime of the necessary and sufficient conditions for entering and exiting a sliding mode, and the computation, at runtime, of the smooth equivalent dynamics. We have shown by a special hierarchical application of convex combinations that unique solutions can be found in general cases when the switching function takes the form of finitely many intersecting manifolds so that an efficient numerical treatment of the sliding motion constrained on the entire discontinuity region (including the switching intersection) is guaranteed.

Finally, the simulation results - reported here on a set of representative case studies - showed that our approach is efficient and precise enough to provide a chattering bath avoidance, to perform a special numerical treatment of the constrained motion along the discontinuity surface, as well as its robustness in achieving an accurate detection and localization of the switch points for both entering to- and exiting from- the sliding region for the case of a single manifold of discontinuity as well as the case of switching intersection.



(a)



(b)

Figure 5. The sliding mode simulation of Case Study 2 with $m_1 = m_2 = m_3 = 1[\text{kg}]$, $k_1 = k_2 = k_3 = k_{12} = k_{13} = k_{23} = 0.01[\text{N} \cdot \text{m}^{-1}]$, $F_{c_1} = 0.14[\text{N}]$, $F_{c_2} = 0.13[\text{N}]$, $F_{c_3} = 0.12[\text{N}]$, $v_d = 0.5\text{m}/\text{sec}$, and $x_0 = [4.7799 \ 0.2797 \ 4.0038 \ 1.7144 \ 1.2922 \ 4.1263]^T$. In (a): The time evolution of the relative velocity v_{r_1} . In (b): The time evolution of the relative velocity v_{r_2} .

Acknowledgements

This work was supported by the ITEA2/MODRIO project under contract N° 6892, and the ARED grant of the Brittany Regional Council.

References

- Myron Allen and Eli Isaacson. Numerical analysis for applied science. *John Wiley and Sons*, 1998.
- Klaus-Jürgen Bathe and Gunwoo Noh. Insight into an implicit time integration scheme for structural dynamics. *Computers and Structures*, 2012.
- Albert Benveniste, Timothy Bourke, Benoit Caillaud, and Marc Pouzet. Non-standard semantics of hybrid systems modelers. *Journal of Computer and System Sciences*, 2012.
- Martin Biák, Tomáš Hanus, and Drahoslava Janovská. Some applications of filippov’s dynamical systems. *Journal of Computational and Applied Mathematics*, 2013.
- John Charles Butcher. Numerical methods for ordinary differential equations. *John Wiley and Sons*, 2008.
- Chaohong Cai, Rafal Goebel, Ricardo Sanfelice, and Andrew Teel. Hybrid systems: limit sets and zero dynamics with a view toward output regulation. *Springer-Verlag*, 2007.
- François Cellier and Ernesto Kofman. Continuous system simulation. *Springer Verlag*, 2006.
- Mario di Bernardo, Chris Budd, Alan Champneys, Piotr Kowalczyk, Arne Nordmark, Gerard Olivar Tost, and Petri Piironen. Bifurcations in nonsmooth dynamical systems. *Industrial and Applied Mathematics*, 2008.
- Aleksei Fedorovich Filippov. Differential equations with discontinuous right-hand sides. *Mathematics and its Applications*, Kluwer Academic, 1988.
- Marcel Guardia, Tere Seara, and Marco Antonio Teixeira. Generic bifurcations of low codimension of planar filippov systems. *Journal of Differential Equations*, 2011.
- Karl Henrik Johansson, Andrey Barabanov, and Karl Johan Åström. Limit cycles with chattering in relay feedback systems. *IEEE TRANSACTIONS ON AUTOMATIC CONTROL*, 47(9), 2002.
- Autar Kaw and Egwu Eric Kalu. Numerical methods with applications (1st edition). *WordPress.*, 2008.
- Hai Lin and Panos J. Antsaklis. Hybrid dynamical systems: Stability and stabilization. *The Control Systems Handbook, Second Edition: Control System Advanced Methods*. CRC Press, 2009.
- Ben Morris. Hybrid invariant manifolds in systems with impulse effects with application to periodic locomotion in bipedal robots. *IEEE Transactions on Automatic Control*, 2009.
- Claus-Dieter Munz, Florian Hindenlang, and Gregor Gassner. A runge-kutta based discontinuous galerkin method with time accurate local time stepping. *Numerical Methods for Hyperbolic Equations: Theory and Applications.*, 2011.
- Peter Schrammel. *Logico-Numerical Verification Methods for Discrete and Hybrid Systems*. PhD dissertation, 2012.
- Vadim Utkin. Sliding mode in control and optimization. *Springer, Berlin*, 1992.
- Daniel Weiss, Tassilo Küpper, and Hany Hosham. Invariant manifolds for nonsmooth systems with sliding mode. *Mathematics and Computers in Simulation*, 2014.
- Fu Zhang, Murali Yeddanapudi, and Pieter Mosterman. Zero-crossing location and detection algorithms for hybrid system simulation. *IFAC W. Cong.*, 2008.
- Jun Zhang, Karl Henrik Johansson, John Lygeros, and Shankar Sastry. Zeno hybrid systems. *International Journal of Robust and Nonlinear Control*, 2001.

Job-Scheduling of Distributed Simulation-Based Optimization with Support for Multi-Level Parallelism

Peter Nordin¹ Robert Braun¹ Petter Krus¹

¹Department of Management and Engineering, Linköping University, Sweden,
{peter.nordin, robert.braun, petter.krus}@liu.se

Abstract

In many organizations the utilization of available computer power is very low. If it could be harnessed for parallel simulation and optimization, valuable time could be saved. A framework monitoring available computer resources and running distributed simulations is proposed. Users build their models locally, and then let a job scheduler determine how the simulation work should be divided among remote computers providing simulation services. Typical applications include sensitivity analysis, co-simulation and design optimization. The latter is used to demonstrate the framework. Optimizations can be parallelized either across the algorithm or across the model. An algorithm for finding the optimal distribution of the different levels of parallelism is proposed. An initial implementation of the framework, using the Hopsan simulation tool, is presented. Three parallel optimization algorithms have been used to verify the method and a thorough examination of their parallel speed-up is included.

Keywords: Job-scheduling, parallelism, distributed simulation, optimization

1 Introduction

Design optimization is a powerful development tool, which can greatly increase the benefits of simulation. However, the usability is often limited by long execution times. A common solution is to utilize parallel execution, for example by using parallel optimization algorithms. Each simulation model in itself may, however, also be parallelized. Furthermore, multiple optimization jobs can also be executed simultaneously. To benefit the most from these methods, an intelligent scheduler for multi-level parallelism is required.

In many organizations the overall computer performance is poorly utilized a large part of the time. Computers are often used for tasks with low requirements, such as word processing, and spend a lot of time in idle mode.

This work presents a framework, illustrated in Figure 1, utilizing available network computers for multi-level parallelism during optimization. Job-level, algorithm-level

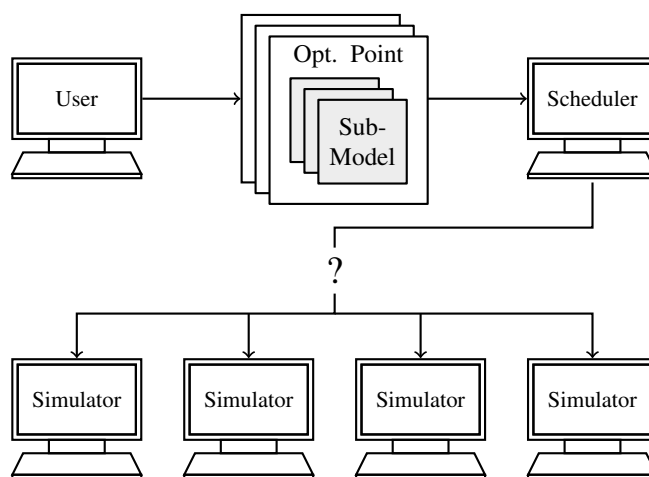


Figure 1. The core of the framework is the job scheduler. It must decide how jobs should be distributed based on available simulation resources and their performance.

and model-level parallelism is supported. The most beneficial combination of these will depend on properties of the model as well as the current state, performance and availability of simulation-service providers on the network. The algorithm used for optimization will also have a large impact on performance. For this reason, a thorough investigation of three parallel optimization algorithms is included. Two of these are custom made for the sake of the experiments, while one is state-of-the-art and naturally parallel.

The intention is to create a small-scale software with few dependencies that can easily be deployed on an office network. One goal is to support simulation models from different tools through the use of Functional Mock-up Interface (FMI) for co-simulation (Blochwitz et al., 2009).

In (Sadashiv and Kumar, 2011), a thorough comparison between the cluster and grid computing concepts is given together with examples on tools and simulation environments for such systems. Computing clusters are often built up of a homogeneous collection of computer nodes located at the same place accessed through a front-end. From the outside, usually only the front-end is visible. A

job-queuing system is responsible for managing jobs and distributing the workload among the nodes.

In a grid network, computers can be located at different places, but they all dedicate some computational power to a common governing system, a middle-ware, responsible for assigning jobs to available resources. One example of such a system is the volunteer-computing framework BOINC (Anderson, 2003). Users around the world can download a client and choose from many projects which to volunteer resources to. Grids are typically heterogeneous by nature. The participating computers may have vastly different performance and availability.

Using dedicated computing clusters would of course be beneficial, as the computational performance and availability would be reliable. Work stations on an office network should, however, be considered as a small-scale grid with a less reliable source of computational power. Computers may come and go sporadically and their perceived performance may at any time be reduced due to workload caused by their respective local user.

For parallel optimization, a third party scheduler could be problematic. Most algorithms require all parallel tasks to run synchronized. They should also have about the same execution time, since the overall speed will be limited by the slowest task.

1.1 Related Work

In (Fourer et al., 2010), a framework for distributed optimization as software services is presented. The authors identify the need for and develops standardized protocols to enable different types of optimization services (different solvers, high-level modelling languages and architectures) to register in a common registry service. The framework is built on the XML format and Web Service standards. The work focus on problems expressed in common high-level modeling languages for optimization. In contrast our work focuses on simulation based optimization of non-linear black-box models particular to specific simulation tools. Such models are difficult to generalize into high-level optimization languages. Instead of letting servers provide optimization algorithms, they provide access to one or more simulation tools.

In (Gehlsen and Page, 2001), a Java language specific framework for distributed discrete-event simulation optimization is presented. A Genetic Algorithm (GA), which is naturally parallel, is used. An optimization manager constructs and evaluates designs. An experiment manager constructs simulation tasks that are sent to a distribution manager using Java Remote Method Invocation (RMI) to simulate the tasks on available remote machines running an instance of the simulation tool.

In (Yücesan et al., 2001), a Java and web-based simulation optimization interface is presented. It allows the user to choose combinations of optimization algorithms and simulation models from databases. The key contribution

is the Optimal Computation Budget Allocation (OCBA) algorithm, which allocates simulation jobs to available simulators, called the Computation Budget. New promising designs that based on statistics are likely to improve the overall simulation quality are prioritized. The total number of simulations is reduced as evaluation of non-promising designs is avoided.

The referenced works all provide a registry of simulation servers that clients can fetch available simulation resources from. A central manager then decides how to distribute the work. Clients communicate either directly with the servers in a peer-to-peer manner or by relaying all communication through the manager. The framework presented in this paper uses a similar approach.

A different approach is presented in (Eldred et al., 2000) where the challenges and possibilities of utilizing multiple levels of parallelism on massively parallel super computers have been investigated. They define four levels of parallelism, *algorithmic coarse-grained*, *algorithmic fine-grained*, *function eval. coarse-grained* and *function eval. fine-grained*. The presented implementation made it possible to recursively divide the workload at each parallelism level. That is, at the highest level only coarse-grained parallelization of the optimization algorithm is regarded but at the next lower-level each one of the previously parallelized parts do their own parallelization and scheduling into the next lower level.

For this paper, the first and last of those parallelism levels are the most relevant. Coarse-grained algorithm parallelism represents evaluation of multiple parameter sets with the same model concurrently, or running multiple optimization jobs at the same time (algorithm-level or job-level). Fine-grained function evaluation represents parallelization within a simulation model (model-level).

1.2 Delimitations

Many simulation tools use variable step-size control. Their execution time will therefore depend on the model parametrization. As a consequence, the points in the parameter space may require different amounts of time to evaluate. This variation is, however, difficult to predict. Fine-grained model parallelism through the use of the transmission line element method in Hopsan can also reduce such effects. For this reason, it has not been considered further.

Coarse-grained model parallelism, i.e. spreading the model evaluation over multiple servers, has been left for future work. This becomes beneficial when a model contains individual sub-models with a long evaluation time, making communication overhead negligible. It would also be required if models contain sub-models from different disciplines and co-simulation using different tools is needed.

Experiments have only been performed on homogeneous computer networks. In principle, the proposed algo-

rithm should work similarly on heterogeneous networks. Verifying this with experiments remains a future project.

The Hopsan tool supports importing co-simulation FMI sub-models, so called Functional Mock-up Units (FMUs). While the goal is to support such models directly in the framework, a Hopsan model must currently be used as a master.

2 Framework Architecture

The idea is to run one server providing access to one or more simulation tools on each available computer in the network. Each server provides a number of simulation slots that represent the processor cores made available.

When a simulation server is started it contacts an address server to register which simulation tools it provides. The address server will request status periodically to keep track on availability, speed and the number of available simulation slots.

When a client requires access to remote simulation, it first requests a list of available servers matching some requirements on speed and available number of slots. Then it connects to each desired server individually to request and reserve the needed slots. If a request is granted, the server will launch a separate simulation worker process. All further communication will then be directly between the client and the worker.

The reason for using an external worker process is to keep the server alive even if the simulation would lead to a crash or lock-up. The worker will report back when it is finished so that the server can reopen the simulation slots. If the worker stops responding due to some failure, the server can terminate it by force to free up resources.

The intention is to use tool specific implementations of optimization algorithms. The optimization is thus assumed to be handled by the client. The job scheduler is not part of the optimization algorithms. The tool running the optimization can, however, use it to run the model evaluations.

2.1 Decentralized and Centralized Modes

The framework can work in two modes. If no centralized job distributor is used, each client is responsible for requesting fresh server status before trying to reserve a slot. The information from the address server may be outdated. Clients send a *request and reserve* command to temporarily reserve the needed slots. An actual request can then be sent once the client has determined the work distribution. This prevents other clients from stealing a seemingly open slot. In this decentralized case, illustrated by Figure 2, clients obtain resources on a first-come-first-serve basis. A client will take as many servers and slots as it needs. Job-level parallelism is only possible as long as there are free slots. The decision whether to use algorithm parallelism, model parallelism or both is taken by each client.

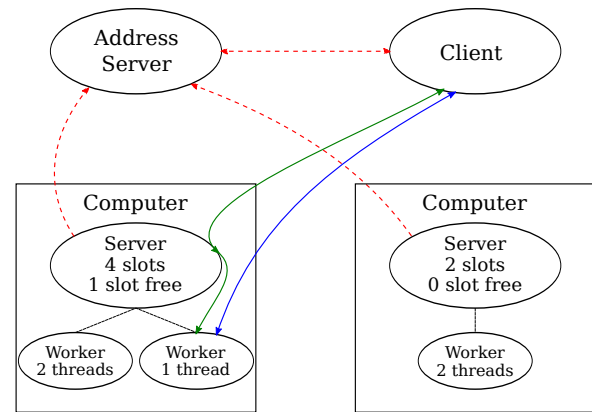


Figure 2. In the decentralized network, clients communicate directly with the servers and the simulation worker processes. A client might look up servers from a predefined list or request them from an address server.

If a centralized job distributor is used, all slot requests go through this master, which keeps track of available resources. In this case, shown in Figure 3, the clients should let the job distributor choose which servers to use. When all servers are busy, job-level parallelism could still be allowed by redistributing ongoing work when new jobs arrive. A system for prioritizing jobs is, however, needed in this case.

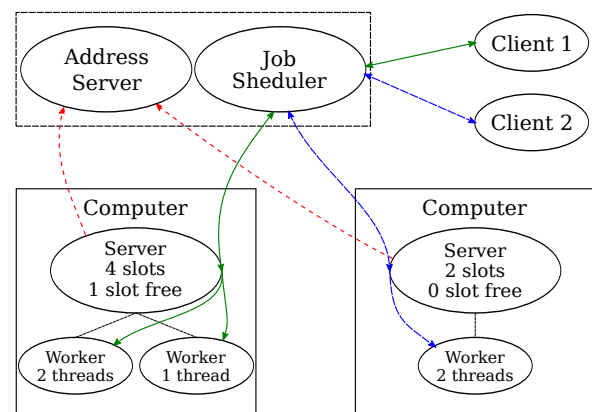


Figure 3. In the centralized network, the job scheduler is responsible for allocating jobs to simulation slots. Clients have no information about available servers and all communication is relayed through the job scheduler.

2.2 Cluster Nodes and Subnets

Simulation servers connected to a Local Area Network (LAN) can report their IP address and port directly to the address server. If a cluster or a subnet behind a firewall is present on the network, the available cluster nodes or subnet computers must either be exposed through port forwarding on the front-end computer or router, or by a relaying address server as illustrated in Figure 4. In this framework it is not possible for the front-end to expose simulation slots from the underlying servers directly. That would

confuse the scheduler and make it interpret the simulation slots as a possibility for model parallelism. Such parallelism is currently only supported within one machine. Also, any built-in job scheduling system on a cluster front-end would have to be bypassed.

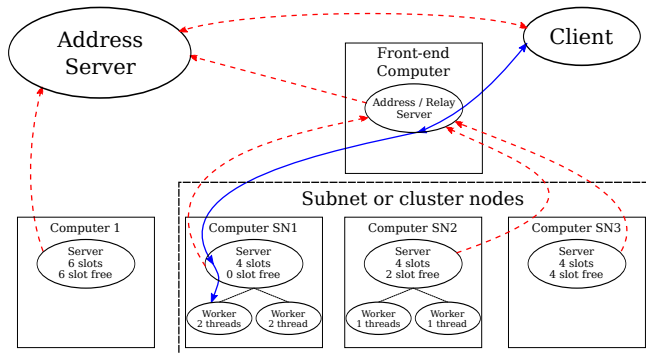


Figure 4. If the network contains subnets or cluster nodes that are not available through port forwarding, an address server instance with access to both networks must be used as a relay.

2.3 Continuous Performance Monitoring

Before a job starts, all participating servers should have supplied benchmark results indicating their performance. However, as the intended target is a work-place network of computers, the performance of the ongoing simulation work must be continuously monitored. Computers may at any time unexpectedly disconnect or slow down due to external use. The work may then need to be rescheduled. For this reason, the scheduler or clients can request simulation progress from each worker to determine if one is significantly lagging behind the others.

A computer with a fast benchmark score may still be unsuitable due to external use. An extension would therefore be to monitor the average CPU utilization. It is, however, difficult to estimate for how long demanding external work will continue.

2.4 Implementation

The framework has been implemented in C++ to work together with the Hopsan (Eriksson et al., 2010) simulation tool. The framework is centred around the message passing library ZeroMQ (Hintjens, 2013). This library can be used for both inter-thread, inter-process and inter-machine communication. It supports a variety of protocols and language bindings are available for many common languages. The library also has built-in support for useful communications patterns, such as the *request-reply* pattern. In this mode incoming requests are automatically queued on a socket until the previous requests have received their reply. A *router* type socket also facilitates asynchronous I/O on the same port. This is useful when setting up a relay server for passing messages between networks.

All network components communicate over TCP/IP. ZeroMQ makes it possible to start servers and clients in any order, making it easy to resume communication when they come and go. While the network components are all written in C++, the use of ZeroMQ makes it possible to include software written in other languages. ZeroMQ can be built with no external dependencies which simplifies implementation and deployment. It can also be extended with support for authentication and encryption.

It is assumed that the optimization algorithms are implemented by the client, in this case the Hopsan simulation tool. The framework implementation consists of:

- The simulation service provider (server) application
- A worker process for the Hopsan simulation core
- The address server, for tracking the available providers on the network
- A client library, simplifying communication with the servers and workers
- The job-scheduler module as a library, currently tightly coupled to the Hopsan simulation tool

The messages exchanged in the framework are currently specific to Hopsan, but should be generalizable for similar tools. Examples are:

- Simulation slot request / reservation, including preferred number of threads for model parallelism
- Sending simulation models and assets like data input files, sub-model libraries and FMUs used by a model
- Simulation control; start, stop and step times, abort or single step instructions for real-time control
- Set and retrieve model parameters
- Status from servers; the number of total/open slots, what services they provide, benchmark speed
- Status from workers; simulation progress
- Retrieving simulation results, variable names, units and values
- Real-time streaming of simulation input and output (if possible)

3 Parallel Optimization Methods

Parallel optimization algorithms are required to evaluate the scheduling algorithm. Two common families of optimization algorithms have been investigated: direct search and population based methods. Only non-gradient based methods have been included. These are more efficient in solving non-linear problems, and can be applied also on problems which are not differentiable.

3.1 Direct Search Methods

Direct search optimization (Hooke and Jeeves, 1961) refers to methods where the parameter space is searched by a number of trial points. At each iteration, an algorithm is used to move one or more points depending on the location of the best known point. This is useful for discrete or non-continuous models, where the gradient cannot easily be obtained. Advantages typically include few evaluations and simple parameterization. On the downside, the possibilities for parallelization are often limited.

The most well-known direct search method is the Nelder-Mead Simplex algorithm for unconstrained problems (Nelder and Mead, 1965). It searches the n -dimensional parameter space with $k = n + 1$ points called the “simplex”. The worst point is reflected through the centroid of the remaining points. Depending on the outcome, the simplex can be expanded, contracted or reduced.

A related method for constrained problems is the Complex method (Box, 1965). In contrast to the simplex method it uses at least $k = n + 2$ points and a reflection factor $\alpha > 1$. This causes a continuous enlargement of the complex. If the reflected point is still the worst, it is retracted iteratively towards the centroid, which compensates for the enlargement. This reduces the risk of the complex collapsing into a subspace when a constraint is reached. Retractions can also be weighted towards the best known point, to prevent the complex from collapsing into the centroid (Guin, 1968). The method can be further improved by adding a random factor and a forgetting factor, commonly referred to as the Complex-RF method (Krus and Ölvander, 2003).

Even though the algorithm is sequential, it can be parallelized with minor modifications. Parallel implementations of the Simplex algorithm has been conducted by (Dennis and Torczon, 1991) using multi-directional search and by (Lee and Wiswall, 2007) by reflecting multiple points at each iteration. Another possibility is to use multiple reflection factors, or to use task prediction methods where possible future evaluations are predicted by assuming a certain outcome of the current step. Multiple retraction steps towards the centroid can also be evaluated in parallel. Here methods using task prediction, multi-retraction and a combination of the first two methods have been tested.

With the task prediction method, candidates are generated iteratively by assuming the outcome of the previous reflection. Figure 5 illustrates the method. First the worst point (x_3) is reflected through the centroid of the other points. It is now assumed that the new point x'_3 is better than the second worst point x_1 . Therefore x_1 can be reflected through x_2 , x_4 and x'_3 . This process is repeated for all four original points. Should the number of simulation slots exceed the number of points, additional candidates are generated by iteratively moving the first reflected point towards the centroid. All candidates are then evaluated in

parallel. If results show that one of the reflected candidates is still the worst, the remaining reflected points are discarded. Moving the reflected points iteratively towards the centroid can then easily be performed in parallel. If it is the first reflected point that shall be moved, the additional candidates can be used to speed up this process further. The iteration will continue until a point that is better than the previously worst point is found.

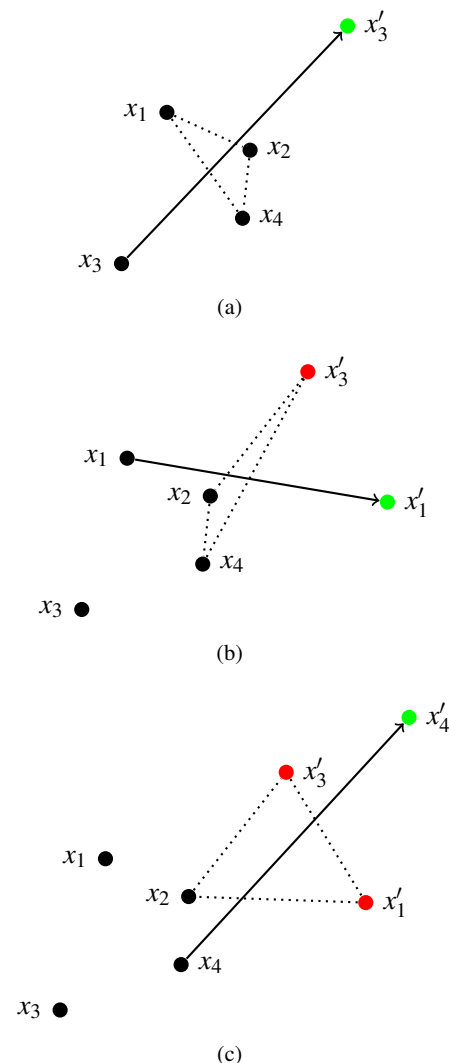


Figure 5. Task-prediction parallel Complex-RF algorithm. By assuming an outcome of a reflection, the next point can be reflected in advance.

Parallelizing retraction steps is trivial, since each step is independent of the previous ones. The method is illustrated by Figure 6. An unlimited number of steps can be computed in parallel. Once a retraction point that is no longer the worst point in the complex is found, all remaining points are discarded.

Results showed that the parallel efficiency of both methods decrease with an increasing number of processing units. Higher speed-up can be achieved by using both methods together and letting them share the available CPUs. In these experiments each method use half

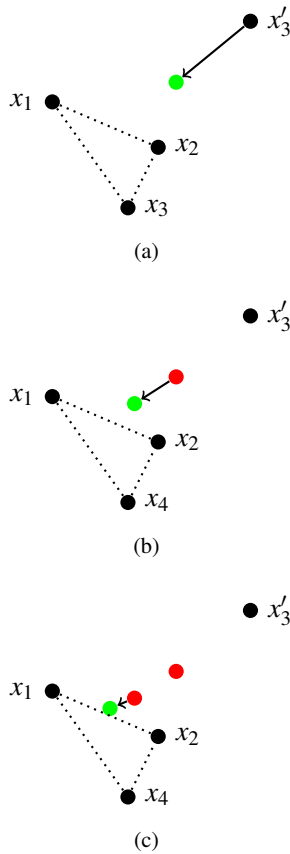


Figure 6. When retracting towards the centroid using the Complex-RF method, multiple steps can be evaluated in parallel.

of the CPUs. Obviously other methods may provide better results, but this has not been considered further in this paper.

The direct search methods were tested on three optimization problems; the sphere function (Equation 1), the Rosenbrock function (Equation 2) and a simulation model of a hydraulic position servo, shown in Figure 7. In the latter, the objective is to minimize the error between reference position and actual position while also maximizing the total energy efficiency of the system. Five parameters are used; proportional and integral control parameters K_p and K_i , piston areas A_1 and A_2 and pump displacement D_p .

$$\begin{aligned}
 &\text{minimize} && \mathbf{F}(\mathbf{x}) = (x_{error}(\mathbf{x}), \eta_{tot}(\mathbf{x}))^T \\
 &&& \mathbf{x} = (K_p, K_i, A_1, A_2, D_p)^T \\
 &\text{subject to} && 0 \leq K_p \leq 1 \times 10^{-2} \\
 &&& 0 \leq K_i \leq 1 \times 10^{-3} \\
 &&& 1 \times 10^{-5} \leq A_1 \leq 1 \times 10^{-2} \\
 &&& 1 \times 10^{-5} \leq A_2 \leq 1 \times 10^{-2} \\
 &&& 1 \times 10^{-6} \leq D_p \leq 1 \times 10^{-3}
 \end{aligned}$$

The three models were optimized with each algorithm 100 times for each number of simulation slots, ranging from 1 to 8. Optimization parameters as suggested by

(Box, 1965) and (Krus and Ölvander, 2003) are used, see Table 1. Results are shown in Figures 8, 9 and 10.

k	$2n$	r_{fac}	0.1
α	1.3	γ	0.3

Table 1. Number of points, reflection factor, randomization factor and forgetting factor used in experiments.

$$F(x_1, x_2) = x_1^2 + x_2^2 \quad (1)$$

$$F(x_1, x_2) = 100(x_2 + x_1^2)^2 + (x_1 - 1)^2 \quad (2)$$

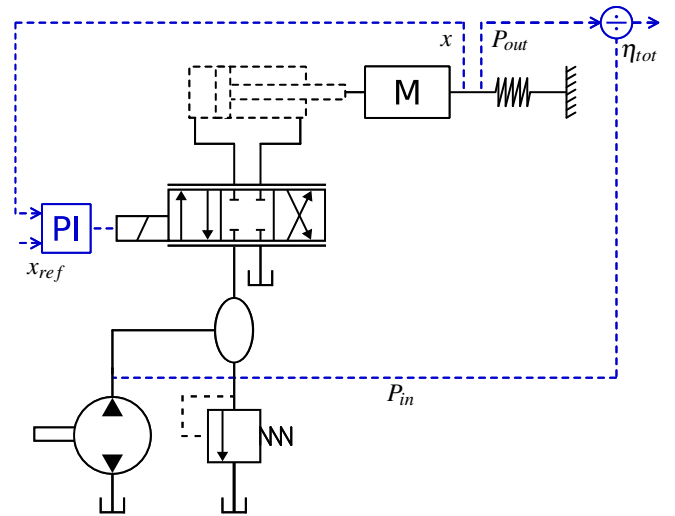


Figure 7. A model of a hydraulic position servo used to evaluate the parallel optimization algorithms.

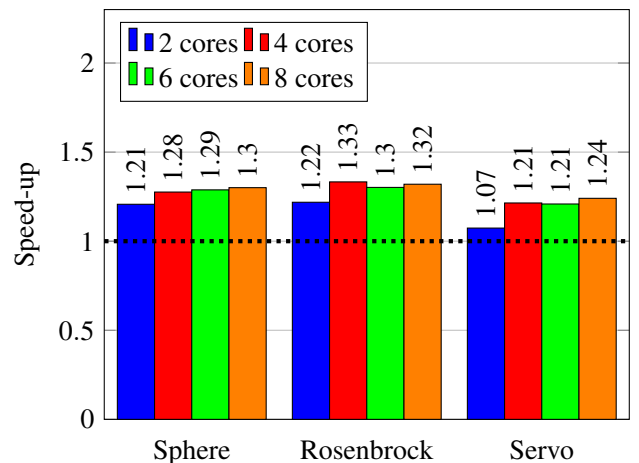


Figure 8. Algorithm speed-up with the task prediction method.

3.2 Population Based Methods

Population based methods is a family of optimization methods where a population of independent points are

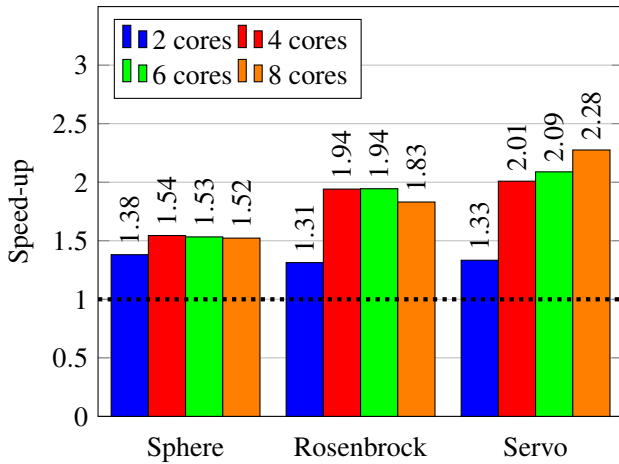


Figure 9. Algorithm speed-up with the multi-retraction method.

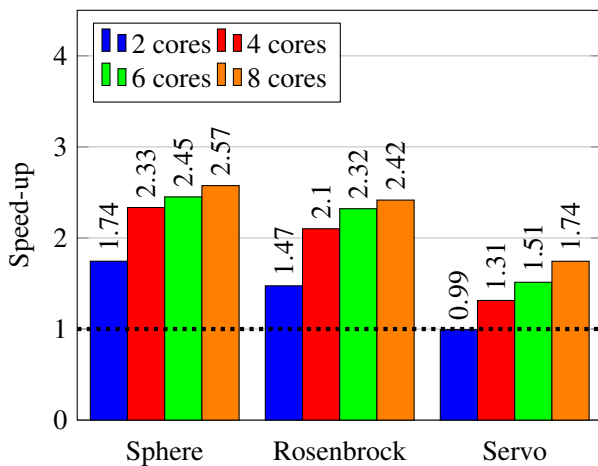


Figure 10. Algorithm speed-up with a combination of task prediction and multi-retraction. This is by far the most efficient method.

used to search the parameter space. At each iteration, all points are evaluated independently of each other. The outcome is then used to generate a new population, which is used in the next iteration. Due to the independent evaluations, population based methods are naturally parallel. Another benefit is that they are intuitive, since they often resemble physical, social or biological phenomena. Examples of population based methods are Differential Evolution (DE) (Storn and Price, 1997), Genetic Algorithms (GAs) (Goldberg, 1989) and Particle Swarm Optimization (PSO) (Kennedy and Eberhart, 1995).

In this paper a PSO algorithm has been used as an example. Results can, however, be generalized to any naturally parallel optimization method. With PSO, each point (denoted “particle”) has a position and a velocity vector, see Figure 11. At each iteration the velocity is changed depending on the particle’s own best known position and the best known position in the swarm. This resembles gravitational pull. Each particle also has an inertial weight, that prevents rapid change in velocity. Particles are then

moved according to the velocity before next iteration. Parallel speed-up can be assumed to be linear, and is only limited by the number of particles in the swarm. It should be pointed out that even though population based methods have higher speed-up than direct search methods, they also require significantly more iterations. Thus, they are not necessarily more efficient than direct search methods.

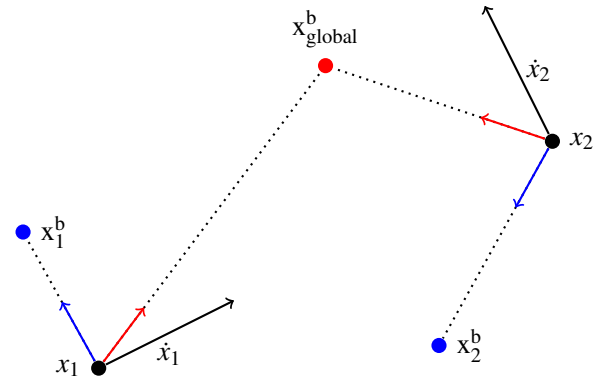


Figure 11. Population-based methods, such as particle swarm optimization, evaluate all points independently and are naturally parallel.

4 Work Scheduling

Efficient scheduling of the workload will have great impact on execution times. This task is complicated for several reasons. The number of available computers and/or processor cores may be limited. Computers may also have different performance or different number of cores. Furthermore, several clients may want to run different optimization jobs at the same time. The proposed solution is to estimate the speed-up factor for various work distributions on available resources.

Optimizations can be parallelized either on algorithm-level or model-level. Speed-up from parallelism will thus depend on both the algorithm and the model. A third alternative is to run several optimizations in parallel and pick the best result (algorithm coarse-grained or job-level parallelism). This has not been considered further in this paper.

Speed-up of the algorithm comes from either reducing the total number of sequential evaluations, or from reducing the number of needed iterations by searching the parameter space more efficiently. For this reason the *equivalent number of iterations with parallelism* $n_{eval,p}$ is defined:

$$n_{eval,p} = \frac{n_{eval}}{SU_a(p_a)} \quad (3)$$

At model-level, the speed-up is defined as the ratio between sequential and parallel execution time. The number of processor cores will determine the magnitude of the speed-up. In most cases it can be assumed that models

cannot be parallelized over several computers. Communication latency over the network induces overhead, which makes this efficient only for large models.

$$t_{sim} = \frac{t_{base}}{SU_m(p_m)} \quad (4)$$

The total execution time for an optimization can be calculated by combining Equations 3 and 4. At each iteration the algorithm will have to wait for the slowest simulation to finish. Thus, the maximum simulation time must be used according to Equation 5. The communication time for sending results over the network may also matter, but is assumed to be negligible for large simulation problems.

$$t_{opt} = n_{eval,p} \max_{0 < i < k} t_{sim,i} + t_{comm} \quad (5)$$

For a homogeneous computer network, where all computers have the same computational speed and number of cores, Equation 5 can be simplified into Equation 6:

$$t_{opt} = n_{eval,p} t_{sim} \quad (6)$$

Finding the optimal task distribution is a combinatorial optimization problem. It can be expressed either as minimizing the execution time or as maximizing the speed-up. For heterogeneous systems, where computers have different performance and number of cores, it can be formulated as follows:

$$\begin{aligned} & \text{maximize} \quad SU(p_a, \mathbf{p}_m) = SU_a(p_a) \min_{0 < i < k} SU_{m,i}(p_{m,i}) \\ & \text{subject to} \quad p_a \frac{1}{k} \sum_{i=0}^k p_{m,i} \leq \sum_{i=0}^{n_p} (n_{c,i}) \\ & \quad p_{m,i} \leq n_{c_i} \text{ for } i = 0, \dots, n_p \end{aligned}$$

Again, the formulation can be simplified for homogeneous systems:

$$\begin{aligned} & \text{maximize} \quad SU(p_a, p_m) = SU_a(p_a) SU_m(p_m) \\ & \text{subject to} \quad p_a p_m \leq n_p n_c \\ & \quad p_m \leq n_c \end{aligned}$$

For a homogeneous system, it is sufficient to loop through different values for p_m , and calculate the largest possible corresponding p_a . The total speed-up can then be computed as the product of $SU_a(p_a)$ and $SU_m(p_m)$. Pseudo code for this is shown in Listing 1.

Listing 1. A scheduling algorithm that computes the optimal combination of algorithm and model parallelism (p_a^* and p_m^*) for homogeneous computer networks.

```
SU* = 0
for (p_m=1; p_m ≤ n_c; ++p_m) {
    p_a = n_p floor(n_c / p_m)
    SU = SU_a(p_a) SU_m(p_m)
    if (SU > SU*) {
        SU* = SU
    }
}
```

```
p_m* = p_m
p_a* = p_a
}
```

Much of this code can be re-used for heterogeneous systems. Instead of using the same p_m for each computer, different maximum values (p_m^{max}) are tested. This limits the maximum number of cores each model can use. The number of parallel models that should run on each computer is then calculated. The sum of these gives the total value for p_a . Finally, SU_m is computed as the minimum speed-up from all computers. Pseudo-code for heterogeneous scheduling is shown in Listing 2.

Listing 2. For heterogeneous computer networks an approximate scheduling can be computed by limiting maximum level of model parallelism (p_m^{max}).

```
SU* = 0
for (p_m^max=1; p_m^max ≤ n_c^max; ++p_m^max) {
    p_a = floor(∑_{i=0}^{n_p} n_{c,i} / min(p_m^max, n_{c,i}))
    SU = SU_a(p_a) SU_m(p_m^max)
    if (SU > SU*) {
        SU* = SU
        p_m* = p_m^max
        p_a* = p_a
    }
}
```

5 Results

Two experiments were conducted, one theoretical and one practical. First, the scheduling algorithm was numerically verified by letting it calculate probable speed-up for two test models on a fictional computer network. Subsequently, the scheduler was implemented and tested by running optimizations on real hardware.

5.1 Numerical Verification

The scheduling algorithm was numerically verified by using two example models; the position servo model mentioned previously, and a model of a hydraulic mining rock drill. The latter is a large model with good opportunities for model-level parallelism. Speed-up on a quad-core processor was measured to be 2.60. The model is provided by industrial partners, and is used in real product development. For the first model, however, model-level parallelism is not beneficial due to the low number of sub-models. Execution time appear to be independent of the number of cores.

As a theoretical example the scheduler was executed for four homogeneous computers with four cores each. By using pre-defined speed-up factors, the optimal work distribution can be obtained from a look-up table. All three optimization algorithms mentioned in Section 3 were examined. The PSO algorithm was assumed to use 16 particles. Speed-up of the algorithms was assumed to be the

same for the rock drill as for the position servo. Results are shown in Table 2. As expected, the rock drill is calculated to achieve the best performance when using the maximum number of cores at model-level. The position servo, however, benefits more from a high degree of algorithm parallelism. When using PSO, parallelism at algorithm level is always more beneficial.

		Position Servo				Rock Drill				
		p_m	SU_m							
p_a		SU_a	1	2	3	4	1	2	3	4
Complex-RFP	1	1.00	1.00	1.00	1.04	0.96	1.00	1.92	2.23	2.60
	2	0.99	0.99	0.99	1.03	0.95	0.99	1.90	2.21	2.49
	3	1.19	1.19	1.19	1.24	1.14	1.19	2.28	2.65	3.09
	4	1.31	1.31	1.31	1.36	1.26	1.31	2.52	2.92	3.41
	5	1.42	1.42	1.42	-	-	1.36	2.73	-	-
	6	1.51	1.51	1.51	-	-	1.45	2.90	-	-
	7	1.67	1.67	1.67	-	-	1.60	3.21	-	-
	8	1.74	1.74	1.74	-	-	1.67	3.34	-	-
PSO (with 16 particles)	1	1.00	1.00	1.00	1.04	0.96	1.00	1.92	2.23	2.60
	2	2.00	2.00	2.00	2.09	1.92	2.00	3.83	4.46	5.2
	3	2.00	2.00	2.00	2.09	1.92	2.00	3.83	4.46	5.2
	4	4.00	4.00	4.00	4.17	3.84	4.00	7.66	8.91	10.4
	5	4.00	4.00	4.00	-	-	4.00	7.66	-	-
	6	5.33	5.33	5.33	-	-	5.33	10.23	-	-
	7	5.33	5.33	5.33	-	-	5.33	10.23	-	-
	8	8.00	8.00	8.00	-	-	8.00	15.33	-	-
	9	8.00	8.00	-	-	-	8.00	-	-	-
	10	8.00	8.00	-	-	-	8.00	-	-	-
	11	8.00	8.00	-	-	-	8.00	-	-	-
	12	8.00	8.00	-	-	-	8.00	-	-	-
	13	8.00	8.00	-	-	-	8.00	-	-	-
	14	8.00	8.00	-	-	-	8.00	-	-	-
	15	8.00	8.00	-	-	-	8.00	-	-	-
	16	16.00	16.00	-	-	-	16.00	-	-	-

Table 2. Speed-up factor as a function of work distribution for the combined Complex-RFP and PSO algorithms. Optimal distributions are shown in red.

5.2 Load Balancing Experiments

To verify the load balancing and rescheduling capabilities of the framework, a network of eight dual-core computers with equal performance was used. The experiment model was a slightly modified position servo model with a dual-core model-level speed up 1.12. Model-level parallelism is achieved through the use of the transmission line element method (Krus et al., 1990) and multi threading (Braun et al., 2011). The model is optimized with both the combined Complex-RFP and the PSO methods. Algorithm speed-up for the Complex-RFP algorithm is taken from Table 2. While the PSO algorithm is assumed to have linear speed-up in itself, in practice this depends on the number of particles used and the number of available computers according to Equation 7. The speed-up is the ratio between the sequential execution time of all models and the longest queue required on any of the simulation servers during parallel execution. The initial algorithm-level parallelism was set to six in both cases, leaving two computers unallocated.

$$SU_{pso,actual} = \frac{p_a}{\text{ceil}\left(\frac{p_a}{\min\left(n_p \text{ floor}\left(\frac{n_c}{p_m}\right), p_a\right)}\right)} \quad (7)$$

Figure 12 shows the total iteration time with the Complex-RFP method including evaluation and transfer of results over the network. One participating computer after another becomes overloaded by external work. Before *c*, the load can be shifted to the free computers and no slowdown occur. After *c*, since the algorithm speed-up is low for this method, the algorithm is reinitialized to use fewer parallel models. At *f* it finally becomes more beneficial to increase the number of parallel models again in comparison to maintaining dual-core model-level parallelism. For a model this small and fast the transfer of result data cannot be neglected. The results show between *c* and *f* that the total time is decreasing slightly with fewer parallel models as less data needs to be transferred.

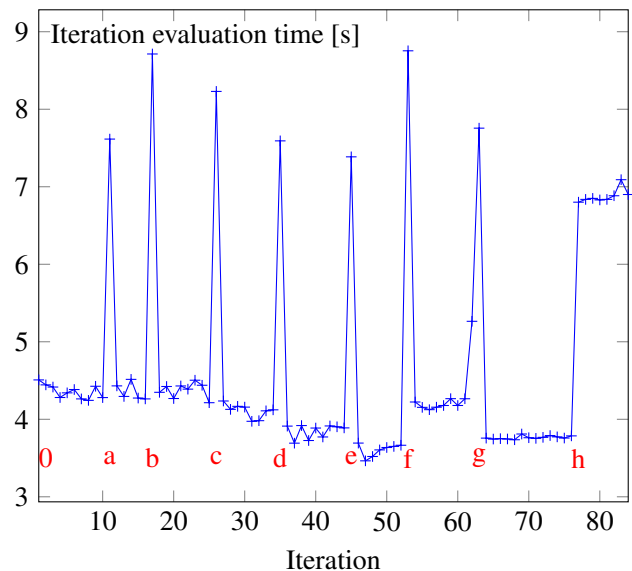


Figure 12. Evaluation time for one iteration using the combined Complex-RFP algorithm, beginning with six parallel evaluations. The letters *a-h* each represent one additional network computer becoming overloaded. Load balancing or parallelization reduction is shown in Table 3.

Figure 13 shows the same experiment for the PSO algorithm. Since it is naturally parallel, the number of particles (parallel models) is kept fixed at six. The speed-up in this case comes purely from the possibility of executing models in parallel. When computers become unavailable the scheduler will try to balance the load so that queues are avoided. Since it is unlikely that a model-level speed-up larger than the number of cores used can be achieved, the method always favors the highest possible algorithm parallelism. At *c*, free computers are no longer available and the scheduler switches to single-core simulation, which is slightly slower but allows to maintain parallel execution. At *f*, the scheduler is forced to begin queuing models for execution and the evaluation time is doubled.

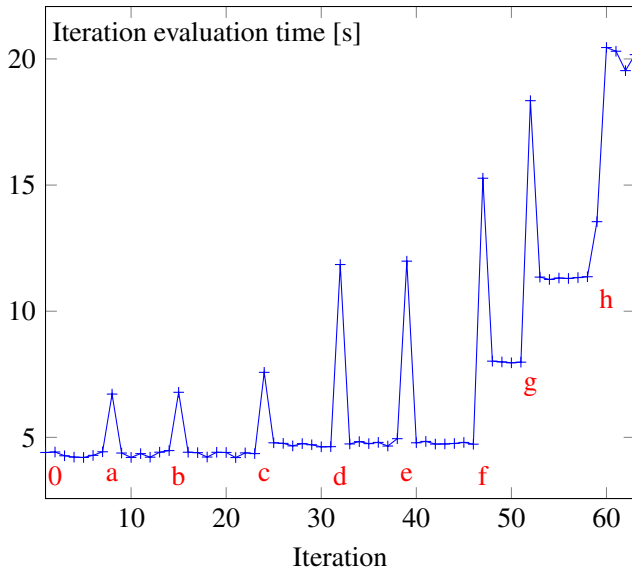


Figure 13. Evaluation time for one iteration using the PSO algorithm with six parallel models. The letters *a–h* each represent one additional network computer becoming overloaded. Load balancing results are shown in Table 3.

In both figures, the spikes represent approximately double execution time, since when a server is lost the current iteration is restarted. At *h*, only one computer remains and when it becomes heavily loaded no better alternatives exist. The chosen parallelism for each rescheduling is given in Table 3.

		0	a	b	c	d	e	f	g	h
	$n_p \times n_c$	16	14	12	10	8	6	4	2	1
C-RFP	p_m	2	2	2	2	2	2	1	1	1
	p_a	6	6	6	5	4	3	4	2	2
PSO	p_m	2	2	2	1	1	1	1	1	1
	p_a	6	6	6	6	6	6	3	2	2

Table 3. The combination of model-level and algorithm-level parallelism that gives the best speed-up depending on availability of computers on the network. Each column represents a point in Figures 12 and 13.

6 Conclusions

A framework for work scheduling of multi-level parallel optimizations has been developed. The scheduler takes the number of available processor cores on each computer into account. Therefore, parallelism on both model-level and algorithm-level can be used to maximize performance. An extension could be to also support solver-level parallelism, for example parallel matrix operations. This could be solved using GPU cards, which would add an additional level to the scheduler.

For homogeneous computer networks, an optimal scheduling can be found by testing all combinations. Heterogeneous networks, however, require heuristic schedul-

ing methods. Thus, an optimal solution cannot be guaranteed.

The speed-up from parallel optimization algorithms depend to a great extent on the model being optimized. Especially, the combination of algorithm and model has a great influence on performance improvement. Thus, different algorithms are efficient for different models. Some knowledge of the model properties are therefore required.

Experiments show that the framework is able to deal with computers on the network suddenly becoming overloaded. The scheduler is able to re-balance the computation load over the remaining resources.

While the implementation is specific for the Hopsan simulation environment, the methodology can be generalized to support other tools. The FMI standard makes it possible to run optimizations with FMUs from other programs embedded in a Hopsan model. Extending the implementation to allow simulation of the FMUs directly is an important continuation of this work. This will, however, require each FMU to contain information of its performance and parallelizability. Including such information in the FMI standard could be one possibility.

Nomenclature

k	Number of points
n	Number of parameters
α	Reflection factor
r_{fac}	Randomization factor
γ	Forgetting factor
p	Degree of parallelization
n_{eval}	Number of evaluations
$n_{eval,p}$	Equivalent evaluations with parallelism
p_a	Degree of parallelization of algorithm
p_m	Degree of parallelization of model
SU_a	Speed-up of algorithm
SU_m	Speed-up of model
SU_{opt}	Speed-up of optimization
t_{sim}	Simulation time
t_{base}	Sequential simulation time
t_{opt}	Optimization time
n_c	Number of processor cores
n_p	Number of processors or computers

References

- David P Anderson. Public computing: Reconnecting people to science. In *Conference on Shared Knowledge and the Web*, pages 17–19, 2003.
- T. Blochwitz, M. Otter, M. Arnold, C. Bausch, C. Clauß, H. Elmqvist, A. Junghanns, J. Mauss, M. Monteiro, T. Neidhold, D. Neumerkel, H. Olsson, J.-V. Peetz, and S. Wolf. The functional mockup interface for tool independent exchange of simulation models. In *8th International Modelica Conference 2011*, Como, Italy, September 2009.

- M. J. Box. A new method of constrained optimization and a comparison with other methods. *The Computer Journal*, 8 (1):42–52, 1965. doi:10.1093/comjnl/8.1.42.
- Robert Braun, Peter Nordin, Björn Eriksson, and Petter Krus. High Performance System Simulation Using Multiple Processor Cores. In *The Twelfth Scandinavian International Conference On Fluid Power*, Tampere, Finland, May 2011.
- John E Dennis, Jr and Virginia Torczon. Direct search methods on parallel machines. *SIAM Journal on Optimization*, 1(4): 448–474, 1991. doi:10.1137/0801027.
- MS Eldred, WE Hart, BD Schimel, and BG van Bloemen Waanders. Multilevel parallelism for optimization on MP computers: Theory and experiment. In *Proc. 8th AIAA/USAF/NASA/ISSMO Symposium on Multidisciplinary Analysis and Optimization, number AIAA-2000-4818, Long Beach, CA, volume 292, pages 294–296, 2000.* doi:10.2514/6.2000-4818.
- B. Eriksson, P. Nordin, and P. Krus. Hopsan NG, A C++ Implementation Using The TLM Simulation Technique. In *The 51st Conference On Simulation And Modelling*, Oulu, Finland, 2010. URL <http://urn.kb.se/resolve?urn=urn:nbn:se:liu:diva-60644>.
- Robert Fourer, Jun Ma, and Kipp Martin. Optimization services: A framework for distributed optimization. *Operations Research*, 58(6):1624–1636, 2010. doi:10.1287/opre.1100.0880.
- Björn Gehlsen and Bernd Page. A framework for distributed simulation optimization. In *Proceedings of the 33rd conference on Winter simulation*, pages 508–514. IEEE Computer Society, 2001. doi:10.1109/WSC.2001.977331.
- David E. Goldberg. *Genetic Algorithms in Search, Optimization and Machine Learning*. Addison-Wesley Longman Publishing Co., Inc., Boston, MA, USA, 1st edition, 1989. ISBN 0201157675.
- J. A. Guin. Modification of the complex method of constrained optimization. *Computer Journal*, 10(4):416, 1968. ISSN 00104620. doi:10.1093/comjnl/10.4.416.
- Pieter Hintjens. *ZeroMQ: Messaging for Many Applications*. "O'Reilly Media, Inc.", 2013.
- Robert Hooke and T. A. Jeeves. "Direct Search" Solution of Numerical and Statistical Problems. *J. ACM*, 8(2):212–229, April 1961. ISSN 0004-5411. doi:10.1145/321062.321069.
- J. Kennedy and R. Eberhart. Particle swarm optimization. In *Neural Networks, 1995. Proceedings., IEEE International Conference on*, volume 4, pages 1942–1948 vol.4, 1995.
- P. Krus, A. Jansson, J-O. Palmberg, and K. Weddfelt. Distributed simulation of hydromechanical systems. In *The Third Bath International Fluid Power Workshop*, Bath, England, 1990.
- Petter Krus and Johan Ölvander. Optimizing optimization for design optimization. In *Design Engineering Technical Conferences and Computers and Information in Engineering Conference, 2003*. ASME Press, 2003. doi:10.1115/DETC2003/DAC-48803.
- Donghoon Lee and Matthew Wiswall. A parallel implementation of the simplex function minimization routine. *Computational Economics*, 30(2):171–187, 2007. doi:10.1007/s10614-007-9094-2.
- J. A. Nelder and R. Mead. A simplex method for function minimization. *The Computer Journal*, 7(4):308–313, 1965. doi:10.1093/comjnl/7.4.308.
- N. Sadashiv and S.M.D. Kumar. Cluster, grid and cloud computing: A detailed comparison. In *Computer Science Education (ICCSE), 2011 6th International Conference on*, pages 477–482, Aug 2011. doi:10.1109/ICCSE.2011.6028683.
- Rainer Storn and Kenneth Price. Differential evolution—a simple and efficient heuristic for global optimization over continuous spaces. *Journal of global optimization*, 11(4):341–359, 1997. doi:10.1023/A:1008202821328.
- Enver Yücesan, Yuh-Chuyn Luo, Chun-Hung Chen, and Insup Lee. Distributed web-based simulation experiments for optimization. *Simulation Practice and Theory*, 9(1):73–90, 2001. doi:10.1016/S0928-4869(01)00037-4.

Validation Techniques Applied on the Saab Gripen Fighter Environmental Control System Model

Robert Hällqvist¹ Magnus Eek¹ Ingela Lind¹ Hampus Gavel¹

¹Saab Aeronautics, Linköping, Sweden

Abstract

The Environmental Control System (ECS) of the Saab Gripen fighter provides a number of vital functions, such as provision of coolant air to the avionics, comfort air to the cockpit, and pressurization of the aircraft fuel system. To support system design, a detailed simulation model has been developed in the Modelica-based tool Dymola. The model needs to be a “good system representation”, during both steady-state operation and relevant dynamic events, if reliable predictions are to be made regarding cooling performance, static loads in terms of pressure and temperature, and various other types of system analyses. A framework for semi-automatic validation of the ECS model against measurements is developed and described in this paper. The framework extends a proposed formal methodology of semi-automatic model validation against in-situ measurements to the model development process implemented at Saab. Applied methods for validating the model in steady-state operation and during relevant dynamic events are presented in detail. The developed framework includes automatic filtering of measurement points defined as steady-state operation and visualization techniques applied on validation experiments conducted in the previously mentioned points. The proposed framework both simplifies continuous validation throughout the system development process and enables a smooth transition towards a more independent verification and validation process.

Keywords: Verification and Validation, Coverage, Domain of Validity, Historical Data Validation

1 Introduction

Model-Based System Engineering (MBSE) is playing an increasingly important role at Saab Aeronautics. Modeling and Simulation (M&S) is used already in early system development phases to increase the understanding of complex, highly integrated, and strongly coupled systems' behavior. In addition, a growing number of design decisions are taken relying on simulation results as simulating a system under investigation often is less costly than physical testing of the

actual system (Carlsson, Andersson, Gavel and Ölvander, 2012). Such an outspoken strategy imposes high demands on the simulation models to cover their *intended use*, see section 2.2. Model Verification and Validation (V&V) then become critical activities.

Model validation is an iterative process that continues for at least as long as the system that the model represents is under development. There is therefore a need to automate the validation process in order to assess the model validity with respect to the current system configuration in a convenient manner. As long as model validation requires a significant manual engineering effort, V&V activities will be “rare events” during system development. A high degree of automation is a necessary prerequisite for a continuous model V&V process. Increasing the level of automation would significantly simplify the execution of V&V activities, allowing for an increase in simulation result credibility with relatively little effort.

The methodology presented in this paper is a result of automation efforts performed when validating the Gripen Environmental Control System (ECS) model statically and the dynamic events for which the model needs to be a good system representation according to its intended use. The presented semi-automatic framework for ECS model validation is a proposed formal extension to the model development process implemented at Saab, see Figure 1. The model validation presented here is performed against existing in-situ measurements on a system level. The presented framework is developed specifically for the Gripen ECS simulation model. However, much of the work is considered to be generic and may hopefully guide validation efforts of other physics-based system simulation models for which *in-situ measurements* exist.

2 Theoretical Background

To provide a context for the presented validation methodology, the simulation model development workflow is visualized in Figure 1 (Carlsson,

2013). This workflow quantifies the model development process implemented at Saab Aeronautics, beginning with definitions of intended use and requirements specifications, all the way to system level model validation against reference data. A serious validation effort of equation-based simulation models requires such a bottom-up approach. Extensive system level validation should therefore preferably not be performed until after at least a sub-model by sub-model validation has been executed. Prior to the

sub-model validation, validation should be performed on a component level.

This paper presents a pragmatic decomposition of the *Model Validation* step of the model development process, see Figure 1. Existing validation measures and techniques are modified and applied, rendering a formal proposal of a semi-automatic validation procedure of physics based models.

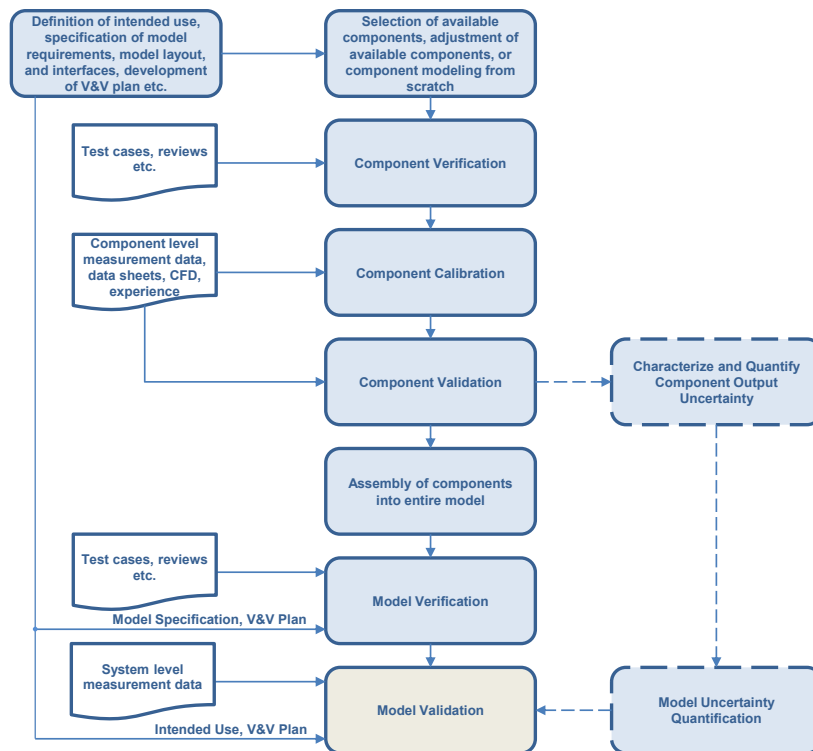


Figure 1: A general process for simulation model specification, development, V&V, and uncertainty quantification (Carlsson, 2013).

2.1 The concepts of Verification and Validation

The concepts of verification and validation (V&V) are fundamental to the work presented in this paper. As there are several available definitions of verification and validation, the interpretations related to the work presented here are explained in the following paragraphs.

The term validation is interpreted as the process of determining the model's validity within its range of usage, i.e. to determine if the model represents the physical system in the operational point, and during the dynamic events of interest, "well enough". The term "well enough" is here defined by relevant validation measures in relation to the model's intended use. This is generally in line with the definitions provided by NASA (2008), SISO (2013), and the

DoD (2007). There are numerous techniques for model validation with varying levels of formality. This paper focuses on model validation using measurement data from the real-world system, sometimes referred to as *historical data validation* or *predictive validation*, depending on the order of execution (Sargent, 2010).

In practice, model verification can be difficult to separate from model validation. However, in this work verification is related to ensuring a correct implementation and that the model requirements are met.

In order to ensure objectivity in V&V, it is important to have a certain degree of independence in the V&V process. What is a suitable level of independence varies depending on for example the type of organization, application, model's intended use, and the level

of formality required. Arthur and Nance (2000) defines independent Verification and Validation (IV&V) as “a series of technical and management activities performed by someone other than the developer of a system with the objective of: improving the quality of the system, and assuming that the delivered product satisfies the users operational needs.”

2.2 Model Intended Use

A model’s purpose (or intended use) should serve as input to the model’s development process as well as later model level validation activities, see Figure 1. The intended use should also serve as the foundation when deciding which modeling technique to implement when developing the model. The model’s intended use should therefore be considered a prerequisite to model development and latter activities (Carlsson, 2013). However, it is often practically impossible to develop a complete set of well-defined intended uses in the initial phase of model development. In later phases, when the model is available to users, new areas of use of the model will probably be found. It is nonetheless important to obtain as complete a picture of the intended use as possible prior to model development (Carlsson et al., 2012).

2.3 Model Coverage

A simulation model is intended to operate within some domain of operation. This domain of operation is usually limited by the physical bounds of the model inputs; for example, an aircraft system simulation model dependent on aircraft Mach number and altitude is normally not intended to produce valid results outside of the aircraft’s flight envelope. Model coverage is here referred to as a measure of how well the model’s operational domain is covered by a given set of validation experiments (the model’s domain of validity). Four criteria that any model coverage metric should take into account are: conducting validation experiments at an untested model operational point should always improve coverage; diverse validation experiments yield better coverage than clustered validation settings; regions of extrapolation result in a degradation of coverage; the metric should be objective (Atamturktur, Egeberg, Hemez and Stevens, 2015). The sensitivity-adjusted nearest neighbor metric to quantify coverage proposed by Atamturktur, Hemez, Unal and Williams (2009) accounts for all of the listed criteria except the penalization of extrapolation. This suggested metric is modified to include a penalty regarding extrapolation, a metric favoring dispersed

validation experiments over clustered. The resulting coverage description is given as

$$\eta_c = \frac{1}{g} \sum_{i=1}^g \min(d_{E,i}) + d_{ZI,i} \quad (1)$$

which provides an objective measure of model coverage accounting for all four of the previously described criteria (Atamturktur et al., 2015). The coverage measure is denoted η_c in Equation 1. The metric decreases with increasing coverage of the operational domain. If every point within the operational domain is validated, then the metric is zero. The total number of grid points within the model’s domain of operation is denoted g . The coverage metric is normalized by the total number of grid points ensuring that the metric remains unaffected by the resolution of the domain of operation. The area encapsulated by the red line in Figure 2 represents a hypothetical model domain of validity resulting from validation simulations conducted with settings corresponding to the circles in the figure. The distance $d_{E,i}$ is the length from grid point i to the closest validation point, see the dashed line in the figure.

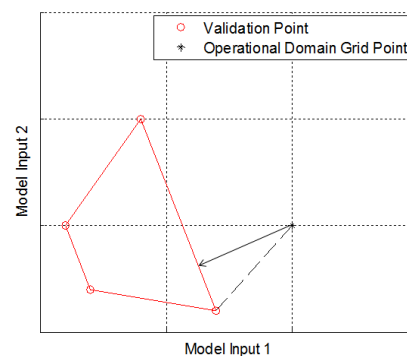


Figure 2: Operational domain grid point depicted outside of a hypothetical model domain of validity

The distance $d_{ZI,i}$ denotes the shortest distance between grid point i and the model domain of validity, see the solid arrow in the figure. This distance serves as an extrapolating penalty, punishing clustered arrangements of validation experiments.

3 Validation Measures

The validation measures define how well the model represents the corresponding physical system in terms of its dynamics and statics.

The measures implemented in the developed framework are partitioned into a set of steady-state and dynamic measures. The steady-state measures describe the model’s accuracy with

respect to the true system in steady-state operational points. Steady-state operation is here considered operation where all model inputs affecting observable system states vary within pre-defined bounds, see section 5.6.

The dynamic measures describe the accuracy of modeled dynamic behavior compared to measurement data from the true system. Which dynamic events to consider for validation are determined by the model's intended use.

3.1 Signal Level Measures

Typical validation measures used to quantify a model's steady-state validity on a signal level are:

- Absolute errors. The difference between simulated values of validation quantities and the corresponding measured values
- Relative errors. The relative error is defined as the absolute error normalized with the measured value.

Typical validation measures used to quantify a model's dynamic validity are:

- Relative error of overshoot/undershoot during a step in the reference
- Comparisons of simulation and reference data settling times during a step in the reference or during an event pushing the investigated signal away from its set-point
- Comparisons of rise time during a step in the reference or during an event pushing the investigated signal away from its set-point
- Comparisons of oscillations frequencies and amplitudes.

3.2 System Level Measures

As described in section 2.3, coverage is a quantity describing to what degree the model has been validated within its domain of operation. Coverage as defined in Equation 1 is in itself a relevant metric quantifying to which extent the model has been validated. Moreover, the metric may be modified to account for experimental

uncertainty (Egeberg, Atamturktur and Hemez, 2013). This modification is the source of inspiration for the system level validation metric implemented in the ECS model's validation methodology

$$\eta_c = \frac{1}{g} \sum_{i=1}^g \min(d_{E,i})(1 + V_E) + d_{Zl,i} \quad (2)$$

where V_E represents any relevant validation metric, for example the worst value (on a system level) of any static validation measure in each operational point E . In Equation 2, V_E is a validation measure that decreases with increasing model accuracy relative to the true system. Keeping V_E as generic as possible is advantageous if the measure is to be compared in between models. This modified coverage metric significantly reduces the amount of information needed to overview the assessed model validity.

4 Industrial Application Example: The Environmental Control System

4.1 System Description

At large, the Gripen Environmental Control System provides its subscribers with the desired amount of air, conditioned to the correct temperature and pressure. Subscribers to ECS conditioned air are typically the fuel system, on board oxygen generating system, anti-g system, avionics, etc. These subscribers often have different requirements regarding mass flow, temperature, and pressure of the supplied air. The difference in requirements is addressed as the air is extracted from the ECS, to the individual subscribers, at different points within the system.

The ECS input air is bleed from the engine or the Auxiliary Power Unit depending on the aircraft's operational point. This air is conditioned through a series of heat exchangers, a compressor-turbine set-up, a condenser, a series of valves, and controlling software. A schematic view of the system at hand is presented in Figure 3.

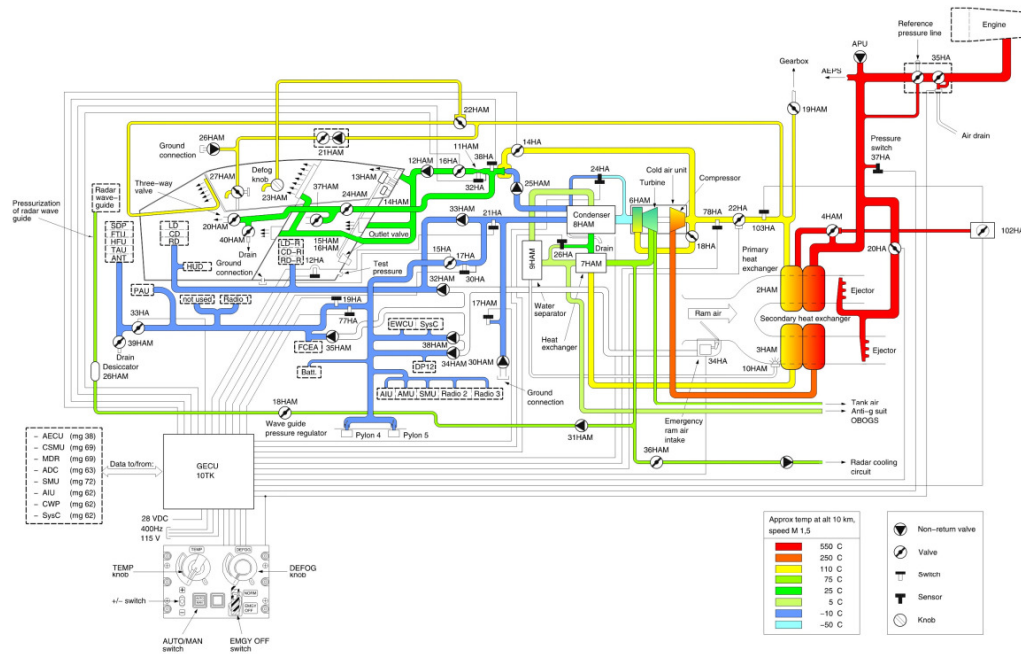


Figure 3: Schematic overview of P-ECS.

4.2 Simulation Model

The available ECS models are developed in the Modelica-based modeling tool Dymola. The ECS models were developed implementing the workflow depicted in Figure 1 and described in (Andersson and Carlsson, 2012, Carlsson et al., 2012). A total of three different fidelity level models representing the ECS exist:

1. High fidelity physics-based model for use in the Dymola simulation environment
2. High fidelity physics-based model for export to simulators without real-time performance.
3. Low fidelity model for export to Hardware In the Loop (HIL) and soft simulators with real-time performance.

The intended uses of the three ECS models are defined by a set of use cases. Based on these use cases, the intended uses of the detailed ECS model for use in Dymola can be summarized as follows:

- Conceptual design concerning H/W and S/W
- Export model benchmarking. The high fidelity ECS model should work as data supplier for V&V activities of less detailed system models

- Analysis of system static and transient pressures, temperatures, and mass flows during hardware malfunctions
- Analysis of system static and transient pressures, temperatures, and mass flows during software faults
- Prediction of system static cooling performance and pressure load levels
- Identification of oscillations and transients occurring as a result of software events or rapid changes in flight conditions.

These use cases are general in nature, which causes problems when quantifying the model accuracy bounds specifying if the model under investigation represents the true system “well enough”.

The validation strategies presented in this paper are applied on model no. 1. This particular model is a high fidelity Modelica model intended to represent the true systems statics as well as selected dynamic events. The ECS is a large, non-linear, MIMO system containing strong cross-couplings and widely varying time constants, aspects that are accounted for in the model. The resulting model has more than 100 inputs and 100 outputs, approximately 9000 time varying variables, and 14 non-linear systems of equations. The model is very computationally expensive, not only as a consequence of the previously mentioned characteristics, but also as a result of the incorporated controlling software.

The controlling software is sampled at 30Hz and events are generated at the time of each sample.

Model no. 2 is somewhat simplified compared to no. 1 as it needs to comply with a fixed step solver. The model's time constants are deliberately increased in order to reduce the model's stiffness, which enables the previously mentioned solver type to be used. The primary consequence is that the model's representation of system dynamics is reduced in accuracy compared to the true system and the non-export high fidelity model.

Finally, model no. 3 is designed to represent the system principal behavior in order to achieve real-time performance for use in simulators. Its physics are severely simplified and the model mainly supplies nominal values, depending on operational point, of system key quantities. Even though greatly simplified, this model is of great use during early software development as well as system fault simulations and integration testing.

The closed loop system representation includes sub-models of the system hardware as well as the controlling software developed in Simulink, see Figure 4.

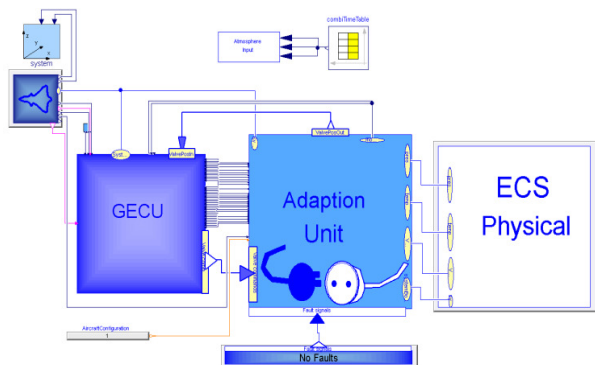


Figure 4: Top level of closed-loop ECS Dymola model.

The sub-model *ECS Physical* is a replaceable model representing the physical part of the ECS. Any of the three ECS simulation models defined at the beginning of section 4.2 can be simulated in this closed loop environment as they are declared as replaceable classes with identical interfaces to their surrounding environment.

The controlling software is integrated into the closed loop model by using a static library (*.lib) file referencing the compiled software object files. The static library is referenced in Dymola through the available annotations feature, which allows the user to link in their own C-libraries (Dassault, 2013).

The component outlined with an aircraft in the left corner of Figure 4 reads data regarding the aircraft's operational point from a comma-separated value (*.csv) file, see section 5.3 for a more detailed description of how the flight conditions are specified. Atmospheric boundary conditions are incorporated into the closed loop simulation environment through the *systems* component located in the top left corner of Figure 4. This component provides interpolated values of ambient pressure, temperature, and humidity according to pre-defined atmospheric profiles.

The model of the physical parts of the ECS is shown in Figure 5. The model's graphical layout is designed to resemble the schematics of Figure 3 to the extent possible.

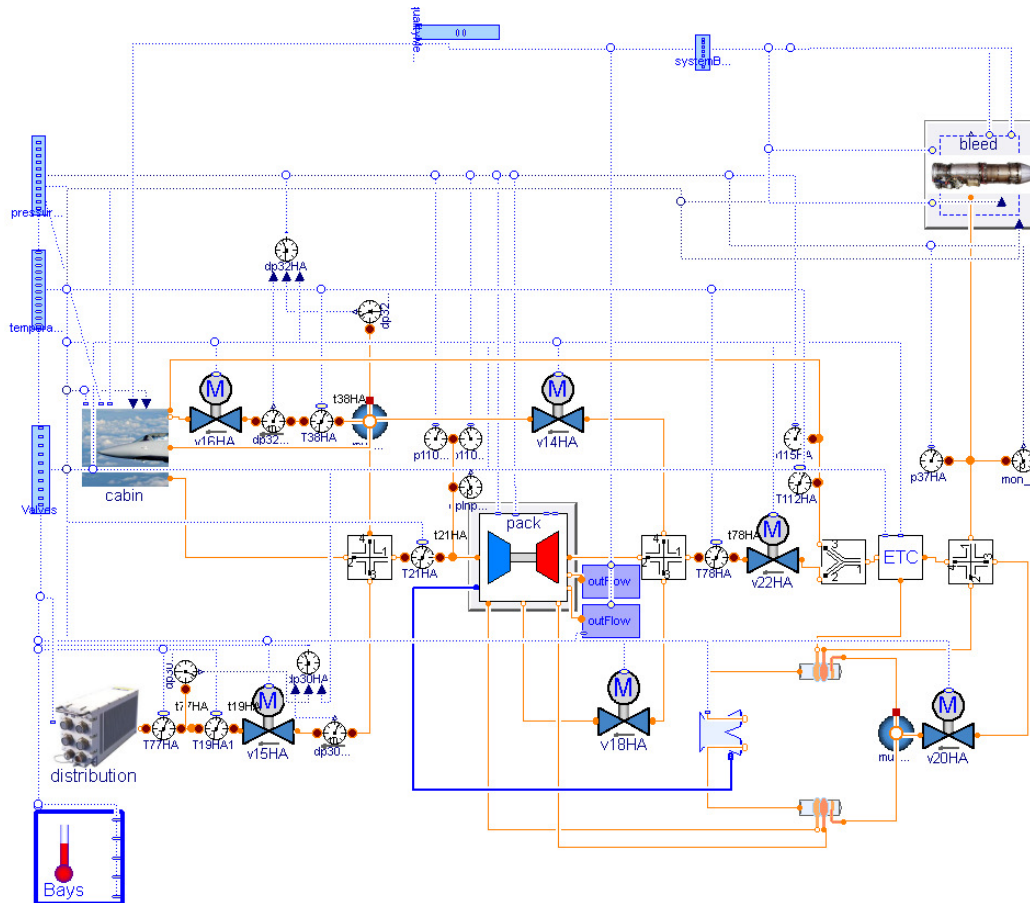


Figure 5: The detailed physical ECS hardware model.

5 Proposed Validation Framework

Using the ECS model as a guiding example, this section presents the developed framework for model validation using measurement data. As is, executing a validation simulation and adding the resulting validation points to the domain of validity is a semi-automatic process. The workflow of this process is presented in Figure 6. This workflow is a proposed generic decomposition of the final step *Model Validation* of the model development process presented in Figure 1. The seven different steps are described in detail in this section.

The validation framework is developed in Matlab as it provides a convenient platform for pre- and post-processing of data. Dassault Systèmes supplies m-functions along with the standard installation of Dymola that enables an interface between Matlab and Dymola allowing a complete validation simulation to be executed from Matlab.

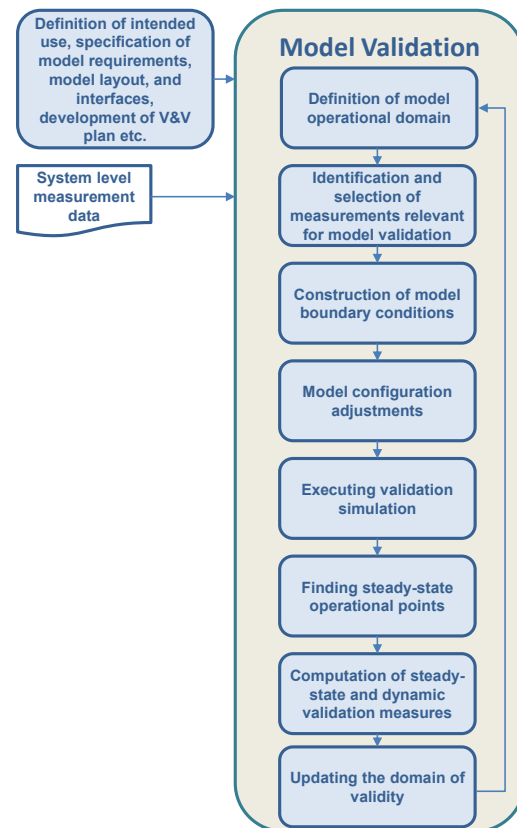


Figure 6: Proposed validation framework.

5.1 Definition of model operational domain

The model's operational domain is spanned by all input variables affecting observable system states. Which these model inputs are should be specified prior to any system level validation activity, they are essential when finding relevant reference data and a necessity when computing coverage as well as the system level validation metric presented in section 3.2.

In the case of the high-fidelity ECS model, these inputs are partitioned into atmospheric inputs (ambient pressure, temperature, and humidity) and inputs controllable by the pilot (altitude, Mach number, and Power Lever Angle). Furthermore, the atmospheric conditions are omitted from the definition of ECS operational domain as they are assumed to remain constant during flight at constant altitude. Atmospheric models are used to get the coupling between ambient conditions and altitude, which model is applied is dependent on the test site ambient ground conditions on the day of the test, see section 5.3.

5.2 Identification and selection of measurements relevant for model validation

Naturally, measurement data containing the steady-state working points where the model needs to be validated should be used for validation. The ECS needs to be a good system representation throughout the aircraft's operational envelope as the model's intended use does not specify especially significant areas of the system domain of operation. Operational points scattered throughout the envelope are therefore an advantage in order to maximize coverage, see section 2.3.

Measurement data including events generating transient phenomena or oscillations in pressures, mass flows or temperatures are relevant to validation. As the model's purpose includes identification of oscillations occurring as a result of software events or rapidly changing flight conditions, model validity during flight conditions knowingly resulting in system oscillations and transients is crucial. A typical event resulting in pressure oscillations propagated throughout the ECS is the switch of bleed supply air from auxiliary power unit to engine. This event, and others like it, are of particular interest.

The available missions feasible for ECS model validation have not been flown specifically to generate ECS model validation data. Even though a plethora of available measurements

exist, they stem from differently configured aircraft with varying measurement set-ups, factors that need to be considered when identifying measurements for validation purposes. These missions are scanned for the steady-state points and dynamic events of interest with the help of tools within the presented framework. The developed Matlab framework includes functions aiding in the identification process, functions presenting maximum/minimum values of model inputs affecting observable system states as well as their maximum/minimum time derivatives. The information regarding time derivatives is used to identify dynamic phenomena, for example steep dives, bleed supply switches, etc. The developed functions also provide the steady-state points found in each scanned mission. The availability of new steady-state points enables computation of the coverage increase connected to validation simulations in these operational points.

The available in-situ measurements contain information regarding pressure levels, mass flows, and temperatures from sensors distributed throughout the system. Like all measured quantities, these measurements are not exact. No extensive effort has been made to quantify the present measurement uncertainties. The information available in sensor data-sheets is investigated and these uncertainties are determined to be small in comparison to the known model errors.

5.3 Construction of model boundary conditions

Necessary model boundary conditions are automatically generated from the measurements selected for validation. Information regarding Mach number, Power Lever Angle (PLA) and bleed pressure, and altitude are logged during flight. Engine bleed temperature levels are computed by combining the relation describing adiabatic compression (Burden, 2009), an example of a non-linear addition to the model,

$$\frac{T_1}{T_2} = \left(\frac{P_1}{P_2}\right)^{\frac{\gamma-1}{\gamma}} \quad (3)$$

with known data of compressor efficiency. The inlet and outlet temperatures are denote T_1 and T_2 respectively in Equation 3. The specific heat is represented by γ , and the inlet and outlet pressure by P_1 and P_2 , respectively. Once established, the model input boundary conditions are stored in a *.csv file which is a convenient format for Dymola to read during model compilation.

As described in section 4, atmospheric boundary conditions are incorporated into the simulation through pre-defined atmospheric models. However, the atmospheric conditions (during any given flight to be used for validation activities) are rarely close enough to any of the available models. Offsets regarding humidity, ambient pressure, and ambient temperature can therefore easily be defined. Ground level data regarding ambient conditions are used to specify the offsets. Such data is available from the Swedish Meteorological and Hydrological Institute (SMHI, 2015).

5.4 Model configuration adjustments

Considering the ECS, model adjustments matching the ECS model to the system configuration used when producing measurements for validation are necessary, both in terms of hardware and controlling software. For example, different aircrafts are equipped with different avionics equipment. This affects the software control set-point of coolant flow as well as the avionics distribution pressure drop characteristics. Such model modifications tuning the model to the specific aircraft configuration should be separated from model calibration against measurements.

5.5 Execution of validation simulation

Simulating a flown mission is done through Matlab using the m-function *dymolaM.m* which executes a command specified as input to the function in Dymola.

The implemented order of succession when executing a mission simulation is as follows:

1. The model is translated along with the boundary conditions generated from in-situ measurements (see Section 5.3) of the considered mission by calling the Dymola function *translateModel*.
2. The result file content is specified through the Dymola function *experimentSetupOutput*. Dymola is capable of storing data regarding variable derivatives, states, inputs, outputs, etc., which if all are enabled result in large result files. If long simulations with high resolution outputs are to be simulated, disabling saving of non-important data is essential in order to avoid memory problems.
3. The mission is simulated through the command *simulateModel*.

The used Dymola functions are described in (Dassault, 2013).

The simulation output is easily read into the Matlab workspace using the *dymload* function. The data structure of the loaded results is somewhat non-intuitive; however, the function *dymget* extracts simulation results for a specific variable from the workspace results.

5.6 Finding steady-state points

Static points are automatically filtered from the measurements. Steady-state points are here referred to as operational points where the conditions on the standard deviations,

$$\begin{aligned}\sigma(Alt) &\leq 10 \\ \sigma(Mach) &\leq 0.009 \\ \sigma(PLA) &\leq 1.5,\end{aligned}\tag{3}$$

of all (by the pilot) controllable closed-loop model inputs: altitude, Mach number, and PLA, are fulfilled. The conditional bounds of Equation 8 are determined through input sensitivity analysis and Subject Matter Experts (SME's) at Saab. A minimum steady-state time span is established which is significantly longer than the system time constants. If the conditions regarding standard deviation are fulfilled for the minimum steady-state time span, this time span is considered to be steady-state. The conditions are computed sequentially in time until they are no longer fulfilled. A continuous steady-state time span is identified by means of a sliding window that monitors the steady-state constraints of Equation 3. The resulting steady-state values are computed as the mean value of the identified continuous time span. Time series plots of altitude and Mach number during part of a flown mission are presented in Figure 7. The conditions on standard deviation regarding altitude are fulfilled for the specified time span (see the left-hand side of the figure); however, the conditions on Mach number are not fulfilled. This particular time span is therefore not defined as a steady-state time span. This filtering algorithm is verified on sets of measurements known to contain static points where it is deemed to fulfill its purpose.

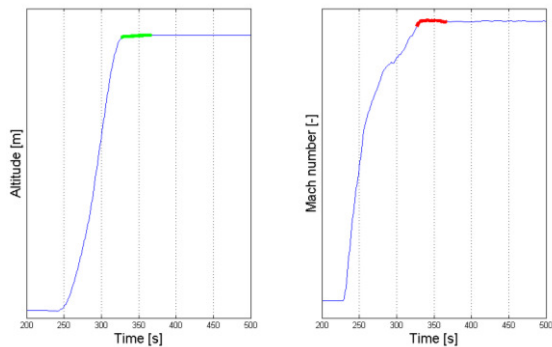


Figure 7: 300-second time span of measurements from flown mission used for model validation.

5.7 Computation of steady-state and dynamic validation measures

The static signal level and system level validation measures, specified in section 3, are automatically computed (through tools developed within the context of the framework) for each found steady-state operational point along with the coverage metric specified in Equation 1. The validation metric V_E implemented in the system level metric of Equation 2 is a weighted sum of all relative errors between model and true system. The weight is implemented to emphasize the impact of large relative errors on the metric. A drawback of such a definition is that some subjectivity is introduced to the measure; the metric is therefore also computed omitting the weight. These measures provide a comprehensible overview of the model's static validity.

The model intended use serves as the foundation when selecting time segments for dynamic validation. In practice, specific representative events known to produce dynamic phenomena are investigated as the signal level dynamic measures are computed at manually selected time segments. The post-processing framework plots the mission time evolution of all relevant variables used in the validation process. Transients of interest are found manually from time series plots of measurements and simulation results and the signal level dynamic validation metrics are computed. Such a time series plot of measured and simulated values of cockpit temperature is provided in Figure 8.

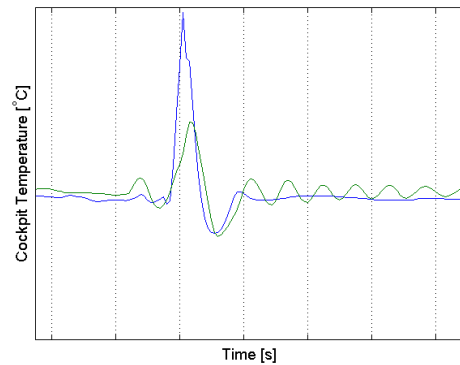


Figure 8: Cockpit temperature during part of a flown mission: green represents measurement data, and blue model simulation results.

Since the simulation results of cockpit temperature have a further dampened character than the corresponding measured quantity, comparing settling times is suitable. Other dynamic measures relevant to this particular event are difference in maximum amplitude, and oscillation frequency.

5.8 Adding to the model domain of validity

All data relevant for post-processing of a simulated mission is available through the steps described in section 5.1 through 5.7. All computed relative and absolute errors in system mass flows, temperatures, and pressure are appended to a *.csv file containing all previously validated steady-state operational points, including information regarding model coverage and the computed system level static validation metric. The file contains all the information necessary to formulate the model's steady-state domain of validity. Figure 9 illustrates a static domain of validity plotted on top of the operational domain. This figure provides information regarding model coverage at a less detailed level than the coverage metric specified by Equation 1 as it is unaffected by changes in validation domain density. Such a figure serves as an intuitive complement to the above metric.

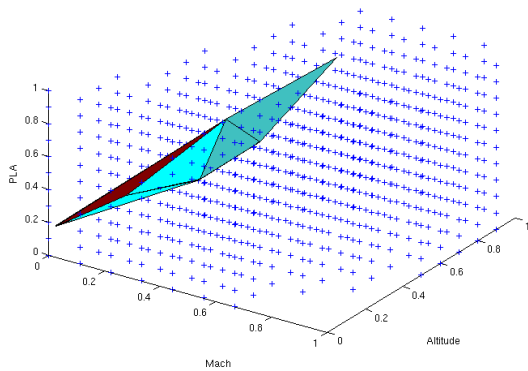


Figure 9: The static validation domain of the ECS model.

As is, one dynamic domain of validity needs to be specified for each investigated event or dynamic phenomenon. The signal level validation metrics are the sole source of information regarding model dynamic validity. Updating such dynamic domains of validity is a tedious process and requires a significant amount of manual effort and system knowledge. However, no alternative method is implemented at this point in time.

6 Discussion and Conclusions

In this paper, a framework for semi-automatic model validation using measurement data from a real-world system is proposed. To ensure industrial applicability, the framework is based on experience from an extensive validation of a detailed system simulation model. The framework covers validation of both steady-state and transient behavior.

In order to reduce the effort required in thorough model validation activities, an increased degree of automation is essential as models need to be repeatedly validated throughout the system development process if well-justified model-based design decisions are to be made. The proposed framework provides a semi-automatic workflow that simplifies the shift towards a more independent V&V approach. Traditional validation measures and techniques suitable for automatic validation have been selected, modified, and implemented in the framework. As a result of the developed methodology, less strict requirements on V&V personnel system expertise are called for during V&V activities. Relieving model developers of repetitive work not only increases objectivity in model validation, but also frees experienced model developers for other tasks that require their knowledge of the modeled system. Parts of the developed framework are currently being used at Saab Aeronautics during validation of

other detailed physics-based simulation models for which measurement data from rig testing exists.

To further increase the degree of automation in the ECS model validation procedure, the selection of an atmospheric model for a specific validation experiment needs to be further automated. No automatic coupling between weather data and model boundary conditions currently exists. Furthermore, the main issues to resolve before the process can be fully automatic are related to selection of aircraft software configuration. There is currently no method to automatically modify the controlling software when matching the model to a specific aircraft configuration.

In addition to the issues listed earlier, improved definitions of dynamic events relevant to validation need to be specified in the model's intended use if the validation of transient behavior is to be further automated. If one or more dynamic operational domains can be clearly and meaningfully specified, there is great potential to automate the identification of dynamic events and the updating of the corresponding dynamic validation domain(s).

The current knowledge regarding present measurement uncertainties in ECS flight data is solely based on supplier information. A pragmatic approach to determining the measurement uncertainties on a more detailed level should be studied in the future.

Acknowledgements

The research leading to these results has received funding from Saab Aeronautics and the National Aviation Engineering Research Programme (NFFP) jointly driven by the Swedish Armed Forces, the Swedish Defence Materiel Administration (FMV), and the Swedish Governmental Agency for Innovation Systems (VINNOVA), (NFFP6 2013-01211).

The authors would like to thank Anders Järlestål for his invaluable input regarding aircraft environmental control systems and Carl-Philip Forss for his help with refining the developed validation framework

References

- Andersson, H., Carlsson, M., *Saab Aeronautics Handbook for Development of Simulation Models: Public Variant*, LIU-IEI-R--12/00159--SE, Linköping University, Linköping, Sweden, 2012.
- Arthur, J.D., Nance, R.E., *Verification and validation without independence: a recipe for failure. 2000*

Winter Simulation Conference, Orlando, FL, USA, 2000.

Atamturktur, H.S., Hemez, F.M., Unal, C., Williams, B.J., Predictive maturity of computer models using functional and multivariate output, *Proceedings of the 27th International Modal Analysis Conference (IMAC-XXVII)*, Orlando, FL, USA, 2009.

Atamturktur, S., Egeberg, M.C., Hemez, F.M., Stevens, G.N., Defining coverage of an operational domain using a modified nearest-neighbor metric, *Mechanical Systems and Signal Processing*, **50–51**: p. 349-361, 2015.

Burden, T., *Termodynamik med kompressibel strömning*, Vol. Ver. 1.2, Institutionen för mekanik, Kungliga Tekniska Högskolan (KTH), 2009.

Carlsson, M., *Methods for Early Model Validation: Applied on Simulation Models of Aircraft Vehicle Systems*, Tekn. Lic. no 1591, Linköping University, Linköping, Sweden, 2013.

Carlsson, M., Andersson, H., Gavel, H., Ölvander, J., Methodology for Development and Validation of Multipurpose Simulation Models, *Proceedings of the 50th AIAA Aerospace Sciences Meeting*, Nashville, TN, USA, 2012.

Dassault, *Dymola User Manual*, Vol. Vol. 1, Ver. 14, p. 586, Dassault Systèmes, 2013.

DoD, *Department of Defence Directive Number 5000.59*, Under Secretary of Defense for Acquisition, Technology, and Logistics USD(AT&L), US Department of Defence (DoD), 2007.

Egeberg, M.C., Atamturktur, S., Hemez, F.M., Defining coverage of a domain using a modified nearest-neighbor metric, *Proceedings of the Society for Experimental Mechanics Series*, 2013.

NASA, *Standard for Models and Simulations*, NASA-STD-7009, National Aeronautics and Space Administration, Washington, DC, USA, 2008.

Sargent, R.G., Verification and Validation of Simulation Models, *Proceedings of the 2010 Winter Simulation Conference*, Baltimore, MD, USA, 2010.

SISO, *GM-VV Vol. 3: Reference Manual, Reference for Generic Methodology for Verification and Validation (GM-VV) to Support Acceptance of Models, Simulations and Data*, SISO-REF-039-2013, Simulation Interoperability Standards Organization, 2013.

SMHI 2015, *Swedish Meteorological and Hydrological Institute (SMHI)*, www.smhi.se.

Integrated model of bioenergy and agriculture system

Hafthor Ægir Sigurjonsson¹ Brian Elmegaard¹ Lasse Røngaard Clausen¹

¹DTU Mechanical Engineering, Technical University of Denmark (DTU), Denmark,
{hafsig, be, lrc}@mek.dtu.k

Abstract

Due to increased burden on the environment caused by human activities, focus on industrial ecology designs are gaining more attention. In that perspective an environmentally effective integration of bioenergy and agriculture systems has significant potential. This work introduces a modeling approach that builds on Life Cycle Inventory and carries out Life Cycle Impact Assessment for a consequential Life Cycle Assessment on integrated bioenergy and agriculture systems. The model framework is built in Python which connects various freely available software that handle different aspects of the overall model. C-TOOL and Yasso07 are used in the carbon balance of agriculture, Dynamic Network Analysis is used for the energy simulation and Brightway2 is used to build a Life Cycle Inventory compatible database and processes it for various impacts assessment methods. The model is successfully demonstrated using a manure utilization case study where the manure is used to produce biogas and then heat and power, whereas its digestate is used as an organic fertilizer to a wheat field. The case study is compared with direct manure to wheat field application.

Keywords: Life cycle assessment, energy efficiency, sustainability

1 Introduction

Environmental conscious design of industrial systems has gained more interest in recent years and the development of industrial ecosystems and eco-industrial parks are now relevant topics for policy-makers. This is in large part due to increasing public awareness of the environmental burden from human activity on the environment. Denmark's future energy plan for 2050 is to be completely independent of fossil fuels for all energy consumption in the country (Danish Ministry of Climate. Energy and Buildings). This includes all electricity and heat consumption, along with transportation fuels. For this to be possible and make sense, the utilization of energy resources needs to be environmentally effective and the available options going forward need to be thoroughly investigated. Along with this focus on more environmentally friendly energy system in Denmark, the environmental burden of its agricultural in-

dustry also needs to be addressed, which today releases about 15% of the total national greenhouse gas emissions (Government (2013a)). A climate change mitigation potentials inter-ministerial working group report identified a few connections with the energy industry to mitigate those emissions (Government (2013b)).

Finding the best possible integration between these two industries in terms of net environmental impact is the motivation of this work. Systems are analyzed using the Life Cycle Assessment framework (LCA) (Rebitzer et al. (2004)) using the Brightway2 software (Mutel (2015)). Building the Life Cycle Inventory (LCI) (Suh and Huppes (2005)) requires detailed models of the inputs and outputs of the agricultural and energy systems, along with possible interactions between them. Integration between bioenergy and agriculture can be done in various ways. In this work the focus has been on producing electricity and district heat by using residual resources in the agricultural system and thus not affect its capacity to produce food and related products. Additionally, the organic residues from the biomass conversion in the energy system are returned back to the agricultural system to ensure that most of the essential elements, e.g. macro-nutrient, for agricultural activities are recycled. The agricultural system base model is a field which mainly produces wheat grain, located in Zealand Denmark. In its reference state, it is fertilized with mineral fertilizers and has expected yield according to the national agricultural guidelines (NaturErhvervstyrelsen (2013)). The LCI model is built on top of an extensive model gathered from the Ecoinvent3 database (Weidema et al. (2013)) and follows their basic modeling principles, in addition to a comprehensive atmospheric carbon balance modeling procedure adopted from (Cherubini et al. (2011) and Petersen et al. (2013)) and using results generated by the soil carbon balance simulation software C-TOOL (Petersen et al. (2002) and Petersen et al. (2005)). The energy system utilizes biomass resources and can be either based on biochemical or thermochemical conversion (or both) before heat and power generation in a gas engine or a steam cycle and will always deliver its residues to the agricultural system as organic fertilizer. Modeling of the energy system is done in the Dynamic Network Analysis (DNA) (Elmegaard and Houbak (2005)). Like the agricultural system the energy

system LCI model is built on top of a model gathered from Ecoinvent3 but using results from DNA. The Life Cycle Impact Assessment (Pennington et al. (2004)) results are given in four levels, from a normalized and weighted end-point result combining seventeen different environmental indicators into one numerical result to disaggregating the most important indicators to specific inputs and outputs of the system analyzed using midpoint level LCIA. This is to allow for evaluation of the total environmental impact and what inputs and outputs are mostly effecting that outcome.

This articles describes the methodology of the integrated agriculture and bioenergy environmental impact assessment model. How the LCIs are built from mass, energy and substance balances of the sub-systems, and how the four levels LCIA analysis gives overall environmental impact and the major contributors to that impact as a result. The model is demonstrated by analyzing manure based biogas production and utilization. Additionally, a direct manure to field application is analyzed as a reference case.

2 Method

2.1 Case description

The modeling and analysis methods introduced in this paper are demonstrated by a case study on biogas production and utilization from pig manure, and a reference case with direct pig manure to field application. The objective of the analysis is to report the environmental impact change to one hectare agricultural field and to identify the main impacts and contributors to the final result. A simple flow chart of the system can be seen in Figure 1.

The system for each case is divided into three sub-systems, i.e. agricultural, storage and transportation, and energy. The energy sub-system consist of the biochemical conversion of biomass to biogas, and heat and power generation. Before the pig manure is converted to biogas and digestate, it is stored and then de-watered in a decanter. The liquid manure is stored in an outdoor storage before it is applied to the agricultural sub-system. However, the solid manure is converted in an anaerobic digester to biogas and digestate. The digestate follows the same process as the liquid manure, but the biogas is combusted in a gas engine producing electricity and district heat.

The agricultural sub-system is a cereal grain production using conventional practices. For the analysis the manure is modeled as a recycled content (Frischknecht (2010)), i.e. only the impacts it induces follow the flow and other parts of the pork production are excluded. Moreover, as raw manure, liquid manure or digestate are applied to the field its effective macro-nutrient content replaces mineral fertilizer and modifies the field emissions.

2.2 Model formulation

2.2.1 Agricultural sub-system model

The objective of this model is to produce a Life Cycle Inventory (LCI) of the system described by the user. A database is used to form the base of a LCI, which is then manipulated and modified based on the actual condition and substance balances of the system. To describe that process the agricultural sub-system model is divided into three modeling sections representing, nutrients-, carbon- and heavy metals balance which will deliver new unit processes and elementary flows for the LCI.

The nutrient balance model is based on the macro-nutrients required to grow crops, i.e. nitrogen (N), phosphorus (P) and potassium (K). The flow of these nutrients through the system are governed by conservation of mass and each substance is modeled individually. Only N is modeled to change in the control volume by immobilization and mineralization in the agricultural soil, for both P and K the outputs are equal to the inputs.

The reference mineral fertilization is based on national guidelines for fertilization (NaturErhvervstyrelsen (2013)) and the change in nutrient balance is regulated by the mineral fertilizer input. Uptake by harvest, grain and straw (if harvested), are a part of the nutrient output of a field. The uptake by grain is based on the yield and its chemical composition. Yields are assumed based on the soil type using national guidelines (NaturErhvervstyrelsen (2013)) and chemical composition is extracted from a biomass database adopted from (Vassilev et al. (2010)). Same principles apply to straw, along with extraction efficiency, i.e. how much of the total straw are harvested. For P model, leaching, surface run-off and erosion are included and estimated based on (Nemecek and Schnetzer (2012)). Figures 2 and 3 display the phosphorus inputs and output of the agricultural sub-system.

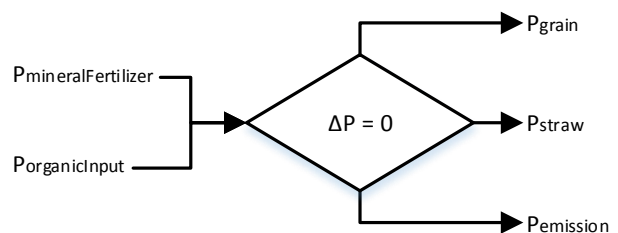


Figure 2. Phosphorus balance in the agricultural sub-system.

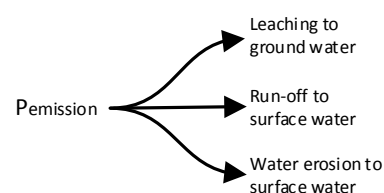


Figure 3. Phosphorus emissions in the agricultural sub-system.

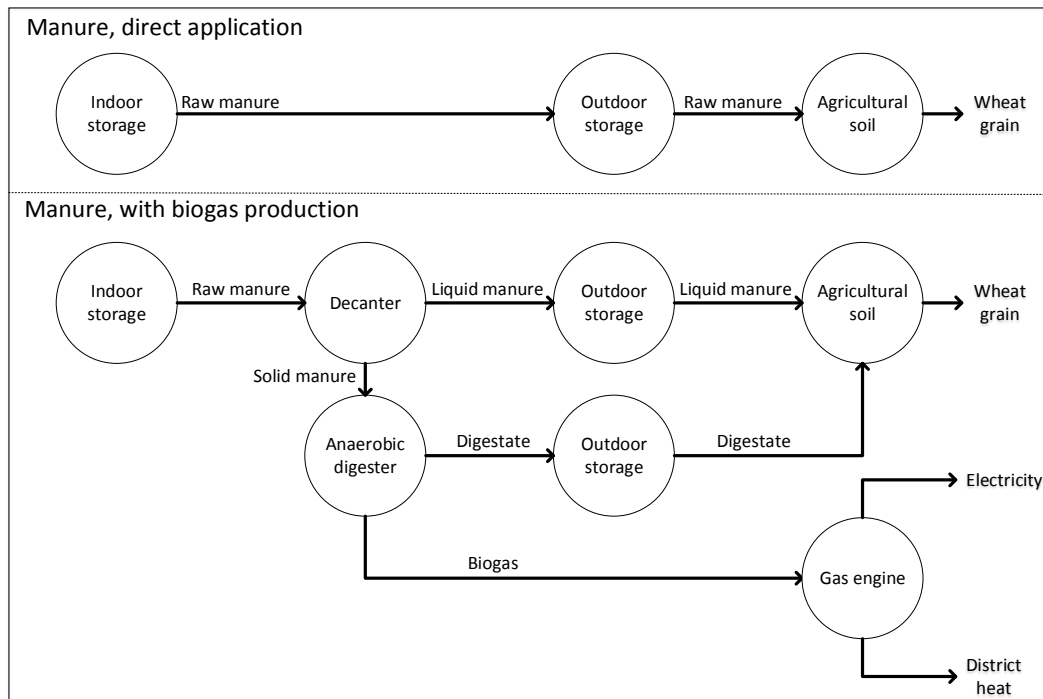


Figure 1. Flow diagram for the case study and the reference.

K model also includes leaching as an emission, but the calculations are based on a method adopted from (de Willigen (2000)) recommended by Food and Agriculture Organization (FAO) in Assessment of nutrient balances: Approaches and methodologies (Roy et al. (2003)). Figures 4 and 5 display the potassium inputs and output of the agricultural sub-system.

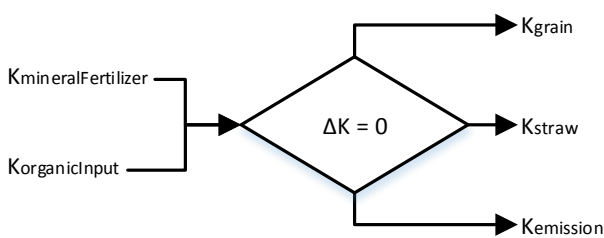


Figure 4. Potassium balance in the agricultural sub-system.

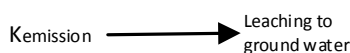


Figure 5. Potassium emissions in the agricultural sub-system.

Nitrogen outputs include leaching (NO_3^-), along with nitrous oxide (N_2O), nitrogen gas (N_2) and ammonia (NH_3) emissions. These nitrogen outputs are calculated in different ways depending on the input resource. Figures 6 and 7 display the nitrogen inputs and output of the agricultural sub-system.

For pig manure sourced inputs (raw slurry, liquid fraction, solid fraction, digestate, liquid digestate and solid digestate) the nitrogen outputs were calculated using the

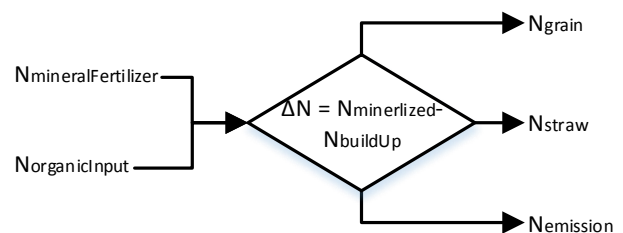


Figure 6. Nitrogen balance in the agricultural sub-system.

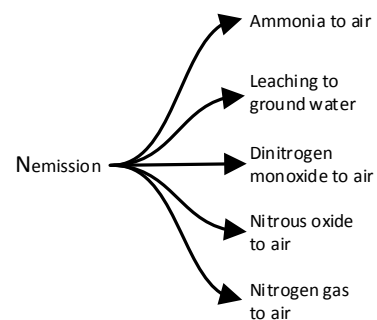


Figure 7. Nitrogen emissions in the agricultural sub-system.

same methods as in (Hamelin et al. (2011)). The methods of assessing direct field emissions for LCIs of agricultural production sub-system (Nemecek and Schnetzer (2012)) are used for mineral and cereal straw sourced inputs.

The carbon (C) balance model is based on the flow through the whole system and follows the law of mass conservation. Similarly to the nutrient balance model the C output of the agricultural sub-system is based on the uptake (photosynthesis) by harvest and associated emis-

sion. However, the input is equal to the total carbon captured by photosynthesis of the whole growth on the field (harvest and residues) in addition to any organic or inorganic C input through fertilization. The uptake is based on the chemical composition, yield and extraction efficiency in the same manner as described above. Figures 8 and 9 display the carbon inputs and output of the agricultural sub-system. Additionally, to describe the photosynthe-

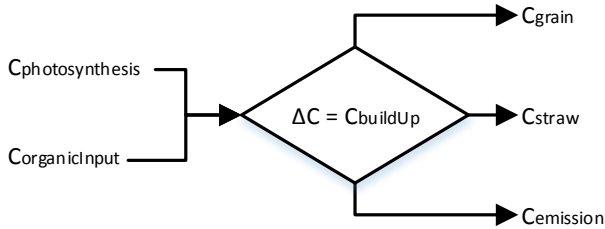


Figure 8. Carbon balance in the agricultural sub-system.

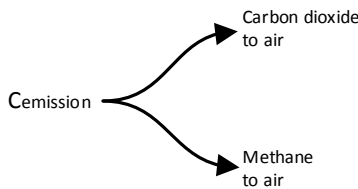


Figure 9. Carbon emissions in the agricultural sub-system.

sis the growth period displayed in Figure 10 is simulated based on the Schnute model (Schnute (1981)), a versatile growth model based on statistically stable parameters. C

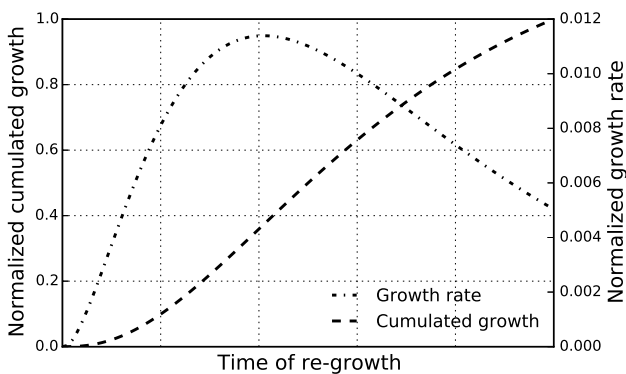


Figure 10. Carbon captured by photosynthesis in the agricultural and forestry sub-system.

emissions from the agricultural sub-system is based on the respiration of decaying residues and organic fertilizer. The magnitude of these residues is based on the straw extraction efficiency and any other organic input to the soil. C decay from the residues and other organic carbon inputs are simulated by C-TOOL (Petersen et al. (2002, 2005)), a software for whole-profile carbon storage simulation in temperate agricultural soils. This also needs to be considered for other biomass potentially utilized in the overall

system. C balance for a wood chips feedstock is thus modeled in a forest sub-system. That model follows the same principles as the agricultural sub-system but uses data extracted from Yasso07 (Liski et al. (2005)), a carbon and decomposition software for forest soils, to simulate the decay of forest residues. It can be seen in Figure 11, that the

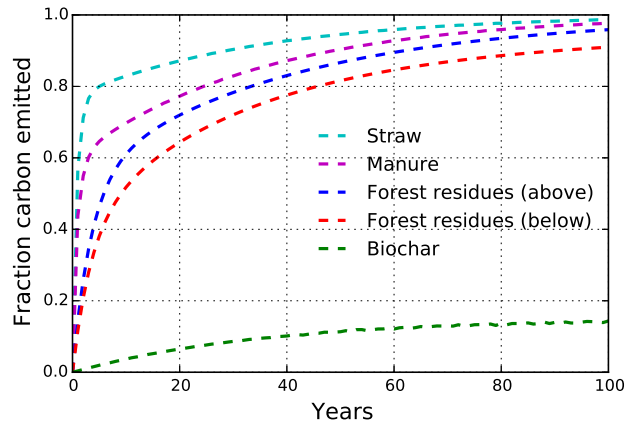


Figure 11. Carbon emissions from decomposition in the agricultural and forestry sub-system.

carbon emission from decaying biomass is gradual over time. The impact factor related to greenhouse gas emissions is in reference of pulse emission of carbon dioxide, i.e. all carbon is emitted in the first year, but the influence on climate change is then based on the integrated radiative forcing of carbon dioxide in the atmosphere. Thus the load of carbon dioxide in the atmosphere needs to adequately accounted for in the case of biomass decay carbon dioxide emissions. When emitted it starts to be absorbed by earth's many sink, e.g. ocean and terrestrial forests, this is simulated by the impulse response function (Joos et al. (1996, 2001)) which needs to be combined with the biomass decay emissions to get their atmospheric load over a time horizon. Figure 12, displays the atmospheric load of carbon emission from different sources in reference to pulse emitted CO₂. The global warming potential

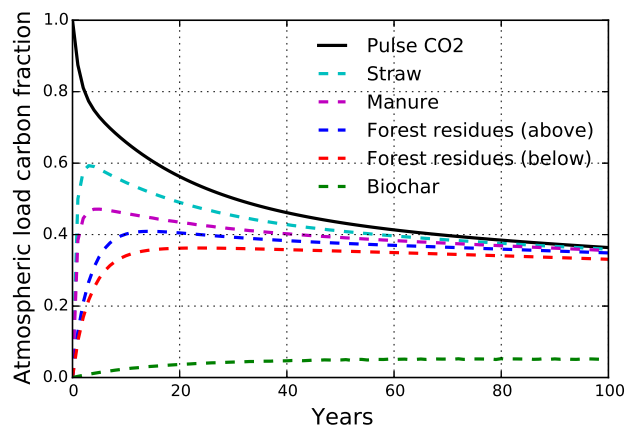


Figure 12. Atmospheric load due to carbon dioxide emissions.

for the biomass decay carbon dioxide emission can then be calculated by referencing their atmospheric load to that of the pulse carbon dioxide. The global warming potential of the different biomass decay emissions is displayed graphically over time in Figure 13.

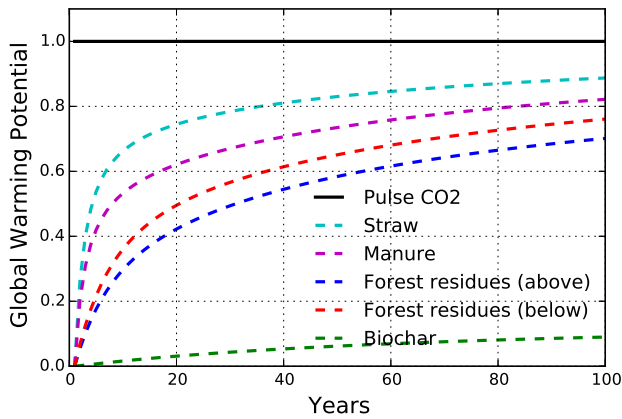


Figure 13. Evolution of the global warming potential over time.

It can be seen in Figure 13 the curve representing manure ends at a value about 0.81. This indicates that the global warming potential of 1 kg manure carbon dioxide decay is about 0.81 kg carbon dioxide equivalent. However, there are two elements to the total global warming potential of a biomass and the other is the sub-sequent re-growth of carbon in the biomass type. This is described in Figure 10 above, and for carbon in manure which mainly comes from annual rotation agricultural crops the value is -1 as its carbon is captured within a year.

The Heavy metals balance model is like the other balance models based on the flow through the whole system and follows the law of mass conservation. The heavy metals modeled are: Cadmium (Cd), copper (Cu), zinc (Zn), lead (Pb), nickel (Ni), chromium (Cr) and mercury (Hg). Inputs to the agricultural field are based on the heavy metals content of fertilizers, pesticides, seeds and disposition. The heavy metals can either accumulate or diminish from the soil based on the balance and are accounted for as emission to the soil (can be positive or negative). For the reference system the emissions are modeled according to ecoinvent modules which use SALCA-heavy metal (Nemecek and Schnetzer (2012)) as its reference. The emission is divided between soil emissions, leaching to ground water and erosion to surface water. Figures 14 and 15 display the heavy metals inputs and output of the agricultural sub-system. The leaching and erosion are modeled in SALCA-heavy metal based on constants, so when inputs change in the reference system the accumulation or demission in soil is only affected, thus causing increase or decrease in soil emissions.

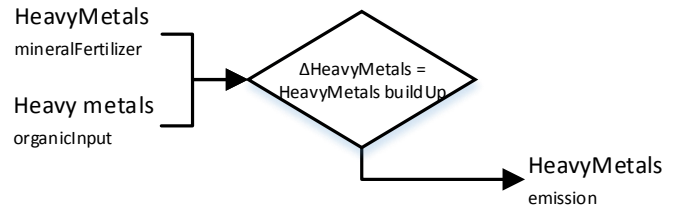


Figure 14. Heavy metals balance in the agricultural sub-system.

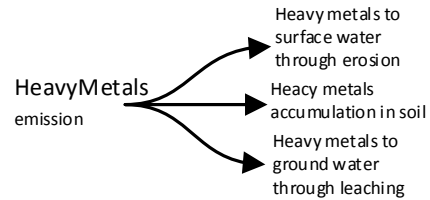


Figure 15. Heavy metals emissions in the agricultural sub-system.

2.2.2 Energy sub-system model

The energy sub-system is modeled with the Dynamic Network Analysis (DNA) energy system simulation tool (Elmegaard and Houbak (2005)). By using DNA it is possible to use the library of energy components already modeled there. Specific models of the energy sub-system for use in this project are modeled in DNA. In all of those pre-made models, the inputs requirements are the ultimate chemical composition, energy content and specific heat of the resource utilized. Optionally, the operation parameters which are to be varied can be defined. The ultimate chemical composition of the resource used is found in the same way as in Section 2.2.1. Additionally, the Higher Heating Value (HHV) and specific heat (cp) are estimated on a dry basis with the following equations from (Friedl et al. (2005)) and (Dupont et al. (2014)) for each resource, respectively.

$$HHV_{dry} = 341.7 \cdot C + 1322.1 \cdot H + 119.8 \cdot (O + N) - 123.2 \cdot S / 10000 - 15.3 \cdot A \quad (1)$$

Where C, H, O, N, S, A are the carbon, hydrogen, oxygen, nitrogen, sulfur and ash content of the resource given by its ultimate chemical composition.

$$CP = (5.340 \cdot T(K) - 299) / 1000 \quad (2)$$

DNA already handles all mass and energy balances over the whole energy sub-system it simulates and delivers the properties of each state of the energy sub-system and all necessary information about its products, e.g. electricity, district heat, digestate, biochar and ash, and fuel.

DNA provides information about the emissions from the power plant. For a thermochemical conversion system the power plant consists of a gasifier and either a steam cycle or a gas engine, and for a biochemical conversion system the power plant consist of an anaerobic digester

and either a steam cycle or a gas engine. By doing all this, DNA handles the nutrient and carbon balance through the power plants. It is worth noting that the nutrient balance differs in one significant way for power plants using biochemical- or thermochemical conversions. This can be observed in Figures 16a and 16b. It can be seen the fig-

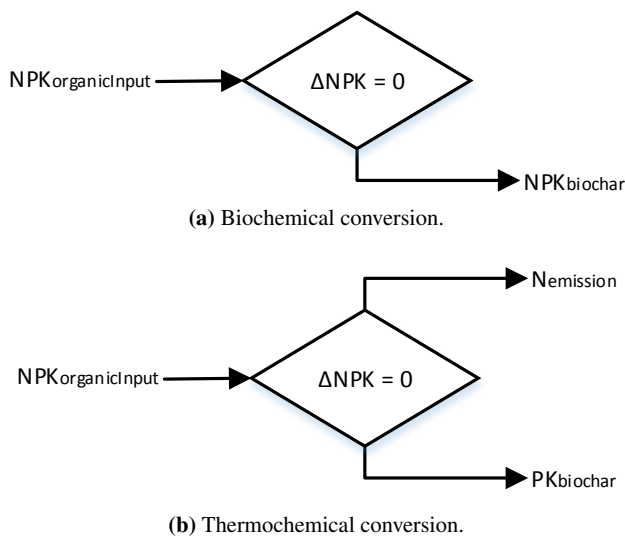


Figure 16. Nutrient balance for inputs to the power plants.

ures that the nitrogen input is lost as emissions when the resource is thermochemically converted, whereas it is retained in the digestate, making it available to the agricultural sub-system again, when biochemically converted.

As mentioned in above the carbon balance for the power plants is performed in DNA. The inputs and outputs from DNA are the carbon input of the organic material to be converted and then either digestate or biochar for biochemical or thermochemical conversion respectively, and emissions which can be both carbon dioxide and methane or just carbon dioxide corresponding to Figure 9 in Section 2.2.1.

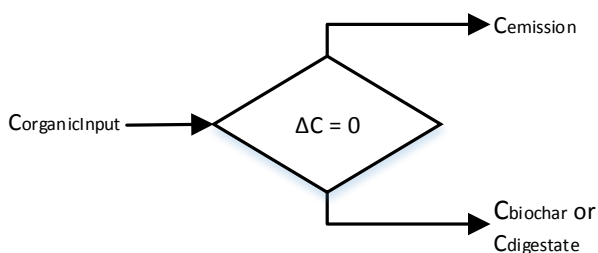


Figure 17. Carbon balance for inputs to the power plants.

2.2.3 Storage and transportation sub-system model

The P and K nutrient balance of the storage and transportation sub-system are modeled with an organic input and an organic output, which are equal for both P and K. However for the decanter the distribution between liquid and

solid fraction differs according to (Hamelin et al. (2011)), which also gives the distribution for N. Most often the balance for N is equivalent to P and K, but special attention is drawn to storage of manure type resources. In those cases N emissions need to be accounted for, which are the same as introduced in Sections 2.2.1 and 2.2.2 except nitrate leaching is added. Figures 18 and 19 display the nitrogen inputs and output of the storage and transportation sub-system. It can be seen in the figures that there

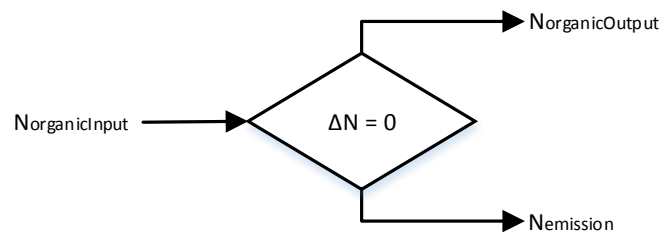


Figure 18. Nitrogen balance in the storage sub-system.

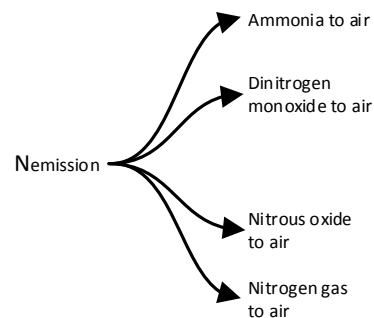


Figure 19. Nitrogen emissions in the storage sub-system.

are a-lot of similarities to Figures 6 and 7 and the amounts are calculated according to (Hamelin et al. (2011)) like for pig manure sourced emissions from agricultural field, but these emission are specific to indoor and outdoor storage.

The carbon balance is equivalent to the nitrogen balance, but with emissions corresponding to Figure 9 and the magnitude of the emissions are calculated according to (Hamelin et al. (2011)).

2.3 Performance analysis model

LCIA results are given in four levels, where the total endpoint results are disaggregated to each impact category and sub-system. Before the results are disaggregated to the main impact categories for each input and output of the LCI at midpoint level. Figure 20 displays the elements of the four level LCIA method.

First the total endpoint results are given. Those results give the total environmental impact asserted by the system analysed. These endpoint results are given in relation to its subcategories, i.e. ecosystem quality, human health and resources, which are then given for each sub-system. Those results are then further disaggregated into their impact subcategories; for ecosystem quality, i.e. agricul-

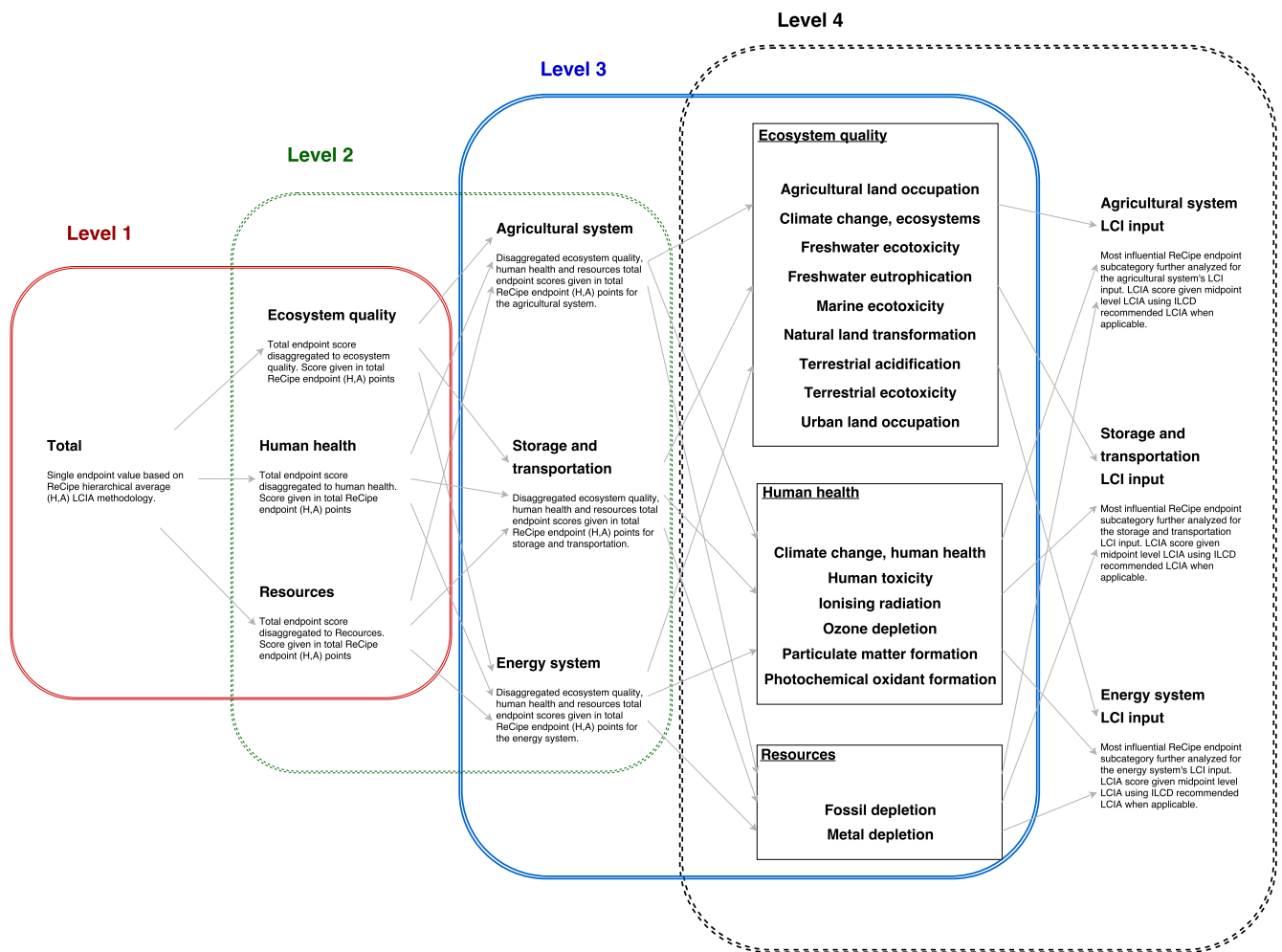


Figure 20. Elements of the four level LCIA method.

tural land occupation, climate change, freshwater ecotoxicity, freshwater eutrophication, marine ecotoxicity, natural land transformation, terrestrial acidification, terrestrial ecotoxicity and urban land occupation; for human health, i.e. climate change, human toxicity, ionizing radiation, ozone depletion, particulate matter formation and photochemical oxidant formation; and for resources, i.e. fossil depletion and metal depletion. Level four then takes the most important impact categories and gives midpoint results for each input and output of the LCI. By doing this the elements of greatest influences to the environmental impact can be identified. For endpoint results the ReCiPe method Goedkoop et al. (6 January 2009) is used and the International Reference Life Cycle Data System (ILCD) recommended methods (Hauschild et al. (2010)) are used for the midpoint results.

3 Model implementation

Python 2.7 was used to design of the integrated agricultural and bioenergy model. The open source advanced life cycle assessment software Brightway2 Mutel (2015)

is imported as a module, which enables easy communication with the Ecoinvent3 database Weidema et al. (2013) once uploaded. Communication to other software within the model script is done by interacting with the operating system and with file manipulation using the `os` and `shutil` python modules, respectively. `Pandas` is used for data structures and as a data analysis tool to import and manipulate data within the python script, and the `numpy` module is used for all numerical calculation. A basic flowchart of the main processes it goes through when used is displayed in Figure 21. Figure 21 uses five different objects to describe various functions in the model. Those functions are; internal process, external process, decision, input/output and local database. The meaning behind internal processes is that these objects are created in and operate fully in the python script the model is written in by the author. However, external processes operate outside the model script and an object has been made for communication within the model script. Local databases are also outside of the script model but no processes are operating within them as they simply pass on data to either internal or external processes that operate on them. The decision function basically contains information on what

makes when compiling the LCIA results before they are displayed to the user.

4 Case study results

LCI tables are given in Appendix A.1 for both the case study and the reference case. Those tables display the inputs and outputs for each sub-system, where the values are given as a changes from conventional wheat production in Denmark. The LCIA results are given in reference to the LCIA levels described in Section 2.3 and in Figure 20. Figure 22 gives the Level 1 endpoint results of the direct field application reference and the biogas production and utilization case.

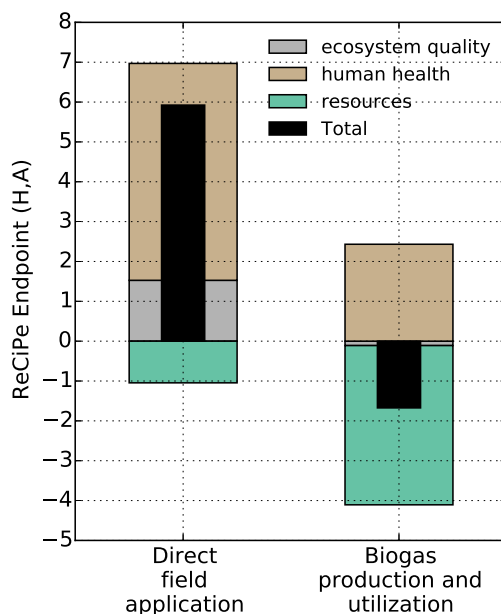


Figure 22. Life Cycle Assessment endpoint results (Level 1).

It can be seen in Figure 22 that the total score of the case study has a lower overall environmental impact than its reference and has a net mitigating environmental effect, whereas the reference has an intensifying effect.

Figure 23 gives the results of the Level 2 analysis, by disaggregating the results from Figure 22 into the main sections of the overall system, i.e. agricultural sub-system, storage and transportation, and energy system, for the three aggregated endpoint categories.

It can be seen in the 23 that the case study outperforms its reference in all three aggregated endpoint LCIA categories. Further, the distribution between the sections indicates large changes in the agricultural sub-system for the ecosystem quality and human health categories, but the largest changes are in the energy sub-system for the resources category. This can be further investigated in a Level 3 analysis. Figures 24 - 26 disaggregate the results from Figure 23 into subcategories of ecosystem quality, human health and resources, respectively. In Figure 24

it can be seen that the greatest contributor to the ecosystem quality impact is climate change and there is very little impact in the other subcategories. In the agricultural sub-system both the case study and its reference show a mitigating effect on climate change, but the case study offers considerably greater mitigation. However, in storage and transportation the impact is intensified. There the case study is less intensive than its reference, but for the energy sub-system the case study also has an intensifying effect whereas the reference does not have an impact as it has no processes in the energy sub-system. To further investigate those results it is relevant to take a closer look at the climate change impact in a Level 4 analysis.

Figure 27 in the Appendix, displays the results using the midpoint category IPCC's global warming potential over a 100 time horizon, for each section. But disaggregated to the inputs and outputs of the system in relation to the LCI. In Figure 27a the difference in the impact of the agricultural sub-system can be found to be due to the carbon dioxide emission and the mineral nitrogen fertilizer input. The amount of carbon dioxide emitted from the agricultural sub-system can be found in tables 3 and 4, but the reason can be found in Section 2.2.1. There it is stated that the carbon dioxide emission from the agricultural sub-system is carbon respiration from decaying organic matter in the soil. Digested manure has less carbon than raw manure because a large portion of it is transformed into biogas in the anaerobic digester. The amount of substituted mineral nitrogen fertilization is given in tables 1 and 2. The reason for greater substitution in the case study can be found in the nitrogen balance of the agricultural sub-system described in Section 2.2.1, there it is stated that less nitrogen in the digested manure is immobilized in the soil compared to nitrogen in raw manure and thus more nitrogen is available to the growing plants. It can be observed in Figure 27b that the difference in impact is due to the difference in methane emission. In Section 2.2.3 it is stated that the carbon balance of the storage units is based on Hamelin et al. (2011), where the digested manure has mostly slowly degradable volatile solids and the emissions are based on the amount of volatile solids stored.

The greatest impact factors in the energy sub-system found by observing Figure 27c are the carbon dioxide emission and the substitution of natural gas fueled heat and power generation. The carbon emission is from the carbon that was taken from the manure in the anaerobic digester is the reason for the decrease in carbon emission between the case study and the reference in the agricultural sub-system. What is interesting is that although the net carbon emission from the agricultural and energy sub-systems is greater in the case study the substitution of fossil fueled heat and power generation counterweights that and contributes in making the biogas production and utilization case superior to its reference in terms of climate change impact.

Figure 25 displays the human health environmental im-

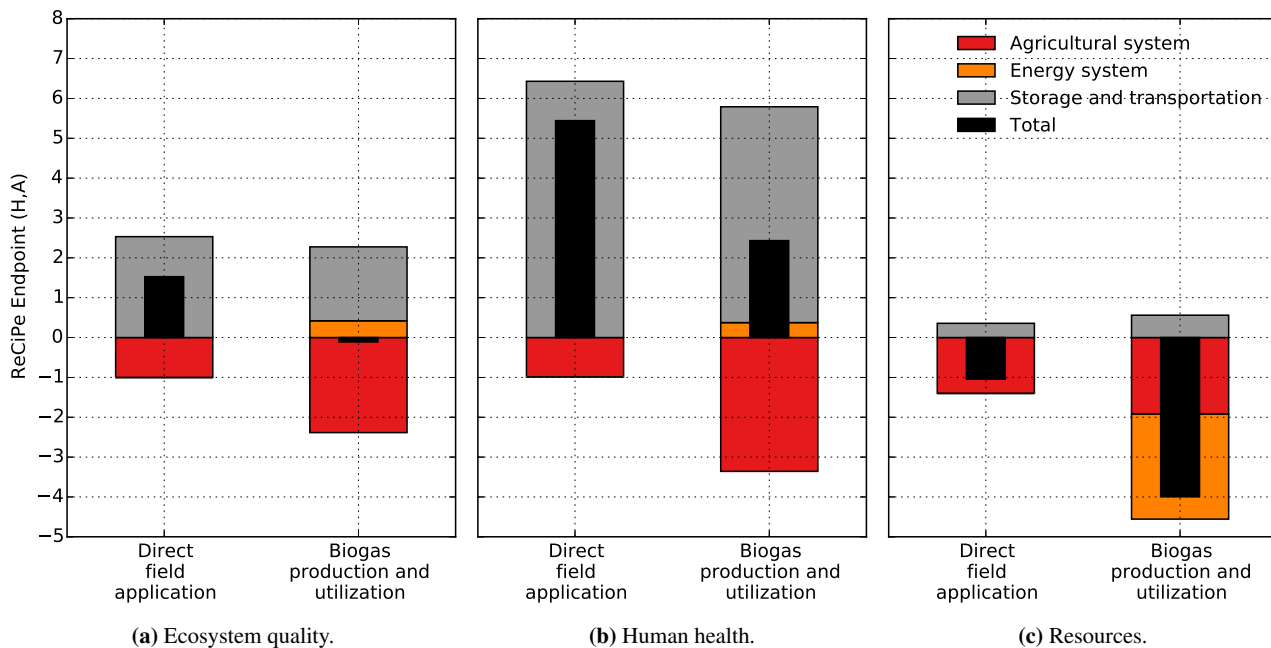


Figure 23. Disaggregated Life Cycle Assessment ecosystem quality endpoint results (Level 2).

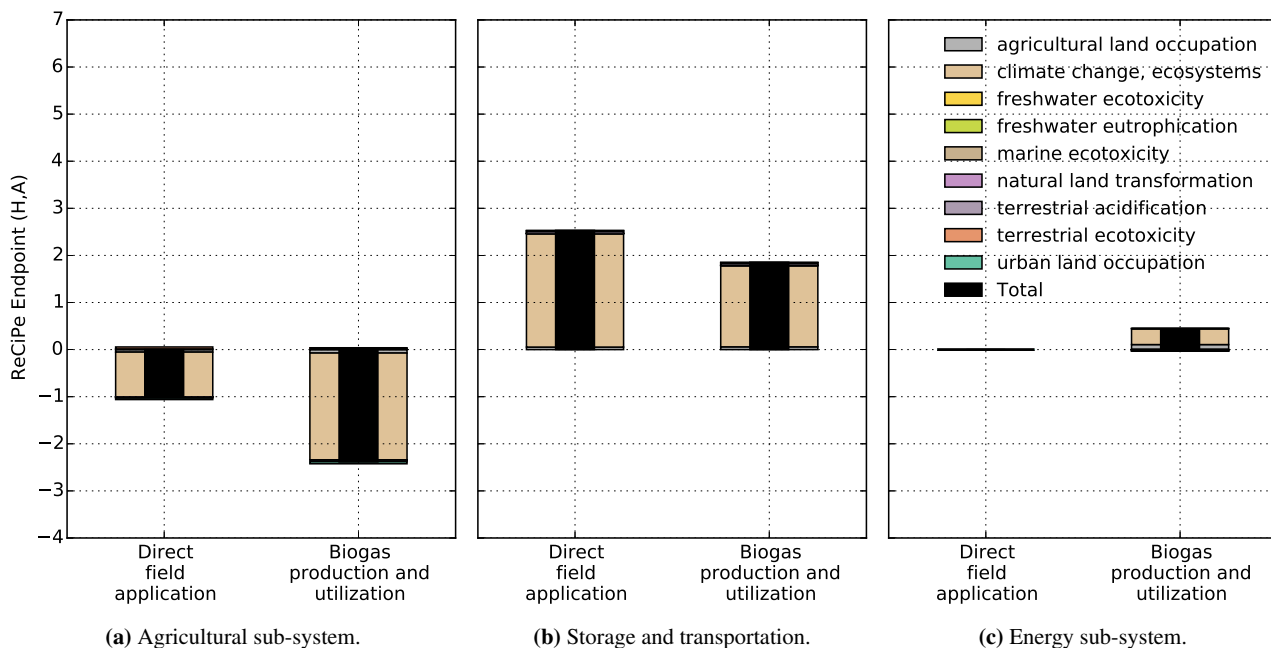


Figure 24. Disaggregated Life Cycle Assessment human health endpoint results.

fact and it can be seen that particulate matter formation and climate change are the largest contributors. Having discussed the climate change impact in depth above, the Level 4 analysis is on the particulate matter formation part of the total environmental impact. From the Figures in 28 it can be seen the main contributor to particulate matter formation is ammonia emission in the agricultural sub-system, and storage and transportation sub-system. The emission of ammonia is calculated in the nitrogen balance in described in Section 2.2.1 and 2.2.3 both are based on

Hamelin et al. (2011) which refers to national guidelines of nitrogen accounting.

In Figure 26, which displays the environmental impact on resources, it can be observed that the greatest category of the two available is fossil depletion. Furthermore, that category is also where the greatest difference is observed between the case study and the reference. From the Figures in 29 the decrease in nitrogen mineral fertilization and the substitution of fossil resources for heat and power generation are most influential.

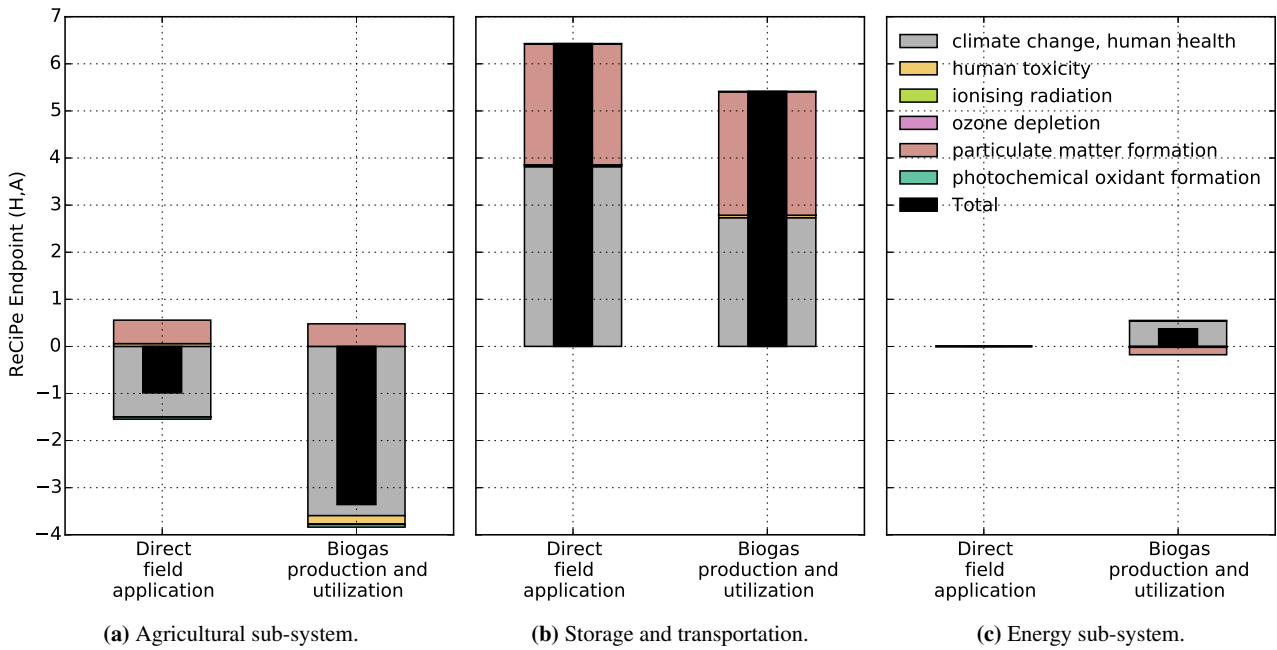


Figure 25. Disaggregated Life Cycle Assessment resources endpoint results.

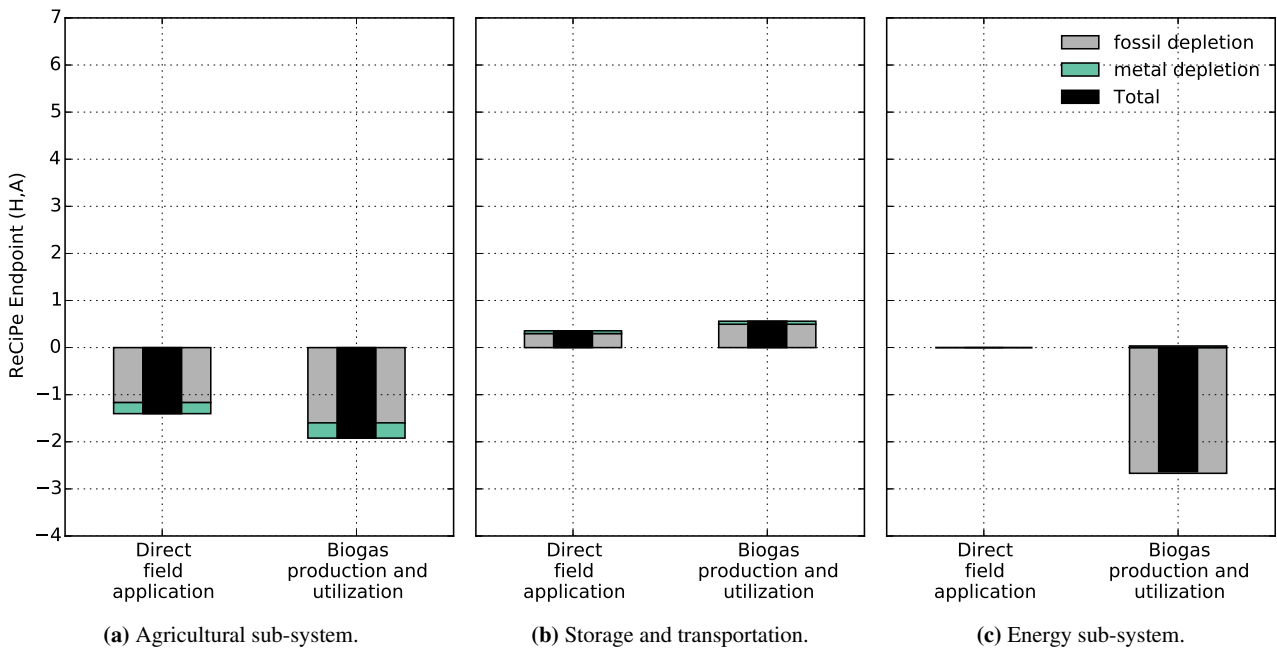


Figure 26. Disaggregated Life Cycle Assessment endpoint results.

5 Discussion

When observing the results of the case study, it seems that for a system like these, analyzing the environmental impact categories climate change and fossil depletion, as particulate matter formation was basically the same for the case study and its reference, might be sufficient to reach an informed decisions. There is a general acceptance of the climate change impact method from IPCC and every impact assessment method in general use, uses that approach.

However, this is not the case for resource depletion environmental impact. For that impact category it is generally recognized that improvements are needed (Hauschild et al. (2010)). Although generally not recognized to reflect resource scarcity, which is a requirement by the ILCD for an impact method, exergy and cumulative exergy could be used to reflect the efficiency of resource utilization in a life cycle sense and thus aid in the decision making. It could be added to the overall analysis but outside of the LCA results where an impact method reflecting scarcity would

be used.

Displaying the results using four levels as introduced in Section 2.3 gives a great deal of insight into the system analyzed. It can also help in finding weaknesses in the modeling, e.g. if one of the greatest contributors is based on uncertain data or the greatest impact is calculated with LCIA method which will need further development. It is also worth noting that the level of detail could be decrease by jumping from level one to level 4 result and showing only the top contributors for main impacts for simplicity.

As mentioned in the introduction, all parts of the processes in the model are freely available. This includes all the external software used. However, the LCI database used in this case study was Ecoinvent3. To be able to use Ecoinvent3 a user will need a license, which is not free of charge. To get around this there are new and constantly expanding freely available LCI databases, e.g. ELCD, USDA, Agribalyse and bioenergiestat.

6 Conclusion

The article introduces a model that successfully uses only freely available software to model Life Cycle Assessment of an integrated bioenergy and agriculture sub-system. This was demonstrated with a case study of biogas production from manure and field application of the residual digestate, in reference to direct manure to field application.

The case study unveiled the studied case to be better in terms of overall environmental impact than its reference, where the greatest difference from the reference were observed in the climate change and fossil depletion impact categories.

The model still uses ecoinvent, a commercial LCI database. But with new freely available LCI database, the possibility for a completely free software based on the model introduced is getting greater.

References

- Francesco Cherubini, Anders H. Stromman, and Edgar Hertwich. Effects of boreal forest management practices on the climate impact of CO₂ emissions from bioenergy. *Ecological Modelling*, 223(1):59–66, December 2011. ISSN 03043800. doi:10.1016/j.ecolmodel.2011.06.021.
- Danish Ministry of Climate, Energy and Buildings. OUR FUTURE ENERGY. Technical report, Danish Ministry of Climate, Energy and Buildings, Copenhagen.
- P. de Willigen. An analysis of the calculation of leaching and denitrification losses as practised in the NUTMON approach. *Rapport-Plant Research International*, (18), 2000.
- Capucine Dupont, Rodica Chiriac, Guillaume Gauthier, and François Toche. Heat capacity measurements of various biomass types and pyrolysis residues. *Fuel*, 115:644–651, January 2014. ISSN 00162361. doi:10.1016/j.fuel.2013.07.086.
- Brian Elmegaard and Niels Houbak. Dna: A general energy system simulation tool. *Proceedings of SIMS 2005*, pages 43–52, 2005.
- A. Friedl, E. Padouvas, H. Rotter, and K. Varmuza. Prediction of heating values of biomass fuel from elemental composition. *Analytica Chimica Acta*, 544(1-2):191–198, July 2005. ISSN 00032670. doi:10.1016/j.aca.2005.01.041.
- Rolf Frischknecht. LCI modelling approaches applied on recycling of materials in view of environmental sustainability, risk perception and eco-efficiency. *The International Journal of Life Cycle Assessment*, 15(7):666–671, June 2010. ISSN 0948-3349. doi:10.1007/s11367-010-0201-6.
- M. J. Goedkoop, R. Heijungs, M. Huijbregts, A. De Schryver, J. Struijs, and R. Van Zelm. Recipe 2008, a life cycle impact assessment method which comprises harmonised category indicators at the midpoint and the endpoint level; first edition report i: Characterisation. Technical report, 6 January 2009. Homepage: <http://www.lcia-recipe.net/>.
- The Danish Government. The Danish Climate Policy Plan Towards a low carbon society. Technical report, Danish Government, Copenhagen, 2013a. Retrieved from: http://www.ens.dk/sites/ens.dk/files/policy/danish-climate-energy-policy/danishclimatepolicyplan_uk.pdf.
- The Danish Government. Catalogue of Danish Climate Change Mitigation Measures. Technical report, Danish Government, Copenhagen, 2013b. Retrieved from: http://www.ens.dk/sites/ens.dk/files/policy/danish-climate-energy-policy/dk_climate_change_mitigation_uk.pdf.
- Lorie Hamelin, Marianne Waesnes, Henrik Wenzel, and Bjorn M Petersen. Environmental consequences of future biogas technologies based on separated slurry. *Environmental science & technology*, 45(13):5869–77, July 2011. ISSN 1520-5851. doi:10.1021/es200273j.
- Michael Hauschild, GOEDKOOP Mark, GUINEE Jerome, HEIJUNGS Reinout, HUIJBREGTS Mark, JOLLIET Olivier, MARGNI Manuele, and DE SCHRYVER An. Recommendations for Life Cycle Impact Assessment in the European context - based on existing environmental impact assessment models and factors (International Reference Life Cycle Data System - ILCD handbook), October 2010. ISSN 1018-5593.
- Fortunat Joos, Michele Bruno, Roger Fink, Ulrich Siegenthaler, Thomas F. Stocker, Corinne Le Quere, and Jorge L. Sarmiento. An efficient and accurate representation of complex oceanic and biospheric models of anthropogenic carbon uptake. *Tellus B*, 48(3):397–417, July 1996. ISSN 0280-6509. doi:10.1034/j.1600-0889.1996.t01-2-00006.x.
- Fortunat Joos, I. Colin Prentice, Stephen Sitch, Robert Meyer, Georg Hooss, Gian-Kasper Plattner, Stefan Gerber, and Klaus Hasselmann. Global warming feedbacks on terrestrial carbon uptake under the Intergovernmental Panel on Climate Change (IPCC) Emission Scenarios. *Global Biogeochemical Cycles*, 15(4):891–907, December 2001. ISSN 08866236. doi:10.1029/2000GB001375.

- Jari Liski, Taru Palosuo, Mikko Peltoniemi, and Risto Sievänen. Carbon and decomposition model Yasso for forest soils. *Ecological Modelling*, 189(1-2):168–182, November 2005. ISSN 03043800. doi:10.1016/j.ecolmodel.2005.03.005.
- Chris Mutel. Brightway2, 2015. Homepage: www.brightwaylca.org.
- NaturErhvervstyrelsen. Vejledning om gødsknings- og harmoniregler. Technical report, Ministeriet for Fødevarer, Landbrug og Fiskeri, 2013.
- Thomas Nemecek and Julian Schnetzer. Methods of assessment of direct field emissions for LCIs of agricultural production systems. *Data v3. 0*, 2012.
- D.W. Pennington, J. Potting, G. Finnveden, E. Lindeijer, O. Joliet, T. Rydberg, and G. Rebitzer. Life cycle assessment part 2: Current impact assessment practice. *Environment International*, 30(5):721 – 739, 2004. ISSN 0160-4120. doi:<http://dx.doi.org/10.1016/j.envint.2003.12.009>.
- Bjorn M. Petersen, Jorgen E. Olesen, and Tove Heidmann. A flexible tool for simulation of soil carbon turnover. *Ecological Modelling*, 151(1):1–14, May 2002. ISSN 03043800. doi:10.1016/S0304-3800(02)00034-0.
- Bjorn M. Petersen, Lars S. Jensen, Søren Hansen, Anders Pedersen, Trond M. Henriksen, Peter Sørensen, Isabelle Trinsoutrot-Gattin, and Jørgen Berntsen. CN-SIM: a model for the turnover of soil organic matter. II. Short-term carbon and nitrogen development. *Soil Biology and Biochemistry*, 37(2):375–393, February 2005. ISSN 00380717. doi:10.1016/j.soilbio.2004.08.007.
- Bjorn Molt Petersen, Marie Trydeman Knudsen, John Erik Hermansen, and Niels Halberg. An approach to include soil carbon changes in life cycle assessments. *Journal of Cleaner Production*, 52:217–224, August 2013. ISSN 09596526. doi:10.1016/j.jclepro.2013.03.007.
- G. Rebitzer, T. Ekvall, R. Frischknecht, D. Hunkeler, G. Norris, T. Rydberg, W.-P. Schmidt, S. Suh, B.P. Weidema, and D.W. Pennington. Life cycle assessment: Part 1: Framework, goal and scope definition, inventory analysis, and applications. *Environment International*, 30(5):701 – 720, 2004. ISSN 0160-4120. doi:<http://dx.doi.org/10.1016/j.envint.2003.11.005>.
- R. N. Roy, R.V. Misra, J.P. Lesschen, and E.M. Smaling. Assessment of soil nutrient balance: Approaches and methodologies. Technical report, Food and Agriculture Organization of the United Nations, 2003. Retrieved from: <ftp://ftp.fao.org/docrep/fao/006/y5066e/y5066e00.pdf>.
- Jon Schnute. A Versatile Growth Model with Statistically Stable Parameters. *Canadian Journal of Fisheries and Aquatic Sciences*, 38(9):1128–1140, September 1981. ISSN 0706-652X. doi:10.1139/f81-153.
- Sangwon Suh and Gjalt Huppes. Methods for life cycle inventory of a product. *Journal of Cleaner Production*, 13(7):687 – 697, 2005. ISSN 0959-6526. doi:<http://dx.doi.org/10.1016/j.jclepro.2003.04.001>.
- Stanislav V. Vassilev, David Baxter, Lars K. Andersen, and Christina G. Vassileva. An overview of the chemical composition of biomass. *Fuel*, 89(5):913–933, May 2010. ISSN 00162361. doi:10.1016/j.fuel.2009.10.022.
- B.P. Weidema, Ch. Bauer, R. Hirschier, Ch. Mutel, T. Nemecek, J. Reinhard, C.O. Vadenbo, and G. Wernet. The ecoinvent database: Overview and methodology, Data quality guideline for the database version 3, 2013. Homepage: www.ecoinvent.org.

A Appendix

A.1 LCI data

Table 1. Life Cycle Inventory for processes, direct field application.

	Unit	Agricultural	Storage and trans.
market for potassium chloride, as K ₂ O	kilogram	-75.735	0.000
liquid manure spreading, by vacuum tanker	cubic meter	21.283	0.000
market for phosphate fertiliser, as P ₂ O ₅	kilogram	-43.510	0.000
market for nitrogen fertiliser, as N	kilogram	-116.115	0.000
market for fertilising, by broadcaster	hectare	-3.263	0.000
transport, tractor and trailer, agricultural	ton kilometer	0.000	445.265
market for electricity, low voltage	kilowatt hour	0.000	15.916
market for liquid manure storage and processing...	cubic meter	0.000	0.001

Table 2. Life Cycle Inventory for emissions, direct field application.

	Unit	Agricultural	Storage and trans.
Phosphate	kilogram	0.134	0.000
Carbon dioxide, fossil	kilogram	-3151.968	0.000
Zinc	kilogram	1.216	0.000
Copper	kilogram	0.183	0.000
Ammonia	kilogram	12.568	0.000
Dinitrogen monoxide	kilogram	0.322	0.000
Mercury	kilogram	0.001	0.000
Nitrogen oxides	kilogram	-0.274	0.000
Nitrate	kilogram	-1.264	0.000
Chromium	kilogram	-0.007	0.000
Carbon dioxide, from soil or biomass stock	kilogram	2376.740	0.000
Lead	kilogram	0.001	0.000
Cadmium	kilogram	-0.001	0.000
Nickel	kilogram	0.010	0.000
Methane, from soil or biomass stock	kilogram	0.000	69.100
Ammonia	kilogram	0.000	31.519
Dinitrogen monoxide	kilogram	0.000	3.676
Nitrogen oxides	kilogram	0.000	1.932
Nitrogen	kilogram	0.000	5.410
Carbon dioxide, from soil or biomass stock	kilogram	0.000	57.454

Table 3. Life Cycle Inventory for processes, biogas production and utilization.

	Unit	Agricultural	Storage and trans.	Energy
market for fertilising, by broadcaster	hectare	-3.475	0.000	0.000
liquid manure spreading, by vacuum tanker	cubic meter	21.685	0.000	0.000
market for potassium chloride, as K ₂ O	kilogram	-75.735	0.000	0.000
market for phosphate fertiliser, as P ₂ O ₅	kilogram	-43.510	0.000	0.000
market for nitrogen fertiliser, as N	kilogram	-129.017	0.000	0.000
market for polyacrylamide	kilogram	0.000	0.000	20.002
transport, tractor and trailer, agricultural	ton kilometer	0.000	0.000	427.653
market for electricity, low voltage	kilowatt hour	0.000	0.000	64.168
market for liquid manure storage and processing...	cubic meter	0.000	0.000	0.001
anaerobic digestion plant construction, agricul...	unit	0.000	0.000	0.000
heat and power co-generation, natural gas, 1MW ...	megajoule	0.000	-7548.223	0.000
heat and power co-generation, natural gas, 1MW ...	kilowatt hour	0.000	-1822.929	0.000
heat and power co-generation unit construction,...	unit	0.000	0.000	0.000
heat and power co-generation unit construction,...	unit	0.000	0.000	0.000
heat and power co-generation unit construction,...	unit	0.000	0.000	0.000
market for lubricating oil	kilogram	0.000	0.533	0.000
market for waste mineral oil	kilogram	0.000	-0.533	0.000

Table 4. Life Cycle Inventory for emissions, dbiogas production and utilization.

	Unit	Agricultural	Storage and trans.	Energy
Lead	kilogram	-0.000	0.000	0.000
Cadmium	kilogram	-0.001	0.000	0.000
Chromium	kilogram	-0.011	0.000	0.000
Carbon dioxide, fossil	kilogram	-3151.968	0.000	0.000
Phosphate	kilogram	0.134	0.000	0.000
Nickel	kilogram	0.004	0.000	0.000
Carbon dioxide, from soil or biomass stock	kilogram	1533.367	0.000	0.000
Nitrogen oxides	kilogram	-0.281	0.000	0.000
Ammonia	kilogram	10.933	0.000	0.000
Copper	kilogram	0.106	0.000	0.000
Nitrate	kilogram	19.052	0.000	0.000
Dinitrogen monoxide	kilogram	0.730	0.000	0.000
Zinc	kilogram	0.703	0.000	0.000
Mercury	kilogram	0.001	0.000	0.000
Methane, from soil or biomass stock	kilogram	0.000	0.000	36.086
Carbon dioxide, from soil or biomass stock	kilogram	0.000	0.000	34.204
Nitrogen oxides	kilogram	0.000	0.000	1.706
Nitrogen	kilogram	0.000	0.000	4.778
Ammonia	kilogram	0.000	0.000	32.096
Dinitrogen monoxide	kilogram	0.000	0.000	3.357
Methane, from soil or biomass stock	kilogram	0.000	5.719	0.000
NMVOC, non-methane volatile organic compounds, ...	kilogram	0.000	0.036	0.000
Platinum	kilogram	0.000	0.000	0.000
Sulfur dioxide	kilogram	0.000	1.067	0.000
Carbon monoxide, from soil or biomass stock	kilogram	0.000	0.854	0.000
Dinitrogen monoxide	kilogram	0.000	0.044	0.000
Nitrogen oxides	kilogram	0.000	0.267	0.000
Carbon dioxide, from soil or biomass stock	kilogram	0.000	1492.460	0.000

A.2 LCIA level 4 results

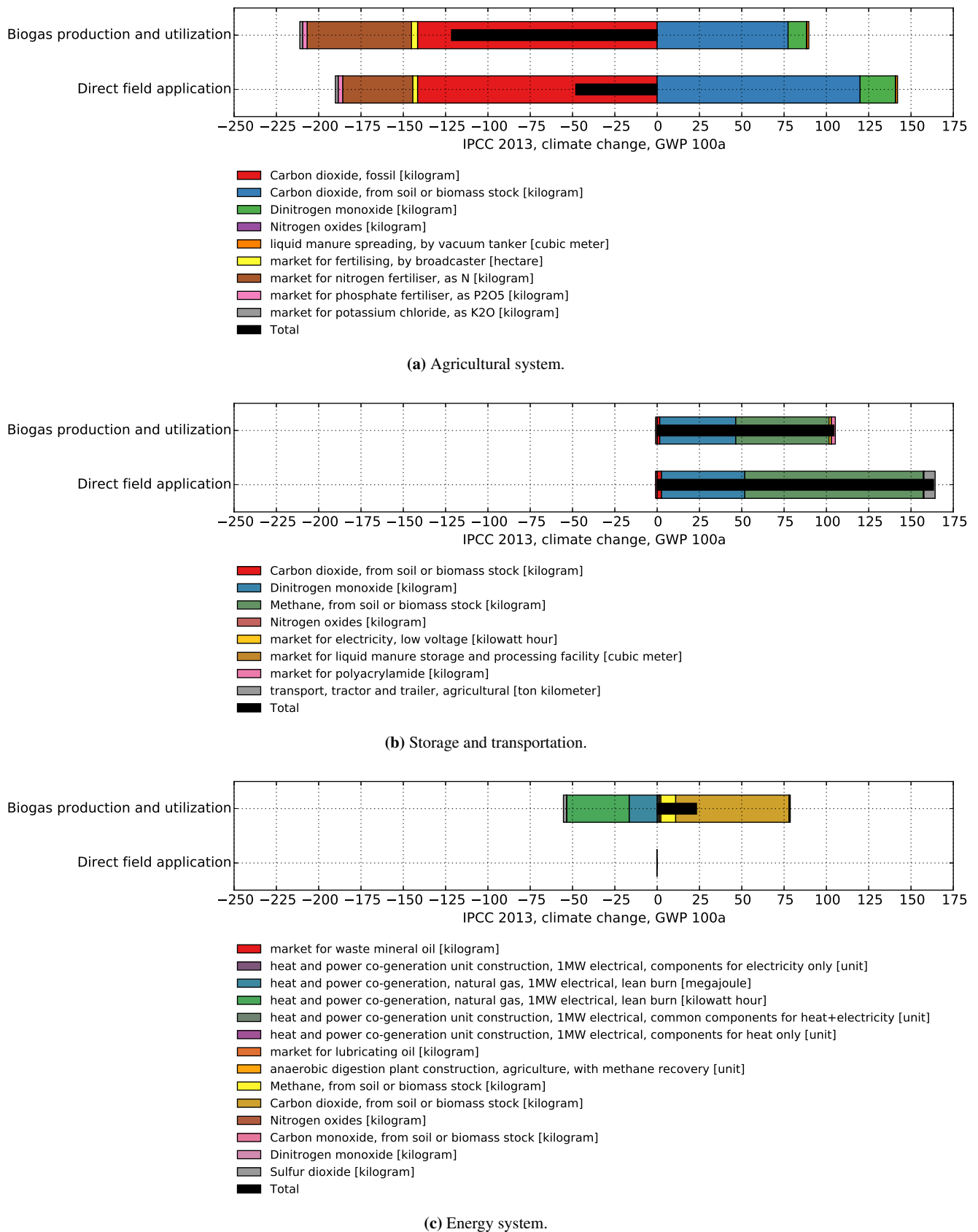
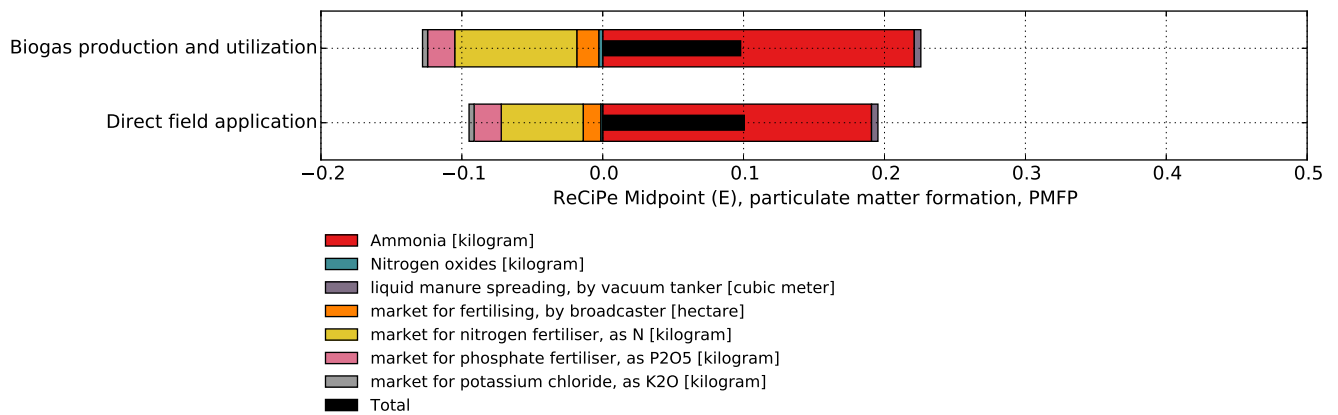
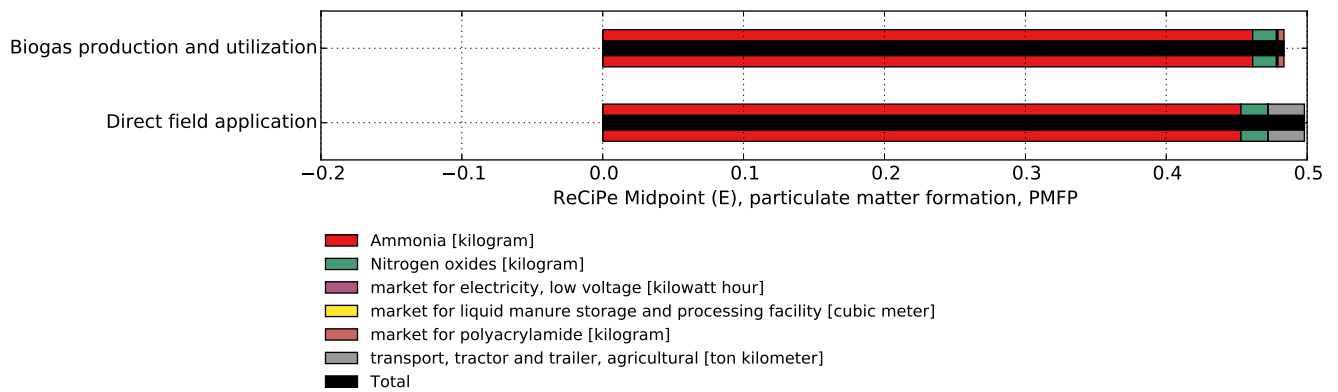


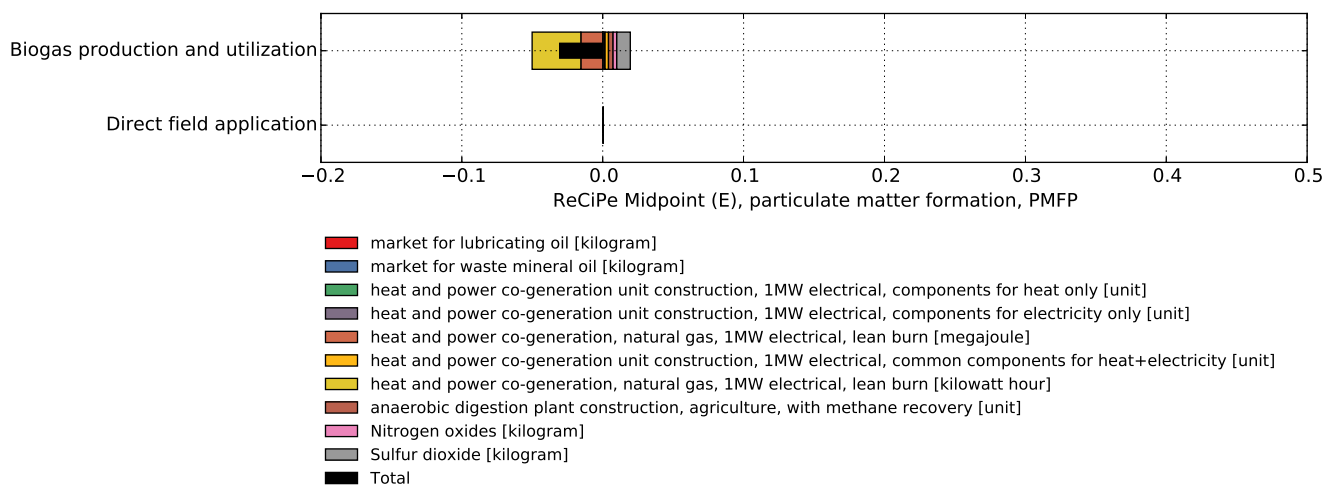
Figure 27. Level 4 climate change, disaggregated LCIA midpoint results in kg Carbon dioxide-equivalence per hectare.



(a) Agricultural system.



(b) Storage and transportation.



(c) Energy system.

Figure 28. Level 4 particulate matter formation, disaggregated LCIA midpoint results in kg PM10-equivalence per hectare.

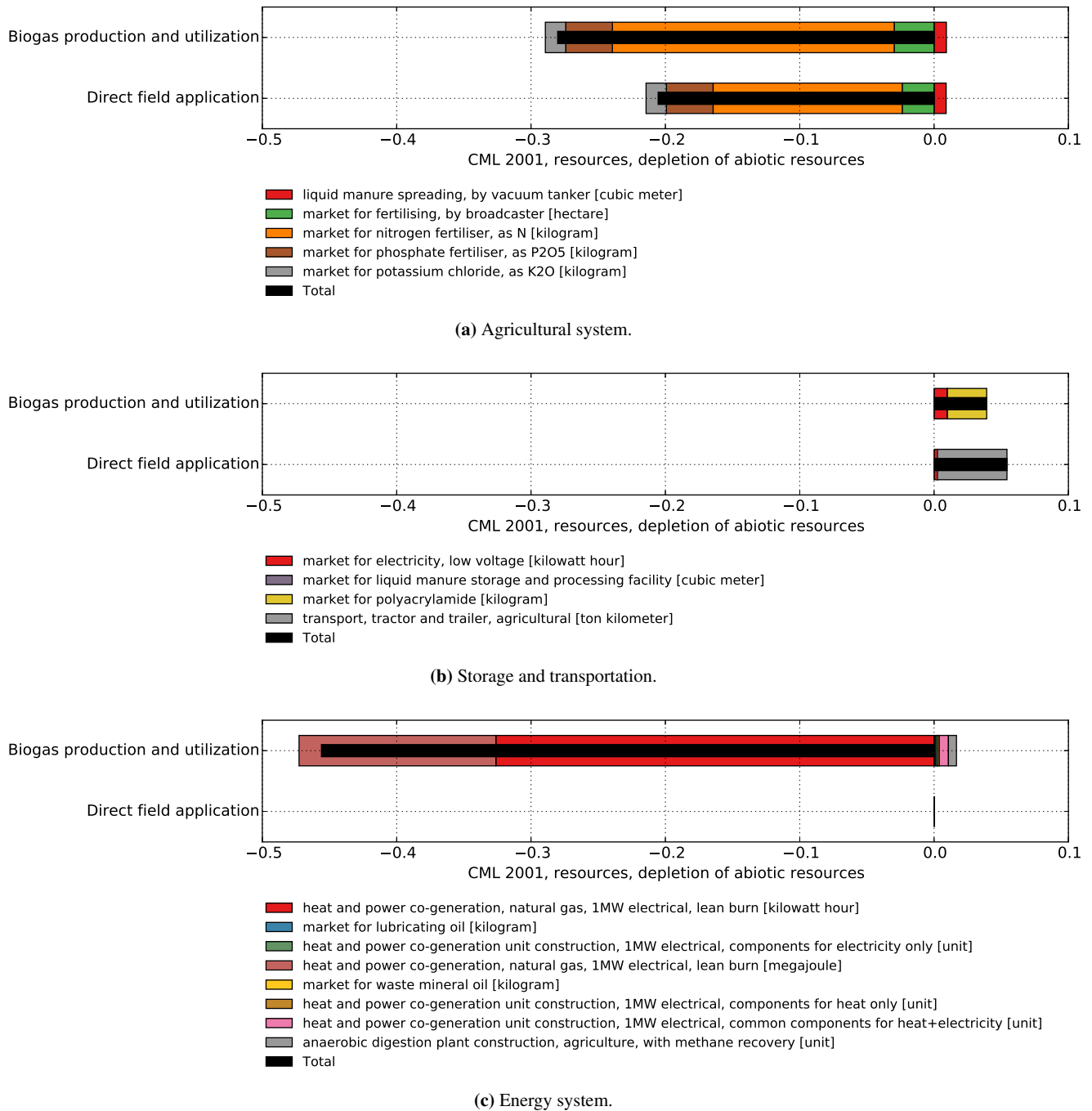


Figure 29. Level 4 depletion of abiotic resources, disaggregated LCIA midpoint results in kg Antimony-equivalence per hectare.

Modeling of the Energy Consumption within the Framework of the Energy Efficiency Management

Yuliia Pavlova¹ Wilhelm Rondeel¹ Oleg Kotsar²

¹Faculty of Technology, Telemark University College, Norway, pavlova.yuliia.kpi@gmail.com, wilhelm.rondeel@hit.no

²Institute for Energy Saving and Energy Management, NTUU “Kyiv Polytechnic Institute”, Ukraine, kovpers@ukr.net

Abstract

Insufficient level of energy efficiency in Ukraine requires a reformation of power sector in order to develop the mechanisms that could stimulate market players for efficient resource usage. For this purpose, it is advisable to use the experience of other energy markets, which is based on the offering of saved electrical energy or reduced capacity as a resource in the market. Thus, it is important to determine accurately the expected and actual demand reduction and amount of saved energy. This study contains the comparative analysis of the existing approaches for determination and measurement of the data necessary for solving the mentioned tasks. Therefore, the paper investigates methods for modeling of energy consumption of the Ukrainian objects where energy efficient projects are implemented. The main contribution of this paper is in the usage of forecasting methods for the development of the expected energy use models of such objects. In the case of the certain type of objects the accuracy of the research results exceeds the accuracy of the results, obtained through usage of the existing approaches in a pure form.

Keywords: energy efficiency, electricity market, modeling of energy use, energy saving.

Abbreviations

<i>ASHRAE</i>	American Society of Heating, Refrigerating and Air-Conditioning Engineers
<i>BCM&BM</i>	Bilateral Contract Market and Balancing Market
<i>EE</i>	Energy efficient
<i>IPMVP</i>	International Performance Measurement and Verification Protocol
<i>M&V</i>	Measurement and Verification
<i>MAD</i>	Mean Absolute Derivation
<i>MAPE</i>	Mean Absolute Percentage Error
<i>MSE</i>	Mean Squared Error
<i>PJM</i>	Pennsylvania-New Jersey-Maryland
<i>SSE</i>	Sum Squared Error

1 Introduction

Providing of reliable power supply according to demand in compliance with acceptable consequences for the environment, needs more efficient usage of electricity (Denysiuk, 2013). Insufficient level of energy efficiency in Ukraine, in its turn, requires an immediate reformation of the Ukrainian power sector in order to stimulate final consumers to decreasing of fossil fuel unit costs and reduction of harmful emissions. One of the most efficient ways of power sector development is the liberalization of the energy markets that was realized in the vast majority of countries. Taking into account current introduction of the liberalized electricity market in Ukraine it is advisable to use the experience of the best energy efficiency managing practices of the other markets for determining and developing the instruments and mechanisms that could stimulate Ukrainian market players for the efficient resource usage.

2 Management of the Energy Efficiency in the World Electricity Markets

Nowadays large attention in energy markets is devoted to stimulation of energy saving and energy efficiency. Creation of the incentives is carried out directly through competition and by means of implementation of different mechanisms for energy saving management. Particularly, in some competitive energy markets of the USA a consumer's ability to reduce its demand for electricity is equivalent to the ability of a generator to increase its electricity output. Therefore the rules of such markets allow final consumers to sell demand resources, creating in this way a competition for the generation companies.

In the American electricity markets Pennsylvania-New Jersey-Maryland (PJM) and New England participation of demand resources is being carried out through selling of energy efficient (EE) resources in the capacity markets. In other words final consumers offer permanent continuous reduction of their demand and electricity consumption during the defined period that have to be achieved due to the EE projects (Bastian, 2010). In such a manner final consumers can not only save costs as a result of changing their load,

but also obtain additional compensation. Such mechanisms has led to decreasing of non-productive power costs, fossil fuel savings, harmful emissions reduction and avoiding of expenses on building new power stations (SPEER, 2013). Some European energy markets in the framework of energy saving activity implement the programs of imposing obligations, which are related to achieving of the determined goals (in harmful emissions reduction and decreasing of fossil fuel usage) due to EE measures. In distinction of the American markets, such European scheme can function in several forms together with various tradable mechanisms and attracting different market participants and entities (Bertoldi, Rezessy, 2009).

Taking into account positive experience of the world markets, it is advisable to develop in the Bilateral Contract Market and Balancing Market (BCM&BM), which is being implemented in Ukraine, the mechanisms of EE resources trading in order to stimulate consumers for the implementation of EE technologies. In that way the quantity of saved electrical energy (or capacity) can be paid for market participants according to certain rules in order to return some compensation for their expenses on energy saving measures. Similar to American energy markets, the value of saved electrical energy can be accounted in the BCM&BM for the estimation of the obtained energy efficiency level. For this purpose it's necessary to analyze and compare the existing methods and approaches for determining the amount of savings and to develop methodology of their application in the BCM&BM.

3 The Analysis of the Approaches for Determining Energy Efficient Resources Value

The section presents the comparative analysis of the existing approaches and methods for determination and measurement of the data which are necessary for quantifying the demand reduction and amount of saved electrical energy. Consequently, the possibilities of their usage in different forms for the Ukrainian energy consumption objects are investigated.

3.1 The Fundamental Principles of the Existing Approaches

Participation of the EE resources in energy markets requires the determination and verification of the value of EE resource, usually expected demand reduction in MW during the defined hours. Requirements and rules of the EE resources participation in energy markets are mostly determined by guidelines developed by relevant authorities. However, the majority of these documents are based on the materials of International Performance Measurement and Verification Protocol (IPMVP), which is a methodological document of Efficiency Valuation Organization (EVO, 2014). IPMVP proposes the approaches for determination and calculation of the

achieved energy savings (i.e. value of EE resources) due to the EE projects. IPMVP describes general requirements and principles of Measurement and Verification (M&V) activity of the achieved results, offers four possible M&V options and determines the requirements for the results reporting. Another basic document is guideline of American Society of Heating, Refrigerating and Air-Conditioning Engineers «ASHRAE Guideline 14-2002. Measurement of Energy and Demand Savings» (ASHRAE, 2002). It is based on the same requirements and M&V options as IPMVP, but it contains more detailed instructions. It is worthwhile to say that above mentioned documents do not offer the precise algorithms of actions for each type of EE project. But they contain general requirements that should be followed by all EE resource suppliers.

Let us analyze the main approaches for determination of the achieved energy savings and M&V options that are offered in IPMVP and ASHRAE Guideline. This will allow to estimate further possibility of their usage by BCM&BM participants. So far as energy savings represent the absence of energy use, they cannot be directly measured. Above mentioned documents offer approaches that involve determination of the EE resource value by comparison of the expected energy use that would have occurred in the reporting period without EE project realization, and actual energy use during the reporting period after EE project realization. The Figure 1 presents the fundamentals of the determination of the achieved savings. During the baseline period (before the EE project realization) and reporting period consumer, who provides EE resource, carries out measurements of the energy use and the independent variables that can influence it. The object's main operating conditions are also determined. After the end of the baseline period, a mathematical model of the baseline energy use is developed on the ground of actual data. This model determines the dependence between energy use and key operating parameters and independent variables.

For the purpose of determination of the expected baseline energy use, the measured independent variables of the reporting period are inserted into the mathematical model of the baseline energy use. In such a manner the baseline energy use is adjusted for the set of reporting conditions. In order to take into account and to reflect the influence of the other factors on energy consumption, various adjustments should be used. For example, such adjustments can be used in the cases of production level increase, changes in object size or equipment etc. The selection of the most appropriate M&V option, which will be used within the chosen approach, is significant for the determination of the achieved savings. In the case when the existed options are not appropriate for the precise projects, EE resource supplier can offer alternative methodology (Bastian, 2010).

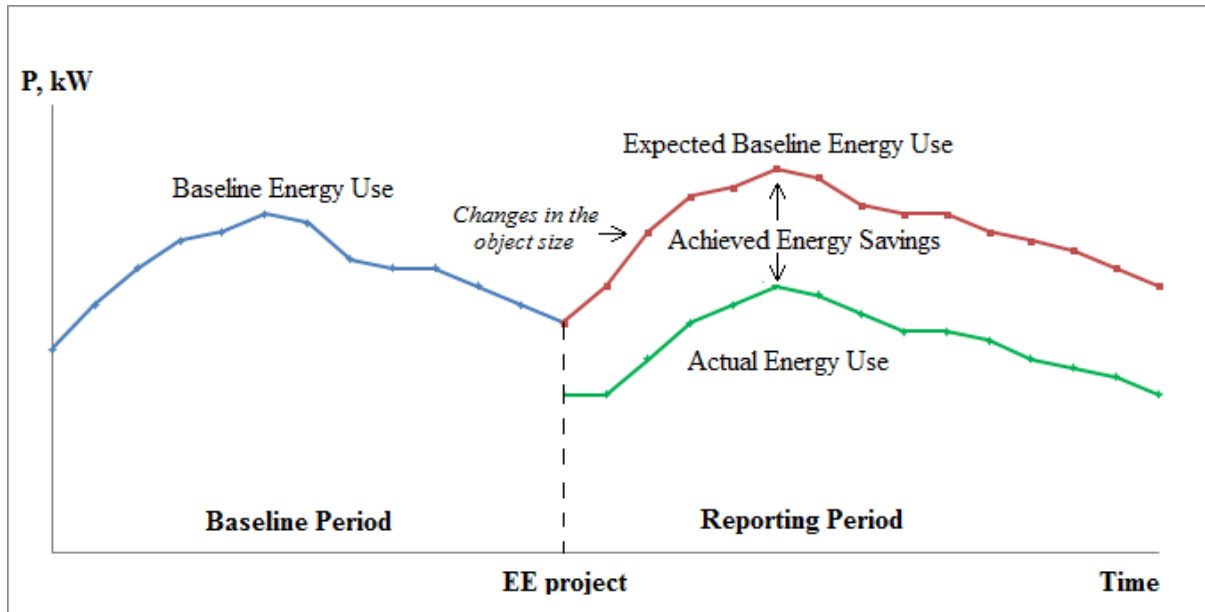


Figure 1. The determination of the achieved energy savings after EE project realization.

3.2 The Analysis of the Conditions and Tasks that Can Occur during Modeling of Energy Consumption of the Object

The analysis of IPMVP and ASHRAE Guideline allows to establish, that the existing approaches and M&V options mostly require measurements of energy use and independent variables that influence it. These values are necessary for the development of the models of energy use and for the next calculation of the EE resource value. In particular, option A of IPMVP, which is based on the simplified calculations, foresees measurement of the main independent variables, because within this option energy consumption is calculated on the basis of the measured data of the chosen variables and other estimated parameters. Option B foresees straightforward measurement of the energy use of the precise equipment or part of the object during the baseline and reporting periods and their following comparison. But for increasing of the results certainty and their adjustment for the reporting conditions, in the majority of cases relevant adjustments are added. They are mainly determined on the ground of the measured independent variables that influence energy use. Option C is similar to option B, but it is used when the measurement of energy use of the precise object part is not possible. Therefore, in this case it is necessary to use the appropriate adjustments for updating of the obtained results. Calculation of the adjustments and estimation of the independent variables are carried out by mathematical modeling, predominantly regression analysis. For this purpose, measurement of the independent variables is also necessary. Option D is the most costly and complicated, because it includes modeling of the

energy use in software with following simulation. It is used quite seldom, mostly in the cases of absence of the baseline data.

Therefore, the described analysis affirms that within the approaches and M&V options, which are provided by IPMVP, it is necessary to conduct measurement of the independent variables that influence energy use, particularly operating hours, weather conditions, production output etc. However, if to review appliance of the existing approaches in the Ukrainian electricity market, it should be mentioned, that in a majority of the energy consuming objects, such measurements are not carried out. But their capacity is being measured mainly with 30-minutes averaging. Therefore, application of the offered options in their current form can require some expenses for the realization of additional measurements of other variables. Furthermore, for the development of the mathematical models of energy use usually it is necessary to possess a set of data for a long past period (for example, months, year). But as far as participants of the Ukrainian electricity market already conduct measurements of the capacity, it is advisable to use such data for determination of the EE resource value. Among options that are provided by IMPVP, for the existing data it is possible to use only option B, because it foresees measurement of the energy use of the whole object and in some cases affords an opportunity to determine EE resource value without independent variables measurements. Particularly, in the cases, when energy use can be considered as sustainable and can be taken as equal to actual baseline energy use without making any adjustments. Let's get a view of the usage of the option B in the case of commercial object.

4 Development of the Forecasting Model of the Object's Energy Use

In the framework of this research the electrical consumption of tradable object is examined. The object under consideration is a supermarket that contains several departments and different types of electrical appliances. Figure 2 presents the load curve of the supermarket for one month with 30-minutes measurement interval. This load curve is a time series that contains 1440 data values.

After analyzing of the object's consumption pattern, investigation of its operating conditions and factors that influence it, this load curve can be characterized as the time series which contains periodical changes in data that tend to be repeated every week. Furthermore, the load curve during the day contains peak periods that are similar from day to day. Therefore, according to IPMVP, due to changes in the character of the object's energy use and dependence on different factors, it is necessary to add adjustments into the model of the baseline energy use. But measurements of the independent variables for these adjustments were not carried. Thus, in the authors' opinion for this and similar objects it can be advisable to use option B in adapted form. Particularly, it is being offered to determine the expected baseline energy use through forecasting. Subsequently it is necessary to check the adequacy of forecasting model and compare the forecasting results with the results, which could be obtained in the case of the usage of the option B for this object in the existing simplified form. It should be mentioned that for the load forecasting for different types of objects it is necessary to choose the most appropriate forecasting method according to particular features of the object, such as type of object, specifics of work, changes in energy use, type of load curve, dependence on different factors etc.

For the forecasting of the load of this supermarket one of the most extended forecasting methods has been chosen – exponential smoothing. Exponential smoothing is a procedure for continually revising a forecast in the light of more recent experience. It

assigns exponentially decreasing weights as the observation is getting older. In other words, recent observations are given relatively more weight in forecasting than the older observations (Kalekar, 2004). For the determination of the energy use model, autocorrelation analysis has been done for this time series. With the purpose of separation seasonal and trend components, autocorrelation analysis has been conducted for the different periods of pre-history and with delays for different periods. Autocorrelation coefficient was calculated according to the equation:

$$r_k = \frac{\sum_{t=k+1}^n (Y_t - \bar{Y})(Y_{t-k} - \bar{Y})}{\sum_{t=1}^n (Y_t - \bar{Y})^2} \quad (1)$$

where:

r_k - coefficient of autocorrelation of the delay for k periods;

\bar{Y} - average value of time series;

Y_t - actual value at the time moment t;

Y_{t-k} - value for k periods earlier then at the time moment t-k (Hanke *et al*, 2001).

From the Figure 2 it is possible to determine, that the load curve is similar from day to day, i.e. every 48 values, therefore autocorrelation analysis has been conducted for 48 (1 day), 96 (2 days) and 144 (3 days) values of time series with the delaying for the periods $r=1..48$ and $r=49..96$. From the Table 1 it is visible, that for the first several delay periods r_1, r_2, r_3 , autocorrelation coefficients are significantly different from 0, and with the increasing of delay period they are decreasing gradually. Therefore, according to (Hanke *et al*, 2001), this proclaims presence of the trend component. The results of the analysis also indicate that the value of the autocorrelation coefficients is increasing the nearer the delay period is getting to 48th or 48-fold. This affirms the presence of the seasonal component in the time series which is repeated every 48 values, i.e. daily.

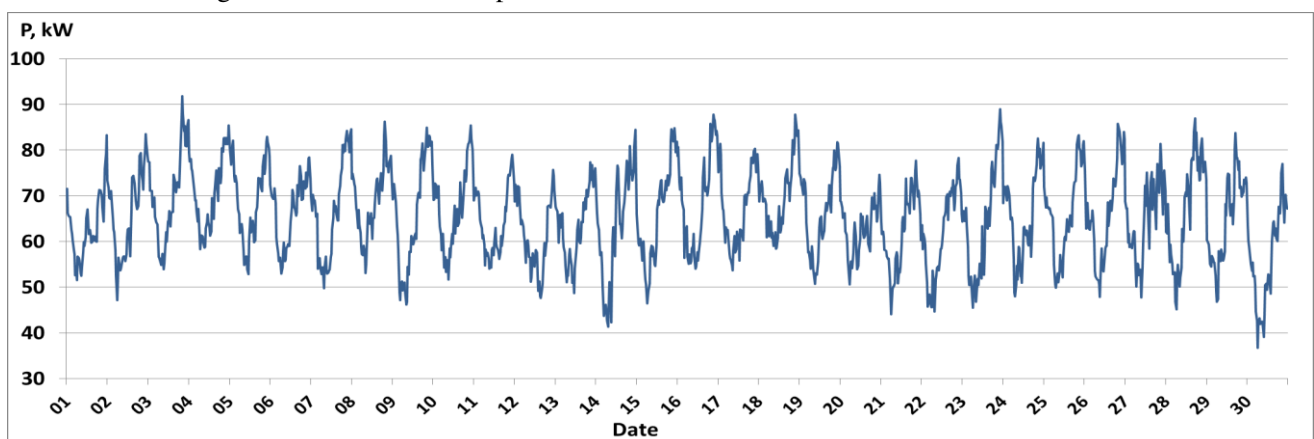


Figure 2. Energy demand of the supermarket for the one month period.

Table 1. The Autocorrelation Coefficients for the Time-series with 144 Values.

	<i>Time-series</i> =48	<i>Time-series</i> =96	<i>Time-series</i> =144
r₁	0,817	0,905	0,921
r ₂	0,642	0,767	0,821
r ₃	0,488	0,644	0,741
r ₄	0,408	0,618	0,676
...
r ₂₃	-0,034	-0,357	-0,396
r ₂₄	-0,061	-0,339	-0,386
r ₂₅	-0,092	-0,330	-0,386
...
r ₄₄	0,086	0,292	0,427
r ₄₅	0,097	0,326	0,457
r ₄₆	0,09	0,365	0,493
r ₄₇	0,076	0,385	0,514
r₄₈		0,365	0,518
r ₄₉		0,316	0,510
r ₅₀		0,265	0,476
r ₅₁		0,224	0,417
...
r ₉₄		0,022	0,164
r ₉₅		0,015	0,169
r₉₆		0	0,175

According to specific of this object functioning, its consumption has similar behavioral model from week to week. Thus, in the framework of this research, the same additional autocorrelation analysis has been conducted for the identification of the seasonal component that is repeated weekly. The analysis has been done for the time-series of the load data for 3 weeks with the delay for the periods r=1..336. Time-series correspondingly had the next amount of data: 336 (1 week), 672 (2 weeks) and 1008 (3 weeks). As it is shown in the Table 2, the nearer the delay period is getting to 336th or 336-fold, the value of the autocorrelation coefficients are increasing. Therefore, it can be asserted, that time-series contains week season cycle.

Table 2. The Autocorrelation Coefficients for the Time-series with 1008 Values.

	<i>Time-series</i> =336	<i>Time-series</i> =672	<i>Time-series</i> =1008
r₁	0,935	0,936	0,935
r ₂	0,856	0,861	0,859
r ₃	0,798	0,805	0,801
r ₄	0,740	0,750	0,744
...
r ₃₃₃	0	0,322	0,448
r ₃₃₄	0,002	0,342	0,475
r ₃₃₅	0,003	0,353	0,49
r₃₃₆		0,354	0,49
r ₃₃₇		0,346	0,474

r ₃₃₈		0,328	0,451
r ₃₃₉		0,304	0,421
...	
r ₆₆₉		0,001	0,24
r ₆₇₀		0,002	0,248
r ₆₇₁		0,001	0,254
r₆₇₂			0,254
r ₆₇₃			0,235
r ₆₇₄			0,216
...			...
r ₁₀₀₆			0,0003
r ₁₀₀₇			0
r₁₀₀₈			0

Consequently, the conduction of the autocorrelation analysis allowed to emphasis in the time-series the presence of the seasonal and trend components. Thus, for the forecasting of the energy use of this object, the method of exponential smoothing with inclusion of trend and seasonal variations has been chosen - Holt-Winters method with multiplicative model.

The specific equations for the Holt-Winters method are:

- overall smoothing:

$$L_t = \alpha \frac{Y_t}{S_{t-s}} + (1 - \alpha)(L_{t-1} + T_{t-1}) \quad (2)$$

- trend estimation:

$$T_t = \beta(L_t - L_{t-1}) + (1 - \beta)T_{t-1} \quad (3)$$

- the estimation of seasonality:

$$S_t = \gamma \frac{Y_t}{L_t} + (1 - \gamma)S_{t-s} \quad (4)$$

- the forecast for the *p* future periods:

$$\hat{Y}_{t+p} = (L_t + pT_t)S_{t-s+p}, \quad (5)$$

where:

L_t - the new smoothed value or the estimation of the current level;

α - the smoothing constant for the data, $0 < \alpha < 1$;

Y_t - the actual value of series in the moment *t*;

β - the smoothing constant for the trend estimate, $0 < \beta < 1$;

T_t - the trend estimate;

γ - the smoothing constant for the seasonality estimate, $0 \leq \gamma \leq 1$;

S_t - the seasonal estimate;

p - the periods to be forecast into the future;

s - the length of seasonal period;

\hat{Y}_{t+p} - the forecast for *p* periods in the future (Hanke et al, 2001).

Within the investigation, the forecast model was developed on the base of the actual data for the period from the 1st until 21st day (3 weeks). This model was used for the forecasting for the next period, from 22nd until 28th day (the 4th week).

When using the Equation 1, the first actual value was accepted as initial smoothed value. Therefore, the trend estimation T_t is equal 0 (Hanke *et al*, 2001). As far as the load curve contains corresponding weekly changes, the duration of the seasonal period is equal to the amount of the obtained measurements during one week – 336. According to (Hanke *et al*, 2001), the seasonal estimate S_t for the first seasonal period is taken equal to 1. The optimal values of the model parameters α , β , γ have been chosen by the minimization of the accuracy indices, particularly forecast errors. They are equal to 0,05; 0,029; 0,71 correspondingly. The selection of parameters is observed in details in (Hanke *et al*, 2001).

For the estimation of the adequacy of the model and accuracy of the forecasted results the following indices were used:

Mean Absolute Percentage Error:

$$MAPE = \frac{1}{n} \sum_{t=1}^n \frac{|e_t|}{Y_t} \cdot 100 \quad (5)$$

Mean Absolute Derivation:

$$MAD = \frac{1}{n} \sum_{t=1}^n |e_t| \quad (6)$$

Mean Squared Error:

$$MSE = \frac{1}{n} \sum_{t=1}^n e_t^2 \quad (7)$$

Sum Squared Error:

$$SSE = \sum_{t=1}^n e_t^2 \quad (8)$$

Coefficient of Determination:

$$R^2 = 1 - \frac{SSE}{\sum_{t=1}^n (Y_t - \bar{Y})^2} \quad (9)$$

where:

n - the amount of the forecasted values;

Y_t - the actual value of series in the moment t ;

\bar{Y} - the average value of Y ;

\hat{Y}_t - the forecast value for the moment t ;

$|e_t|$ - forecast error, $|e_t| = Y_t - \hat{Y}_t$ (Hanke *et al*, 2001).

For determination of the forecast accuracy the obtained results were compared with the data of actual energy use for the period from the 22nd until 28th day. The Figure 3 presents the object's actual and forecasted load curves. Although the forecast model was developed on the base of the actual data for the period from the 1st until the 21st day, this figure presents the actual load curve for the period from the 15th day for clarity.

For the estimation of the possibility of the option B usage in the adapted form, the results of the expected baseline energy use, obtained through forecast, can be compared with the results, which could be obtained in the case of the option B usage in the existed pure form. As it was mentioned above, the simplified form of the option B foresees the equating of the expected baseline energy use to the actual baseline energy use without adjusting. In this research two cases of the option B usage in a simplified form were envisaged: when the values of the expected baseline energy use for the period from the 22nd until 28th day were taken equal to the actual data of the previous periods: from the 8th until 14th and from the 15th until 22nd day. The obtained results are presented in the Table 3.

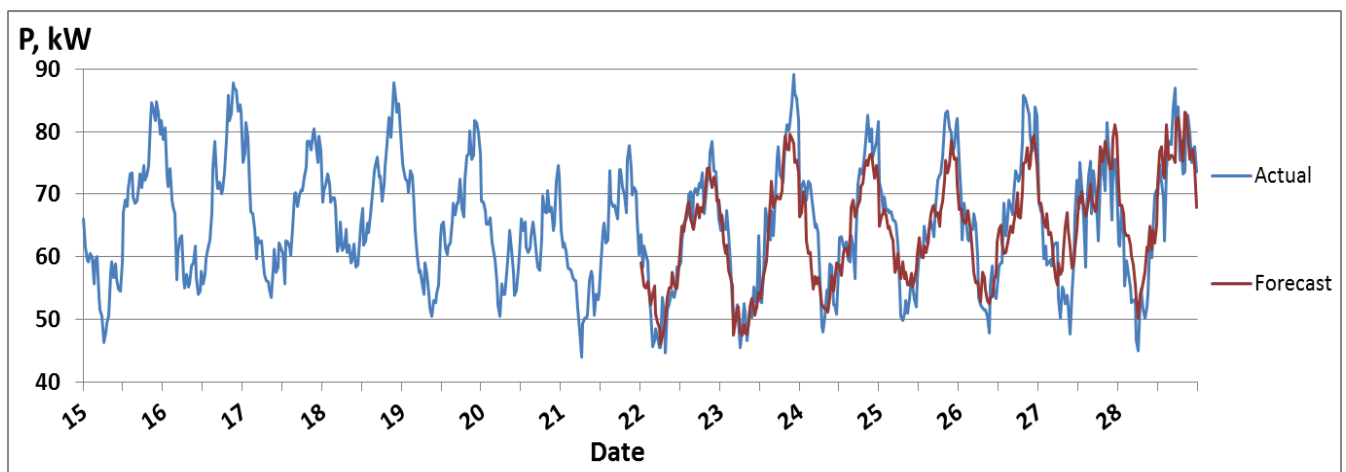


Figure 3. Actual and Forecasted Load Curves.

Table 3. Energy Demand, kW.

<i>Data</i>	<i>Period</i>	<i>Actual data</i>	<i>Values obtained through forecasting</i>	<i>Values were taken equal to the actual data from the 8th until 14th</i>	<i>Values were taken equal to the actual data from the 15th until 22nd</i>
22	1	63,6	59,14	73,68	66
22	2	58,32	56,71	74,88	61,56
22	3	61,68	55,41	73,44	59,64
22	4	60,48	55,10	72,48	59,16
22	5	59,28	56,05	72	60,6
....
25	145	71,94	64,92	68,94	68,76
25	146	70,44	66,37	70,86	70,56
25	147	67,38	67,12	71,82	71,64
25	148	69,66	67,60	70,08	73,2
25	149	67,44	66,53	70,86	71,64
.....
28	332	79,8	75,60	73,32	69,84
28	333	75,12	76,69	75,24	71,16
28	334	77,16	77,02	80,76	70,44
28	335	77,52	74,25	84,48	66
28	336	73,56	67,97	74,88	60,36

Table 4. The Indices of the Forecast Model Accuracy.

<i>Indices</i>	<i>The values obtained through forecasting (based on the actual data for the 3 previous weeks)</i>	<i>The values were taken equal to the actual data from the 8th until 14th day</i>	<i>The values were taken equal to the actual data from the 15th until 22nd day</i>
MAPE	6,53	8,86	8,24
MAD	4,20	5,64	5,22
MSE	26,7	54,25	42,34
R ²	0,76	0,50	0,61
Range of the errors values	-13,78...12,50	-20,16...20,88	-15,84...20,7

For the comparison of the results, that obtained through usage of the option B in the existing and adapted forms, the accuracy indices were analyzed. As it is presented in the Table 4, all three accuracy indices MAPE, MAD, MSE for the results obtained through forecast with Holt-Winters method are lower than the relevant indices for the energy use that was taken equal to actual baseline energy use. The smaller values indices MAPE, MAD, MSE have the more accurate results are provided by this model usage. The value of the determination coefficient R² indicates the adequacy of the forecasting results and can have the value between 0 and 1. The model is considered to be adequate if R² is close to 1. As we can see from the Table 4, the range of the errors values is the most narrow for the results obtained through forecasting. As we can see from the Table 4, for this object the results, obtained through forecasting, are more accurate than the results, obtained through the usage of the option B in the existing form, particularly by equating the

expected energy use to the actual energy use without adjustments. In the cases when the other sets of actual data are available for model development (for example, the data of a shorter/longer period) it is possible to use the same forecasting method for the model development but with finding the new optimal values of model parameters α , β , γ .

5 Conclusions

The analysis of the electricity market activity in the field of energy saving and increasing of energy efficiency allows to define the main mechanisms and results of the attraction of energy efficiency for participation in the markets. It is expected, that implementation of the mechanisms for trading of the EE resources, saved due to EE projects, into the BCM&BM will stimulate market participants for energy saving activity and energy efficiency improvement.

In such a manner, the usage of the consumers' technical abilities to reduce demand and to increase the level of energy efficiency will result in decreasing fossil fuel usage, harmful emission reduction, delaying of the growth rate of the electricity demand and reduction of the expenses on building new generation.

The investigation of the existing approaches for the determination of the EE resources value has allowed to specify the set of conditions and tasks, that can occur during their usage at the Ukrainian energy consumption objects. Particularly, the difference between the organization of the energy use measurements and the distinction of the available data sets restrict the usage of the existing approaches and M&V options in the pure form.

Taking into consideration the above mentioned restrictions, the usage of the existing options in the adapted form was offered. Particularly, the usage of forecasting methods during the determination of the expected baseline energy use model. In the case of the certain type of object this allowed to obtain the results which satisfy the adequacy requirements. The accuracy of these results exceeds the accuracy of the results, obtained through the usage of the existing options. For the other types of objects it is advisable to choose the most appropriate forecasting methods according to particular features of the objects.

Consequently, the usage of the forecasting can allow final consumers, that implement EE projects, to estimate in advance the expected EE resource value and to plan the activity for the trading of such resource in the energy market.

Besides that, under conditions of the BCM&BM, the existence of the premature precise data of the expected demand reduction can provide a possibility to estimate more accurately trends of the increasing of the load and correct the plans of the exploitation and building of new generation capacities.

References

- American Society of Heating, Refrigerating and Air-Conditioning Engineers (ASHRAE). *ASHRAE Guideline 14-2002. Measurement of Energy and Demand Savings*, June 2002. Available at the official website of ASHRAE: <https://www.ashrae.org>
- Jeff Bastian. *PJM Manual 18B: Energy Efficiency Measurement & Verification. Revision: 01*, 2010.
- Paolo Bertoldi and Silvia Rezessy. *Energy Saving Obligations and Tradable White Certificates*, 2009, Joint Research Centre of the European Commission. p. 62.
- S. Denysiuk. *Policy Formation Increase Energy Efficiency – Current Challenges Guidelines and European. Power Engineering: Economics, Technique, Ecology*, vol. 2, No. 33, pp. 7-22, 2013.
- Efficiency Valuation Organization (EVO). *International Performance Measurement and Verification Protocol, EVO 10000 – 1:2014*, June 2014. Available at the official website of EVO: <http://www.evo-world.org>
- John E. Hanke, A.G.R., Dean W. Wichern, *Business Forecasting. 7th ed.* 2001, New Jersey: Prentice Hall.
- Prajakta S. Kalekar, *Time series forecasting using holt-winters exponential smoothing*. Kanwal Rekhi School of Information Technology, 2004. 4329008: p. 1-13.
- South-central Partnership for Energy Efficiency as a Resource (SPEER), *Toward a More Efficient Electric Market: New Frameworks for Advancing Energy Efficiency in Texas*, June 2013. Available at: <http://eepartnership.files.wordpress.com/2013/06/toward-a-more-efficient-electric-market-june-2013.pdf>

Modeling for control of run-of-river power plant Grønvollfoss

Liubomyr Vytvytskyi¹ Roshan Sharma¹ Ingunn Granstrøm² Bernt Lie¹

¹Faculty of Technology, Telemark University College, Norway, {124022, roshan.sharma, Bernt.Lie}@hit.no

²Skagerak Kraft AS, Norway, Ingunn.Granstrom@skagerakenergi.no

Abstract

Design of optimal operation and control of a run-of-river hydro power plant depends on good models for the elements of the plant. River reaches are often considered to be shallow channels with free surface flow. A typical model for such reaches thus use the Saint Venant model, which is a 1D model based on the mass and momentum balances. This combination of free surface and momentum balance makes the problem numerically challenging to solve.

Here, the finite volume method with staggered grid is used to illustrate the dynamics of the river upstream from the Grønvollfoss run-of-river power plant in Telemark, Norway, operated by Skagerak Energi. A model of the same river in the Grønvollfoss power plant has been studied previously, but here the geometry of the river is changed due to new information from Skagerak Energi. The numerical scheme for solving the model has been further developed.

In addition, the behavior of the dynamic model is compared to data from experiments, carried out on the Grønvollfoss run-of-river power plant. The essence of the experiments is to consider the time taken from an increase in the input volumetric flow, to a measured change in level in front of the dam at Grønvollfoss.

The model is manually tuned by changing the Strickler friction factor, the river length and the type of river slope/width (constant/varying) in order to fit the water level ahead of the Grønvollfoss dam from experimental data. Least squares model fitting is also used for the model with the constant slope and width of the river and this model shows good fitting after the manual tuning.

The results of the improved model (numerically, tuned to experiments), is a model that can be further used for control synthesis and analysis.

Keywords: Run-of-river hydropower, Saint Venant Equations, Modeling, Simulation.

1 Introduction

1.1 Background

There are in total operating over 1500 hydro power plants in Norway today, with a total capacity of more than 28GW. Water power plants have an annual production of 129TWh in 2013, which constitutes some 96% of the production of electricity¹. Most hydropower production comes from large hydropower plants with water reservoirs. Small hydropower plants is a generic term for plants that have small production capacity. There are in total operating over 1100 such smaller hydropower plants in Norway today and production from these accounts for about 7% of the total hydropower production².

Skagerak Energi is operating two run-of-river hydro power plants in river Tinnelva flowing out of lake Tinnsjøen in Eastern Telemark. The uppermost, Årlifoss, has a 16.2 m water fall, and provides inlet flow to the pondage of Grønvollfoss; the Grønvollfoss power plant is in question here. Grønvollfoss is situated 5 km downstream from Årlifoss, and has a water fall of 22.6 m. The installed power in Grønvollfoss is 2x16MW (i.e. two turbines), and the average annual production is 172GWh.

It is of interest to keep the level in front of the dam in Grønvollfoss as high as possible to give as high a turbine pressure as possible to maximize power production. In addition, the dam level should be as constant as possible to avoid variation in production, and loss of water flowing over the dam. It is important to control the level/production because both the production and the inflow of water from upstream disturbs/upsets the level.

1.2 Previous work

The dynamic model for such run-of-river system has an important role in control and optimization. In a previous paper (Lie et al., 2013), a model for the Grønvollfoss power plant has been developed using the Saint-Venant equations and the staggered grid scheme. Discretization

¹ <https://www.regjeringen.no/nb/tema/energi/fornybar-energi/fornybar-energiproduksjon-i-norge/id2343462/>

² https://www.regjeringen.no/nb/tema/klimatekologi/miljo/naturmangfold/innsiktsartikler-naturmangfold/fornybar-energiproduksjon-i-norge/id2076808/?regj_oss=20

of the Saint-Venant equations using the staggered grid scheme has been studied in Farina et al. (2011). The Quick and Superbee algorithms are more complex, but better algorithms for solving the Saint-Venant equations (Johansen et al., 2012a). Even better are adaptive WENO schemes (Johansen et al., 2015). In Xu et al. (2012), the problem of estimating the levels of three cascaded river reaches by using the Saint-Venant model has been described. Large rivers with several run-of-river plants constitute large scale control and optimization problems; the application of e.g. Model Predictive Control has recently been studied for such systems (De Schutter et al., 2011).

1.3 Overview of paper

In this work, the geometry of the system has been substantially updated from that of Lie et al. (2013), and the resulting model has been compared to experiments on the system. The paper is structured as follows: Section 2 consists of a system description of the run-of-river power plant. Section 3 describes formulation of the model with basic simulations for verification. The experiments from the power plant and their application for validation of the model are provided in Section 4. Conclusions are drawn in Section 5.

2 System description

A typical view of run-of-river power plant is presented in Figure 1. This type of hydro power plant has high flow rate, which passes through the turbine and spins the rotor. The turbine transfers the kinetic energy from water to rotational mechanical power, which then will be transferred to electric power in the generator.

After this the water returns to the river via a short tailrace

The Grønvollfoss power plant is situated in the river Tinnelva and is the second power plant in this river. That is why this power plant does not have a dedicated reservoir, but instead uses the outlet flow from the Årlifoss power plant as input; Årlifoss is situated upstream the river.

2.1 Functional description

For this run-of-river system, there are some *inputs* (control inputs, disturbances) and *outputs* (measured and performance (quality) outputs), which can affect and describe the functionality, as shown in Figure 2. The control inputs could be the outlet flow rate through the turbine \dot{V}_{out} and possibly the flood gate opening at Grønvollfoss power plant. Also flow from the Årlifoss power plant, which is inlet flow rate \dot{V}_{in} , can be assumed as control input if both plants are considered as one unit. However, this flow can also be a disturbance if the Grønvollfoss power plant is considered independently. Measured outputs can e.g. be the power production in the Grønvollfoss power plant, the level ahead of the Grønvollfoss dam, and also any other level measured in the river/dam between Årlifoss and Grønvollfoss, e.g. the level exactly after Årlifoss power plant. The power production can also be considered a performance output, which will show the result of one of the main goals: production maximization. The variation of the level ahead of the Grønvollfoss dam can be a performance output, because this level should be as constant as possible to avoid variation in production, which is also the main goal of the control challenge.

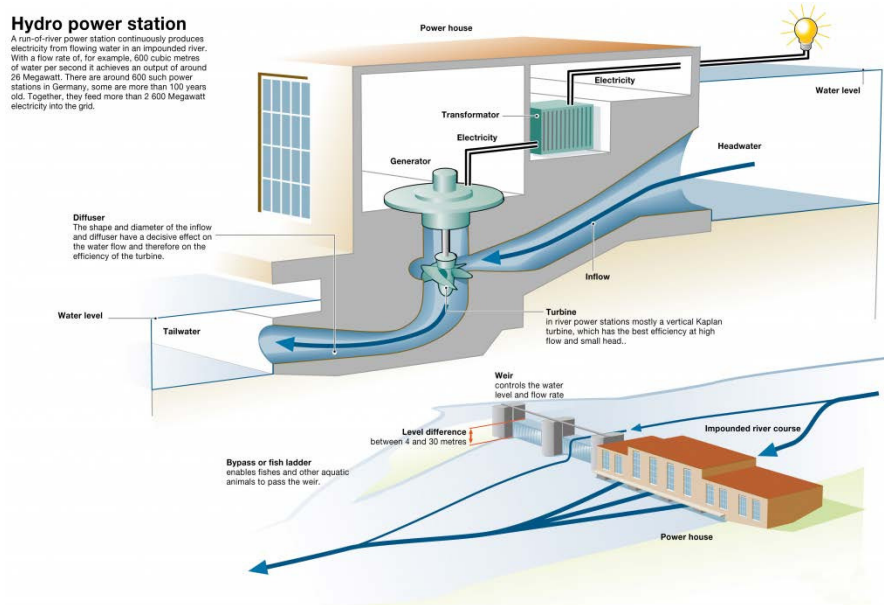


Figure 1. Run-of-river power plant³.

³ <http://www.commercialrenewableenergy.co.uk/hydro-power/>

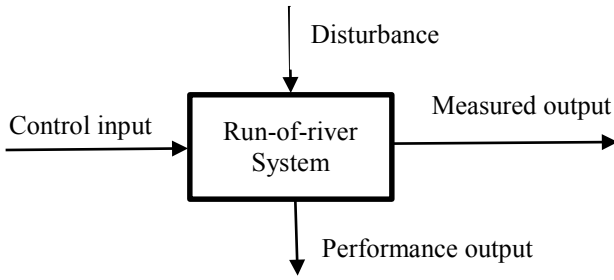


Figure 2. Functional description of run-of-river system.

Here, the Grønvollfoss power plant is chosen to be considered as an independent unit. The control inputs are therefore the outlet flow rate through the turbine \dot{V}_{out} and the flood gate opening at Grønvollfoss power plant; the disturbance consists of inlet flow rate \dot{V}_{in} . The power production in the Grønvollfoss power plant, and the level ahead of the Grønvollfoss dam is measured.

2.2 System description

The following information about the system is provided by Skagerak Energi and maps on the Internet. All of the provided parameters are approximations. The water level before the Grønvollfoss dam is around 19 meters above the river bed (level of riverbed in this place is 125.5 m.a.s.l.^{4,5} and level of water is thus 144.5 m.a.s.l.⁶). There is also information about the level of the river surface (145.7 m.a.s.l.) and riverbed (143 m.a.s.l.) exactly after the Årlifoss power plant. In this case, the height difference between the two power plants (Årlifoss and Grønvollfoss) is around 17.5 meters. There is also information about the length of the river between the two power plants, $L=5$ kilometers, and the width of the river is on average $w=166$ m, which is found from the known length and surface area of the river, which is equal 0.83 km² (this area is provided by Skagerak Energi). We will consider two cases: one with constant width and slope of the river, and another case where both the river width and the river slope may vary. In the first case of constant width and slope, the slope is given by Figure 3, and the width is given to be $w = 166$ m.

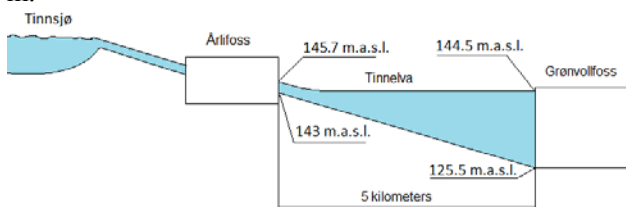


Figure 3. The schematic view of river geometric.

⁴ Meters above sea level

⁵ <http://gis3.nve.no/nivellement/220.pdf> The map of river from 1924, when the power plants have not been built and which shows the water level at that time.

In the second case, we allow both the river width and the river slope to vary. Because on maps of the river, the width is simplified as is shown in Figure 4.

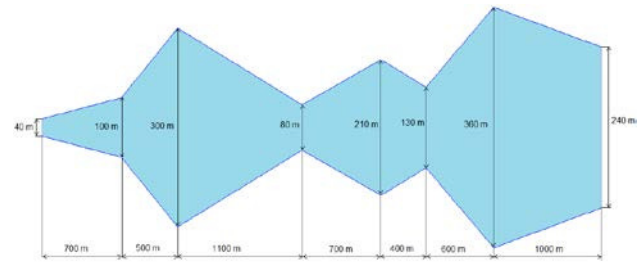


Figure 4. The schematic view of the width variation.

In reality, the slope of the river also varies along the river. For this work, the river map from year 1924 has been studied and then the slope is approximated as shown in Figure 5. For the first part of the river reach with length $L_1=2500$ m, the height drop is $H_1=7$ m, with slope angle $\theta_1 = \sin^{-1}(H_1/L_1)$. Then, for the next part, the slope changes the angle with the length $L_2=500$ m and the height drop $H_2=6.5$ m, to $\theta_2 = \sin^{-1}(H_2/L_2)$. Finally, for the last part with length $L_3=2000$ m, the height drop $H_3=4$ m, and the slope angle of slope $\theta_3 = \sin^{-1}(H_3/L_3)$.

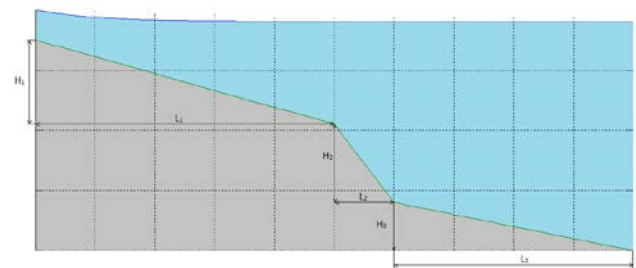


Figure 5. The schematic view of river slope.

2.3 Experiment description

To check and improve accuracy of the run-of-river model, the model will be validated and tuned against experiments on the Grønvollfoss power plant. Only one experiment was permitted.

This experiment consists in changing the inlet flow rate to the system \dot{V}_{in} for some time, and measuring the change of the level in front of the Grønvollfoss dam and also the time for which changes in inlet flow rate will start to influence the level in front of the dam.

The experiment table with all values for experiment is in Table 1.

It should be noted that the water level ahead of the Grønvollfoss dam was decreased by 15 cm before the experiment (to 144.35 m.a.s.l.) to avoid overflow the

6

<http://atlas.nve.no/SilverlightViewer/?Viewer=NVEAtlas>

dam after increasing the inlet flow rate. In addition, the inlet volumetric flow rate is controlled by increasing or decreasing power production, thus the values of the flow rates are approximations. There is also information that the water level ahead of the Grønvollfoss power plant is measured by a sensor and logged every 5 s. These results are filtered and are defined as a moving average of 300 values every 100 ms (the average of levels during last 30 s).

Table 1. Experiment table.

Inlet volumetric flow rate, m^3/s	Outlet volumetric flow rate, m^3/s	Time interval for changing, min	Initial level ahead of the dam, m.a.s.l
120-160-120	120	15	144.35

3 Modeling

3.1 Control volumes

To create a model of the shallow river system, the Saint-Venant equations will be used. These equations describe the behavior of the river and consists of both mass and momentum balances, and are tricky to solve numerically. The Finite Volume method with staggered grid is common for solving such kinds of problems. The staggered grid is the scheme where the grid for mass balance is shifted with regard to momentum balance's grid as it is shown in Figure 6, where the blue segments (control volumes) on top of the figure is the grid for the mass balance and the skewed red segments below is the grid for the momentum balance.

The level h , volumetric flow rate \dot{V} and their variation along the x -axis are shown in Figure 6. Here x is in the interval from zero to L and also is presented as grid i in interval $i=1, 2, \dots, 11$. In addition, the figure shows the variation of pressure p along x or i .

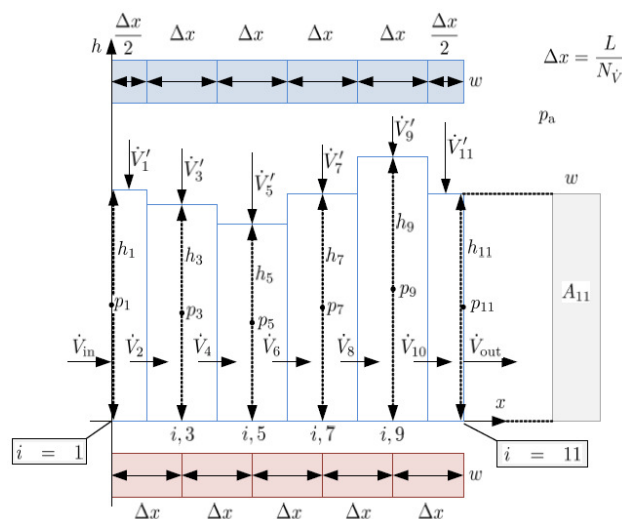


Figure 6. The scheme of Staggered grid (Lie et al., 2013).

As is seen from Figure 6, the number of control volumes for the mass balance/levels (N_h) is one larger than for the momentum balance/volumetric flows ($N_{\dot{V}}$). In the figure $N_{\dot{V}} = 5$ and each of these segments has length Δx . For levels, $N_h = N_{\dot{V}} + 1 = 6$ and here for the first and last segments, the length is $\frac{\Delta x}{2}$ and all other segments have length Δx .

In addition, in Figure 7 is shown the slope of river bed θ and the gravity vector g .

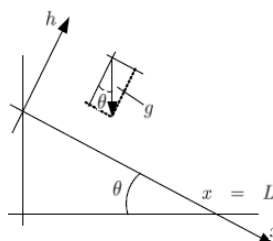


Figure 7. The slope geometry (Lie et al., 2013).

3.2 Model formulation

Some simplifying assumptions are introduced for developing the Saint-Venant equations (Lie et al., 2013):

- The run-of-river system is considered as a shallow river, which means that the water level and width of the river is much smaller than the length of the river, and the slope of the river is not too steep. This also means that the depth of the river has little variation. In this case, the hydrostatic pressure approximation can replace the vertical variation of the water motion, and the flow velocity is approximated by the depth-averaged flow velocity (Stelling et al., 2003).
- The fluid is incompressible and the streamline curvature is small. In addition, formulas related to steady flow (e.g. the Manning Formula and the Chézy Formula) can be used to estimate the effect of friction.
- Coriolis force is neglected. Only gravity force is taken into consideration.

Stelling and Duinmeijer studied the staggered conservation scheme for the discretization of the Saint-Venant equations in van't Hof et al. (2012). The discretization of the Saint-Venant equations for the mass balance with Finite Volume method results in:

$$\frac{dh_i}{dt} = \frac{\dot{V}_{i-1} - \dot{V}_{i+1} + \dot{V}_i}{w \cdot \Delta x} \quad (1)$$

for $i = 3, 5, \dots, 2N_{\dot{V}} - 1$. For the first and last level, equation (1) will be as follows:

$$\frac{dh_1}{dt} = \frac{\dot{V}_{in} - \dot{V}_2}{w \cdot \frac{\Delta x}{2}} + \frac{\dot{V}'_1}{w}$$

$$\frac{dh_{2N_V+1}}{dt} = \frac{\dot{V}_{2N_V} - \dot{V}_{out}}{w \cdot \frac{\Delta x}{2}} + \frac{\dot{V}'_{2N_V+1}}{w}$$

The discretization of the Saint-Venant equations for the momentum balance with the Finite Volume method result is in:

$$\frac{d\dot{V}_i}{dt} = \frac{\dot{M}_{i,i} - \dot{M}_{o,i}}{\Delta x} + g \cdot \cos \theta \cdot w \cdot \frac{h_{i-1}^2 - h_{i+1}^2}{2 \cdot \Delta x} + \bar{A}_i \cdot g \cdot \sin \theta - \frac{g}{C_i^2} \frac{\bar{\varphi}_i}{\bar{A}_i^2} |\dot{V}_i| \dot{V}_i \quad (2)$$

which is valid for $i = 2, 4, \dots, 2N_V$. In this equation, the momentum input and output flow per density are defined as follows:

$$\frac{\dot{M}_{i,i}}{\rho} = \begin{cases} \frac{\dot{V}_{in}}{A_1}, & i = 2 \\ \frac{|\dot{V}_{i-2}|}{A_{i-2}} \cdot \max(\dot{V}_{i-2}, 0) \\ + \frac{|\dot{V}_{i+2}|}{A_{i+2}} \cdot \max(-\dot{V}_{i+2}, 0), & i = 4, 6, \dots, 2N_V - 2 \\ \frac{|\dot{V}_{2N_V-2}|}{A_{i-2}} \cdot \max(\dot{V}_{2N_V-2}, 0), & i = 2N_V \end{cases} \quad (3)$$

$$\frac{\dot{M}_{o,i}}{\rho} = \begin{cases} \frac{\dot{V}_i^2}{A_i}, & i = 2, 4, \dots, 2N_V - 2 \\ \frac{\dot{V}_{out}}{A_{2N_V+1}}, & i = 2N_V \end{cases} \quad (4)$$

Also here, cross sectional area A , wetted perimeter φ and their averages between neighboring segments ($\bar{A}, \bar{\varphi}$) are defined as:

$$A_i = w \cdot h_i \quad (5)$$

$$\varphi_i = w + 2h_i \quad (6)$$

$$\bar{h}_i = \frac{h_{i-1} + h_{i+1}}{2} \quad (7)$$

$$\bar{A}_i = \bar{h}_i \cdot w \quad (8)$$

$$\bar{\varphi}_i = \frac{\varphi_{i-1} + \varphi_{i+1}}{2} \quad (9)$$

The Chézy friction coefficient C , which is defined in relation to Strickler's friction factor k_S is shown below:

$$C_i = k_S R_i^{\frac{1}{6}} \quad (10)$$

where $R_i = \frac{A_i}{\varphi_i}$ and it is the hydraulic radius.

If it is assumed that N_V goes to infinity, the model will become as follows:

$$\frac{\partial h}{\partial t} = -\frac{1}{w} \frac{\partial \dot{V}}{\partial x} + \frac{\dot{V}'}{w} \quad (11)$$

$$\frac{\partial \dot{V}}{\partial t} = -\frac{\partial}{\partial x} \left(\frac{\dot{V}^2}{A} \right) - g \cdot A \cdot \cos \theta \cdot \frac{\partial h}{\partial x} + A \cdot g \cdot \sin \theta - \frac{g}{C^2} \frac{\varphi}{A^2} |\dot{V}| \dot{V}$$

with boundary conditions:

$$\begin{aligned} \dot{V}_{x=0} &= \dot{V}_{in} \\ \dot{V}_{x=L} &= \dot{V}_{out} \end{aligned} \quad (13)$$

3.3 Operational data and parameters

After the run-of-river model is given by the Finite Volume discretization, it is possible to describe it by different elements such as states, inputs, and parameters.

The states of the model are as follows:

- h_i – the water level along the river, where $i = 1, 3, \dots, 2N_V + 1$.
- \dot{V}_i – the volumetric flow rate along the river, where $i = 2, 4, \dots, 2N_V$.

The inputs for the model are:

- \dot{V}_{in} – inlet volumetric flow rate.
- \dot{V}_{out} – outlet volumetric flow rate.
- \dot{V}'_i – lateral inflow per length unit, where $i = 1, 3, \dots, 2N_V + 1$.

The model parameters are:

- w – width of the river.
- θ – angle of river slope.
- ρ – density of water.
- g – the gravitational acceleration.
- k_S – Strickler friction factor.

The values for each model parameters will be specified in Table 2. Also the nominal operating parameters are presented in Table 3.

3.4 Model simulation and verification

Some basic simulation is done to verify the model. All parameters are as in Table 2 and Table 3, the simulation is started from steady state, and after 10 min the inlet volumetric flow rate \dot{V}_{in} is suddenly changed from the normal value, which is equal 120 m³/s (in steady state, all the volumetric flow rates are equal to this value), to 160 m³/s. This new flow rate lasts for 15 minutes, then the inlet flow rate is reduced back to 120 m³/s (as designed in the experiment). There is also some time for

increase and decrease in the inlet flow rate; this takes 10 seconds. It should be noted that all simulations are done in MATLAB using the “ode23” solver. Here and in the subsequent simulations, the whole river length is divided into 100 nodes, which means that $N_V = 100$ and $\Delta x = 50$ m. The result of the simulation of the model with constant width and slope is shown in Figure 8 where the top plot shows the water level ahead of the Grnvollfoss dam as a function of time. The bottom plot shows how different volumetric flow rates (for inlet, for 1st, 2nd, 50th, 99th and last 100th segments) change with time.

Table 2. Parameters for run-of-river model.

Variable	Value	Unit	Comments
g	9.81	m/s^2	the gravitational acceleration
ρ	1000	k/m^3	density of water
w	166	m	width of the river
H	17.5	m	height of the river
L	5000	m	length of the river
θ	$\sin^{-1} \frac{H}{L}$	–	angle of river slope
k_S	20	$m^{1/3}/s$	Strickler friction factor

Table 3. Nominal operating parameters for run-of-river model.

Variable	Value	Unit	Comments
\dot{V}_{in}	120	m^3/s	inlet volumetric flow rate
\dot{V}_{out}	120	m^3/s	outlet volumetric flow rate
\dot{V}'_i	0	$m^3/(s \cdot m)$	lateral inflow per length unit
$h(x = L)$	19	m	steady state level ahead of the dam
\dot{V}	120	m^3/s	steady volumetric flow rate

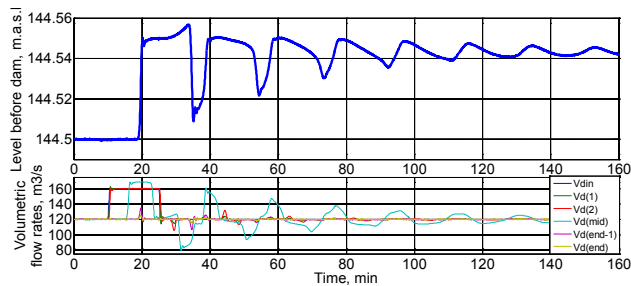


Figure 8. The simulation the model with constant width and slope, $k_S=20 m^{1/3}/s$.

From Figure 8, the simulation results show that around 10 min is needed from the change in the inlet flow rate to the water level ahead of the dam starts to increase. Steady state is reached after more than two hours, when the oscillations have decayed. These oscillations describe a wave, which is initiated by the inlet flow jump, and reflections from the Grnvollfoss dam back and forth to Årlifoss. The jump of the inlet flow rate leads to an increase in the water level ahead of the dam of around 4 cm. This increase is also seen from results of the water level along the whole river, as is shown in Figure 9.

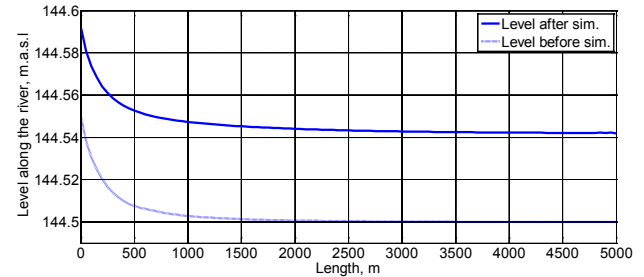


Figure 9. The water level along the river before and after jump of the inlet flow rate.

4 Model fitting

4.1 Experimental data

The experimental results of power production in the Årlifoss power plant are shown in Figure 10. Here, it is seen that before the experiment was started, the power production was around 18 MW and at the time 10:04:45 AM the production was increased to 22.5 MW within a time lapse of 30 seconds. The new value of power production was kept stable for around 15 minutes and then at 10:19:55 AM it was decreased to the initial value, around 18 MW. This decrease took around 20 seconds. These values of power production 18 MW and 22.5 MW correspond to approximately 120 and 160 m^3/s of volumetric flow rate respectively.

The water level just after the Årlifoss power plant is also measured, but unfortunately, the water level can not be logged and can only be observed from the screen of the monitoring panel in the Årlifoss power plant, where the results from the level sensor is presented without any filtering. Nevertheless, the observation of this level shows that it increases during the jump of inlet flow rate with around 15 cm. After decreasing the flow in the Årlifoss power plant back to 120 m^3/s , this water level also decreases to the previous level (around 145.7 m.a.s.l.).



Figure 10. Measured power production in the Årlifoss power plant during experiment.

The results of the experiment for the water level ahead of the Grønvollfoss dam are presented in Figure 11. Here the time 0 min means the actual time 9:54:45 AM of the experiment day. The increase from 120 to 160 m³/s of inlet flow rate starts at 10:04:45 AM, which is after 10 min in the figure. Then after around 15 minutes, at 10:19:55, the inlet flow decreases to the original 120 m³/s, which is after 25 min in the figure. As it is shown in the figure, the water level ahead of the Grønvollfoss dam starts increasing at a time around 20 min, which is 10 minutes after the inlet flow rate was increased. Then oscillations are seen in the water level ahead of the dam. These oscillations describe a wave, which is initiated by the inlet flow jump, and reflections from the Grønvollfoss dam back and forth to Årlifoss. This process continues with damping until a new steady state is reached. The period time of each oscillation is around 21 minutes and the steady state is reached after more than 80 minutes. The jump of the inlet flow rate leads to an increase in the water level ahead of the dam of around 3 cm.

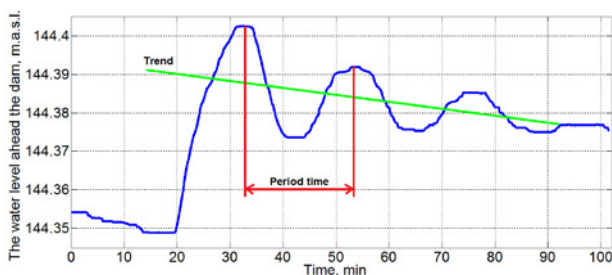


Figure 11. The plot of experimental result of the water level ahead of the Grønvollfoss dam.

Here, from Figure 11, it should be also noted that the trend of oscillations goes a little bit down (the average of maximum and minimum values of one oscillation becomes lower for every next oscillation). This trend can be caused by an outlet flow rate which is a little bit bigger than the inlet flow rate to the system, e.g. $\dot{V}_{in} = 120$ m³/s but $\dot{V}_{out} = 121$ m³/s.

4.2 Manual tuning of the model

Now the model should be tuned to fit the experimental data. We start with changing the Strickler friction factor, continue with type of slope or width behavior (constant or non-constant width and slope) and also include the river length. It should be mentioned that decreasing or increasing the Strickler friction factor or the river length could compensate the approximations with the width and slope, which effectively introduce reflection of waves, which can be interpreted as increased friction. That is why the observed Strickler factor (from the literature: in range 20-80 m^{1/3}/s) can be less than 20 m^{1/3}/s and the river length can be more than 5 km.

First of all, the model with constant width and slope is tuned by changing the Strickler factor, due to this model being the simplest, which is beneficial for use in model based control. All the other parameters are used as during previous simulations, but the steady state water level ahead of the dam is reduced to 144.35 m.a.s.l. as it was in experiment. The time of increasing and decreasing the inlet volumetric flow rate should be also changed to 30 seconds for increasing and 20 seconds for decreasing as it is seen from experimental data (see Figure 10). Also as in previous simulations, the number of nodes is the same and equal to 100. Simulations are done in MATLAB using the “ode23” solver. The result of comparing the water level ahead of the Grønvollfoss dam from the constant model with chosen Strickler factor equal to 16 m^{1/3}/s and the experimental results is shown in Figure 12.

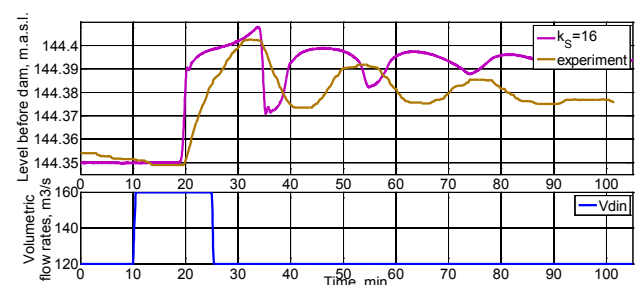


Figure 12. Comparison of the tuned model with constant width and slope against experimental result.

Figure 12 shows that the real data from experiment is not really the same as the model result, especially the period time of the oscillations, which is longer for the experiment, and the level increasing, which is around 4 cm in the simulation result as opposed to around 3 cm in the experimental data. The benefits are that the amplitude of oscillations and the time of reaching the wave dam is approximately the same. One more disadvantage is that the model result of water level after the Årlifoss power plant does not match the experimental data (the difference is more than 1 m), where this level should be higher (around 145.7 m.a.s.l.) and should not increase a lot after the inlet flow rate jump was finished. The steady state level along the river is in Figure 13.

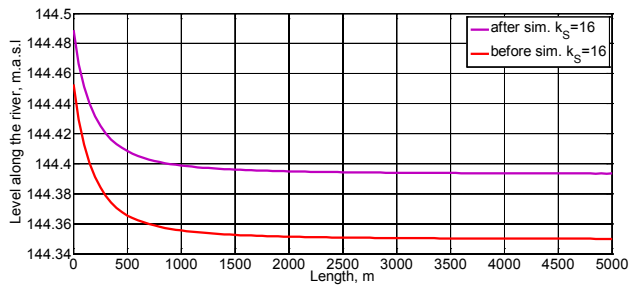


Figure 13. The steady water level along the river before and after jump of the inlet flow rate.

Next, the model with non-constant slope and width is tuned with experimental data. This model was tuned using the Strickler factor, and the best fit was achieved with Strickler factor equal to $14 \text{ m}^{1/3}/\text{s}$. The comparison between varying width/slope model after tuning of the Strickler constant, with experiment results is shown in Figure 14. The steady river level computed from this tuned model are shown in Figure 15.

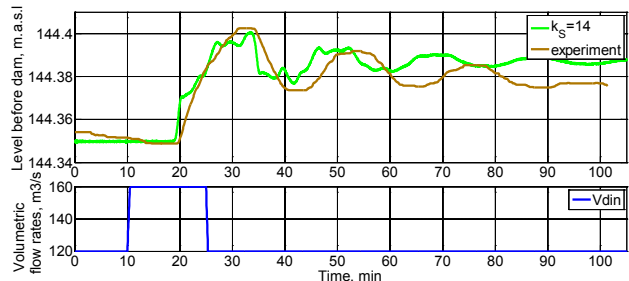


Figure 14. Comparison of the tuned model with varying width and slope against experimental result.

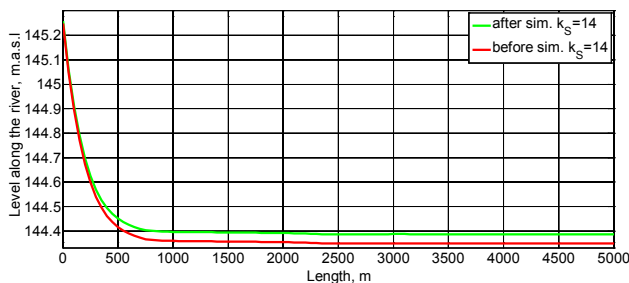


Figure 15. The steady water level along the river before and after jump of the inlet flow rate.

Figure 14 and Figure 15 show that in comparison to experimental data, the model results are quite good and match the real points better than the model with constant slope/width. There are still the same deficiencies as in the model with constant slope and width:

- The oscillation period is still shorter than in the real results, but longer than in the constant model;
- The level increase is still higher from the model results than in experiment, but here this difference is around 0.5 cm, which is better than in the constant model;
- The water level after the Årlifoss power plant is still lower than expected from the real data, but here it is around 0.5 m difference ($145.7 - 145.2 \text{ m.a.s.l.}$), which is better than in the model with constant slope/width.

And also one positive thing is that this water level after the Årlifoss plant comes back to the initial value after the inlet flow rate jump was finished.

Also after analysis the experimental results, it was seen that the trend of oscillations goes a little bit down (see Figure 11), so it is in interest to try also to make small difference between inlet and outlet volumetric flow rates. That is why the outlet flow rate is increased on $1 \text{ m}^3/\text{s}$ to $121 \text{ m}^3/\text{s}$. The results of the water level ahead of the dam in this case are shown in Figure 16 for the model with constant slope and width, and in Figure 17 for the model with non-constant slope and width.

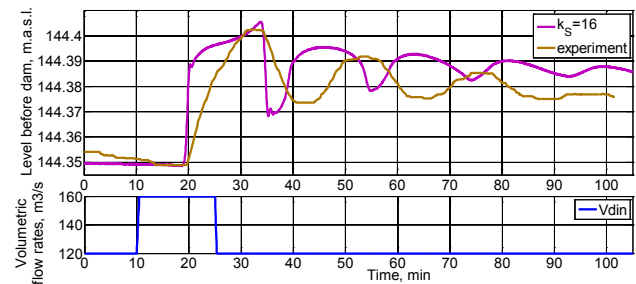


Figure 16. Validation of the model with constant width and slope with the experimental results, when $\dot{V}_{out} = 121 \text{ m}^3/\text{s}$.

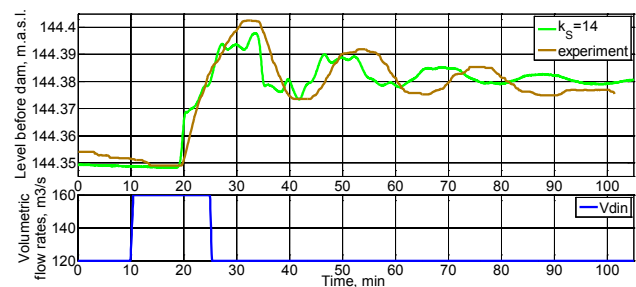


Figure 17. Validation of the model with varying width and slope with the experimental results, when $\dot{V}_{out} = 121 \text{ m}^3/\text{s}$.

As it is seen from Figure 16, the increase of the outlet volumetric flow rate does not show much better results for the constant width/slope model.

But from Figure 17 this increase in the outlet volumetric flow rate of just $1 \text{ m}^3/\text{s}$ make the simulation results fit better the experimental data for the varying width/slope model. In particular, this is seen at the new level ahead of the dam after the jump of inlet flow rate. But simulation results in this figure still show too short oscillation period.

The simplest way to adjust the oscillation period is to change the length of the river. Although this makes the model somewhat unphysical, changing the length can be thought of as compensating for other model simplifications. The best fit for the constant width/slope model is found with a length of 6.3 km, which is shown in Figure 18. Here, the water level ahead of the dam from the model fits the experimental data quite well. Still there is mismatch with the water level just after the Årlifoss dam, however this water level is of less interest

and the main point should be given to the water level ahead of Grønvollfoss.

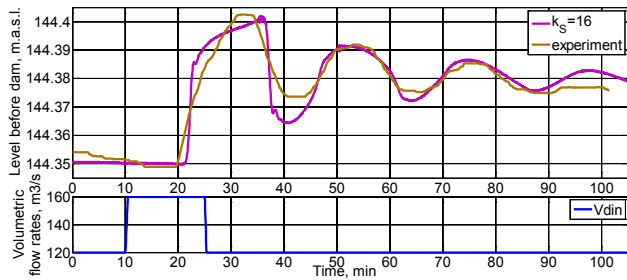


Figure 18. Validation of the constant width/slope model with experimental results, when $\dot{V}_{out} = 121 \text{ m}^3/\text{s}$ and length of river equal 6300 m.

The results of the model with varying slope and width for the same river length equal to 6.3 km are shown in Figure 19. Here it can be seen that the increase of the river length makes this model fit the experimental data better relating to the oscillation period, but worse the water level.

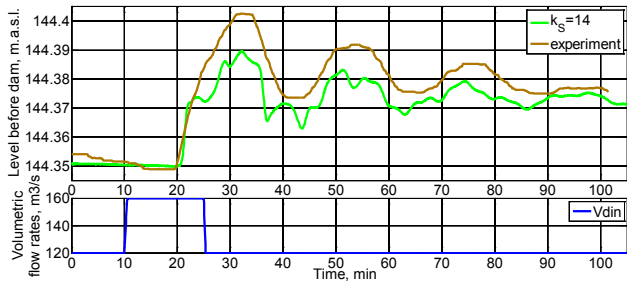


Figure 19. Validation of the model with varying slope and width with experimental results, when $\dot{V}_{out} = 121 \text{ m}^3/\text{s}$ and length of river equal 6300 m.

From all this tuning we can make the conclusion that the geometry of the river is very important for these models. However, the geometry information can be simplified by tuning the friction term with the Strickler factor, the river length or the value of constant width.

4.3 Least squares model fitting

After basic model validation with trial and error is done, the results from the model with constant slope and width looks pretty well. That is why, the least squares error algorithm is used to tune the Strickler factor, the river length and the value of the constant width of the river for this simple model (constant width/slope).

The least squares error algorithm is nothing but just an optimization problem for minimization sum of squares error between the model and the experimental results of the water level ahead of the Grønvollfoss dam. This algorithm is developed in MATLAB using the *MultiStart* function, which is solved the optimization problem from different start points, due to this problem has many local solutions. These start points are specified as a vector, which include different combinations of the Strickler factor, the river length and width based on

previous studying. And that is why the first initial value for this optimization problem are taken from the best fitting results of the model from previous model validation part: $k_{S,0} = 16 \text{ m}^{1/3}/\text{s}$, $L_0 = 6.3 \text{ km}$ and $w_0 = 166 \text{ m}$.

The vectors of results for the water level ahead of the dam from the model and experiment should have the same size. That is why, the model will be simulated with time step equal to 5 sec. and for the time equal to 6085 sec. (as in the results from experiment). The error will be taken not for the whole simulated time length, but only from time equal to 20 min. when the water level ahead of the dam starts to increase due to the jump of the inlet flow rate (see Figure 18).

The results of the least squares error algorithm are presented in Figure 20, where the sum of squares errors is equal to 0.0121 and the optimal values for the Strickler factor, the river length and width are $k_S = 13.513 \text{ m}^{1/3}/\text{s}$, $L = 6300.09 \text{ m}$ and $w = 161.5 \text{ m}$. Here the inlet flow is shown in the bottom plot and the outlet volumetric flow is $\dot{V}_{out} = 121 \text{ m}^3/\text{s}$.

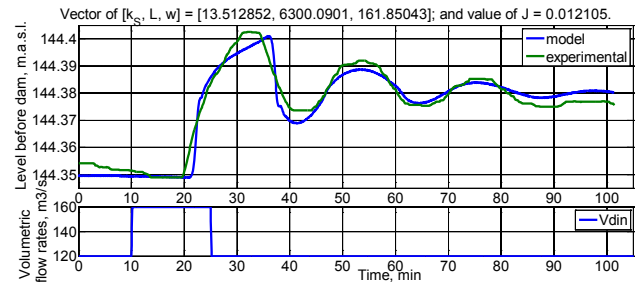


Figure 20. The results of the least squares model fitting.

It should be noted that the sum of squares errors for the best fitting results of the model from previous model validation part is equal to 0.0207 ($k_S = 16 \text{ m}^{1/3}/\text{s}$, $L = 6.3 \text{ km}$ and $w = 166 \text{ m}$). Therefore, the least squares error algorithm helps to find the parameters that leads to better model fitting.

4.4 Further testing of model

Next, the number of nodes is decreased to just 20 to make the model as fast as possible. And results of simulating this model are compared with the results from the model with 100 nodes and with experimental data, Figure 21.

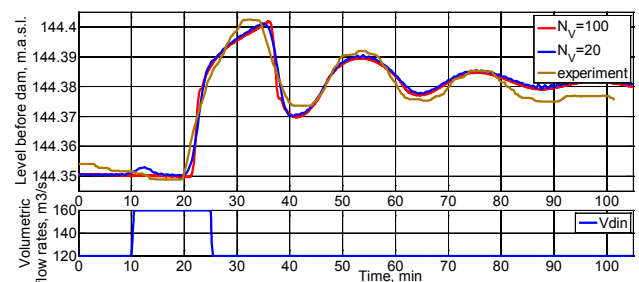


Figure 21. Comparing the results depends on the number of nodes.

Figure 21 shows that there are almost no difference between results from the model with 100 nodes and 20 nodes. Although some accuracy is lost with fewer nodes, the simulation time is 6-7 times less for the model with 20 compartments.

5 Discussion and conclusions

In this paper, the use of the Saint-Venant equations for a run-of-river system has been explored. The Finite Volume method with staggered grid was used to discretize and solve the Saint-Venant equations. The substantially new geometry of the river was provided by Skagerak Energi, and also an experiment on the system was done to compare the model results with reality.

The effect of varying slope and width on the model was also studied. Using this possibility of slope and width variation and also with changing the Strickler factor and the river length, the model was tuned against the experimental data. After this tuning, the model fitted the experimental data reasonably well.

The validation shows that the geometry of the river is very important for these models. However, the geometry information can be simplified by tuning the friction term with the Strickler factor, the river length or the value of constant width.

6 Future work

When the run-of-river model is tuned against experimental results, it can be used to design model based control for the Grønvollfoss power plant. It is possible to linearize the model for use in advanced control, but it is also possible to use the non-linear model directly.

References

- De Schutter, B. and Scattolini, R. Introduction to the special issue on hierarchical and distributed model predictive control. *Journal of Process Control*, 2011. 21(5): pp. 683-684.
- Farina, M., Ferrari-Trecate, G., Romani, C., Scattolini, R. Moving horizon estimation for distributed nonlinear systems with application to cascade river reaches. *Journal of Process Control*, 2011. 21(5): pp. 767-774.
- Johansen A. O. Implementation and test of a fifth order Central WENO scheme for solving hyperbolic balance laws. *Added Values P/S, Lysholt Alle 10, Dk-7100, Vejle, Denmark*, February 2015.
- Johansen, A. O., Elmegaard B. and Sørensen, J. N., 2012a, Implementation and test of a higher order hybrid solver for hyperbolic and parabolic balance laws. *International Journal for Computers & Mathematics with Applications*, 1-32.
- Lie, B., Ruan, Y., and Andreassen, I. (2013): Modeling for control of run-of-river power plant". Proceedings, 54th International Conference of Scandinavian Simulation Society (SIMS 2013), October 16-17 2013, Bergen, Norway.

Stelling, G. S. and Duinmeijer, S. P. A. A staggered conservative scheme for every Froude number in rapidly varied shallow water flows. *International Journal for Numerical Methods in Fluids*, 2003. 43(12): pp. 1329-1354.

van't Hof, B. and Veldman, A.E. Mass, momentum and energy conserving (MaMEC) discretizations on general grids for the compressible Euler and shallow water equations. *Journal of Computational Physics*, 2012.

Xu, M., Negenborn, R.R., van Overloop, P.J., van de Giesen, N.C. De Saint-Venant equations-based model assessment in model predictive control of open channel flow. *Advances in Water Resources*, 2012.

Near Well CFD Simulation of SAGD Extra Heavy Oil Production

Amila C Kahawalage¹ Vidar Mathiesen² Britt Halvorsen¹

¹Department of Process, Energy and Environment, Telemark University College, Norway,
amilachandra@gmail.com, Britt.Halvorsen@hit.no

²InflowControl AS, Norway, vidar.mathiesen@inflowcontrol.no

Abstract

Near well computational fluid dynamic simulation for extra heavy oil production using steam assisted gravity drainage was studied with ANSYS Fluent software. Computational fluid dynamic simulation can predict the multiphase flow behavior in the well annulus and the base pipe when the well involves an Autonomous Inflow Control Valve which is a promising approach for enhanced oil recovery. Volume of Fluid multiphase model was used to simulate the fluid behavior. Three different case studies were carried out by changing the volume fraction and the orientation of the valve. The mixing region of the two immiscible fluids is increased if the water volume fraction of the inlet from the reservoir to wellbore is increased. Simulation results showed that the valve orientation has an impact on oil/water separation.

Keywords: Extra heavy oil, computational fluid dynamics, Steam Assisted Gravity Drainage, Autonomous Inflow Control Valve, Volume of Fluid model

1 Introduction

Conventional oil deposits are depleting gradually as the oil consumption has been increasing due to rapid growth of global population, industry and technology. As a result, the demand for non-conventional oil is increased. Non-conventional oil can be categorized mainly as bitumen and heavy oil. Billions of oil barrels of heavy oils and bitumen have been deposited in the earth. However, it is not as easy to extract non-conventional oil as conventional oil. Bitumen and heavy oil can be extracted using several methods such as steam stimulation, steam assisted gravity drainage (SAGD), hot water flooding and in situ combustion (Butler, 1991).

1.1 Background

Generally in the SAGD process which is the focal point of interest in this study, two horizontal wells are drilled as shown in Figure 1. When high pressure steam is injected to one wellbore (upper), oil is heated and drained into the second (lower) wellbore due to reduction of viscosity and then pumped out.

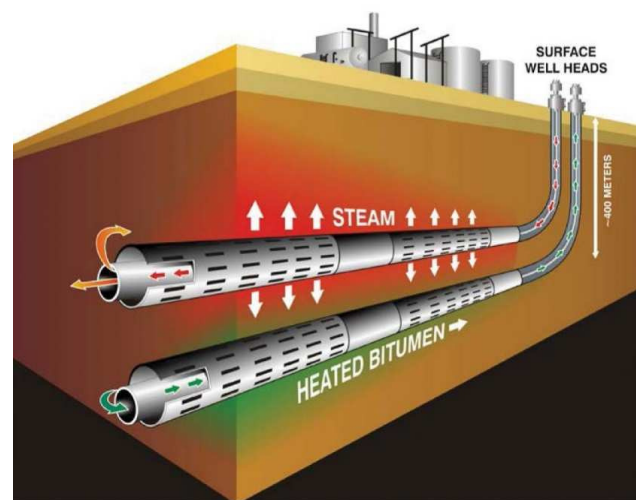


Figure 1: SAGD operation
(Drilling Engineering Association, 2012)

Bitumen and heavy oil are highly viscous at reservoir conditions. By steam injection, bitumen and heavy oil are converted to low viscous fluids, which are mobile through the pipes from reservoir to ground. Injected steam is condensed and drained with oil to the production well. Hence, not only oil but also water is pumped out. If production well produces an oil water mixture, then there will be an additional cost for oil/water separation at the production site, and also the possibilities are high for ground water pollution with oily water coming out from the production well. To overcome this problem, Inflow Control Device (ICD) was introduced by Norsk Hydro in Troll field in 1990s. (Al-Khelaiwi, 2013)

After introduction of ICD by Norsk Hydro, the technology has been continuously developing and the Autonomous Inflow Control Device (AICD) is a typical example of this development. AICD does not require control from the surface as it is basically operated based on change in the fluid characteristics. AICD in oil and gas fields has the ability to choke the influx of gas or water to the production pipe. However, Inflow Control Valves (ICVs) provide solutions to this. ICVs can be

controlled remotely or autonomously. Autonomous inflow control valves (AICVs) (Aakre et al., 2013) are capable to differentiate between fluids based on the physical properties of the fluids, such as density and viscosity.

1.2 Objective

The AICV functionality highly depends on the flow behavior around the valve and near well. Theoretically, if any well segment with AICV receives water, the valve should close autonomously, and the production from this segment will stop. Volume fraction of each phase as well as physical properties of the fluids affect the flow behavior. In this study, this scenario is analyzed by varying the process conditions because the operation of AICV can be improved and shortcomings can be reduced by analyzing the flow behavior.

2 Basic Principle and Geometry of AICV

Following description includes the operational mechanism of AICV which is manufactured by InflowControl AS, Norway. The AICV functionality is established on the difference in the pressure drop in a laminar flow restrictor compared to turbulent flow restrictor. Pressure drop through the laminar flow restrictor can be estimated using equation (1).

$$\Delta p = \frac{32\mu vL}{D^2} \tag{1}$$

Pressure drop through the pipe segment is given in equation (2)

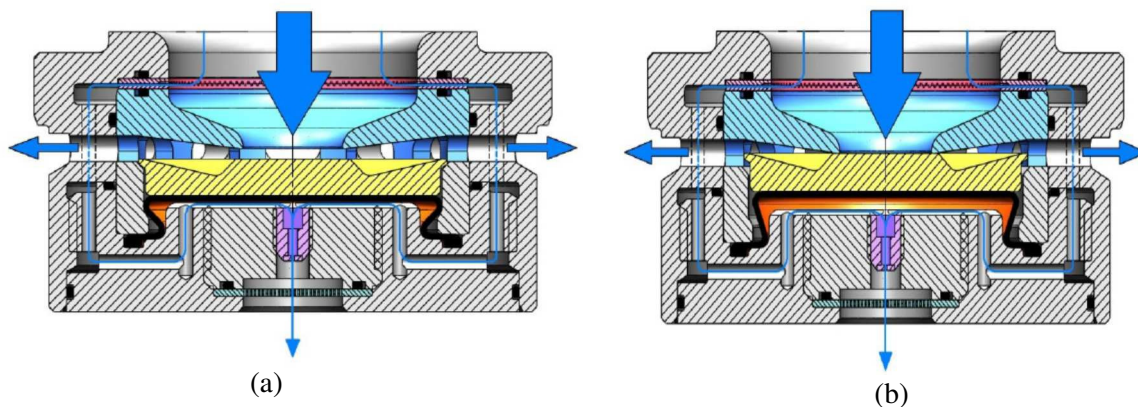


Figure 3. Open and close position of AICV: (a) open; (b) close (Aakre et al., 2014)

$$\Delta p = k \frac{1}{2} \rho v^2 \tag{2}$$

where μ is the fluid viscosity, v is the fluid velocity, ρ is the fluid density and L and D are the length and diameter of the laminar flow element respectively and k

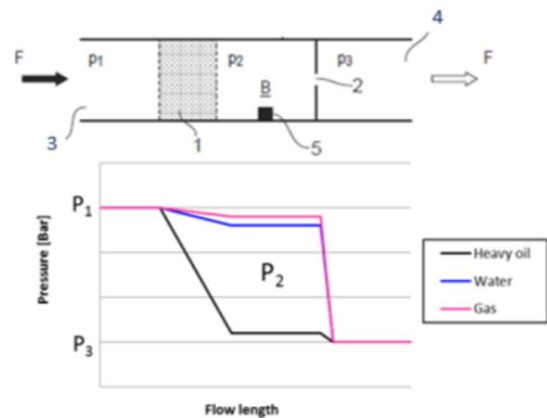


Figure 2. Combination of laminar and turbulent flow restrictors in series (Aakre et al., 2014)

is a geometrical constant. Figure 2 represents the laminar and turbulent flow restrictors in series. According to Figure 2, position 1 and 2 represents the laminar and turbulent flow restrictors respectively; position 3 represents the inlet to the valve from the annulus and position 4 indicates the outlet from the valve to the base pipe. Fluid properties and flow rates influence the pressure in chamber B. This pressure is the key element which is used to control the valve. When the pressure drop through the laminar flow element is high as in heavy oil, the valve is open. When low viscous fluids such as gas or water flows through the laminar flow element the pressure drop is low but the pressure in chamber B is high enabling the valve to be closed. Figure 3 illustrates the open and closed positions

of the AICV (Aakre et al., 2014). According to Figure 3(a), the thickest blue arrow shows the inlet of the main flow to the valve, and the two horizontal arrows show the outlet of the main flow to the base pipe. Location which are marked by dashed line in Figure 4, are referred as nozzles hereafter in this paper.

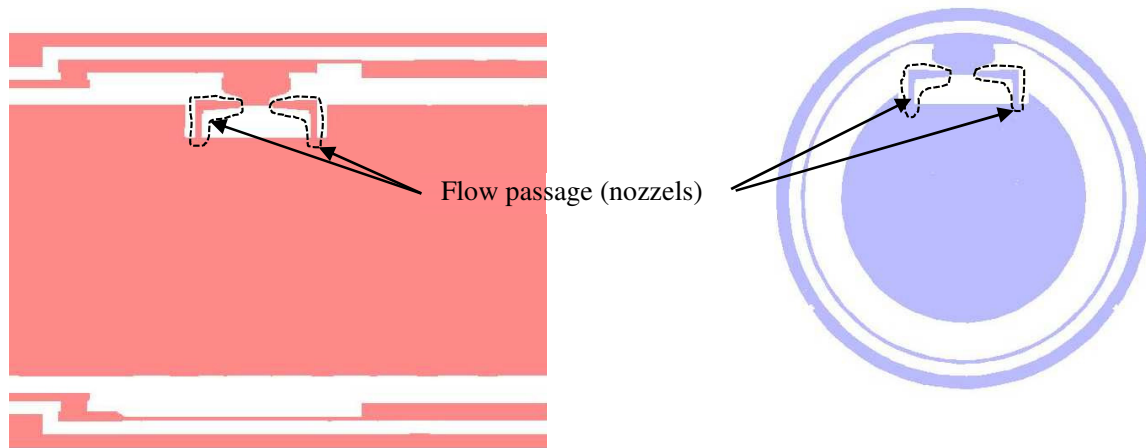


Figure 4 .Representation of nozzles for two different sections

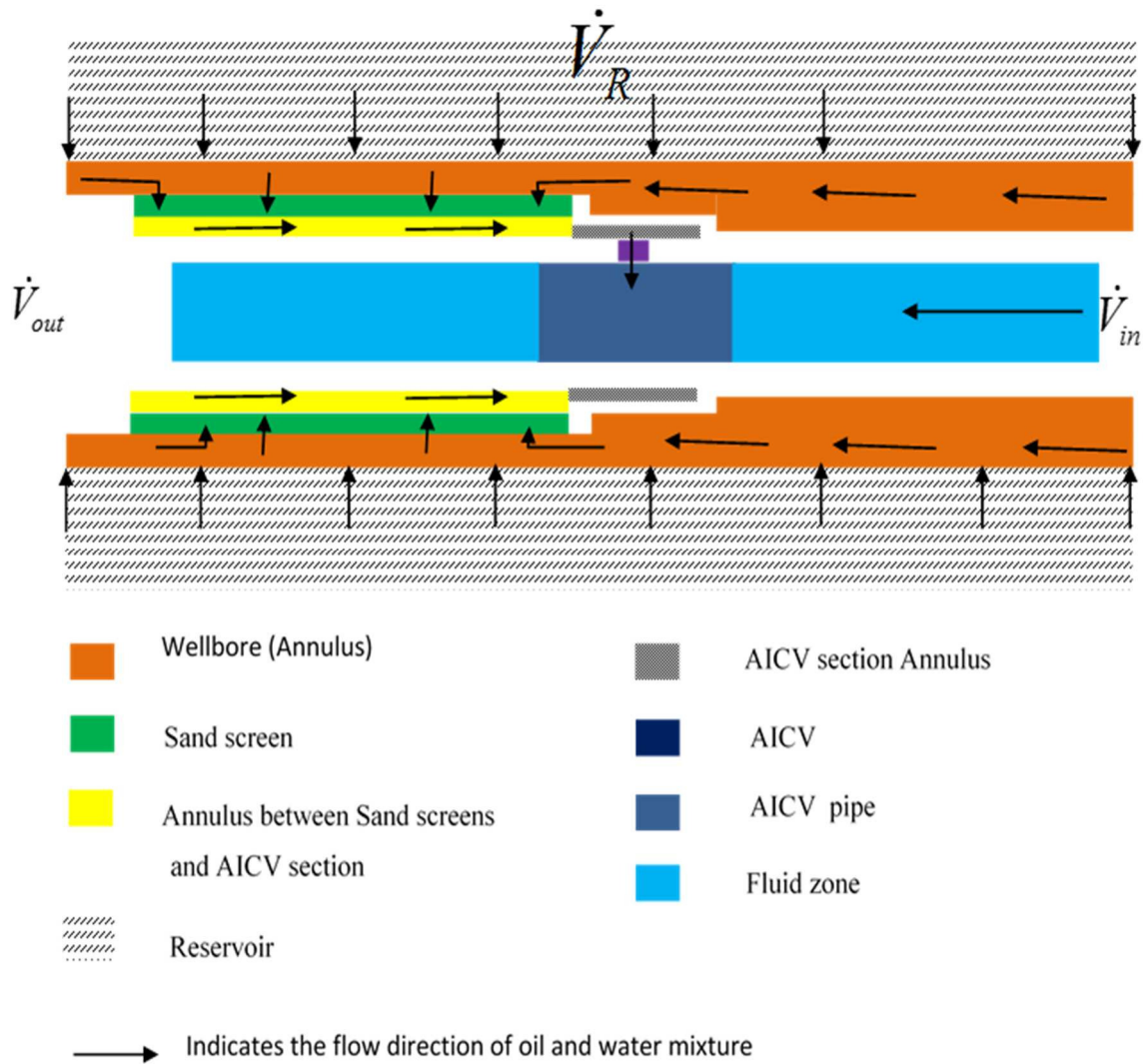


Figure 5. Overview of the simulation model

3 Methodology and ANSYS Fluent Setup

3.1 Simulation Procedure

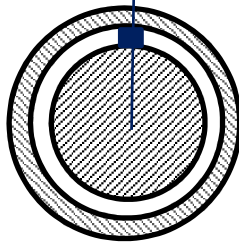
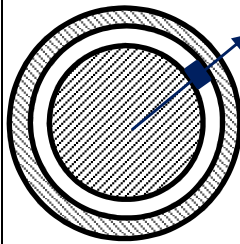
The complete model used for this study, is described in this section. Oil and water mixture which comes from the reservoir is collected in the wellbore and enters into the annulus through the sand screen. Finally the mixture goes to the production pipe through the AICV and gets mixed with oil which comes from other segments of the well (Figure 5). The near well temperature was considered as constant as 213 °C. Three boundary conditions are defined in the model and they are described in Table 1.

Table 1. Description of inlets and outlets

Inlet/Outlet	Description
Inlet I	Total flow rate comes from the reservoir into the wellbore. Volume flow rate (\dot{V}_R) is fixed for all simulations and its value is 1 m ³ /h. \dot{V}_R is divided into two inlets according to the volume fraction of each fluid.
Inlet II	Extra Heavy oil and water flow rate that comes from other well segments (\dot{V}_{in}) are also kept constant and the value is 3 m ³ /h. It is assumed that there are no water in the inlet (\dot{V}_{in}).
Outlet I	Its condition is kept as a pressure outlet and its value is 28 bar (gauge).

However, only the AICV geometry are considered in the simulations but not the AICV function. To observe how the simulation is affected by the volume fraction of each fluid in Inlet I, the volume fractions were changed while keeping the total volume flow rate constant. Simulations were performed when the AICVs were mounted with different orientations in the base-pipe so that the valve position was also changed, to investigate the flow behavior according to the valve orientation. This is shown in Table 2.

Table 2. Different valve positions

Position A	Position B
	
	AICV is positioned 45° angle from the vertical. ($\theta = 45^\circ$)

The flow behavior was investigated and the description of all the case studies is shown in Table 3.

3.2 Geometry Modeling and Meshing

The total geometry model consists of six main parts as shown in Figure 5. The main parts are the AICV section, the inlet pipe, the outlet pipe, the annulus between the

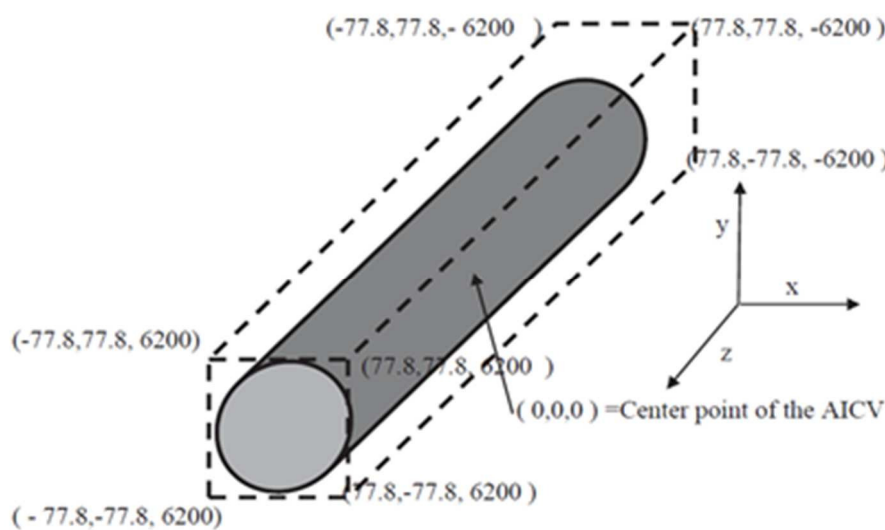


Figure 6. Coordination of the model boundaries (dimensions are in mm)

The objective of the simulations is to investigate the flow behavior of heavy oil and water in the entire model.

sand screen and the AICV section, the sand screen and the wellbore. Each part was modelled separately as

multibody parts and finally assembled into one geometry. Coordination of the model boundaries is shown in Figure 6.

Meshing was created using ANSYS Meshing Tool. The min size, max face size, max size and growth rate were set to 0.001m, 0.0065 m, 0.01 m and 1.2 respectively in the global setting for all simulations. Each part was meshed separately. The element number and number of nodes for CASE 1 and CASE 2 were 1304220 and 1179132 respectively. The element number and number of nodes for CASE 3 were 1300200 and 1304778. Cross section of the generated mesh is shown in Figure 7.

Table 3. Different case studies for simulations

Parameter	CASE 1	CASE 2	CASE 3
Oil volume fraction in Inlet I	0.7	0.5	0.7
Water volume fraction in Inlet I	0.3	0.5	0.3
AICV position	A	A	B

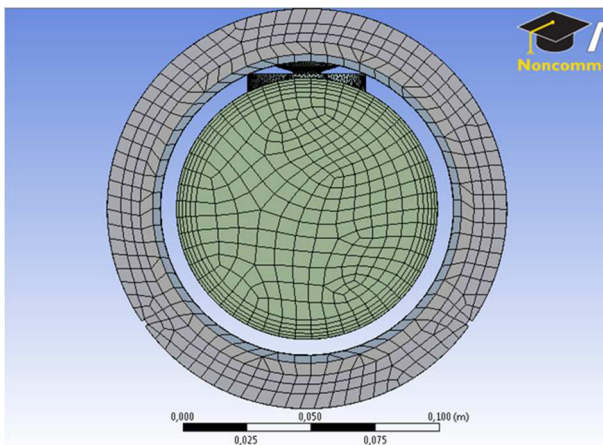


Figure 7. Cross section of generated mesh

3.3 ANSYS/Fluent Setup

All the simulations were performed with pressure based solver because both heavy oil and water can be considered as incompressible liquids. Simulations were carried out with transient mode to achieve proper steady state. The volume of fluid (VOF) multiphase model was selected as stratified oil and water multiphase flow was considered in horizontal pipes (Mohammed et al., 2011). Heavy oil density and viscosity were defined according to the temperature and pressure (213 oC and 28 barg) as given in Table 4.

The sand screen was modeled as a porous media in the CFD simulation. For the modeling purposes slotted sand screen was selected which has 3% open area (PetroWiki, 2015, Xie et al., 2007), with the dimension of 3.81 cm, 0.03556 cm and 1 cm as length, width and depth respectively. Power law was used to define the porous media.

Table 4. Fluid properties for case studies (213 °C and 28 barg)

Fluid	Density [kg/m ³]	Viscosity [cp]
Water	848	0.1255
Extra heavy oil	826	8.35

The three main boundary conditions in the simulation are described in Table 1. Inlet I has two sub inlets for water and heavy oil. For the water and oil inlet, the boundary type was selected as mass flow and the flow direction was set to be normal to the boundary.

SIMPLE (Semi-Implicit Method for Pressure-Linked Equations) was selected as the Pressure Velocity Coupling method for the simulations in CASE 1 and CASE 2. SIMPLEC (Semi-Implicit Method for Pressure-Linked Equations Consistent) was selected for CASE 3. PRESTO! (PREssure STaggering Option), Power law and Modified HRIC (High Resolution Interface Capturing) was selected as the Spatial Discretization methods for pressures, momentum and volume fraction respectively.

Table 5. Maximum normalized equation residuals

Property	Normalized equation residuals
Continuity	10 ⁻⁵
X,Y and Z velocity	10 ⁻⁵
K	10 ⁻⁴
Epsilon	10 ⁻⁴
Vf-phase-2	10 ⁻⁴

Convergence was decided based on two criteria. The normalized equation residuals for the momentum, continuity, turbulence and volume fraction equations were monitored and would desirably drop as shown in Table 5. However, this criterion alone is not enough for deciding the validity of the solution. For some cases the residual criterion might never be fulfilled even though the solution is valid and for other cases the solution can be incorrect even though the residuals are low. Therefore, volume fraction of oil and mixture velocity at position (0,0,0) was also monitored. When these monitored values remained constant for more than 100 time steps, the simulation was considered at steady state and converged.

Table 6. Description of planes and lines

Plane No	Description
Plane 01	Z=0 plane; goes through the AICV
Plane 02	Z=1000 mm plane, goes through the base pipe, sand screen and well annulus
Plane 03	X=0 plane; goes through the AICV as well as base pipe centerline

4 Results and Discussion

The simulation results are discussed in this section. For better explanation, data were extracted from several planes for each case, and the location of each plane in the 3D structure are shown in Figure 8 and Table 6.

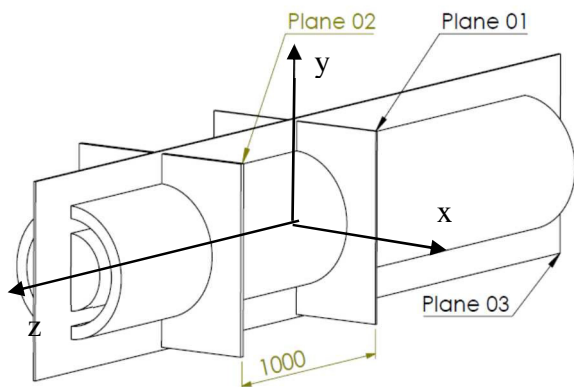


Figure 8. Overview of planes

Figure 9(a) and (b), show the oil phase which remains on the top and the water phase which stays at bottom in the wellbore. In CASE 1 and CASE 2, the inlet oil

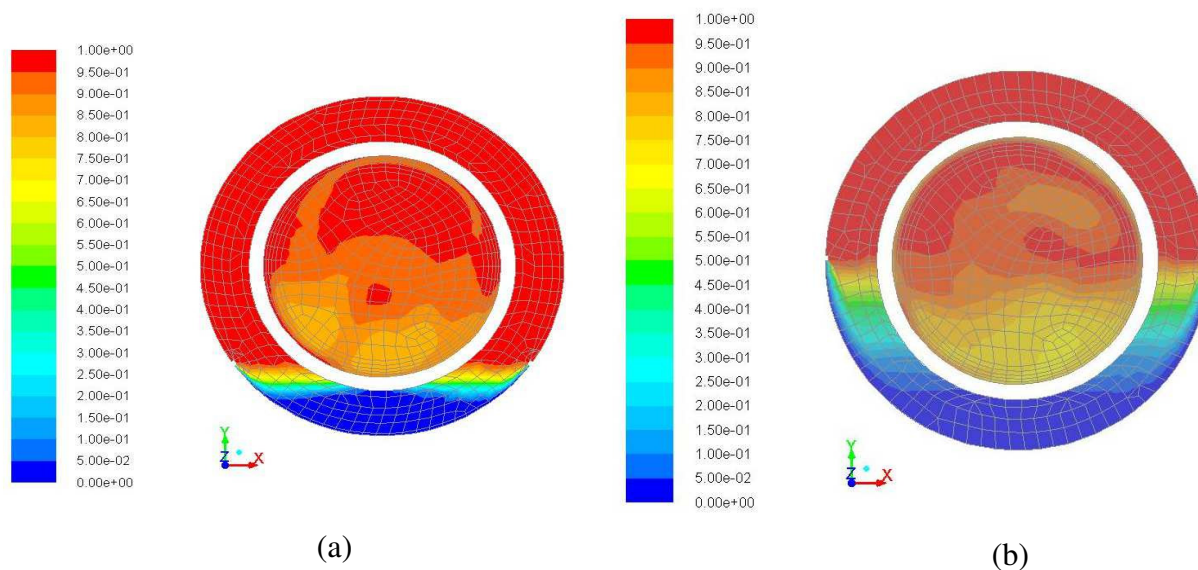


Figure 9. Extra heavy oil volume fraction through plane 02 for; (a) CASE 1 and (b) CASE 2

volume fraction from reservoir is 0.7 and 0.5 respectively. The interface layer between oil and water is thicker in CASE 2 than in CASE 1. Water separation in the production pipe is observed in both cases and the water level is higher in CASE 2.

Figure 10 (a) and (b) show oil volume fraction in the cross sectional plane going through the centerline of the AICV for CASE 1 and CASE 2 respectively. As described above, oil and water separation in the

wellbore and also in the AICV annulus section is observed. Higher water level are obtained in the AICV annulus section in CASE 2 compared to CASE 1. This is because the water volume fraction in Inlet I is 50% in CASE 2 and 30 % in CASE 1. When considering the AICV region, CASE 2 has more water than CASE 1. It can be seen in CASE 2 that the oil and water mixture through the AICV, is mixing with the oil flow in the pipe. The mixing region is larger in CASE 2 because of the higher volume flow rate of water to the well.

Figure 11(a) and (b) show the oil volume fraction of the cross sectional plane which goes through plane 03 for CASE 1 and CASE 2 respectively. Through this plane two nozzles are indicated. Considering CASE 1 only one nozzle injects oil/water mixture whereas in CASE 2 both nozzles inject mixed flow. Also in CASE 2 there is a larger mixing region than in CASE 1. The longer mixing region is due to higher volume flow rate of the water in CASE 2 than in CASE 1.

Figure 10(a) and Figure 12(a) show the oil volume fraction of the cross sectional plane going through the plane 01 for CASE 1 and CASE 3 respectively. It can be observed that water gets separated in the right side in the AICV annulus in CASE 3 but in CASE 1 water gets separated in the bottom. This indicates that water is

injected to the production pipe through the lower nozzle in CASE 3, which implies that water has chosen the easiest way to enter the production pipe. In the other cases, the nozzles are located on the top of the pipe whereas in CASE 3 the nozzles are located close to the bottom of the pipe, hence water entering from these nozzles gets separated more quickly than in the other cases (refer Figure 11(a) and Figure 12(b)).

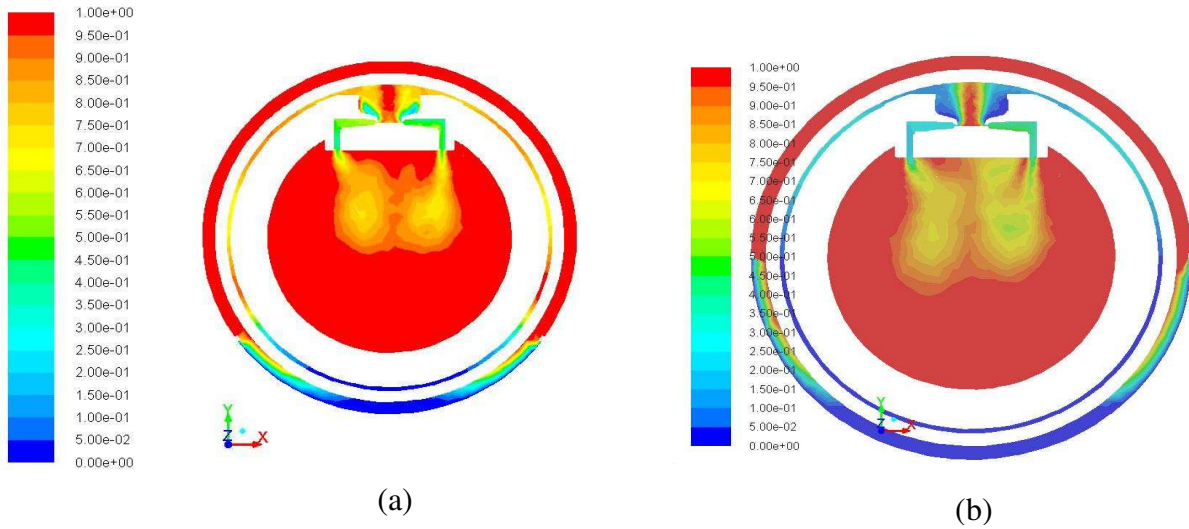


Figure 10. Extra heavy oil volume fraction through plane 01 for; (a) CASE 1 and (b) CASE 2

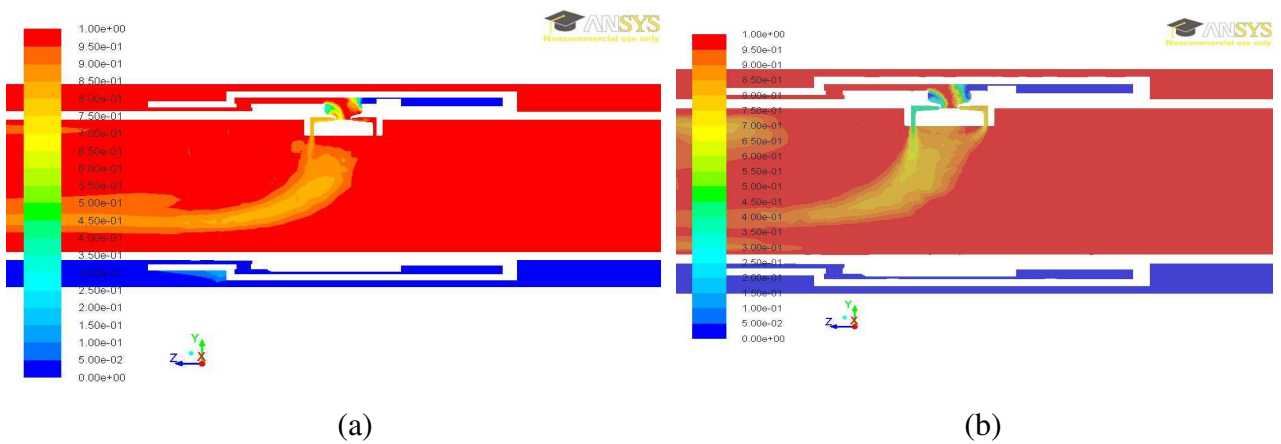


Figure 11. Extra Heavy Oil volume fraction through the Plane 03 for; (a) CASE 1 (b) CASE 2

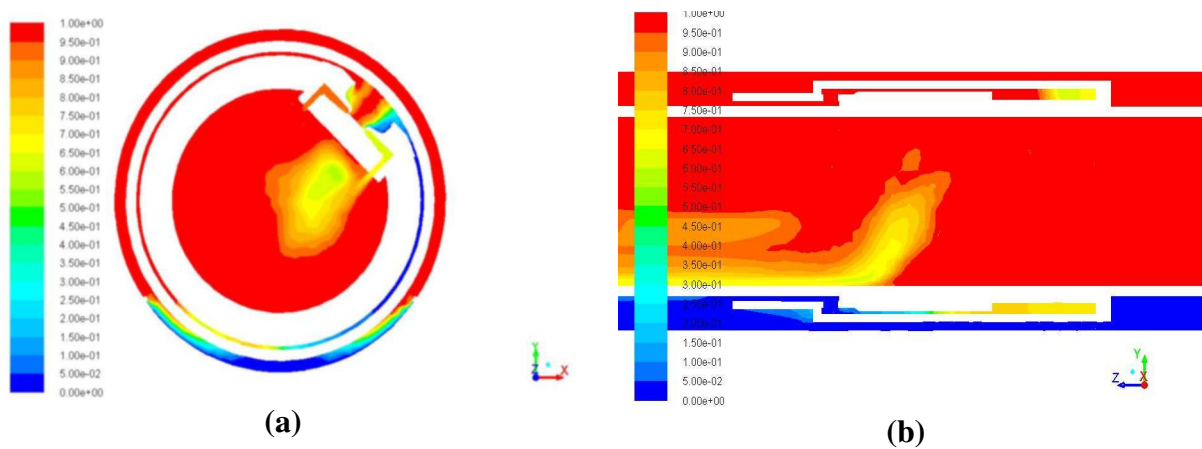


Figure 12. Extra Heavy Oil volume fraction for CASE 3 through the plane (a) 01 (b) 03

5 Conclusion

In this study, CFD simulations were carried out using ANSYS Fluent to investigate the flow behavior in production of extra heavy oil with AICV in combination with the SAGD process in the near well area.

The simulation results show that VOF model can be used for prediction of flow behavior in near well reservoir. The denser fluid which is water gets separated at the bottom of the wellbore and the oil accumulates on the top. When the water volume fraction at the inlet from reservoir to the wellbore is increased, the mixing region is increased. When the valve orientation is changed it affects the oil/water separation process.

References

- AAKRE, H., HALVORSEN, B., WERSWICK, B. & MATHIESEN, V. 2013. Smart Well With Autonomous Inflow Control Valve Technology. SPE Middle East Oil and Gas Show and Conference. Bahrain: Society of Petroleum Engineers.
- AAKRE, H., HALVORSEN, B., WERSWICK, B. & MATHIESEN, V. 2014. Autonomous Inflow Control Valve for Heavy and Extra-Heavy Oil. SPE Heavy and Extra Heavy Oil Conference. Colombia: Society of Petroleum Engineers.
- AL-KHELAIWI, F. T. M. 2013. A Comprehensive Approach to the Design of Advanced Well Completions. Doctor of Philosophy, Heriot-Watt University.
- BUTLER, R. M. 1991. Thermal Recovery of oil and Bitumen, New Jersey, Prentice-Hall. Inc.
- MOHAMMED, A., AL-YAARI, BASEL, F. & ABU-SHARKH 2011. CFD Prediction of Stratified Oil-Water Flow in a Horizontal Pipe. Asian Transactions on Engineering, 5, 68-75.
- PETROWIKI. 2015. Slotted liners and wire wrapped screens [Online]. Texas: Society of Petroleum Engineers. Available: http://petrowiki.org/Slotted_liners_and_wire_wrapped_screens [Accessed 01 April 2015].
- XIE, J., JONES, S. W., MATTHEWS, C. M., WAGG, B. T., PARKER, P. & DUCHARME, R. 2007. Slotted liner design for SAGD wells. In: OIL, W. (ed.) World Oil. Houston.

Gasification of biomass for production of syngas for biofuel

Umesh Adhikari¹ Marianne S. Eikeland¹ Britt M. Halvorsen¹

¹ Department of Process Energy and Environmental Technology, Telemark University College, N-3901 Porsgrunn, Norway

Abstract

Steam gasification is used to produce a high-quality synthesis gas. In this work, the emphasis is on the composition of syngas production which can be further processed for the conversion of biomass to transport biofuels. Biomasses such as wood chips are heated in a gasification reactor to produce a mixture of gases, mainly CO, CO₂, H₂, and CH₄.

Flow sheets for steam gasification of woody biomass have been developed and the process have been simulated using Aspen Plus. The Peng-Robinson equation of state with Boston-Mathias is selected for the model. The model describes the hydrodynamic parameter and reaction kinetics modeling.

Gasification temperature, steam to biomass ratio (STBR), and steam temperature are the most important operating parameters that are considered and studied to examine the gasifier performance. The impact of these process parameters on gasification is determined by sensitivity analysis. The simulation results show that a synthesis gas with a high content of H₂ and CO is obtained for the optimized gasification process.

Keywords: Steam gasification, Aspen Plus, Product gas

1 Introduction

Energy demand is increasing day by day in today's world and energy crisis may come in near future. Together with this, emissions of different gases such as carbon dioxide cause global warming and climate change. Traditional fuels such as petroleum, coal and natural gas are the principal sources of world's energy demand in the current situation (Hu, Yu, & Lu, 2012).

There is a need for alternative sources of energy in near future, and one of the alternative fuels can be biomass. Biomass gasification is one of the appropriate solutions. As an alternative energy source, biomass can be used in power plants for combined heat and power production.

A Lot of progress has been made on biomass gasification during the past few decades. Among the different gasifier types such as fixed bed, fluidized bed and dual fluidized bed gasifiers, development of dual fluidized bed gasifier not only increased the efficiency but also made it possible to gasify various types of biomass such as wood, agricultural residues, and municipal solid wastes.

In Dual Fluidized Beds (DFB) heat is provided to the gasification reactor by circulating hot bed materials (Pröll, Rauch, Aichernig, & Hofbauer, 2007). The main idea of this gasification system is to produce the nitrogen free of syngas for biofuel production.

1.1 Biomass to biofuel

Biochemical and Thermochemical conversion are two different ways of converting biomass into biofuel. Conversion of biomass into liquid or gaseous fuels by anaerobic digestion or fermentation is a biochemical conversion process. In the thermochemical process, biomass solid raw material is converted to fuel gas or syngas (CO, H₂, and CO₂). The syngas that is produced can be converted to fuels like synthetic gasoline and diesels (Kumar, Jones, & Hanna, 2009). For this application, Fischer-Tropic (FT) is one of the most popular processes.

Synthesis gas mainly produced from biomass gasification, coal gasification and natural gas reforming is further used for the production of hydrocarbons. Researchers have shown their interest in (FT) technology due to fast depletion of fossil fuels, increasing the price of crude oil and global warming problem in today's world (Choudhury & Moholkar, 2013).

1.2 Principle of Steam gasification of Biomass

The general process description of the steam gasification is shown in Figure 1-1. The principle is the same as for a dual fluidized bed gasifier having a combustion and a gasification reactor. Here, biomass is devolatilized in RYield (Reactor) where conversion of non-conventional stream biomass into conventional components (C, H₂, O₂, N₂, S) takes place. The gasification process is simulated using a Gibbs reactor in which steam is supplied to the reactor and char combustion takes place in reactor RStoic with the supply of air. The heat that is produced during the combustion is used in the gasifier for the gasification reaction. Finally, flue gas (N₂, CO₂, and excess O₂) and solid (bed materials) is separated by using cyclone separator.

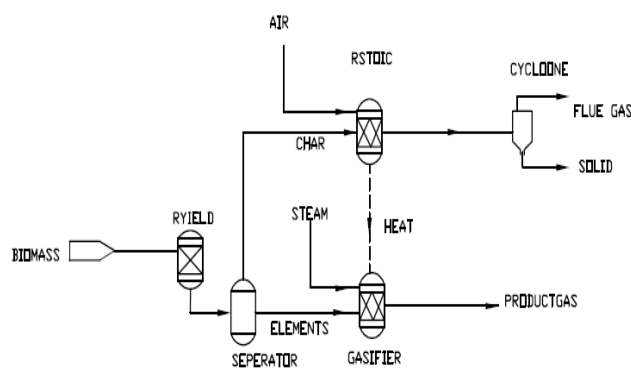


Figure 1-1: Steam gasification of biomass

1.3 Reaction chemistry

Steam is used for the gasification process. The equilibrium reaction takes place in the Gibbs reactor. A detailed description of the reactions in the gasification process is given by the reaction (R1), (R2), (R3), (R4) and (R5). The chemical reaction for endothermic and exothermic reactions are given in Table 1-1 (Zanzi, Sjöström, & Björnbom, 2002). In the steam gasification, reaction (R1) is dominant and if the gasification medium is air or oxygen then (R2) is the dominant reaction. Reaction (R3) occurs with freshly devolatilized char. For the generation of more H_2 , the reaction (R4) plays a major role. Reactions (R1), (R2) and (R5) are highly endothermic whereas (R3) and (R4) are mild exothermic (Basu, 2010).

The general reaction in biomass gasification is shown as in Equation 1 (Authier & Lédé, 2013).

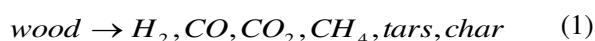


Table 1-1. Chemical Reaction

Chemical reactions	Symbol
Steam gasification $C(s) + H_2O \Leftrightarrow CO + H_2$	(R1)
CO_2 gasification $C(s) + CO_2 \Leftrightarrow 2CO$	(R2)
Methanation $0.5C(s) + H_2 \Leftrightarrow 0.5CH_4$	(R3)
Water gas shift $CO + H_2O \Leftrightarrow CO_2 + H_2$	(R4)
Methane-reforming $CH_4 + H_2O \Leftrightarrow CO + 3H_2$	(R5)

2 Aspen Plus Simulation

Aspen Plus simulation software is selected for modeling the gasifier in this research. In many research projects, this software is being used for modeling coal and biomass gasification. It is a sequential modular simulator that has links to a variety of specialized software like heat exchanger design, dynamic simulation and batch process modeling. (Schefflan). In this process simulation is carried out first by specifying material and energy streams on the simulator blocks. Peng-Robinson equation of state with Boston-Mathias (PR-BM) has been selected as the property package to calculate properties of different components during the gasification process. The simulated process diagram is shown in Figure 2-1.

The following assumptions have been considered for the process simulated in Aspen Plus.

- Isothermal and Steady state process.
- Pressure drop are neglected.
- Instantaneous devolatilization of biomass. The main volatile products are H_2 , CO , CO_2 , CH_4 .
- Heat loss from the reactors is neglected.
- Char contains only carbon and ash.
- Tars and other heavy products are assumed as non-equilibrium.

HCOALGEN and DCOALIGT property models have been chosen for both biomass and ash that are non-conventional to estimate the biomass enthalpy of formation, specific heat capacity and density.

Calculators and design specification blocks are used in the model simulation. Calculators have been used to calculate the product composition after the breakdown of elements and to determine the air mass flow rate. FORTRAN statements are entered to operate the calculator for breakdown of elements. Design specification block have been used for executing the steam flow rate. Details can be found in the Master Thesis (Adhikari, 2015).

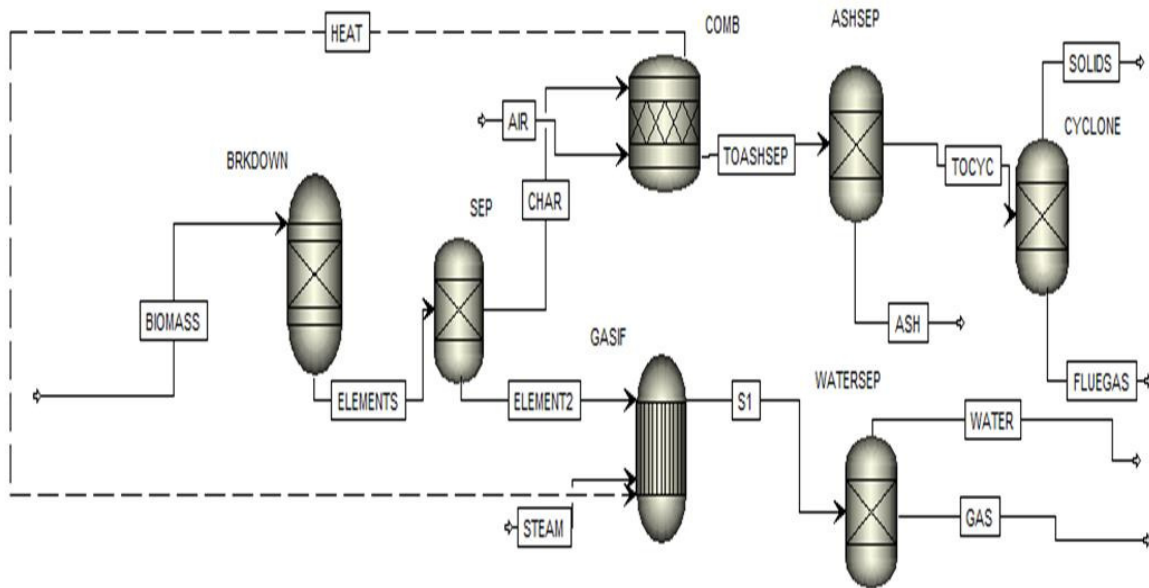


Figure 2-1: Simulated Process Diagram

Table 2-1 gives an overview of the reactor blocks used in the simulations.

Table 2-1. Aspen Plus Reactor Block

Description	Reactor Block ID
This reactor model is useful when reaction stoichiometry and kinetics are unknown and yield distributions elements or data are known.	RYIELD
The model is mainly useful when reaction stoichiometry is unknown, but pressure and temperature are known. It models single phase chemical equilibrium by minimizing Gibbs free energy.	RGIBBS
SEP have been used in the simulation to split a portion of char into the gasifier and combustor. ASHSEP have been used to separate the ash, WATERSEP is used to separate water from gas and CYCLONESEP to separate the product mixture.	SEPARATOR
This reactor model is mainly used for modeling the char combustion.	RSTOIC

Biomass is specified as non-conventional components in ASPEN Plus. Ultimate and Proximate analysis is

defined as biomass in the simulation model. The information about this analysis is given in Table 2-2 and Table 2-3(Doherty, Reynolds, & Kennedy, 2013).

Table 2-2. Biomass composition (Ultimate Analysis) defined in Aspen Plus

Ultimate Analysis (Dry basis)	Biomass (wt %)	Ash (wt %)
Carbon	51.19	0
Hydrogen	6.08	0
Oxygen	41.3	0
Nitrogen	0.2	0
Sulphur	0.02	0
Chlorine	0.05	0
Ash	1.16	100

Table 2-3. Biomass composition (Proximate Analysis) defined in Aspen Plus

Proximate Analysis (Dry basis)	Biomass (wt %)	Ash (wt %)
Volatile matter	80	0
Fixed carbon	18.84	0
Ash	1.16	100
Moisture	20	0

2.1 Feed Specification

Biomass feed before starting of the simulation have been specified. Biomass with a flow rate of 1500kg/hr. temperature 25°C and pressure 1 atm is specified.

2.2 Break down of Elements

The 'RYield' reactor is used to model the breakdown of the elements. It converts the non-conventional biomass into conventional components that are determined and set using a calculator block.

2.3 Gasification

For gasification, RGibbs model is used as the main reactor that handles three phase chemical equilibrium. This reactor calculates the syngas composition by minimizing the Gibbs free energy and assumes complete chemical equilibrium. Gasification Reactions (R1), (R2), (R3), (R4), (R5) have been taken with zero temperature approach for all the reactions. The principal product of the char gasification is the syngas (H₂ and CO) which also contains other elements like H₂O, N₂, S, Cl₂, CO₂, CH₄, and ash. The mass fractions of all these elements are given in Table 2-4.

Table 2-4. Mass fraction of the elements resulted from simulation

Elements	Mass fraction
H ₂	0.04
CO	0.32
H ₂ O	0.45
N ₂	0.0013
S	0.08
CO ₂	0.11
CH ₄	0.00

2.4 Combustion

The RStoic model has been used for the combustion process. The model involves that 'no chemical reactions' are specified and the option of a generation of combustion reactions is selected. The air stream 'AIR' is fed to this block reactor with the composition of 0.79 N₂ and 0.21 O₂ and temperature of 450°C is specified (Pröll & Hofbauer, 2008).

3 Simulation Analysis

The model have been used to perform a sensitivity analysis. To study the gas production, four main gases (H₂, CO, CO₂, CH₄) as stated by (Lv et al., 2004) are considered. Mainly the influence of reactor temperature, steam temperature and steam to biomass

ratio (STBR) on the product gas composition is studied.

3.1 Gasification Temperature

The gasification temperature highly influences on the syngas composition. To determine the effect on the composition, the temperature is varied from 600 to 1100°C. The results are presented in Figure 3-1.

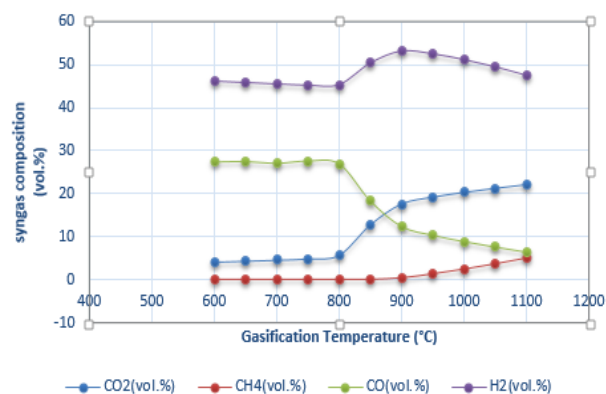


Figure 3-1. Effect of gasification temperature on syngas composition

Over this range, the minimum composition of H₂ is (45.81 vol. %), and the maximum is (53.27 vol. %). The minimum and maximum compositions for CO, CO₂, and CH₄ are 6.44%-27.64%, 4.16%-22.11% and 0-5.08% respectively. From the results, it is clear that the temperature of the gasifier should be maintained at 800-850°C to produce a higher amount of product gas. The Lower temperature cannot provide the required heat energy for the gasification reaction and therefore, produces less amount of product gas (mainly CO and H₂).

3.2 Steam Temperature

The influence on the syngas composition with variation in steam temperature is shown in the Figure 3-2. The steam temperature was varied from 450 to 1000°C to check the volume percent of syngas composition.

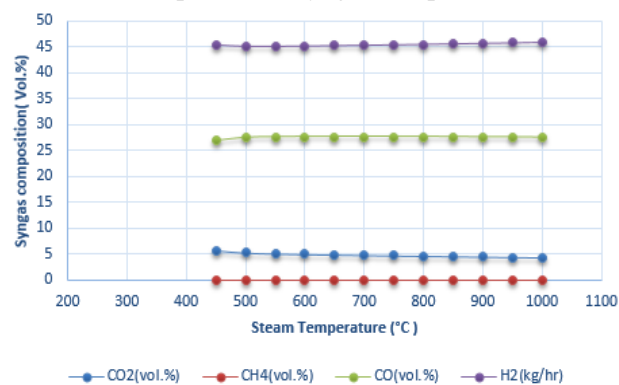


Figure 3-2. Plot of product gas composition versus steam temperature

As can be seen from the figure, the steam temperature does not have any significant influence on the syngas composition. It is therefore not of big importance to preheat the steam to a high temperature before feeding it to the reactor.

3.3 Steam to Biomass Ratio (STBR)

STBR has a significant impact on the syngas composition. Over the STBR range, H₂ increases from 45.39 to 48.64 vol. %. There is no influence of STBR on the composition of CH₄. However, there is a gradual increase in the CO₂ content. From the STBR value of about 0.7 there is a sharp decrease in the CO composition as is shown Figure 3-3.

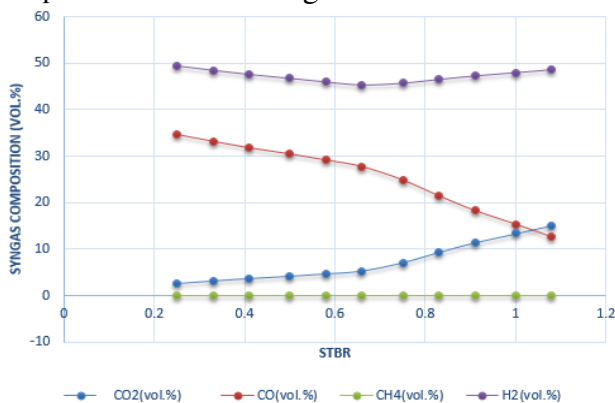


Figure 3-3. Effect of STBR on syngas composition

The amount of hydrogen increases with increased steam injection and the amount of carbon monoxide decreases which can be explained by the water-gas shift reaction (R4). According to reaction (R3) increasing amount of steam increases the fraction of hydrogen in the syngas.

4 Comparison of the result

Steam gasification is used to produce a high-quality product gas (CO, H₂, CO₂, and CH₄) and these gas are further processed for production of synthesis fuel. For this gas quality, gas composition and purity are the main important parameter. The main objective is to look at the generated product gas composition. The product gas composition that is obtained from the simulation is compared with the experimental result in the Table 4-1.

Table 4-1. Experimental and model value of producer gas composition

Components	Experimental value(vol% dry basis)(Schuster, Löffler, Weigl, & Hofbauer, 2001)	Model results(vol% dry basis)
Hydrogen (H ₂)	56.18	58.37
Carbon monoxide(CO)	31.17	34.11
Carbon dioxide (CO ₂)	12.42	7.24
Methane(CH ₄)	0.11	Negligible
Others	0.11	0.28

There are still more challenges and questions regarding the improvement of simulation. The result that is obtained from the simulation can be modified to improve the simulation results. For this verification of the result is necessary which may be possible in the real plant experiment. Simulation based on the kinetic model can be studied. Also, simulation of gasification process can be done with CO₂ capture process to study the behavior of syngas production.

5 Conclusions

A simulation study considering biomass (wood) as the raw material to a Dual fluidized-bed gasifier was carried out using the proximate and ultimate analysis in the model. The process simulation tool Aspen Plus was used in this study. Different unit operation blocks were combined and the required kinetic expressions and hydrodynamic models were developed to carry out the simulations. The simulation results show that a synthesis gas with a high content of H₂ and CO on a dry basis.

The mixture of gas can be further processed for conversion of biomass to transport biofuel such as gasoline, diesel and jet fuels and the process FT (Fischer-Tropsch Synthesis) is getting more popular during recent years for production of renewable fuels.

The impact of gasification temperature, steam temperature, steam to biomass ratio (STBR) on the gasification process are determined by sensitivity analysis. The optimum gasification temperature is found to be about 800°C and the optimum STBR about 0.65.

References

- Adhikari, U. (2015). Gasification of biomass for production of syngas for biofuel *Master Thesis* (pp. 27-50): Telemark University College, Faculty of Technology, Porsgrunn, Norway, 2014.
- Authier, O., & Lédé, J. (2013). The image furnace for studying thermal reactions involving solids. Application to wood pyrolysis and gasification, and vapours catalytic cracking. *Fuel*, *107*, 555-569.
- Basu, P. (2010). *Biomass gasification and pyrolysis: practical design and theory*: Academic press.
- Choudhury, H. A., & Moholkar, V. S. (2013). An Optimization Study of Fischer–Tropsch Synthesis Using Commercial Cobalt Catalyst. *2*(1), 31-39.
- Doherty, W., Reynolds, A., & Kennedy, D. (2013). Aspen plus simulation of biomass gasification in a steam blown dual fluidised bed. 212-220.
- Hu, J., Yu, F., & Lu, Y. (2012). Application of Fischer–Tropsch synthesis in biomass to liquid conversion. *Catalysts*, *2*(2), 303-326.
- Kumar, A., Jones, D. D., & Hanna, M. A. (2009). Thermochemical biomass gasification: a review of the current status of the technology. *Energies*, *2*(3), 556-581.
- Lv, P., Xiong, Z., Chang, J., Wu, C., Chen, Y., & Zhu, J. (2004). An experimental study on biomass air–steam gasification in a fluidized bed. *Bioresource technology*, *95*(1), 95-101.
- Pröll, T., & Hofbauer, H. (2008). H₂ rich syngas by selective CO₂ removal from biomass gasification in a dual fluidized bed system—process modelling approach. *Fuel Processing Technology*, *89*(11), 1207-1217.
- Pröll, T., Rauch, R., Aichernig, C., & Hofbauer, H. (2007). Performance characteristics of an 8 MW (th) combined heat and power plant based on dual fluidized bed steam gasification of solid biomass. 937-944.
- Schefflan, R. Introduction to Aspen Plus. *Teach Yourself the Basics of Aspen Plus™*, 1-19.
- Schuster, G., Löffler, G., Weigl, K., & Hofbauer, H. (2001). Biomass steam gasification – an extensive parametric modeling study. *Bioresource technology*, *77*(1), 71-79. doi: [http://dx.doi.org/10.1016/S0960-8524\(00\)00115-2](http://dx.doi.org/10.1016/S0960-8524(00)00115-2)
- Zanzi, R., Sjöström, K., & Björnbom, E. (2002). Rapid pyrolysis of agricultural residues at high temperature. *Biomass and Bioenergy*, *23*(5), 357-366.

Temperature Effects in Anaerobic Digestion Modeling

Wenche Hennie Bergland Carlos Dinamarca Rune Bakke

Department of Process, Energy and Environmental Technology, Telemark University College, Norway,

Wenche.Bergland@hit.no, Carlos.Dinamarca@hit.no, Rune.Bakke@hit.no

Abstract

Temperature effects on kinetic coefficients for the biochemical processes particle disintegration, hydrolysis and substrate uptake reactions were included in the anaerobic digestion model 1 (ADM1). It was evaluated on data from a pilot experiments in a 220 liter AD sludge bed reactor treating dairy manure for 4 months of varying loads and temperatures; 25, 30 and 35 °C. Implementing individual temperature effects for each biochemical reaction gave the best fit for both biogas production and intermediate products. Simulated overall soluble and particulate organic carbon removal, pH and acetate are close to measured values while propionate is underestimated. Temperature has a moderate influence on steady state biogas production in sludge bed AD (1.6 % per degree at 30 – 35 °C and 3.4 % per degree at 25 – 30 °C), implying the net energy gain can peak at $T < 35$ °C in some cases.

Keywords: Anaerobic digestion, sludge bed, temperature dependence, ADM1.

1 Introduction

Anaerobic digestion (AD) can be used to recover energy as methane from organic wastes and thereby reduce greenhouse gas emissions by contributing to more sustainable waste handling.

Anaerobic degradation of organic matter into biogas is carried out by a consortium of microorganisms, which degrade complex organic macro-molecules by extracellular (disintegration, hydrolysis) and intracellular (acidogenesis, acetogenesis, methanogenesis) enzyme mediated biochemical reactions (Fig. 1). The Anaerobic Digestion Model No.1 (ADM1) (Batstone et al., 2002) is a common platform of modelling, simulations and understanding AD. It was developed by the International Water Association (IWA).

ADM1 was developed primarily to model digestion of sludge from wastewater treatment plants where the standard process temperatures are 35 °C, or 55 °C, presumed optimal for respectively meso- and thermophilic digestion. Energy optimized AD may, however, not be such, e.g. 35 °C for mesophilic. Higher temperatures (35 - 42 °C) are sometimes preferred while lower digestion temperature than microbial optima for which standard model parameters are available may also

be favorable in some cases. Anaerobic reactors fed with low energy substrates, such as cow manure slurry, can possibly be an example of the latter since a large portion of the potential energy might be required to heat the reactor to 35 °C in cold climates. The potential for reducing heating requirements is therefore examined by testing and modeling AD at temperatures lower than 35 °C claimed to be the mesophilic optimum (Lin et al., 1987).

ADM1 contains several biochemical reactions, physiochemical equilibriums and gas-liquid transfer processes which all are affected by temperature. Increased knowledge about AD process parameters temperature dependency is generally required for adequate AD modeling using the standard ADM1 at temperatures other than 35 °C.

Temperature effects on the biogas production is known (Henze and Harremoës, 1983) but the effects on individual kinetic coefficients for particle disintegration, hydrolysis and substrate uptake reactions might be required to adequately simulate AD with both particulate and dissolved organics in the substrate where it is not known which is the rate-limiting reaction.

Temperature dependency for the kinetics in AD is often described using one Arrhenius equation (Banik et al., 1998; Grant and Lin 1995; Kettunen and Rintala, 1997) for exponential growth in the mesophilic area up to 30 °C, but in order to include both the opposing synthesis and degradation processes the temperature dependency for the biochemical reactions in the whole mesophilic range should be modelled using double Arrhenius equations (1) (Hinshelwood, 1946; Pavlostathis and Giraldo-Gomez, 1991).

$$\rho = A_1 \exp\left(\frac{-E_{a1}}{RT}\right) - A_2 \exp\left(\frac{-E_{a2}}{RT}\right) \quad (1)$$

ρ = microbial activity, A is the frequency factor, E_a is the apparent activation energy, R is the gas constant and T is the absolute temperature.

This temperature effect on each individual degradation reaction are studied to some degree (Donoso-Bravo et al., 2009; Rebac et al., 1995, Lin et al., 1987) but by using varying models for the temperature effect. Intermediate products are measured here to evaluate the model's ability to simulate individual degradation reaction.

It is probably sufficient that the rate limiting degradation step is modeled utilizing the proper temperature effect(s). It is however not always obvious what the rate-limiting step is. Hydrolysis and disintegration are often assumed rate limiting for particle rich substrates, such as manure, but this may be altered by pre-treatment. Particle rich manure filtrate, for which the rate-limiting step is unknown, is used as feed in this study.

Modelling AD at thermophilic (45 - 70 °C) and psychrophilic (4 - 15 °C) temperatures with possible other degradation paths (Vavilin et al., 1997) is not attempted here. Temperature effects on diffusion are assumed insignificant in the range investigated.

An intention is that the model can be used to reveal optimal sludge bed AD temperatures, such as to investigate the potential for reducing heating requirements by reactor operation at temperatures below 35°C.

The purpose of this study is to quantify temperature effects on AD modelling by establishing and testing an extended ADM1 ("ADM1-T") to account for temperature effects on model parameters.

The model is tested on data from a 220 liter AD sludge bed reactor treating dairy manure filtrate for 4 months of varying loads and with step temperature changes between 25, 30 and 35 °C.

Additional aims are:

- (1) Distinguish between physical and biological effects of temperature;
- (2) Evaluate temperature effects in sludge bed AD and
- (3) Look for limiting reaction steps for process capacity by testing and modeling AD at different loads and temperatures.

This should improve our general understanding of how, where and when temperature influences AD processes.

2 Materials and Methods

Temperature dependent kinetic parameters for both biochemical and physico-chemical processes are retrieved from literature survey. Other relevant model parameters are retrieved from batch tests and compared against continuous AD using dairy manure filtrate.

2.1 Model Parameters

2.1.1 Biochemical kinetic parameters

Kinetic temperature dependent parameters for biochemical processes in ADM1-T are K_{dis} , K_{hyd} , k_m , K_d , Y and K_s , which are recommended in ADM1 for 35 °C and used as a reference (Table 1). K_{dis} and K_{hyd} are for 1.st order extracellular reactions disintegration and hydrolysis (2).

$$\rho = k_{dis,hyd} \cdot X_{dis,hyd} \quad (2)$$

ρ = disintegration rate or hydrolysis rate of solid substrate (kg COD solid substrate $m^{-3} d^{-1}$ where COD = chemical oxygen demand), $X_{dis,hyd}$ = solid substrate concentration (kg COD solid substrate m^{-3}), $K_{dis,hyd}$ = temperature dependent kinetic parameter for disintegration or hydrolysis (d^{-1}). Disintegration is typically considered the rate-limiting step for substrates containing mainly particles, while hydrolysis of proteins, lipids and carbohydrates is the rate limiting in high rate digesters and then only disintegration of decaying microorganisms is accounted for (Batstone et al., 2002).

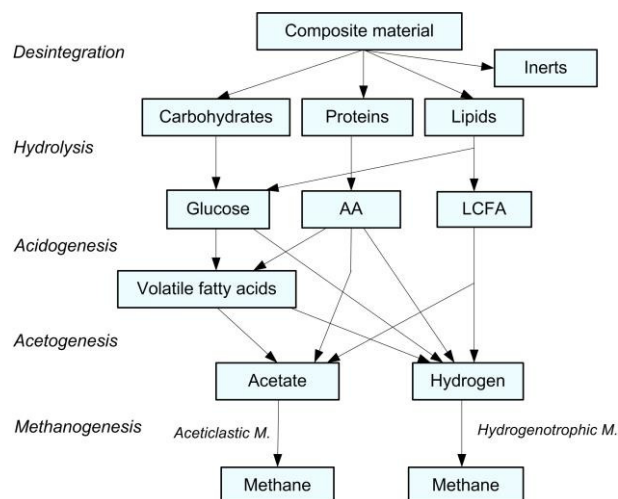


Figure 1. COD flow diagram of the Anaerobic Digestion Model No.1 (Adapted from Batstone et al., 2002) showing the biochemical reactions for which temperature effects have been included as arrows.

Each intracellular enzyme mediated biochemical reaction (acidogenesis, acetogenesis, methanogenesis) (Fig. 1) is generally approximated by a Monod type saturation function where the reaction rate of substrate uptake by organism, ρ (kg COD substrate $m^{-3} d^{-1}$), can be described as:

$$\rho = k_m \cdot X \cdot \frac{S}{S+K_s} \cdot I \quad (3)$$

Equation (3) contains the maximum substrate uptake rate constant k_m (kg COD substrate kg COD biomass $^{-1} d^{-1}$), X = biomass concentration (kg COD biomass m^{-3}), S = substrate concentration (kg COD substrate m^{-3}), K_s = half saturation constant (kg COD substrate m^{-3}) and I = inhibition factor. The growth of biomass, X , is expressed through the yield, Y (kg COD biomass X kg^{-1} COD substrate) of uptake of substrate, while biomass death is described by K_d (d^{-1}) (Table 1).

Temperature effects on K_{hyd} and k_m are retrieved from literature sources. The hydrolysis kinetic parameter is also tested by a set of laboratory experiments to find both the k_{hyd} for this substrate and the effect of low temperature. A Hinshelwood double

Arrhenius function is recommended (Batstone et al., 2002) as the temperature dependency for the biochemical reactions expressed through k_m . The affinity for the substrate parameter K_S is therefore not altered. Monod (1949) assumes a saturation relationship between substrate concentration and growth rate while growth yield remained constant over a wide range of substrate concentrations that requires a constant K_S . We extend this assumption to temperature and evaluate if temperature effects on yield can be ignored. The death of biomass K_d has a constant small value in ADM1. The temperature effect, if any, is assumed small and not altered.

Table 1 Biochemical processes temperature dependent kinetic parameters.

Parameter	Biochemical	Expression	Denomination
K_{dis}	disintegration	2	d^{-1}
K_{hyd}	hydrolysis	2	d^{-1}
k_m	max substrate uptake rate constant	3	kg COD substrate $m^{-3} d^{-1}$
K_S	half saturation constant	3	kg COD substrate m^{-3}
Y	biomass growth yield		kg COD biomass kg^{-1} COD substrate
K_d	death rate of biomass		d^{-1}

Relative factors of the relevant temperatures, 35, 30 and 25 °C are calculated from reported temperature effect (Henze and Harremoës, 1983) on the overall biogas production (Table 2). These factors are applied for all the kinetic parameters K_{dis} , K_{hyd} and k_m for all the degradation steps since the limiting reaction is unknown as a first approach.

Table 2. Relative temperature factors for kinetic parameters for the overall biogas production. Calculated from Henze and Harremoës (1983).

Temperature (°C)	25	30	35
Temperature factor	0.42	0.87	1

Temperature effects on the kinetic parameters that are different for each degradation equation are also implemented. Relative temperature effects for hydrolysis, acidogenesis and acidoclastic methanogenesis of respectively starch, glucose and acetic acid through batch tests at 15-45 °C (Donoso-Bravo et al., 2009) is used to calculate temperature factors for each reaction (Table 3). Relative temperature effects on individual reactions are also reported by Rebac et al. (1995) for butyrate, propionate and acetate

degraders at 10–40 °C. Calculated relative factors from these temperature effects are also in Table 3. Reactions that were not found were estimated by using factors from “nearby” reactions in Fig. 1: The same temperature effect as for sugar uptake is used on amino acids and fatty acids uptake. The same temperature effect for hydrogen uptake as for acetate uptake is also used.

Table 3. Relative change of the kinetic parameters K_{dis} , K_{hyd} and k_m with temperature. Calculated from reported data in (A) Donoso-Bravo et al. (2009), and (B) Rebac et al. (1995).

Process	Temperature (°C)			Ref.
	25	30	35	
Disintegration, K_{dis}	Same as for hydrolysis of carbohydrates			
Hydrolysis of carbohydrates, $K_{hyd, su}$	0.48	0.74	1.00	A
Hydrolysis of protein, $K_{hyd, pr}$	Same as for hydrolysis of carbohydrates			
Hydrolysis of lipids, $K_{hyd, li}$	Same as for hydrolysis of carbohydrates			
Sugar Uptake, k_m	0.21	0.22	1.00	A
Amino acid uptake, k_m	Same as for sugar uptake			
Fatty acid uptake, k_m	Same as for sugar uptake			
Butyrate uptake, k_m	0.67	0.86	1.00	B
Propionate uptake	0.70	0.90	1.00	B
Aceticlastic methanogens, k_m	0.69	0.93	1.00	A
Aceticlastic methanogens, k_m	0.48	0.70	1.00	B
Hydrogenotroph methanogens, k_m	Same as for aceticlastic methanogens			

Three different simulations were done;

H: using the same temperature effect (Table 2) for all the degradation steps.

D: using all the temperature effects from Table 3 but with methanogenesis from Donoso-Bravo et al. (2009)

R: using all the temperature effects from Table 3 but with methanogenesis from Rebac et al. (1995)

2.1.2 Physio-chemical parameters

The temperature dependencies of the temperature dependent kinetic parameters k_a and k_H (Table 4) are in the standard ADM1 while the temperature dependency of the mass transfer coefficient $k_{L,a}$ is implemented here.

Physico-chemical equilibrium is modeled based on the law of mass action for aqueous substances and on Henry’s law to model the solubility of a gas in water. Both are temperature dependent; which are given by equations (4) and (5) respectively.

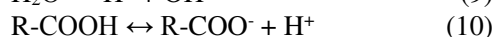
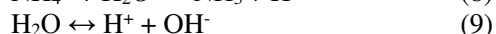
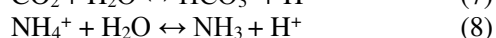
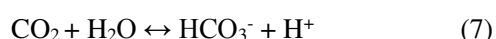
$$k_a = \frac{[B^-] \cdot [H^+]}{[S_{total}] - [S_{ion}]} \quad (4)$$

$$S_{total} = k_H \cdot P \quad (5)$$

Where both K_a and k_H are temperature dependent according to van Hoff's equation (Eq. 6).

$$\ln \frac{k_2}{k_1} = \frac{\Delta H^\circ}{R} \cdot \left(\frac{1}{T_1} - \frac{1}{T_2} \right) \quad (6)$$

The equilibriums reactions (7-9) have temperature correction implemented while carboxylic acids (10) temperature dependency is assumed small and not taken into account (Batstone et al., 2002).



Dynamic gas transfer is also dependent on temperature, accounted for by the temperature dependency of the overall mass transfer coefficient, k_{LA} (Eq.11), according to Saravanan et al. (2000).

$$k_{LA} = 0.56 \cdot T + 27.9 \quad (11)$$

Table 4. Temperature dependent physico-chemical processes parameters.

Parameter	Physico-chemical	Expression in Equations
k_a	Equilibrium constant	(4)
k_H	Henry's constant	(5)
k_{LA}	Mass transfer coefficient	(11)

2.1.3 Non temperature dependent parameters

The conditions with longer sludge retention time (SRT) than hydraulic retention time (HRT) is implemented in ADM1 as $SRT = tres_x + HRT$, recommended with $tres_x = 40$ days for high rate, sludge bed reactors. The validation experiment was carried out in a sludge bed reactor, but not at high rate, so lower $tres_x$ is also evaluated.

ADM1 uses the same fixed stoichiometry to model product distribution for 35 and 55 °C. These stoichiometric values were assumed appropriate for the range from 25 to 35 °C also.

2.2 Biodegradability and hydrolysis

Long-term batch tests using 100 ml medical syringes as batch reactors were performed on dairy manure filtrate at room temperature (~23 °C) and at 35 °C to determine the biodegradable amount and the kinetic hydrolysis

parameter for this substrate. 30 ml of manure filtrate was added to the syringe and the gas production was monitored regularly. The soluble and total chemical oxygen demand, COD_S and COD_T , (representing the energy content of the waste) was measured before and after the test. The not degradable fraction of the substrate was calculated based on remaining COD. The COD_T removed is equivalent to the biogas potential. To determine how much of the COD came from either the soluble ($B_{0soluble}$) or the solid ($B_{0particle}$) fractions, a factor $f = B_{0soluble}/B_{0particle}$ was estimated by COD particle and liquid contents at start and end of the experiment.

The hydrolysis kinetic factor K_h was calculated using:

$$B = B_0 (1 - e^{-kt}) \quad (12)$$

at temperatures 23 and 35 °C. B_0 is the total biogas production and B is the biogas production at the given time t .

2.3 AD sludge bed experiment

2.3.1 AD reactor design operation

The dairy manure feed was from the organic milk producer Foss Farm in Skien, Norway. The cattle were fed grass and clover ensilage and 25 % "dairy concentrate" (19 % protein). The manure was flushed into an indoor temporarily storage tank, diluting the manure with flush water by 14 % on average (Bergland et al., 2014). The manure was stored for 1-6 weeks in the storage tank before treated in a rotating vacuum drum filter (mesh light opening of 1.4 mm) to remove the coarse solids. The filtrate was used as AD feed (substrate) in this study.

The dairy manure AD was performed in a sludge bed reactor as an integral part of a process to generate fertilizers and biogas, as described by Haugen et al. (2013) (Fig. 2).

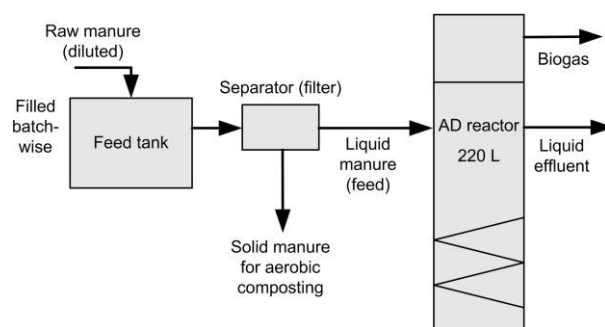


Figure 2. The sludge bed AD process of this pilot plant treating dairy cow manure was the subject of this study.

The AD reactor had a liquid volume of 254 liter with 400 mm Ø and 2000 mm height consisting mainly of a lower liquid volume for suspended biomass. A plastic support medium for biofilm growth was integrated with solids, gas and liquid separation at the top. The process

had been operated for 2 year at 35°C following 70 days at 25 °C before the 130 days operation reported here allowing the culture to adapt to cow manure filtrate as substrate.

The reactor was operated at the mesophilic temperatures 25, 30 and 35 °C during this test. The load was from zero up to a load corresponding to a hydraulic retention time (HRT) of 8.5 days. The reactor was semi-continuously operated by pulse feeding with the feeding pump controlled as a binary (On/Off) device.

2.3.2 Monitoring and analysis

A comprehensive online- and offline-testing scheme was used to monitor the AD reactor. Biogas production ($L d^{-1}$), gas composition (fractions of CO_2 and CH_4), liquid flow and reactor temperature were monitored continuously online as described by Haugen et al. (2013). Substrate and effluent samples were collected 1-2 times a week. Total chemical oxygen demand (COD_T), soluble COD (COD_S), total solids (TS), volatile solids (VS), total suspended solids (TSS), volatile suspended solids (VSS), pH, alkalinity, NH_4^+-N and VFA's (acetate, propionate, butyrate, iso-butyrate, valerate, iso-valerate) were analyzed as described in Bergland et al. (2015).

3 Results

3.1 Biodegradability and hydrolysis input to the model

The batch tests gave a total biodegradable fraction of 0.26 of the COD_T . The non-degradable is therefore 74 % for the manure substrate COD used. The fractions of protein, carbohydrates and lipids in the biodegradable fraction are set to 0.27 (f_{pr}), 0.51 (f_{ch}) and 0.22 (f_{li}) respectively (Table 6) as found for slurry cattle manure (Møller et al., 2003). Tests of the temperature dependency revealed that 96 % \pm 2 % of the biogas production at 35 °C were achieved at 23 °C in the batch tests, confirming that yields are quite insensitive to temperature. The effect is implemented as 96 % at 25 °C and 98 % at 30 °C. The fraction of biodegradable from particles is below 0.38 and the rest from soluble organics, determined based on the COD contents before and after the batch test (Table 5). 0.3 is used as biodegradable fraction from particles and 0.7 from dissolved COD in the model.

Table 5. Dairy manure filtrate parameters used to calculate the COD content of the degradable and non-degradable fractions of particulates and dissolved organics of the AD reactor substrate.

Property	Before	After	ΔCOD
COD_T	50	37	13
COD_S	14	6	8
$COD_T - COD_S =$ $COD_{particles}$	36	31	

Hydrolysis kinetics were also found from the batch test that lasted 91 days, excluding data from the first 2-3 weeks (when hydrolysis is not the rate-limiting step). Using least square method on Eq.12 (Chap 2.2) gives estimation of k_{hyd} to be $0.13 d^{-1}$ at 35 and $0.05 d^{-1}$ at 23 °C (Fig. 3). This is in the range of k_{hyd} found for straw and grass tested by Veecken and Hamelers (1999) at temperatures 20 – 40 °C.

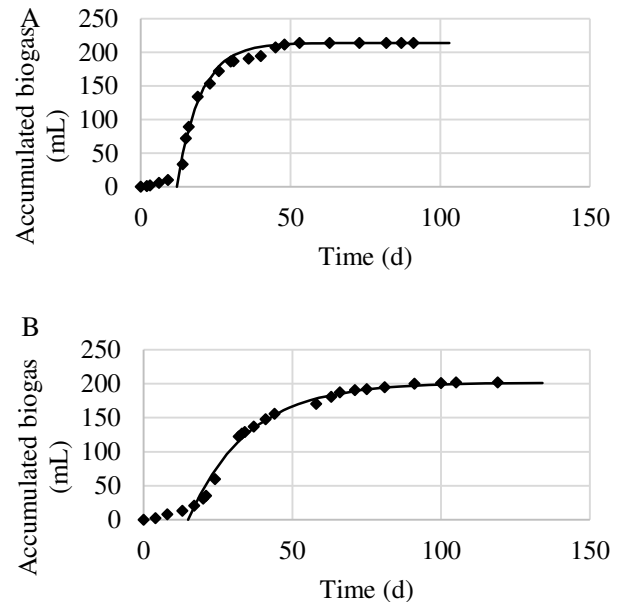


Figure 3. Batch test data and fitted line for 35 °C (A) and 23 °C (B) used to calculate k_{hyd} .

The average hydrolysis factor for sludge is $k_{hyd} = 0.183$ at 35 °C (Batstone et al., 2002). The k_{hyd} values for cow manure used here are therefore changed by multiplying the various coefficients for sludge with the factor $0.13/0.183$ at 35 °C to: $k_{hyd, ch} = 0.18$ from $0.25 d^{-1}$, $k_{hyd, li}$ to 0.07 from 0.1 and $k_{hyd, pr}$ to 0.14 from $0.2 d^{-1}$ for all the simulations. The k_{hyd} values are similarly adjusted down for the lower temperatures with relative factors of 1 at 35 °C, 0.74 at 30 °C and 0.47 at 25 °C which is almost identical to the temperature effect found by Donoso-Bravo et al. (2009) for carbohydrates (Table 3).

The batch results (Fig. 3) also confirms that temperature influence AD kinetics much more than stoichiometry (k_{hyd} is reduced by 60 % while yield by 4 % at 23 °C compared to at 35 °C).

3.2 AD sludge bed reactor data input to the model

The biogas production and effluent concentrations of the pilot AD are presented with the simulated results in Figure 5 - 6 during the given load and temperature step changes (Fig. 4). Some scattering in measured AD substrate composition may be due to real, uncontrolled, fluctuations in the influent with seasonal and other

changes in farm operation. Sampling and measurement errors are also likely on particle rich manure samples. Such fluctuations are reduced through the AD reactor, as expected. The inlet fluctuations are considered noise, so the inflow concentrations are therefore smoothed by median values, floating by the amount of samples indicated after each property, for $\text{NH}_4\text{-N}$ (20), COD_T (6), COD_S (4), acetate (20), propionate (20) and butyrate (20).

Table 6. Substrate inflow content to the AD reactor in the simulation.

Parameter	Content	Formula	Denominator
X_c	composite	0	g COD L ⁻¹
X_pr	protein	$f_{pr} \cdot 0.11 \cdot (\text{COD}_T - \text{COD}_S)$	g COD L ⁻¹
X_li	lipid	$f_{li} \cdot 0.11 \cdot (\text{COD}_T - \text{COD}_S)$	g COD L ⁻¹
X_ch	carbohydrates	$f_{ch} \cdot 0.11 \cdot (\text{COD}_T - \text{COD}_S)$	g COD L ⁻¹
X_I	solid inert	$0.86 \cdot (\text{COD}_T - \text{COD}_S)$	g COD L ⁻¹
S_I	soluble inert (from solid)	$0.03 \cdot (\text{COD}_T - \text{COD}_S)$	g COD L ⁻¹
COD_T	total	50.6 ± 2	g COD L ⁻¹
COD_S	soluble	13.9 ± 2	g COD L ⁻¹
S_I	soluble inert (from liquid)	$0.1 \cdot (\text{COD}_S - \text{COD}_{VFA})$	g COD L ⁻¹
S_su	sugar	$0.18 \cdot f_{ch} \cdot (\text{COD}_S - \text{COD}_{VFA})$	g COD L ⁻¹
S_aa	amino acids	$0.18 \cdot f_{pr} \cdot (\text{COD}_S - \text{COD}_{VFA})$	g COD L ⁻¹
S_fa	long chain fatty acids	$0.18 \cdot f_{li} \cdot (\text{COD}_S - \text{COD}_{VFA})$	g COD L ⁻¹
S_ac	acetic acid	3.3 - 3.6	g COD L ⁻¹
S_pro	propionic acid	1.44 - 1.50	g COD L ⁻¹
S_bu	butyric acid	0.64 - 0.65	g COD L ⁻¹
S_IC	HNO_3^-	0.058	M
S_IN	$\text{NH}_4 + \text{NH}_3$	0.07 ± 0.001	M

The reactor was started more than two years before the test period used here. Simulations of a preliminary period (340 days before the results presented here) were used to adjust pH and CO_2 concentration of the biogas

and thereby establish model steady state conditions that correspond to that observed at what is defined as time zero in this study (Fig. 5 and 6). The CO_2 concentration in the biogas was adjusted by adding a constant inflow substrate HCO_3^- level (Table 6). The modeled effluent pH level was forced to match measured values by adjusting the addition of a constant concentration of ions in the inflow substrate. The active reactor biomass concentrations were also tuned to match steady state performance, found to add up to a level below 10 g COD L⁻¹ reactor. This is well below the upper limit of 40 g COD L⁻¹ reactor for sludge bed AD (Kleerebezem et al., 2006).

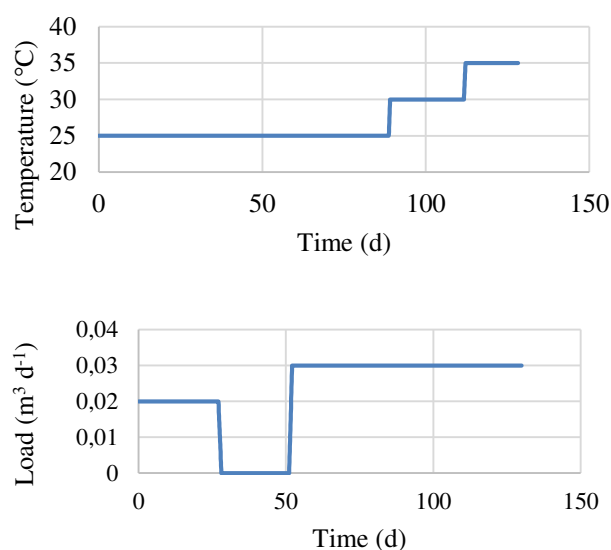


Figure 4. Temperature (°C) and load (m³ d⁻¹) during the experiment.

3.3 Simulation of AD reactor

Sludge retention time (SRT), a key factor in sludge bed AD processes is evaluated and quantified first to have a SRT calibrated model to investigate temperature effects next.

3.3.1 Sludge retention time

The process simulation is observed to be highly dependent on SRT, a parameter that is unknown and uncontrolled in most sludge bed reactors such as tested here. The simulated gas production has a good fit to the experimental values (Fig. 5 A) independent of SRT modelling approach at steady state. The model's ability to predict process changes, however, was quite different depending on SRT. SRT has the largest effect on the effluent acetate concentration, with SRT calculated from $\text{tres}_x = 20$ being closest to the experimental values. The recommended way of simulating SRT using $\text{tres}_x = 40$ (Batstone et al., 2002) has the lowest fit to the experimental values for biogas production but good fit to the acetate concentration. The observation that SRT influence acetate, the reactant for most of the methane production, especially, suggests that

methanogenesis can be especially sensitive to load transitions and SRT.

SRT is calculated using $tres_x = 15$, since it gave the best correlations, for the remaining simulations to evaluate the impact of the various temperature corrected kinetic constants. A lower $tres_x$, implying lower SRT than that proposed by Batstone et al. (2002) seem reasonable for the present case since HRT was higher than typical for sludge bed AD.

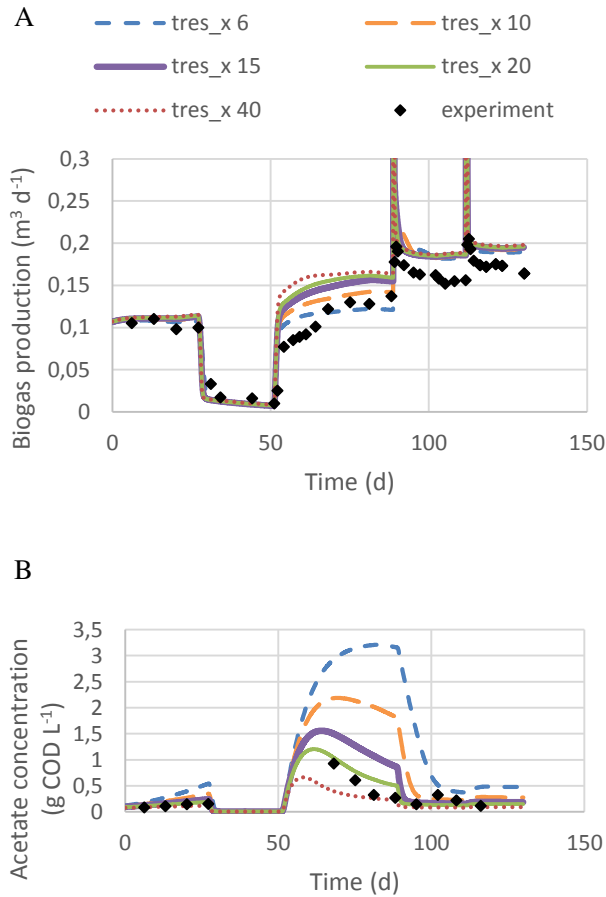


Figure 5. Biogas production rate (A) and effluent acetate concentrations (B) using temperature dependency from Henze and Harremoës (1983). Experimental (diamond) and simulated (lines).

3.3.2 Temperature effects

The simulated biogas production and effluent concentrations (Fig. 6) for the various temperature models shows good fit to the measured values. The various temperature effect parameters (Donoso-Bravo et al., 2009; Rebac et al., 1995; Henze and Harremoës, 1983) differ most in simulating acetate concentrations, but less on the overall biogas production rate.

The simulated transient peaks in biogas production following temperature increases are in the same range as observed (Fig. 6). Peak shape depends, however, on numeric also: Step size in the simulation below 0.001

day gives reasonable fit (Fig. 6). Larger model numerical step size overestimates this initial peak. The experimental temperature steps lasted for 0.4 and 0.5 days from 25 to 30 °C and 30 to 35 °C, respectively.

The three simulations “H”, “D” and “R” gave the same biogas production except for “H” at 30 °C which coincidence with the original ADM1 model. The original model gave higher biogas production at both 25 °C and 30 °C but similar to the others at 35 °C as expected (Fig. 6).

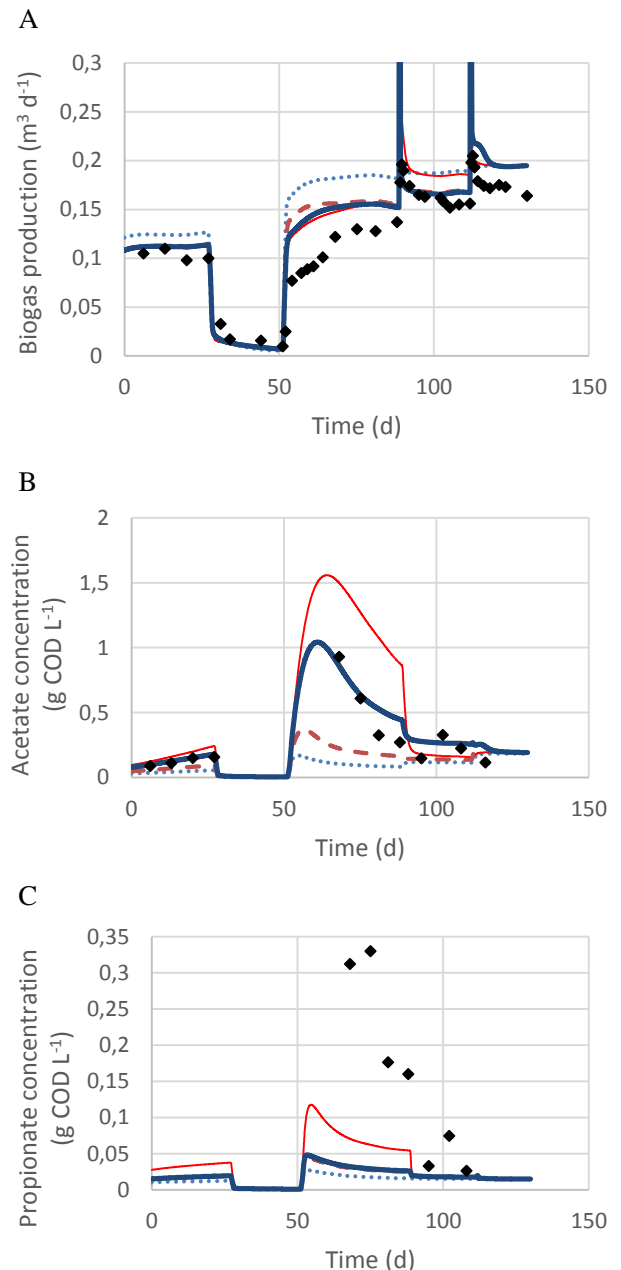


Figure 6. Biogas production rate (A) and effluent acetic (B) and propionic (C) concentration values temperature dependency using original model, Rebac et al. (1995), Donoso-Bravo et al. (2009), Henze and Harremoës (1983) with $tres_x = 15$ d. Experimental (♦) and simulated (lines); original , D ---, H —, R —

The biogas production, relative to 35 °C, from simulation and experimentally (Table 7) shows that the simulated relative temperature change for “H” is less affected by temperature than the published biogas production temperature effect used to adjust the kinetic factors (Table 2). This approach with the same temperature factor on each biochemical reaction is however better than the original model, but with less accuracy than using individually temperature effects for each reaction as for “R”.

Table 7. Simulation and experimental results on the temperature effect on biogas production rate.

Model	25 °C	30 °C	35 °C
R	0.79	0.85	1
D	0.81	0.86	1
H	0.80	0.95	1
Original model	0.95	0.97	1
AD experiment	0.77	0.92	1

The tested temperature model parameters using the simulation “R” is predicting the key intermediate, acetate, best. Significant deviations are only found in the simulations of the intermediate product propionate (Fig. 6) with elevated propionate following the load increase. The predictions are less than half of that observed. Note, however, that these levels are low and close to detection limit for propionate. Simulated overall soluble and particulate organic carbon removal and pH are close to measured values.

The original ADM1 model with only temperature correction for physio-chemical reactions did not simulate the observed temperature effects as well as the new version made here to also include temperature effects on the bio-reactions. It did however predict the transient gas production peak as well as the extended model, implying that this peak has a physical explanation. It is explained by reduced solubility of gasses with increased temperature causing gas release.

The elevated transient acetate suggests that methanogenesis is the rate-limiting step of the process investigated here, but the results are not conclusive except during the transient response to the step load increase (Fig. 5 - 6). It is normally either the disintegration, hydrolysis, degradation of propionic acid or the methanogenesis that is the limiting AD reaction (Batstone et al., 2002). The temperature effects on biogas production rate reported by Henze and Harremoës, (1983) may indicate hydrolysis as the rate-limiting step and not the methanogenesis for substrates with high particulates content (such as is the case in manure). The relatively small fraction of particles degraded in our experiment may however change this, possibly making methanogenesis the rate limiting

process step. This analysis does, therefore, not revealed which biochemical step is rate-limiting during the various phases of the experiment. It can, however, be argued that it is not important to know which step is rate limiting as long as appropriate temperature corrections are applied on the kinetic parameters of all the potentially rate-limiting steps. The reasonably good fit with experimental observations supports this claim.

4 Conclusion

The calibrated model, using recommended ADM1 parameters with standard temperature effect models, yields good fit of simulated and measured biogas production. Simulated overall soluble and particulate organic carbon removal, pH and intermediate products accumulation are also close to measured values. The main deviations between measured and modeled values, observed in transient acetate accumulations, were sensitive both to sludge retention time (SRT) and temperature effect modeling. Temperature effects on microbial substrate uptake rate kinetics accounts for the observed steady state gas generation levels.

Implementing individual temperature effects for each biochemical reaction gave the best fit for both biogas production and effluent acetate concentration. The original ADM1 model did not simulate the observed temperature effect as well as the modified models. All the modified models confirmed the experimental observation that temperature has a moderate influence on steady state biogas production in sludge bed AD (1.6 % reduced production per degree at 35 – 30 °C and 3.4 % per degree at 30 – 25°C). It is not revealed which biochemical step is rate-limiting but that seems irrelevant in ADM1 simulations.

The influence of temperature on steady state biogas production in the sludge bed AD was predictable using standard modeling parameters and moderate (1.6 % per degree at 30 – 35 °C and 3.4 % per degree at 25 – 30 °C). This imply that the net energy gain can peak at T < 35 °C in some cases and that such maxima can be found by the temperature extended ADM1.

Acknowledgements

The project was supported by the Norwegian Agricultural Agency, Innovation Norway, The Research Council of Norway, Ministry of Education and Research and Telemark University College. The authors wish to thank farmer Knut Vasdal for the good cooperation in carrying out the experiment and Associate Professor Finn Haugen for the automatic process monitoring and control.

References

Banik, G., Viraraghavan, T., Dague, R. (1998). Low temperature effects on anaerobic microbial kinetic

- parameters. *Environmental Technology*, 19(5), 503-512.
- Batstone, D., Keller, J., Angelidaki, I., Kalyuzhnyi, S., Pavlostathis, S., Rozzi, A., . . . Vavilin, V. (2002). *Anaerobic Digestion Model No. 1 (ADM1)*. Tech. rep., IWA Publishing.
- Bergland, W., Dinamarca, C., Bakke, R. (2014). Efficient biogas production from the liquid fraction of dairy manure. *Renewable Energy & Power Quality Journal (RE&PQJ)*, 12.
- Bergland, W., Dinamarca, C., Toradzadegan, M., Nordgård, A., Bakke, I., Bakke, R. (2015). High rate manure supernatant digestion. *Water Research*, 76, 1-9.
- Donoso-Bravo, A., Retamal, C., Carballa, M., Ruiz-Filippi, G., Chamy, R. (2009). Influence of temperature on the hydrolysis, acidogenesis and methanogenesis in mesophilic anaerobic digestion: parameter identification and modeling application. *Water Science and Technology*, 60(1), 9-17.
- Grant, S., Lin, K. (1995). Effects of temperature and organic loading on the performance of upflow anaerobic sludge blanket reactors. *Canadian Journal of Civil Engineering*, 22(1), 143-149.
- Hafner, S., Bisogni, J. (2009). Modeling of ammonia speciation in anaerobic digesters. *Water Research*, 43(17), 4105-4114.
- Haugen, F., Bakke, R., Lie, B. (2013). Adapting Dynamic Mathematical Models to a Pilot Anaerobic Digestion Reactor. *Modeling, Identification and Control*, 34(2), 35-54.
- Henze, M., Harremoes, P. (1983). Anaerobic treatment of wastewater in fixed film reactors - A literature review. *Water Science and Technology*, 15(8-9), 1-101.
- Hinshelwood, C. (1947). *The Chemical Kinetics of the Bacterial Cell*. London: Oxford University Press.
- Kettunen, R., Rintala, J. (1997). The effect of low temperature (5-29 degrees C) and adaptation on the methanogenic activity of biomass. *Applied Microbiology and Biotechnology*, 48(4), 570-576.
- Kleerebezem, R., van Loosdrecht, M. (2006). Critical analysis of some concepts proposed in ADM1. *Water Science and Technology*, 54(4), 51-57.
- Lin, C., Noike, T., Sato, K., Matsumoto, J. (1987). Temperature characteristics of the methanogenesis process in anaerobic-digestion. *Water Science and Technology*, 19(1-2), 299-310.
- Monod, J. (1949). The Growth of Bacterial Cultures. *Annual Review of Microbiology*, 3, 371-394.
- Møller, H., Sommer, S., Ahring, B. (2004). Methane productivity of manure, straw and solid fractions of manure. *Biomass & Bioenergy*, 26(5), 485-495.
- Pavlostathis, S., Giraldo-Gomez, E. (1991). Kinetics of anaerobic treatment: A critical review. *Critical Reviews in Environmental Control*, 21(5-6), 411-490.
- Rebac, S., Ruskova, J., Gerbens, S., Vanlier, J., Stams, A., Lettinga, G. (1995). High-rate anaerobic treatment of waste-water under psychrophilic conditions. *Journal of Fermentation and Bioengineering*, 80(5), 499-506.
- Saravanan, V., Hemachandran, B., Raj, A., Sundaram, S. (2000). Liquid phase volumetric mass transfer coefficient in dairy effluent stream. *Bioprocess Engineering*, 23(2), 175-176.
- Vavilin, V., Lokshina, L., Rytov, S., Kotsyurbenko, O., Nozhevnikova, A., Parshina, S. (1997). Modelling methanogenesis during anaerobic conversion of complex organic matter at low temperatures. *Water Science and Technology*, 36(6-7), 531-538.
- Veeken, A., Hamelers, B. (1999). Effect of temperature on hydrolysis rates of selected biowaste components. *Bioresource Technology*, 69(3), 249-254.

Simulation of gasification of livestock manure with Aspen Plus

Hildegunn H. Haugen¹ Britt M. Halvorsen¹ Marianne S. Eikeland¹

¹Faculty of Engineering and Technology, Telemark University College, Norway
Hildegunn.H.Haugen@hit.no

Abstract

Gasification is a flexible technology where all types of organic waste including biomass from manure can be used as feed to the reactor. The recovery of energy from solid waste offers several benefits including substantial reduction in the total quantity of waste and reduction in environmental pollution. The most suitable application of the product gas from the reactor is dependent on the quality and composition of the gas.

In this study, gasification of manure and wood chips is simulated. In the gasification process, the carbonaceous feedstock is fluidized with steam at 850°C. The simulations are performed using Aspen Plus. The focus has been to study the heating values and the fractions of the different components in the product gas. The results are discussed and different modifications of the process parameters in the simulations are considered. Sensitivity analyses with respect to the steam to biomass ratio have been performed.

Keywords: Gasification, livestock manure, biomass, Aspen Plus

1 Introduction

Biomass is a renewable energy resource. Depletion of fossil fuels reserves and environmental issues requires optimal utilization of biomass to replace use of fossil fuels (Wang et al, 2010). Production of renewable energy from livestock manure gives reduction in emissions of greenhouse gases as methane and nitrogen monoxide. In addition, more energy from renewable resources are produced (Triolo et al, 2013).

Intensified livestock industry and increased consumption of meat and animal products gives surplus of animal manure. This surplus can be used as an energy resource. The main part in animal manure is animal slurry (feces and urine). In addition the manure can contain sand, cleaning water, bedding materials (straw and branches). The quality of the manure depends also on how it is handled, diets and type of livestock (Triolo et al, 2013).

The conventional way to handle animal slurry for energy purposes is wet fermentation. Direct combustion is not so appropriate for most animal manures since the dry matter content in the sample is too low. To enrich

the dry matter content, the liquid fraction needs to be separated from the solids. This manure can be separated into solid and liquid in the farmhouse by different practical solutions. Mechanical separation is a common separation technique. Dry matter, phosphorous and nitrogen are separated from the slurry fractions (Hjorth et al, 2011).

The main aim of this study is to use Aspen Plus for simulation of biomass gasification (Doherty et al, 2013). Combustion, pyrolysis and gasification can be used to convert biomass into energy product (Wang et al, 2010).

The gasification process is simulated as a steam blown dual fluidized bed reactor at atmospheric pressure. The application of the product is determined based on composition of the product gas.

2 Biomass gasification

Gasification of biomass is a thermochemical process that gives gaseous products. Carbonaceous materials in the biomass are converted into gaseous products with acceptable heating values. The produced gas can be used in gas engines or turbines to produce electricity or in production of liquid fuel for transport. (Ptasinski et al, 2007).

Energy is stored in biomass, since plants absorb energy from the sun through the photosynthesis process. Biomass sources can be woody plants, agriculture plants, sludge and manure. The different types of biomass have different heating values, chemical compositions, moisture content and ash content. Organic matter in the biomass shows small variations. The difference in moisture content and ash content are normally large. Manure can contain an essential part of water. To avoid a low gasification efficiency, the moisture content in the biomass needs to be reduced before gasification. (Ptasinski et al, 2007).

3 Biomass feed

Biomass values used for studying the gasification are proximate analysis and ultimate analysis of pig manure and poultry manure (Xiao et al. 2008), (Font-Palma, 2012). Data from gasification of wood chips are used for model validation (Doherty et al, 2013).

Xiao et al. have carried out experimental studies using pig manure. The raw pig manure was mechanically pretreated to separate feces and urine and then composted for two weeks. Samples used for

gasification was dried, crushed and assorted in different sizes. The size fraction used for gasification was 0.5 – 1.0 mm. Characteristics of pig manure samples are presented in Table 1.

Poultry manure consists of manure and litter from chicken production. The organic matter in the manure is high and makes it suitable for gasification. The concentrations of potassium (K), calcium (Ca) and

phosphorous (P) in the ash is also high and are therefore suitable as fertilizer in the agriculture production (Font-Palma, 2012). Values used in the simulation are presented in Table 1. Doherty et al present proximate and ultimate analysis for wood chips.

Table 1. Characteristics of pig manure, poultry litter and wood chips.

<i>Components</i>	<i>Pig manure</i> (Xiao et al. 2008)	<i>Poultry manure</i> (Font-Palma, 2012)	<i>Wood chips</i> (Doherty et al, 2013)
<i>Proximate analyses (wt %)</i>			
Volatile matter	65.78	64.97	80
Fixed carbon	16.07	13.46	18.84
Ash	18.15	21.57	1.16
Moisture	21.61	27.4	20
<i>Ultimate analyses (wt %)</i>			
Carbon, C	36.45	37.05	51.19
Hydrogen, H	4.89	5.06	6.08
Oxygen, O	37.89	31.44	41.3
Nitrogen, N	4.52	3.66	0.2
Sulphur, S	0.88	0.45	0.02
Chlorine, Cl	-	0.97	0.05
Ash	15.36	21.37	1.16
Lower Heating Value, LHV [MJ/kg]	14.46	14.79	19.09

3.1 Gasification process

Gasification of biomass results in a mixture of combustible gases (Wang et al, 2010). Gasification converts the internal chemical energy of the carbon in the biomass into combustible gases (Puig-Arnavat et al). Biomass is heated in a gasifier at a high temperature with a controlled volume flow of oxidant (air, oxygen or steam). The produced gas includes hydrogen (H₂), carbon monoxide (CO), carbon dioxide (CO₂), methane (CH₄), water vapor (H₂O), nitrogen (N₂), higher hydrocarbons and impurities such as tars, ammonia (NH₃), hydrogen sulphide (H₂S) and hydrogen chloride (HCl) (Doherty et al, 2013). Gasification is in general a very complex process due to combination of different mechanisms like mass transfer, chemical reactions and heat transfer. Input values used for gasification

simulation are literature values from proximate and ultimate analyses.

The produced gas can reach different compositions and yields. Important factors are type of biomass, composition, type of oxidation agent, reaction temperature and pressure. (Wang et al, 2010). The chemistry in biomass gasification involves both biochemical and thermochemical reactions (McKendry, 2002). Simulations with Aspen Plus are based on the FICFB (Fast Internally Circulation Fluidized Bed) gasification process (Doherty et al, 2013). This model uses Gibbs free energy minimization method. It means that thermochemical processes for conversion of biomass is used to predict the composition of the producer gas (Doherty et al, 2013), (McKendry et al, 2002). If steam is used as gasification agent, the five chemical reactions showed in Table 2 can be considered.

Table 2. Chemical reactions in steam gasification of biomass, adapted from (Dorthey et al, 2013), (Thapa 2015)

Reactions	Chemical equations	Reaction type	$\Delta H_{R, 850}$ [kJ/mol]
Steam gasification	$C + H_2O \leftrightarrow CO + H_2$	Heterogeneous reaction	+118.5
Boundard	$C + CO_2 \leftrightarrow 2CO$	Heterogeneous reaction	+159.5
Methanation	$C + 2H_2 \leftrightarrow CH_4$	Heterogeneous reaction	-87.5
Water-gas shift	$CO + H_2O \leftrightarrow CO_2 + H_2$	Homogeneous reaction	-33.6
Methane reforming	$CH_4 + H_2O \leftrightarrow CO + 3H_2$	Homogeneous reaction	+ 225.5

The four main processes in the gasifier is drying, pyrolysis, combustion (oxidation) and gasification (reduction) (Doherty et al, 2013), (Kaushal, Priyanka et al., 2011). Figure 1 shows a schematic gasifier setup of a circulating fluidized bed gasifier.

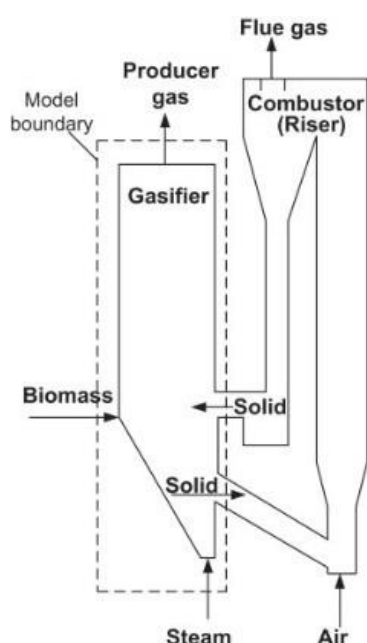


Figure 1 Schematic gasifier setup (Kaushal, Priyanka et al., 2011).

The typically moisture content in the biomass ranges from 5 – 35%. Drying happens at a temperature of 100-200 °C and reduces the moisture content to < 5% (Dorthey et al, 2013). The moisture content changes phase from liquid to gas. In addition to the added steam, the moisture contributes to the reactions in the gasifier. Pyrolysis happens at a temperature of (200-500 °C). Here the biomass is devolatilized to char and volatile gases. Gasification and combustion reactions are physically separated, to produce a producer gas with a low content of nitrogen (Dorthey et al, 2013). Typically, temperatures in the gasifier is 800-900 °C. The gasification takes place in a fluidized bed and the main reactions taking place are described in table 2. The bed

material is circulated to the combustor where carbon attached to the bed material surface is burned off. Flue gas is removed. Hot bed material is recirculated back to the gasifier. The hot bed material supply the gasifier with necessary heat to the endothermic reactions.

4 Aspen plus simulation

The Aspen Plus model used in the simulation is based on the work of Doherty and described in more details by Doherty et al, 2013. In the simulation performed, pig and poultry manure are used as feed, but simulation with wood chips has also been performed to compare our model with the model of Dorethy et al 2013. Deviations is observed in the results with wood chips from the two models. The difference is due to the definition of the conversion of non-conventional components to conventional components in the first unit operation.

The stream class used in Aspen Plus is MIXCISLD, implying streams of gas mixture and solid carbon. The property method used is Redlich-Kwong-Soave (RKS) cubic equation of state with Boston-Mathias alpha function (RKS-BM).

The following assumptions were made for the Aspen simulation (Dorthey et al, 2013):

- The system is isothermal and operates under steady state conditions.
- Operation at atmospheric pressure, pressure drops are neglected.
- Tar formation is not considered.
- Char is 100% carbon.
- Heat loss from the gasifier is neglected.

4.1 Flow Sheet

The Aspen Plus flow sheet used in the simulation is presented in Figure 2 and is based on the model described by Doherty et al, 2013. The 'MANURE' is defined as a non-conventional stream and the ultimate and proximate analyse is given in Table 1. The thermodynamic condition for the manure stream was specified to 25 °C and 1 bar.

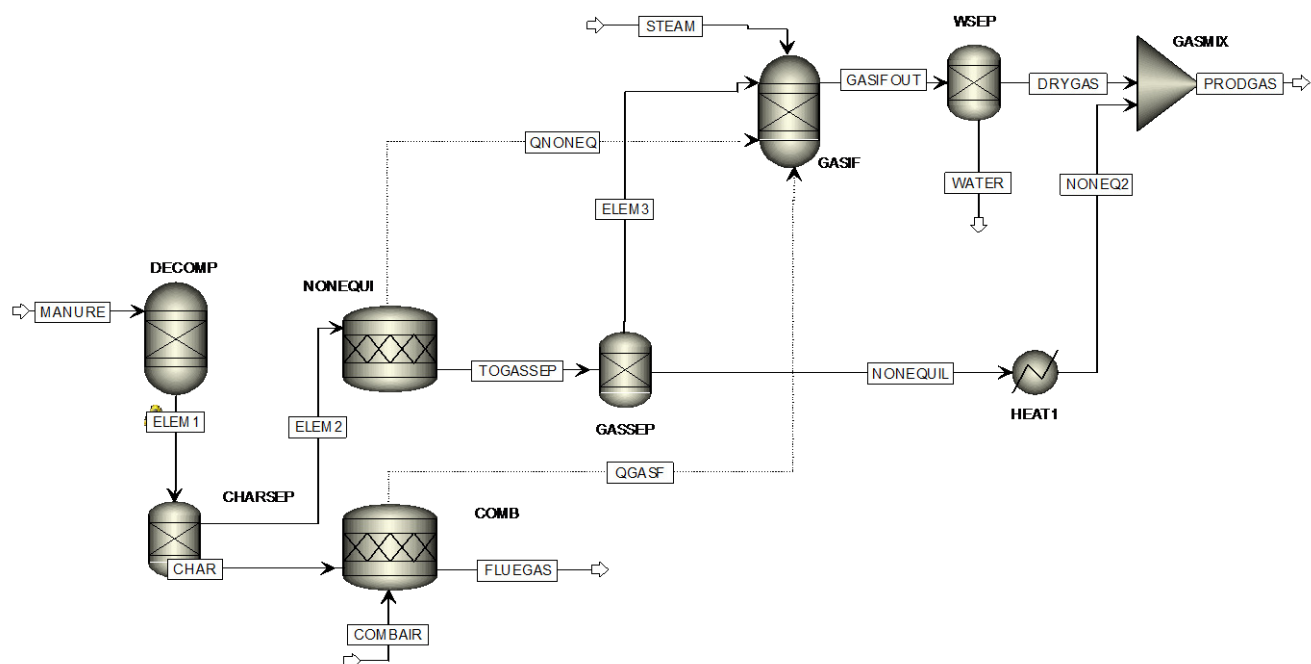


Figure 2. The Aspen Plus flow sheet.

In the RYield reactor 'BRKDOWN' the non-conventional components convert to conventional components. It is assumed that all hydrogen in the non-conventional component are converted to H_2 , all oxygen are converted to O_2 , all nitrogen are converted to N_2 , all chlorine are converted to Cl_2 , sulphur to elementary S and carbon to elementary C. The conversion are set using a calculator block (Doherty et al, 2013, Aspen tech, 2010). The outlet stream 'ELEM1' are fed to 'CHARSEP' where a portion of the char and all ash are separated out. The char and ash are directed to a combustion reactor RStoic titled 'COMB'. The air stream 'COMBAIR' is also fed to the same block. The air and char react, and the heat produced in this reactor is available for the gasification reactor by the heat stream 'QGASIF'. The char split fraction is set using a design specification, and varied until the temperature in the gasification reactor 'GASIF' is $850^\circ C$. The 'FLUEGAS' is the exhaust gas from the combustion process.

The material stream 'ELEM2' is directed to an RStoic reactor 'NONEQUIL' where all the nitrogen gas, chlorine gas and sulphur are converted to ammonia (NH_3), hydrogen chloride (HCl) and di hydrogen sulfide (H_2S) by the reaction with hydrogen. The stoichiometric reactions are defined in Table 3.

The heat produced in these reactions is made available for the gasification reactor by connecting the two blocks with the heat stream 'QNONEQ'. NH_3 , HCl and H_2S are removed from the main fuel stream by the separator 'GASSEP'.

'ELEM3' is the main flow stream that is fed to the gasifier 'GASIF' which is a RGibb reactor. This stream contains mainly carbon, H_2 , O_2 and water. Steam is also added to the 'GASIF' to gasify the manure and fluidise the bed. Reactions described in Table 2 is added in the RGibb reactor. After the RGibb reactor, water is removed in a separator 'WSEP' to determine the gas composition on a dry basis.

Table 3 Reactions for nitrogen, sulphur and chlorine (Doherty et al, 2013)

Chemical element	Formation reactions
Nitrogen, N_2	$0.5N_2 + 1.5H_2 \leftrightarrow NH_3$
Sulphur, S_2	$S + H_2 \leftrightarrow H_2S$
Chlorine, Cl_2	$Cl_2 + H_2 \leftrightarrow 2HCl$

Information of the process parameters are given in Table 4. The steam flow is given with a steam to biomass (e.g. manure) ratio (STBR) of 0.4. The STBR is defined as the mass flow rate of biomass moisture plus injected steam divided by the dry biomass flow rate (Doherty, 2013). The steam temperature is set to $450^\circ C$ and the pressure is 1 bar.

The stream 'NONEQUIL' is heated in a heater 'HEAT1' to make it possible to mix the 'DRYGAS' with NH_3 , HCl and H_2S in 'GASMIX' to 'PRODGAS'.

Table 4. Process parameters used in Aspen Plus simulation.

	<i>Pig</i>	<i>Poultry</i>	<i>Wood chips</i>
Manure in pr. reactor [kg/h]	1000	1000	1000
STBR	0.4	0.4	0.4
Steam in reactor [kg/h]	97.46	16.40	120
Reactor temperature [°C]	850	850	850
Reactor pressure [bar]	1	1	1

5 Results and Discussion

The feed compositions of the pig and poultry manures are presented in Table 1. The proximate analysis shows that the poultry manure has a higher moisture and ash content and lower content of fixed carbon compared to pig manure. Wood chips has higher concentration of volatile components, more fixed carbon and significantly lower content of ash. The ultimate analyses show that the concentration of carbon in pig manure and poultry manure is approximately the same. The main difference between the two types of manure is that the pig manure has higher oxygen concentration and the poultry manure has higher ash content. Wood chips have significantly higher concentration of carbon compared to the manures. The content of nitrogen, sulphur, chlorine and ash are low in wood chips. The measured LHV of pig manure, poultry manure and wood chips are 14.46, 14.79 and 19.09 MJ/kg respectively.

Table 5 presents the results from simulations using pig manure, poultry manure and wood chips on dry and ash free basis as feed to the gasification process.

Table 5. Results of the main components after gasification

<i>Components</i>	<i>Pig (sim¹)</i>	<i>Poultry (sim¹)</i>	<i>Wood Chips (sim¹)</i>
CH ₄ (vol % dry basis)	0	0.04	0.14
CO (vol % dry basis)	42.86	32.40	39.72
CO ₂ (vol % dry basis)	5.36	9.42	5.18
H ₂ (vol % dry basis)	45.75	53.20	54.77
NH ₃ (ppm dry)	55605	42527	1721
H ₂ S (ppm dry)	4729	2284	75
HCl (ppm dry)	na ²	4453	170
LHV [MJ/m ³]	10,34	9.83	10,97
Gasification temperature [°C]	850	850	850

¹sim = simulated, ²na = not available.

Result from simulations shows that gasification of pig manure and poultry manure, and wood chips gives about the same lower heating values. The product gas from gasification of pig manure has higher CO and lower H₂

content compared to the product gas from the poultry manure. The concentration of CH₄ are insignificant for all cases, which is favourable for downstream processing to bio fuel. The gas composition from woodchips is comparable with the gas composition of the manures, but have higher H₂ concentration than pig manure and higher CO concentration than poultry manure.

Comparison of the product gas from manures shows that the pig manure gives higher concentration of NH₃ and H₂S than the poultry manure. Since the poultry manure has a certain content of Cl, the product gas also includes HCl. It is necessary to remove HCl, NH₃ and H₂S from the product gas if further processing to other specified products.

Table 6 shows typical dry composition of producer gas from the Guessing steam gasification process, which is based on wood chips (Pröll, T *et al*, 2004)

Table 6. Typical dry composition of producer gas from the Guessing steam gasification process (Pröll, T *et al*, 2004).

<i>Components</i>	<i>Experimental values</i>
CH ₄ (vol % dry basis)	10...11
CO (vol % dry basis)	24...26
CO ₂ (vol % dry basis)	20...22
H ₂ (vol % dry basis)	38...40
Others (vol % dry basis)	1...8
LHV [MJ/m ³]	12.9-13.6
Gasification temperature [°C]	850

Significant variations in the gas composition are observed when comparing the steam gasification process in Güssing with the simulations. Especially in the real plant, a significant amount of CH₄ obtained. In the simulation, the concentration of H₂ and CO reaches higher values than in a real plant, whereas the CO₂ content is lower. The simulation of the gasifier uses Gibbs reactor, which applies Gibbs free energy minimization to calculate equilibrium. The reactions in the gasification process are complex and by using the Gibbs reactor, it is not necessary to specify the stoichiometry or the reaction rates. However, this will also imply that considerations due to reactions kinetics are not evaluated.

Sensitivity analysis for pig and poultry manure and wood chips are performed using Aspen Plus. The reactor temperature is 850 °C. Figures 3 to 5 shows the steam to biomass ratio (STBR) as function of volume fraction of CH₄, CO, CO₂ and H₂ in the produced gas.

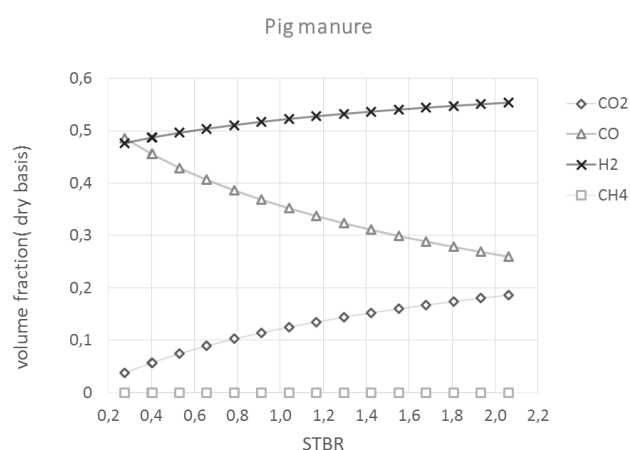


Figure 3. STBR as a function of volume fraction (dry basis) of CH₄, CO, CO₂ and H₂ for pig manure.

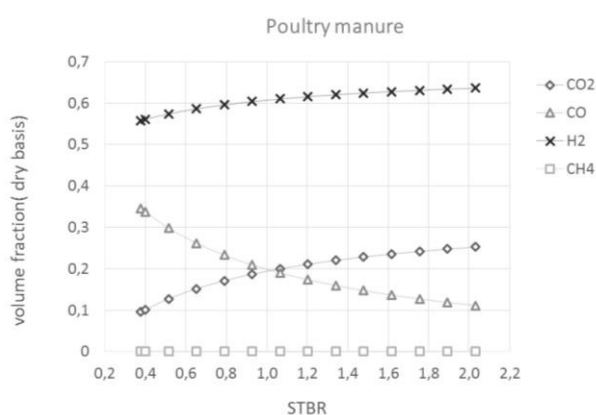


Figure 4. STBR as a function of volume fraction (dry basis) of CH₄, CO, CO₂ and H₂ for poultry manure.

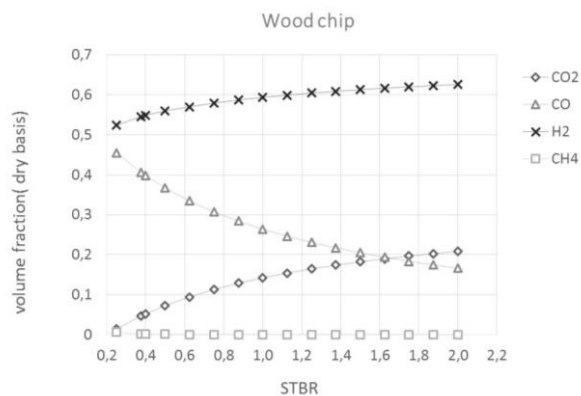


Figure 5. STBR as a function of volume fraction (dry basis) of CH₄, CO, CO₂ and H₂ for wood chips.

All types of biomass show the same trend regarding the gas composition. H₂ and CO₂ concentrations increase with increased STBR. CO and CH₄ decrease with increased STBR. Poultry manure gives the highest H₂ production, and the lowest CO content, while pig manure gives highest CO content, and lowest H₂ production. The CO₂ content is highest for the poultry manure.

From the reaction equations given in Table 2, an increase in the steam will give a reduction in CO concentration and an increase in the CO₂ concentration due to the water gas shift reaction. The figures show that a ratio of CO/CO₂ equal to 1 will take place at different STBR. For pig manure, this will be at a STBR at 2.8, for poultry manure at 1.0 and for wood chips at 1.6. This ratio is for all cases at a CO concentration of approximately 20 vol %.

Depending of the application of the produced gas the composition of the product is crucial. For production of chemicals for instant methanol, a ratio of H₂/CO of 1 is preferable, for other products the ratio differ. For production of heat and power, a high concentration of combustible gases is desirable. Related to the simulation given here, a low STBR is preferred.

6 Conclusion

Pig and poultry manures, together with woodchips, have been simulated in Aspen Plus based on the FICFB (Fast Internally Circulation Fluidized Bed) gasification process (Doherty et al, 2013). A model is developed using the Gibbs free energy minimization method to consider the possibility of using different types of biomass in a gasification process. Pig and poultry manures, together with woodchips, have been simulated in Aspen Plus to consider the possibilities to use different types of biomass in a gasification process.

The simulations of the gasification process with the three types of biomasses give comparable results regarding gas composition. Pig manure gives the highest CO concentration, while wood chips give the highest H₂ concentration. The lower heating value of the product gas is also comparable for the biomasses. Manure has relatively high concentration of NH₃ and H₂S and needs further cleaning processes compared to wood chips. This will give higher production costs.

Sensitivity analyses to study the composition of the produced gas as a function of steam to biomass ratio (STBR) show all an increase in H₂ and CO₂ concentrations and a decrease in CO concentration, with increasing STBR as expected.

References

- Aspen tech, Aspen Plus Getting Started Modeling Processes with Solids. Version Number: V7.2 July 2010
- Doherty, Wayne, Reynolds A., Kennedy D. Aspen plus simulation of biomass gasification in a steam blown dual technological developments, A. Méndez-Vilas (Ed.), Formatex Research Centre, pp. 211-220, 2013.
- Font-Palma, Carolina, kinetics and modelling of gasification of poultry manure and litter: An overview. Energy Conversion and Management Volume 53, Issue 1, January 2012, Pages 92–98. doi:10.1016/j.enconman.2011.08.017

- Hjorth, Maibritt, Christensen, K. V., Christensen, M. L., Sommer, Sven G., Solid-Liquid Separation of Animal Slurry in Theory and Practice, Sustainable Agriculture Volume 2, (953-986), 2011.
- Jarunghammachote, S., Dutta, A. Equilibrium modeling of gasification: Gibbs free energy minimization approach and its application to spouted bed and spout-fluid bed gasifiers. Science Direct, Energy Conversion and Management 49 (2008) 1345–1356.
- Kaushal, Priyanka, Proell, Tobias, Hofbauer, Hermann, Application of a detailed mathematical model to the gasifier unit of the dual fluidized bed gasification plant. Biomass and Bioenergy Volume 35, Issue 7, July 2011, Pages 2491–2498. doi:10.1016/j.biombioe.2011.01.025
- McKendry, Peter, Energy production from biomass (part 3): gasification technologies, Bioresource Technology, Volume 83, Issue 1, May 2002, Pages 55–63. doi: 10.1016/S0960-8524(01)00120-1
- Puig-Arnabat, Maria, Bruno, Joan Carles, Coronas Alberto. Review and analysis of biomass gasification models, Renewable and Sustainable Energy Reviews. Volume 14, Issue 9, December 2010, Pages 2841–2851. doi:10.1016/j.rser.2010.07.030
- Proell Tobias, Rauch Reinhard, Aichernig Christian, Hofbauer Hermann, Coupling of biomass steam gasification and an SOFC - gas turbine hybrid system for highly efficient electricity generation Proceedings of ASME Turbo Expo 2004: Power for Land, Sea, and Air June 14–17, 2004, Vienna, Austria
- Ptasinski, Krzysztof J., Mark Prins J., Pierik Anke. Exergetic evaluation of biomass gasification, Energy Volume 32, Issue 4, April 2007, Pages 568–574. doi:10.1016/j.energy.2006.06.024
- Thapa, Rajan Kumar. Optimization of Flow Behavior in Biomass Gasification Reactor. Doctoral Dissertation at Telemark University College, Faculty of Technology 2015:2, ISBN 978-82-7206-394-7.
- Triolo, Jin M, Pedersen, Lene, Sommer Sven G. Characteristics of Animal Slurry as a key biomass for biogas production in Denmark. pp. 307-326, 2013. doi.org/10.5772/54424
- Wang Lijun, Shabbazi, Milford, Hanna A. Characterization of corn stover, distiller grains and cattle manure for thermochemical conversion, 2010, Biomass and Bioenergy, Volume 35, Issue 1, January 2011, Pages 171–178. doi:10.1016/j.biombioe.2010.08.018
- Xiao, Xianbin, Dung, Duc Le, Li Liyun, Meng, Xianliang, Cao Jingpei, Morishita Kayoko, Takarad, Takayuki. Catalytic steam gasification of biomass in fluidized bed at low temperature: Conversion from livestock manure compost to hydrogen-rich syngas, 2010. doi.org/10.1016/j.biombioe.2010.05.001.

Modeling and simulation of Triclosan kinetics and distribution in humans using a PBPK model

Samee Maharjan[¶], Roshan Sharma[¶], Trine Husøy[‡], Hubert Dirven[‡], Monica Andreassen[‡], Bernt Lie[¶]
[¶] Telemark University College, Norway

[‡] Dept. of Food, Water and Cosmetics; Norwegian Institute of Public Health (NIPH)

Abstract

Triclosan is an antibacterial additive which is widely used in personal care products (PCPs) such as soaps, perfumes etc. Previous studies have indicated that triclosan might have potential to adverse effects on the human health. Some traces of triclosan are found in human plasma and milk at a concentration which is likely to be related to the use of PCPs.

In this study, a Physiologically Based Pharmacokinetic or Toxicokinetic (PBPK/TK) model is developed to assess the concentration of triclosan in human organs after exposure through the skin (dermal) or the oral canal. The absorbed chemical is metabolized in the liver and leaves as conjugates and then excreted through kidney in the urine. The simulation is done using MATLAB. Lastly, the developed model is fitted using least square techniques in MATLAB using synthetic data generated from the model itself with or without the addition of random noise.

Keywords: Triclosan, PBPK, Model fitting

1 Introduction

The excess use of chemicals in PCPs, it has attracted concern from pharmacists, chemists and environmentalists. Human exposure to common household chemicals is a potential health risk. Triclosan is one of these chemicals which are widely used as an antibacterial compound in cosmetic products. Triclosan is an off white chlorinated aromatic compound, which consists of two benzene rings linked by an oxygen atom, with three chlorine atoms and a hydroxyl group attached. It was first used in 1970s in hospitals since then become a widely used anti bacterial agent. While people who use triclosan products daily have higher levels of the chemical in their bodies, even consumers who do not use triclosan on their skin are exposed to it through food, water, and even household dust¹.

Physiologically Based Pharmacokinetic /Toxicokinetic (PBPK/TK) Models are commonly used in the pharmaceutical and toxicological sciences to understand the distribution of chemicals in the human body. Mathematically based differential equations are used to depict pharmacokinetic processes in terms of physiological and biochemical parameters. PBPK/TK

modeling can be taken as an example of using simple modeling technique for model development and then simulate accordingly. These models are widely used in the field of toxicology and risk assessment. In (Mielke & Gundert-Remy, 2012), three different case studies for two chemicals are presented. One case study is done for the effect of Bisphenol A on the newly born child, whereas other two are the assessing the concentration of Bisphenol A and Coumarin in the body organs through dermal penetration. For all three case studies a PBTK model is used with required physiological and chemical parameters. Basically these models described the distribution of a chemical, in the human organs according to its absorption, metabolism and excretion. The results from such simulations are basically the chemical concentrations that will eventually stay in the body after exposure and distribution to target organs for toxicity. A PBPK/TK model comprises the physiology of the body and the toxicokinetic properties of the chemical. It is not possible to determine the risk of the chemical based on the modeling. To do that we need real exposure data and compare this with the toxicity of the compound. If the human exposure are low, the risk is also low, independent of the knowledge of the distribution at a certain dose.

In this paper, we develop a PBPK/TK model for assessing the distribution of triclosan in the human organs after exposure through both the oral and the dermal route. In Section 2, a description of the system under study is given. In section 3, a detail of model development using species balance for each organ is shown. All the simulation results are given in Section 4 whereas sensitivity analysis and model fitting for uncertain parameters are discussed in Section 5. Lastly the results of the paper are discussed in section 6.

2 System Description

Studies show that after almost 2 hours of dermal application in rats, traces of triclosan are seen in the blood system. By 24 hours, 23 % of the applied dose appeared in blood whereas remaining dose is resided in the skin. Metabolism of triclosan mainly takes place in the liver but a small amount is also metabolized in the skin itself. The percentage of glucuronide are found to be higher than that of sulfate (4.1% vs. 0.9 % at 24 hrs) in blood, this suggests that most of the formed sulfate remains in skin but glucuronide diffuse more

¹ www.newsweek.com

² Outermost layer of skin.

readily into blood by virtue of hydrophilicity. Absorption of triclosan in the human skin is approximately 5 times slower than in the rats. This is because rats possess thinner stratum corneum² and larger number of hair follicles than humans (Moss, Howes, & Williams, 2000). For oral application, the triclosan dose is directly transported to the liver where metabolism takes place before entering the systemic circulation through first pass metabolism. Thus, the amount of free triclosan found in blood after oral exposure is less than the amount after dermal application for the same dose. The ratio between the two conjugates varies from species to species. Different studies show that for humans, almost all the applied dose is converted into conjugates with approximately 90% as glucuronides and 10% as sulfates. In contrast, 78-90% of the triclosan was found as sulfate conjugates in mice (Rodricks, Swenberg, Borzelleca, Maronpot, & Shipp, 2010). Triclosan excreted predominantly as its conjugates. Irrespective to the route of application, the major route of elimination in humans is through urine while in rats triclosan is excreted in faeces. Triclosan in rat will therefore undergo enterohepatic circulation³. In the intestine of rats the conjugated triclosan is de-conjugated by glucuronidases and sulphatases, and the free triclosan is re-absorbed (Moss et al., 2000).

Metabolism of Triclosan

The main metabolites of triclosan are the conjugation products triclosan sulfate and triclosan glucuronide Figure 1. The conjugation of triclosan is described as follows. A family of enzymes known as SULT (sulfotransferase) catalyze the transfer of a sulfonate group (-SO₃⁻) from PAPS (3-phosphoadenosine-5'-phosphosulfate) to triclosan, forming the conjugate triclosan sulfate with the release of PAP (3-phosphoadenosine-5-phosphate). Denoting triclosan by T and triclosan sulfate by TS, we can write the overall reaction as,

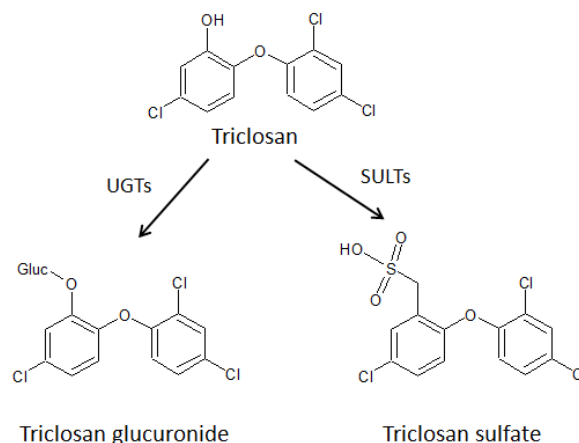
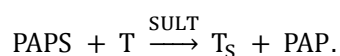
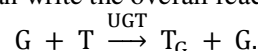


Figure 1: Metabolism of triclosan into glucuronides and sulfates (After Fang et al., 2010).

Similarly, an enzyme known as UGT (Uridine 5'-diphospho-glucuronosyl transferase = UDP-glucuronosyl transferase) catalyzes the transfer of the glucuronosyl acid component of UDP-glucuronic acid to triclosan, forming the conjugate triclosan glucuronide as well as a residual of UDP-glucuronic acid. Denoting UDP-glucuronic acid by G, the conjugate triclosan glucuronide by T_G, and the residual of UDP-glucuronic acid by \bar{G} , we can write the overall reaction as,



In both cases, triclosan (T, substrate) is absorbed on the enzyme surface and is inserted into the active site. Provided that triclosan has been absorbed into the active site, we assume that a co-substrate (PAPS or G) also is adsorbed at the active site, forming a substrate/co-substrate complex. Next, a reaction takes place in this complex formed at the active site, and conjugated triclosan (T_S or T_G) is formed together with a co-product (PAP or \bar{G}) and these then desorb from the active site. Under the conditions of constant enzyme concentration and constant co-factor concentration, the overall reaction rate referring to triclosan can be written as,

$$\hat{r}_j = \hat{r}_{\text{max}} \frac{c_T}{c_T + K_{T,j}},$$

where $[\hat{r}_j]$ is given in mole/(time and protein mass), and $j \in \{S, G\}$. The individual reaction rates are thus:

$$\hat{r}_\text{S} = \hat{r}_{\text{max,S}} \frac{c_T}{c_T + K_{T,S}}$$

$$\hat{r}_\text{G} = \hat{r}_{\text{max,G}} \frac{c_T}{c_T + K_{T,G}}$$

In (Wang, Falany, & James, 2004), the rate constants are given for human liver as From Table 1 it should be observed that the molar rates of generation are given as

$$\dot{n}_j^g = \hat{r}_j \cdot m_{P,j},$$

where $m_{P,j}$ is the relevant mass of protein in the liver. Sulfonation takes place in the human liver cytosol while glucuronidation takes place in the liver

² Outermost layer of skin.

³ the circulation of substances from the [liver](#) to the [bile](#), followed by entry into the [small intestine](#), absorption by the [enterocyte](#) and transport back to the liver.

microsomes. Due to the fact that sulfatation occurs in cytosol and glucuronidation occurs in membranes of the liver, the protein mass for the two enzymes would differ (Wang et al., 2004). These protein masses is needed because the \hat{r}_{max} and K_T is taken from human in vitro liver studies. If we had data from formation of conjugates in human blood, we would not need these factors.

Ideally, we would like to relate $m_{p,j}$ to the mass m_h of the liver as an organ instead (hepatic mass), in other words to ξ_j satisfying

$$m_{p,j} = \xi_j m_h .$$

In (Cubitt, Houston, & Galetin, 2009), the hepatic cytosolic scaling factor was found in the range $\xi_{h,s} \in \{45,134\}$ mg protein in liver cytosol per g of liver, with a mean weighted value $\xi_{h,s} = 80.7 \times 10^{-3}$. They also report a typical fraction protein in intestine cytosol per g intestine to be $\xi_{i,s} = 18 \times 10^{-3}$. It should be observed that the rate numbers given in Table 1 do not necessarily carry over from liver to intestine. In (Barter et al., 2007), experimental results are cited in the range $\xi_{h,G} \in \{19,77\}$ mg protein in liver microsomes per g of liver. The value probably varies among individuals, with age, and by gender. A possible useful value may be $\xi_{h,G} = 30 \times 10^{-3}$. In (Johnson, Tucker, Tanner, & Rostami-Hodjegan, 2005) variation in liver size (m_h) for humans is discussed.

Table 1: Michaelis-Menten reaction parameters for triclosan metabolism in human liver (Wang et al., 2004).

	$K_{T,j,li} \left[\frac{\mu\text{mol}}{\text{L}} \right]$	$\hat{r}_{max,j,li} \left[\frac{\text{pmol}}{\text{min mg protein}} \right]$
Sulfonation (S)	8.5 ± 3.2	95.1 ± 28.4
Glucuronidation (G)	107 ± 2.2	739 ± 163

3 Model development

Figure 2 illustrates the topology of a network of organs describing the transport of chemicals from its absorption through the skin and/or the GI tract to its excretion through the kidney. After absorbing chemical through the skin, triclosan along with its conjugates passes through the skin and mix with the central blood system.

The central blood system then transports these chemicals into almost every organ. The circulation process continues until the entire dose intake has been eliminated. The excretion of chemical is via the kidney through urine. Triclosan is relative hydrophilic and does not accumulate in the body and is rapidly metabolized and excreted. Thus we can assume that the membrane between tissue and capillary of an organ is of no barrier. For this kind of chemicals, their kinetics can be best described by a perfusion-rate-limited

kinetics. A single compartmental model is used for model development process.

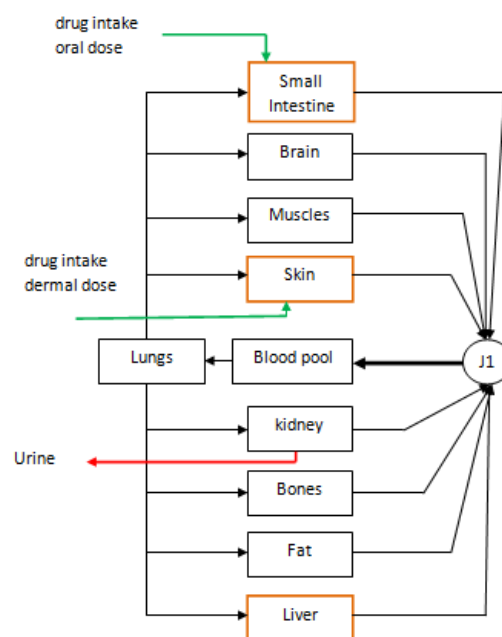


Figure 2: Flow of chemical intake (Beard, 2012).

Species Balance

The general species balance in molar form,

$$\frac{dn_j}{dt} = \dot{n}_j^i - \dot{n}_j^e + \dot{n}_j^g .$$

Here,

\dot{n}_j^g = Number of moles generated of species j.

\dot{n}_j^i = Influx number of moles per unit time of species j.

\dot{n}_j^e = Efflux number of moles per unit time of species j.

For non metabolic organs

The number of moles expressed in the form of concentration as,

$$\dot{n}_j^i = \dot{V}c_j^i$$

$$\dot{n}_j^e = \dot{V}c_j^* .$$

Here $c_j^* = \frac{c_j}{\lambda}$, λ is the partition coefficient and as there will be no any chemical reformation,

$$\dot{n}_j^g = 0$$

thus the reaction can be described by the equation,

$$\frac{dn_j}{dt} = \dot{V}(c_j^i - c_j^*).$$

Here $j = \{\text{free triclosan (T), triclosan sulfate (T}_s\text{), triclosan glucuronide (T}_G\text{)}\}$.

For metabolic organs

For the liver and the skin where there is breakdown of free triclosan into its conjugates, the reactions can be represented by,

$$\frac{dn_{T,k}}{dt} = \dot{V}(c_{T,k}^i - c_{T,k}^*) - \dot{n}_{T,k}^g + \dot{n}_{d2s}$$

$$\frac{dn_{T_{G,k}}}{dt} = \dot{V}(c_{T_{G,k}}^i - c_{T_{G,k}}^*) + \dot{n}_{T_{G,k}}^g$$

$$\frac{dn_{T_{S,k}}}{dt} = \dot{V}(c_{T_{S,k}}^i - c_{T_{S,k}}^*) + \dot{n}_{T_{S,k}}^g$$

Here 'k' is for the liver and the skin. \dot{n}_{d2s} is the amount of chemical applied either through the skin or the mouth.

The excretion is through the kidney as urine.

$$\dot{n}_{j,k2u} = \theta_{k2u} c_{j,ins}^*$$

Flow Junction

The flow topology has one junction at the inlet to the blood pool. For this junction, no matter is accumulated. Steady state species balances for this junction lead to:

$$\begin{aligned} \dot{n}_{k,bp}^e &= \dot{n}_{k,ins}^e + \dot{n}_{k,br}^e + \dot{n}_{k,mu}^e + \dot{n}_{k,sk}^e + \dot{n}_{k,ki}^e + \dot{n}_{k,bo}^e \\ &\quad + \dot{n}_{k,fa}^e + \dot{n}_{k,li}^e \\ \dot{n}_{k,bp}^e &= \dot{n}_{k,lu}^i \end{aligned}$$

Here subscript "k" denotes the possible substrate i.e. free triclosan, glucuronide and sulfate.

4 Simulation and Analysis

Model parameter

Table 2 shows the standard model parameters used for PBPK model development for human. All the standard parameters are extracted from (Mielke et al., 2011). Additional parameters that are used in implementing metabolism and excretion of triclosan in human body are given in Table 1. So far no specific data for skin is provided, thus 20% of corresponding parameter of liver is used for reaction kinetics in the Skin. The chemical excretion coefficient from kidney to urine is estimated from the standard chemical excretion coefficient of rats by using the tissue volume ratio for scaling.

Tissue volume of kidney for rats = 2.77 ml

Tissue volume of kidney for humans = 310 ml

θ_{k2u} for rats = 0.490 ml/s (Beard, 2012)

θ_{k2u} for human = $0.490 \times 310 / 2.77 = 54.8$ ml/s

Effective permeation for the conjugates is different from their parent chemical. As there is lack of the exact value for the effective permeation of triclosan conjugates, a chemical excretion coefficient of parent compound which is scaled by 4 is used.

Table 2: Standard parameters for human (Mielke et al., 2011) .

Organ		Volume of tissue Vt [L]	Flowrate [L/hr]	Partition Coefficient [λ] [-]
No.	Name			
1	Brain	1.45	46.8	0.73
2	Muscle	29.2	65.8	0.29
3	Bone	9.33	7.8	0.23
4	Fat	18.2	19.5	4.20
5	Skin	2.7	20	0.77
6	Kidney	0.31	74.1	0.51
7	Small Intestine	3.7	20	0.57
8	Liver	1.8	99.5	0.57
9	Lung	1.432	353.5	1.16
10	Blood pool	5	353.5	-

Operating condition

The following operating conditions are used in the model:

- Initial states: all are zero.
- Body weight (bw):73 kg
- Chemical dose 0.1 g / kg bw is supplied continuously for 2 hours.

Simulation results

The simulations are carried out using MATLAB for both oral and dermal application. The level of concentration in the simulation is presented as the number of accumulated moles of chemicals (T , T_S and T_G) in each organ scaled by the mass of administered chemical. Figure 3, Figure 4 and Figure 5 contains the information for free triclosan, triclosan glucuronide and triclosan sulfate respectively for human organs. Due to relatively high volume and low flow rate, the muscles and the fats contain high number of free triclosan and conjugates. As their plots are not compatible with the plots of remaining organs, a separate is used to show the level of chemicals in them. The difference in the level triclosan and its conjugates in the human blood after the oral and dermal exposure are shown in Figure 7.

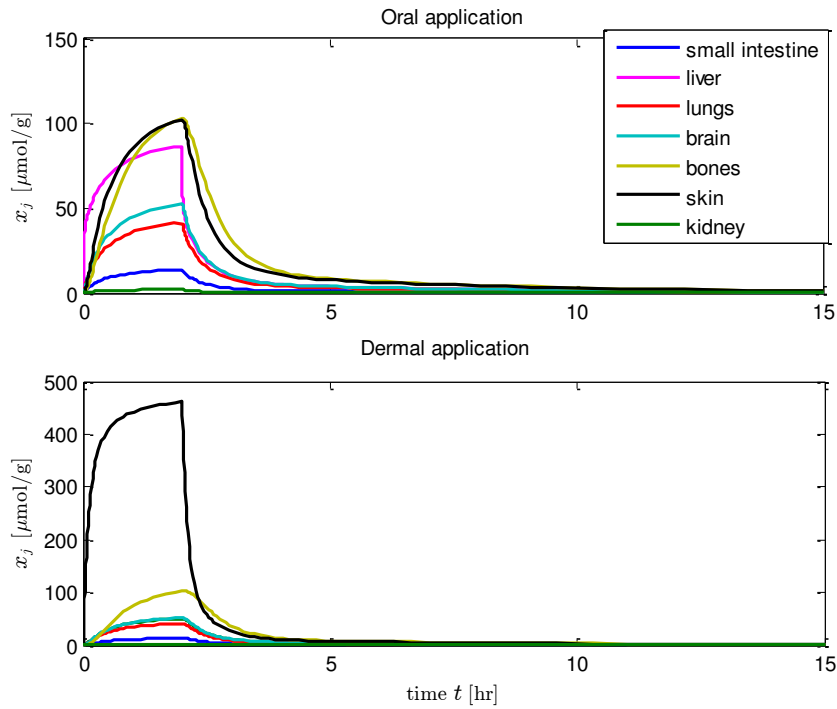


Figure 3: All accumulated molar mass of free triclosan scaled by total mass of administered chemical in human.

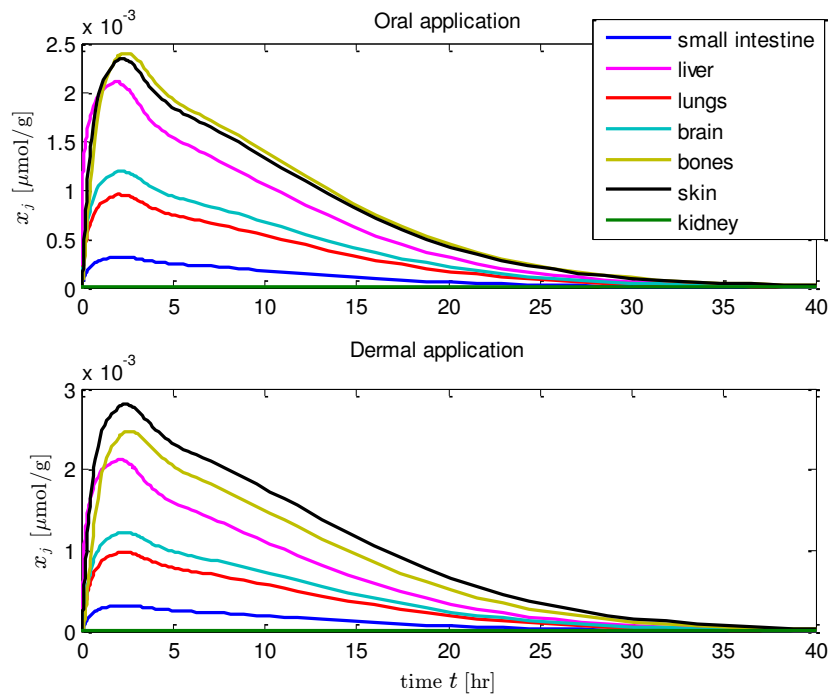


Figure 4: All accumulated molar mass of triclosan glucuronide scaled by total mass of administered chemical in human.

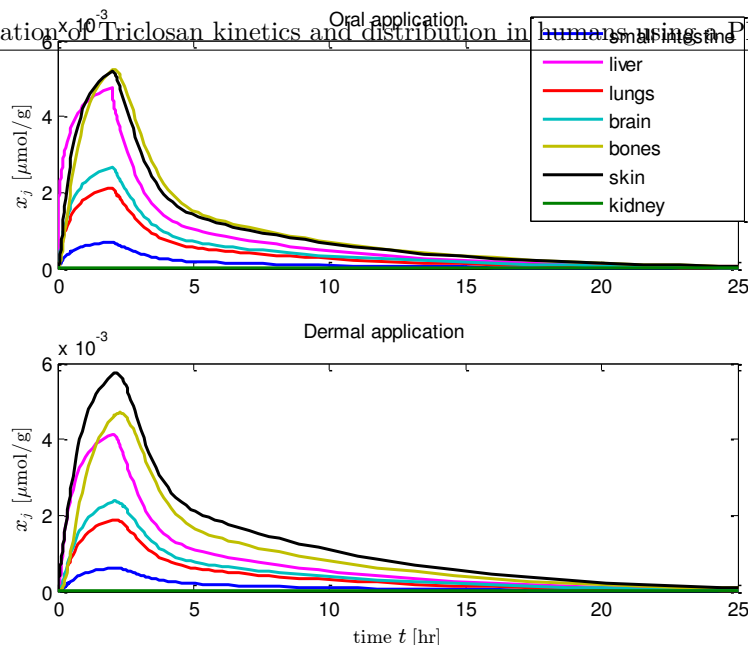


Figure 5: All accumulated molar mass of triclosan sulfate scaled by total mass of administered chemical in human.

Fats

Muscles

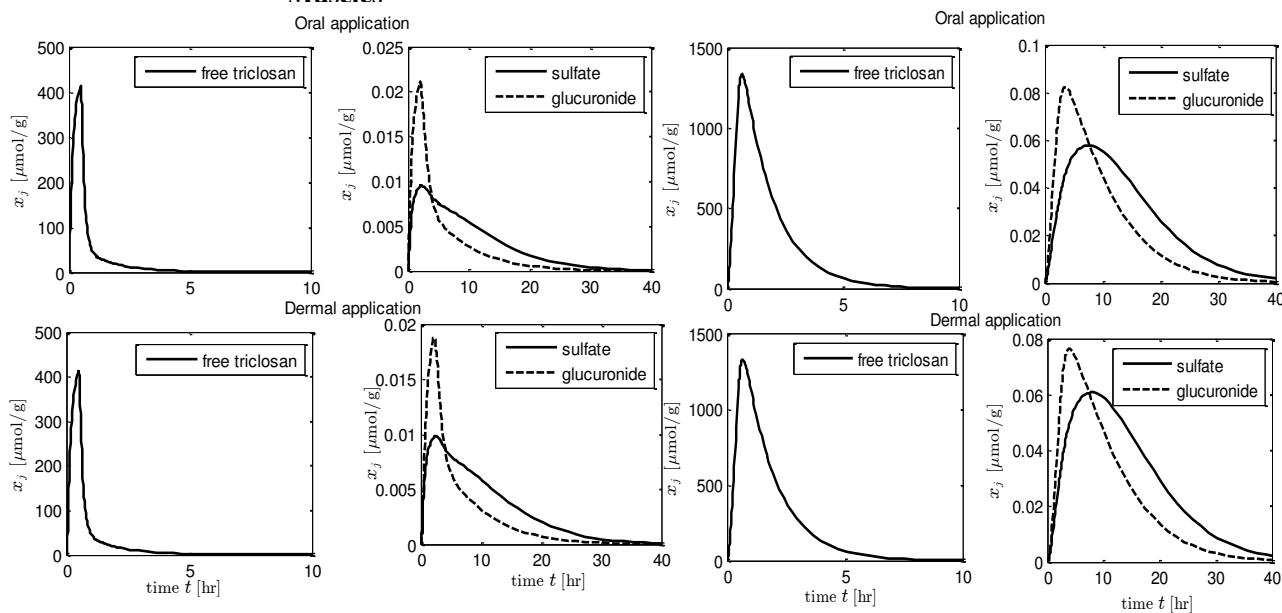


Figure 6: All accumulated molar mass scaled by total mass of administered chemicals in the muscles and the fats.

5 Parameter Estimation

5.1 Sensitivity analysis

Morris method is used for the sensitivity analysis of uncertain parameters. Here the concentration of free triclosan and its two conjugates in the liver are the chosen output for the analysis. The sensitivity analysis is performed by calculating the elementary effect (EE) for each uncertain parameter. The sensitivity measure using Morris method is only qualified not quantified (how much a given factor is more important than

others). Let the parameters be P_i where $i = \{1, \dots, 9\}$ for 9 uncertain parameters and output as the function of these parameters as $f(P_i)$. Then elementary effect for first parameter, can be calculated as,

$$EE_1^j = \frac{f(P_1 + \Delta, P_2^j, \dots, P_9^j) - f(P_1^j, P_2^j, \dots, P_9^j)}{\Delta}$$

Here $j = \{1, 2, \dots, k\}$ if 'k' number of random values for first parameter are considered within its upper and lower bound. So for 100 random values, there will be 100 EEs for the first parameter which will be later normalized.

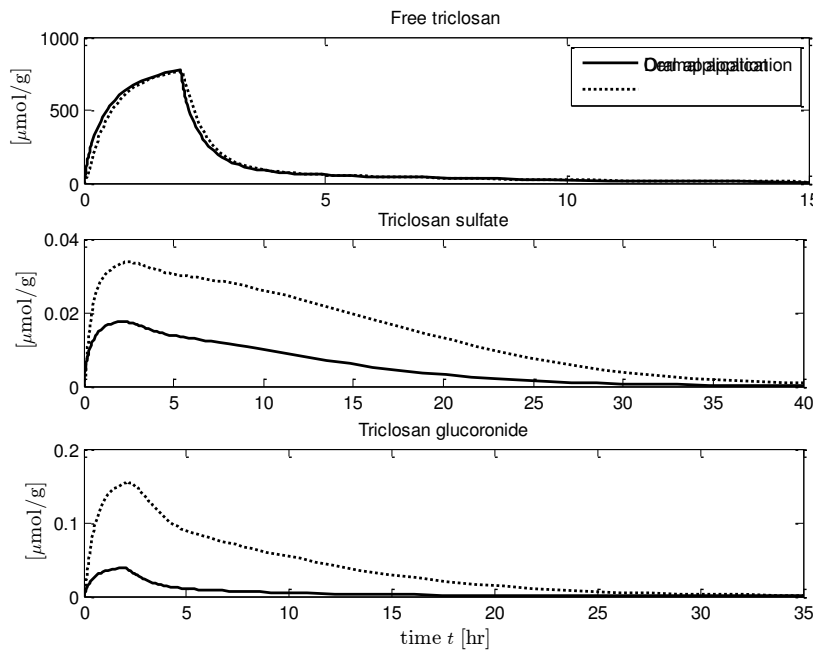


Figure 7: All accumulated molar mass scaled by total mass of administered chemicals in the human blood for the oral and dermal application.

If standard deviation is relatively small, the effect of that particular parameter on the output is "mildly nonlinear". If the standard deviation is relatively large, then the effect of the parameter on the output is "strongly non linear" (Ekstrom, 2005). Overall large measure of the mean of the EEs indicates a parameter with an important (overall) influence on the output. A high measure of the standard deviation of EEs may indicate that a parameter is highly interacting with other parameters. It may also indicate that the effect of this parameter is non linear (Morris, 1991).

Figure 8 shows the standard deviation of all uncertain parameters.

5.2 Model fitting

For least square method which is a widely used way to fit parameters, with following procedures: take differences between predicted values of y and observed values of y , square them and add up all the quantities for each of the data points. With data points (x_i, y_i) , the predicted value of y is $g(x_i; \mathbf{a})$, and the sum of squares is

$$L(\mathbf{a}) = \sum_{i=1}^N (y_i - g(x_i; \mathbf{a}))^2$$

Obviously, the sum of squares depends on the parameter vector \mathbf{a} , so we write L as a function of \mathbf{a} .

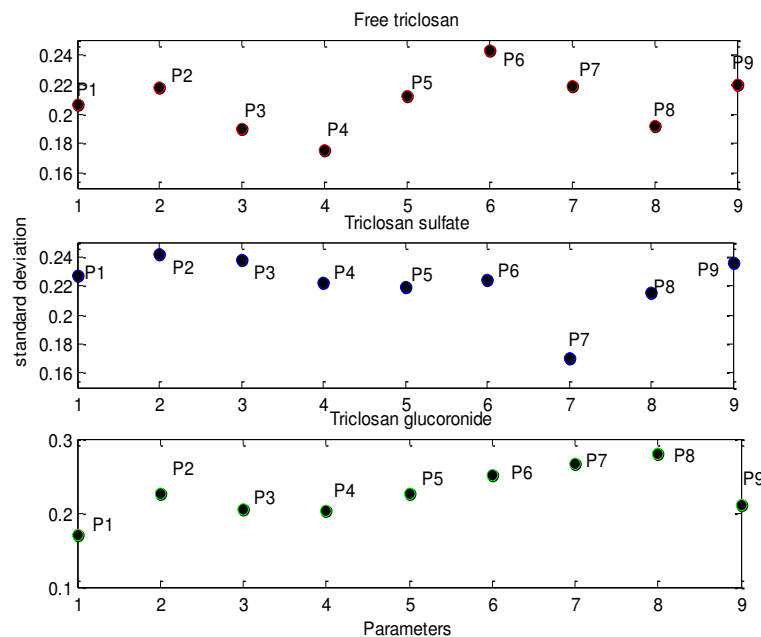


Figure 8: Standard deviation of EE for all uncertain parameters

$$P_1 - \hat{r}_{\max,G,li} \quad P_2 - K_{T,G,li} \quad P_3 - \hat{r}_{\max,S,li} \quad P_4 - K_{T,S,li} \quad P_5 - \hat{r}_{\max,G,sk} \\ P_6 - K_{T,G,sk} \quad P_7 - \hat{r}_{\max,S,sk} \quad P_8 - K_{T,S,sk} \quad P_9 - \theta_{kzu}$$

The task is to find the minimum of $L(a)$ over different values of a . In general, this is not straightforward, unless the function g is linear.

Due to the lack of experimental data, synthetic data from the simulation with all parameter are sampled every hour and placed as predicted output. According to the sensitivity analysis, parameter P5 have almost same standard deviation in all three outputs whereas P7 and P8 show high standard deviation so these three parameters are taken for the model fitting. Assuming that these parameters are unknown ones, the model is

glucuronide drops down faster than triclosan sulfate so after few hours the concentration of triclosan sulfate is higher. The pattern is same for almost all the organs. There is difference in the concentration level for the oral and the dermal route. In most of the organs, the concentration of free triclosan is relatively low whereas those of conjugates are relatively higher for the dermal application than oral application. The skin contains extremely high number of moles of free triclosan than other organs if the route of application is dermal. The Michaelis-Menten reaction parameters for triclosan

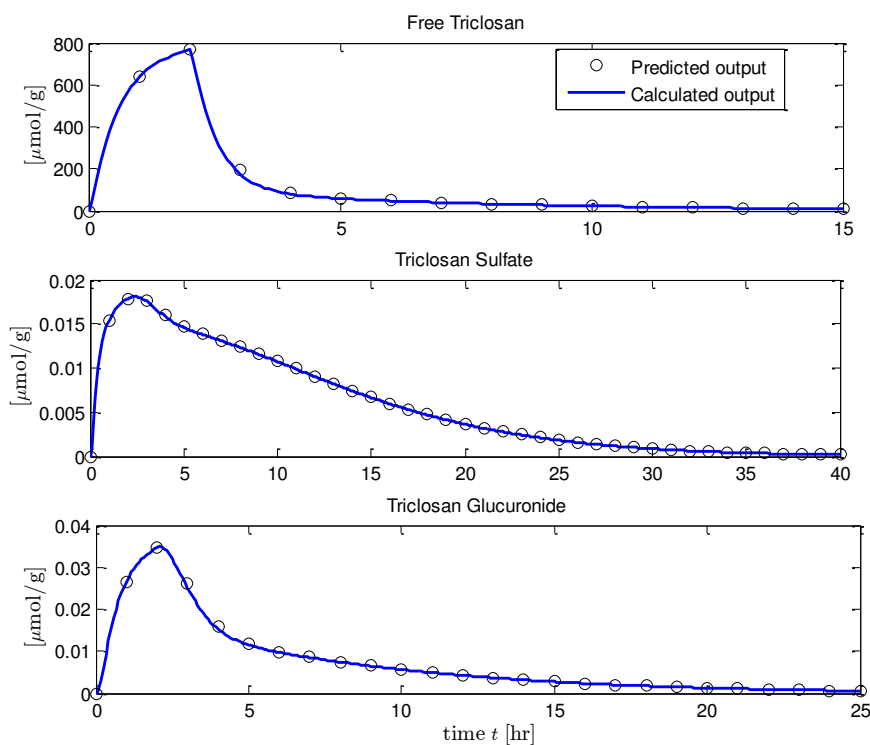


Figure 9: Synthetic measurements vs. model fitted output in the blood.

fitted with curve of synthetic data. The analysis is done for the concentration of free triclosan and its two conjugates in the blood as it will be easier to get sampling data from the blood. First simulation is done without adding any external noise to the predicted output (Figure 9) whereas second simulation is done with the addition of random noise into the predicted output (Figure 10). The random noises are generated between 0 to approximately 5% of peak value of calculated output when there was no noise.

6 Results and Discussion

The concentration of free triclosan seems to be very high during first few hours of exposure, but is rapidly distributed and excreted. The organ concentration of triclosan glucuronide was higher than that of triclosan sulfate. After exposure, the concentration of triclosan

metabolism in human skin shows higher standard deviation that means small deviation in these parameters can affect the model drastically. This might be due to the fact that the sensitivity analysis is done for dermal application in which free triclosan is firstly metabolized in the skin.

Simulations show that within 15 hours of application 90% of the administered chemicals are metabolized into its conjugates. For no noise or very little noise in the sampled output model fitting works fine for 3 unknown parameters but there was some deviation from predicted output when noise is increased. So we cannot be sure about using model fitting for those models where there is possibility of high noise.

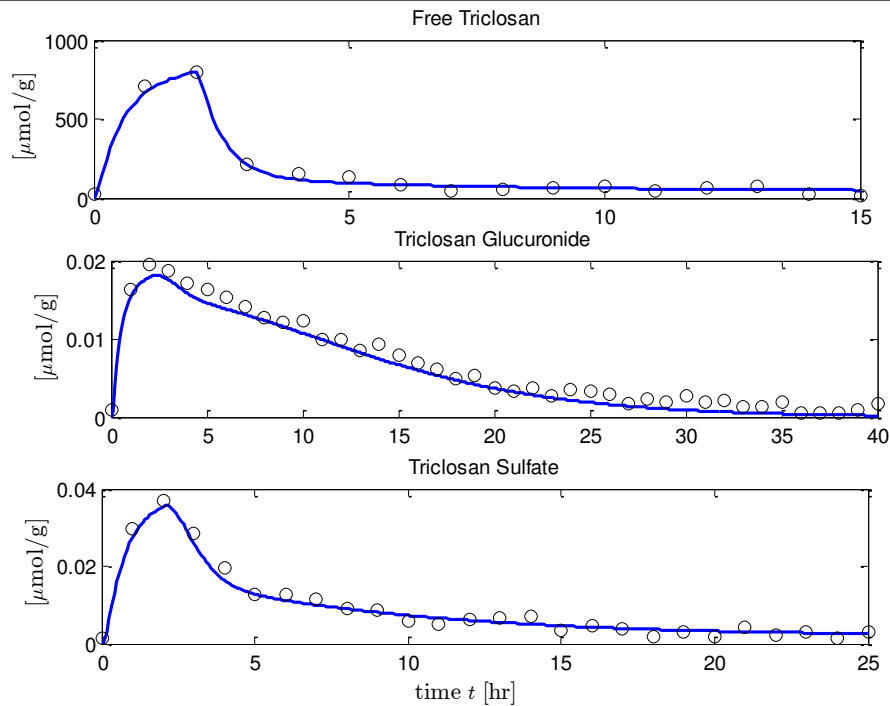


Figure 10: Synthetic measurements with addition of random noise vs. model fitted output in the blood

7 Conclusion

In this study, we demonstrate the concentration level of triclosan and its conjugates in the human organs with PBPK modeling. Large organs like muscles and fats contain relatively high concentration than other remaining organs. Due to the unavailability of verified and experimental data the validation of developed model was not possible to be done.

8 References

- Barter, ZE, Bayliss, MK, Beaune, PH, Boobis, AR, Carlile, DJ, & Reisfeld, Brad. (2007). "Scaling Factors for the Extrapolation of In Vivo Metabolic Drug Clearance From In Vitro Data: Reaching a Consensus on Values of Human Microsomal Protein and Hepatocellularity Per Gram of Liver". *Current Drug Metabolism*, 8, 33-45.
- Beard, Daniel A. (2012). *Biosimulation Simulation of Living Systems*. Cambridge United Kingdom: Cambridge University Press.
- Cubitt, Helen E., Houston, J. Brian, & Galetin, Aleksandra. (2009). "Prediction of Human Drug Clearance by Multiple Metabolic Pathways: Integration of Hepatic and Intestinal Microsomal and Cytosolic Data". *Drug Metabolism and Disposition*, 39, 864-873.
- Ekstrom, Per-Anders. (2005). "Eikos: A Simulation Toolbox for Sensitivity Analysis in MATLAB". *FACILIA AB*.
- Fang, JL, Stingley, RL, Beland, FA, Harrouk, W, Lumpkins, DL, & Howard, P. (2010). "Occurrence, efficacy, metabolism, and toxicity of triclosan". *Journal of Environmental Science and Health*, 28(3), 147-171.
- Johnson, Trevor N., Tucker, Geoffrey T., Tanner, M. Stuart, & Rostami-Hodjegan, Amin. (2005). "Changes in Liver Volume from Birth to Adulthood: A Meta-Analysis". *Liver Transplantation*, 12(11), 1481-1493.
- Mielke, Hans, Abraham, Klaus, Gotz, Mario, Vieth, Barbel, Lampen, Alfonso, Luch, Andreas, & Gundert-Remy, Ursula. (2011). "Physiologically based toxicokinetic modelling as a tool to assess target organ toxicity in route-to-route extrapolation- The case of coumarin". *Toxicology Letters*, 202, 100-110.
- Mielke, Hans, & Gundert-Remy, Ursula. (2012). "Physiologically Based Toxicokinetic Modelling as a Tool to Support Risk Assessment :Three Case Studies". *Journal of Toxicology*, 2012, 11.
- Morris, Max D. (1991). "Factorial Sampling Plans for Preliminary Computational Experiments". *Technometrics*, 33, 161-174.
- Moss, T, Howes, D, & Williams, F. M. (2000). "Percutaneous Penetration and Dermal Metabolism of Triclosan (2,4,4'-Trichloro-2'-hydroxydiphenyl Ether)". *Food and Chemical Toxicology*, 30, 360-370.
- Rodricks, Joseph V, Swenberg, James A, Borzelleca, Joseph F, Maronpot, Robert R, & Shipp, Annette M. (2010). "Triclosan: A critical review of the experimental data and development of margins of

safety for consumer products". *Critical Reviews in Toxicology*, 40, 422-484.

Wang, Li-Quan, Falany, Charles N., & James, Margaret O. (2004). "Triclosan as a substrate and inhibitor of 3'-phosphoadenosine 5'-phosphosulfate-sulfotransferase and udp-glucuronosyl transferase in human liver fractions". *Drug Metabolism and Disposition*, 32, 1162-1169.

Near Well Simulation and Modelling of Oil Production From Heavy Oil Reservoirs

A.Malagalage^{1,2} Britt M. Halvorsen²

¹Tel-Tek, Porsgrunn, Norway, Anjana.t.malagalage@tel-tek.no

²Telemark University College, Faculty of Technology, Norway, Britt.Halvorsen@hit.no

Abstract

Heavy oil reservoirs cover up 2/3 of the world's hydrocarbon reservoirs. When heavy oil is produced through horizontal wells with water drive, a water breakthrough is expected.

Conventional inflow control devices (ICDs) can only delay a water breakthrough. The disadvantage of ICDs is the inability to control the water inflow, after the water breakthrough. Autonomous inflow control valve (AICV) is designed to choke or stop the inflow as soon as the water breakthrough occurs.

To evaluate the performance of AICVs OLGA-Rocx simulations were conducted. Simulations show that the AICVs have a superior potential in limiting the water inflow to the base pipe (86% reduction in water accumulation compared to normal ICDs). AICVs are more effective in heterogeneous and fractured reservoirs as it can restrict the early water breakthrough. In homogeneous reservoirs, AICVs' function reduces oil production rate compared to the ICD system, however, the lifetime of the well is increased.

Keywords: Near well simulation, Inflow control, heavy oil production, OLGA, ROCX, AICV

1 Introduction

Until recently heavy crude oil production was not considered economical and little interest was shown in heavy oil field explorations. It is estimated that the heavy crude oil and bitumen reserves cover up 2/3 of the total crude oil reserves in the world. Development of oil recovery technologies and the continuous growth of the oil demand have increased the economic value of heavy oil. This has resulted in a significant boost in the heavy oil recovery.

When producing heavy oil, water/gas breakthrough can happen easily as water/gas have a higher mobility compared to heavy oil. When water/gas breakthrough occurs, oil production is reduced. Inflow control devices (ICDs) have to be used to overcome the issues of water/gas breakthrough.

Conventional ICDs are capable of delaying water/gas breakthrough but once the breakthrough occurs there is no other solution but to choke the total

flow. Hence various developments have been emerged in the field of inflow control technology such as inflow control valves (ICVs). InflowControl has developed an autonomous inflow control valve (AICV) which can increase the oil recovery while overcoming the problem of water/gas inflow. The objective of AICV is to minimize the water/gas inflow from the zones where the breakthrough has occurred and to allow oil production from the other zones. It is interesting to study the effectiveness of AICVs compared to conventional ICDs, under different conditions. (Mathiesen 2013b)

2 Literature review

2.1 Heavy oil production and its challenges

Basically the major crude oil types can be categorized as light oil, heavy oil, extra heavy oil and natural bitumen. Currently Canada and Venezuela are the two major countries which explore heavy oil fields and in Canada about 700,000 barrels of heavy crude oil are produced per day (A. Hart 2013). Recovering heavy oil is a challenging and a costly process due to its higher viscosity. In a horizontal well, the distance that the oil has to move to reach the wellbore is relatively low. Therefore horizontal wells can be considered as a better technique to recover heavy oil. The main advantage of horizontal drilling over conventional vertical drilling is its higher production rates. As a result operating costs are relatively less compared to vertical drilling. The major obstacle in drilling a horizontal well is the higher capital costs compared to vertical wells. Generally the cost of drilling a new horizontal well from the surface is 1.5 to 2.5 times the cost of drilling a new vertical well. (S.D.Joshi 2003)

In most of the oil reservoirs oil is in contact with water and/or gas. As both water and gas have lower viscosities and hence higher mobility, water/gas breakthrough can occur during heavy oil recovery. Due to the toe-heel effect, higher oil production rate is obtained at the heel section of the well. Hence in a homogeneous reservoir, the initial water breakthrough will occur near the heel of the well.

2.2 Inflow control technologies

In order to control the wellbore inflow profile, inflow control devices were introduced in early 90's. The basic working principle of different ICDs is to restrict the inflow by creating an additional pressure drop. As a result wellbore pressure distribution will be adjusted causing an evenly distributed inflow profile along the horizontal well.

According to (P. Fernandes 2009) an ICD can be effective when the pressure drop across the pipe line is relatively higher than the pressure difference between the well and the reservoir. Highly permeable reservoirs with long wells provide a favorable condition for ICDs. Furthermore if the frictional pressure drop is relatively low compared to the drawdown, ICDs can even restrict the oil flow instead of delaying water inflow. If the permeability distribution can be understood, ICDs can be effectively used in heterogeneous reservoirs to delay the water breakthrough. It can be concluded that the ICDs are not a universal solution for water breakthrough problem.

ICD is a fixed instrument. Once it is installed in a particular application, neither its location nor its relationship between the pressure drop and the flow rate can be changed. That is the reason for ICDs not being able to prevent water/gas inflow. Another type of inflow control technology that has been developed in order to overcome this drawback is the inflow control valve (ICV). Those are sliding-sleeve valves installed along the pipeline. By using a downhole monitoring system, ICVs can be operated by a controlling system which is located at the surface. ICVs exhibit a flexibility to operate according to the changing properties in the reservoir. ICVs are more expensive than ICDs and ICDs are more simple and reliable compared to ICVs as they have no moving parts, therefore ICDs have a less installation risks. (P. Fernandes 2009, F. T. Al-Khelaiwi 2010)

The newest inflow control technique is to use autonomous instruments which can adjust their functionality autonomously according to the dynamics of the wellbore. Autonomous inflow control devices are being developed by companies such as Halliburton and Statoil. Statoil has produced a rate controlled production (RCP) valve which chokes the low viscous flows while permitting high viscous flow to go through the valve. It operates autonomously based on the Bernoulli Effect. (M. Halvorsen 2012)

2.3 Autonomous inflow control valve (AICV)

AICV is a completely self-operating device, which has been designed by combining the features of both AICD and ICV. Its autonomous functionality is achieved by designing it in a way to distinguish between fluids based on their density and viscosity. Fundamental theory behind the operation of AICV is the difference

between the pressure drop in a laminar flow restrictor and a turbulent flow restrictor.

Pressure drop within the laminar flow restrictor is analogous to a pipe segment and the pressure drop is given by the equation (1).

$$\Delta P = \frac{32 \cdot \mu \cdot v \cdot L}{D^2} \quad (1)$$

In a turbulent restrictor, pressure drop can be related with a thin orifice plate and the relevant pressure drop is given by equation (2).

$$\Delta P = K \cdot \frac{1}{2} \cdot \rho \cdot v^2 \quad (2)$$

Where,

- ΔP : Pressure drop
- K : Geometric constant
- D : Diameter of the tube
- L : Length
- μ : Viscosity
- v : Fluid velocity
- ρ : Density

According to these relations, pressure drop within a laminar flow restrictor depends on the viscosity and the velocity of the fluid. In a turbulent restrictor, the pressure drop depends on the density and the velocity of the fluid.

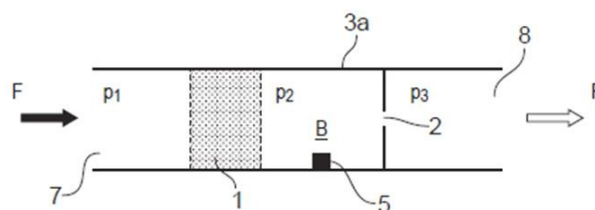


Figure 1. Combination of laminar and turbulent restrictors in series (Mathiesen 2013a)

AICV consists of a component which can be considered as a laminar flow restrictor and a turbulent flow restrictor connected in series which is shown in Figure 1. Laminar flow restrictor is represented by section 1 while the turbulent restrictor is represented by section 2. As the fluid enters the inlet (section 7) it has to go through both flow restrictors. Depending on the fluid characteristics, pressure in chamber B will vary. Pressure in chamber B is used to control the valve. When a high viscous fluid (oil) goes through the laminar flow restrictor, a higher pressure drop will occur according to (1). When a low viscous fluid (water) passes through the laminar flow restrictor, it will result in a relatively low pressure drop. When a low viscous fluid (water) passes through the laminar flow restrictor, it will result in a relatively low pressure drop resulting a higher pressure in the chamber.

AICV is designed to be opened when the pressure in chamber B (P_2) is relatively lower than the pressure in the inlet section (P_1). That is when a higher pressure drop occurs via the laminar flow restrictor at section 1,

AICV will kept open. When oil flows through the restrictors, relatively higher pressure drop occur through section 1 due to its high viscosity. As a result the pressure in chamber B will be lowered and the valve will be kept open. When a low viscous fluid (gas/water) flows through the restrictors relatively lower pressure drop will occur through the laminar restrictor. This will result in a relatively higher pressure in chamber B, which will force the valve to be closed. (Mathiesen 2013a)

2.4 Near-well simulations

Conventional reservoir and well simulators are not sophisticated enough to simulate phenomena like coning where dynamic wellbore-reservoir interactions play a major role. A steady state inflow performance relationship (IPR) is being used in conventional dynamic well flow models. This method does not account for the dynamics in the near well zone. At the same time steady state lift curves are used by the conventional reservoir models to represent a tubing performance relationship (TPR) which again does not consider the flow dynamics in the wellbore. This drawback can be overcome by combining a transient wellbore flow model with a near-well reservoir model. (B. Hu 2007)

OLGA-ROCX is one of the leading commercially available transient wellbore-reservoir flow models. In (R. A. F. S. Moghaddam 2013) OLGA-ROCX has been used to study the application of ICD in heavy oil production and it was successfully implemented for oil with viscosity of 100cp and 500cp. A thorough analysis between AICVs and ICDs were done in (Mathiesen 2013a) using OLGA-ROCX under different conditions in the well. As successful simulations have been conducted with AICV and ICD, OLGA-ROCX was used to conduct the simulations in this research.

3 Development of the OLGA-Rocx model

3.1 Development of the reservoir model

3.1.1 Grid

The dimensions of the considered reservoir are mentioned in Table 1. Generally an AICV is installed per a zone having a length of 12.4 m of the well. It is difficult to simulate a real well with several AICVs as it requires significant amount of computational resources. Hence an equivalent AICV was selected to represent 8 AICVs. Therefore the length of the well zone containing the equivalent AICV is 99.2 m.

Table 1. Dimensions of the reservoir

Length of the reservoir (x)	992 m
Height of the reservoir (z)	20 m
width of the reservoir (y)	80 m

The horizontal well that is being simulated is located parallel to the x-direction. Location of the well in yz-plane is shown in Figure 2.

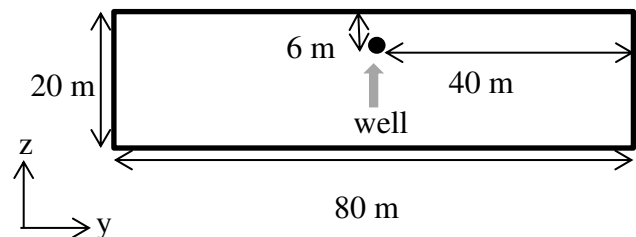


Figure 2. Location of the well in the yz-plane

When developing the mesh for the simulations, a mesh converging towards the center can be applied in y-direction to have a finer mesh around the well. For x and z-directions uniform meshes were applied. The mesh was divided into 29 elements along the y-axis and it was divided into 10 elements along both x and z directions. The final mesh is shown in Figure 3.

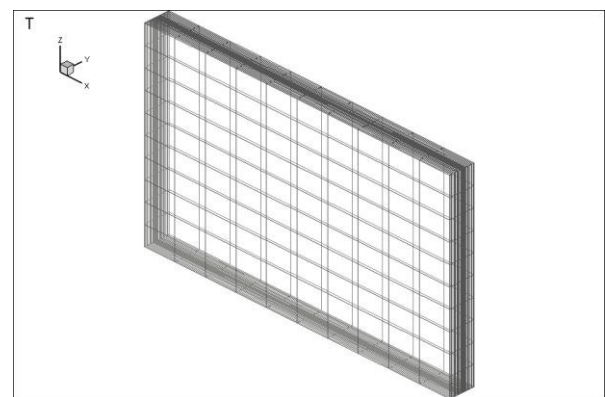


Figure 3. 3D view of the grid

3.1.2 Fluid properties

Under the fluid properties, black-oil model was selected. Black-oil model is a simplified model which can be used for systems which are not highly volatile (Peaceman 2000). The basic properties of heavy oil and the conditions of the reservoir that were considered in the simulations are given in Table 2.

Table 2. Reservoir and oil properties used for simulations

Oil viscosity	150 cp (at 130 bar, 100 ⁰ C)
Oil specific gravity	0.92
Gas specific gravity	0.64
GOR (Sm ³ /Sm ³)	50

For simulating a case with water drive, two feed steam have to be defined. The respective feed streams are defined in Rocx as tabulated in Table 3.

Table 3. Feed streams

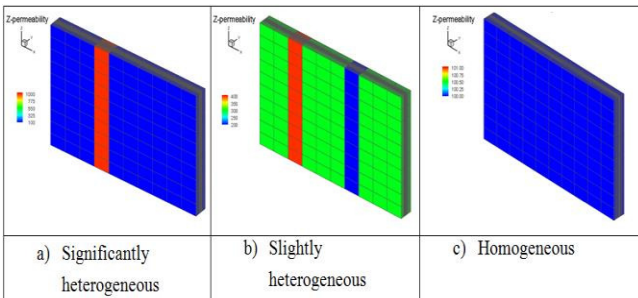
Stream	Fraction type	Fraction	Watercut
Oil	GOR	50	0.0001
Water	GLR	0.0001	0.99

3.1.3 Reservoir properties

For all the simulations, porosity of the reservoir was considered as 0.3 which is constant throughout the reservoir. Three types of reservoirs based on their permeability profiles were considered in this study. Those three types are,

- Heterogeneous reservoir with a highly permeable zone (fractured reservoir)
- Heterogeneous reservoir with a relatively high permeable zone and with a relatively lower permeable zone.
- Homogeneous reservoir

In each cell of all reservoirs, permeability in horizontal directions (k_H) (x and y directions) was considered 10 times higher than the vertical permeability (k_V) (z-direction) of that particular cell. Vertical permeability profiles of the three reservoirs are shown in Figure 4.

**Figure 4.** Vertical permeability profiles of the reservoir

3.1.4 Initial and boundary conditions

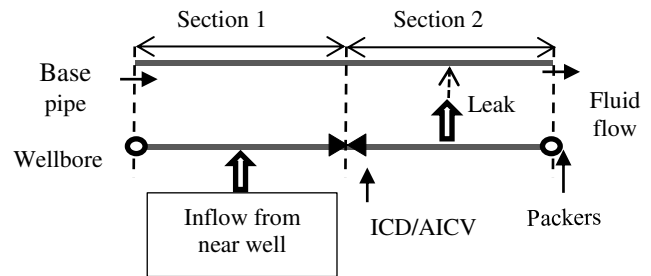
Initially black oil feed is defined as 100% oil and initially reservoir is considered to be completely saturated with oil. The pressure in the reservoir is 130 bar and the temperature is 100°C

3.2 Development of the well and wellbore model

3.2.1 Wellbore-pipeline model

To represent the wellbore a pipe with a length of 992m and diameter of 0.1m was taken and its roughness was set as 2.8e-05 m. The reservoir model has discretize the well into 10 zones, and each zone is divided into two sections. As a result the well is divided in to 20 hypothetical sections. A pipe with the same dimensions

was taken to represent the base pipe and its roughness was defined as 0.045m. Similar to the wellbore, it is also divided into 20 sections. By using Figure 5, which shows a single zone of the well, the concept of this model can be described.

**Figure 5.** Simplified model of a single section of the well

In Table 4. It is described how the model in Figure 5. is developed within OLGA GUI environment by using inbuilt OLGA modules.

Table 4. Reservoir/well model on OLGA

Component	OLGA module	Description
Inflow source	Nearwell source	Reservoir model (Rocx file) is coupled with this.
Leak	Leak	Diameter – 3.5 cm , CD ¹ - 1 NO mass transfer between the phases. Connects to the pipeline
ICD/ AICV	Valve/PID Controlled valve	Valve size is used to decide the required pressure drop through the ICD (typically 20mm). CD – 0.84 For AICV, valve opening is controlled through a PID controller.
Packers	Valve (closed)	Opening – 0 (fully closed), Diameter – 0.1 m

3.2.2 AICV modeling

Parameters of the PID controller used to model the AICVs are defined in Table 5. to get the controlling performance. These parameters were obtained by using trial and error method.

¹ CD – coefficient of discharge

Table 5. PID controller parameters

Parameter	Value (AICV)	Value (for flow choking in ICD)
Amplification	-0.01	-0.0001
Bias (Initial signal)	1	1
Integral constant (s)	50	500
Maximum signal (maximum opening)	1	1
Minimum signal (minimum closing)	0.01	0.01

3.3 Simulated cases

Three main cases were simulated, focusing on three different types of inflow control technologies which are listed in Table 6. A reference case having ICDs with 20mm opening, and without choking the total flow was also simulated.

Table 6. Type of inflow control technologies

Case	Description
Case 1 (ICD _{ch})	Well having ICDs (20mm opening) combined with choking of the total flow from the reservoir.
Case 2 (ICD _{ch,res})	Installing an ICD having a relatively higher flow restriction at the high permeable zone while installing normal ICDs in the rest of the zones. Total product rate is also choked when the total flow rate exceeds the desired value.
Case 3 (AICV _{1%})	Well with AICVs having a relative opening of 1% when the AICV is in closed position.

4 Simulation results

4.1 Comparing the basic performances of AICVs and ICDs in fractured reservoirs

4.1.1 Accumulated oil and water

In Figure 6. accumulated volumes of oil and water are plotted for the cases mentioned in Table 6.

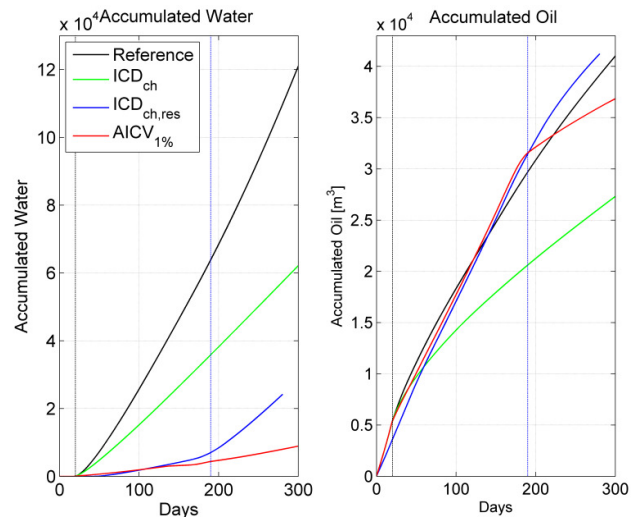


Figure 6. Accumulated oil and water for comparison

According to the Figure 6. it is observed that all the considered inflow control technologies have the capability to reduce the water inflow compared to the reference case. Among the considered inflow control technologies, AICVs have the highest potential in reducing the water inflow. On the other hand, normal ICDs with choked flow have reduced the accumulated oil volume significantly, while the other two methods have been deviated from the reference case slightly

The deviations of the accumulated oil and water volumes, for the different inflow control technologies, can be expressed with respect to the reference case. The relative deviations and the average water cut of the total flow are summarized in the Table 7. These results were obtained on the 281st day of the operation.

Table 7. Accumulated oil/water comparison

Case	Change of oil accumulation [%]	Change of water accumulation [%]	Average water cut [%]
ICD _{ch}	-33.2	-47.7	68.7
ICD _{ch,res}	5.2	-77.9	37.0
AICV _{1%}	-8.1	-92.7	18.2

The restrictions imposed on the fluid inflow to control the water production, have affected a reduction in oil production as well. Based on the amount of accumulated water, the AICVs display a remarkably higher potential in restricting the water inflow.

By considering the results obtained from Case 1, it can be seen that choking the total flow will not only reduce water production but will also limit the oil production. When it comes to quality of the final product, the reference case has an average water cut of 73.71%. This simulation shows that having relatively low restrictive uniform ICDs with flow choking is not a suitable solution for the water inflow problem in fractured reservoirs.

It is interesting to see that by replacing the normal ICD in the high permeable zone with a more restrictive ICD, the results have been dramatically changed. It has enhanced the accumulated oil volume while the other two inflow control technologies have reduced the amount of oil production. According to Figure 6, until the second breakthrough occurs on the 160th day, flow pattern of the AICV case and the non-uniform ICD case (ICD_{ch,res}) follow a similar path.

4.1.2 Oil and water flow rates

Changes of the oil and water flow rates throughout the production time, especially when the water breakthrough takes place, indicate the positive and negative features of the AICV and non-uniform ICD methods. Oil and water flow rates of the two cases are presented in Figure 7.

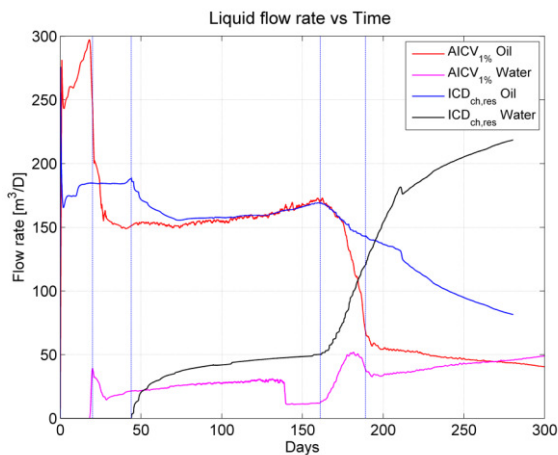


Figure 7. Oil and water flow rate of AICV and ICD_{ch,res} methods

Installing a more restrictive ICD having a higher pressure drop, in the high permeable zone, has delayed the early water breakthrough down to 44 days. Due to the higher pressure through the new ICD; oil production rate has also been reduced.

Non-uniform ICD method has been able to produce 63.46% more oil compared to AICV methods, at the time of the early water breakthrough. On the other hand it inherits low oil production rates and the inability to control the water inflow when the breakthrough happens. From a practical point of view, it is difficult to locate the exact position of the high

permeable zones and hence it is challenging to install more restrictive ICDs within particular zones.

Even though the non-uniform ICD method has been able to delay the first breakthrough, by the time of the second breakthrough happens, it has produced more water and less oil compared to AICV system. In Figure 7, it can be observed that when the second breakthrough happens on the 160th day, the oil production rate rapidly reduces and water flow rate rapidly increases. When observing the relative opening area of the AICVs with respect to time, it takes 20 days for them to reach the closed position (minimum opening). If an AICV takes a relatively long period of time to reach its closed position, water production rate will also be increased. At the same time, if an AICV has a relatively very small opening at the closed position, oil production rate will also be reduced significantly along with the water inflow rate. As a result the amount of oil being produced after the valves are closed down, is less than the non-uniform ICD method. This is a factor which has to be considered based on the economics of the production. With a smaller opening of the AICV, both oil and water flow rates will be reduced and if the opening area of the valve is set to a higher value at the closed position, it will increase the water and oil production rates.

4.2 Effects of design parameters of AICV

4.2.1 Pressure drop and minimum opening area

In an AICV, pressure drop across the valve and the allowable flow at the closed position are design parameters, which can be adjusted depending on the application. Two cases were simulated to see the effect of having a higher pressure drop over the AICV (AICV_{1%,res}) and the effect of having a better closing valve (0.25% minimum opening, AICV_{0.25%}) at the high permeable zone.

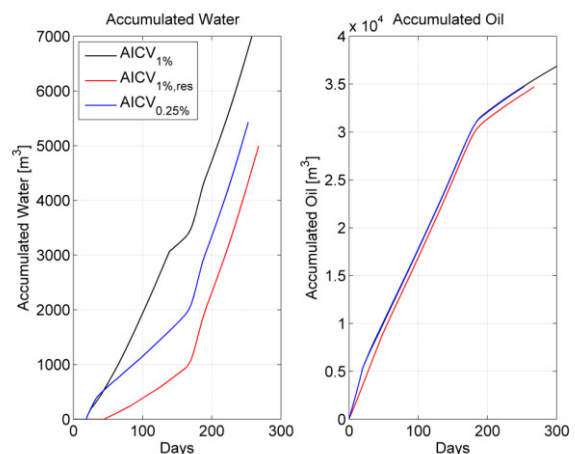


Figure 8. Accumulated water and oil with respect to AICV parameters

The accumulated oil and water profiles of these two cases are presented in Figure 8. with respect to the accumulated oil and water profiles of uniform AICVs with 1% minimum opening.

When considering the amount of accumulated water, it can be concluded that having a higher pressure drop is more effective than having a fine closing. This phenomenon is highly dependent on the reservoir and fluid properties. In this particular well, reducing the minimum opening down to 0.25% ,has no effect on the amount of oil accumulated. Having a higher pressure drop has also reduced the oil accumulation slightly.

If it is required to produce more oil at a higher production rate , minimum opening of the AICVs in the low permeable zones, have to be increased. A case was simulated by having an AICV with both higher pressure drop and a lower opening at the high permeable zone and having AICVs with 2% opening in rest of the zones. The obtained results are plotted with respect to the results in Figure 8. and it is presented in Figure 9.

As expected the new combination has yielded a higher oil production, but it has also increased the water production as well. The acceptable water cut and the minimum opening area of the AICVs have to be decided based on the economics of the production process.

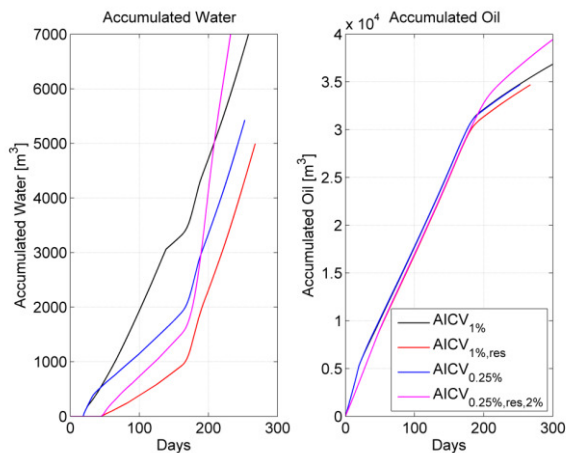


Figure 9. Accumulated oil and water with 2% opening AICV

4.2.2 Response time

Once the water starts to flood into the AICV, it takes a certain period of time for the valve to respond to the change of the fluid properties. As a result the valve will not close as soon as the water breakthrough occurs. In Figure 10, oil and water flow rates of two identical cases having AICVs with different response times are presented. As it can be seen, if the valve closes slowly, water production rate rapidly increases and as a result water accumulation will be increased. However after the AICVs reach their closed positions, both water and oil flow rates will reach the same value regardless of the response time.

From a practical point of view the difference between the two response times might not be significant. But from a simulation point of view, PID controller which is used to represent the AICV has to be tuned properly. Otherwise closing will not be similar to the actual closing function of the AICV and significant errors could occur in the accumulated flows.

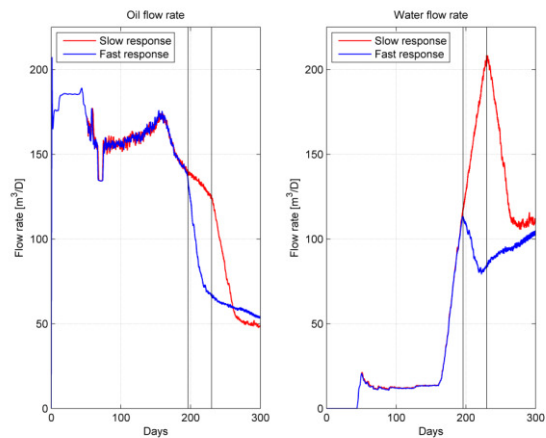


Figure 10. Oil and water flow rates under different response times

4.3 Functionality of the AICVs and ICDs in homogeneous reservoirs

For the simulations, a reservoir with a vertical permeability of 100mD was considered as shown in Figure 4. Accumulated oil and water quantities are plotted in Figure 11. and, the AICVs have reduced the amount of water that is being produced. According to the results obtained, AICVs have been able to reduce the water accumulation by almost 47%. As a side effect of the inflow control, oil production has also been reduced by 7%.

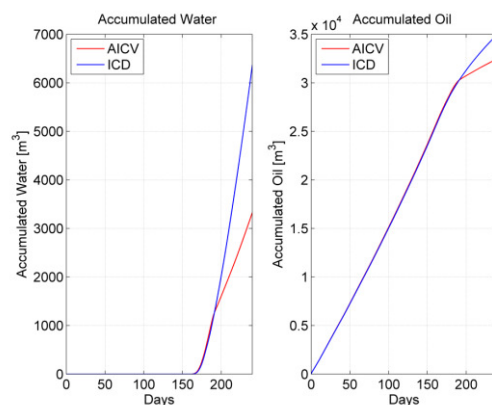


Figure 11. Accumulated water and oil profiles of homogeneous reservoirs

As seen in Figure 11. until the AICVs are closed down, both ICDs and AICVs follow the same flow

pattern. Once the AICVs are closed down both oil and water inflows are choked down. Therefore the oil accumulation will be less than the normal ICDs. The changes of liquid flow rates are shown in Figure 12.

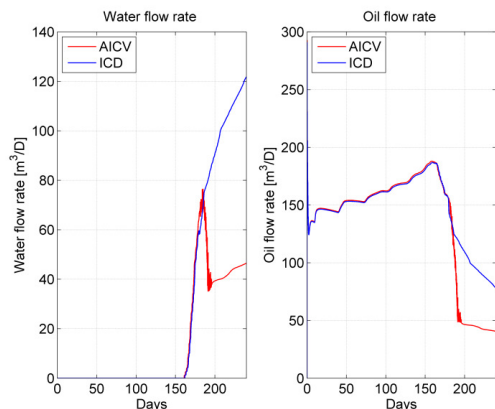


Figure 12. Water and oil flow rates of homogeneous reservoirs

ICDs have only been able to delay the water inflow and once the water starts flooding into the well it has no control over it. Hence water inflow rate is continuously increases while the oil production rate is gradually decreasing. Due to AICV's capability to restrict the inflow, water flow rate is suddenly dropped down to a lower value, when the AICV is closed down. Due to the low viscosity of water, its production rate is gradually increases. As a result when the valve is in the closed position where it cannot restrict the inflow further, water production rate will increase gradually. However AICVs have been able to restrict the water inflow rate down to a significantly lower value compared to the ICDs. As the AICVs are closed down, oil production is also reduced down and continuously decreases due to the production of water.

4.4 Functionality of the AICVs and ICDs in heterogeneous reservoirs

As shown in Figure 4, an intermediate reservoir between a fractured and a homogeneous reservoir was also taken for the simulations. The accumulated oil and water volumes are presented in Figure 13.

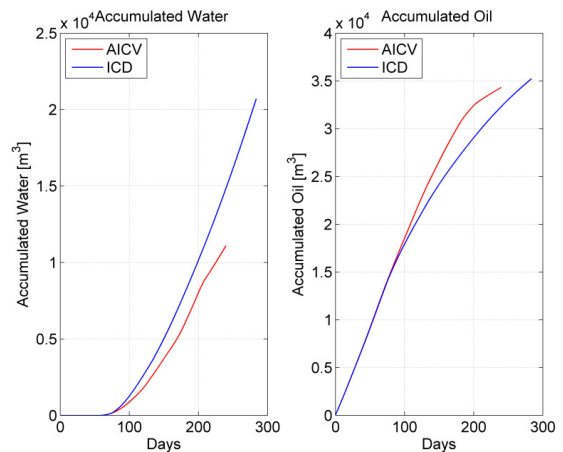


Figure 13. Accumulated water and oil profiles of heterogeneous reservoir

Compared to the accumulated liquid profiles in homogeneous reservoir AICVs in heterogeneous reservoirs have the potential to produce more oil compared to ICDs. The liquid flow rate profiles of the considered heterogeneous reservoir are presented in Figure 14.

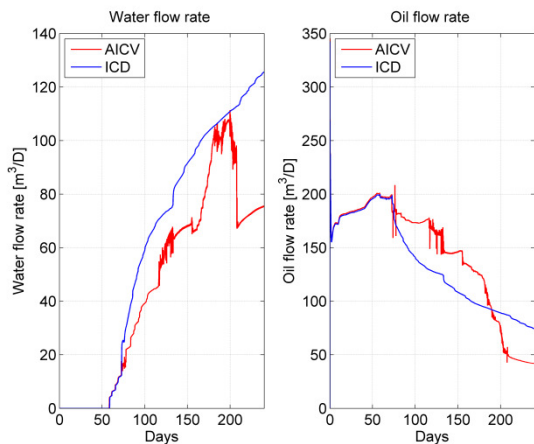


Figure 14. Water and oil flow rates of heterogeneous reservoir

As there are three different permeable zones three water breakthroughs occur during the production. First one occurs on the 55th day and the last one is initiated on 160th day. AICVs will be completely closed by the 210th day. That is why a sudden increase and decrease in water production rate is observed on 160th day and on 210th day respectively. Until the third breakthrough, AICVs have maintained a higher oil production rate. In the ICD system oil production rate has decreased due to the choking of the total flow.

By considering the results obtained for the three types of the reservoirs, AICVs can be effectively used in both fractured and heterogeneous reservoirs. Even though they reduce the water production in

homogeneous reservoirs, they reduce the amount of oil produced as well.

5 Discussion

Under all the conditions, which were taken into consideration during the simulations, AICVs have produced less water than all the other inflow control technologies.

Compared to the uniform ICD system, AICVs have been able to produce more oil in both fractured and heterogeneous reservoirs. In homogeneous reservoirs, as the AICVs choke the inflow of the all the zones simultaneously, oil production rate is reduced compared to the ICDs. This phenomenon can also be seen in the long run operation of heterogeneous and fractured reservoirs. By increasing the allowable flow through the AICV when it is in closed position, it will be able to produce more oil provided that it will produce more water as well.

It has been shown that if it is possible to install an AICV or/and ICD having a relatively higher flow restriction, in the high permeable zone, early water breakthrough in fractured reservoirs can be delayed. It will also increase the amount of oil produce at the time of breakthrough. Also a much lower water inflow rate can be achieved, compared to uniform AICV/ICD systems. The main drawback of this system is that it is difficult to locate the exact location of the high permeable zones and it is also difficult to install a particular inflow control instrument in an exact location.

To conduct accurate simulations of the AICVs, it is important to tune the PID controlling system that is used to represent the AICV. False tuning will lead to slow responses or too many fluctuations, causing significant errors in the final results. Currently the tuning has to be conducted by trial and error method combined with PID condoling theory.

6 Conclusion

Based on the obtained results, it can be concluded that the AICVs can be successfully implemented to minimize the water inflow into the base pipe. Due to the choking of the inflow, AICVs will restrict the oil production down to a certain limit as well. By having a higher minimum opening area when the AICV is in closed position, restriction towards the oil production can be minimized. The acceptable limit of the water cut of the final product, has to be decided according to the economic factors.

AICVs are more suitable to be used in heterogeneous and fractured reservoirs. In homogeneous reservoirs it will choke the oil inflow from all the zones and therefore the total oil production is rapidly reduced. If it is possible to have ICDs or AICVs having higher flow restriction properties, installed in the high permeable zone, much better

inflow control action can be obtained in fractured reservoirs. But practically it is difficult to install the correct type of AICV at the correct position. But the advantage of AICV is that it will close the water producing zone and produce oil from the other zones

Response time of the AICV plays a vital role in the effectiveness of the AICV. At the time of closing the AICVs, if the water flow rate is almost equal to the oil flow rate, reservoir will produce more water even after the inflows are choked. (due to the minimum allowable flow through AICV).

All the results obtained by the simulations are required to be validated by conducting experimental work. And further study has to be conducted in homogeneous reservoirs, to see how the performance of the AICV can be enhanced.

Abbreviations

AICV	: Autonomous Inflow Control Valve
GLR	: Gas Liquid Ratio
GOR	: Gas Oil Ratio
ICD	: Inflow Control Device
ICV	: Inflow Control Valve

References

- A. Hart. 2013. "A review of technologies for transporting heavy crude oil and bitumen via pipelines." *Journal of Petroleum Exploration and Production Technology*:1-10. doi: 10.1007/s13202-013-0086-6.
- B. Hu, J. Sagen, G. Chupin, T. Haugset, A. Ek, and T. Sommersel. 2007. "Integrated Wellbore-Reservoir Dynamic Simulation,," Asia Pacific Oil and Gas Conference and Exhibition.
- F. T. Al-Khelaiwi, V. M. Birchenko, M. R. Konopczynski, and D. Davies. 2010. "Advanced Wells: A Comprehensive Approach to the Selection Between Passive and Active Inflow-Control Completions." *SPE Production & Operations* 25:305-326. doi: <http://dx.doi.org/10.2118/132976-PA>.
- M. Halvorsen, G. Elseth, and O. M. Nævdal. 2012. "Increased oil production at Troll by autonomous inflow control with RCP valves." SPE Annual Technical Conference and Exhibition.
- Mathiesen, H. A. Vidar. 2013a. "Increased oil recovery of an old well, recompleted with Autonomous Inflow Control Valve (AICV)." ADIPEC 2013 Technical

- Conference, Abu Dhabi, United Arab Emirates.
- Mathiesen, V. 2013b. "Autonomous gas/water shut-off in field with gas/water breakthrough." SPE Aberdeen Summit Series Seminar.
- P. Fernandes, Z. Li, and D. Zhu. 2009. "Understanding the roles of inflow-control devices in optimizing horizontal-well performance." PE Annual Technical Conference and Exhibition.
- Peaceman, D. W. 2000. *Fundamentals of numerical reservoir simulation*: Elsevier.
- R. A. F. S. Moghaddam, H. Aakre, B. M. Halvorsen. 2013. "Near well simulations of heavy oil production with ICD completion." *Computational Methods in Multiphase Flow VII* 79:499-509.
- S.D.Joshi. 2003. "Cost/benefits of horizontal wells." SPE Western Regional/AAPG Pacific Section Joint Meeting.

Improved model for solar heating of buildings

Bernt.Lie@hit.no

Telemark University College, Porsgrunn, Norway

Abstract

A considerable future increase in the global energy use is expected, and the effects of energy conversion on the climate are already observed. Future energy conversion should thus be based on resources that have negligible climate effects; solar energy is perhaps the most important of such resources.

The presented work builds on a previous complete model for solar heating of a house; here the aim is to introduce ventilation heat recovery and improve on the hot water storage model. Ventilation heat recovery reduces the heat loss due to ventilation, as expected. Here, a recovery efficiency of 0.5 is used, although a more realistic number is perhaps 0.7. The improved hot water storage model increases the exergy of the storage tank by assuming a vertical temperature distribution. Further improvements are possible by introducing a simple thermocline tracking algorithm, effectively allowing for variable volumes of the temperature zones in the hot water storage tank. Currently, the model does not allow for very good temperature control; this is due to a lack of freedom in the control inputs.

Keywords: Solar heating, Building models, Model efficiency, Control.

1 Introduction

The observed increase of greenhouse gases in the atmosphere in tandem with an increase in global temperature, has led to a concern about the temperature development for the rest of the century with the possible consequence of increased ocean level, more violent weather, etc. To counter these predictions, there is an emphasis on reducing the use of fossil fuel and thereby stop the increase in CO₂ level of the atmosphere.

Solar energy is a freely available alternative to fossil energy. One possible way to utilize solar energy is to capture the irradiance in a solar collector, and store the energy by heating up water in a storage tank. Such hot water can be used for heating, for showering, etc. The intermittent nature of irradiance is partially handled by such storage of energy, but it is usually necessary to combine solar energy with auxiliary forms such as electricity or fossil fuel to ensure sufficient availability of power. Because of fluctuations in energy prices (spot marked), it may be possible to take advantage of predictions of irradiance to reduce the energy bill: if we know that tomorrow will be sunny, we can reduce the heating by electricity or fossil fuel – or at least make sure that we use such auxiliary forms when their cost is low.

The complexity level of models for solar heating of buildings range from simple models for energy planning over decades to detailed studies of the individual components in such systems. Of particular interest is the study of models suitable for on-line use. For large scale solar collector plants, concentrated solar power systems are used [18], while for domestic heating, flat plate solar collectors or evacuated collectors are cheaper. Here, we focus on domestic heating. The fitting of an industry standard flat plate solar collector model to experimental data is discussed in [12], while [21] and [20] discuss more complex models for transient studies. Both [5] and [7] give useful background in solar radiation and design of such collectors. Models of storage tanks are discussed e.g. in [7], see also [8], [2], and [19]. Software libraries with detailed building models are available, but for control studies, the discussion in [15], [16] is particularly relevant. Disturbances are important in building models. Domestic hot water load profiles are treated in [11]; seasonal variations and optimization is important for design [6] and [9]. Variation in solar irradiance and ambient temperature are typically measured; see e.g. [7]; day to day prediction of solar irradiance is treated in [1]. In [13], a relatively complete model structure for on-line use is given. With respect to on-line use of models, [4] use a simple model of a building together with prediction of outdoor temperature and varying electric spot prices to study possibilities for cost savings through advanced control, with emphasis on efficient algorithms, while [10], [17] and [14] discuss the use of Model Predictive Control of a system for thermal capturing of solar energy with auxiliary energy supply.

Although relatively complete in structure, the model in [13] has a number of limitations. (i) Heat integration during ventilation is not included, and heat loss through ventilation is of major importance, (ii) the water storage model is homogeneous in temperature; real storage tanks may exhibit a large spatial variation in temperature, (iii) heat transfer is computed using fixed numbers, but heat transfer varies with fluid flow, (iv) variation in fluid flow rates is not included, (v) the solar collector model is static. It is of interest to improve on the model in [13]; in this paper, points (i) and (ii) above are addressed. Stratification is known to occur in hot water tanks. In [19], a plug flow model modified with thermal diffusion is used to approximate this effect; a very high order discretized model (600 states) is used as a reference model, and a lower order model with some 60 states and adaptive thermocline front tracking is proposed. The results do, however, indicate that for a storage tank with indirect heating via a heat exchanger, a low order model, possibly with thermocline front tracking, may suffice. It is quite common to approximate the storage tank with 2–3

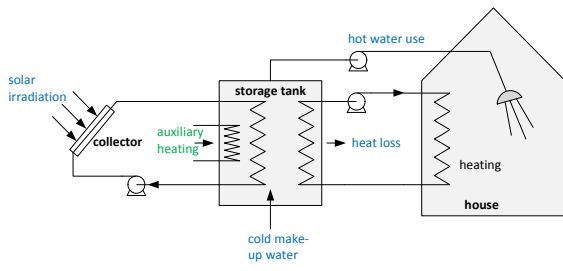


Figure 1: Blue font indicates disturbance variable, while green font indicates control variable. Heat losses are due to temperature differences to ambient temperatures. The storage tank is assumed to be instantly re-filled with cold make-up water, which may have a varying temperature.

well mixed, fixed size tanks.¹

The paper is organized as follows. First, a description of the system with solar heating, storage tank and building is given, with some background information. Next, simple modifications of the unit models for the storage tank and the ventilation system are presented and discussed. Then the modified full model is given, and simulation results are given. Finally, some conclusions are drawn.

2 System description

2.1 System elements

The system for mixed solar and electric (auxiliary) heating of a domestic building as reported in [13], is depicted in Figure 1. The reason for introducing heat exchangers to separate the fluids of the collector circuit and the heating circuit from the utility hot water of the storage tank (“indirect heating”), is to allow for use of anti freeze and algae reducing components in these circuits. The reported model in [13] had a number of deficiencies, and here an improved description of the ventilation system and the storage tank will be introduced.

A simple improvement of the ventilation system could be to introduce an energy recovery efficiency η_v . A storage tank with heat exchangers is depicted in Figure 2, and is modified to include stratification in comparison with [13]. The water in the storage tank consists of a cold zone of more or less homogeneous temperature at the bottom separated by a thermocline (large temperature gradient) from the hot zone of more or less homogeneous temperature at the top. This is an improvement compared to the storage tank in [13] where the storage tank was assumed to be perfectly well mixed. It is still assumed that the tube side temperature is constant throughout, i.e. that the collector fluid has homogeneous temperature throughout the tube side and that the floor fluid has homogeneous temperature throughout the tube side. The auxiliary heating has, however, been modified so that it only operates in the hot zone.

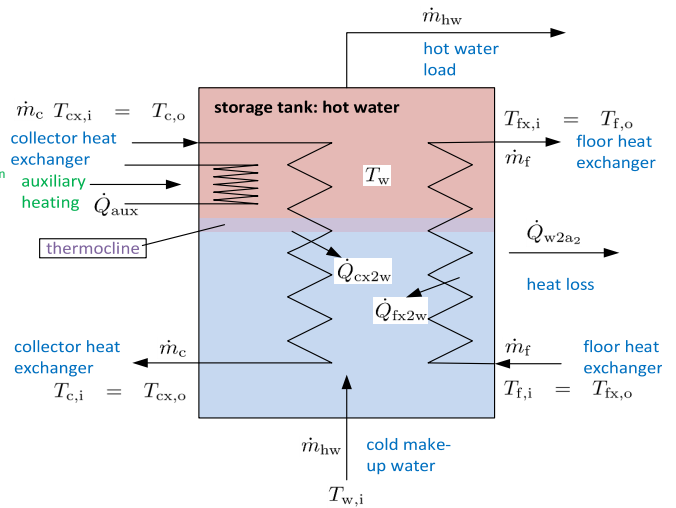


Figure 2: Sketch of storage tank, including thermocline which separates the cold zone (bottom; blue color) and the hot zone (top; red color).

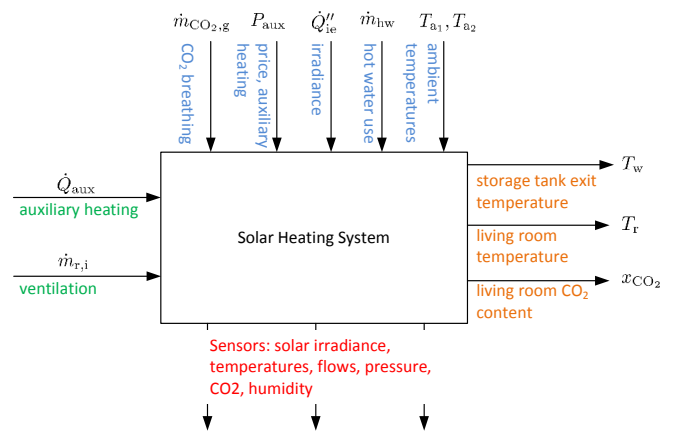


Figure 3: Functional description of the solar heating system with auxiliary heating input.

2.2 Functional description

From a system theoretic point of view, it is useful to present the system as a block diagram with inputs and outputs — inputs and outputs will vary with time; Figure 3 illustrates this causal relationship with disturbances on the top of the block, control inputs (manipulating inputs) at the left side, while performance outputs (orange) are shown on the right side of the system block and available sensor signals (red) at the bottom of the block. This functional description is the same as in [13], and is unaffected by the modification of the ventilation system and the storage tank.

3 Unit models

3.1 Storage tank thermal energy balance

A thermocline as indicated in Fig. 2 is the result of density variations wrt. temperature, and buoyancy effects thereof. In general, such a thermal stratification is complex, and requires a description involving mass, momentum and energy balances in 3D. For on-line use, a common simplification

¹Suggested in personal communication by U. Eicker.

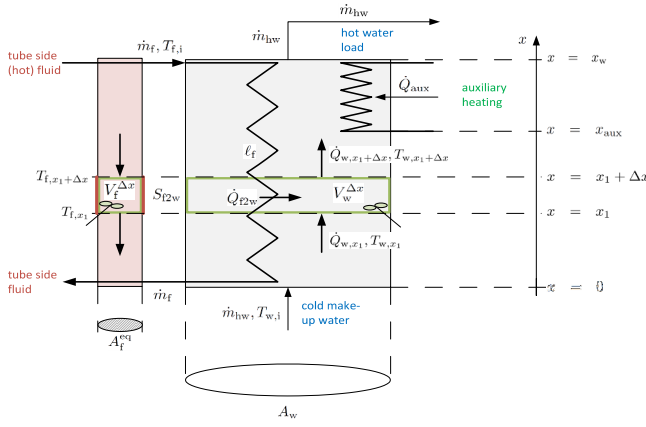


Figure 4: Principle layout of storage tank.

is to assume that the feed/exit diffusers are constructed so that 1D models are reasonably accurate, and neglect the momentum balance. Furthermore, it is common to assume the density is constant. This leads to a 1D energy balance, [19]. In the sequel, if quantity q is an *extensive* quantity, \dot{q} denotes the flow rate of q . Furthermore, for a general quantity q , q' denotes the quantity per length unit, q'' denotes the quantity per unit area (length squared), etc. Figure 4 illustrates the principle layout of the storage tank, with stored water (“shell side” of heat exchanger), subscript w, in heat exchange with fluid (“tube side”), subscript f.

3.2 Storage tank distributed model

In Fig. 4, a 1D distribution of the temperature in the vertical direction ($x \in [0, H]$) is indicated, with discretization into well mixed slices of height Δx . The well mixed volume of water in the interval $x \in [x_1, x_1 + \Delta x]$ is indicated by $V_w^{\Delta x}$, while the well mixed volume of the heat exchanging fluid in the same x interval is indicated by $V_f^{\Delta x}$. The cross sectional area of the water tank, orthogonal to the x axis, is A_w . For the tube side of the heat exchanger coil, an equivalent cross sectional area is A_f^{eq} defined such that $V_f^{\Delta x} = A_f^{\text{eq}} \Delta x$.

By letting $\Delta x \rightarrow 0$, the complete model with a tube side hot fluid can be summarized as

$$\frac{m_w \hat{c}_{pw}}{x_w} \frac{\partial T_w}{\partial t} = -\dot{m}_{hw} \hat{c}_{pw} \frac{\partial T_w}{\partial x} + \dot{Q}'_{f2w} + \dot{Q}'_{aux} - A_w \frac{\partial \dot{Q}''_w}{\partial x} \quad (1)$$

$$\dot{Q}''_w = -k_w \frac{\partial T_w}{\partial x} \quad (2)$$

$$\frac{m_f \hat{c}_{pf}}{x_w} \frac{\partial T_f}{\partial t} = \dot{m}_f \hat{c}_{pf} \frac{\partial T_f}{\partial x} - \dot{Q}'_{f2w} \quad (3)$$

where

$$\dot{Q}'_{f2w} = \frac{UA|_{f2w}}{x_w} (T_f - T_w) \quad (4)$$

with boundary conditions

$$T_w(t, x=0) = T_{w,i} \quad (5)$$

$$\dot{Q}''_w(t, x=x_w) = 0 \quad (6)$$

$$T_f(t, x=x_w) = T_{f,i} \quad (7)$$

and initial conditions given by $T_w(t=0, x)$, $\dot{Q}''_w(t=0, x)$ and $T_f(t=0, x)$. If the tube side fluid is cold, we need to reverse the tube side fluid and replace \dot{m}_f with $-\dot{m}_f$, with boundary condition at $x=0$; $T_f(t, x=0) = T_{f,i}$.

By assuming steady operation, the model simplifies to

$$\frac{d\dot{Q}''_w}{dx} = \frac{\dot{m}_{hw} \hat{c}_{pw}}{k_w A_w} \dot{Q}''_w + \frac{UA|_{f2w}}{A_w x_w} (T_f - T_w) + \frac{1}{A_w} \dot{Q}'_{aux} \quad (8)$$

$$\frac{dT_w}{dx} = -\frac{1}{k_w} \dot{Q}''_w \quad (9)$$

$$\frac{dT_f}{dx} = \frac{UA|_{f2w}}{x_w \dot{m}_f \hat{c}_{pf}} (T_f - T_w) \quad (10)$$

with

$$\dot{Q}''_{w, x=x_w} = 0 \quad (11)$$

$$T_{w, x=0} = T_{w,i} \quad (12)$$

$$T_{f, x=x_w} = T_{f,i} \quad (13)$$

The model in Eqs. 1–3 can be discretized in space by reversing the $\Delta x \rightarrow 0$ limit.

3.3 Storage tank concentrated model

Next, introduce the hypothesis that the tube side fluid temperature T_f varies little through the coil, while the shell side water temperature T_w is more or less homogeneous in the region $[0, x_{aux}]$ and is different but more or less homogeneous within the region $[x_{aux}, x_w]$. This hypothesis leads to a concentrated model

$$\frac{dT_{w,\ell}}{dt} = \frac{\dot{m}_{hw} \hat{c}_{pw}}{m_w \frac{x_{aux}}{x_w} \hat{c}_{pw}} (T_{w,i} - T_{w,\ell}) + \frac{UA|_{f2w}}{m_w \frac{x_{aux}}{x_w} \hat{c}_{pw}} \frac{x_{aux}}{x_w} (T_f - T_{w,\ell}) \quad (14)$$

$$\frac{dT_{w,u}}{dt} = \frac{\dot{m}_{hw} \hat{c}_{pw}}{m_w \frac{x_w - x_{aux}}{x_w} \hat{c}_{pw}} (T_{w,\ell} - T_{w,u}) + \frac{UA|_{f2w}}{m_w \frac{x_w - x_{aux}}{x_w} \hat{c}_{pw}} \frac{x_w - x_{aux}}{x_w} (T_f - T_{w,u}) + \frac{1}{m_w \frac{x_w - x_{aux}}{x_w} \hat{c}_{pw}} \dot{Q}'_{aux} \quad (15)$$

$$\frac{dT_f}{dt} = \frac{\dot{m}_f \hat{c}_{pf}}{m_f \hat{c}_{pf}} (T_{f,i} - T_f) - \frac{UA|_{f2w}}{m_f \hat{c}_{pf}} \frac{x_{aux}}{x_w} (T_f - T_{w,\ell}) - \frac{UA|_{f2w}}{m_f \hat{c}_{pf}} \frac{x_w - x_{aux}}{x_w} (T_f - T_{w,u}), \quad (16)$$

with initial states $T_{w,\ell}$, $T_{w,u}$ and T_f given at zero time.

By assuming steady operation, the concentrated model reduces to linear equations, and can easily be reformulated into the matrix form

$$M \begin{pmatrix} T_{w,\ell} \\ T_{w,u} \\ T_f \end{pmatrix} = \begin{pmatrix} \dot{m}_{hw} \hat{c}_{pw} T_{w,i} \\ \dot{Q}'_{aux} \\ \dot{m}_f \hat{c}_{pf} T_{f,i} \end{pmatrix} \quad (17)$$

Table 1: Nominal parameters for storage tank of solar heating system.

Parameter	Value	Unit
A_w	x_w^2	m^2
A_f^{eq}	$\frac{\pi r_p^2 \ell_f}{x_w}$	m^2
\hat{c}_{pf}	3.5	$\frac{\text{kJ}}{\text{kg} \cdot \text{K}}$
\hat{c}_{pw}	4.19	$\frac{\text{kJ}}{\text{kg} \cdot \text{K}}$
k_w	0.6×10^{-3}	$\frac{\text{kW}}{\text{m} \cdot \text{K}}$
ℓ_f	30	m
m_w	$60 \cdot N_{\text{pers}}$	kg
N_{pers}	2	–
r_p	$\frac{13}{2} \times 10^{-3}$	m
S_{f2w}	$2\pi r_p \cdot \ell_f$	m^2
U_{f2w}	0.25	$\frac{\text{kW}}{\text{m}^2 \cdot \text{K}}$
x_{aux}	$\frac{3}{4} x_w$	m
x_w	$\sqrt[3]{\frac{m_w}{\rho_w}}$	m
ρ_f	1060	kg/m^3
ρ_w	10^3	kg/m^3
\wp_w	$\frac{S_{f2w}}{x_w}$	m

 Table 2: Nominal operating conditions for storage tank. μ_x is the Heaviside function.

Quantity	Value	Unit
\dot{m}_f	$\frac{2 \times 10^3}{3600}$	kg/s
\dot{m}_{hw}	$\frac{50}{24 \cdot 3600} N_{\text{pers}}$	kg/s
\dot{Q}_{aux}	$2\mu_x x_{\text{aux}}$	kW
\dot{Q}'_{aux}	$\frac{\dot{Q}_{\text{aux}}}{x_w - x_{\text{aux}}}$	$\frac{\text{kW}}{m}$
$T_{f,i}$	70	$^\circ\text{C}$
$T_{w,i}$	10	$^\circ\text{C}$
$T_f(t=0, x)$	$T_{f,i}$	$^\circ\text{C}$
$T_c(t=0)$	$T_{f,i}$	$^\circ\text{C}$
$T_w(t=0, x)$	$T_{w,i}$	$^\circ\text{C}$
$T_{w,\ell}(t=0)$	$T_{w,i}$	$^\circ\text{C}$
$T_{w,u}(t=0)$	$T_{w,i}$	$^\circ\text{C}$

where the elements of matrix M are:

$$M_{11} = \dot{m}_{\text{hw}} \hat{c}_{pw} + UA|_{f2w} \frac{x_{\text{aux}}}{x_w} \quad (18)$$

$$M_{12} = 0 \quad (19)$$

$$M_{13} = -UA|_{f2w} \frac{x_{\text{aux}}}{x_w} \quad (20)$$

$$M_{21} = -\dot{m}_{\text{hw}} \hat{c}_{pw} \quad (21)$$

$$M_{22} = \dot{m}_{\text{hw}} \hat{c}_{pw} + UA|_{f2w} \frac{x_w - x_{\text{aux}}}{x_w} \quad (22)$$

$$M_{23} = -UA|_{f2w} \frac{x_w - x_{\text{aux}}}{x_w} \quad (23)$$

$$M_{31} = -UA|_{f2w} \frac{x_{\text{aux}}}{x_w} \quad (24)$$

$$M_{32} = -UA|_{f2w} \frac{x_w - x_{\text{aux}}}{x_w} \quad (25)$$

$$M_{33} = \dot{m}_f \hat{c}_{pf} + UA|_{f2w} \frac{x_{\text{aux}}}{x_w} \quad (26)$$

4 Storage tank simulation

4.1 Parameters and operating conditions

Examples of parameter values for the storage tank are given in Table 1.

Examples of operating conditions are given in Table 2.

In Table 2, T_c is the temperature of the concentrated model.

4.2 Steady operation

The two point boundary value steady models are solved using routine `bvp4c` in MATLAB of The MathWorks.² Figure 5 illustrates the steady temperatures in the storage tank (T_w) and the tube side of the heat exchanger (T_f) when $\dot{Q}_{\text{aux}} = 2 \text{ kW}$.

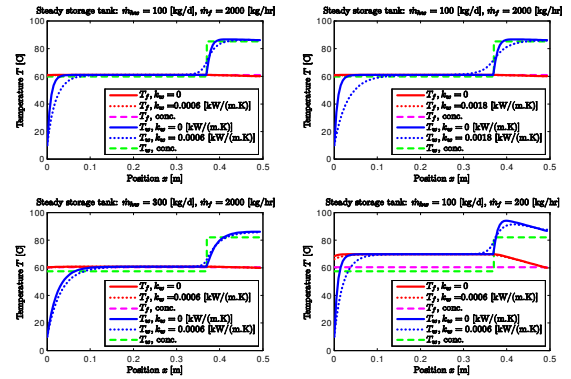


Figure 5: Steady temperatures in storage system: T_w (blue, concentrated: green) and T_f (distributed: red, concentrated: magenta); without diffusion (solid) and with diffusion (dotted). Auxiliary heat $\dot{Q}_{\text{aux}} = 2 \text{ kW}$. Subplot (1, 1): nominal case; subplot (1, 2): tripled diffusion coefficient k_w ; subplot (2, 1): tripled hot water consumption \dot{m}_{hw} ; subplot (2, 2): 10% tube side flow \dot{m}_f .

²See www.mathworks.com.

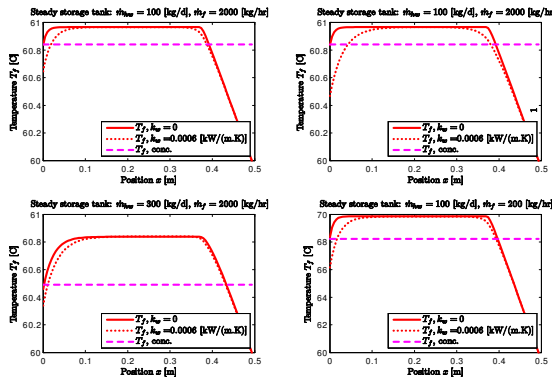


Figure 6: Details of steady tube side temperature T_f (distributed: red, concentrated: magenta); without diffusion (solid) and with diffusion (dotted). Auxiliary heat $\dot{Q}_{aux} = 2$ kW. Subplot (1, 1): nominal case; subplot (1, 2): tripled diffusion coefficient k_w ; subplot (2, 1): tripled hot water consumption \dot{m}_{hw} ; subplot (2, 2): 10% tube side flow \dot{m}_f .

Figure 6 gives a more detailed view of the tube side temperature with and without diffusion, with $\dot{Q}_{aux} = 2$ kW.

The results in plot (1, 1) of Figure 5 seem to indicate that the nominal storage tank system with volume given by $x \in [0, x_{aux}]$ is relatively well mixed — except perhaps for a small region near $x = 0$, and that the nominal system and volume given by $x \in [x_{aux}, x_w]$ is relatively well mixed. In other words: it may be possible to simplify the model into a two compartment model. Likewise, the tube side seems to have a relatively constant temperature throughout, leading to a third compartment. However, if the heat diffusion is important (plot (1, 2) in the figures), or the hot water consumption \dot{m}_{hw} increases dramatically (plot (2, 1) in the figures), or the flow rate \dot{m}_f of the hot water fluid decreases dramatically (plot (2, 2)), then such a coarse three compartment model is probably too simple. It should be remembered that these conclusions are based on a steady model. It remains to see whether the inertia of the system can be captured by a coarse three compartment model.

4.3 Transient operation

The dynamic models are solved using the solver `ode15s` in MATLAB of The MathWorks.³ Solving the discretized dynamic model with $N = 50$ slices and for the nominal conditions, leads to the results in Figs. 7–8.

Comparisons of the transients of the distributed model with the concentrated model are given Figs. 9–10.

If we reduce the tube fluid flow rate \dot{m}_f to 10% of the nominal value, the results are as in Figs. 11–12.

Finally, it is of interest how changing various quantities affect the system when the system starts from steady state. Figures 13–14 show the effect of a 10 °C drop in $T_{f,i}$ when starting from nominal steady state.

Changes in other inputs show minor response and relatively similar response in the distributed model and the concentrated model, except for changes in \dot{m}_{hw} where the re-

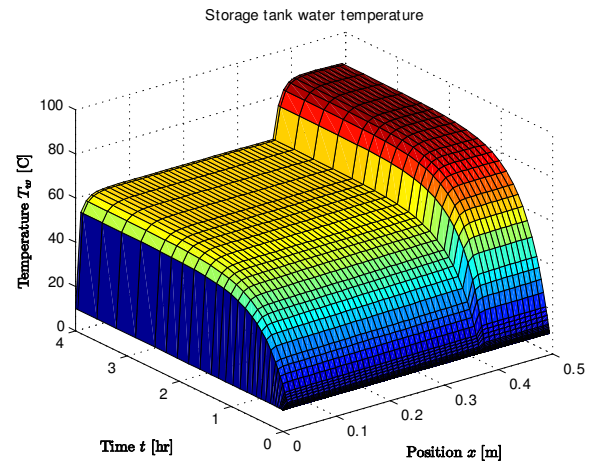


Figure 7: Transient temperature distribution T_w ; $N = 50$. Conditions as in Figs. 5–6, subplot (1, 1).

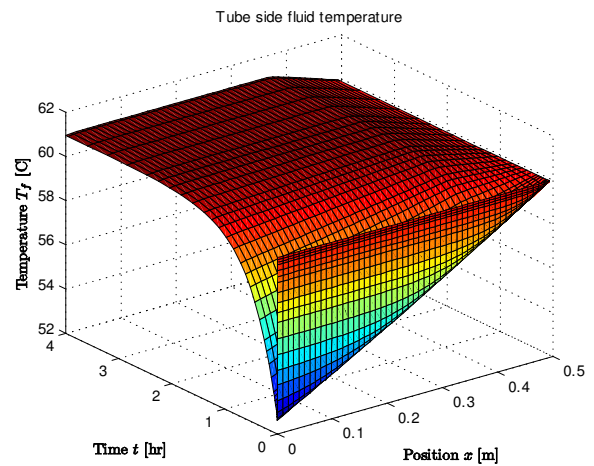


Figure 8: Transient temperature distribution T_f ; $N = 50$. Conditions as in Figs. 5–6, subplot (1, 1).

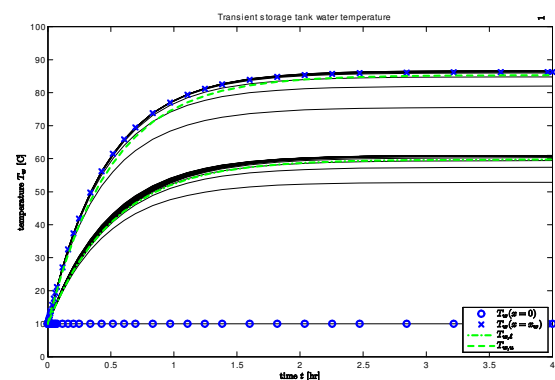


Figure 9: Transient storage tank water temperature distribution (solid black), with indications of inlet temperature $T_{w,i}$ (circle, blue) and outlet temperature T_w ($x = x_w$) (x, blue), as well as lower concentrated temperature $T_{w,l}$ (dash-dot, green) and upper concentrated temperature $T_{w,u}$ (dashed, green). Conditions as in Figs. 5–6, subplot (1, 1).

³See www.mathworks.com.

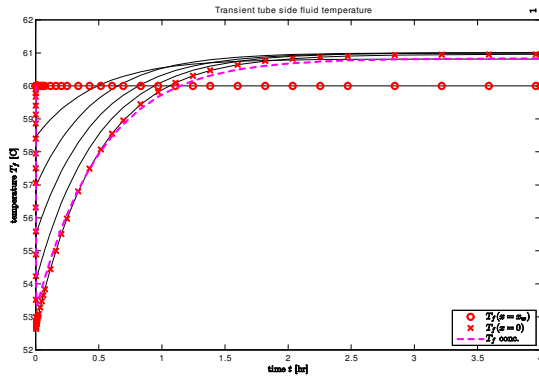


Figure 10: Transient tube side fluid temperature distribution (solid black), with indications of inlet temperature $T_{f,i}$ (circle, red) and outlet temperature $T_f(x=0)$ (x, red), as well as concentrated model temperature T_f (dashed, magenta). Conditions as in Figs. 5–6, subplot (1, 1).

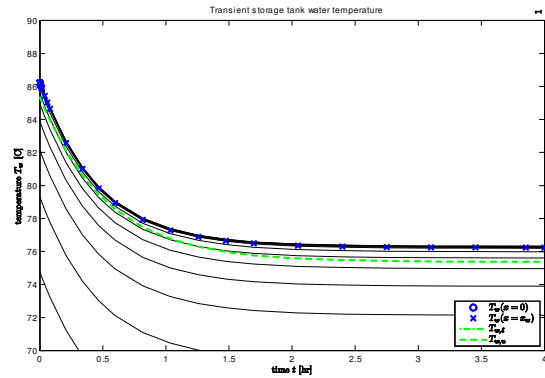


Figure 13: Transient storage tank water temperature distribution (solid black), when starting from nominal steady state, and experiencing a 10°C drop in inlet temperature $T_{w,i}$. Response in outlet temperature $T_w(x=x_w)$ (x, blue), as well as upper concentrated temperature $T_{w,u}$ (dashed, green).

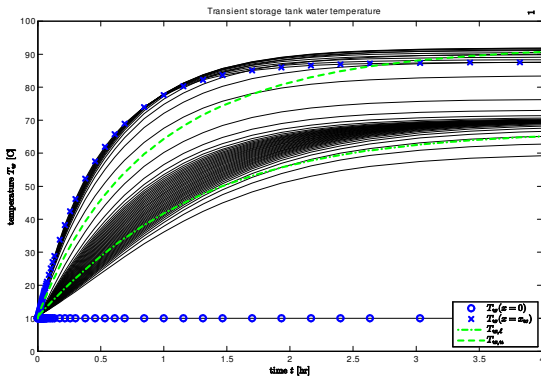


Figure 11: Transient storage tank water temperature distribution (solid black), with indications of inlet temperature $T_{w,i}$ (circle, blue) and outlet temperature $T_w(x=x_w)$ (x, blue), as well as lower concentrated temperature $T_{w,l}$ (dash-dot, green) and upper concentrated temperature $T_{w,u}$ (dashed, green). Conditions as in Figs. 5–6, subplot (2, 2).

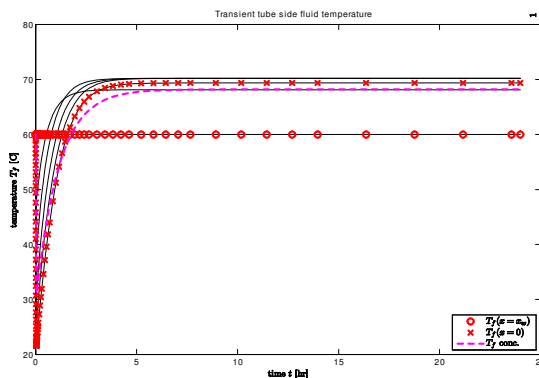


Figure 12: Transient tube side fluid temperature distribution (solid black), with indications of inlet temperature $T_{f,i}$ (circle, red) and outlet temperature $T_f(x=0)$ (x, red), as well as concentrated model temperature T_f (dashed, magenta). Conditions as in Figs. 5–6, subplot (2, 2).

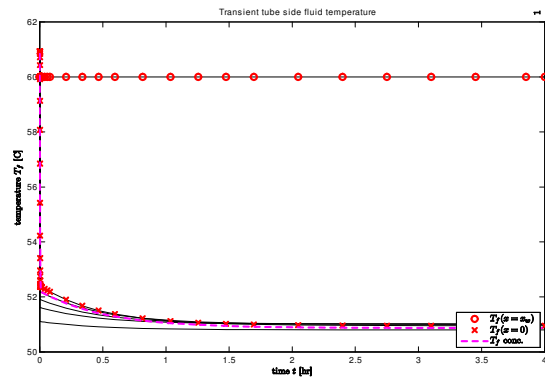


Figure 14: Transient tube side fluid temperature distribution (solid black), when starting from nominal steady state, and experiencing a 10°C drop in inlet temperature $T_{f,i}$. Response in inlet temperature $T_{f,i}$ (circle, red) and outlet temperature $T_f(x=0)$ (x, red), as well as concentrated model temperature T_f (dashed, magenta).

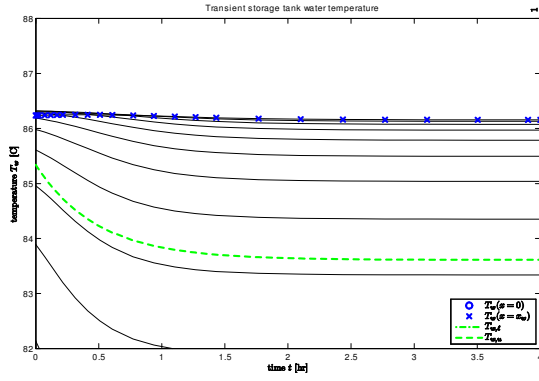


Figure 15: Transient storage tank water temperature distribution (solid black), when starting from nominal steady state, and experiencing a doubling of the hot water mass flow \dot{m}_{hw} . Response in outlet temperature $T_w(x = x_w)$ (x, blue), as well as upper concentrated temperature $T_{w,u}$ (dashed, green).

response in $T_w(x = x_w)$ is minor for the distributed model and relatively pronounced for the concentrated model, Fig. 15.

4.4 Comparing models

In [19], a simple model of a water storage tank with stratification is discussed, and an adaptive algorithm for tracking the thermocline is developed. Tracking of the thermocline is particularly important for the case of recirculating the heated water into the bottom of the storage tank. However, when the energy in the heated water is transferred through a heat exchanger, as discussed in this work, the thermocline will be much less pronounced.

With a heat exchanger, and in steady operation, Figure 6 indicates that assumptions of constant storage tank water temperature below the auxiliary heating region as well as a different and constant temperature in the auxiliary heating region, and constant tube fluid temperature throughout may be reasonably good for most conditions — except for (unrealistically) low flow rate for the tube fluid. Figures 8–10 indicate that under nominal conditions, the reduced order 3 state model captures both the steady state conditions and the inertia of the system reasonably well. However, in the case of low flow rate for the tube fluid, the reduced order model has too slow dynamics for the storage tank effluent temperature. Figures 13–15 indicate that for most input changes, the concentrated 3 state model is reasonably good, except for at capturing the outlet temperature for changes in the hot water flow rate \dot{m}_{hw} .

The plots of the transients of the fluid temperature T_f , Figs. 8, 10 and 12 do indicate the presence of some fast dynamics and thus a stiff system, and it is probably possible to reduce the order of the model. This possibility is not pursued here, though, and the reduced order model is used as is in the system simulations.

5 System simulation

5.1 Improved storage tank model

With reference to [13], the original *storage tank* description had states T_w , T_{cx} and T_{fx} denoting well mixed storage tank water temperature, collector heat exchanger fluid temperature, and floor heating heat exchanger fluid, respectively. In the improved storage tank model, based on the concentrated model in Eqs. 14–16, will have states $T_{w,\ell}$, $T_{w,u}$, T_{cx} and T_{fx} . For the collector fluid in the heat exchanger:

$$\begin{aligned} \frac{dT_{cx}}{dt} = & \frac{\dot{m}_c}{m_{cx}} (T_c - T_{cx}) \\ & - \frac{UA|_{cx2w} \frac{x_{aux}}{x_w}}{m_{cx} \hat{c}_{p,cx}} (T_{cx} - T_{w,\ell}) \\ & - \frac{UA|_{cx2w} \frac{x_w - x_{aux}}{x_w}}{m_{cx} \hat{c}_{p,cx}} (T_{cx} - T_{w,u}), \end{aligned}$$

for the floor fluid in heat exchanger:

$$\begin{aligned} \frac{dT_{fx}}{dt} = & \frac{\dot{m}_f}{m_{fx}} (T_f - T_{fx}) \\ & - \frac{UA|_{fx2w} \frac{x_{aux}}{x_w}}{m_{fx} \hat{c}_{p,fx}} (T_{fx} - T_{w,\ell}) \\ & - \frac{UA|_{fx2w} \frac{x_w - x_{aux}}{x_w}}{m_{fx} \hat{c}_{p,fx}} (T_{fx} - T_{w,u}), \end{aligned}$$

and for the water in the storage tank:

$$\begin{aligned} \frac{dT_{w,\ell}}{dt} = & \frac{\dot{m}_{hw}}{m_w \frac{x_{aux}}{x_w}} (T_{w,i} - T_{w,\ell}) \\ & + \frac{UA|_{cx2w}}{m_w \hat{c}_{pw}} (T_{cx} - T_{w,\ell}) \\ & + \frac{UA|_{fx2w}}{m_w \hat{c}_{pw}} (T_{fx} - T_{w,\ell}) \\ & - \frac{UA|_{w2a2}}{m_w \hat{c}_{pw}} (T_{w,\ell} - T_{a2}) \\ \frac{dT_{w,u}}{dt} = & \frac{\dot{m}_{hw}}{m_w \frac{x_w - x_{aux}}{x_w}} (T_{w,\ell} - T_{w,u}) \\ & + \frac{UA|_{cx2w}}{m_w \hat{c}_{pw}} (T_{cx} - T_{w,u}) \\ & + \frac{UA|_{fx2w}}{m_w \hat{c}_{pw}} (T_{fx} - T_{w,u}) \\ & - \frac{UA|_{w2a2}}{m_w \hat{c}_{pw}} (T_{w,u} - T_{a2}) \\ & + \frac{1}{m_w \frac{x_w - x_{aux}}{x_w} \hat{c}_{pw}} \dot{Q}_{aux}. \end{aligned}$$

5.2 Ventilation energy recovery

With reference to [13], the improved *building model* only needs a change in the description of the *air temperature*,

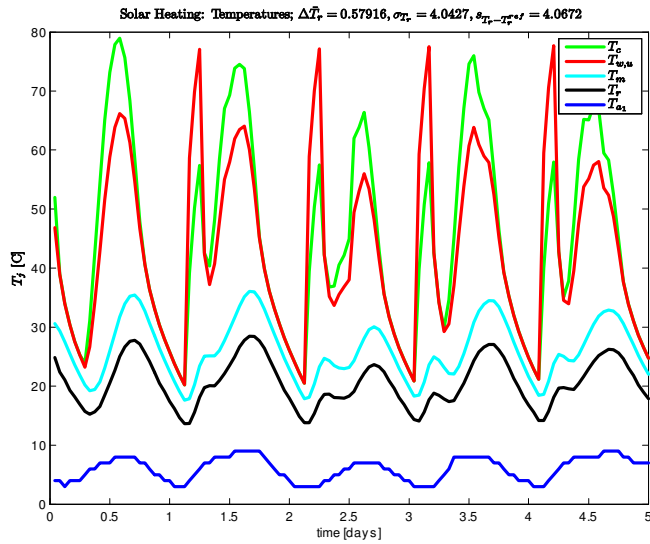


Figure 16: Temperatures at various positions in the system with realistic disturbance inputs.

which changes to

$$\begin{aligned} \frac{dT_r}{dt} = & \frac{\dot{m}_{r,i}}{m_r} (T_{a1} - T_r) \times (1 - \eta_v) \\ & + \frac{UA|_{m2r}}{m_r \hat{c}_{p,r}} (T_m - T_r) \\ & - \frac{UA|_{r2a1}}{m_r \hat{c}_{p,r}} (T_r - T_{a1}), \end{aligned}$$

where zero ventilation energy recovery as used in [13] is equivalent to setting $\eta_v = 0$, while complete energy recovery is equivalent to setting $\eta_v = 1$. In the subsequent simulations, $\eta_v = 0.5$, which is unrealistically low.

5.3 Simulation

Except for the obvious changes of model parameters necessitated by the changes in ventilation heat recovery and storage tank, the model parameters, operating conditions, and disturbances are as in [13].

Figures 16–18 indicate the operation of the system when using a thermostat controller to control the room temperature to ca. 20 °C, and can be compared to the results in [13].

Using the improved model in this work with thermostat control, the standard deviation of the offset from the reference room temperature is $s_{T_r - T_r^{ref}} = 4.1$ °C, with a mean auxiliary heating of $\bar{Q}_{aux} 0.4$ kW. The ventilation heat loss seems to be $\bar{Q}_{vent} \approx 1.0$ kW. With the original model of [13], the similar numbers were $s_{T_r - T_r^{ref}}^{2014} = 3.8$ °C, $\bar{Q}_{aux}^{2014} 1.17$ kW and $\bar{Q}_{vent} \approx 1.5$ kW. Obviously, these numbers can not be used to tell which model is best. However, it is clear that the energy consumption is reduced with the new model: this is a result of a combination of ventilation heat integration and allowing for temperature distribution in the storage tank⁴. The fact that the temperature

⁴Temperature distribution/stratification implies less entropy loss due to mixing, and thus a higher exergy = available energy.

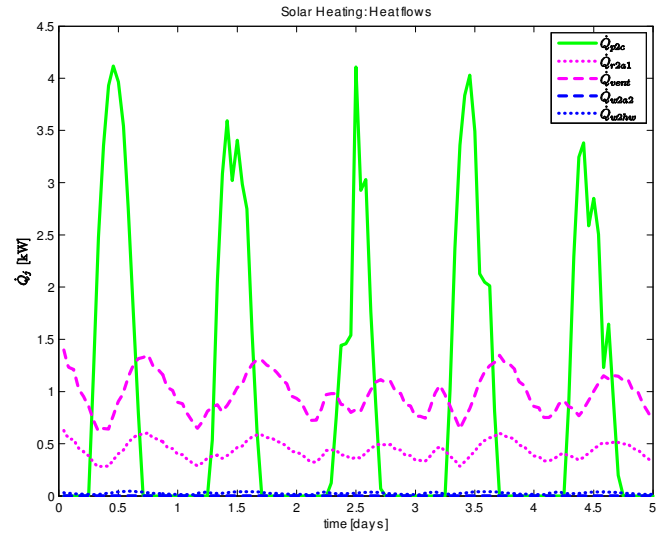


Figure 17: Heat flows at various positions in the system with realistic disturbance inputs.

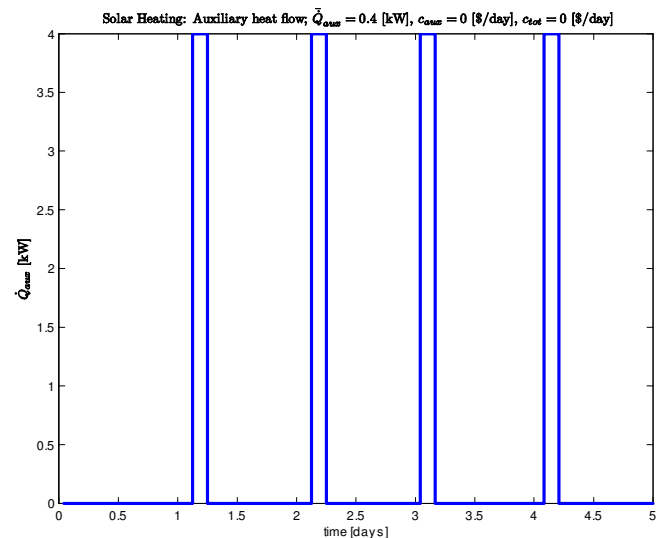


Figure 18: Auxiliary heat input to storage tank using thermostat controller.

variation increases in the improved model simply reflects the fact that for the given conditions, the solar energy is too plentiful to allow good control: to improve the control, it is necessary to be able to reduce the heat flow from the collector. In these simulations, the efficiency of the ventilation heat integration is set to $\eta_v = 0.5$. In simple ventilation heat integration systems, a realistic efficiency factor is typically $\eta_v = 0.7$ or so. With heat pumps, η_v can be even higher, at the cost of a slightly increased electricity consumption.

6 Conclusions

This paper discusses two improvements in a previously published model of solar heating of buildings applied to on-line control and optimization: inclusion of energy recovery from ventilation, and a more realistic water storage tank model. Simulation results of a 1D distributed storage tank model seem to indicate that a two compartment model is sufficiently accurate for control design, although variation in the hot water consumption ideally requires a two compartment model with varying volumes for the two compartments — this is similar to using a thermocline tracking algorithm. Simulation results of the complete system with a thermostat controller verifies expected changes in the system behavior. However, good control of the system can not be expected unless it is also possible to reduce the influence of the solar irradiance: the peak irradiance is too strong, so that the room temperature becomes too high.

Although the model has been improved, future improvements are possible. Here, it is important to make a distinction between improvements which are necessary to make the model realistic, and design changes necessary to make the system better controllable. The list of improvements from the introduction to this paper are still relevant. A higher ventilation heat recovery should be used, and it should be considered to introduce thermocline tracking/variable zone volumes in the storage tank. Also, it is possible that the heat exchanger for the floor heating system should not pass through the hot zone.

To improve controllability, it may be necessary to reduce the circulation of the solar collector fluid.

References

- [1] Arachchige, D.D.K. (2014). *An Approach to Day Ahead Forecasting of Solar Irradiance with an Application to Energy Gain in Solar Thermal Collectors*. M.Sc. thesis, University of Agder, Faculty of Engineering and Science, Grimstad.
- [2] Bayón, R., and Rojas, E. (2013). “Simulation of thermocline storage for solar thermal power plants: From dimensionless results to prototypes and real-size tanks”. *International Journal of Heat and Mass Transfer*, **Vol. 60**, pp. 713–721. <http://dx.doi.org/10.1016/j.ijheatmasstransfer.2013.01.047>.
- [3] Defra (2008). *Measurement of Domestic Hot Water Consumption in Dwellings*. Department for Environment, Food and Rural Affairs (Defra), UK.
- [4] de Oliveira, V., Jäschke, J., and Skogestad, S. (2013). “Dynamic online optimization of a house heating system in a fluctuating energy price scenario”. Preprints of the 10th IFAC International Symposium on Dynamics and Control of Process Systems, The International Federation of Automatic Control, December 18–20, 2013, Mumbai, India, pp. 463–468.
- [5] Duffie, J.A., and Beckman, W.A. (2013). *Solar Engineering of Thermal Processes, 4th edition*. John Wiley & Sons, Hoboken, NJ.
- [6] Durão, B., Joyce, A., Farinha Mendes, J. (2014). “Optimization of a seasonal storage solar system using Genetic Algorithms”. *Solar Energy*, **Vol. 101**, pp. 160–166.
- [7] Eicker, U. (2014). *Energy Efficient Buildings with Solar and Geothermal Resources*. John Wiley & Sons Ltd., Chichester, UK. ISBN 9781118352243.
- [8] Han, Y.M., Wang, R.Z., and Dai, Y.J. (2009). “Thermal stratification within the water tank”. *Renewable and Sustainable Energy Reviews*, **Vol. 13**, pp. 1014–1026. doi:10.1016/j.rser.2008.03.001.
- [9] Cheng Hin, J.N., and Zmeureanu, R. (2014). “Optimization of a residential solar combisystem for minimum life cycle cost, energy use and exergy destroyed”. *Solar Energy*, **Vol. 100**, pp. 102–113.
- [10] Holth, E. (2009). Model Predictive Control of mixed solar and electric heating. MSc thesis, NTNU, Norway.
- [11] Jordan, U., and Vajen, K. (2000). “Influence of the DHW load profile on the fractional energy savings: a case study of a solar combi-system with trnsys simulations”. *Solar Energy*, **Vol. 69**, Nos. 1–6, pp. 197–208.
- [12] Kratzenberg, M.G., Beyer, H.G., and Colle, S. (2006). “Uncertainty calculation applied to different regression methods in the quasi-dynamic collector test”. *Solar Energy*, **Vol. 80**, pp. 1453–1462.
- [13] Lie, B., Pfeiffer, C., Skeie, N.-O., Beyer, H.-G. (2014). “Models for Solar Heating of Buildings”. Proceedings, 55th International Conference of Scandinavian Simulation Society (SIMS 2014), October 21–22 2014, Aalborg University, Denmark. Published by *Linköping Electronic Press*, www.ep.liu.se/ecp/108/ecp14108.pdf, pp. 28–38.
- [14] Lie, B., Pfeiffer, C., Beyer, H.-G. (2014). “Using history based irradiance forecasts for supporting the predictive control of solar thermal systems”. *Proceedings, EuroSun 2014*, September 16–19, Aix-les-Bains, France.

- [15] Perera., D.W.U., Pfeiffer, C., and Skeie, N.-O. (2014). “Modelling the heat dynamics of a residential building unit: Application to Norwegian buildings”. *Modeling, Identification and Control*, **Vol. 35**, No. 1, pp. 43–57, ISSN 1890-1328. doi:10.4173/mic.2014.1.4.
- [16] Perera., D.W.U., Pfeiffer, C., and Skeie, N.-O. (2014). “Modeling and simulation of multi zone buildings for better control”. *Proceedings, SIMS 2014, Aalborg, Denmark, October 21–22, 2014*.
- [17] Pichler, M.F., Lerch, W., Heinz, A., Goertler, G., Schranzhofer, H., Rieberer, R. (2014). “A novel linear predictive control approach for auxiliary energy supply to a solar thermal combistorage”. *Solar Energy*, **Vol. 101**, pp. 203–219.
- [18] Powell , K.M., and Edgar, T.F. (2012). “Modeling and control of a solar thermal power plant with thermal energy storage”. *Chemical Engineering Science*, **Vol. 71**, pp. 138–145.
- [19] Powell , K.M., and Edgar, T.F. (2013). “An adaptive-grid model for dynamic simulation of thermocline thermal energy storage systems”. *Energy Conversion and Management*, **Vol. 76**, pp. 865–873. <http://dx.doi.org/10.1016/j.enconman.2013.08.043>.
- [20] Saleh, A.M. (2012). *Modeling of Flat-Plate Solar Collector Operation in Transient States*. M.Sc. thesis, Purdue University, Indiana.
- [21] Zima, W., and Dziewa, P. (2010). “Mathematical modelling of heat transfer in liquid flat-plate solar collector tubes”. *Archives of Thermodynamics*, **Vol. 31**, No. 2, pp. 45–62. doi: 10.2478/v10173-010-0008-7.

Near well simulation of CO₂ injection for Enhanced Oil Recovery (EOR)

L.B.J. Chathurangani¹ Britt M. Halvorsen¹

¹Telemark University College, Faculty of Technology, Norway, {132348, Britt.Halvorsen}@hit.no

Abstract

Relative low recovery rates are a major challenge in oil industry. Estimates show that more than half of the oil remains in the reservoir after shut down. Therefore there are strong incentives for using CO₂ injection for Enhanced Oil Recovery (EOR). CO₂ injection also contributes to the control of the greenhouse effect.

Generally CO₂ is injected as a supercritical fluid. At sufficiently high pressures and temperatures, it achieves miscibility with oil.

In this research simulations are performed using OLGA-Rocx. The effect of CO₂ injection is represented through the change of oil relative permeability and the pressure effect of the injection well. Higher oil production is obtained when the residual oil saturation is reduced. The simulations indicate that, CO₂ should be injected as early as possible to increase the oil production. A rapid oil production rate can be achieved if the injection well is located on the top of the reservoir. Also the oil production is proportional to the injection pressure.

Keywords: CO₂-EOR, Near well simulation, Relative permeability curves, OLGA, ROCX

1 Introduction

Energy is a crucial requirement of our everyday lives and mainly this energy comes from crude oil. Oil is generally referred as a non-renewable resource. According to International Energy Statistics, in year 2013 the total global oil supply was approximately 91,000 thousand barrels per day (Administration 2014). Reservoir estimations conducted in 2013 suggest that US is able to produce oil for another 12 years using conventional recovery techniques. Similarly Canada has reserves for 4 years excluding oil sands; Saudi Arabia and Kuwait have reserves for another 77 and 105 years respectively (Conglin Xu 2013). Thus it is very essential to improve technologies to recover more oil from existing production fields.

Primary production is the first phase of the productive life of an oil field and in that phase oil is produced without any injection to the reservoir formation. The natural pressure in the reservoir is sufficient for the oil in the formation to flow into the production wellbore. Oil can be recovered up to 20% of the oil originally in the rock (OOIP) in this phase and this depends on the characteristics of the rock

formation and properties of the oil. Once the wells start to produce oil, the pressure in the formation is reduced causing a continuous decrease in the oil production rate. Water flooding is done for maintaining the reservoir pressure in the secondary phase to produce more oil. This phase has a potential of recovering further 15% - 20% of the OOIP.

Even after completion of the primary and secondary phases of the oil production, 65% or more of the OOIP is left in the reservoir formations (Institute for 21st century energy). The reasons for this poor oil recovery are that the oil is bypassed due to poor sweep efficiency, oil which is physically unconnected to the well bore and oil which is trapped by viscous, capillary and interfacial tension forces. The characteristics of the oil are changed using an injectant to recover a significant amount of oil remaining in the formation (Melzer 2012). These technologies are called Tertiary recovery or Enhanced Oil Recovery (EOR) methods and can be categorized into three types. These types are thermal methods, chemical methods and miscible gas flooding. CO₂, N₂ and Hydrocarbon gasses can be used as miscible gases.

2 Background

2.1 CO₂ Enhanced Oil Recovery (EOR)

CO₂- EOR has been used by the oil and gas industry for over 45 years (Sean I. Plasynski 2008). The two major countries having several projects regarding CO₂ EOR are United States and Canada. CO₂ is considered as an excellent solvent for miscible floods and CO₂ injection is a promising EOR mechanism. CO₂ is injected into the depleted oil fields through one or more injection wells which are located around the production well as the oil production is going down. This has the ability of recovering an additional 15% to 20% of OOIP (Institute for 21st century energy). In addition to production of energy by recovering more oil by applying CO₂ EOR, it has direct environmental benefit by sequestering CO₂ permanently in the old oil formation. According to estimations, the U.S and Canada have the potential to sequester more than 82 billion tons of Carbon (Sean I. Plasynski 2008).

2.2 Properties of CO₂

Pure CO₂ is a non-combustible gas having no colour or odour. The molecular weight of CO₂ is 44.010 g/mol and in given pressure and temperature CO₂ is denser

than air. Figure 1 shows the influence of pressure and temperature on the density of CO₂.

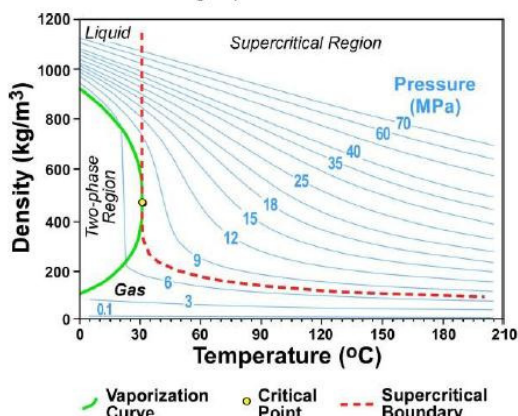


Figure 1. Relation of the density of carbon dioxide to temperature and pressure (Steve Whittaker 2013)

Below the critical temperature, CO₂ can exist either as a gas or liquid. After exceeding the critical temperature CO₂ exists as a gas. However when pressure is exceeding the critical pressure, the CO₂ becomes a supercritical fluid. Critical properties of CO₂ are given in Table 1.

Table 1. Critical properties of CO₂ (Mathiassen 2003)

Parameter	Value
T _C	31.05 °C
P _C	73.9 bar
V _C	94 cm ³ /mol

CO₂ at its supercritical pressure and temperature is completely miscible with oil. Because of that, oil moves through the rock pore spaces more easily yielding more oil production. (Institute for 21st century energy). As the reservoir fluids are produced through the production wells, the reservoir pressure will decline. Then the injected CO₂ has the ability to reconvert into gaseous state and provides a gas lift which is similar to original reservoir natural gas pressure (Alomair and Iqbal 2014).

The main advantage of CO₂ compared to other gasses is its ability to extract heavy hydrocarbon components up to the range C30. Some of the main characteristics of CO₂ which are effective in extracting oil from porous rock are mentioned below (Holm and Josendal 1974).

- CO₂ promotes swelling

Oil swelling occurs due to solubility of CO₂ in oil. Pressure, temperature and the oil composition are the main key parameters which effect on the degree of swelling. Swelling is important because the residual oil saturation is inversely proportional to the swelling factor.

- CO₂ reduces oil viscosity

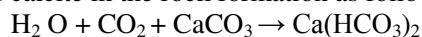
The dissolving of CO₂ in oil reduces the oil viscosity as well. But the overall viscosity reduction depends on the initial oil viscosity. The reduction of oil viscosity will be larger if the initial oil viscosity is high.

- Interfacial tension reduction

CO₂ has the ability to reduce the interfacial tension by dissolving in oil. This has significant influence on the relative permeability curves and increases the oil relative permeability.

- CO₂ exerts an acidic effect on rock

CO₂ dissolves in water and forms carbonic water in the front section of CO₂ injection. This leads to dissolution of calcite in the rock formation as following reaction.



These rates of reactions in carbonated rocks are faster than in sand-stones. Because of this, the porosity and the permeability of the formation can be changed due to CO₂ injection.

- CO₂ reduces the effect of gravity segregation

CO₂ has the ability to reduce density difference between oil and water by dissolving in oil and water. This leads to reduced chance of gravity segregation.

2.3 Mechanisms

The main mechanisms of CO₂- EOR depend on the conditions of injecting CO₂, the reservoir conditions (pressure and temperature) and the oil composition. Generally CO₂ is not miscible with reservoir oil at the first contact. At sufficiently high pressures and temperatures, CO₂ achieves dynamic miscibility with oil through multiple contacts. The minimum pressure at which CO₂ and oil are completely mixed with each other at any proportion is called the minimum miscibility pressure (MMP). Injection of CO₂ at a pressure equal to or above the MMP is called miscible CO₂ EOR and CO₂ flooding at a pressure below the MMP is called immiscible CO₂ EOR.

2.3.1 Miscible CO₂ EOR

CO₂ EOR can be achieved when CO₂ is flooded into a reservoir having low viscous oil, at a pressure equal to or higher than MMP. Mixing reservoir oil with CO₂ does not happen instantaneously. When the reservoir oil is in contact with the injected CO₂, the oil begins to dissolve into the dense CO₂ and the dense CO₂ begins to dissolve into the oil. Eventually the oil and the injected CO₂ become one single phase due to repeated contacts with time. The instance where CO₂ is completely mixed with oil, is termed as miscible CO₂ EOR. Under this process vaporization of crude oil, development of miscibility, and reduction of interfacial

tension occurs within the reservoir. This leads to more oil production due to more efficient sweep of oil (Steve Whittaker 2013).

When miscible CO₂ EOR is performing, several compositional zones are developed in the displacement direction within the reservoir as shown in Figure 2. As the first point of contacting CO₂ with reservoir oil, a miscible front will be generated. In this front lighter hydrocarbon molecules will be transferred gradually from the oil to CO₂. Then this front will dissolve in oil and act as a single phase under favourable pressure and temperature conditions. This makes it easier for the oil to move towards the production wells.



Figure 2. Illustration of the zones that develop in miscible CO₂ flooding (Steve Whittaker 2013)

Most of the oil recovery operations are designed to maintain the reservoir pressure above the MMP in order to operate under fully miscible conditions. These pressure conditions can be achieved naturally in the reservoirs below about 800m of depth.

2.3.2 Immiscible CO₂-EOR

When the reservoir pressure is not sufficient to exceed the MMP or the reservoir contains oil having high density and viscosity (heavy oil) immiscible CO₂-EOR is carried out. Even though the miscibility between oil and CO₂ is not significant; CO₂ will dissolve in the oil phase. Hence reduction of crude oil viscosity and swelling occur and these are the most important effects under the immiscible CO₂ EOR process (Alomair and Iqbal 2014). In addition to that the reservoir oil is pushed effectively towards the production well by the injected CO₂. Therefore due to these mechanisms, an additional portion of the remaining oil in the reservoir can be recovered. In generally, immiscible CO₂-EOR is much less efficient compared to miscible CO₂-EOR in recovering the residual oil.

2.4 Benefits of CO₂-EOR

The main advantage of CO₂ EOR is the economic benefits due to additional oil production by extending the productive life of the existing oil fields. In addition to the economic benefits, environmental benefits are also achieved. These benefits include permanent sequestering of captured CO₂ in the old oil formation without releasing it into the atmosphere. Hence the effect due to greenhouse gas on the global warming can be reduced. Old production wells can be converted into CO₂ injection wells. Hence there is no need to drill new wells which would lead to land degradation.

Therefore energy production, energy security and environmental sustainability can be enhanced via CO₂-EOR.

2.5 Limitations of CO₂ EOR

Supplying CO₂ to the place where the oil fields are located is one of the major challenges for CO₂ EOR. Availability of low cost CO₂ is the main challenge. This includes all cost for purchasing and transportation. To obtain a great performance the purity of CO₂ should be higher than 95%. Thus, purifying cost should also be considered. From the amount of CO₂ currently used for EOR, about 75% is extracted from naturally occurring deposits located near the oil fields in order to ensure economic feasibility. The rest is the captured CO₂ from industrial processes such as power plants fertilizer, manufacturing plants, etc. (Sean I. Plasynski 2008)

The problems associated with CO₂ EOR are gravity tonguing and viscous fingering. These are due to high mobility, lower density and viscosity of CO₂ compared to the oil in the reservoir. In order to avoid these problems to some extent and improve the sweep efficiency, the following methods are carried out:

- WAG (Water Alternating Gas) process
In order to improve sweep efficiency water and CO₂ are injected to the formation as alternating slugs.
- Injection of foaming solutions together with CO₂
By adding foaming solutions in more permeable areas of the reservoir, the mobility of CO₂ can be reduced. Hence sweep efficiency can be improved. (Mathiassen 2003)
- Installation of well packers and inflow control devices

CO₂ EOR is not suitable for all oil fields and the effectiveness of CO₂ EOR depends on several factors such as oil composition, depth, temperature and other characteristics of the reservoir (Steve Whittaker 2013). The characteristics of the reservoir such as reservoir heterogeneities, porosity, permeability and wettability must be considered when designing a CO₂ EOR system.

3 Development of the model in OLGA-Rocx

The impact of CO₂ injection as an enhanced oil recovery mechanism is analysed via near-well simulations. In this chapter, the development procedure of the simulation models is described.

3.1 Simulation tools

The model of the near-well reservoir was developed in Rocx and coupled with the wellbore model in OLGA. The simulation results are presented through TECPLOT and OLGA.

The objective of this study is to conduct computational simulations to study the effect of CO₂ injection as an EOR technique. The study is focused on the fluid movement within the reservoir and the effect of different parameters on the amount of oil produced. A relatively small well section is sufficient to conduct the study and more importantly, by using a smaller well section the required computational time is reduced.

In this work an oil reservoir with a thickness of 20m was considered. It was assumed that there is an enormous aquifer below the oil layer. The length of the well was taken as 25m.

3.2 Development of the near-well reservoir model

Initially a base case without any CO₂ injection was developed and simulated in order to compare the results of the more complex simulations using different CO₂ injection parameters.

3.2.1 Dimensions of the reservoir

The considered reservoir contains a horizontal production well (a pipe) along the x-direction having a length of 25m. The production well is located in the middle of the y-axis and at 6m below the top of the reservoir. In Figure 3 a sketch of the reservoir is presented.

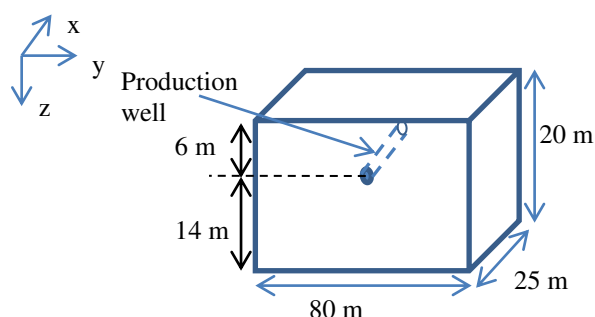


Figure 3. Dimensions of the reservoir

It is assumed that an enormous aquifer is located below the considered reservoir (at the bottom plane of the reservoir). Therefore pressure due to the water drive at the bottom of the reservoir is considered to be constant 158 bar. For the oil production, the pressure difference between the base pipe and the water drive pressure is approximately 10 bar. Hence, the base pipe pressure corresponds to 148 bar.

3.2.2 Grid

The geometry illustrated in Figure 3 was defined in Rocx through the rectangular coordinate system. The grid of the reservoir was divided into 1, 39 and 20 elements in x, y and z directions respectively.

The elements in x and z directions were considered to have constant length. In order to study the close surrounding of the well bore in greater details, the grid

spacing in the y direction was defined to make a finer grid in the centre. The view of the grid in the (y,z) plane is presented in Figure 4.

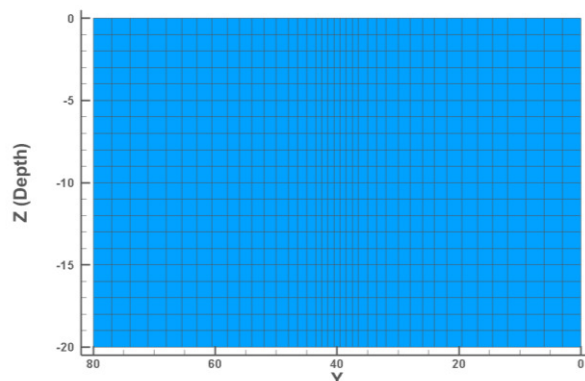


Figure 4. Mesh of the yz plane

3.2.3 Fluid properties

The properties of the oil, associated gas and water were specified and the black oil model was used for the simulations. The defined fluid properties and the reservoir conditions are summarised in Table 2.

Table 2. Fluid properties and the reservoir conditions

Label	Value (unit)
GOR	50 Sm ³ / Sm ³
Gas specific gravity	0.64
Oil specific gravity	0.85
Measured oil viscosity	10 cp
Measured at temperature	48.9 °C
Measured at pressure	158 bar

For these simulations a homogeneous reservoir was considered with porosity of 0.15% (Gu and Deo 2009). Permeabilities in the x,y and z directions of each cell were defined as 400 mD, 400 mD and 40 mD respectively.

3.2.4 Relative permeability curves

Two sets of relative permeabilities are required for three phase flow calculations in the reservoir. Those are,

- The water relative permeability (k_{rw}) and oil-water relative permeability (k_{row})
- The gas relative permeability (k_{rg}) and liquid-gas relative permeability (k_{rog})

Relative permeability values were defined as a function of water or gas saturation. The respective relative permeability curves are shown in Figure 5 (Gu and Deo 2009). Since the location of the crossover point and endpoint of the relative permeability values are functions of wettability of the rock formation (Kasiri and Bashiri 2011), this reservoir formation can be considered as a water-wetted reservoir.

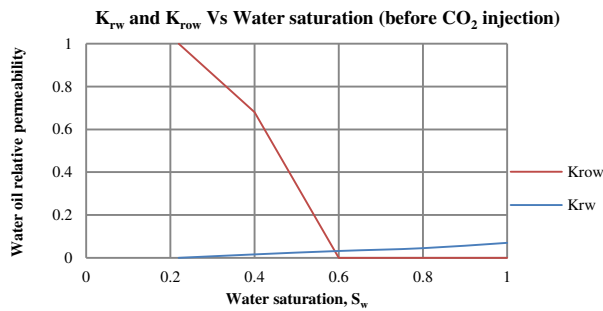


Figure 5. The water relative permeability (k_{rw}) and oil-water relative permeability (k_{row}) (Gu and Deo 2009)

For all the simulations the relative permeability curves shown in Figure 6 were used for the gas phase.

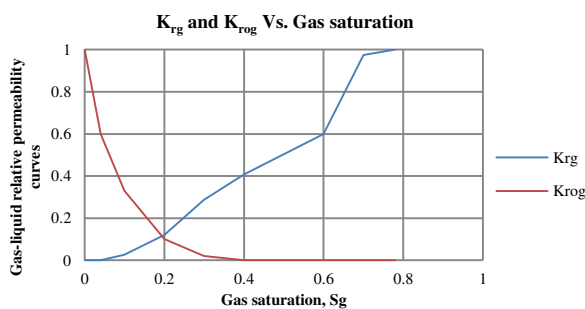


Figure 6. The gas relative permeability (k_{rg}) and liquid-gas relative permeability (k_{rog}) (Gu and Deo 2009)

3.2.5 Initial and boundary conditions

The initial pressure and the temperature of the reservoir were set as 158 bar and 48.9^oC respectively. It is assumed that the reservoir is completely filled with oil initially.

According to the defined reservoir, the production well is parallel to the x -axis. The (y,z) coordinates of the well are (20,6) in the (y,z) plane. The diameter of the well is 0.1m. The pressure and the temperature of the well are 158 bar and 48.9^oC respectively.

Pressure at the bottom boundary of the reservoir is considered to be constant and equal to 158 bar due to large aquifer below the oil reservoir. Therefore in Rocx this boundary condition is defined as a reservoir having a water-feed at the bottom plane ($Z=20$). The temperature of the boundary is the same as in the reservoir and equals to 48.9^oC.

3.3 Development of the CO₂ injection cases in Rocx

These cases were developed to study the effect of different CO₂ injection parameters on oil production. The effect of CO₂ injection was represented via the changes in the relative permeability curves and the pressure source through the injection well.

3.3.1 Change of relative permeability curves

As OLGA-Rocx does not support injection of CO₂ directly, a different approach had to be followed by changing the relative permeability curves.

For these simulations it was assumed that the residual oil saturation will be reduced from 0.4 to 0.1 compared to the reference case. The modified relative permeability diagram is shown in Figure 7.

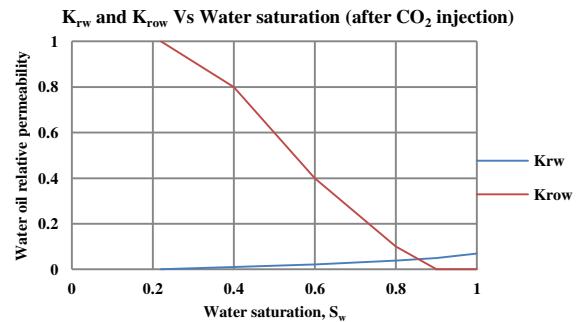


Figure 7. Water -oil relative permeability curves after CO₂ injection

3.3.2 Effect of CO₂ injection as a pressure source

By injecting a gas feed, the pressure effect on the CO₂ injection can be simulated. As the CO₂ gas feed cannot be directly defined in Rocx, a gas feed was defined with the properties of super critical CO₂ at 158 bar and 48^oC.

Under these simulations, the location of the CO₂ injection was defined in the (y,z) plane by changing the (y,z) coordinated. These were defined as pressure (reservoir) boundary conditions.

3.4 Development of the well and wellbore model in OLGA

The version of OLGA 7.3.1 was used as the main program to run the simulations and the model of the well and well bore were developed as shown in Figure 8.

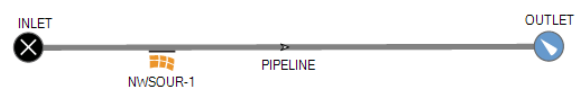


Figure 8. Layout of the model developed in OLGA

Then the pipe line was configured to have a length of 25 m in the x direction. The settings of the components were defined through the Model Browser. The reservoir model developed in Rocx was coupled with the near-well source.

The properties of the fluids and the reservoir conditions were defined according to the model developed in Rocx.

4 Simulation results

The results of the OLGA-Rocx simulations are illustrated and analysed in this section to study the effect of CO₂ injection as an EOR mechanism.

4.1 Effect of residual saturation

The effect of CO₂ injected is simulated via changing the relative permeability curves. Both the curvature and the residual oil saturation of the relative permeability curves can be changed due to CO₂ injection. In this section, the effect of the change of the residual oil saturation is considered.

In practice, it is economical to produce as much oil as possible using water drive. Therefore CO₂ was injected after the water breakthrough has occurred.

The accumulated volumes of oil and water produced with CO₂ injection is compared with the reference case which has no CO₂ injection. The comparison of the results is presented in Figure 9. One can clearly see that by decreasing the residual oil saturation, oil production has been enhanced significantly while the water production has been reduced. The change of oil and water production curves can be explained by the new relative permeability curves presented in Figure 7. Oil has a higher permeability compared to the water up to the water saturation of 0.8 and oil will be produced up to a water saturation of 0.9. In the reference case, oil production was terminated when the water saturation reaches 0.6. Therefore the decrease of residual oil saturation has increased the oil production while reducing the water production.

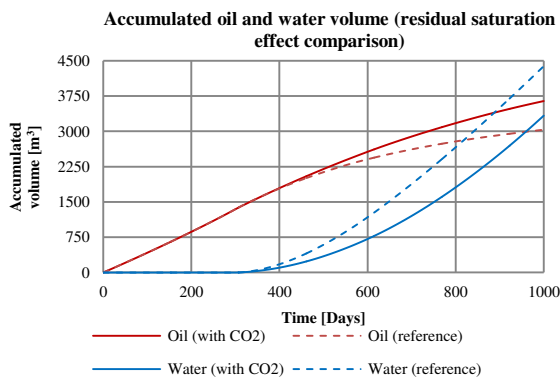


Figure 9. Residual oil saturation effect - accumulated fluid volume comparison

For economical purposes, it is important to analyze the oil production as a function of the water cut of the final product. In Figure 10 the accumulated oil volume of the two cases (CO₂ injection and reference case) are presented against the in-situ water cut.

It is clearly seen that the injection of CO₂ has significantly increased the quality of the final product. That is, when reaching a particular water cut, CO₂ injection has produced a higher amount of accumulated oil compared to the reference case.

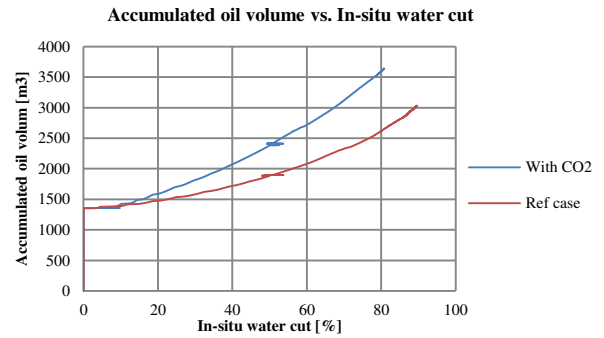


Figure 10. Accumulated oil volume vs. In-situ water cut

4.2 Effect of the curvature of the relative permeability curve

The chemical and physical properties of oil in the reservoir can change as CO₂ gets dissolved in oil. As a result the curvature of the relative permeability curves (their shapes) can be changed. A set of simulations were conducted using different types of relative permeability curves as shown in Figure 11.

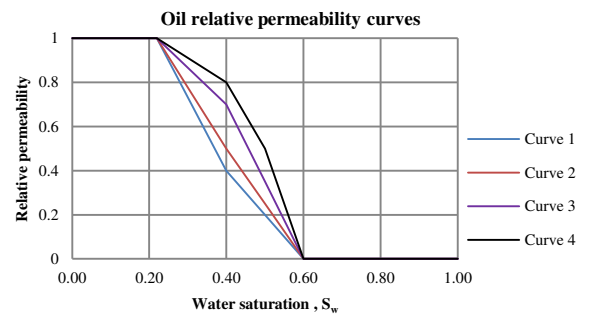


Figure 11. Oil relative permeability curves

The accumulated oil volumes related to the respective relative permeability curves are plotted in Figure 12 together with the accumulated oil volumes of the reference case and the residual saturation case which was presented in section 4.1.

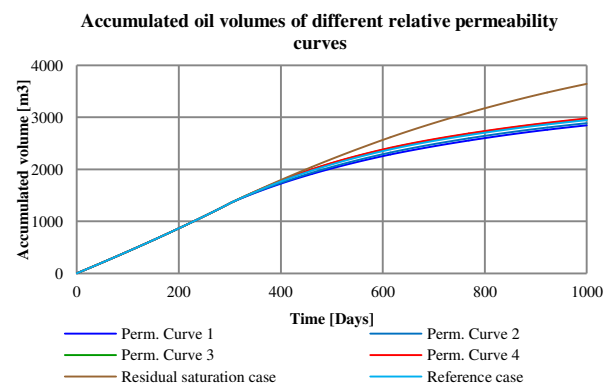


Figure 12. Accumulated oil volumes of different relative permeability curves

Based on the results illustrated in Figure 12 it can be concluded that the reduction of the residual oil

saturation has a significant higher impact on the oil production than the changes in the curvature of the relative permeability curves. When the shape of the relative permeability curve changes from a shape of concave up towards a shape of concave down, both the accumulated oil and water volumes increase gradually. The difference between the results of the considered four curves is relatively insignificant compared to the effect of the residual oil saturation.

Since the water is also an important parameter, average water cut of the different cases are presented in Figure 13.

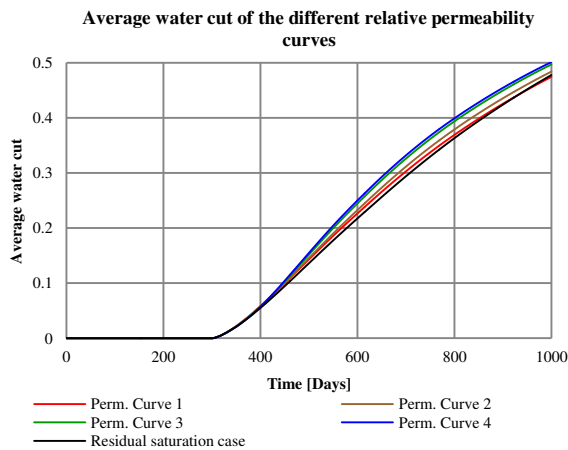


Figure 13. Average water cut of the different relative permeability curves

The average water cut of the system increases gradually when the shape of the relative permeability curve moves from a shape of concave down, decreasing towards a shape of concave up. Hence it can be concluded that even though concave down, decreasing curves produce more oil, they tend to produce at a relatively higher water cut as well. More important, it is interesting to observe that the case with lower residual saturation produces with the lowest water cut.

4.3 Effect of CO₂ injection time

The above simulation shows that additional amount of oil can be produced by injecting CO₂ to the formation (due to the reduction of residual oil saturation). It is interesting to study how the oil production will behave when the CO₂ is injected at a different time. For the study the simulation was conducted with CO₂ injection at different times and with a residual oil saturation of 0.1. Initial saturation profile for each simulation was obtained from the reference case using Tecplot. The initial oil saturation profiles are shown in Figure 14.

In Figure 15 the accumulated volume of produced oil is compared with the reference case which has no CO₂ injection. Regardless of the time of CO₂ injection, all the simulations have produced more oil than the reference case. Even though the difference between the

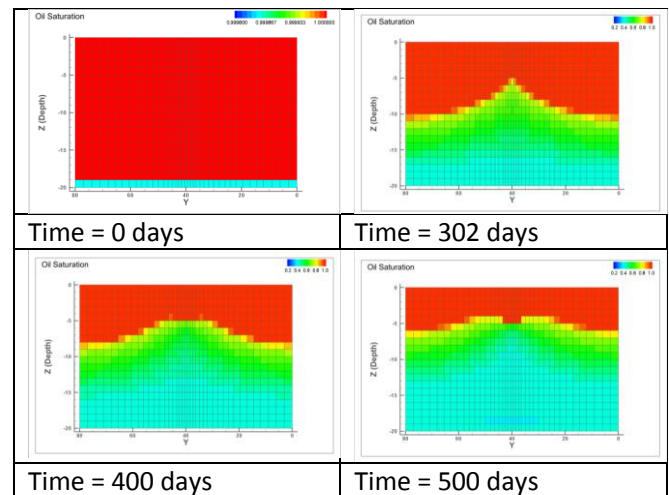


Figure 14. Initial saturation profiles for CO₂ injection time

amounts of oil produced is small for the cases with CO₂ injection, one can see that the earlier the CO₂ is being injected, the higher the oil production will be.

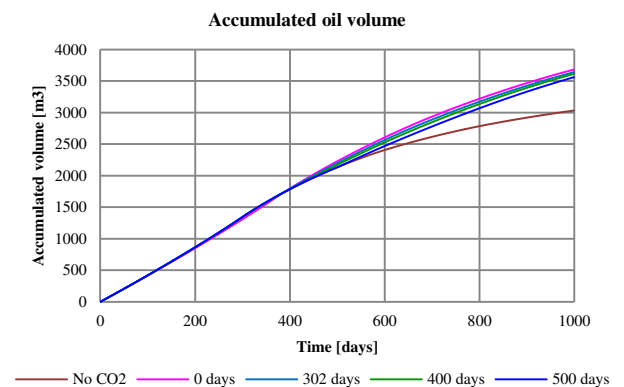


Figure 15. Accumulated oil volume (CO₂ injection time)

From the accumulated water profile presented in Figure 16 it can be observed that the amount of water produced with all the simulations having CO₂ injection is lower than the accumulated water volume of the reference case. Simulations with early CO₂ injection times tend to produce less amount of water compared to CO₂ injection simulations at later times. Another important factor is that the water breakthrough time has been delayed by 100 days by introducing CO₂ at the beginning of the simulations.

At any oil saturation value in the reservoir, injection of CO₂ makes oil more permeable. Hence CO₂ injection causes higher oil mobility leading to higher oil production. With time the oil saturation decreases due to the oil production. Therefore if CO₂ is injected early where the oil saturation is high, relatively more oil can be recovered. In addition, less water will be produced from the reservoir.

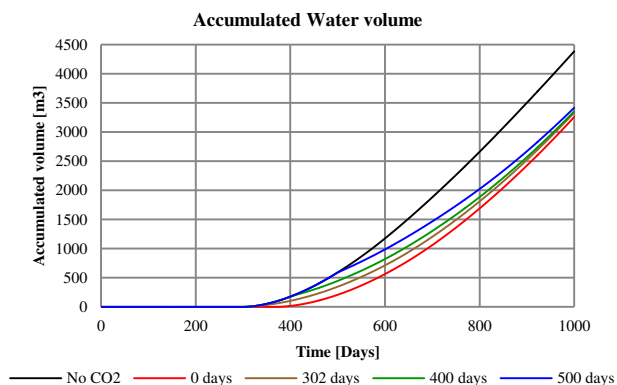


Figure 16. Accumulated water volume (CO₂ injection time)

4.4 Effect of the CO₂ injection location

For the following simulations, CO₂ was injected on the 302th day of the oil production where the water breakthrough takes place.

Figure 14 shows the oil saturation profile of the yz plane of the reservoir at the point of water breakthrough. In order to push the oil towards the well, CO₂ can be injected into the upper part of the reservoir to depth of maximum Z = 10. Simulations were conducted with different injection points to study the effect of the CO₂ injection location. The (y,z) coordination of the injection points (location of the injection well) of the simulations are, (1,1), (1,8), (1,9) and (1,10). In Figure 17 the accumulated oil profiles of these simulations are compared with reference case.

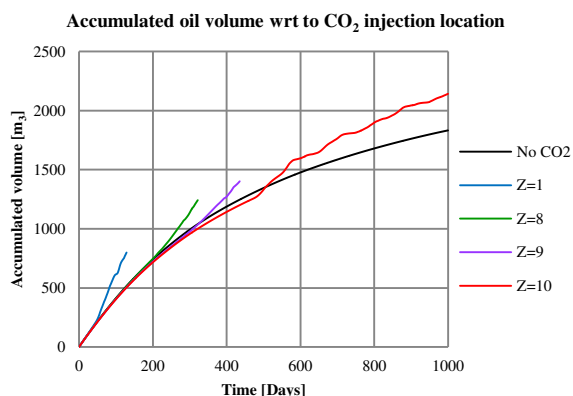


Figure 17. Accumulated oil volume wrt to CO₂ injection location

The figure clearly shows that when the gas injection well is located at the top of the reservoir, higher oil production rate can be obtained. But all these simulations tend to be instable as the gas feed reaches the production well. Hence it was impossible to conduct the simulations for the whole time period. However, the trend in the curves indicates that higher oil production can be obtained if the gas injection well is located at the top of the reservoir. When a pressure source is located in the top of the reservoir, more oil should be produced and the upward water flow should

be restricted. This phenomenon can be observed through the simulation results.

4.5 Effect of the CO₂ injection pressure

Another important factor in CO₂ injection is the pressure of the gas feed. For the simulations the location of the gas injection well was considered to be at the position (Z=10 and Y=1) to prevent simulation instabilities.

Figure 18 illustrates the profiles of the accumulated oil volume under different injection pressures compared with the accumulated oil volume obtained in the reference case.

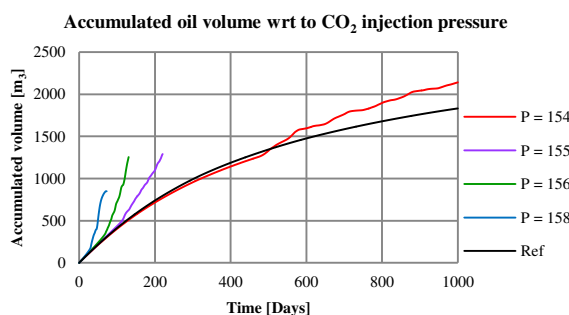


Figure 18. Accumulated oil volume wrt to CO₂ injection pressure

The figure clearly shows that as the inlet pressure increases, the rate of oil production increases rapidly. Due to the instabilities of the simulations, higher pressure simulations tend to stop. For the case with pressure of 154 bar, it can be seen that it still produces more oil compared to the reference case after 1000 days. Based on the trend of the lines, it can be assumed that as the pressure of the gas stream increases, higher amount of oil can be recovered from the reservoir. It is interesting to note that as the inlet pressure is decreased below 154 bar, the simulation crashes within a short period of time. This can be explained by considering the initial pressure distribution at the point of water breakthrough of the reservoir which is presented by Figure 19.

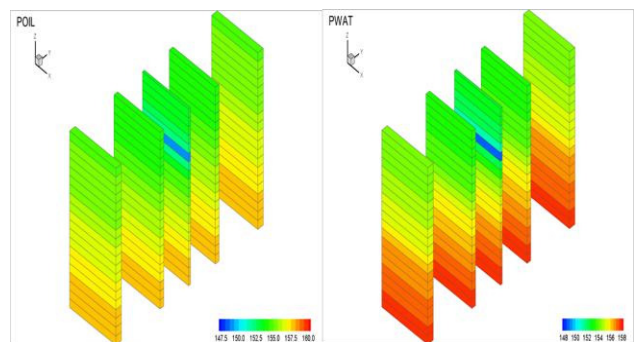


Figure 19. Pressure profile at water breakthrough

The result shows that, even though the initial pressure of the reservoir is defined as 158 bar, it is reduced down to around 154 bar in the top part of the

reservoir, at the point of water breakthrough. Therefore CO_2 cannot be injected to the reservoir at a pressure below 154 bar. The pressure in the reservoir reduces further with time and as a result of that more oil will be produced with time compared to the reference case due to the pressure effect of the injection well. The blue coloured cell indicates the production well, where the pressure is lowest.

Simulation data for 250 days are presented in Figure 20 for the analysis of water production. According to this figure, it can be concluded that as the inlet pressure increases, accumulated water flow will be reduced.

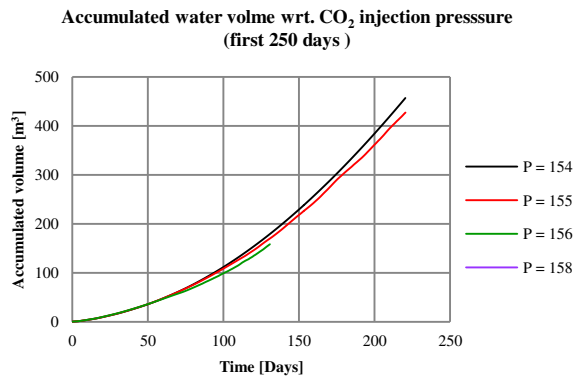


Figure 20. Accumulated water volume wrt CO_2 injection pressure (first 250 days)

4.6 CO_2 storage within the reservoir

CO_2 -EOR is not only an oil recovery mechanism but also a possible partial solution for global warming. The ability to store CO_2 within the reservoir is an additional advantage of CO_2 -EOR. The gas saturation profile after CO_2 has been injected is shown in Figure 21.

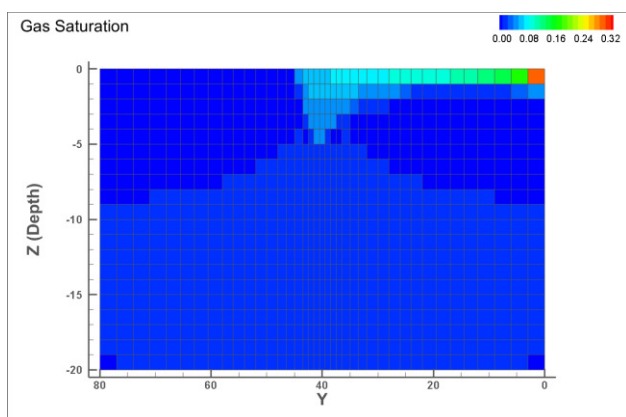


Figure 21. Gas saturation profile after CO_2 injection

The CO_2 injection well is located at the coordinates of (1,1) in the (y,z) plane. Gas gradually moves towards the production well and forms a gas cone. Due to the instabilities of the simulations in OLGA-Rocx when the gas reached the production well, further analysis could not be conducted. Installation of inflow control devices to prevent gas breakthrough could lead to proper gas storage and higher oil production.

5 Discussion

Based on the results of the simulations both the residual oil saturation and the curvature of the relative permeability curve are important parameters in CO_2 EOR as they affect the oil and water production from the well. Higher amount of oil can be recovered from the reservoir with lower water cut if the residual saturation of the oil can be reduced via CO_2 injection. Reduction of the residual oil saturation reduces the immobile oil content in the reservoir. At the same time oil will have a higher permeability compared to water even at lower oil saturations (Figure 7.). The effect of the residual saturation is extremely significant compared to the effect of the curvature shape of the relative permeability curve. If the residual oil saturation is high, oil permeability reduces rapidly as the oil saturation reduces, regardless of the curvature of the relative permeability curve. Hence residual oil saturation is more important factor than the shape of the permeability curve.

Both the location and the pressure of the CO_2 injection well have a significant impact on the oil production as well. A CO_2 injection well with higher injection pressure located at the top of the reservoir facilitates more oil production and less water production. When the injection well is located at the top of the reservoir, it can push oil in the top layer of the reservoir towards the production well. If the injection well is located at the middle of the reservoir, it will create an obstacle for the oil in the top of the reservoir to reach the production well. Due to the pressure effect of the injection well, water flowing from the bottom of the reservoir will be restricted.

Better results can be obtained from CO_2 EOR if CO_2 is injected as early as possible. At the early stages of the production, the oil saturation of the reservoir is higher and CO_2 injection can further enhance the permeability of the oil. If CO_2 is injected later, the effect of the permeability enhancement is not strong enough to compete with the permeability of water. The point at which the CO_2 should be injected is an economical factor. Generally it would be economical to produce oil with natural water drive as the water breakthrough occurs, and then CO_2 can be injected to enhance the oil recovery.

6 Conclusion

In this research work the effect of the CO_2 injection is represented through the changes in the relative permeability curves (i.e. residual oil saturation and the curvature of the permeability curve) and through the pressure effect of the CO_2 injection. All the simulations were conducted with a homogeneous, water-wet reservoir.

The most important parameter to be considered during CO_2 EOR is the residual oil saturation. The success of the CO_2 EOR system depends on its ability

to reduce the residual oil saturation. Compared to the effect of the residual oil saturation, the effect of the curvature of the relative permeability curve is insignificant.

The optimum location of the CO₂ injection well and its injection pressure can be estimated via computational simulations. Based on the simple OLGA-Rocx simulations it is better to locate the injection well at the top of the production well. Higher gas injection pressure will produce oil rapidly but it can cause operational issues. Based on the simulations it can be seen that the gas can be injected at the reservoir pressure and as the pressure in the reservoir decreases, the pressure impact of the gas stream will be significant.

Since OLGA-Rocx is not fully compatible for CO₂ injection, these results have to be verified through more acceptable simulation tools such as Eclipse and with experimental results. Still this work produces a fundamental framework for the simulation of CO₂ injection via OLGA-Rocx platform.

References

- Administration, US Energy Information. 2014. "International Energy Statistics." Accessed 15/04/2015.
<http://www.eia.gov/cfapps/ipdbproject/iedindex3.cfm?tid=5&pid=53&aid=1>.
- Alomair, Osamah, and Maqsood Iqbal. 2014. "CO₂ Minimum Miscible Pressure (MMP) Estimation using Multiple Linear Regression (MLR) Technique." SPE Saudi Arabia Section Technical Symposium and Exhibition.
- Conglin Xu, Laura Bell. 2013. "Worldwide reserves, oil production post modest rise." *Oil & Gas Journal* Accessed 02/04/2015.
<http://www.ogj.com/articles/print/volume-111/issue-12/special-report-worldwide-report/worldwide-reserves-oil-production-post-modest-rise.html>.
- Gu, Zhiqiang, and Milind Deo. 2009. Applicability of Carbon Dioxide Enhanced Oil Recovery to Reservoirs in the Uinta Basin, Utah (OFR-538).
- Holm, LW, and VA Josendal. 1974. "Mechanisms of Oil Displacement By Carbon Dioxide." *Journal of Petroleum Technology* 26 (12):1,427-1,438.
- Institute for 21st century energy, U.S. Chamber of Commerce. "CO₂ Enhanced Oil Recovery."
- Kasiri, N, and A Bashiri. 2011. "Wettability and Its Effects on Oil Recovery in Fractured and Conventional Reservoirs." *Petroleum Science and Technology* 29 (13):1324-1333.
- Mathiassen, Odd Magne. 2003. "CO₂ as injection gas for enhanced oil recovery and estimation of the potential on the Norwegian continental shelf." *Trondheim, Norway*.
- Melzer, L Stephen. 2012. "Carbon dioxide enhanced oil recovery (CO₂ EOR): Factors involved in adding carbon capture, utilization and storage (CCUS) to

enhanced oil recovery." *Center for Climate and Energy Solutions*.

Sean I. Plasyński, Darin Damiani. 2008. *Carbon Sequestration Through Enhanced Oil Recovery*. edited by U.S: Department of Energy National Energy Technology Laboratory.

Steve Whittaker, Ernie Perkins. 2013. *Technical aspects of CO₂ enhanced oil recovery and associated carbon storage*.

The Kelvin-Voigt Model's Suitability to Explain the Viscoelastic Properties of Anticorrosion Bitumen at Large Shear Strain in Subsea Cables and Umbilicals

Magnus Komperød¹

¹Technological Analyses Centre, Nexans Norway AS, Norway, magnus.komperod@nexans.com

Abstract

Bitumen is used as anticorrosion to protect steel armor wires in subsea cables and umbilicals. Bitumen's viscoelastic behavior influences the mechanical properties of the cables, in particular the bending stiffness. UFLEX2D is a software tool for mechanical analyses of cables and similar structures, which can include the viscoelastic effect of bitumen using a Kelvin-Voigt model. This paper evaluates how well the Kelvin-Voigt model is able to resemble bitumen's viscoelastic properties. It is concluded that the Kelvin-Voigt model's lack of temperature dependence can be managed, while the model's handling of strain amplitude is too simple to fully explain bitumen's behavior. It is also concluded that the Kelvin-Voigt model has limited abilities to resemble the frequency response of bitumen.

Keywords: Arctic Engineering; Bitumen; Bode Diagram; Cross Section Analysis; Kelvin-Voigt Model; Offshore Technology; Rheology; Subsea Cable; Umbilical.

1 Introduction

Umbilicals are cable-like structures consisting of electric and fiber optic signal cables, as well as steel tubes for transportation of fluids and for running subsea hydraulic equipment. Power umbilicals also include electric power phases for energizing subsea electric units, such as compressors. Umbilicals are essential for offshore oil and gas production.

Connecting power grids across seas requires subsea power cables. Such cables consist of one or several power phases, where each phase is a stranded conductor made of copper or aluminum covered by an electric insulation system. Subsea power cables are also used in direct electrical heating (DEH) systems, which is a technology for flow assurance in oil and gas pipelines. Please refer to Nysveen et al. (2007) for an introduction to DEH systems. Figure 1 shows a DEH riser cable having four phases, each consisting of a stranded copper conductor with a XLPE insulation system.



Figure 1. DEH riser cable with four phases. The cable also includes steel tubes and fiber optic signal cables. The two black arrows in the figure indicate the two layers of galvanized steel armor wires.

Umbilicals and subsea cables commonly include armor wires, which main purpose is to carry the cable's axial load and thereby reduce the axial tension in the other cable elements. Armor wires may also be used to tune the cable's submerged-weight-to-diameter ratio, which influences the cable's dynamic behavior in the sea. Armor wires are usually arranged in one to four armor layers, which are located right inside the cable's outer sheath. The two black arrows in Figure 1 indicate the two layers of armor wires in the DEH riser cable.

Armor wires are commonly made of galvanized steel. This material has favorable mechanical properties and is

cost-effective. However, as the steel wires are constantly submerged in seawater, the galvanization may be insufficient corrosion protection. Therefore the armor wires may be coated in bitumen, which serves as corrosion protection.

Because bitumen is a viscoelastic material it changes the shear forces between the armor wires and their neighboring cable elements, compared to the frictional shear forces that arise when bitumen is not present on the contact surfaces. Shear forces between cable elements due to friction and how these shear forces influence the cables' mechanical properties are extensively covered in the literature. See for example Féret and Bournazel (1987) and Kebabze (2000).

Literature on how shear forces of bitumen and other viscoelastic materials influence cables is sparse. Olsen et al. (2014), Konradsen and Ouren (2014), and Komperød et al. (2015) cover identification of bitumen's viscoelastic properties. The latter paper focuses on identification of bitumen's properties at equally large shear strain as in real-life cables. Mullins et al. (2015) develop models of the force required to pull an bitumen-coated armor wire out of a cable. Hedlund (2015) models the bending moment vs. bending curvature characteristics for cables with bitumen-coated armor wires. The latter work is based on Mullins et al. (2015). Also, some work on this issue has been carried out by MARINTEK as part of the implementation of bitumen's viscoelastic properties in the UFLEX2D software. Please refer to Appendix A for a brief note on UFLEX2D.

For mechanical cable models to include the effect of bitumen, these models must include material models of bitumen's viscoelastic properties. The UFLEX2D software uses the Kelvin-Voigt model to describe these properties. The contribution of the present paper is to evaluate how well the Kelvin-Voigt model is able to explain the viscoelastic properties of bitumen identified in Komperød et al. (2015).

2 Nomenclature

Table 1 presents the nomenclature used in this paper. Complex numbers are indicated with tilde, for example \tilde{G} . The following notation applies to the shear strain: γ is the shear strain as function of t . γ_0 is the center-to-peak amplitude of γ . $\tilde{\gamma}$ is the phase vector (phasor) notation of γ . Similar notation is used for the shear stress, τ .

When it is essential to distinguish between G^* and φ of the Kelvin-Voigt model vs. G^* and φ of the empirical model, the subscripts KV and E are used. When at no risk of confusion, the angular frequency, ω , may be referred to as the frequency.

Table 1. Nomenclature.

c_i, d_i	Parameters of the empirical model.
\tilde{G}	Bitumen's complex shear modulus [Pa].
G^*	Bitumen's shear stress amplitude to shear strain amplitude ratio [Pa].
G_E^*	G^* as modeled by the empirical model [Pa].
G_{KV}^*	G^* as modeled by the Kelvin-Voigt model [Pa].
G'	Bitumen's storage modulus [Pa].
G''	Bitumen's loss modulus [Pa].
j	Imaginary unit [-], $j^2 \stackrel{\text{def}}{=} -1$.
T	Temperature of bitumen [$^{\circ}\text{C}$].
T_1	Specific value of T used in examples [$^{\circ}\text{C}$].
t	Time [s].
$\gamma, \gamma_0, \tilde{\gamma}$	Bitumen's shear strain [-].
γ_1	Specific value of γ_0 used in examples [-].
η	Bitumen's viscosity [Pa s].
$\tau, \tau_0, \tilde{\tau}$	Bitumen's shear stress [Pa].
φ	Phase shift between shear stress and shear strain of bitumen [rad].
φ_E	φ as modeled by the empirical model [rad].
φ_{KV}	φ as modeled by the Kelvin-Voigt model [rad].
ω	Angular frequency [rad/s].
ω_1, ω_2	Specific values of ω used in examples [rad/s].

3 Properties of the Kelvin-Voigt Model

The Kelvin-Voigt model is on the form

$$\tau(t) = G' \gamma(t) + \eta \frac{d\gamma(t)}{dt}, \quad (1)$$

where G' is the material's shear storage modulus and η is its viscosity. The Kelvin-Voigt model is a linear, time-invariant (LTI) model as the model parameters G' and η are time-invariant, and

$$\begin{aligned}
 & G'(a\gamma_1(t) + b\gamma_2(t)) + \eta \frac{d}{dt}(a\gamma_1(t) + b\gamma_2(t)) \quad (2) \\
 & = a \left(G'\gamma_1(t) + \eta \frac{d\gamma_1(t)}{dt} \right) + b \left(G'\gamma_2(t) + \eta \frac{d\gamma_2(t)}{dt} \right).
 \end{aligned}$$

Eq. 2 states that the response of the input sequence $a\gamma_1(t) + b\gamma_2(t)$ is equal to a times the response of the input sequence γ_1 plus b times the response of the input sequence γ_2 . Hence, the Kelvin-Voigt model obeys the superposition principle.

3.1 Behavior at Sinusoidal Strain

Assume that the strain is applied in a sinusoidal manner. The strain can then be written as

$$\gamma(t) = \gamma_0 \cos(\omega t), \quad (3)$$

where γ_0 is the center-to-peak amplitude and ω is the angular frequency. Inserting Eq. 3 into Eq. 1 gives

$$\begin{aligned}
 \tau(t) &= G'\gamma_0 \cos(\omega t) + \eta \frac{d}{dt} \gamma_0 \cos(\omega t) \quad (4) \\
 &= G'\gamma_0 \cos(\omega t) - \eta \omega \gamma_0 \sin(\omega t) \\
 &= G'\gamma_0 \cos(\omega t) - G''\gamma_0 \sin(\omega t).
 \end{aligned}$$

In the third line of Eq. 4 the shear loss modulus is introduced as $G'' \stackrel{\text{def}}{=} \eta \omega$.

Euler's formula is

$$e^{jx} = \cos(x) + j \sin(x), \quad (5)$$

which gives

$$\begin{aligned}
 e^{-jx} &= \cos(-x) + j \sin(-x) \quad (6) \\
 &= \cos(x) - j \sin(x).
 \end{aligned}$$

Solving Eqs. 5 and 6 for $\cos(x)$ and $\sin(x)$ gives the well-known identities

$$\cos(x) = \frac{e^{jx} + e^{-jx}}{2}, \quad (7)$$

$$\sin(x) = \frac{e^{jx} - e^{-jx}}{2j}. \quad (8)$$

Inserting Eqs. 7 and 8 into Eq. 4

$$\begin{aligned}
 \tau(t) &= G'\gamma_0 \frac{e^{j\omega t} + e^{-j\omega t}}{2} - \eta \omega \gamma_0 \frac{e^{j\omega t} - e^{-j\omega t}}{2j} \quad (9) \\
 &= G'\gamma_0 \frac{e^{j\omega t} + e^{-j\omega t}}{2} + j\eta \omega \gamma_0 \frac{e^{j\omega t} - e^{-j\omega t}}{2} \\
 &= \frac{\gamma_0}{2} [(G' + j\eta \omega)e^{j\omega t} + (G' - j\eta \omega)e^{-j\omega t}] \\
 &= \frac{\gamma_0}{2} G_{\text{KV}}^* [e^{j\varphi_{\text{KV}}} e^{j\omega t} + e^{-j\varphi_{\text{KV}}} e^{-j\omega t}] \\
 &= \gamma_0 G_{\text{KV}}^* \frac{e^{j(\omega t + \varphi_{\text{KV}})} + e^{-j(\omega t + \varphi_{\text{KV}})}}{2} \\
 &= \gamma_0 G_{\text{KV}}^* \cos(\omega t + \varphi_{\text{KV}}).
 \end{aligned}$$

On the fourth line of Eq. 9, the factors $(G' \pm j\eta \omega)$ are written on polar form where the following notation is used

$$\begin{aligned}
 G_{\text{KV}}^* &\stackrel{\text{def}}{=} \sqrt{G'^2 + \eta^2 \omega^2} \quad (10) \\
 &= G' \sqrt{1 + \left(\frac{\eta}{G'}\right)^2 \omega^2},
 \end{aligned}$$

$$\varphi_{\text{KV}} \stackrel{\text{def}}{=} \arctan\left(\frac{\eta}{G'} \omega\right). \quad (11)$$

The physical interpretations are that G^* is the shear stress amplitude to shear strain amplitude ratio, and φ is the phase shift between the shear stress and the shear strain. These interpretations are valid for any model, while the calculations of G_{KV}^* and φ_{KV} from Eqs. 10 and 11 are specific to the Kelvin-Voigt model.

The derivatives of G_{KV}^* and φ_{KV} w.r.t. ω will be used later in this paper. These derivatives are

$$\frac{dG_{\text{KV}}^*}{d\omega} = \frac{\eta^2 \omega}{\sqrt{G'^2 + \eta^2 \omega^2}}, \quad (12)$$

$$\frac{d\varphi_{\text{KV}}}{d\omega} = \frac{\eta}{G' \left(1 + \left(\frac{\eta}{G'}\right)^2 \omega^2\right)}. \quad (13)$$

The sinusoidal functions $\gamma(t)$ of Eq. 3 and $\tau(t)$ of Eq. 9 can be written on phase vector (phasor) form as

$$\tilde{\gamma} = \gamma_0 e^{j\omega t}, \quad (14)$$

$$\tilde{\tau} = \gamma_0 G_{\text{KV}}^* e^{j(\omega t + \varphi)}. \quad (15)$$

The complex shear modulus, \tilde{G} , is defined as the ratio of these phase vectors, i.e.

$$\begin{aligned} \tilde{G} &\stackrel{\text{def}}{=} \frac{\tilde{\tau}}{\tilde{\gamma}} & (16) \\ &= \frac{\gamma_0 G^* e^{j(\omega t + \varphi)}}{\gamma_0 e^{j\omega t}} \\ &= G^* e^{j\varphi} \\ &= G' + j\eta\omega. \end{aligned}$$

The upper three rows of Eq. 16 apply to any model, while the fourth row is specific to the Kelvin-Voigt model.

Figure 2 shows a Bode diagram of the Kelvin-Voigt model based on Eqs. 10 and 11. From physics, it is known that both parameters G' and η are non-negative. The second line of Eq. 10, as well as Eq. 11, tell how the Bode diagram will be influenced by changing the parameters: Increasing (decreasing) the ratio $\frac{\eta}{G'}$ will shift the Bode diagram to the left (to the right). Increasing (decreasing) both parameters with the same factor, so that G' increases (decreases), while the ratio $\frac{\eta}{G'}$ is fixed, will shift the magnitude plot upward (downward). In other words: *The Bode diagram may be shifted by changing the parameters, but its shape will always be as illustrated in Figure 2.* The only exceptions are (i) $\eta = 0$, which gives $G_{KV}^* = G'$ and $\varphi = 0$ for any ω , and (ii) $G' = 0$, which gives $G_{KV}^* = \eta\omega$ and $\varphi = \frac{\pi}{2}$ rad, i.e. 90° , for any ω .

The asymptotic behavior is also inherent in the Kelvin-Voigt model and can not be changed by changing the parameters (except for the special cases $G' = 0$ and $\eta = 0$):

1. At low frequencies G_{KV}^* will approach G' .
2. At low frequencies the phase shift, φ_{KV} , will approach 0 rad.
3. At high frequencies G_{KV}^* will approach $\eta\omega$.
4. At high frequencies φ_{KV} will approach $\frac{\pi}{2}$ rad, i.e. 90° .
5. As seen from Eq. 12, G_{KV}^* has a stationary point at $\omega = 0$, and is strictly increasing with ω for $\omega > 0$, provided that $\eta > 0$.
6. As seen from Eq. 13, φ_{KV} is strictly increasing with ω , provided that $\eta > 0$.

This means that any material which viscoelastic properties violate the Bode diagram of Figure 2 and / or the asymptotic behaviors described above can not be correctly modeled by the Kelvin-Voigt model.

4 Bitumen's Properties at Large Shear Strain

This section explains bitumen's viscoelastic properties at large shear strain based on the results of Komperød et al. (2015).

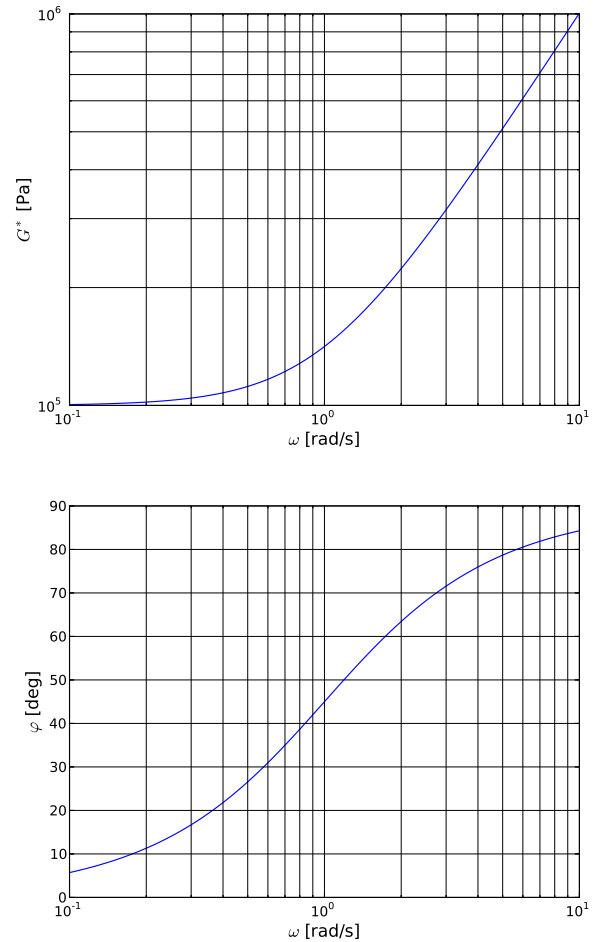


Figure 2. Bode diagram of the Kelvin-Voigt model using the parameters $G' = 1.0 \times 10^5$ and $\eta = 1.0 \times 10^5$. Please note that the second axis (y-axis) of the phase plot is scaled in [deg], while [rad] is used in the calculations of the main text.

4.1 Model Identification

The author and his colleagues have developed a new laboratory instrument for identification of bitumen's viscoelastic properties, G^* and φ . The advantage of the new laboratory instrument compared to traditional low-strain rheometers is that the new laboratory instrument can measure the viscoelastic properties of bitumen subject to equally large shear strain as in real-life cables. The shear strain of traditional low-strain rheometers is much smaller than the shear strain in cables. Hence, the viscoelastic properties identified in such rheometers may not be representative for bitumen's behavior in cables.

Komperød et al. (2015) present the basic principle of the new laboratory instrument and derive how to calculate bitumen's viscoelastic properties from the sensor measurements of the laboratory instrument. Komperød et al. (2015) also present an empirical model of G_E^* and φ_E as function of the shear strain amplitude, γ_0 , the angular frequency, ω , and the bitumen temperature, T . This model is based on experiments in the new laboratory instrument

which was run for 48 different combinations of γ_0 , ω , and T . Two parallels were run for each of the 48 combinations, i.e. in total 96 experiments were run.

The model identified from these 96 experiments is

$$G_E^* = c_0 - c_1\gamma_0 + c_2\gamma_0\omega - c_3T + c_4T^2, \quad (17)$$

$$\varphi_E = d_0 + d_1\gamma_0 - d_2\omega + d_3T. \quad (18)$$

In Eqs. 17 and 18, c_i and d_i are real, positive parameters, which are identified using the ordinary least squares method (OLS). That is, for each of the 96 experiments, γ_0 , ω , and T are known inputs to the laboratory instrument, while one value for G_E^* and one value for φ_E are identified from each experiment. Hence, the experiment output G_E^* and the regressors γ_0 , $\gamma_0\omega$, T , and T^2 are known for 96 experiments, which are used to identify the parameters c_0 , c_1 , c_2 , c_3 , and c_4 using OLS. Similarly, the experiment output φ_E and the regressors γ_0 , ω , and T are also known for 96 experiments, which are used to identify the parameters d_0 , d_1 , d_2 , and d_3 using OLS.

The model of Eqs. 17 and 18 is a simple, empirical model, which model structure is chosen to ensure numerical convergence and to be simple to give practical interpretations. It is emphasized that the model structure is not based on analytical models of bitumen's properties. However, the model gives reasonable explanation of bitumen's behavior within the operating range of the laboratory experiments. Please refer to Komperød et al. (2015) for detailed explanation of the model identification and model validation.

4.2 Model Interpretation

In Eq. 17, c_0 is a constant term. The term $-c_1\gamma_0$ expresses that G^* will decrease as the shear strain amplitude increases. That is, the shear stress amplitude will grow slower than the shear strain amplitude.

The product $\gamma_0\omega$ expresses bitumen's strain rate (strain per time unit). Hence, the term $c_2\gamma_0\omega$ means that bitumen will set up larger shear forces if it is strained rapidly than if strained slowly.

The first and second derivatives of G_E^* w.r.t T are

$$\frac{\partial G_E^*}{\partial T} = -c_3 + 2c_4T, \quad (19)$$

$$\frac{\partial^2 G_E^*}{\partial T^2} = 2c_4. \quad (20)$$

The first derivative is negative for the temperature range covered by the laboratory experiments. This means that bitumen will set up larger shear forces at lower temperatures than at higher temperatures for the same strain. Hence, bitumen will behave more like a "glue" as the temperature decreases. As seen from Eq. 20, the second derivative is positive for all values of T . This means

that the first derivative will become more negative as the temperature decreases. In other words, G_E^* grows with increasing rate as the temperature decreases.

As emphasized in Komperød et al. (2015), G_E^* does not depend directly on the frequency, ω , but on the product $\gamma_0\omega$, which expresses the strain rate.

Eq. 18 is straight forward to interpret: The phase shift, φ_E , increases for increased strain amplitude, γ_0 , and for increased temperature, T . For increased frequency, ω , the phase shift will decrease.

4.3 Comparison with the Kelvin-Voigt Model

Comparing the empirical model, i.e. Eqs. 17 and 18, which is based on laboratory experiments, with the Kelvin-Voigt model of Eqs. 10 and 11 shows some significant differences:

1. In the empirical model both G_E^* and φ_E depend on the temperature, while the Kelvin-Voigt model does not include temperature-dependence at all. Hence, a set of Kelvin-Voigt model parameters, G' and η , can only be valid for one single temperature, not a temperature interval.

If the Kelvin-Voigt model is to be used for variable temperatures, the model parameters G' and η must be adjusted to the temperature variations. This may be implemented as the parameters being continuous functions of the temperature, i.e. $G' = G'(T)$ and $\eta = \eta(T)$. Tables may also be used, where G' and η are listed for various temperature points. Interpolation may be used between these temperature points.

2. In the empirical model G_E^* and φ_E also depend on the strain amplitude, γ_0 , while the Kelvin-Voigt model does not depend on γ_0 . This is a bigger issue than the temperature-dependence discussed above, because it is reasonable (with a few exceptions) to assume that the temperature is nearly homogeneous over a pitch length of the cable. However, bitumen's shear strain varies significantly over a pitch length: It is largest at the cable's neutral axis of bending and zero at the points farthest away from the neutral axis.
3. As discussed above, Eq. 17 shows that G_E^* of the empirical model depends on the strain rate, which is expressed through the product $\gamma_0\omega$, but G_E^* does not depend on the frequency, ω , alone. Comparing with G_{KV}^* of the Kelvin-Voigt model, Eq. 10, shows that this model depends only on ω , not on the product $\gamma_0\omega$.

This issue means that if the strain amplitude, γ_0 , is constant, G_E^* of the empirical model and G_{KV}^* of the Kelvin-Voigt model will depend on the frequency, ω . But if γ_0 is allowed to vary, the behaviors of the two models will differ. As explained above, the strain amplitude will be largest at the cable's neutral axis of

bending and zero farthest away from the neutral axis. Hence, the assumption of constant strain amplitude over a pitch length of the cable will not be met in a real-life cable.

4. For the empirical model, the derivative of G_E^* w.r.t. ω is

$$\frac{\partial G_E^*}{\partial \omega} = c_2 \gamma_0. \quad (21)$$

Comparing Eq. 21 with Eq. 12 shows that the two derivatives are quite different. $\frac{\partial G_{KV}^*}{\partial \omega}$ depends on the frequency, ω , while $\frac{\partial G_E^*}{\partial \omega}$ depends on the strain amplitude, γ_0 . However, both derivatives are positive, which means that G^* is strictly increasing with the frequency for both models (except that the Kelvin-Voigt model has a stationary point at $\omega = 0$). Also, for both models, $\frac{\partial G^*}{\partial \omega}$ is constant w.r.t. ω for high frequencies. That is, G^* increases proportional with ω for high ω .

5. Inspecting Eq. 18 shows that the terms d_0 , $d_1 \gamma_0$, and $d_3 T$ give positive contributions to the phase shift, φ_E . The contribution from the term $-d_2 \omega$ is zero for $\omega = 0$ and strictly decreasing for increasing ω . Hence, the phase shift has a positive value given by $d_0 + d_1 \gamma_0 + d_3 T$ for $\omega = 0$, and thereafter decreases as ω increases. However, for the frequency range covered by the empirical model, the phase shift is always positive.

The behavior of the Kelvin-Voigt model is very different from the empirical model w.r.t. the phase shift. The phase shift of the Kelvin-Voigt model is given by Eq. 11. The function $\arctan(\cdot)$ is zero when the argument is zero and then increases towards its asymptote of $\frac{\pi}{2}$ in a strictly increasing, nonlinear manner as the argument increases.

The phase shift of the empirical model is positive for zero frequency and then decreases for increasing frequency, while the phase shift of the Kelvin-Voigt model is zero for zero frequency and then increases for increasing frequency. Therefore, although the two models are very different w.r.t. phase shift, the phase shift graphs of the models will cross each other at one specific frequency. Hence, the Kelvin-Voigt model can resemble the phase shift of the empirical model at one single point in the frequency domain. However, the Kelvin-Voigt model can never resemble the empirical model over any frequency interval, because the models' derivative w.r.t. frequency always have opposite signs (plus or minus).

For the empirical model of Eq. 17, the derivative of G_E^* w.r.t. the strain amplitude, γ_0 , is

$$\frac{\partial G_E^*}{\partial \gamma_0} = -c_1 + c_2 \omega. \quad (22)$$

Setting Eq. 22 equal to 0 and solving for ω gives $\omega = \frac{c_1}{c_2}$. Hence, for this particular frequency, G_E^* becomes insensitive to the strain amplitude, γ_0 . That is, for this frequency the issue of higher strain amplitude at the cable's neutral axis of bending than farther away from the neutral axis will vanish, because G_E^* is insensitive to γ_0 if $\omega = \frac{c_1}{c_2}$. This desirable frequency is somewhat higher than the frequency of the cable's cyclic behavior as hanging from an offshore installation. Still, the effect that the term $c_2 \omega$ counteracts the term $-c_1$ is favorable.

Figure 3 shows a Bode diagram of a Kelvin-Voigt model, as well as an empirical model on the form of Eqs. 17 and 18. The Kelvin-Voigt model has the same model parameters as in Figure 2. The magnitude plot shows that the G^* graphs of the two models behave somewhat similarly, but are not identical. The φ graphs of the two models are very different, which is in accordance to point 5 above. However, as predicted, the phase shift graphs cross each other, meaning they yield the same phase shift at one specific frequency, in this case at $\omega = 1$.

5 Fitting the Kelvin-Voigt Model to the Empirical Model

The issues discussed in Section 4.3 conclude that the Kelvin-Voigt model can not resemble the empirical model over a frequency interval. In particular the phase shift, φ , fits poorly as the Kelvin-Voigt model and the empirical model have opposite signs of $\frac{\partial \varphi}{\partial \omega}$. Still, as will be shown below, the Kelvin-Voigt model is suitable if only one specific frequency is to be modeled, not a frequency interval. Further, if the phase shift is disregarded, then G_{KV}^* of the Kelvin-Voigt model can resemble G_E^* of the empirical model well over a limited frequency range.

Mathematically speaking, the two Kelvin-Voigt model parameters, G' and η , provide two degrees of freedom for how to fit the Kelvin-Voigt model to the empirical model. In other words: Two requirements, formulated as two equations, can be met.

5.1 Fitting G_{KV}^* and φ_{KV} for one Specific ω

Assume that the model parameters c_i and d_i of Eqs. 17 and 18 are identified from laboratory experiments or otherwise. The problem addressed in this section is how to calculate the parameters of the Kelvin-Voigt model, G' and η , so that the Kelvin-Voigt model resembles the empirical model for a specific strain amplitude, γ_1 , a specific frequency, ω_1 , and a specific temperature, T_1 . This means that the two requirements to be met can be expressed as

$$G_{KV}^*(\omega_1) = G_E^*(\gamma_1, \omega_1, T_1), \quad (23)$$

$$\varphi_{KV}(\omega_1) = \varphi_E(\gamma_1, \omega_1, T_1), \quad (24)$$

where the right hand side of these equations are obtained by inserting γ_1 , ω_1 , and T_1 into Eqs. 17 and 18.

The next issue is to solve for the Kelvin-Voigt parameters G' and η . Inserting Eq. 24 and $\omega = \omega_1$ into Eq. 11 and rewriting gives

$$\tan(\varphi_E) = \frac{\eta}{G'} \omega_1. \quad (25)$$

Inserting Eqs. 23 and 25 into Eq. 10

$$\begin{aligned} G_E^* &= G' \sqrt{1 + \tan^2(\varphi_E)} \\ &= G' \sqrt{1 + \frac{\sin^2(\varphi_E)}{\cos^2(\varphi_E)}} \\ &= G' \sqrt{\frac{\cos^2(\varphi_E) + \sin^2(\varphi_E)}{\cos^2(\varphi_E)}} \\ &= G' \sqrt{\frac{\cos^2(\varphi_E) + \sin^2(\varphi_E)}{\cos^2(\varphi_E)}} \\ &= G' \sqrt{\frac{1}{\cos^2(\varphi_E)}} \\ &= \frac{G'}{\cos(\varphi_E)}, \end{aligned} \quad (26)$$

which gives

$$G' = G_E^* \cos(\varphi_E). \quad (27)$$

Inserting Eq. 27 into Eq. 25

$$\tan(\varphi_E) = \frac{\sin(\varphi_E)}{\cos(\varphi_E)} = \frac{\eta}{G_E^* \cos(\varphi_E)} \omega_1, \quad (28)$$

which gives

$$\eta = \frac{G_E^* \sin(\varphi_E)}{\omega_1}. \quad (29)$$

Hence, Eqs. 27 and 29 provide explicit expressions for the Kelvin-Voigt model parameters, G' and η , which are based on G_E^* and φ_E calculated by the empirical model.

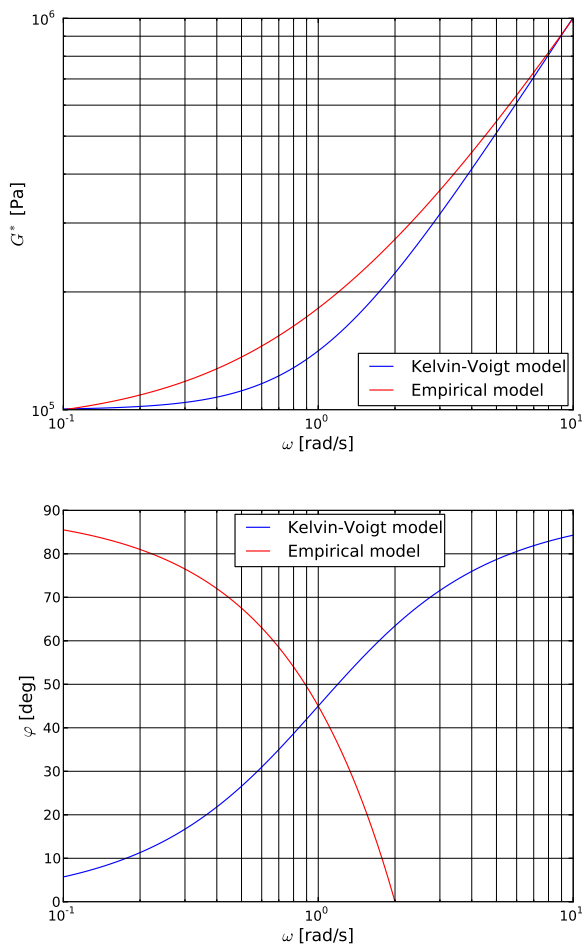


Figure 3. Bode diagram of a Kelvin-Voigt model and an empirical model. The Kelvin-Voigt model has the same model parameters as in Figure 2.

Example 1 The parameters of the Kelvin-Voigt model are to be calculated so that the Kelvin-Voigt model resembles the empirical model at the frequency $\omega_1 = 0.5$ for some specified values of strain amplitude, γ_1 , and temperature, T_1 .

Solution: $\omega = 0.5$ as well as the specified values of γ_1 and T_1 are inserted in Eqs. 17 and 18. These equations then provide G_E^* and φ_E for $\omega = 0.5$. Then insert the calculated G_E^* and φ_E , as well as $\omega_1 = 0.5$, into Eqs. 27 and 29 to obtain the Kelvin-Voigt model parameters G' and η . Figure 4 shows Bode diagram of the Kelvin-Voigt model with the new parameters. Although the graphs of the Kelvin-Voigt model and the empirical model are very different, both G^* and φ match perfectly for $\omega = 0.5$. End of Example 1.

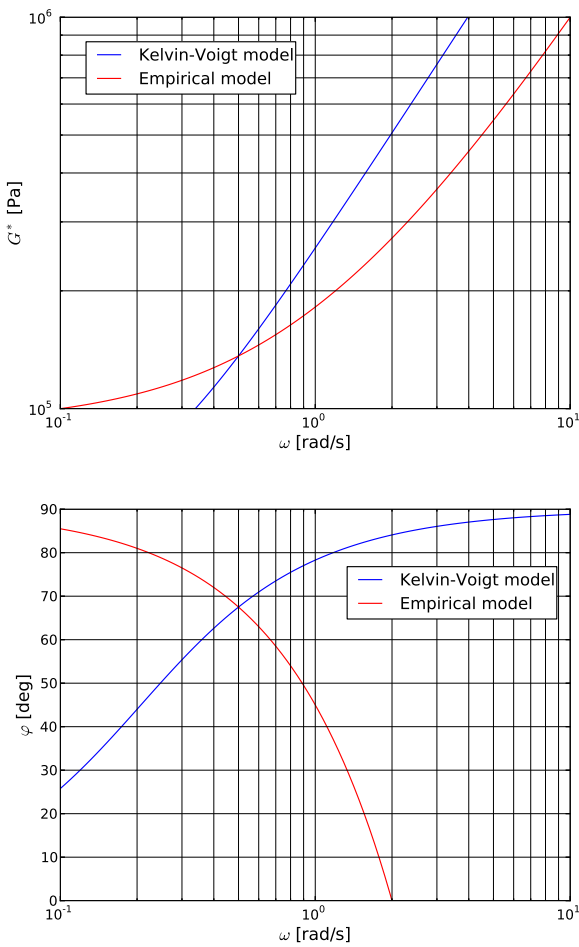


Figure 4. Bode diagram of the Kelvin-Voigt model obtained in Example 1.

5.2 Fitting G_{KV}^* as a First Order Taylor Polynomial

The method proposed in Section 5.1 tunes the parameters G' and η to make the Kelvin-Voigt model resemble both G_E^* and φ_E of the empirical model at one specific frequency, ω_1 . However, as seen from Figure 4, the Kelvin-

Voigt model fits the empirical model poorly for any frequency that is not very close to ω_1 .

The present section suggests an alternative approach to the method of Section 5.1. That is to disregard the fit of φ_{KV} for the benefit of better fit for G_{KV}^* . By better fit, it is here meant that G_{KV}^* of the Kelvin-Voigt model shall resemble the empirical model well not only in one single frequency point, but over a limited frequency interval. As two requirements can be met, these requirements are chosen as:

$$G_{KV}^*(\omega_1) = G_E^*(\gamma_1, \omega_1, T_1), \quad (30)$$

$$\left. \frac{dG_{KV}^*}{d\omega} \right|_{\omega=\omega_1} = \left. \frac{\partial G_E^*}{\partial \omega} \right|_{\gamma_0=\gamma_1, \omega=\omega_1, T=T_1}. \quad (31)$$

Eq. 30 means that G_{KV}^* of the Kelvin-Voigt model and G_E^* of the empirical model shall have the same value at the chosen frequency. This requirement is identical as in Section 5.1. Eq. 31 means that the slope of G_{KV}^* of the Kelvin-Voigt model and the slope of G_E^* of the empirical model shall be identical at the chosen frequency, ω_1 .

As seen from Eq. 17, G_E^* is a linear function in ω (the apparent curvature of G_E^* in the Bode diagrams arises because the diagrams have logarithmic axes). Hence, Eqs. 30 and 31 above mean that G_E^* is mathematically equivalent to the linearization, i.e. the first order Taylor expansion, of G_{KV}^* .

As in Section 5.1, the strain amplitude, γ_1 , the frequency, ω_1 , and the temperature, T_1 , which the Kelvin-Voigt model shall be valid for must be chosen and inserted into Eq. 17, which provides the value of G_E^* . The derivative $\frac{\partial G_E^*}{\partial \omega}$ of the empirical model is $c_2\gamma_0$, which becomes $c_2\gamma_1$ after inserting $\gamma_0 = \gamma_1$.

Eqs. 30 and 31 are then inserted into Eqs. 10 and 12, respectively. These equations are then solved for the Kelvin-Voigt parameters, G' and η , as follows: Inserting Eq. 10 into Eq. 12 gives

$$\left. \frac{\partial G_E^*}{\partial \omega} \right|_{\omega=\omega_1} = \frac{\eta^2 \omega_1}{G_E^*(\omega_1)}, \quad (32)$$

$$\eta^2 = \frac{G_E^*(\omega_1)}{\omega_1} \left. \frac{\partial G_E^*}{\partial \omega} \right|_{\omega=\omega_1}, \quad (33)$$

$$\eta = \sqrt{\frac{G_E^*(\omega_1)}{\omega_1} \left. \frac{\partial G_E^*}{\partial \omega} \right|_{\omega=\omega_1}}. \quad (34)$$

Squaring Eq. 10 and inserting Eq. 33

$$G_E^*(\omega_1)^2 = G'^2 + \frac{G_E^*(\omega_1)}{\omega_1} \left. \frac{\partial G_E^*}{\partial \omega} \right|_{\omega=\omega_1} \omega_1^2, \quad (35)$$

$$G'^2 = G_E^*(\omega_1) \left(G_E^*(\omega_1) - \left. \frac{\partial G_E^*}{\partial \omega} \right|_{\omega=\omega_1} \omega_1 \right), \quad (36)$$

$$G' = \sqrt{G_E^*(\omega_1) \left(G_E^*(\omega_1) - \left. \frac{\partial G_E^*}{\partial \omega} \right|_{\omega=\omega_1} \omega_1 \right)}. \quad (37)$$

From Eq. 17 it is trivial to verify that the factor inside the parenthesis of Eq. 37 is equal to G_E^* for $\omega = 0$. Further, because $\frac{\partial G_E^*}{\partial \omega} \geq 0$, the expressions inside the square roots of Eqs. 34 and 37 are ensured to be nonnegative if $G_E^* \geq 0$ for $\omega = 0$. Hence, Eqs. 34 and 37 provide the Kelvin-Voigt model parameters that satisfy Eqs. 30 and 31.

Example 2 The parameters of the Kelvin-Voigt model are to be calculated so that the Kelvin-Voigt model resembles G_E^* and $\frac{\partial G_E^*}{\partial \omega}$ of the empirical model at the frequency $\omega_1 = 0.5$ for some specified values of strain amplitude, γ_1 , and temperature, T_1 .

Solution: $\omega = 0.5$ as well as the specified values of γ_1 and T_1 are inserted in Eqs. 17 to obtain G_E^* . Further, $\frac{\partial G_E^*}{\partial \omega}$ is calculated as $c_2 \gamma_1$. Then the calculated G_E^* and $\frac{\partial G_E^*}{\partial \omega}$, as well as $\omega_1 = 0.5$, are inserted into Eqs. 34 and 37, which provide the Kelvin-Voigt model parameters G' and η . The Bode diagram of the Kelvin-Voigt model with the new parameters is shown in Figure 5. The magnitude plot shows that G_{KV}^* of the Kelvin-Voigt model resembles the empirical model well over a limited interval centered at $\omega = 0.5$. As the two models have different second derivatives, $\frac{\partial^2 G_E^*}{\partial \omega^2}$, the two models will eventually drift apart as moving away from the point $\omega = 0.5$. The cost of this improvement of G_{KV}^* is that the phase shift, ϕ_{KV} , fits poorly at $\omega = 0.5$ as shown in Figure 5. End of Example 2.

It is seen from Figure 5 that G_{KV}^* is larger than G_E^* for all ω , except for $\omega = 0.5$, where $G_{KV}^* = G_E^*$. The following proves that this inequality always holds. From Taylor's theorem (see for example Section 10.9 of Thomas et al. (2010)) it follows that G_{KV}^* can be written as

$$G_{KV}^*(\omega) = G_{KV}^*(\omega_1) + \left. \frac{dG_{KV}^*}{d\omega} \right|_{\omega=\omega_1} (\omega - \omega_1) + \frac{1}{2} \left. \frac{d^2 G_{KV}^*}{d\omega^2} \right|_{\omega=\omega_c} (\omega - \omega_1)^2, \quad (38)$$

where $\omega_1 < \omega_c < \omega$ if $\omega_1 < \omega$, and $\omega < \omega_c < \omega_1$ if $\omega_1 > \omega$.

As G_E^* is a linear function in ω , it can be written as

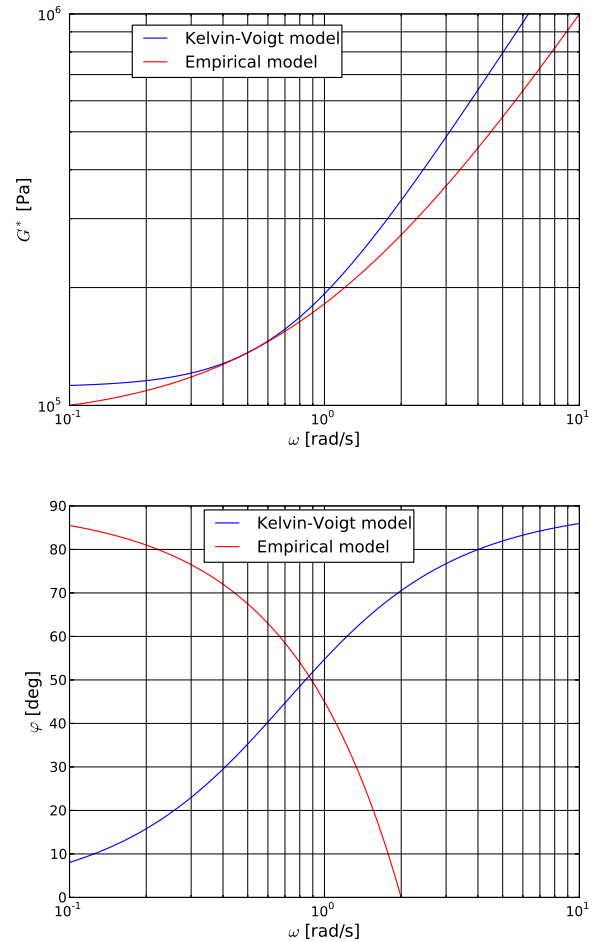


Figure 5. Bode diagram of the Kelvin-Voigt model obtained in Example 2.

$$G_E^*(\omega) = G_E^*(\omega_1) + \left. \frac{\partial G_E^*}{\partial \omega} \right|_{\omega=\omega_1} (\omega - \omega_1). \quad (39)$$

Subtracting Eq. 39 from Eq. 38, and using Eqs. 30 and 31 gives

$$G_{KV}^*(\omega) - G_E^*(\omega) = \frac{1}{2} \left. \frac{d^2 G_{KV}^*}{d\omega^2} \right|_{\omega=\omega_c} (\omega - \omega_1)^2. \quad (40)$$

The second derivative of G_{KV}^* is

$$\frac{d^2 G_{KV}^*}{d\omega^2} = \frac{G'^2 \eta^2}{(G'^2 + \eta^2 \omega^2)^{\frac{3}{2}}}, \quad (41)$$

which is positive for any finite ω . Hence, the right hand side of Eq. 40 is positive for any ω and for any ω_c , except for $\omega = \omega_1$, where the right hand side is zero. The practical interpretation of this result is that G_{KV}^* is larger than G_E^* for any frequency, ω , except for $\omega = \omega_1$, where $G_{KV}^* = G_E^*$. In many cases, large G^* will give conservative analysis results. Hence, for these cases the approach presented in this section is conservative.

5.3 Fitting G_{KV}^* at Two Frequencies

In Section 5.2, the two requirements to decide the parameters of the Kelvin-Voigt model are that G^* and $\frac{\partial G^*}{\partial \omega}$ should be equal for the Kelvin-Voigt model as for the empirical model at some specified frequency, ω_1 . The present section derives an alternative method to the method of Section 5.2. The two requirements of the method of the present section are that G_{KV}^* of the Kelvin-Voigt model shall resemble the empirical model at two different frequencies, ω_1 and ω_2 , where $\omega_2 > \omega_1$. That is

$$G_{KV}^*(\omega_1) = G_E^*(\gamma_1, \omega_1, T_1), \quad (42)$$

$$G_{KV}^*(\omega_2) = G_E^*(\gamma_1, \omega_2, T_1). \quad (43)$$

The strain amplitude, γ_1 , and the temperature, T_1 , which the Kelvin-Voigt model shall be valid for must be chosen and inserted into Eq. 17. Then by also inserting the two frequencies ω_1 and ω_2 in Eq. 17, the equation provides the values for $G_E^*(\omega_1)$ and $G_E^*(\omega_2)$.

Next, Eqs. 42 and 43 are inserted into Eq. 10, together with $\omega = \omega_1$ and $\omega = \omega_2$, respectively. Squaring Eq. 10 then gives

$$G_E^*(\omega_1)^2 = G'^2 + \eta^2 \omega_1^2, \quad (44)$$

$$G_E^*(\omega_2)^2 = G'^2 + \eta^2 \omega_2^2. \quad (45)$$

Solving Eqs. 44 and 45 for the Kelvin-Voigt parameters G' and η yields

$$G' = \sqrt{\frac{G_E^*(\omega_1)^2 \omega_2^2 - G_E^*(\omega_2)^2 \omega_1^2}{\omega_2^2 - \omega_1^2}}, \quad (46)$$

$$\eta = \sqrt{\frac{G_E^*(\omega_2)^2 - G_E^*(\omega_1)^2}{\omega_2^2 - \omega_1^2}}. \quad (47)$$

It can be mathematically proved that the expressions under the square roots of Eqs. 46 and 47 are nonnegative. These proofs are omitted here. Hence, Eqs. 46 and 47 provide the model parameters of the Kelvin-Voigt model.

Example 3 The parameters of the Kelvin-Voigt model are to be calculated so that G_{KV}^* resembles G_E^* at the frequencies $\omega_1 = 0.2$ and $\omega_2 = 1$ for some specified values of strain amplitude, γ_1 , and temperature, T_1 .

Solution: γ_1 and T_1 , as well as ω_1 and ω_2 , are inserted into Eq. 17 to obtain $G_E^*(\omega_1)$ and $G_E^*(\omega_2)$. Then the calculated $G_E^*(\omega_1)$ and $G_E^*(\omega_2)$, as well as ω_1 and ω_2 , are inserted into Eqs. 46 and 47, which provide the Kelvin-Voigt model parameters G' and η . The Bode diagram of the Kelvin-Voigt model with the new parameters is shown in Figure 6. The figure shows that G_{KV}^* intersects G_E^* at

$\omega_1 = 0.2$ and at $\omega_2 = 1$. G_{KV}^* resembles G_E^* quite well also between these two frequencies.

In the phase shift plot of Figure 6, the two models intersect within the interval $[\omega_1, \omega_2]$. However, this is a coincidence that does not follow from the mathematical derivation. The phase shift diagrams of Figures 5 and 6 are almost identical. This is also a coincidence as the ratio $\frac{\eta}{G'}$ happens to be near identical in Example 3 and as in Example 2. End of Example 3.

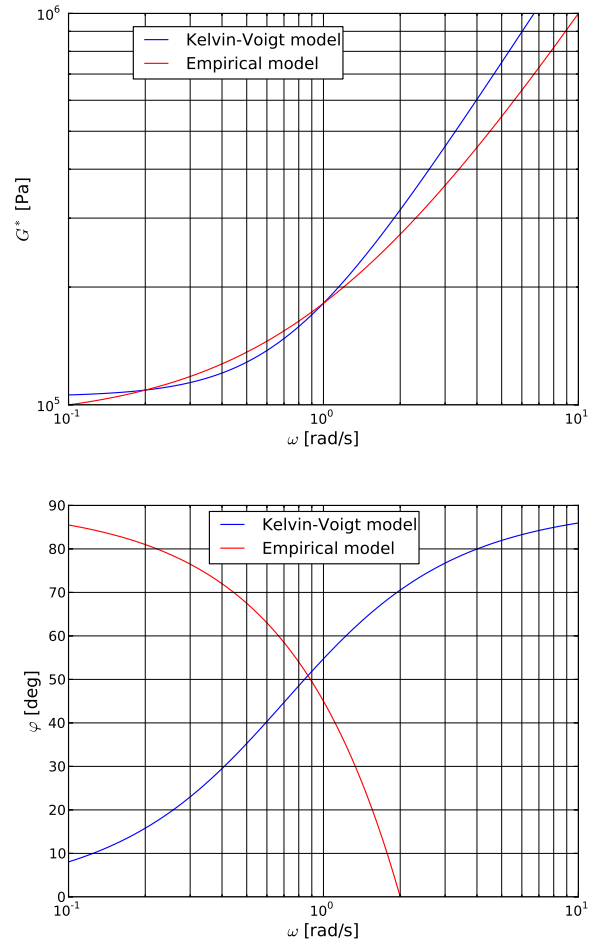


Figure 6. Bode diagram of the Kelvin-Voigt model obtained in Example 3.

It is seen from Figure 6 that the Kelvin-Voigt model underestimates G^* in the open interval (ω_1, ω_2) , and overestimates G^* for $\omega < \omega_1$ and for $\omega > \omega_2$. The following proves that this holds for any empirical model on the form of Eq. 17, and for any ω_1 and ω_2 , provided that the parameter c_2 of the empirical model is positive.

It follows from Eq. 41 that $\frac{d^2 G_{KV}^*}{d\omega^2}$ is positive for any finite ω . Hence, $\frac{dG_{KV}^*}{d\omega}$ is strictly increasing. From Eq. 17 it follows that $\frac{\partial G_E^*}{\partial \omega}$ is a positive constant w.r.t. ω .

The assumption of the present section is that $G_{KV}^* = G_E^*$ for the frequencies ω_1 and ω_2 . That is

Subtracting Eq. 59 from Eq. 58, and using Eq. 49 gives

$$G_{KV}^*(\omega_1) - G_E^*(\omega_1) = 0, \quad (48)$$

$$G_{KV}^*(\omega_2) - G_E^*(\omega_2) = 0. \quad (49)$$

Rolle's theorem (see Section 4.2 of Thomas et al. (2010)) states that

$$\left. \frac{\partial}{\partial \omega} [G_{KV}^*(\omega_c) - G_E^*(\omega_c)] \right|_{\omega=\omega_c} = 0, \quad (50)$$

for some $\omega_c \in (\omega_1, \omega_2)$. Because $\frac{dG_{KV}^*}{d\omega}$ is strictly increasing and $\frac{\partial G_E^*}{\partial \omega}$ is constant, it follows that

$$\frac{\partial}{\partial \omega} [G_{KV}^*(\omega) - G_E^*(\omega)] < 0 \quad \forall \omega < \omega_c, \quad (51)$$

$$\frac{\partial}{\partial \omega} [G_{KV}^*(\omega) - G_E^*(\omega)] > 0 \quad \forall \omega > \omega_c. \quad (52)$$

Further,

$$G_{KV}^*(\omega) = G_{KV}^*(\omega_1) + \int_{\omega_1}^{\omega} \frac{dG_{KV}^*}{d\omega} d\omega, \quad (53)$$

$$G_E^*(\omega) = G_E^*(\omega_1) + \int_{\omega_1}^{\omega} \frac{\partial G_E^*}{\partial \omega} d\omega. \quad (54)$$

Subtracting Eq. 54 from Eq. 53, and using Eq. 48 gives

$$G_{KV}^*(\omega) - G_E^*(\omega) = \int_{\omega_1}^{\omega} \frac{\partial}{\partial \omega} [G_{KV}^*(\omega) - G_E^*(\omega)] d\omega. \quad (55)$$

From Eq. 51 it follows that the integrand of Eq. 55 is negative if $\omega < \omega_c$. Hence, the integral is negative if $\omega_1 < \omega \leq \omega_c$, and it is positive if $\omega > \omega_1$. Therefore,

$$G_{KV}^*(\omega) - G_E^*(\omega) > 0 \quad \forall \omega < \omega_1, \quad (56)$$

$$G_{KV}^*(\omega) - G_E^*(\omega) < 0 \quad \forall \omega \in (\omega_1, \omega_c]. \quad (57)$$

A similar reasoning for $\omega > \omega_c$ gives

$$G_{KV}^*(\omega) = G_{KV}^*(\omega_2) + \int_{\omega_2}^{\omega} \frac{dG_{KV}^*}{d\omega} d\omega, \quad (58)$$

$$G_E^*(\omega) = G_E^*(\omega_2) + \int_{\omega_2}^{\omega} \frac{\partial G_E^*}{\partial \omega} d\omega. \quad (59)$$

$$G_{KV}^*(\omega) - G_E^*(\omega) = \int_{\omega_2}^{\omega} \frac{\partial}{\partial \omega} [G_{KV}^*(\omega) - G_E^*(\omega)] d\omega. \quad (60)$$

By Eq. 52 the integrand of Eq. 60 is positive for $\omega > \omega_c$. Therefore, the integral is positive if $\omega > \omega_2$, and negative if $\omega_c \leq \omega < \omega_2$. Hence,

$$G_{KV}^*(\omega) - G_E^*(\omega) > 0 \quad \forall \omega > \omega_2, \quad (61)$$

$$G_{KV}^*(\omega) - G_E^*(\omega) < 0 \quad \forall \omega \in [\omega_c, \omega_2]. \quad (62)$$

Combining Eqs. 56 and 57 with Eqs. 61 and 62 gives

$$G_{KV}^*(\omega) < G_E^*(\omega) \quad \forall \omega \in (\omega_1, \omega_2), \quad (63)$$

$$G_{KV}^*(\omega) > G_E^*(\omega) \quad \forall \omega \notin [\omega_1, \omega_2]. \quad (64)$$

This derivation proves that the Kelvin-Voigt model will always underestimate G^* between the frequencies ω_1 and ω_2 . Further, the Kelvin-Voigt model will always overestimate G^* for frequencies smaller than ω_1 and larger than ω_2 . In some applications it will be conservative to use large G^* . In these cases, the Kelvin-Voigt model will be non-conservative for frequencies between ω_1 and ω_2 .

Subtracting Eq. 48 from Eq. 49, dividing by $\omega_2 - \omega_1$, and rewriting yields

$$\frac{G_{KV}^*(\omega_2) - G_{KV}^*(\omega_1)}{\omega_2 - \omega_1} = \frac{G_E^*(\omega_2) - G_E^*(\omega_1)}{\omega_2 - \omega_1}. \quad (65)$$

Taking the limit $\omega_2 \rightarrow \omega_1$

$$\lim_{\omega_2 \rightarrow \omega_1} \frac{G_{KV}^*(\omega_2) - G_{KV}^*(\omega_1)}{\omega_2 - \omega_1} = \lim_{\omega_2 \rightarrow \omega_1} \frac{G_E^*(\omega_2) - G_E^*(\omega_1)}{\omega_2 - \omega_1}, \quad (66)$$

$$\left. \frac{dG_{KV}^*}{d\omega} \right|_{\omega=\omega_1} = \left. \frac{\partial G_E^*}{\partial \omega} \right|_{\omega=\omega_1}. \quad (67)$$

Eq. 67 in combination with Eq. 48 state that the method of Section 5.2 is a special case of the method derived in the present section: Taking the limit $\omega_2 \rightarrow \omega_1$ of the method of the present section gives the method of Section 5.2.

6 Further Work

The work presented in this paper, together with the work presented in Olsen et al. (2014), Konradsen and Ouren (2014), and Komperød et al. (2015), are part of Nexans

Norway AS' effort to include the viscoelastic properties of bitumen in models of subsea cables and umbilicals.

The work of the present paper will be continued by modeling the mechanical properties of subsea cables and umbilicals with bitumen-coated armor wires using the UFLEX2D software. Because UFLEX2D requires bitumen's viscoelastic properties to be modeled by the Kelvin-Voigt model, the results of this paper are essential for modeling the effect of bitumen using UFLEX2D.

7 Conclusion

The contribution of the present paper is to evaluate the Kelvin-Voigt model's suitability to describe the viscoelastic properties of bitumen used as corrosion protection in subsea cables and umbilicals. This work is based on an empirical model developed by the author and his colleagues. This empirical model is published in Komperød et al. (2015).

The empirical model shows that bitumen's viscoelastic properties depend on the shear strain amplitude, shear strain rate, and the temperature. The Kelvin-Voigt model structure is not able to include dependence to strain amplitude nor to temperature. The lack of temperature dependence can be handled in the Kelvin-Voigt model by using different model parameters for different temperatures or by letting these model parameters be temperature-dependent, because it is reasonable (with a few exceptions) to assume that the bitumen temperature is homogeneous over one pitch length of the cable. The lack of strain amplitude dependence is a bigger issue, because bitumen's strain amplitude varies significantly within one pitch length of the cable. No solution to this issue has been found, except for choosing the Kelvin-Voigt parameters conservatively.

Under the assumption of constant strain amplitude, bitumen's frequency dependence in the Kelvin-Voigt model is analyzed and compared to the empirical model using Bode diagrams. Three different approaches are derived and discussed for how to decide the Kelvin-Voigt model parameters in order to resemble the frequency dependence of the empirical model. It is concluded that the Kelvin-Voigt model can resemble the shear stress amplitude to shear strain amplitude ratio and the phase shift between shear stress and shear strain at one single frequency. Alternatively, the Kelvin-Voigt model can resemble the shear stress amplitude to shear strain amplitude ratio over a limited frequency interval if the phase shift is disregarded. It is not possible to resemble the phase shift for more than a single frequency, because the derivative of the phase shift w.r.t. the frequency in the Kelvin-Voigt model inherently has opposite sign (plus or minus) compared to the empirical model.

References

- J. J. Féret and C. L. Bournazel. Calculation of stresses and slip in structural layers of unbonded flexible pipes. *Journal of Offshore Mechanics and Arctic Engineering*, 109:263 – 269, 1987.
- J. Hedlund. Modelling of viscoelastic dynamic bending stiffness for VIV analysis of submarine cables. In *Proceedings of the 9th International Conference on Insulated Power Cables (Jicable '15)*, 2015.
- E. Keadze. *Theoretical modelling of unbonded flexible pipe cross-sections*. PhD thesis, South Bank University, 2000.
- M. Komperød, B. Konradsen, and R. Slora. Viscoelastic large strain model of bitumen used for corrosion protection in subsea cables and umbilicals. In *Proceedings of the ASME 2015 34th International Conference on Ocean, Offshore and Arctic Engineering OMAE 2015*, 2015.
- B. Konradsen and S. V. Ouren. Modeling the effects of temperature and frequency on bitumen-coated helical cable elements. In *Proceedings of the 55th Conference on Simulation and Modelling (SIMS 2014) - Aalborg, Denmark*, 2014.
- J. Mullins, D. Morin, A. Tyrberg, C. Sonesson, and J. Ekh. Bitumen shear mechanics in a dynamic subsea electrical cable. In *Proceedings of the ASME 2015 34th International Conference on Ocean, Offshore and Arctic Engineering OMAE 2015*, 2015.
- A. Nysveen, H. Kulbotten, J. K. Lervik, A. H. Børnes, M. Høyer-Hansen, and J. J. Bremnes. Direct electrical heating of subsea pipelines - Technology development and operating experience. *IEEE Transactions on Industry Applications*, 43:118 – 129, 2007.
- E. Olsen, K. A. Hansen-Zahl, and S. Karlsen. Viscoelastic behaviour of bitumen in dynamic control umbilicals. In *Proceedings of the ASME 33rd International Conference on Ocean, Offshore and Arctic Engineering OMAE 2014*, 2014.
- G. B. Thomas, M. D. Weir, and J. Hass. *Thomas' calculus - global edition - 12th edition*. Pearson Education, Inc., 2010.

A About UFLEX2D

The UFLEX program system originates from a joint MARINTEK and Nexans Norway AS effort kicked off in 1999, resulting in a 2D software module (UFLEX2D) for structural analysis of complex umbilical cross-sections. The first version of the tool was launched in 2001. From 2005 and onwards further development of the 2D module as well as the development of a 3D module (UFLEX3D) has taken place within a Joint Industry Project (JIP). The JIP is still running, and is financed by a group of 10 sponsors covering the following oil and gas industry segments; operators, suppliers, technical service providers.

An optimization framework for tracking droplets in fire water spray images

Joachim Lundberg¹ Marius Lysaker¹

¹Faculty of Technology, Telemark University College, Norway, joachim.lundberg@hit.no

Abstract

The properties of the flow from fire water nozzles, like droplet size and velocity distribution within the spray, are known to influence the fire suppression efficiency. To analyze the flow properties, the water spray is recorded with the use of a high-speed camera and laser light. Typically, each image of the water spray may contain tens of droplets, yielding a huge number of possible droplet paths between adjacent frames, i.e. n droplets in two subsequent frames generates n^2 possible droplet paths with $n!$ possible configurations using brute-force approach. In this paper, we propose an optimization method based on the Hungarian algorithm to calculate the droplet paths. Using this framework, each droplet path is optimized with respect to droplet position, droplet size and droplet velocity.

Keywords: Droplets, Image Processing, Tracking

1 Introduction

The Norwegian petroleum industry has developed a standard for the technical safety of offshore installations (NORSOK S-001, 2008). When dimensioning accidental load with this standard, the deluge or fire water spray may be considered as a risk reducing measure for equipment and pipes, but not for the structural elements or fire partition (NORSOK S-001, 2008). In risk evaluation, proper documentation of the suppression effect and reliability has to be provided when water is used as a fire risk reduction measure. The standard states that the deluge system shall be automatically activated upon confirmed gas detection when it is used for explosion mitigation.

In the literature, the availability of data on fire water spray is limited. Often the spray is described only by the orifice diameter of the fire water nozzles and spray angle. However, the flow properties of the spray (i.e., size and velocity distribution of the droplets) are known to influence the suppression efficiency. Small droplets will follow the gas flow, evaporate quickly, and cool the fire gases. In contrast, large droplets have high momentum and are more likely to reach the source of the fire and to cool objects such as process equipment and pipes.

In the 90's, Jackman (1992) manually measured the droplet sizes and velocities for some commercial nozzles, using an image-based method to determine size

from photographic high-speed film images. Sheppard (2002) found the velocity field and droplet sizes using particle image velocimetry (PIV) and phase Doppler anemometry (PDA). PDA is a common technique for characterizing droplet distributions in sprays. In PDA measurements the droplets scatter the laser light at an angle that can be used to determine the droplet diameter. The light scattering is actually a measure of the curvature of the surface of the droplet; however, this technique has limitations with non-spherical droplets (Kashdan et al., 2007). Non-spherical droplets may be excluded by the data acquisition software, although this results in uncertainty in the PDA measurements. Recently, Zhou et al. (2012) used an image-based method to characterize the spray from a fire sprinkler in the near and far field of the sprinkler tip, with the near field measurements providing input that could be used in numerical fire models.

Image processing techniques are currently being used for analyzing sprays because they are relatively simple and economical compared to other methods like PDA (Koh, 2001). They also have advantages to other techniques regarding non-spherical droplets. However, it can be demanding to use these techniques due to the number of frames that need to be analyzed to get a statistically meaningful distribution (Lee & Kim, 2004). In shadow-imaging techniques, the depth of field effect is one of the major contributions to measurement error. (Lee & Kim, 2004).

To determine the droplet paths for each individual droplet of the spray, an optimization framework based on the Hungarian algorithm will be used. The overall objective is to obtain the spray characteristics of a medium velocity deluge nozzle used on an offshore installation in the North Sea, and make a spray characterizing method with an in-house image processing code.

Other post-processing codes for analyzing shadow-images have been tested. But for fire water spray, only commercial codes where the tracking algorithm is not presented are available.

2 Experimental setup

The experimental setup is located inside a container and consists of the following equipment: a laser with transmitting optics, a deluge nozzle, a high-speed

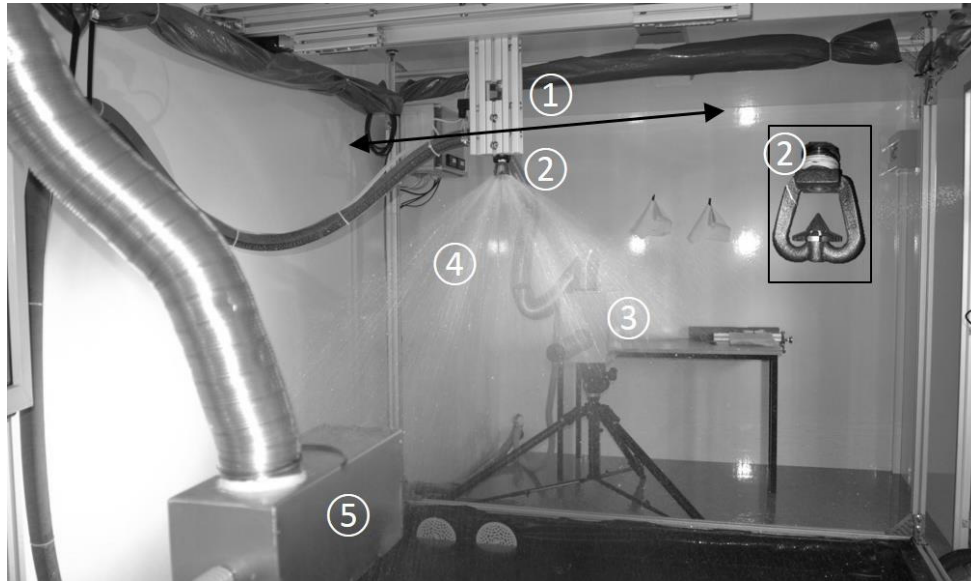


Figure 1. The experimental setup for fire water droplet measurement rig: 1) traverse with nozzle mounting, 2) deluge nozzle, 3) high-speed camera and long-distance microscope lens, 4) deluge spray, 5) laser transmitting optics.

camera, a long-distance microscope lens, a traverse with nozzle mounting and auxiliary equipment. The deluge nozzle is a Tyco MV34-110 medium velocity nozzle. According to the producer, the nozzle produces a cone-shaped spray that is uniformly filled with medium velocity droplets. The sub image in Figure 1 shows a picture of the nozzle.

A high-speed camera is used to capture images of the spray illuminated with a laser as shown in Figure 2. The back illumination is a copper vapor laser (CVL) from Oxford Lasers. The laser generates short light pulses (25 ns) with high effect (20 W) continually at 12.5 kHz. The camera and laser are synchronized to capture images at 12,500 frames per second. The high-speed camera is a Photron APX-RS monochrome camera. Two high magnification microscope lenses were used (Navitar 12 X with a focus range extender and Questar QM-1). The camera and lens have a narrow focus depth to produce sharp images of droplets in the focus plane with limited visibility of the droplets in front of or behind the plane. The technique is shown in Figure 2.

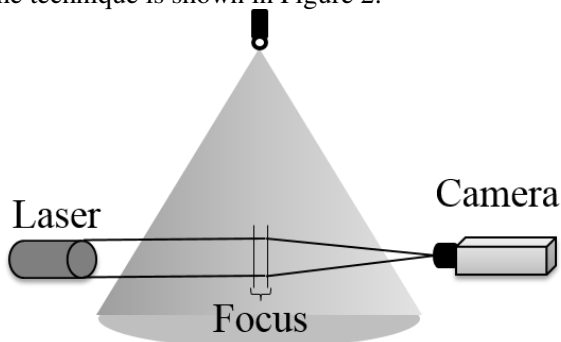


Figure 2. Experimental setup illustrating the narrow focus in the center plane of the spray.

The technique used in this work is called image-based shadow-imaging. The camera will register the shadows of the droplets because the water droplets will scatter the light from the laser.

3 Image processing

The flow properties, like droplet size and velocity, generated with a fire water nozzle are known to vary within the spray (Sheppard, 2002). Therefore, to characterize the flow properties caused by a given fire water nozzle, hundreds of movies must be recorded. Each movie is recorded at a given location in the spray. Since each movie typically consists of 8,000-12,000 frames, millions of images need to be analyzed to obtain the velocity- and size- distribution for all locations of the fire water spray within a certain accuracy. Due to the number of images to be analyzed, an automatic post-processing algorithm is required.

The post-processing algorithm is developed in MATLAB and uses MATLAB image processing toolbox, (Mathworks, 2009). Established and new image processing techniques are used to extract information about the fire water spray from the movies of the droplets. The size of the droplets can be determined by comparing the droplets in the movie to a calibration standard with a known size. The velocity can be found by comparing the position of the droplets in subsequent frames. By recording the measurements of several droplets, it is possible to find the droplet size- and velocity distribution of the spray.

In this paper, we propose an algorithm that automatically calculates the size and velocity distribution in a given water spray movie. In short, the algorithm works as follows:

1. Separate “in-focus” droplets from all “out-of-focus” droplets, and the background in each image.
2. Calculate the size and position of all “in-focus” droplets in each image.
3. Find the velocity by comparing the position of the droplets in temporally adjacent frames.

3.1 Segmentation

The recorded images consist of droplets (both “in-focus” and “out-of-focus” droplets), noise and the background. The background is the image without any droplets or noise. In an ideal image, the “in-focus” droplets are black, the “out-of-focus” droplets are gray and the background is white, meaning that it is easy to identify the “in-focus” droplets. However, in real measurements, due to varying illumination and optical phenomena, the background appears uneven and there is a smooth transition from “in-focus” to “out-of-focus” droplets, see Figure 3.

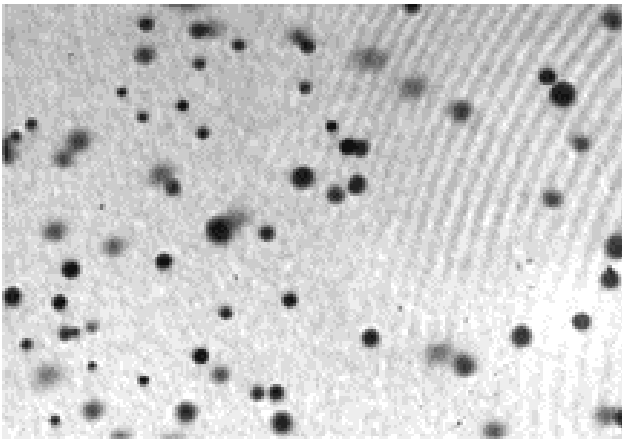


Figure 3. Original image from spray, I_i .

An estimate for the uneven background B is found by averaging all frames within a movie, i.e.

$$B = \frac{1}{n} \sum_{i=1}^n I_i \quad (1)$$

where I_i is the image at frame i and n is the total number of frames in the movie. Then, for each image in the movie, the background is subtracted:

$$J_i = I_i - B, \quad \text{for } i = 1:n. \quad (2)$$

After the background subtraction routine, the images will mainly consist of noise and droplets, see Figure 4.

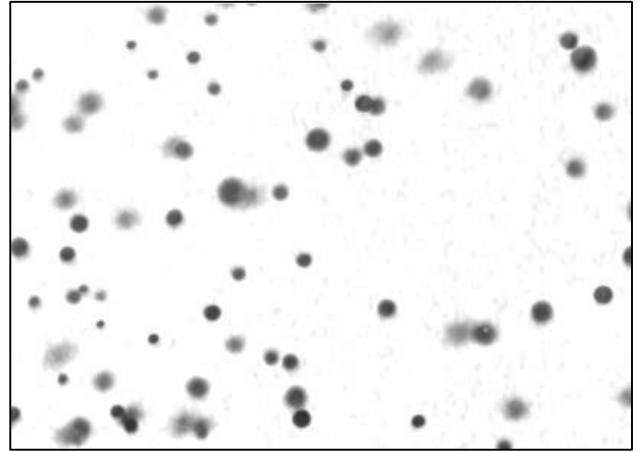


Figure 4. Image processed image J_i , where the background is removed from the original image.

The background B , which is subtracted from all of the images, is shown in Figure 5.

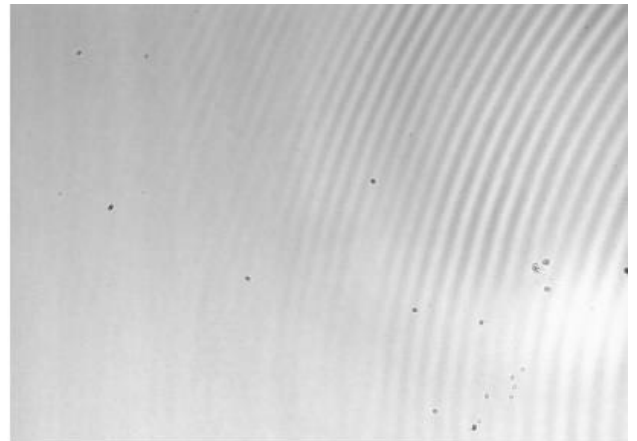


Figure 5. This figure shows the background found by (1).

The droplets can be isolated by applying a thresholding algorithm that divides the image into droplets and background (including noise). The Otsu (1979) algorithm is used to find the threshold value t . The optimal solution of t maximizes the inter-class variance between the droplets and the background (Gonzales & Woods, 2008). The threshold value is then used to divide the gray-scale image $J_i(x, y)$ into background and droplets, where (x, y) represents the pixel coordinates. Every pixel value above the threshold t is classified as background, and pixel value below t is identified as droplets, yielding the binary image

$$T_i(x, y) = \begin{cases} 0 & \text{if } J_i(x, y) < t \\ 1 & \text{if } J_i(x, y) \geq t \end{cases} \quad (3)$$

The threshold algorithm can be used both globally and locally, and thereby determine one global threshold value for an entire image, or one local threshold value for each defined area. The output of the threshold

algorithm is a binary image, i.e. droplets and background, see Figure 6.

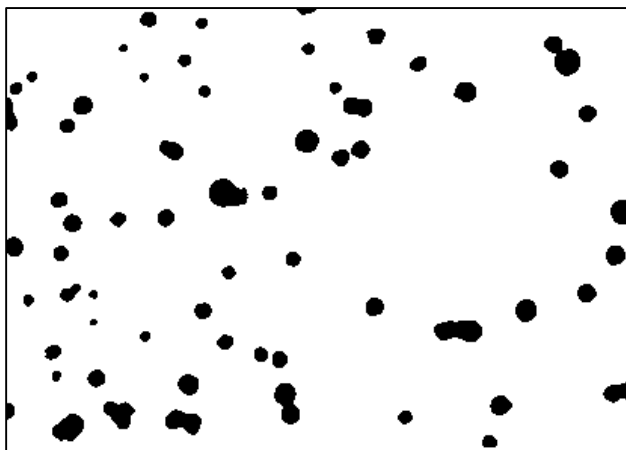


Figure 6. Thresholded image T_i found with (3) showing droplets (black) and background (white).

3.2 In-focus droplets

The basic principle of shadow-imaging is that the camera will have a narrow depth of field that will make a sheet of droplets in focus while droplets in front of or behind this sheet will be blurred away. The thickness of the DOF sheet is dependent on the size and has to be calibrated. To qualify the “in-focus” droplets, the concept of gray-scale gradient at the boundary by Lecouna et al. (2000) is adopted. This method compares the gray-scale or intensity gradient at the boundary of the droplets to the intensity difference of the minimum of the droplet and the background.

Droplets in focus are counted to generate the spray distributions. In the cases examined here, the droplet sizes range from typically 100 to 1200 μm and the velocity is between 1.0 and 15.0 m/s. These intervals will determine the range of droplets the image processing code is limited to find.

The qualified droplets are indexed from one to the number of recognized objects in the image as shown in Figure 7.

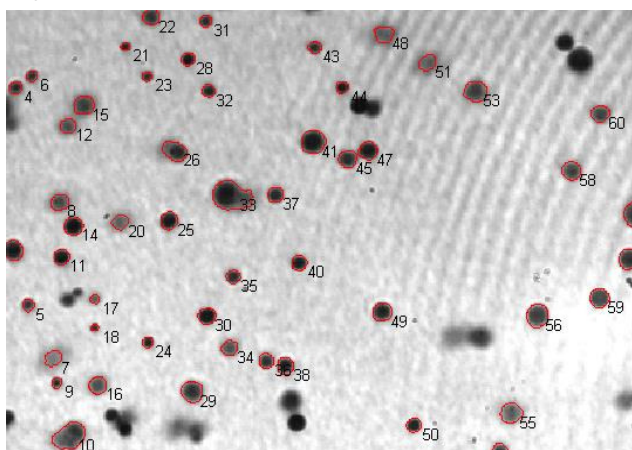


Figure 7. Contours of qualified droplets (with red ring and a number) and an index number superimposed on I_i .

3.3 Droplet matching

To find the velocity of the droplets, the position of each droplet in a given frame is compared with the position of the same droplet in subsequent frames. In this article, the velocity of the droplets in image T_i is calculated with the use of three images, i.e. T_{i-1} , T_i and T_{i+1} . The velocity distribution of the droplets is then obtained by comparing the physical position in the temporally adjacent frames.

Therefore, to calculate the droplet velocity, all “in-focus” droplets have to be tracked between the frames. However, this is a challenging problem, since several possible droplet paths may exist for a given set of droplets, see Figure 8. By using brute-force search, the number of possible configurations of droplet paths for n droplets are $n!$. By using the Hungarian algorithm the number will only be n^2 .

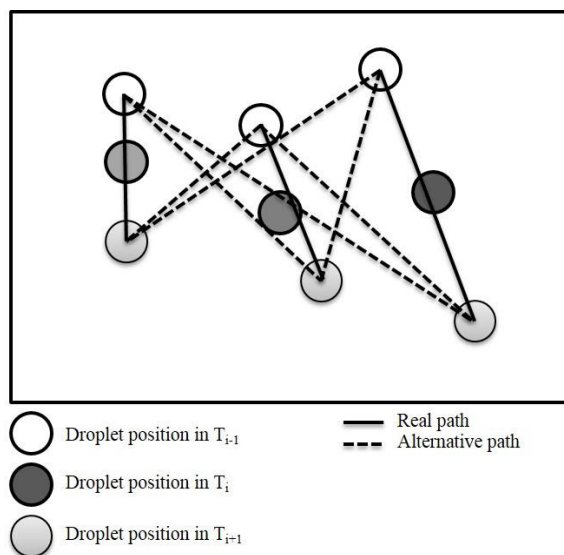


Figure 8. Droplet combinations for illustrations. Possible paths for three droplets in three sub sequential frames.

Please note that, with respect to the flow properties, each droplet has exactly one path, i.e. one single droplet cannot be assigned to several paths. Moreover, the number of “in-focus” droplets may change from frame to frame, as droplets might emerge or disappear in subsequent frames. To overcome these challenges, a multiple tracking framework is applied. Multiple tracking considers all possible paths, and selects the optimal combination. Such an optimization problem can be solved efficiently by, e.g. the Hungarian algorithm (Kuhn, 1955).

3.4 Tracking as an assignment problem

In terms of mathematics, a path between the positions of droplets in subsequent frames can be assigned a cost. In this thesis, the cost for a given path is defined by a combination for the following constraints:

- The direction of the path should not change appreciable from frame to frame.
- The droplet velocity should not deviate much from an average droplet velocity.
- The droplet size should not differ appreciably from frame to frame.
- A droplet cannot be assigned to more than one path.

To find the optimal association of **all** the droplets in adjacent frames, a cost must be calculated for **each** individual path. Let $P = \{p_1, p_2, \dots, p_k\}$, $Q = \{q_1, q_2, \dots, q_l\}$ and $R = \{r_1, r_2, \dots, r_m\}$ denote the sets of k, l and m points (droplets) detected in frame $i - 1$, i and $i + 1$, respectively. The total cost of each path from $p \in P$ to $r \in R$ via $q \in Q$ is given by the penalty matrix $C_{k \times m}$, where

$$C_{k \times m} = \delta \Delta_{k \times m} + \lambda \Lambda_{k \times m} + \gamma \Gamma_{k \times m} \quad (4)$$

and δ, λ and γ are positive constants and the subscript $k \times m$ represents the dimension of the matrixes, i.e. the matrixes have k rows and m columns. In the following, the three matrixes $\Delta_{k \times m}$, $\Lambda_{k \times m}$ and $\Gamma_{k \times m}$ are discussed in more detail.

The elements in $\Delta_{k \times m}$ represents a measure of the smoothness of each path, and paths that change direction from one frame to another are penalized. To calculate the direction of a path, we utilize the fact that every convex combination of two points lies on the line segment between the two points, i.e. $w = \alpha p + (1 - \alpha)r$, with $0 \leq \alpha \leq 1$. By using $\alpha = 1/2$, (assuming no acceleration), a point halfway between p and r is thereby simply given by $w = \frac{p+r}{2}$. If $w \in Q$, it means that there is a droplet in frame i positioned halfway between a droplet $p \in P$ and a droplet $r \in R$, indicating a non-changing direction of the path. Otherwise, with $w \notin Q$, the path changes direction from one frame to another, and the changes are measured as the shortest distance from w to any $q \in Q$, i.e.

$$\Delta_{k \times m} = \begin{bmatrix} d\left(\frac{p_1 + r_1}{2}, q^*\right) & \cdots & d\left(\frac{p_1 + r_m}{2}, q^*\right) \\ \vdots & \ddots & \vdots \\ d\left(\frac{p_k + r_1}{2}, q^*\right) & \cdots & d\left(\frac{p_k + r_m}{2}, q^*\right) \end{bmatrix} \quad (5)$$

where $d(w, q^*)$ denotes the shortest distance from w to any $q \in Q$.

All droplets will move a certain distance between the frames in the high speed movie. However, the droplet velocity depends on the droplet size, i.e. larger droplets move with another velocity than smaller droplets. Each element in $\Lambda_{k \times m}$ in (3) gives the deviation between the

velocity along a given path and a size dependent (prior calculated) velocity distribution by

$$\Lambda_{k \times m} = \begin{bmatrix} |d(p_1, r_1) - v^*| & \cdots & |d(p_1, r_m) - v^*| \\ \vdots & \ddots & \vdots \\ |d(p_k, r_1) - v^*| & \cdots & |d(p_k, r_m) - v^*| \end{bmatrix} \quad (6)$$

where $|d(p, r) - v^*|$ denotes the absolute value of the distance (velocity) by moving from p to r (the framerate is known), minus a size dependent velocity distribution, where the size dependent velocity v^* is based on droplet p and r .

Finally, the elements in $\Gamma_{k \times m}$ are a measure of the mismatch in the size of the droplets connected along a given path. First, let us introduce the following notation

$$A(p, q, r) = \frac{|A(p) - A(q)| + |A(p) - A(r)| + |A(q) - A(r)|}{A(p) + A(q) + A(r)}. \quad (7)$$

where $A(p), A(q)$ and $A(r)$ denotes the area of droplets p, q and r , respectively. With this notation at hand, the matrix $\Gamma_{k \times m}$ is given by

$$\Gamma_{k \times m} = \begin{bmatrix} A(p_1, q^*, r_1) & \cdots & A(p_1, q^*, r_m) \\ \vdots & \ddots & \vdots \\ A(p_k, q^*, r_1) & \cdots & A(p_k, q^*, r_m) \end{bmatrix} \quad (8)$$

where q^* is the droplet $q \in Q$ with the shortest distance to the midpoint between the given p and r .

Please note that all elements in the matrixes $\Delta_{k \times m}$, $\Lambda_{k \times m}$ and $\Gamma_{k \times m}$ are greater or equal to zero. Consequently, all elements, i.e. costs, in the penalty matrix $C_{k \times m}$ are greater or equal to zero. The Hungarian algorithm takes the penalty matrix $C_{k \times m}$ as its only argument and returns the optimum path assignment (see (Kuhn, 1955) for details). The running time of the Hungarian is $O(n^3)$ compared to brute-force search of $O(n!)$.

Figure 9 shows the droplet paths with a red vector found with the Hungarian algorithm. The contours of the segmented droplets and the segmented droplets of the temporally adjacent frames are superimposed for illustrational purposes.

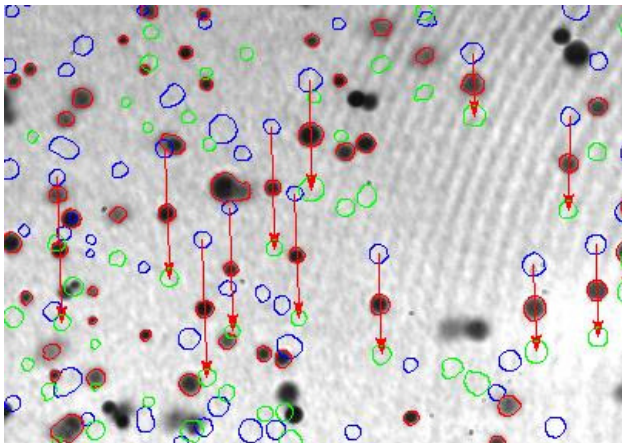


Figure 9. Vectors of droplet paths showing movement from frame $i - 1$ (blue contour) to frame $i + 1$ (green contour) of the droplets in frame i (red contour).

4 Results

This work gives preliminary results for one water pressure of 2.00 bar(g) applied to the fire water nozzle. All the experiments are done one meter below the nozzle tip and at radial positions 0 – 150 cm from the center and at 3 different azimuthal angles (0° , 15° and 30°) compared to the frame arms of the nozzle.

Figure 10 shows the results of droplet size distribution when combining all the measurements from 0 – 150 cm.

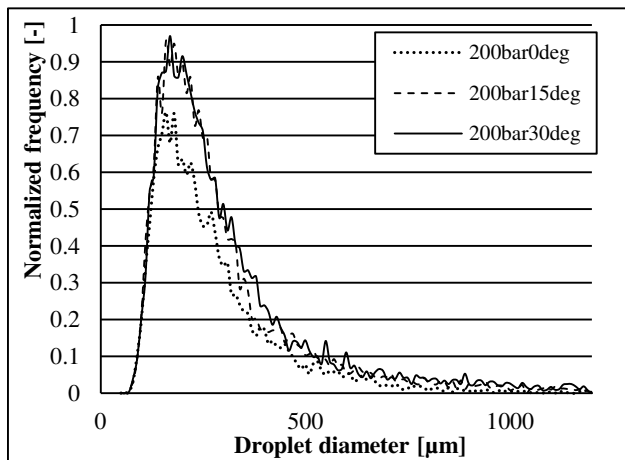


Figure 10. Total droplet size distribution for azimuthal angles of (0° , 15° and 30°) compared to the frame arms of the nozzle.

Figure 11 shows the velocity distribution in the spray. This is for all radial positions and the azimuthal angle 0° .

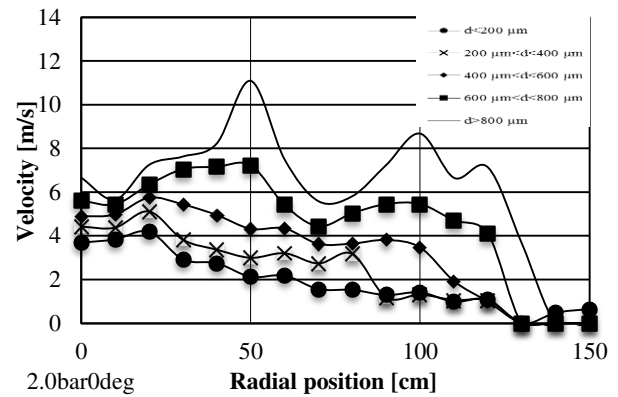


Figure 11. Preliminary experimental results for velocity of droplet size intervals as a function of radial position.

5 Conclusion

The usage of the Hungarian algorithm on a penalty matrix seems to give good results. The droplet paths, velocity and sizes seem to agree with spot checks by monitoring visually how the automatic image processing code perform on the images. The vectors in Figure 9 indicate that all the droplets flow in the same direction. This agrees with the physical properties of this spray. By using the velocity field of Figure 9 as an example, 12 droplet paths are found. To find these 12 paths with the Hungarian algorithm, a 12x12 matrix has to be solved. By using a brute-force search, almost 500 million possible path configurations have to be checked.

References

Gonzalez, R.C. and Woods, R.E. Digital Image Processing (third ed.). Pearson Prentice Hall, Upper Saddle River, NJ, 2008.

Jackman, L.A. Sprinkler Spray Interactions with Fire Gases. Ph.D. Thesis, Explosion and Fire Unit, South Bank University, London, 1992.

Kashdan, J.T., Shrimpton, J.S., Whybrew, A. A Digital Image Analysis Technique for Quantitative Characterisation of High-speed Sprays. Optics and Lasers in Engineering 45(1): 106-115, 2007.

Koh K.U., Kim J.Y., Lee S.Y. Determination of in-focus criteria and depth of field in image processing of spray particles. Atomization and Sprays, 11(4):317–333, 2001.

Kuhn, H.W. The Hungarian method for the assignment problem. Naval Research Logistics Quarterly, 2: 83–97, 1955.

Lecuona, A., Sosa, P.A., Rodriguez, P.A., Zequeira, R.I. Volumetric characterization of dispersed two-phase flows by digital image analysis. Measurement Science and Technology, 11: 1152–1161, 2000.

Lee S.Y., Kim Y.D. Sizing of Spray Particles Using Image Processing Technique. KSME International Journal, 18(6): 879-894, 2004.

Mathworks. MATLAB User's Guide (r2011b). 3 Apple Hill Drive Natick, MA, 2011.

- NORSOK-Standard, Technical Safety S-001 (4th ed). Standards Norway, 2008.
- Otsu, N. A Threshold Selection Method from Gray-Level Histograms. IEEE Transactions on Systems, Man, and Cybernetics 9(1): 62-66, 1979.
- Sheppard, D.T. Spray Characteristics of Fire Sprinklers. National Institute of Standards and Reporting NIST GCR 02-838, Gaithersburg, MD, 2002.
- Zhou, X., D’Aniello, S.P., Yu, H.-Z. Spray Characterization Measurements of a Pendent Fire Sprinkler. Fire Safety Journal 54: 36-48, 2012.

A Study of the Effect of Relative Permeability and Residual Oil Saturation on Oil Recovery

Mahesh P. Ediriweera¹ Britt M. Halvorsen¹

¹Process Technology, Telemark University College, Norway

Abstract

Depletion of the production and the low recovery factor are major challenges faced in petroleum industry. The recovery factor and the lifetime of a well are strongly affected by the reservoir properties such as permeability, porosity, residual oil saturation and the water breakthrough time. This research is done to investigate the influence of the relative permeability on oil recovery. Simulations are done for different relative permeability curves and various residual oil saturations. The main focus is the impact on total flow rates and water breakthrough time. The reservoir simulator Rocx in combination with OLGA is used as the simulation tool. The results show that the total oil production and the water breakthrough time are strongly affected by the relative permeability and residual oil saturation. The impact of relative permeability is much higher than the residual oil saturation in petroleum processing.

Keywords: oil recovery, OLGA/Rocx, reservoir, properties, relative permeability, water breakthrough, water coning

1 Introduction

The offshore petroleum industry is continuously looking for new technologies to enhance the oil recovery and to optimize the operation. The main drawbacks faced by the industry are low oil recovery factor, depletion of oil production, gas coning and water coning. Some previous works have shown that considerable amount of oil still remain in the reservoir after well shutdown. The residual oil saturation and early breakthrough are the main reasons for remaining oil volumes in abandon oil fields. Since the reservoir properties highly influence the oil recovery process, it is interesting to identify the relation between the recovery factor and the reservoir properties. Further, the relative permeability varies with time due to changing in water saturation during the recovery process. If relationships and variations are known, then recovery can be efficiently upgraded by manipulating reservoir properties. Enhanced Oil Recovery (EOR) methods can be used to change the properties such as relative permeability and residual oil saturation. A typical oil reservoir consists of an underlying aquifer and a gas cap. Here in this paper, heavy oil reservoirs

are considered and gas coning is not discussed. Heavy oil reservoirs occupy more than two third of global oil reserves.

The oil recovery factor is the ratio between the amount of oil that can be extracted from a reservoir throughout the lifespan of the well and the total reservoir oil in place. The recovery factor is in general less than 20 percent when heavy oil is produced without any external force (P. Zitha, 2011). The conical water profile of the reservoir, which forms above the aquifer during the extraction process, is known as water cone. The water coning phenomena occurs in oil wells with aquifer as shown in Figure 1. The cone spreads towards the well while the amount of oil is being reduced in the reservoir over the life span of the well. When the water cone hits the wellbore, water mixes with oil and the inflow to the well becomes multiphase flow. After the breakthrough, the water volume ratio of the multiphase flow is increased gradually and the volume percentage of the mixture is introduced as water cut.

The demand of oil and gas would remain until a cost effective feasible energy source is found. Hence, the industry always look for new methods to extract as much oil and gas as possible in an efficient and effective way. Recovery mechanisms have been developing for years in order to extract maximum output by increasing the recovery factor and controlling the water breakthrough. These two features are strong functions of reservoir properties and extraction techniques. The regulated reservoir properties expose the access to control the recovery factor and the coning effect. Therefore, an overall understanding over reservoir properties and extraction techniques is desired before going deeper into the improved oil extraction. Tertiary recovery methods, so called Enhance Oil Recovery, which increase the mobility of residual oil throughout the entire reservoir by changing reservoir properties (P. Zitha, 2011). External force or fluids are used to efficiently capture hydrocarbons using these methods. Relative permeability is one of the reservoir properties which can be controlled with existing techniques in the petroleum industry under tertiary recovery methods.

The purpose of the study is to build an OLGA-Rocx¹ model for a typical Norwegian oil production process to investigate the influence of relative permeability throughout the operation. Various reservoir models can be used to simulate the characteristics of the reservoir over the period. The model is able to predict the behavior of inflow and the property changes in the reservoir during the normal operation. Only horizontal wells are modelled in this project due to the fact that horizontal wells are the most common technology implemented in Norwegian offshore fields. The TECPLOT² module is used as the result visualization tool to plot the simulated reservoir results.

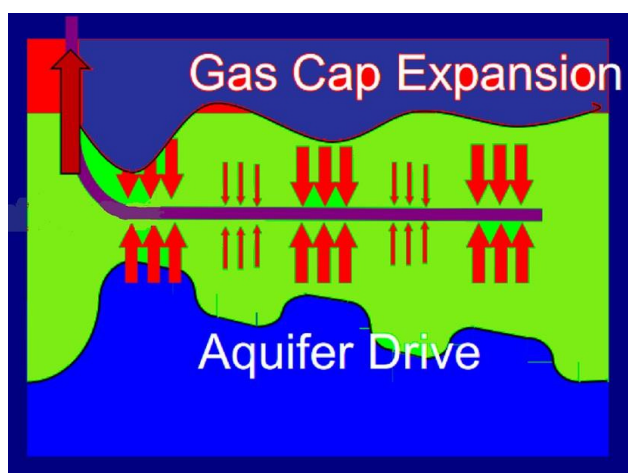


Figure 1. A typical petroleum reservoir with water aquifer and gas cap.

2 Reservoir Properties

Each and every petroleum reservoir has its own characteristics throughout the reservoir volume. These properties are distinguished as rock properties and fluid properties. Porosity, permeability and relative permeability are the most critical rock properties. Pressure, temperature, viscosity, specific gravity, oil and gas concentrations are some key fluid properties for the analysis. Conventionally, crude oil is brownish green or black in color with the specific gravity 0.801-0.985. The distillation process decomposes crude oil into its subcomponents within the boiling point range from 20^oC to 350^oC (Speight e Speight, 2009).

2.1 Porosity and Permeability

In general, the reservoir volumes consist of sandstone which is considered as high porous and high permeable media. Porosity is a measurement of the void spaces in a rock. Relationship for porosity is expressed as the volume fraction given in Equation 1. Tiny spaces in

sandstones hold hydrocarbons and water within the reservoir. Therefore, indirectly the porosity is a dimension of reserved petroleum quantity of the given reservoir. Porosity can be categorized as primary and secondary porosities. Gaps and spaces developed during the sedimentation process is called the primary porosity while the secondary porosity is formed in later stages as dissolving of minerals occurred. Hydrocarbons can only be produced if interconnected pores are available within the reservoir rock. The ratio between interconnected pores and total rock volume is equal to the effective porosity which is the useful property in the oil extraction process. Practically, the porosity value is given in Equation 1 is always higher than the effective porosity.

$$\text{Porosity } (\phi) = \frac{\text{Volume of the Void space } (V_V)}{\text{Total or Bulk Volume of the Rock } (V_T)} \quad (1)$$

Permeability describes the fluid conductivity through a porous media, also known as “absolute/intrinsic permeability”. If high pressure is needed to extract hydrocarbons, it is called low permeable reservoirs and vice-versa. Permeability is directly related to the porosity, it depends on the porous connectivity and the size of the porous volumes. Absolute permeability could be determined by laboratory experiments with the use of inert gases (frequently used nitrogen) (A. B. Zolotukhin, 1997). Permeability can be calculated by Darcy’s law which was developed semi empirically by Darcy in the 19th century for single phase flow and in 20th century for multiphase flow (Lokendra Pal, 2006). The permeability coefficient depends on both material and the fluid properties. The greater the K value is, the higher will the flow rate be.

Darcy’s law is expressed by:

$$Q = \frac{K \Delta P}{\eta \Delta L} A \quad (2)$$

where, Q is the flow rate, K is the permeability coefficient, ΔP = Pressure difference, A is the cross sectional area of the flow, η is the fluid viscosity and ΔL is the flow length.

Permeability is expressed in *Darcy* or *millidarcys* and most of the oil reservoirs are in the range of ten to several hundreds of *millidarcys*. Figure 2 shows the permeability of different types of commonly available rocks.

¹ OLGA-Rocx is a modelling software dedicated for oil field simulation. <http://www.prod.software.slb.com>

² <http://www.tecplot.com>

Permeability	Pervious		Semi-Pervious		Impervious								
Unconsolidated Sand & Gravel	Well Sorted Gravel	Well Sorted Sand or Sand & Gravel	Very Fine Sand, Silt, Loess, Loam										
Unconsolidated Clay & Organic			Peat	Layered Clay	Unweathered Clay								
Consolidated Rocks	Highly Fractured Rocks		Oil Reservoir Rocks	Fresh Sandstone	Fresh Limestone, Dolomite	Fresh Granite							
κ (cm ²)	0.001	0.0001	10 ⁻⁵	10 ⁻⁶	10 ⁻⁷	10 ⁻⁸	10 ⁻⁹	10 ⁻¹⁰	10 ⁻¹¹	10 ⁻¹²	10 ⁻¹³	10 ⁻¹⁴	10 ⁻¹⁵
κ (millidarcy)	10 ⁺⁸	10 ⁺⁷	10 ⁺⁶	10 ⁺⁵	10,000	1,000	100	10	1	0.1	0.01	0.001	0.0001

Source: modified from Bear, 1972

Figure 2. Permeability of common rocks (Logs).

2.2 Relative Permeability

The relative permeability is defined for multiphase flows. The effective permeability of a component of the multi-phase flow is given by the relative permeability. Darcy's law can be modified for a multiphase flow as expressed in Equation 3.

$$Q_i = \frac{K_i \Delta P_i}{\eta_i \Delta L} A \quad i = 1, 2, \dots, n \quad (3)$$

The subscript i indicates the parameters of i th phase and K_i is the of phase permeability of the component i . Several laboratory experiments have shown that the sum of the effective permeability is less than the absolute permeability (A. B. Zolotukhin, 1997).

$$\sum_{i=1}^n K_i < K$$

Relative permeability is the ratio between effective permeability of the respective phase and the absolute permeability as shown in Equation 4. Therefore, the sum of the relative permeability components must also be less than 1. Even though the effective permeability is a function of several parameters such as rock properties, fluid properties, absolute permeability fluid saturation and reservoir condition (pressure, temperature), the relative permeability depends on the fluid saturation and structure of the porous medium (A. B. Zolotukhin, 1997). However, the relative permeability can be assumed as a function of only saturation due to its strong correlation with saturation.

$$K_{ri} = K_i / K \quad (4)$$

Saturation of a particular fluid is denoted as the ratio of fluid volumes to pore volume as expressed in Equation 5. Though several attempts have been made to calculate the relative permeability on a theoretical basis, so far the commonly available data has been

taken from experimental investigations. For two phase flows typical permeability curves are shown in Figure 3.

$$\text{Saturation of Oil } (S_o) = \frac{\text{Volume of Oil}}{\text{Pore Volume}} \quad (5)$$

One important remark on the curve is that the relative permeability becomes zero if the saturation of the corresponding phase is less than a specific value. The value is then said to be the residual saturation of the respective phase.

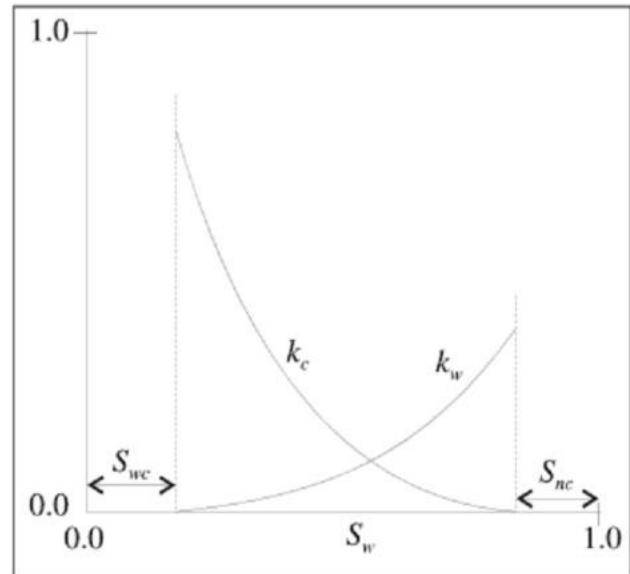


Figure 3. A typical oil-water relative permeability curve (A. B. Zolotukhin, 1997).

3 Modelling and Simulation

Models are built based on the properties found in the Grane field in the North Sea. Table 1. shows the reservoir properties of the Grane field. Even though, homogeneous reservoirs do not exist in real world, adequate parameters are used in simulation to evaluate real world challenges. A reservoir, having the length of 100m, the width of 201m and the height of 30m is considered. The geometry of the field is divided into a 3-dimensional mesh with control volumes. The mesh is selected to obtain accurate results by using finer grids closer to well and coarser grids apart from the well. The considered reservoir with control volume distribution is shown in Figure 4. The horizontal well is placed along the x-axis in the reservoir model. Reservoir properties such as permeability, porosity and relative permeability are included as input parameters to the model. Another two important inputs to the model are initial conditions and boundary conditions. Under the boundary conditions, the properties and the concentrations beyond reservoir margins are defined. If the aquifer is large enough, pressure at the lower boundary can be considered as a constant during the

simulation. The well position in the reservoir block is also given as boundary conditions. The fluid concentration and saturation at initial time are given as initial conditions.

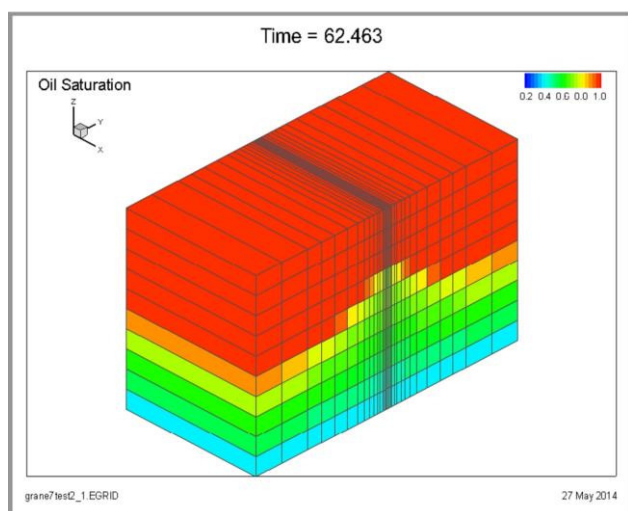


Figure 4. Control volume distribution.

Fluid flow variations along the horizontal well during normal operation can be inspected with the well model of interest. Simulations have been carried out with one Inflow Control Device (ICD) along the horizontal well, even though a real well has number of ICDs. The diameter of the ICD is 9 mm. Based on the single-valve model, more complex models can be simulated in future with less effort. For the comparison, only a variable of interest is changed while keeping all other variables constant in order to avoid the impacts from them. Another attractive feature in the OLGA model is the availability to observe dynamic variations of each subcomponent during simulations. This feature is useful to identify errors and to introduce appropriate parameters of individual subcomponent. Trial and error method is used to introduce convenient parameters for the model.

Table 1. Reservoir properties in Grane field.

<i>Property</i>	<i>Value</i>
Pressure (bar)	176
Temperature (C)	76
Porosity (%)	33
viscosity (cP)	12
Thickness (m)	31
Permeability (D)	10

In order to save the simulation time and the memory space are important in any kind of finite element

methods. Simulations can be done with relatively large time steps to minimize the running time. Even though precise results are not given with large time steps, information taken from the simulations is useful to get general idea and to cut down errors prior to the final simulation. The selection of plotting variables is also decisive to reduce the running time.

This study is mainly focused on the influence of the relative permeability on flow rates, the water breakthrough time and the oil extraction efficiency. Figure 5. shows the relative permeability data found in literature and the graphs are created using polynomial regressions. Three different cases are concerned for the comparison where the residual water and the residual oil values are distinct from each other. At the beginning of well, the well surrounding is saturated with oil. During the simulation oil saturation throughout the reservoir is reduced, while the water saturation starts to increase gradually. However, water will not enter the wellbore until the water saturation around the well exceeds its own residual limit. Theoretically, the oil extraction can be continued till the saturation falls down to its residual limit. Residual oil in the reservoir remains in abandoned oil fields after operation is finished.

4 Results and Discussions

Three cases are simulated for 200 days and the comparison of the results are mainly focused on water breakthrough, liquid flow rates, accumulated liquid volumes and the reservoir oil saturation profiles. The results gave different values/profiles for each case so that the effect of the relative permeability is reflected. Figure 6. shows the accumulated total liquid volumes with respect to time. The average total liquid flow rates are represented by the gradients of respective graphs. The total flow rates prior to breakthrough are approximately $337\text{m}^3/\text{day}$. Gradients of the curves change with time. At the beginning, the flow rate is maintained at constant level until the breakthrough occurs and thereafter the total flow rate starts to fluctuate with time. Subsequently, the total flow rate and oil flow rate achieve different values due to the multiphase flow after the breakthrough.

The reason for the total flow rate deviation, from a constant value after the breakthrough, can be explained with the use of relative permeability and Darcy's equation for multiphase flow. The sum of relative permeability values is lower than absolute permeability. The total flow rate is then the sum of individual flow rates in the multiphase flow. Furthermore, the total flow rate depends on the relative permeability and the viscosities of each component as well. Theoretically, viscosity values would compensate the effect of relative permeability as shown in Equation 3 and might lead to a higher flow rates.

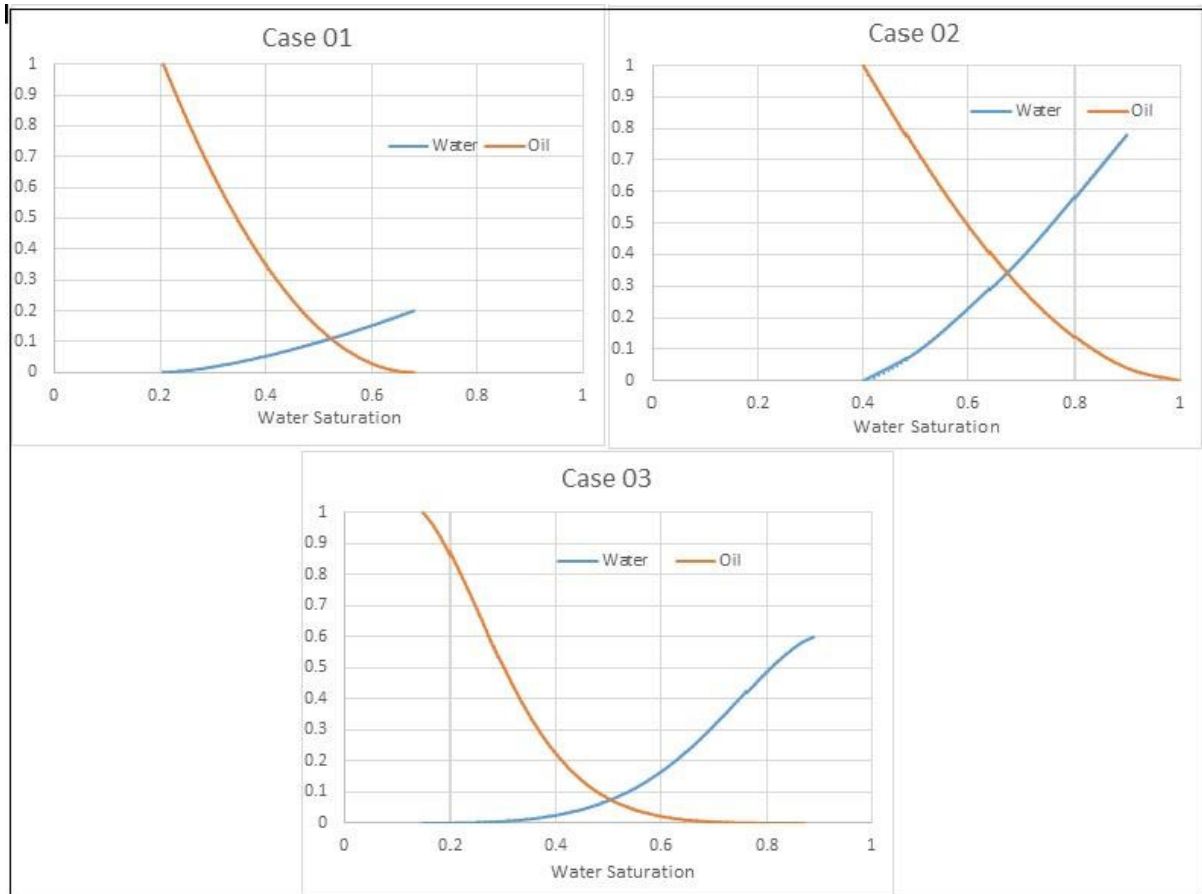


Figure 5. Relative permeability values in three cases.

However, total flow rate is always less than any single phase flow rate in practice. In this paper, oil-water multiphase flows are considered. The simulation results show that the total flow rates are decreased after the breakthrough. It seems that the relative permeability values of the multiphase flow influence in the flow rate reductions. The liquid flow rate is continuously changed after the breakthrough since the water saturation near the well is changed and then the relative permeability varies accordingly. Hence, the flow rate changes after the breakthrough can be well described with the dynamic variation of the relative permeability throughout the reservoir with time. Table 3 shows the information about the water breakthrough for each case. The accumulated oil curves have the same characteristic since oil is the only component before the multiphase condition is achieved. The water saturation throughout the reservoir is an important factor to understand the variation of the breakthrough time. Multiphase phenomenon could be approached within the reservoir even before water enters to the well bore due to the water coning profile. It is important to note that water cone is formed above the aquifer at the beginning of the operation and the water saturation inside the cone should not necessarily be 100% saturated water. Table 3 shows the saturation at the grid (1, 16, 4) where the well is located. Water

saturations noticed at the breakthrough point are equal to the residual saturation for each case. Saturated values at any given time and any location can be picked up by using Tecplot data.

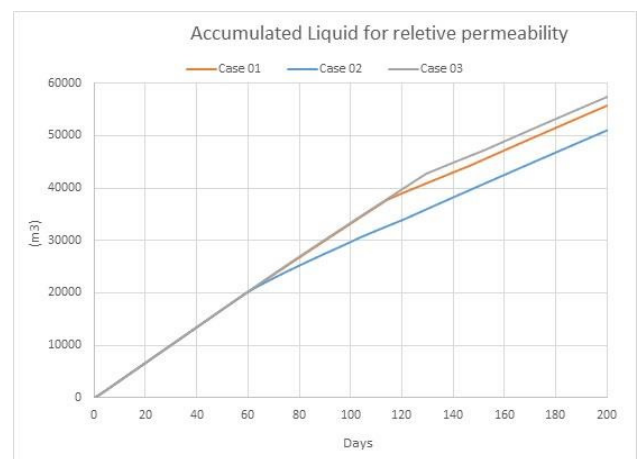


Figure 6. Accumulated Liquid profiles vs life time.

Table 2. Liquid Volumes after 100 days.

Case	Volume (m ³)	
	Liquid	Oil
Case 01	33219	28672
Case 02	29717	25980
Case 03	33367	30973

If water flows with the same speed within the reservoir until breakthrough happens, the water cone must have the same profile for every case. Figure 8 shows the oil saturation profile at the breakthrough time for the given cases. Further, the breakthrough time should be delayed according to the residual saturation so that the latest breakthrough time should occur, for Case 02, which has the highest residual water saturation. However, the latest breakthrough happens, in Case 03, which has the lowest residual water saturation. This deviation implies that the breakthrough is not only affected by the water saturation. This paradox can be explained using relative permeability graphs in Figure 5. Even though the water breakthrough happens at the residual saturation of water at the well-grid, water dispersion throughout the reservoir does not occur in the same rate due to the multiphase flow towards the well. When the oil saturation is closer to the residual level, the relative permeability of water increased exponentially (see Figure 3). When oil approaches its residual limit, the relative permeability of water is stabilized at absolute permeability and starts to act as a single phase flow. This nature of relative permeability leads to early breakthrough. The mobility of the water phase is highly activated at low oil saturations, especially around the residual limit and less activated for high oil saturations. Simulation results have given breakthrough points in the cases 01, 02, and 03 respectively. Therefore, it can be concluded that the influence of water relative permeability is affected than the residual saturation for the water breakthrough. The breakthrough time paradox is fully explained by using relative permeability curves and residual oil saturation of the multiphase within the reservoir before the breakthrough.

Accumulated oil volumes are shown in Figure 7 where the oil flow rates are gradually decreased after the water breakthrough. The reduction of oil flow rates after the breakthrough can be highlighted as a common observation in every case. However, the decreasing rates are different for each case. The highest decreasing rate is shown in case 02 and the lowest is shown in case 03. Total flow rate is also reduced after the breakthrough as discussed earlier. Case 01 and 03 have approximately similar dynamic behaviors in total flow rate curves. Therefore, it is easy to investigate and

compare the oil flow behaviors of these two cases after the breakthrough.

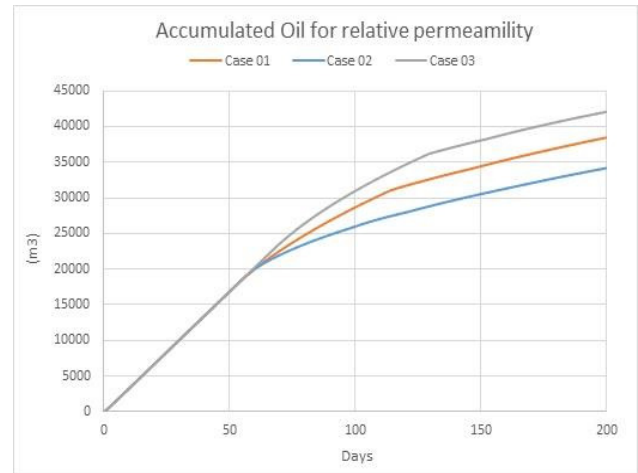


Figure 7. Accumulated Oil profile vs life time.

Gradients of the accumulated oil curves have almost a similar variation and curves are approximately parallel a long after the breakthrough. Accumulated volumes seem to converge to a certain value as shown in Figure 7 and this value is the highest for case 03. Therefore, case 01 produces less oil with the same reservoir size than case 03. Moreover, it can be concluded that the delayed water breakthrough will produce higher oil volume for the same total fluid volume. The oil recovery factor can be upgraded by delaying the water breakthrough.

Even though the residual oil saturation is zero, in case 02, the lowest amount of oil is produced in this case. The observation reveals that lower oil residual reservoirs are not always producing higher oil volumes and the influence of the relative permeability is stronger than the oil residual value in some fields. Result inspections of the oil reservoir saturation profile shows that the narrowest water cone appeared at the earliest breakthrough case for a given well-age.

Table 3. Breakthrough data with different relative permeability.

Case	Water Breakthrough	Liquid Volume at breakthrough (m ³)	Water saturation at well Grid
Case 01	53	18193	0.29
Case 02	55	18688	0.44
Case 03	68	23025	0.26

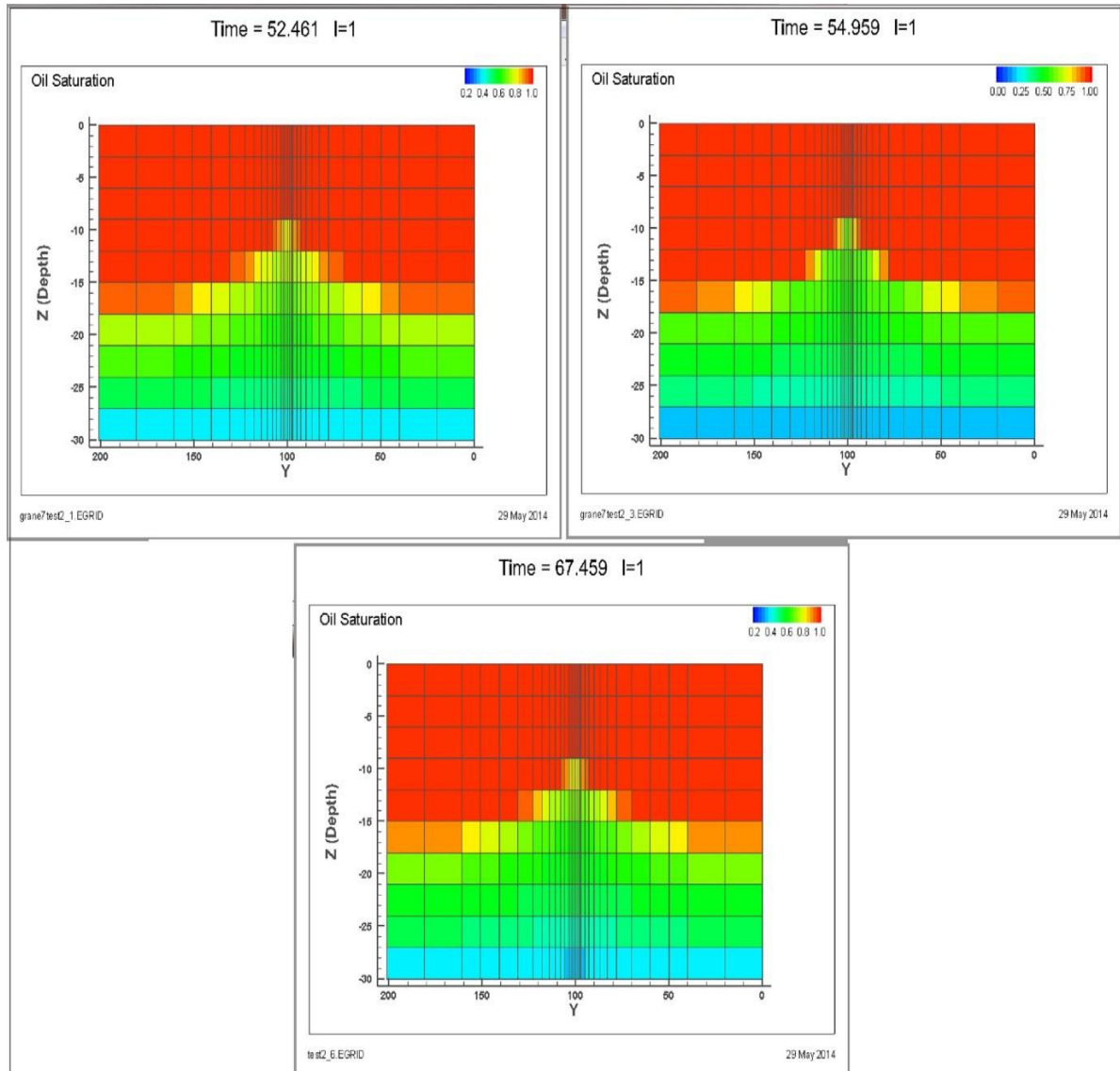


Figure 8. Oil saturation profile closer to breakthrough time (i) case 01(ii) case 02 (iii) case 03.

5 Conclusion

This study was carried out to analyze the oil recovery characteristics in heavy oil reservoirs. A major challenge in oil fields is the decreasing oil production rate with time and the remaining amount of oil after well shutdown. Developing technologies have given some positive results on oil recovery factor. Water flooding and enhanced oil recovery methods are used successfully to increase the recovery. Water breakthrough is a strong challenge faced in heavy oil production and it causes increased water cut during the operation. Multiphase flow demands additional operational cost for separation. On the other hand, if water breakthrough is delayed, higher pure oil volume can be achieved. Therefore, delayed water breakthrough gives lower operational and maintenance costs.

Water breakthrough and multiphase flow strongly depend on relative permeability and the residual oil saturation in the reservoir. In this study, the influence of the relative permeability is investigated using different permeability curves and different residual oil saturations found in literature. The simulation results showed variations of water breakthrough time, accumulated total liquid, accumulated oil and the possible extracted amount of oil in a given reservoir with different permeability curves. Most of the observed behaviors can be explained by multiphase flow. The variation in water breakthrough times is a result of multiphase flow rate within the reservoir before the breakthrough. The influence of relative permeability is critical than the residual oil saturation on water breakthrough time. The results show that the case with minimum residual oil does not give the maximum recovery due to the flow characteristics in the reservoir. The mobility of water is significantly

higher than of viscous oil, and the water can flow towards the well faster than oil from the bottom of the reservoir towards the well. This causes early breakthrough and water can enter to the wellbore even though there is a large amount of oil remaining in the reservoir. Enhanced oil recovery methods can be used to: manipulate the relative permeability, delaying the water breakthrough and obtain better production with high oil quality.

References

A. B. Zolotukhin, J. R. U. Introduction to reservoir engineering. Stavanger 1997.

Logs, E. Oil on my shoes. Disponível em: <
<http://www.geomore.com/porosity-and-permeability-2/>
>. Acesso em: 2014/05/15.

Lokendra Pal, M. K. J., Paul D. Fleming. A Simple method for calculation of the permeability coefficient of porous media. TAPPI, 2006.

P. Zitha, R. F., D. Zornes, K. Brown, and K. Mohanty. Increasing Hydrocarbon Recovery Factors. Society of Petroleum Engineers 2011. Disponível em: <
<http://www.spe.org/industry/docs/recoveryfactors.pdf>
>. Acesso em: 2014/05/20.

Speight, J.; Speight, J. G. Enhanced recovery methods for heavy oil and tar sands. Houston, TX: Gulf Pub. Co. 2009.

Simulation of CO₂ injection in fractured oil reservoir

Nora I. Furuvik¹ Britt M. Halvorsen¹

¹Department of Technology, Telemark University College, Norway,
{Nora.C.I.Furuvik@hit.no,Britt.Halvorsen@hit.no}

Abstract

CO₂-EOR is an attractive method because of its potential to increase the oil production from mature oilfields and at the same time reducing the carbon footprint from industrial sources. CO₂-EOR refers to a technique for injection of supercritical-dense CO₂ into oil reservoirs. Remaining oil from mature oil fields has been successfully produced using CO₂-EOR since early 1970's. The reservoir properties together with fluid properties significantly affect the CO₂-EOR performance. This study focuses on CO₂ injection in carbonate reservoirs including simulations of CO₂-distribution in the rock. Carbonate reservoirs are characterized by low permeability and high heterogeneity causing significant amount of CO₂ to be recycled. The simulations are carried out using commercial reservoir simulation software. Criteria for the performed simulations are a highly heterogeneous carbonate reservoir with fractures. The simulations show that CO₂-injection in combination with closing of fractured zones result in high oil production and good distribution of CO₂ in the reservoir.

Keywords: CO₂ EOR, fractured reservoir, inflow control, near well simulations

1 Introduction

Production of fossil fuels (oil and gas) will be required for many years to meet the high demand of energy worldwide. CO₂-EOR or CO₂-flooding has been widely studied the last 40 years and are already in use in several countries. CO₂-EOR increases oil recovery by injecting CO₂ into the reservoir, either in form of supercritical CO₂ or as carbonated water. CO₂ injection will maintain the pressure, mobilize the oil and release petroleum resources that would otherwise be inaccessible (Jakobsen et al, 2005).

In addition to increased oil recovery, CO₂-EOR has the ability to lower the emission of CO₂ by storing the gas permanently underground after it is utilized. At well-selected storage sites the rock formation are likely to preserve more than 99 % of the injected CO₂ for over 100 years (NETL/DOE, 2010). This is an environmental friendly win-win situation where both oil recovery is increased and the emission of greenhouse gases to the atmosphere is reduced.

The physical properties of the oil reservoir rock (porosity, permeability) determine the effectiveness of the CO₂ injection for the EOR-storage process. Reservoir properties affect the field response to the CO₂-storage process, including oil production rate, CO₂ utilization factor and CO₂ recycle ratio. (Ettehadtavakkol, 2014). This study focuses on CO₂ injection in carbonate reservoirs including simulations of CO₂ distribution in the porous rock. Carbonate reservoirs are characterized by low permeability and high heterogeneity causing significant amount of CO₂ to be recycled. The simulations are carried out using commercial reservoir simulation software. Criteria for the performed simulations are a carbonate reservoir with fractures. The oil production performance from a carbonate reservoir is nearly half the production from sandstone, whereas the CO₂ utilization is about 60% less.

2 Oil recovery

Oil recovery refers to the extraction process of liquid hydrocarbons from beneath the Earth's surface. The extraction process occurs in three different phases; primary, secondary and tertiary oil recovery phase. These three different ways of oil production is illustrated in Figure 1 (China Oilfield Technology, 2013). In the primary phase of oil production, the drive mechanism for oil extraction is the pressure difference between the oil reservoir and the production well. The oil reservoir covers an extended area, thus the reservoir pressure slowly will decline over time. The main pressure drop is located near the production well. Injection of pressurized gas and/or water into the reservoir will rebuild the reservoir pressure and sweep more oil towards the production wells. This recovery phase is known as secondary oil recovery phase or water flooding. After primary and secondary oil recovery phases, there are still significant amounts of oil remained trapped in the reservoir. (Kulkarni, 2003) The remaining oil reserves are trapped in the reservoir pores, and can no longer be forced to migrate toward the production well by water flooding. As oil saturation in the reservoir declines, more oil reserves are trapped by capillary forces or in dead-end pores, resulting in decreased mobility of the remaining oil. (Hill *et al* 2013; Ahmed, 2013; Kulkarni, 2003) At this point, a tertiary phase of oil production can be considered.

Tertiary enhanced oil recovery (EOR) involves techniques for injection of steam (thermal recovery), chemicals (chemical flooding) or miscible gasses

(miscible displacement) to improve the properties of the remaining oil in order to make it flow more freely within the reservoir. (Hill *et al* 2013; Ahmed, 2013)

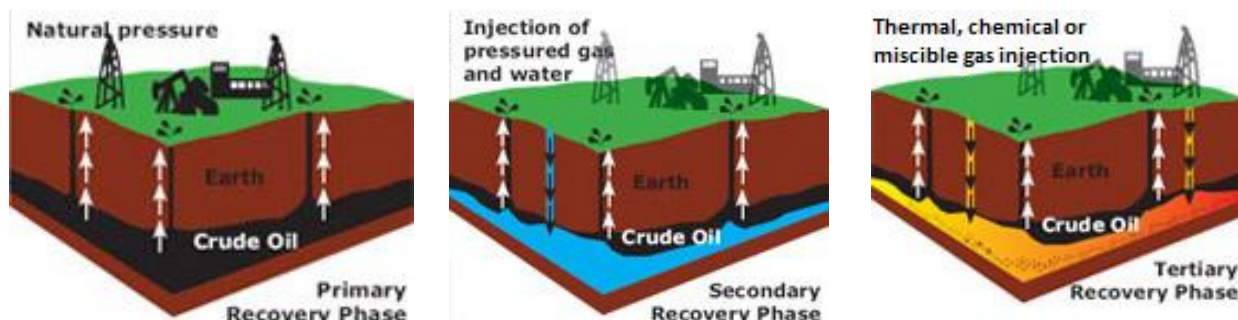


Figure 1. Primary, secondary and tertiary oil production. (China Oilfield Technology, 2013)

The oil viscosity is reduced dramatically with dissolving CO₂ in oil so that the oil flows more freely within the reservoir. When CO₂ comes into contact with crude oil a process of dissolution occurs thereby causing swelling of the oil. This results in expansion in oil volume which means that some fluid has to migrate. The degree of swelling depends on pressure, temperature, hydrocarbon composition and physical properties of the oil. (Pasala, 2010; Melzer 2012; Hill, 2013; Ghoojani, 2011)

Use of supercritical CO₂ for EOR increases oil supply by mobilizing residual oil trapped in inaccessible void spaces. CO₂-EOR also contributes to minimize the impact of greenhouse gas emission by keeping CO₂ out of the atmosphere, as much of the CO₂ is exchanged for the displaced oil and water in the pores, and remains trapped in the deep rock formations (NRG Energy Inc., 2014)

3 Petrophysics

Petrophysics is the study of porous geologic material, its physical properties and its interactions with fluids (gases, liquid hydrocarbons and aqueous solutions). (Tiab *et al*, 2012). Since hydrocarbons are light in density compared to water, the hydrocarbons start to migrate in a porous rock containing water. The hydrocarbons move through fault and fractures in the source rock until they are trapped in a reservoir rock. The reservoir rock is overlain by a seal rock, an impermeable rock layer that does not allow fluids to flow through. The oil and gas accumulates in a trap forming a hydrocarbon reservoir. If there is no such trap along the migration route, the oil and gas will continue their migration out to the surface of the Earth. (Oljeindustriens Landsforening). Accumulation of hydrocarbons in such traps is usually found in coarse-grained, permeable and porous sedimentary rocks. Since the pores most often are water-saturated, the migration of hydrocarbons takes

place in an aqueous environment. Oil, gas and water will separate according to the density difference once they are caught in the trap. This is illustrated in Figure 2. (Hyne, 2001; Selley, 1998)

Gas accumulates in the highest portion of the trap, forming a free gas cap. Because the specific gravity of the water is considerable higher than oil, the oil floats on the surface of the water and accumulates in the middle of the trap, forming the oil reservoir. Salt water goes to the bottom. However, due to void spaces and tiny openings in the rocks, capillary forces resist complete gravitational segregation of the fluid phases. Water is therefore found in small amounts in all zones of the reservoir. (Hyne, 2001; Marshak, 2001; Selley, 1998)

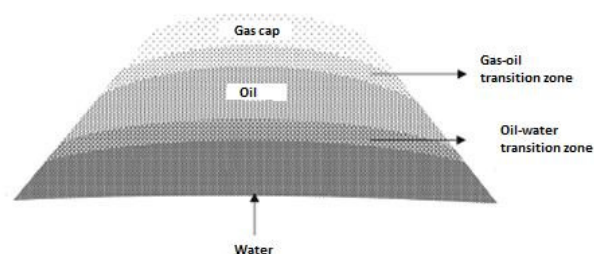


Figure 2. Cross section of a reservoir showing vertical segregation of fluids. (Dandekar, 2013)

3.1 Porosity

A reservoir rock is porous and permeable. For a rock to act as a reservoir it must have pores to store fluids and the pores must be connected to allow transmission of the fluids. Since reservoir rocks are composed of mineral grains and crystals, their properties depend upon the property of the minerals. These properties are highly affected by the reservoir physics, including saturation, relative permeability and porosity. In addition, rock properties also depend on the temperature and pressure, and the type and amount of

contained fluids (oil, gas or water). (Khudaida, et al, 2012).

A porous rock consists of mineral grains and small spaces in between the mineral grains, called void space or pores. Porosity of a rock represents the measure of the void space within the porous rock. Almost all porous material have three basic types of pores; catenary, cul-de-sac and closed pores (Shelley, 1998). A presentation of the three types of pores is given in Figur 3.

Catenary pores include pores connected to other pores with more than one pore channel, Cul-de-sac pores (dead-end pores) are the pores that only connects to other pores through one pore channel. While closed pores include pores that have no connection to other pores at all and are completely isolated from the pore network.

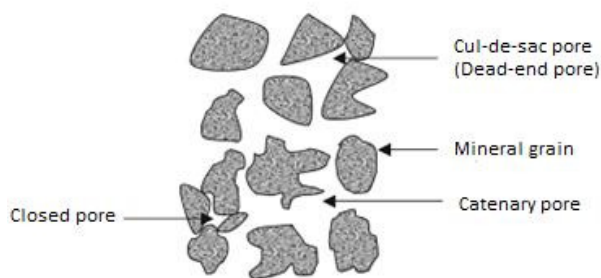


Figure 3. Three basic types of pores. (Dandekar, 2013)

Absolute porosity encompasses all the void spaces, including interconnected pores as well as pores that are sealed off. Absolute porosity is defined as the ratio of the total pore volume (Catenary pores, Dead-end pores and Closed pores) to the bulk volume of the porous rock:

$$\phi_a = \frac{\text{Total pore volume}}{\text{Total or bulk volume}} \quad (1)$$

Effective porosity (ϕ) is the proportion of void spaces that excludes the completely disconnected pores (Closed pores). Effective porosity is defined as the ratio of the void volume of interconnected pores (Catenary pores and Dead-end pores) to the bulk volume of the porous rock:

$$\phi = \frac{\text{Void volume of interconnected pores}}{\text{Total or bulk volume}} \quad (2)$$

Thus, effective porosity measures the void volume that is interconnected to the surface. Even if dead-end pores cannot be flushed out, they can still produce oil by pressure depletion or gas expansion. (Khudaida et al, 2012; Tiab et al, 2012; Hyne, 2001; Shelley, 1998; Dandekar, 2013)

3.2 Saturation

The void spaces within a reservoir rock are always completely saturated by fluids. However, all available

pores are not occupied by hydrocarbon fluids; a certain amount of residual formation water cannot be displaced and is always present in the reservoir. The relative amount of each fluid present in the pores is called saturation. In a hydrocarbon reservoir, oil, gas and water fill a fraction of the total pore volume of the rock (V_{total}):

$$V_{total} = V_{oil} + V_{gas} + V_{water} \quad (3)$$

Fluid saturation is defined as the ratio of the volume occupied by oil, gas or water to total pore volume, which gives following equation for oil saturation (S_{oil}):

$$S_{oil} = \frac{\text{Volume of oil in the reservoir rock}}{\text{Total pore volume of the rock}} \quad (4)$$

Similar expressions can be written for gas saturation (S_{gas}) and water saturation (S_{water}).

The endpoint saturations for each fluid phase are of special interest. The most frequently endpoint saturations are irreducible water saturation, residual oil saturation and critical gas- and condensate saturations. The irreducible water saturation defines the maximum water saturation that can retain without producing water. Residual oil saturation is the remaining oil in the reservoir rock at the end of an extraction process or a specific recovery process. (Ahmed, 2012; Tiab et al, 2012; Hyne, 2001; Kvinge, 2012)

3.3 Wettability

Wettability is the tendency for a fluid to spread or adhere to a solid surface in the presence of other immiscible fluids. Wettability has an impact on the capillary forces, relative permeability, irreducible water saturation, residual oil saturation and the interfacial tension. (HIS Energy; Schlumberger, 2007; Ahmed, 2013). Wettability is related to the rock-fluid interactions, thus it is determined by the interaction between the fluids and the rock surface. When two phases are present in a reservoir rock, interfacial tensions exist. For the two immiscible coexisting fluids, the one with lowest interfacial tension is the wetting phase. Interfacial tension relates to the fluid-fluid interactions, and is a measure of the force that holds the surfaces of the two immiscible fluids together. Low rock-fluid interfacial tension means low surface energy and high tendency for the fluid to wet a surface. (Ahmed, 2013).

3.4 Permeability

In addition to being porous, a reservoir rock must have the ability to transmit fluids through its interconnected pores. This rock property is termed permeability, and in Figure 4 it is seen how interconnected pores can give high rock permeability.

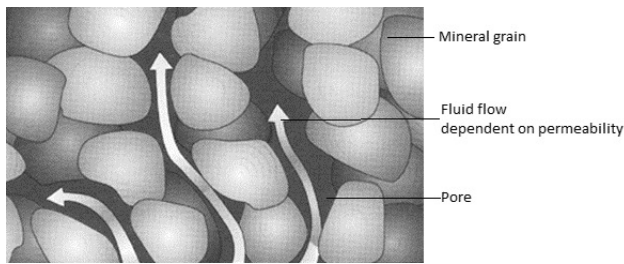


Figure 4. Illustration of a reservoir rocks permeability. (Rocky Mountain Carbon Capture and Sequestration)

Permeability is a measure of how easy a fluid can flow through a porous rock. Permeability is usually expressed in millidarcys (mD). In a 1-dimensional, linear flow, the steady-state flow is calculated according to Darcy's law:

$$Q = A \frac{K \Delta p}{\mu dx} \quad (5)$$

where K is the permeability of the porous rock [D], Q is the volumetric flow rate [cm³/s], A is the cross-sectional area of the core sample [cm²], μ is the viscosity of the fluid [cP], x is the length [cm] and $\frac{dp}{dx}$ is the pressure drop of the core sample [atm/cm].

Absolute permeability defines K when the pores within a reservoir are saturated with one single fluid phase (oil, gas or water). Absolute permeability of a given porous material is a rock property and is independent of the type of fluid.

Effective permeability describes the permeability of each fluid when more than one fluid is present in the reservoir. In a multi-phase system, the permeability highly depends on the relative saturation of each fluid. During the movement through the rock, each fluid will interfere with the other fluids due to capillary forces. These interactions lead to reduction in the flow rate of the each individual phase. Consequently, the effective permeability for each fluid will be lower than the absolute permeability. Multi-phase flow leads to a modification of Darcy's law, by introducing effective permeability instead of absolute permeability:

$$Q_i = A \frac{K_i dp_i}{\mu_i dx} \quad (6)$$

In which i refers to each of the specific fluid phase.

Relative permeability is the ratio of the effective permeability of a particular fluid phase to the absolute permeability, and is given by:

$$K_{rel,i} = \frac{K_i}{K} \quad (7)$$

where $K_{rel,i}$ refers to the relative permeability of the specific fluid phase i . Relative permeability is a dimensionless function. The relative permeability curves in water-wetted and oil-wetted rock are presented in Figure 5 and Figure 6 respectively. S_{orw} represents the residual oil saturation and S_{wc} represents

the irreducible water saturation. The plots show that the wettability has significant impact on the shape of the relative permeability curves. The relative permeability curve of the non-wetting fluid has an s-shape, while the relative permeability curve of the wetting fluid is concave upwards.

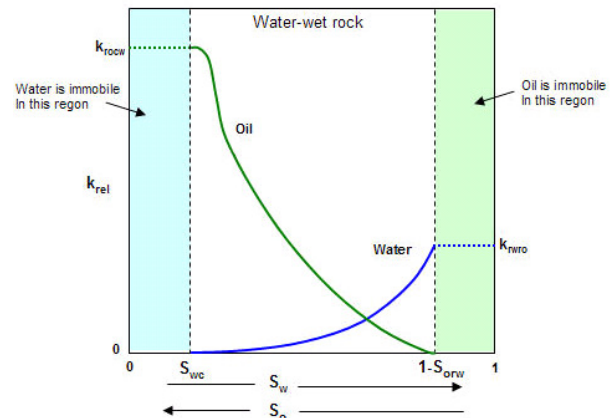


Figure 5. Relative permeability for oil and water in water-wetted rock.

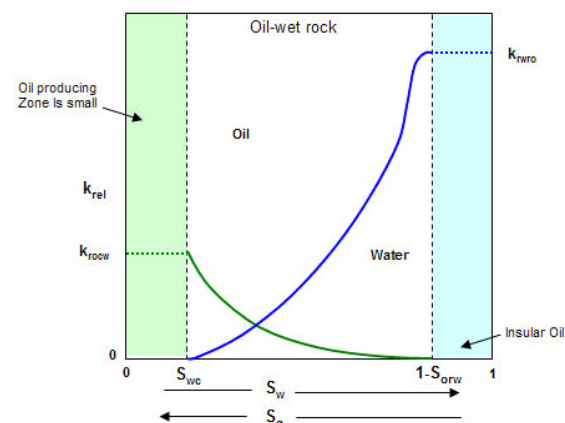


Figure 6. Relative permeability for oil and water in oil-wetted rock.

3.5 CO₂-EOR

Sedimentary rocks are classified by factors like, grain size, sorting, sphericity and porosity. Most oil and gas accumulation have been found in clastic and carbonate reservoirs. The reservoir properties (permeability and heterogeneity in these examples) significantly affect the EOR performance. The low permeability and high heterogeneity of carbonate causes the oil production performance to be small and the CO₂ utilization to be large, compared to sandstone.

CO₂ is usually not miscible on the first contact with the reservoir oil. However, at sufficiently high pressures, CO₂ achieves miscibility with oil for a broad spectrum of reservoirs. Under favorable conditions, the gas will vaporize the low to medium fractions of the reservoir crude. After multiple contacts between the oil and carbon dioxide, a bank of light hydrocarbons and CO₂ will form, and this mixture promotes miscibility

between the CO₂ and the remaining crude oil. Complete miscibility between the oil and CO₂ or hydrocarbon solvents, eliminates interfacial tension and capillary forces and helps to recover, in theory, all of the residual oil. (Pasala, 2010) Supercritical CO₂ is considerably denser than the gaseous CO₂ phase but has lower density and viscosity than the occupant brine saline water in the porous space. As a result of the differences of fluid densities, supercritical CO₂ migrates buoyantly towards the upper confining layer. The preferred depths to inject CO₂ are greater than 800 m (NRG Energy Inc., Texas, 2014) as they provide the required conditions above the critical points of CO₂ for it to stay in supercritical phase. (NRG Energy Inc., Texas, 2014) CO₂ affects the oil and rock by reducing the interfacial tension, reducing the oil viscosity, swelling the oil and by having an acid effect on rock.

4 Simulations

The simulations are carried out using commercial reservoir simulation software, Rocx in combination with OLGA. The OLGA software is the main program, but several additional modules are developed to solve specific cases.

Criteria for the performed simulations are a highly heterogeneous carbonate reservoir with fractures.

4.1 Rocx

Rocx contains detailed information about the geometry of the reservoir. Input parameters to Rocx are reservoir and fluid properties like permeability, porosity, viscosity, initial and boundary conditions. Figure 7 shows the grid and geometry of the simulated reservoir section at initial conditions.

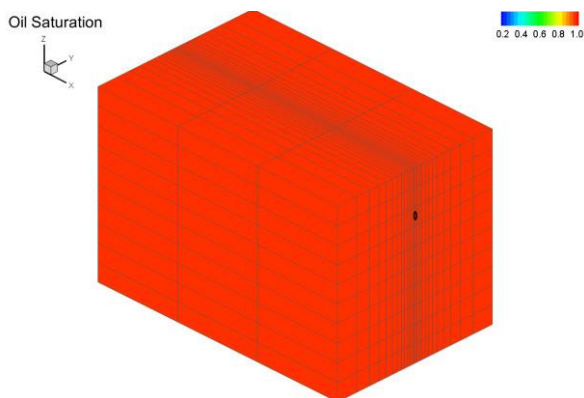


Figure 7. Grid and geometry of the simulated reservoir section.

The geometry of the simulated reservoir is 150 m in length, 106 m in width and 100 m in depth. 3 grid blocks are defined in x-direction, 25 in y-direction and 10 in z-direction. The well is located 70 m from the bottom, as indicated as a black dot in Figure 7. The

radius of the wellbore is 0.15 m. The reservoir is divided into three zones in x-direction, where the mid-zone (second zone) represents the fractured part. Thus the permeability is set much higher in this zone compared to the two other zones. The reservoir and fluid properties for this specific case are presented in Table 1.

Table 1. Reservoir and fluid properties.

Properties	Value
Oil viscosity	10 cP
Reservoir pressure	176 bar
Temperature	76°C
Gas oil ratio (GOR)	16 Sm ³ /Sm ³
Natural gas specific gravity	0.64
Oil specific gravity	0.8
Porosity	0.3
Permeability first zone	100-200 mD
Permeability second zone	10000-20000 mD
Permeability third zone	100-200 mD
Wellbore pressure	136 bar

Data for relative permeability are set manually in table form in Rocx. Oil-wet reservoir is considered in these simulations, and Figure 8 shows the implemented relative permeability curves for oil and water.

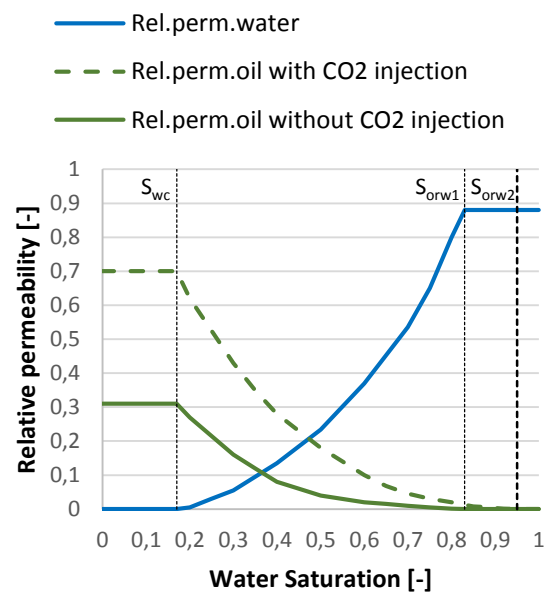


Figure 8. Relative permeability curves in oil-wet carbonate reservoir.

The vertical lines represent the residual oil saturation (S_{orw1} and S_{orw2}) and the irreducible water saturation (S_{wc}). The green lines indicate the relative permeability of oil for two different simulation cases, one where CO₂ is injected to the reservoir (green dotted line) and one without CO₂-injection (green solid line).

The module Rocx is connected to OLGA by the nearwell source, which allows importing the file created by Rocx. In order to get a simulation of a complex fluid flow, OLGA requires both a flowpath and a pipeline. In reality they are the same, but in the simulations the flowpath represents the wellbore and the pipeline represents the annulus. In Figure 9 the

sources implemented in the pipeline indicate the inflow from the reservoir into the annulus. The flow from annulus goes through the valves A, B and C and into the wellbore via the leaks. The valves 1, 2 and 3 are simulate packers and are closed during the simulations. Packers are installed to isolate the different production zones in the well.

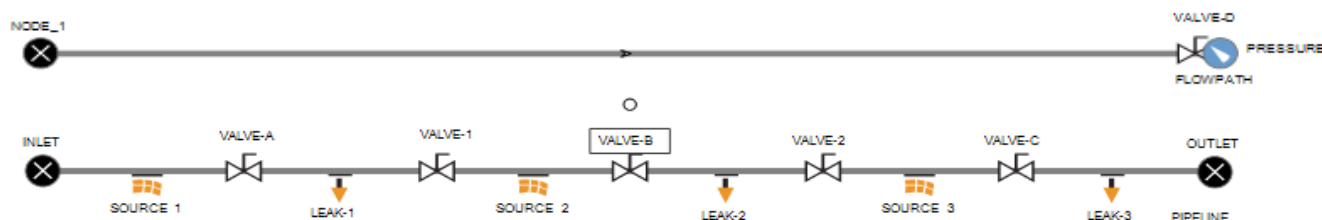


Figure 9. OLGA Study case.

Three different cases (Case 1, 2 and 3) are simulated. The input for simulation in Rocx and OLGA is listed in Table 2. All three cases include the reservoir and fluid properties detailed in Table 1. Case 1 includes the oil relative permeability curve shown as a green solid line in Figure 8. All the valves A, B and C are fully open during the simulation. Case 2 includes the same oil relative permeability curves as for Case 1, but with valve B nearly closed.

In Case 3, CO₂ is injected to the reservoir by assuming that the oil relative permeability curve is significantly changed due to the influence on CO₂ on the fluid properties. The oil relative permeability curve implemented for Case 3 is seen as a green dotted line in Figure 8. Valve B is kept in the same position as for Case 2. The water permeability curve is the same for the three cases and is seen as the blue line in Figure 8. All simulations were run for 300 to 400 days.

Table 2. Input for simulation case 1, 2 and 3.

Simulation Case	Data input to Rocx	Relative permeability curve	CO ₂ injection to reservoir	Position Valve A and C	Position Valve B	Simulation time
Case 1	See table 1	See Figure 8	No	Open	Open	400 days
Case 2	See table 1	See Figure 8	No	Open	Nearly closed	312 days
Case 3	See table 1	See Figure 8	Yes	Open	Nearly closed	366 days

Fractures in the reservoir are a major problem in oil fields using CO₂-EOR. The consequence is that the injected CO₂ moves through the fractures and directly to the production well without getting distributed in the reservoir. The CO₂ is reproduced and will not have any affection on the oil recovery. The fracture in the reservoir is specified as the high permeability zone (second production zone).

The oil industry focuses on developing improved technology for automatically closing down production from water and gas producing zones.

In this study, Case 2 and Case 3 are simulated with the valve placed in the second production zone (Valve B) nearly closed. OLGA does not allow the valve to be completely closed and therefore a negligible opening is used. In the simulation with Case 1 valve B is fully open.

5 Results

For each case the accumulated volume of oil and water are studied and compared. Figure 10 and Figure 11 show the accumulated volume production as a function of time for oil and water respectively. In Case 1 there are no restrictions for the fluid flow. This results in high production flow of oil and water, mainly through the fractures. Due to the high production rate, the water breakthrough occurs after only 22 days. In Case 2 the high permeability zone is choked, giving low oil production and late water breakthrough (after 260 days). The oil permeability curve in Case 3 is changed to account for the effect of CO₂ injection to the reservoir. Valve B is kept nearly closed, as in Case 2. The accumulated volume of oil increases significantly compared to Case 2, whereas the water breakthrough occurs apparently at the same time.

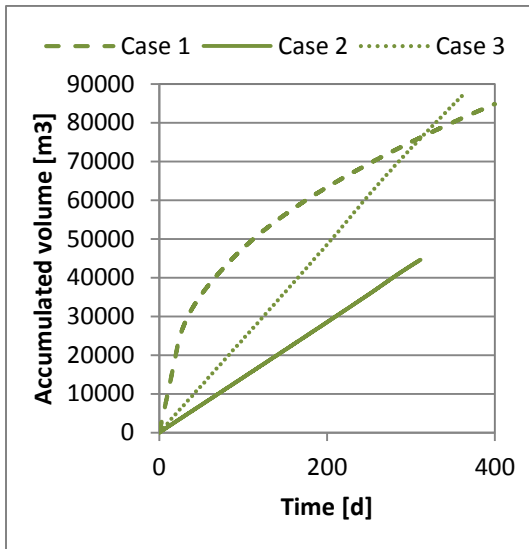


Figure 10. Accumulated volume of oil.

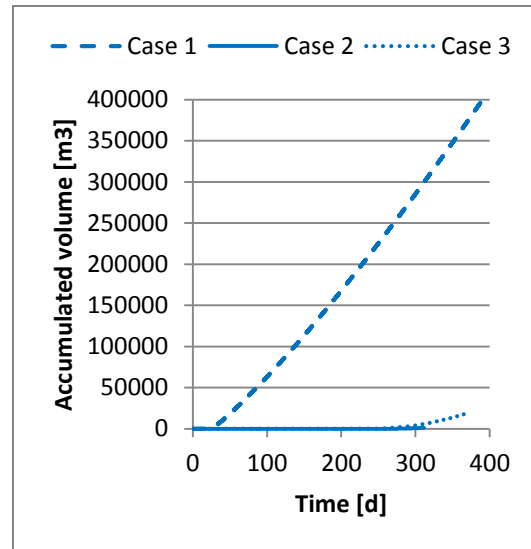


Figure 11. Accumulated volume of water.

In Table 3 the time for water breakthrough in the three different production zones are presented together with the water cut after 310 days of production.

Table 3. Water breakthrough and water cut.

Simulation Case	Water breakthrough in production zone 2[d]	Water breakthrough in production zone 1 and 3[d]	Water cut after 310 days [-]
Case 1	22	98	0,8325
Case 2	260	280	0,2378
Case 3	235	240	0,3962

The water cut is defined as the water volume flow divided by the total liquid flow.

From Table 3 it is seen that after 310 days the water cut are 0.8235 for Case 1, 0.2378 for Case 2 and 0.3962 for case 3. A graphical output of the water cut during the whole simulation is shown in figure 12.

The plots in Figure 12 displays that Case 1 has a high water cut compared to the other cases. This is not economically favorable due to high separation costs and need of very large separation units.

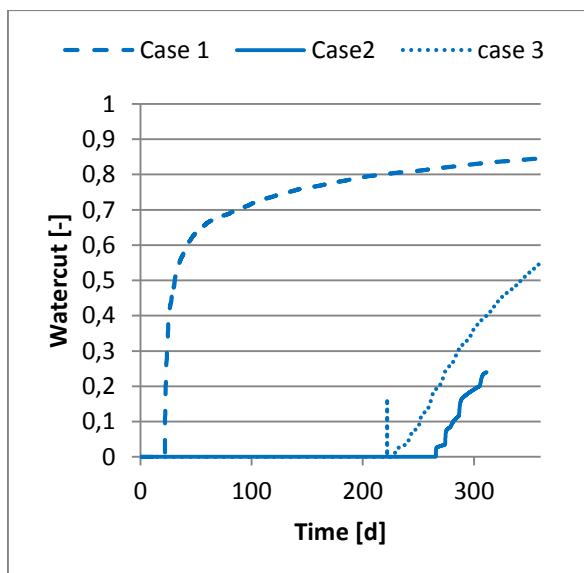


Figure 12. Graphical output of the water cut.

Figure 13 and Figure 14 shows the distribution of water and carbonated water in the reservoir for Case 2 and Case 3 respectively. In Case 3 it is assumed that CO₂ is injected in the water phase, and therefore this water phase is represented as carbonated water. The plots represent the saturation of oil after 312 days of production. As expected, the distribution of water/carbonated water disperses from the high permeable zones to the low permeable neighbor zones in both cases. Case 3 shows high distribution of water in the reservoir compared to Case 2. This is due to injection of CO₂. CO₂ mixes with the oil, making it less viscous and more mobile. The simulations indicate clearly that CO₂ injection in combination with closing of fractured zones result in high oil production and good distribution of CO₂ in the reservoir.

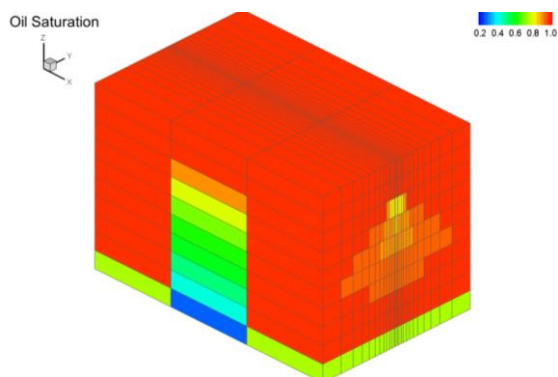


Figure 13. Saturation of oil Case 2 at 312 days.

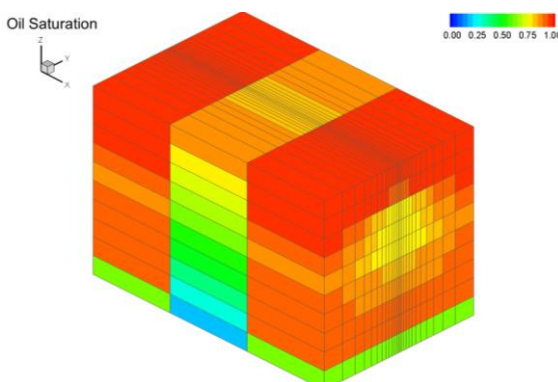


Figure 13. Saturation of oil Case 3 at 312 days.

6 Conclusion

CO₂-EOR is an attractive method because of its potential to increase the oil production from mature oilfields and at the same time reducing the carbon footprint from industrial sources. CO₂-EOR refers to a technique for injection of supercritical-dense CO₂ into an oil reservoir. Remaining oil from mature oil fields has been successfully produced using CO₂-EOR since early 1970's. The reservoir properties (porosity, permeability) together with fluid properties significantly affect the CO₂-EOR performance. This study focuses on CO₂ injection in carbonate reservoirs including simulations of CO₂-distribution in the rock. Carbonate reservoirs are characterized by low permeability and high heterogeneity causing significant amount of CO₂ to be recycled. The simulations are carried out using commercial reservoir simulation software. Criteria for the performed simulations are a highly heterogeneous carbonate reservoir with fractures. The simulations indicate clearly that CO₂ injection in combination with closing of fractured zones result in high oil production and good distribution of CO₂ in the reservoir.

References

Kamal Ahmed, CO₂ injeksjon for økt oljeutvinning i kalk, *Masteroppgave, Institutt for fysikk og teknologi*, Universitet i Bergen, 2013.

China Oilfield Technology, Annual report 2013, Available from: <http://www.chinaoilfieldtech.com/oilrecovery.html>

Glenn-Andre Dåtland Kvinge, En eksperimentell studie av CO₂ lagring i sandstein og kalkstein med bruk av ulike avbildningsteknikker, *Masteroppgave, Institutt for Fysikk og teknologi, Universitet i Bergen*, 2012.

Amin Etehadtavakkol, Larry W. Lake and Steven L. Bryant, CO₂-EOR and storage design optimization, *International Journal of Greenhouse Gas Control*, Vol. 25: p. 79-92, June 2014.

E. Ghoojani and S.H. Bolouri, Experimental study and calculation of CO₂-oil relative permeability, *Petroleum & Coal*, ISSN 1337-7027, 53-(2) : p. 123-131, Sharif University of Technology, Shahid Bahonar University, Kerman, Iran, 2011.

Bruce Hill, Susan Hovorka and Steve Melzer, Geologic carbon storage through enhanced oil recovery, *Energy Procedia*, vol. 37: p. 6808-6830, Elsevier Ltd., USA, 2013

HIS Energy, Available from: http://www.fekete.com/SAN/WebHelp/FeketeHarmony/Harmony_WebHelp/Content/HTML_Files/Reference_Material/General_Concepts/Relative_Permeability.htm.

Norman J. Hyne, Ph.D., Nontechnical Guide to Petroleum Geology, Exploration, Drilling and Production, *Penn Well Corporation*, Second edition, ISBN: 0-87814-823-X, USA, 2001.

Viktor E. Jakobsen, F.H., Marius Holm, Beate Kristiansen, BELLONA, *CO₂ for EOR on the Norwegian shelf -A case study*. 2005: p. 108.

Kamal Jawher Khudaida and Diganta Bhusan Das, A numerical study of capillary pressure-saturation relationship for supercritical carbon dioxide (CO₂) injection in deep saline aquifer, *Chemical Engineering research and Design*, Volume 92, Issue 12: p. 3017-3030, Desember 2012.

Madhav M. Kulkarni, Immiscible and miscible gas-oil displacements in porous media, *Master thesis, Graduate Faculty of the Louisiana State University and Agricultural and Mechanical College*, India, 2003.

Stephen L. Melzer, Carbon Dioxide Enhanced Oil Recovery (CO₂EOR): Factors Involved in Adding Carbon Capture, Utilization and Storage (CCUS) to Enhanced Oil Recovery, *CO₂ Consultants and Annual CO₂ Flooding Conference Director*, Midland,Tx, February 2012

NETL/DOE, *Carbon Dioxide Enhanced Oil Recovery - Untapped Domestic Energy Supply and Long Term Carbon Storage Solution*. 2010.

NRG Fact Sheet, CO₂ Enhanced Oil Recovery, *NRG Energy Inc.*, Texas, 2014, Available from: <http://www.nrgenergy.com>

Oljeindustriens Landsforening, Innføring i Geologi, Faktahefte for Utdanning til olje og gassindustrien, Available from:

<http://www.utog.no/postmann/dbase/bilder/geologihefte-web.pdf>

Sangeeta M. Pasala, CO₂ displacement mechanisms: Phase equilibria effects and Carbon dioxide sequestration studies, *PhD, Department of Chemical Engineering, The University of Utah*, December 2010.

Richard C. Selley, *Elements of Petroleum Geology*, *Academic Press California*, second edition, ISBN: 0-12-636370-6 USA, 1998.

Rocky Mountain Carbon Capture and Sequestration, available from:

<http://rmccs.org/sitecharacterization/experimental3.html>

Schlumberger, Fundamentals of Wettability, *Oilfield Review*, Volume 19, Number 2: p. 66-71, summer 2007.

Djebbar Tiab and Erle C. Donaldson, *Petrophysics, Theory and Practice of Measuring Reservoir Rock and Fluid Transport Properties*, *Gulf Professional Publishing*, Third edition, ISBN: 978-0-12-383848-3, USA, 2012.

Derivation of Arc Length of Helical Cable Element at Cable Bending, with Emphasize on Taylor Series Expansion of the Non-Integrable Infinitesimal Arc Length

Magnus Komperød¹

¹Technological Analyses Centre, Nexans Norway AS, Norway, magnus.komperod@nexans.com

Abstract

Elements of subsea cables and umbilicals can be classified as helical and non-helical. These two element types behave very differently at cable bending. This paper focuses on helical cable elements during cable bending. The arc length of helical elements at cable bending is derived, which leads to an integral that can not be solved analytically. When establishing strains and stresses of helical elements, it is essential that this integral is calculated with very high accuracy. An integration error of 0.01% is unacceptable in many applications. Maclaurin series expansion is used to convert this integral into an integral that can be solved analytically. It is proved that arbitrary integration accuracy can be achieved by increasing the order of the Maclaurin polynomial. Expressions for upper and lower boundaries of the integration error are also provided. The main advantage of the integration approach derived in this paper is that it provides an analytical expression for the integral, which can be used in mechanical analyses of cables and umbilicals.

Keywords: Analytical Integration; Cross Section Analysis; Helical Cable Element; Maclaurin Series Expansion; Offshore Technology; Subsea Cable; Taylor's Theorem; Umbilical.

1 Introduction

Subsea power cables are essential for overseas power transmission, while umbilicals are necessary for offshore oil and gas production. Umbilicals are cable-like structures that consist of different types of elements, such as tubes for hydraulic equipment and transportation of fluids, electric and fiber optic signal cables, and electric power phases for energizing subsea units.

The elements of subsea cables and umbilicals can be categorized as helical elements and non-helical elements. Non-helical elements are parallel to the cable's length direction. Common non-helical elements are the cable's outer sheath and possible center tube or center profile.

Helical elements form helices which helix centers are

equivalent to the cable's cross section center. Helical elements are typically power phases, tubes, electric and fiber optic signal cables, as well as armor wires. Figure 1 shows an umbilical with a non-helical center tube, two layers of helical tubes, and one layer consisting of helical tubes, helical electric signal cables, and a helical fiber optic signal cable. The umbilical also has four layers of helical steel armor wires. The yellow outer sheath is non-helical.

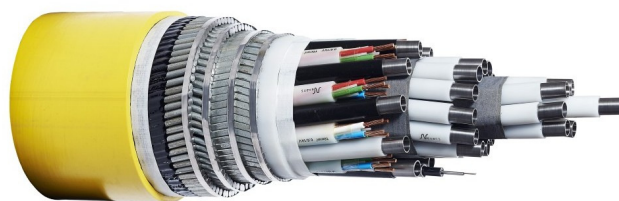


Figure 1. Umbilical with helical tubes, helical electric and fiber optic signal cables, and helical armor wires.

Many cable elements, in particular metallic elements, have mechanical capacity criteria that are not to be exceeded during cable handling, installation, and operation. For metallic elements, these criteria are typically a certain percentage of the elements' respective yield limits. In terms of not exceeding the capacity criteria, helical elements behave more favorably during cable bending than non-helical elements. During cable bending, non-helical cable elements are inherently tensioned at the outer arc and compressed at the inner arc. Helical cable elements can slide inside the cable in such a way that the element's tension at the cable's outer arc are canceled by the element's compression at the cable's inner arc, only limited by possible shear forces, such as friction.

Modeling of helical elements during bending of cables and similar structures are covered in the literature. For example Féret and Bournazel (1987), Kebabze (2000), Sødahl et al. (2010), and Skeie et al. (2012) discuss bending

of cables and similar structures not constrained by end effects. Sævik (1992) and Komperød et al. (2015) discuss bending of cable segments that are confined by end terminations, while Lutchansky (1969) considers stresses in helical elements close to cable clamps.

Strains and stresses of helical elements are essential for modeling the mechanical properties of cables, such as axial stiffness, bending stiffness, torsion stiffness, and capacity (allowed combinations of axial cable tension and cable bending curvature). To obtain correct values for strains and stresses, it is essential to calculate the arc length of the helical elements with very high accuracy. A length error of 0.01% is unacceptable in many cases.

How to calculate the arc length of helical elements in bent cables is derived in the literature, see for example Lutchansky (1969) and Komperød et al. (2015). These derivations lead to an integral that can not be solved analytically. The contribution of the present paper is to use Maclaurin series expansion to rewrite this integral into integrals that can be solved analytically. Sævik (1992) points out that using too few terms of the Maclaurin series may lead to inaccurate results.

The present paper proves mathematically that arbitrary accuracy of the integral can be achieved by increasing the order of the Maclaurin polynomial. It is also derived expressions for upper and lower boundaries that the true element length is ensured to be within. These boundaries narrow as the polynomial order increases. Finally, the proposed method is demonstrated through a numerical example. In the example, the Maclaurin approach is compared to numeric integration using Simpson's method. The latter method also serves the purpose of verifying the former method. The main advantage of the Maclaurin approach, compared to Simpson's method, is that the Maclaurin approach provides an analytical expression for the integral, which can be used in mechanical analyses of cables and umbilicals.

2 Nomenclature

Table 1 presents the nomenclature used in this paper.

3 Assumptions and Simplifications

The mathematical derivation of this paper is subject to the follow assumptions and simplifications:

1. The helical cable elements are assumed to follow loxodromic curves at cable bending. This means that if a helical element slips the beneath surface, it slips parallel to its tangent vector.

The loxodromic approach is one of three common approaches in the literature. Another approach is to assume the helical elements to follow a geodesic

Table 1. Nomenclature.

c	Variable defined in Eq. 13 [-].
k	Exponent [-].
L	Pitch length [m].
l	Cable length [m].
N	Order of Maclaurin polynomial [-].
$P_N(x)$	Maclaurin polynomial of order N [-].
$Q_N(x)$	Reminder of Maclaurin polynomial of order N [-].
$Q_N^{\text{lower}}(x)$	Lower boundary of $Q_N(x)$ [-].
$Q_N^{\text{upper}}(x)$	Upper boundary of $Q_N(x)$ [-].
$\bar{Q}_N(x)$	Variable defined in Eq. 23 [-].
$\bar{Q}_N^{\text{max}}(x)$	Maximum value of $\bar{Q}_N(x)$ [-].
R	Pitch radius [m].
s	Length of helical cable element [m].
$s(\theta_1, \theta_2)$	Length of helical cable element from θ_1 to θ_2 [m].
s_a	Axial component of s [m].
s_h	Circumference component of s [m].
x	Variable defined in Eq. 8 [-].
x^{min}	Minimum value of x on interval $[\theta_1, \theta_2]$ [-].
x^{max}	Maximum value of x on interval $[\theta_1, \theta_2]$ [-].
\bar{x}	Variable defined in Eq. 20 [-].
α	Pitch angle [rad].
θ	Angle in cable's cross section [rad].
θ_1	Lower integration limit [rad].
θ_2	Upper integration limit [rad].
κ	Cable bending curvature [m^{-1}].

curve during cable bending. In the geodesic approach, the helical element slips both parallel and perpendicular to its tangent vector. The third approach is to assume the helical elements to follow a curve that is between the loxodromic curve and the geodesic curve. Please refer to Sævik (1992) for an explanation of loxodromic curves and geodesic curves at cable bending.

2. Displacements of helical cable elements in the cable's radial direction are neglected.
3. The cable is assumed not to twist around its length axis.
4. The cable's path is assumed to have zero torsion, i.e. the cable is assumed to be bent in a two-dimensional plane, not a three-dimensional room.

5. The curvature, κ , may be a constant, or it may be a function of θ , i.e. $\kappa = \kappa(\theta)$. In the latter case, the function $\kappa(\theta)$ must be on a form such that x^n is analytically integrable, where x is defined in Eq. 8 and n is a nonnegative integer.

4 Derivation of the Infinitesimal Arc Length

This section derives the infinitesimal arc length of a helical element in a bent cable. The derivation is strongly inspired by Komperød et al. (2015). Lutchansky (1969) presents a somewhat different derivation, which yields identical result. The derivation of Lutchansky (1969) is longer and somewhat more complex, but it has the advantage of also deriving a parameterization of the helical element, which is not the case for Komperød et al. (2015).

Let l be the length of the cable, and let s be the length of a helical cable element. Over an *infinitesimal* cable length, dl , the cable and its elements follow their respective tangent vectors. Hence, dl and ds are straight lines. ds can be decomposed into two components; ds_a that is parallel to dl , and ds_h that is perpendicular to dl . Figure 2 illustrates the relationship between the lengths l , s , s_a , and s_h . The lengths ds , ds_a , and ds_h are related through Pythagoras' theorem

$$ds = \sqrt{ds_a^2 + ds_h^2}. \quad (1)$$

By definition, the center of a helical element is a radial distance R from the cable's cross section center, where R is the element's pitch radius. The angle θ defines the helical element's position in the cable cross section: For positive bending curvature, i.e. $\kappa > 0$, the helical element is at the cable's outer arc for $\theta = \frac{\pi}{2}$, and at the inner arc for $\theta = -\frac{\pi}{2}$. For negative bending curvature, i.e. $\kappa < 0$, the helical

element is at the cable's outer arc for $\theta = -\frac{\pi}{2}$, and at the inner arc for $\theta = \frac{\pi}{2}$. The helical element is at the cable's neutral axis for $\theta = 0$ and for $\theta = \pi$, regardless of the sign of κ . By definition, θ increases 2π for each pitch length, L , along the cable's length, l . That is, θ and l are related through

$$\frac{\theta}{l} = \frac{2\pi}{L}. \quad (2)$$

Over an infinitesimal cable length, dl , the cable's cross section center follows a circle arc with radius $\frac{1}{\kappa}$. Because the cable's cross section center is a radial distance $\frac{1}{\kappa}$ from the center of the circle arc, the helical element's radial distance is $\frac{1}{\kappa} + R \sin(\theta)$. Hence, s_a is related to l through the relation

$$\begin{aligned} ds_a &= \frac{\frac{1}{\kappa} + R \sin(\theta)}{\frac{1}{\kappa}} dl \\ &= (1 + R\kappa \sin(\theta)) dl. \end{aligned} \quad (3)$$

From Eq. 2 it follows that over a cable length dl , the helical cable element completes an angle $d\theta = \frac{2\pi}{L} dl$. Because the element is located a distance R from the cable's cross section center, the angle $d\theta$ corresponds to an arc length in circumference direction of $ds_h = R d\theta$. Hence,

$$ds_h = \frac{2\pi R}{L} dl. \quad (4)$$

Inserting Eq. 3 and Eq. 4 into Eq. 1 gives the relationship between the helical cable element's length, s , and the cable's length, l , as

$$ds = \sqrt{(1 + R\kappa \sin(\theta))^2 + \left(\frac{2\pi R}{L}\right)^2} dl. \quad (5)$$

The desired result is the length of the helical element, s , from θ_1 to θ_2 , i.e. the integral of Eq. 5, which is

$$s(\theta_1, \theta_2) = \int_{\frac{L}{2\pi}\theta_1}^{\frac{L}{2\pi}\theta_2} \sqrt{(1 + R\kappa \sin(\theta))^2 + \left(\frac{2\pi R}{L}\right)^2} dl, \quad (6)$$

where the integration limits follow from Eq. 2. Please note that the square root of Eq. 6 can not be considered a constant during integration, because θ depends on l . The exceptions are the two special cases of $R = 0$ and $\kappa = 0$, where the square root expression is independent of l and can hence be considered a constant during integration. The physical interpretation of $R = 0$ is that the element is not a helical element, but a non-helical element

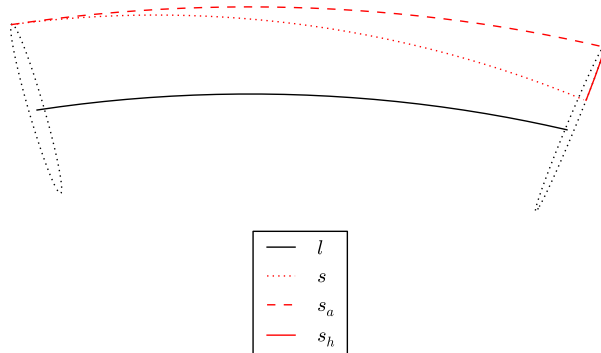


Figure 2. Relationship between l , s , s_a , and s_h .

located in the cable's cross section center. The case $\kappa = 0$ means that the cable is straight (not bent).

To the author's knowledge, it is not possible to integrate Eq. 6 analytically. The main contribution of the present paper is to approximate the integrand using Maclaurin series expansion, and then to estimate the integration error of this approach.

5 Maclaurin Series Expansion

Using Eq. 2 and the relationship $\tan(\alpha) = \frac{2\pi R}{L}$, where α is the element's pitch angle, Eq. 5 can be rewritten to

$$ds = \frac{R}{\sin(\alpha)} (1+x)^{\frac{1}{2}} d\theta, \quad (7)$$

where

$$x \stackrel{\text{def}}{=} \cos^2(\alpha) [2R\kappa \sin(\theta) + R^2\kappa^2 \sin^2(\theta)]. \quad (8)$$

The term $(1+x)^{\frac{1}{2}}$ of Eq. 7 is recognized from the theory of binomial series. That is

$$(1+x)^k = 1 + \sum_{n=1}^{\infty} \binom{k}{n} x^n, \quad (9)$$

where the right hand side is the Maclaurin series of the left hand side, and where

$$\binom{k}{n} \stackrel{\text{def}}{=} \frac{k(k-1)(k-2)\dots(k-n+1)}{n!}. \quad (10)$$

5.1 Proof of Convergence and Estimation of Reminder

When inserting Eq. 8 into Eq. 9, and then inserting Eq. 9 into Eq. 7, the right hand side of Eq. 7 becomes an infinite series of which each term can be integrated analytically w.r.t. θ . However, it is not feasible to sum infinite many terms. Hence, the series of Eq. 9 must be truncated before it is inserted into Eq. 7.

This section uses Taylor's theorem to prove that the right hand side of Eq. 9 converges to the left hand side, and to estimate the reminder (approximation error). In order to use Taylor's theorem, the constraint $-\frac{1}{2} < x < 1$ must be imposed. For subsea cables and umbilicals, R is rarely more than 0.2 m, and κ is rarely more than 0.5 m^{-1} . The absolute value of x is not likely to exceed 0.2, or at least not 0.3. Therefore, the imposed constraint is unlikely to be an issue for real-life cables.

Please note that according to the binomial theorem, the right hand side of Eq. 9 converges to the left hand side for $|x| < 1$ (ProofWiki, 2015). Hence, the convergence proof

of this section is actually superfluous. However, proving convergence using Taylor's theorem also provides a reminder estimate which is essential for Section 6.

For two variables a and x in an open interval, in which $f(x)$ and its first $N+1$ derivatives are continuous, Taylor's theorem states that

$$f(x) = P_N(x) + Q_N(x), \quad (11)$$

where

$$P_N(x) = f(a) + \sum_{n=1}^N \frac{d^n f(x)}{dx^n} \Big|_{x=a} (x-a)^n, \quad (12)$$

$$Q_N(x) = \frac{d^{N+1} f(x)}{dx^{N+1}} \Big|_{x=c} (x-a)^{N+1}, \quad (13)$$

for some c , where $x < c < a$ if $x < a$, and $a < c < x$ if $x > a$ (Thomas et al., 2010). In Eq. 11, P_N is the Taylor polynomial of order N , and Q_N is the reminder of this polynomial.

Inserting $f(x) = (1+x)^k$ and $a = 0$ into Eqs. 11-13, gives

$$(1+x)^k = P_N(x) + Q_N(x), \quad (14)$$

where

$$P_N(x) = 1 + \sum_{n=1}^N \binom{k}{n} x^n, \quad (15)$$

$$Q_N(x) = \binom{k}{N+1} (1+c)^{k-N-1} x^{N+1}, \quad (16)$$

$x < c < 0$ if $x < 0$, and $0 < c < x$ if $x > 0$. Proving that P_N converges to $(1+x)^k$, i.e.

$$\lim_{N \rightarrow \infty} P_N(x) = (1+x)^k, \quad (17)$$

is done by proving that Q_N goes to zero, i.e.

$$\lim_{N \rightarrow \infty} Q_N(x) = 0. \quad (18)$$

Eq. 18 will now be proved. Eq. 16 can be rewritten to

$$Q_N(x) = \binom{k}{N+1} x (1+c)^{k-1} x^N, \quad (19)$$

where

$$\bar{x} \stackrel{\text{def}}{=} \frac{x}{1+c}. \tag{20}$$

By the constraints imposed on x and c

$$\frac{-\frac{1}{2}}{1 + (-\frac{1}{2})} < \bar{x} < \frac{1}{1+0}, \tag{21}$$

which gives

$$|\bar{x}| < 1. \tag{22}$$

For $k - 1 > 0$ the maximum value of $(1 + c)^{k-1}$ in Eq. 19 is less than 2^{k-1} . For $k - 1 < 0$ the maximum value of $(1 + c)^{k-1}$ is less than $(1 + (-\frac{1}{2}))^{k-1} = 2^{|k-1|}$. Hence, regardless of k , the maximum value of $(1 + c)^{k-1}$ is less than $2^{|k-1|}$.

The sequence $\bar{Q}_N(x)$ is defined as

$$\bar{Q}_N(x) \stackrel{\text{def}}{=} \left| \binom{k}{N+1} 2^{|k-1|} \bar{x}^N \right|. \tag{23}$$

Then

$$-\bar{Q}_N(x) \leq Q_N(x) \leq \bar{Q}_N(x). \tag{24}$$

The limit of $\bar{Q}_N(x)$ can be established through the relation

$$\begin{aligned} \lim_{N \rightarrow \infty} \frac{\bar{Q}_{N+1}(x)}{\bar{Q}_N(x)} &= \lim_{N \rightarrow \infty} \frac{\left| \binom{k}{N+2} 2^{|k-1|} \bar{x}^{N+1} \right|}{\left| \binom{k}{N+1} 2^{|k-1|} \bar{x}^N \right|} \\ &= \lim_{N \rightarrow \infty} \left| \frac{k - N - 1}{N + 2} \bar{x} \right| \\ &= |\bar{x}|. \end{aligned} \tag{25}$$

The result of Eq. 25 states that as $N \rightarrow \infty$, $\bar{Q}_N(x)$ will decrease by a factor $|\bar{x}|$ for each increment of N . Hence,

$$\lim_{N \rightarrow \infty} -\bar{Q}_N(x) = \lim_{N \rightarrow \infty} \bar{Q}_N(x) = 0. \tag{26}$$

Using the sandwich theorem for sequences (Thomas et al., 2010, Theorem 2 p. 536), Eqs. 24 and 26 prove Eq. 18. Taking the limit $N \rightarrow \infty$ of Eq. 14 and inserting Eq. 18 proves Eq. 17. This means that as the number of terms in the Maclaurin polynomial, $P_N(x)$, increases, the polynomial approaches $(1 + x)^k$ and the reminder, $Q_N(x)$, approaches zero. For a finite number of terms, the polynomial and the reminder are given by Eqs. 15 and 16, respectively.

Inserting Eqs. 14-16 into Eq. 7 and setting $k = \frac{1}{2}$ gives the infinitesimal length of the helical element, ds

$$\begin{aligned} ds &= \frac{R}{\sin(\alpha)} \left[1 + \sum_{n=1}^N \binom{\frac{1}{2}}{n} x^n \right] d\theta \\ &+ \frac{R}{\sin(\alpha)} \binom{\frac{1}{2}}{N+1} (1+c)^{-N-\frac{1}{2}} x^{N+1} d\theta, \end{aligned} \tag{27}$$

where x is given by Eq. 8. The upper right hand side of Eq. 27 is the Maclaurin polynomial, while the lower right hand side is the reminder of this polynomial.

5.2 Numerical Example of the Maclaurin Polynomial's Accuracy

Figure 3 shows the true value for $\frac{R}{\sin(\theta)}(1+x)^{\frac{1}{2}}$ of Eq. 7 plotted against the corresponding Maclaurin polynomials of orders 1 through 4 for the numerical values stated in Table 2. To the resolution of the figure, only the first order Maclaurin polynomial can be distinguished from the true value. Figure 4 shows the same graphs zoomed in at the maxima. This figure visualizes well the decrease rate of the approximation error as the polynomial order increases. The fourth order polynomial approximates the true value so well that they can not be distinguished even in the zoomed figure.

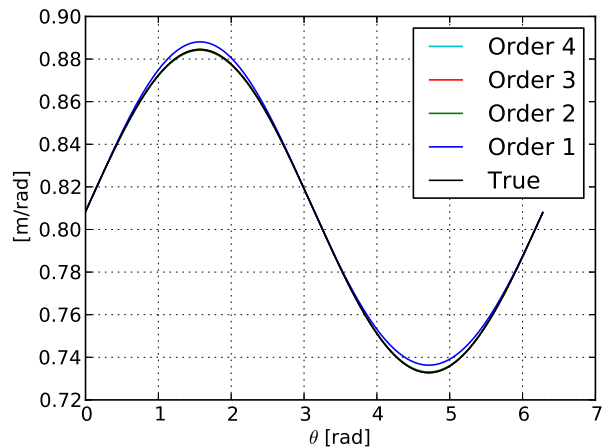


Figure 3. Comparing $\frac{R}{\sin(\theta)}(1+x)^{\frac{1}{2}}$ with Maclaurin polynomials of orders 1 through 4.

Table 2. Values used in numerical examples.

Variable	Value	Unit
α	0.25	rad
R	0.20	m
κ	0.50	m ⁻¹

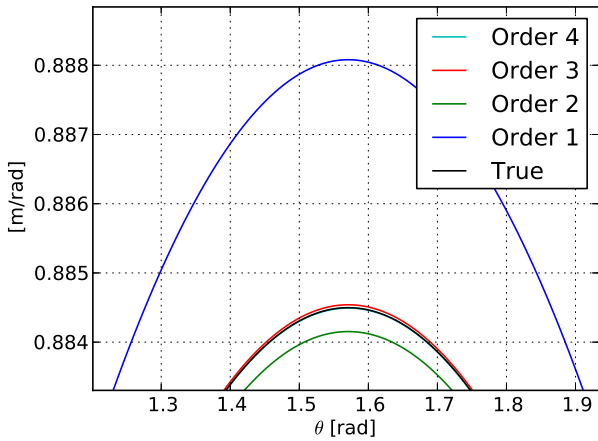


Figure 4. Comparing $\frac{R}{\sin(\theta)}(1+x)^{\frac{1}{2}}$ with Maclaurin polynomials of orders 1 through 4, zoomed in close to the maxima.

6 Integration of the Maclaurin Polynomial

This section considers analytical integration of the Maclaurin polynomial. This integral is an approximation of Eq. 6, which can not be integrated analytically.

6.1 Proof of Convergence after Integration

In this section it is proved that arbitrary accuracy of the helical cable element's length, $s(\theta_1, \theta_2)$, can be achieved by increasing the order of the Maclaurin polynomial, $P_N(x)$.

Inserting Eq. 14 into Eq. 7 and integrating w.r.t. θ from θ_1 to θ_2 , where $\theta_2 > \theta_1$, gives

$$s(\theta_1, \theta_2) = \int_{\theta_1}^{\theta_2} \frac{R}{\sin(\alpha)} P_N(x) d\theta \quad (28)$$

$$+ \int_{\theta_1}^{\theta_2} \frac{R}{\sin(\alpha)} Q_N(x) d\theta.$$

It will now be proved that the upper right term converges to the length of the helical cable element, $s(\theta_1, \theta_2)$, by proving that the lower right term converges to zero. \bar{Q}_N^{\max} is defined as

$$\bar{Q}_N^{\max} \stackrel{\text{def}}{=} \arg \max_{\theta} \bar{Q}_N. \quad (29)$$

Eq. 24 can then be extended to

$$-\bar{Q}_N^{\max} \leq -\bar{Q}_N(x) \leq Q_N(x) \leq \bar{Q}_N(x) \leq \bar{Q}_N^{\max}. \quad (30)$$

Hence,

$$-\bar{Q}_N^{\max} \leq Q_N(x) \leq \bar{Q}_N^{\max}. \quad (31)$$

Multiplying Eq. 31 with the non-negative factor $\frac{R}{\sin(\alpha)}$ gives

$$-\frac{R}{\sin(\alpha)} \bar{Q}_N^{\max}(x) \leq \frac{R}{\sin(\alpha)} Q_N(x) \leq \frac{R}{\sin(\alpha)} \bar{Q}_N^{\max}(x). \quad (32)$$

As this inequality holds for any θ , the inequality will also hold after taking the Riemann sum w.r.t. θ of each expression. As integration can be considered taking the norm limit of the Riemann sum, the inequality will also hold after integration from θ_1 to θ_2 , where $\theta_2 > \theta_1$, i.e.

$$-\int_{\theta_1}^{\theta_2} \frac{R}{\sin(\alpha)} \bar{Q}_N^{\max}(x) d\theta \leq \int_{\theta_1}^{\theta_2} \frac{R}{\sin(\alpha)} Q_N(x) d\theta \leq \int_{\theta_1}^{\theta_2} \frac{R}{\sin(\alpha)} \bar{Q}_N^{\max}(x) d\theta. \quad (33)$$

Because \bar{Q}_N^{\max} by definition is the largest value of \bar{Q}_N for any θ , \bar{Q}_N^{\max} is not a function of θ . Hence, Eq. 33 can be rewritten

$$-\frac{R}{\sin(\alpha)} \bar{Q}_N^{\max}(x) (\theta_2 - \theta_1) \leq \int_{\theta_1}^{\theta_2} \frac{R}{\sin(\alpha)} Q_N(x) d\theta \leq \frac{R}{\sin(\alpha)} \bar{Q}_N^{\max}(x) (\theta_2 - \theta_1). \quad (34)$$

Eq. 26 holds for any θ . Hence,

$$\lim_{N \rightarrow \infty} -\bar{Q}_N^{\max}(x) = \lim_{N \rightarrow \infty} \bar{Q}_N^{\max}(x) = 0. \quad (35)$$

Taking the limit of Eq. 34 and inserting Eq. 35 then gives

$$0 \leq \lim_{N \rightarrow \infty} \int_{\theta_1}^{\theta_2} \frac{R}{\sin(\alpha)} Q_N(x) d\theta \leq 0. \quad (36)$$

Then by the sandwich theorem for sequences it is proved that

$$\lim_{N \rightarrow \infty} \int_{\theta_1}^{\theta_2} \frac{R}{\sin(\alpha)} Q_N(x) d\theta = 0. \quad (37)$$

Taking the limit $N \rightarrow \infty$ of Eq. 28 and inserting Eq. 37 proves that

$$s(\theta_1, \theta_2) = \lim_{N \rightarrow \infty} \int_{\theta_1}^{\theta_2} \frac{R}{\sin(\alpha)} P_N(x) d\theta. \quad (38)$$

The practical interpretation of Eq. 38 is that arbitrary accuracy of the helical cable element's length, $s(\theta_1, \theta_2)$, can be achieved by increasing the order of the Maclaurin polynomial, $P_N(x)$.

6.2 Advantages of the Maclaurin Polynomial Approach

The main motivation for the work presented in this paper is to obtain an *analytical* expression for the length of helical cable elements at cable bending, i.e. an analytical solution to the integral of Eq. 6. This analytical solution can be used in mechanical analyses of cables and umbilicals. The Maclaurin approach proposed in this paper also has some interesting properties w.r.t. integration accuracy which are discussed in this section.

Inserting Eq. 15 into Eq. 38 and solving the integral of the constant term of $P_N(x)$ gives

$$s(\theta_1, \theta_2) = \frac{R}{\sin(\alpha)} (\theta_2 - \theta_1) + \lim_{N \rightarrow \infty} \frac{R}{\sin(\alpha)} \left[\sum_{n=1}^N \binom{k}{n} \int_{\theta_1}^{\theta_2} x^n d\theta \right]. \quad (39)$$

When the cable is straight (not bent), i.e. when $\kappa = 0$, x vanishes. Then the lower right term of Eq. 39 vanishes. Hence, the upper right term is the helical cable element's length when the cable is straight, and the lower right term is the element's elongation as the cable is bent. Negative elongation means compression.

For realistic values of R and κ , the helical cable element's elongation or compression due to cable bending is very small compared to the element's initial length. From Eq. 39 it then follows

$$\left| \lim_{N \rightarrow \infty} \frac{R}{\sin(\alpha)} \left[\sum_{n=1}^N \binom{k}{n} \int_{\theta_1}^{\theta_2} x^n d\theta \right] \right| \ll \frac{R}{\sin(\alpha)} (\theta_2 - \theta_1) \approx s(\theta_1, \theta_2). \quad (40)$$

It may be tempting to neglect the upper term of Eq. 40 for the purpose of simplifying the equation. However, that would be a very serious mistake, because it is this elongation, although very small, that causes the strains and stresses on which the mechanical analyses are based.

An intuitive way to establish the helical cable element's elongation due to cable bending is to integrate Eq. 6 numerically for bent cable and then subtract the element's length at straight cable. As the element's length changes only slightly during cable bending, the numerical integration must be very accurate, otherwise erroneous results are reached. In many cases an integration error of 0.01% will be unacceptable.

The Maclaurin approach presented in this paper has the advantage of analytically separating the helical cable element's length before cable bending (the upper right term of Eq. 39) and the element's elongation or compression due to cable bending (the lower right term of Eq. 39). Further, the Maclaurin approach has the benefit that each term can be integrated analytically, which nearly eliminates numerical errors. However, some error due to truncation of the Maclaurin series is inherent in the proposed method. An approach to calculate this error is presented in Section 6.3.

As will be shown in Section 6.4, numeric integration using Simpson's method also gives very good results.

6.3 Estimation of Error

Section 6.1 proved Eq. 38, with the practical interpretation that arbitrary accuracy of the helical cable element's length, $s(\theta_1, \theta_2)$, can be achieved by increasing the order of the Maclaurin polynomial, $P_N(x)$. The present section considers how to estimate the approximation error of $s(\theta_1, \theta_2)$ due to truncation of $P_N(x)$ at a finite polynomial order, N . The error is given from Eq. 28 as

$$\int_{\theta_1}^{\theta_2} \frac{R}{\sin(\alpha)} Q_N(x) d\theta = s(\theta_1, \theta_2) - \int_{\theta_1}^{\theta_2} \frac{R}{\sin(\alpha)} P_N(x) d\theta. \quad (41)$$

In other words, the purpose of this section is how to estimate the left hand side of Eq. 41, where $Q_N(x)$ is given by Eq. 16. Please note that it is not straight forward to integrate the left hand side of Eq. 41, because $Q_N(x)$ contains the variable c , which is unknown and varies with x . There are several ways to estimate this integral, with different degrees of accuracy, and different degrees of complexity and difficulty. The method proposed below is believed to be a feasible compromise between accuracy and complexity.

The basic principle of the proposed method is to provide upper and lower limits of $Q_N(x)$, which are sufficiently close to the true $Q_N(x)$ to be reasonable accurate, while being simple enough to be integrated analytically.

Define x^{\min} and x^{\max} as the lowest and highest values, respectively, of x within (and including) the integration limits θ_1 and θ_2 . That is

$$x^{\min} \stackrel{\text{def}}{=} \arg \min_{\theta \in [\theta_1, \theta_2]} x, \quad (42)$$

$$x^{\max} \stackrel{\text{def}}{=} \arg \max_{\theta \in [\theta_1, \theta_2]} x. \quad (43)$$

For $k = \frac{1}{2}$, Eq. 16 can be written as

$$Q_N(x) = \binom{\frac{1}{2}}{N+1} x^{N+1} \frac{1}{(1+c)^{N+\frac{1}{2}}}. \quad (44)$$

The binomial factor, $\binom{\frac{1}{2}}{N+1}$, is positive for even N , and negative for odd N . As $c > -\frac{1}{2}$, the factor $\frac{1}{(1+c)^{N+\frac{1}{2}}}$ is always positive. The factor x^{N+1} is negative when N is even and $x < 0$, otherwise positive.

All values on the right hand side of Eq. 44 are known, except for c . While c is unknown, it is known to be within the intervals stated in Section 5.1. That is $x^{\min} \leq x < c < 0$ if $x < 0$, and $0 < c < x \leq x^{\max}$ if $x > 0$, where the inequalities have been extended by using Eqs. 42 and 43.

Let $Q_N^{\text{lower}}(x)$ and $Q_N^{\text{upper}}(x)$ be lower and upper boundaries, respectively, that $Q_N(x)$ always will be within provided that the previously stated constraints are obeyed. In other words, the following inequality always holds:

$$Q_N^{\text{lower}}(x) \leq Q_N(x) \leq Q_N^{\text{upper}}(x). \quad (45)$$

Subject to the constraints imposed on c , it can be shown that

$$\frac{\partial}{\partial c} \frac{1}{(1+c)^{N+\frac{1}{2}}} < 0. \quad (46)$$

This inequality, together with the constrains of c , will be used to derive expressions for $Q_N^{\text{lower}}(x)$ and $Q_N^{\text{upper}}(x)$. The derivation must be divided into four cases, depending on whether N is odd or even, and on whether x is positive or negative:

N is Even, x is Positive

If N is even and $x > 0$, then $\binom{\frac{1}{2}}{N+1} x^{N+1} > 0$. From Eq. 46 it then follows that

$$\frac{\partial}{\partial c} \left[\binom{\frac{1}{2}}{N+1} x^{N+1} \frac{1}{(1+c)^{N+\frac{1}{2}}} \right] < 0. \quad (47)$$

As the derivative is negative, the lower limit, Q_N^{lower} , is found by inserting the highest value for c , and the upper limit, Q_N^{upper} , is found by inserting the lowest value of c . Because $x > 0$, c is constrained by $0 < c < x^{\max}$. Hence,

$$Q_N^{\text{lower}}(x) = \binom{\frac{1}{2}}{N+1} x^{N+1} \frac{1}{(1+x^{\max})^{N+\frac{1}{2}}}, \quad (48)$$

$$Q_N^{\text{upper}}(x) = \binom{\frac{1}{2}}{N+1} x^{N+1}. \quad (49)$$

N is Even, x is Negative

If N is even and $x < 0$, then $\binom{\frac{1}{2}}{N+1} x^{N+1} < 0$. That gives,

$$\frac{\partial}{\partial c} \left[\binom{\frac{1}{2}}{N+1} x^{N+1} \frac{1}{(1+c)^{N+\frac{1}{2}}} \right] > 0. \quad (50)$$

As the derivative is positive, the lower limit is found by inserting the lowest value for c , and vice versa. Because $x < 0$, c is constrained by $x^{\min} < c < 0$. Hence,

$$Q_N^{\text{lower}}(x) = \binom{\frac{1}{2}}{N+1} x^{N+1} \frac{1}{(1+x^{\min})^{N+\frac{1}{2}}}, \quad (51)$$

$$Q_N^{\text{upper}}(x) = \binom{\frac{1}{2}}{N+1} x^{N+1}. \quad (52)$$

N is Odd, x is Positive

If N is odd and $x > 0$, then $\binom{\frac{1}{2}}{N+1} x^{N+1} < 0$. That gives,

$$\frac{\partial}{\partial c} \left[\binom{\frac{1}{2}}{N+1} x^{N+1} \frac{1}{(1+c)^{N+\frac{1}{2}}} \right] > 0. \quad (53)$$

As the derivative is positive, the lower limit is found by inserting the lowest value for c , and vice versa. Because $x > 0$, c is constrained by $0 < c < x^{\max}$. Hence,

$$Q_N^{\text{lower}}(x) = \binom{\frac{1}{2}}{N+1} x^{N+1}, \quad (54)$$

$$Q_N^{\text{upper}}(x) = \binom{\frac{1}{2}}{N+1} x^{N+1} \frac{1}{(1+x^{\max})^{N+\frac{1}{2}}}. \quad (55)$$

N is Odd, x is Negative

If N is odd and $x < 0$, then $\binom{\frac{1}{2}}{N+1} x^{N+1} < 0$. That gives,

$$\frac{\partial}{\partial c} \left[\binom{\frac{1}{2}}{N+1} x^{N+1} \frac{1}{(1+c)^{N+\frac{1}{2}}} \right] > 0. \quad (56)$$

As the derivative is positive, the lower limit is found by inserting the lowest value for c , and vice versa. Because $x < 0$, c is constrained by $x^{\min} < c < 0$. Hence,

$$Q_N^{\text{lower}}(x) = \left(\frac{1}{N+1}\right) x^{N+1} \frac{1}{(1+x^{\min})^{N+\frac{1}{2}}}, \quad (57)$$

$$Q_N^{\text{upper}}(x) = \left(\frac{1}{N+1}\right) x^{N+1}. \quad (58)$$

Multiplying Eq. 45 with the non-negative constant $\frac{R}{\sin(\alpha)}$ gives

$$\begin{aligned} \frac{R}{\sin(\alpha)} Q_N^{\text{lower}}(x) &\leq \frac{R}{\sin(\alpha)} Q_N(x) \\ &\leq \frac{R}{\sin(\alpha)} Q_N^{\text{upper}}(x). \end{aligned} \quad (59)$$

Using the same reasoning as in Section 6.1 ensures that Eq. 59 also holds after integration w.r.t. θ , provided that $\theta_2 > \theta_1$. That is

$$\begin{aligned} \int_{\theta_1}^{\theta_2} \frac{R}{\sin(\alpha)} Q_N^{\text{lower}}(x) d\theta &\leq \int_{\theta_1}^{\theta_2} \frac{R}{\sin(\alpha)} Q_N(x) d\theta \\ &\leq \int_{\theta_1}^{\theta_2} \frac{R}{\sin(\alpha)} Q_N^{\text{upper}}(x) d\theta. \end{aligned} \quad (60)$$

Inserting Eq. 41 into Eq. 60 gives the final result

$$\begin{aligned} \int_{\theta_1}^{\theta_2} \frac{R}{\sin(\alpha)} Q_N^{\text{lower}}(x) d\theta & \\ &\leq s(\theta_1, \theta_2) - \int_{\theta_1}^{\theta_2} \frac{R}{\sin(\alpha)} P_N(x) d\theta \\ &\leq \int_{\theta_1}^{\theta_2} \frac{R}{\sin(\alpha)} Q_N^{\text{upper}}(x) d\theta. \end{aligned} \quad (61)$$

Hence, the uppermost and lowermost integrals of Eq. 61 provide lower and upper limits, respectively, for the difference between the true length of a helical cable element and the approached based on Maclaurin series.

The uppermost and lowermost integrals of Eq. 61 can be integrated analytically as x^{N+1} is the only factor depending on θ in the expressions $Q_N^{\text{lower}}(x)$ and $Q_N^{\text{upper}}(x)$, where x is defined in Eq. 8. However, note that $Q_N^{\text{lower}}(x)$ and $Q_N^{\text{upper}}(x)$ are defined differently for $x > 0$ and for $x < 0$. Hence, the integral must be divided into subintervals if x alters between being positive and being negative within the interval given by the integration limits.

6.4 Numerical Example of Error Estimation

This section presents a numerical example of the method of error estimation which is derived in Section 6.3. The numerical values stated in Table 2 are used in the example. The length of a helical element over one half pitch length in the cable’s outer arc is calculated, that is, the integration limits are $\theta_1 = 0$ and $\theta_2 = \pi$.

Table 3 presents the numerical results. The first column shows the order of the Maclaurin polynomial which the calculation is based on. The second column is the length of the helical element after cable bending calculated by the Maclaurin approach derived in this paper. The third and fourth columns are the lower and upper limits, respectively, of the estimation error. That is, the third column is the first row of Eq. 61, and the fourth column is the third row of this equation. The fifth column is the sum of the second and third columns, while the sixth column is the sum of the second and fourth columns. Hence, the true value of the helical element’s length, $s(\theta_1, \theta_2)$, is ensured to be between the value of the fifth column and the value of the sixth column.

The second column of Table 3 indicates that the calculated length of the helical element converges to a certain value. The most important result of the table is the third and fourth columns, which shows the the estimation error decreases rapidly as the order of the Maclaurin polynomial increases. The fifth and sixth columns show that the interval which the true element length is ensured to be within quickly narrows as the polynomial order increases. These results are expected from the proof in Section 6.1.

Table 4 shows numeric integration of Eq. 6 using Simpson’s method. This numeric method tends to converge to a certain value as the number of discretization intervals increases. This is similar to the Maclaurin approach which tends to converge for increasing polynomial order as shown in the second column of Table 3. By comparing the two tables, it is shown that the Maclaurin approach and Simpson’s method converge to the same value. Simpson’s method here serves as a verification that the Maclaurin approach derived in this paper is correct. The main advantage of the Maclaurin approach over Simpson’s method is that the former provides an analytical solution of the length integral, which can be used in mechanical analyses of cables and umbilicals.

In Table 4 the error is reduced by a factor of approximately 16 for each time the number of discretization intervals is doubled, except for from two to four intervals, where the factor is approximately 21. The calculations of the errors are based on comparison with Simpson’s method using 10^6 intervals. Please note that more decimals are used in these calculations than those shown in Table 4. According to Edwards and Penney (1986), the error of Simpson’s method is approximately proportional to $\frac{1}{n_i^4}$, where n_i is the number of discretization intervals. Hence, according to this theory, the integration error will decrease by a factor of approximately 16 as the number

Table 3. Error estimation using the method derived in Section 6.3. Please refer to the main text for explanation.

	<i>Calculated length [m]</i>	<i>Lower error [m]</i>	<i>Upper error [m]</i>	<i>Lower length limit [m]</i>	<i>Upper length limit [m]</i>
$N = 1$	2.6973895	-0.0060811	-0.0046426	2.6913083	2.6927468
$N = 2$	2.6913083	0.0003238	0.0005077	2.6916321	2.6918160
$N = 3$	2.6918160	-0.0000552	-0.0000294	2.6917608	2.6917866
$N = 4$	2.6917608	0.0000031	0.0000069	2.6917639	2.6917677

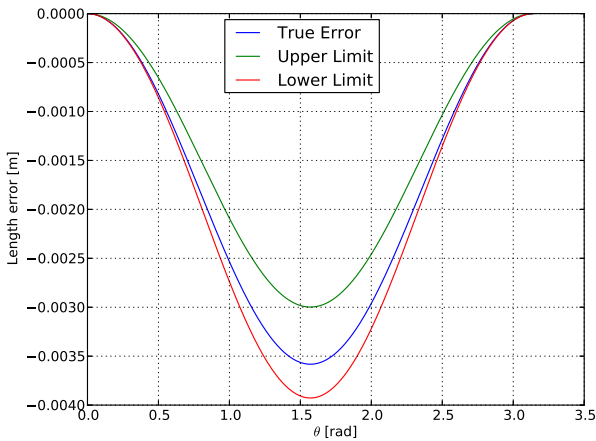


Figure 5. Upper and lower error estimate compared to the true error for $N = 1$.

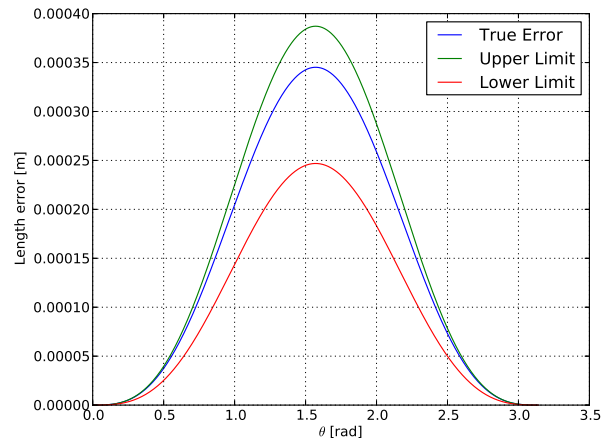


Figure 6. Upper and lower error estimate compared to the true error for $N = 2$.

of intervals is doubled, which is in accordance with the observations.

Table 4. Numeric integration of Eq. 6 using Simpson’s method.

<i>Number of intervals</i>	<i>Calculated length [m]</i>
2	2.6990374
4	2.6921142
8	2.6917874
16	2.6917682
32	2.6917670
64	2.6917669
128	2.6917669

Figures 5 - 8 illustrate Table 3 graphically for different values of N . In each of the figures, the blue curve represents the difference between the true element length and the element length calculated by the Maclaurin expansion. More precisely, the blue curve is $\frac{ds}{d\theta} - \frac{R}{\sin(\alpha)} P_N(x)$. Integrating this term w.r.t. θ from θ_1 to θ_2 gives the second line of Eq. 61. That is, the area between the blue curve and the first axis (x-axis) is the difference between the true length of the helical cable element and the approach based on Maclaurin polynomial as derived in the present paper. Areas above the first axis are considered positive, and areas below the first axis are considered negative.

The red and green curves of Figures 5 - 8 represent the

lower and upper limits of the estimation error. More precisely, the red curve is $\frac{R}{\sin(\alpha)} Q_N^{\text{lower}}(x)$ and the green curve is $\frac{R}{\sin(\alpha)} Q_N^{\text{upper}}(x)$. Integrating these terms w.r.t. θ from θ_1 to θ_2 gives the first row and the third row of Eq. 61, respectively. That is, the first row of Eq. 61 is equal to the area between the red curve and the first axis. Similarly, the third row of Eq. 61 is equal to the area between the green curve and the first axis. Also, the areas between the red curve and the first axis, and between the green curve and the first axis, are equal to the values of the third and fourth columns of Table 3, respectively.

In Figures 5 - 8 the blue curve is always above the red curve and below the green curve. Hence, the area between the blue curve and the first axis is larger than the corresponding area of the red curve, but smaller than the corresponding area of the green curve, taking into consideration that areas below the first axis are considered negative. Hence, the graphs of the four figures are graphical illustrations of the inequality of Eq. 61.

Figures 5 - 8 also summarize the main contribution of this paper: The area between the blue curve and the first axis is the error between the true length of the helical element and the calculation based on the Maclaurin polynomial. This area can not be found using analytical integration. However, the blue curve is always above the red curve and below the green curve. Hence, the red and green curves are limits that the blue curve is ensured to be

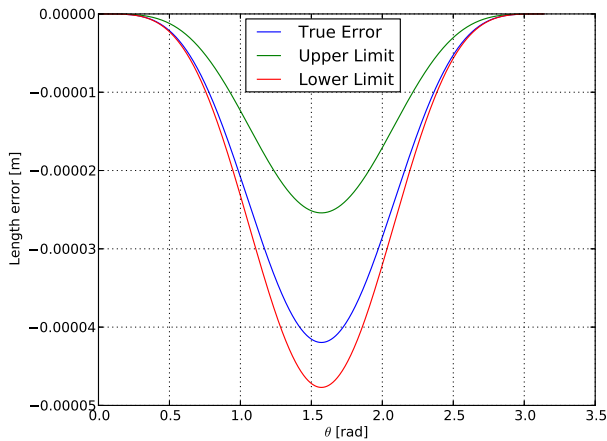


Figure 7. Upper and lower error estimate compared to the true error for $N = 3$.

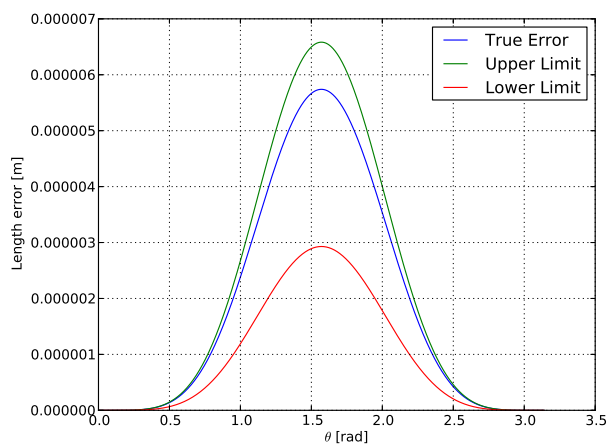


Figure 8. Upper and lower error estimate compared to the true error for $N = 4$.

within. The area between the red curve and the first axis, and the area between the green curve and the first axis, can be calculated using analytical integration. Therefore, the latter two areas are lower and upper limits, respectively, that the error of the Maclaurin polynomial approach is ensured to be within. Figures 5 - 8 also show how the error of the Maclaurin polynomial approach decreases as the polynomial order increases: Note the difference between the scales of the second axes (y-axes) in the four figures.

7 Conclusion

The present paper derives an expression for the arc lengths of helical cable elements at cable bending. This expression is an integral that to the author's knowledge can not be solved analytically. The integrand of the expression is then approximated by a Maclaurin series expansion, which terms can be integrated analytically.

In order to establish correct strains in the helical cable elements, which is essential for mechanical analyses of the cable, the integrals must be calculated with very high accuracy. An integration error of 0.01% will in many cases be unacceptable. In this paper it is proved that arbitrary integration accuracy can be achieved by increasing the order of the Maclaurin polynomial. The paper also derives lower and upper limits of the integration error, which is caused by truncation of the Maclaurin series.

The results of the paper are illustrated in a numerical example. The example compares the proposed Maclaurin approach with numeric integration using Simpson's method. The comparison shows that both the Maclaurin approach and Simpson's method perform very well. The Maclaurin approach has the inherent advantage of providing an analytical expression for the integral, which can be used in mechanical analyses of cables and umbilicals.

References

- C. H. Edwards and D. E. Penney. *Calculus and analytic geometry - 2nd edition*. Prentice-Hall International Ltd., 1986.
- J. J. Féret and C. L. Bournazel. Calculation of stresses and slip in structural layers of unbonded flexible pipes. *Journal of Offshore Mechanics and Arctic Engineering*, 109:263 – 269, 1987.
- E. Kebabzde. *Theoretical modelling of unbonded flexible pipe cross-sections*. PhD thesis, South Bank University, 2000.
- M. Komperød, B. Konradsen, and R. Slora. Theoretical and practical considerations of helical cable elements subject to end effects at cable bending. In *Proceedings of the ASME 2015 34th International Conference on Ocean, Offshore and Arctic Engineering OMAE 2015*, 2015.
- M. Lutchansky. Axial stress in armor wires of bent submarine cables. *Journal of Engineering Industry*, 91(3):687 – 693, 1969.
- ProofWiki. Binomial theorem/general binomial theorem, 2015. URL www.proofwiki.org/wiki/Binomial_Theorem/General_Binomial_Theorem.
- N. Sødahl, G. Skeie, O. Steinkjær, and A. J. Kalleklev. Efficient fatigue analysis of helix elements in umbilicals and flexible risers. In *Proceedings of the ASME 29th International Conference on Ocean, Offshore and Arctic Engineering OMAE 2010*, 2010.
- G. Skeie, N. Sødahl, and O. Steinkjer. Efficient fatigue analysis of helix elements in umbilicals and flexible risers: Theory and applications. *Journal of Applied Mathematics*, 2012.
- S. Sævik. *On Stresses and Fatigue in Flexible Pipes*. PhD thesis, Norwegian Institute of Technology, 1992.
- G. B. Thomas, M. D. Weir, and J. Hass. *Thomas' calculus - global edition - 12th edition*. Pearson Education, Inc., 2010.

Simulation of Transcritical Flow in Hydraulic structures

Cornelius E. Agu¹ Geir Elseth² Bernt Lie³

^{1,3} Faculty of Technology, Telemark University College, Norway, {cornelius.e.agu,bernt.lie}@hit.no

² Statoil AS, Norway, geiel@statoil.com

Abstract

In hydraulic engineering, transcritical flows are often required in some applications. One example is in a Venturi channel where the occurrence of critical depth is used to estimate flow rate in the channel. In this paper, a simple numerical scheme that predicts transcritical flows in hydraulic structures is developed based on the Saint Venant Equations (SVE). The solution of this scheme is aimed to be used in real time to calibrate the model that uses a measured liquid level to estimate flow rate of the fluid in a Venturi channel. The proposed algorithm consists of a set of ordinary differential equations derived from discretizing SVE in space along the channel axis. The results based on this scheme show that the algorithm is capable of predicting flows involving transcritical conditions. Errors associated with the scheme are relatively small in locating shocks in flows with imposed downstream boundary level, and in predicting the transition within the throat of Venturi channels.

Keywords: Transcritical, Saint Venant Equations, Critical Depth, Hydraulic Structures, Boundary Condition

1 Introduction

As it is encountered in natural channels such as river flow, open channel flow usually transits from one flow condition to another due to bed slope changes and variation in channel width. These conditions are classified into subcritical where the flow velocity is less than the gravity wave celerity¹, supercritical in which the flow velocity is greater than the wave speed (celerity) and critical flow condition where the flow velocity and celerity are the same. When there is a change from one flow condition to another, the condition is regarded as transcritical flow.

In artificial hydraulic structures, transcritical flows are often introduced to establish a relationship between flow rate and the free stream level. This condition is widely utilized in Venturi channels and weirs for flow measurements.

The possibility of estimating drilling mud flow rate for kick/loss detection using a Venturi channel flow rate

model has been previously studied, and the studies show that the required tuning parameter for the model depends on the fluid properties due to non-Newtonian behaviour of the fluid (Agu and Lie, 2014; Berg *et al*, 2015). One possibility of making the flow rate model applicable for software development in real time is to calibrate the model with a 1-D unsteady state model that describes the flow in the channel. The Saint Venant Equations have been long established as a good 1-D model that predicts the flow behaviour in an open channel. Most algorithms for simulating the model predict flow accurately in pure subcritical and pure supercritical conditions. Due to its numerical challenges, algorithms available for simulating transcritical flow require either modification of the Saint Venant Equations or imposing internal boundary at critical depth whose location is certainly unknown.

The purpose of this study is to develop a numerical scheme that solves the Saint Venant Equations across a critical flow condition. Such a scheme is used in real time to calibrate the Venturi channel model that uses a measured liquid level to estimate flow rates in the channel, which ensures high accuracy in drilling mud flow rate measurement using a Venturi channel.

(Meselhe *et al*, 1997) developed a two-step predictor-corrector implicit scheme for simulating transcritical flow based on SVE. They included an artificial dissipation terms to suppress numerical oscillations around stiff regions, so to facilitate hydraulic jumps resolutions. (Zerihun and Fenton, 2006) presents a one-dimensional model for steady state transcritical free surface flows based on a Boussinesq-type equation. They argued that due to involvement of a short length within which transcritical flow occurs, the pressure distribution is not hydrostatic and the Saint Venant Equations are not valid. (Sart *et al*, 2010) developed a scheme based on the modified Preissman method. As Preissman scheme solves only pure subcritical and supercritical flows, they adopted the scheme and included the condition for imposing internal boundary condition where critical flow occurs.

In this paper, a numerical scheme for solving transcritical flow using unmodified SVE is presented. The equations are discretized in space using the finite

¹ Wave Celerity = $\sqrt{\frac{Ag}{B}}$, is defined as the velocity of a wave propagating in a flowing liquid relative to the liquid.

volume approach into a set of ordinary differential equations (ODE). The boundary condition equations are formulated based on a combination with physical boundary condition that satisfies the continuity equation. The scheme is simulated and the results are compared with published results and with the experimental values obtained from a Venturi rig set up at Telemark University College, Norway.

In the following sections, the governing equations are presented, and the experimental setup is described. The numerical scheme solution is compared with results from the experiment and from the literature. Finally, some conclusions are drawn.

2 Governing Equations

The unsteady state flow of fluid in an open channel can be described by the one-dimensional Saint Venant Equations (Szymkiewicz, 2010),

$$\frac{\partial A}{\partial t} + \frac{\partial Q}{\partial x} = 0, \quad (1)$$

$$\frac{\partial Q}{\partial t} + \frac{\partial \left(\frac{\beta Q^2}{A} \right)}{\partial x} = gA \sin \theta - gA \cos \theta \frac{\partial h}{\partial x} - gAS_f. \quad (2)$$

Equations (1) and (2) are based on mass conservation and momentum conservation principles, respectively, where Q is the volume flow rate, and A and h are the flow cross sectional area and free surface level, respectively. θ is the channel angle of inclination, and g is the acceleration due to gravity. β is a momentum correction coefficient with a value between 1.03 and 1.07.

For a Newtonian fluid, the frictional slope S_f is given by Manning's equation,

$$S_f = (|V|n_M)^2 R_h^{-4/3}. \quad (3)$$

For a non-Newtonian fluid flow, the internal frictional shearing stresses dominate. Based on power law fluid rheology, S_f is given by Eq. (4) which is derived from the velocity distribution function across the fluid depth as given in (Sisson *et al*, 2012).

$$S_f = \frac{K}{4\rho g R_h} \left(\frac{|V|}{h} \frac{1+2n}{n} \right)^n \quad (4)$$

Here, n_M is Manning's roughness coefficient, h is the free surface liquid level, $V = Q/A$ is the average flow velocity and $R_h = \frac{A}{P_{wet}}$ is the hydraulic radius at each cross section.

2.1 Solution Algorithm - ODE Scheme

The numerical scheme presented here for solving the unsteady state equations (1) and (2) is based on the finite volume method with staggered grid which ensures that the varying slope of the liquid surface is captured (Versteeg and Malalasekera, 2007). Figure 1 shows the grid arrangement.

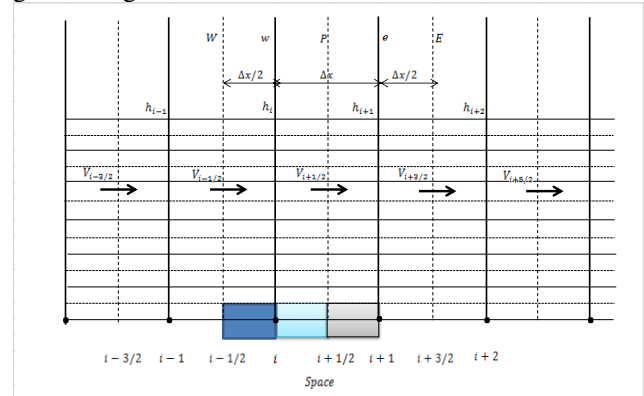


Figure 1: Staggered grid arrangement for mass and momentum control volumes.

For a positive flow², the scheme described by a set of ordinary differential equations (ODE) is given by Eqs. (5)-(10).

$$\frac{dA_i}{dt} = - \frac{Q_{i+1/2} - Q_{i-1/2}}{\Delta x} \quad (5)$$

$$\frac{dQ_{i+1/2}}{dt} = -\beta \frac{(QV)_{i+1} - (QV)_i}{\Delta x} - g\bar{A}_{i+1/2} \cos \theta \frac{h_{i+1} - h_i}{\Delta x} + g\bar{A}_{i+1/2} S_{i+1/2} \quad (6)$$

$$S_{i+1/2} = \sin \theta - S_{f i+1/2} \quad (7)$$

$$Q_i = \frac{Q_{i+1/2} + Q_{i-1/2}}{2} \quad (8)$$

$$\bar{A}_{i+1/2} = f \left(\frac{h_{i+1} + h_i}{2} \right) \quad (9)$$

By a first order upwind condition, the momentum flux, $(QV)_i$ is given as in Eq. (10)

$$(QV)_i = \frac{Q_{i+1/2} + Q_{i-1/2}}{2} V_{i-1/2}. \quad (10)$$

The indices, $i = 1, 2, 3, \dots, N$ indicate the computational nodes along the channel length. The first node in this scheme is at $i = 1$, and it interacts with the left physical boundary. The last node is at $i = N$ which corresponds to the right physical boundary.

The detailed derivation and description of Eqs. (1)-(2) and Eqs. (5)-(10) can be found in (Agu, 2014).

² Positive flow occurs when $\frac{Q_{i+1/2} + Q_{i-1/2}}{2} \geq 0$

2.2 Boundary Equations

At the upstream boundary, the values of $h(x = 0)$ and $Q(x = 0)$ are designated as input corresponding to h_0 and $Q_{1/2}$, respectively. The downstream boundaries are $h(x = L)$ and $Q(x = L)$ corresponding to h_N and $Q_{N+1/2}$, respectively; see Figure 2. Normally, $Q(x = 0)$ is specified along with any of $h(x = 0)$ and $h(x = L)$ depending on the flow condition.

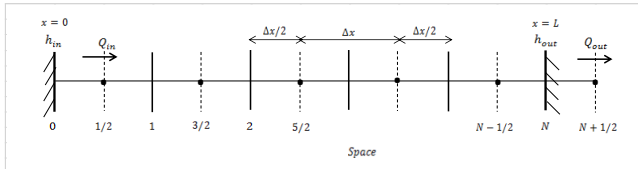


Figure 2: Position of h and Q cells at the domain boundaries.

The boundary equations are only formulated for downstream boundaries where the last computational node correspond to the physical boundary. When $h_N(t)$ is given, $\frac{dA_N}{dt}$ is known. $Q_{N+1/2}(t)$ is obtained from Eq. (11) such that the mass balance, Eq. (5) is satisfied.

$$Q_{N+1/2} = Q_{N-1/2} - \Delta x \frac{dA_N}{dt}. \quad (11)$$

When $Q_{N+1/2}(t)$ is given, A_N is obtained by integrating Eq. (5) over time.

$$A_N = \int \left(-\frac{Q_{N+1/2}(t) - Q_{N-1/2}}{\Delta x} \right) dt \quad (12)$$

For a pure subcritical flow, both upstream and downstream boundaries must be specified with a combination of level and flow rate. In a pure supercritical flow, only the upstream boundary is specified with the flow variables $h(x = 0)$ and $Q(x = 0)$. When the flow transits from subcritical upstream to supercritical downstream, only the upstream flow rate is used to determine the flow behaviour. The downstream boundary flow rate can be obtained from Eq. (13), which is derived from Eq. (6)

$$\frac{dQ_{N+1/2}}{dt} = -\frac{\beta}{2\Delta x} \left(\frac{2Q_{N+1/2}^2}{\bar{A}_{N+1/2}} - \frac{(Q_{N+1/2} + Q_{N-1/2})Q_{N-1/2}}{\bar{A}_{N-1/2}} \right) + g\bar{A}_{N+1/2}S_{N+1/2}. \quad (13)$$

2.3 Simulation Execution

The accuracy of the scheme described by Eq. (5) through Eq. (13) is of first order since the scheme is based on a first order upwind condition. Its stability depends on the initial condition and on the ODE solver for its implementation. The ode23 and ode45 can be

used in pure subcritical and pure supercritical problems. When the problem involves transcritical, the scheme suffers convergence problem when implemented on ode23 or ode45, especially in the region of shock propagation. The ode15s can efficiently be used to implement the scheme in all problems including transcritical cases.

When an adaptive time step is used in the solver, the number of grids used does not affect the stability of the scheme, but the accuracy and speed of execution. Where the problem does not involve shock wave propagation, 50 grids can be sufficient. In stiff problems such as that involving transition from supercritical to subcritical flow condition, larger number of grids in the range of 100 to 500 will be required.

Moreover, the convergence of the scheme to a solution solely depends on the initial condition. A uniform liquid level (not necessary a normal level) can be used to initialize the scheme for any flow rate, but the chosen level must not be less than the highest level (mainly the imposed boundary level) that can be achieved in the flow.

By using the right frictional slope model, the scheme can be used to simulate flows of all conditions characterized by both Newtonian and non-Newtonian fluid behaviours.

3 Experimental Setup

At Telemark University College, Norway, a Venturi channel test rig was set up. The rig is used to validate the model established to predict a flow through an open channel, and to study the possibility of applying a Venturi channel model for estimating the flow rate of drilling mud in an open channel, in both steady and unsteady state conditions.

The rig consists of a trapezoidal channel of total length 3.70 m and height 0.3 m. The geometry of the channel is shown in Figure 3, and the description of parts and dimensions are given in Table 1.

The complete circuit of the rig is made up of a series of equipment including a mud mixing tank, a mud circulating pump (screw type) with capacity up to 1000 kg/min, a 100 liter Venturi channel intake tank and a mud return tank. All the equipment is linked by a set of stainless steel pipes of appropriate sizes between two adjoining equipment. There are a set of sensing instruments measuring different flow properties in real time. A Coriolis mass flow meter measuring up to 600 kg/min was installed between the pump and the channel intake tank to measure the flow rate and density of the flowing fluid. The pressure transmitter at the outlet of the pump keeps track of pressure in the line for safe pump operation. Also, the fluid temperature is monitored with a temperature transmitter at the pump outlet. A differential pressure transmitter on the line before the intake tank monitors the pressure drop over a 3 meter horizontal pipe section, and this gives indication

of viscosity of the flowing fluid. Over the Venturi channel, three ultrasonic level transmitters were mounted on a bar positioned at the center along the axis of the channel. Each of the transmitters can be moved relatively along the bar for measuring the level of flow at any defined position marked on a graduated rule attached to the bar.

The Venturi channel is supported at the upstream end on a hinged support and at downstream end on a pneumatic piston-cylinder assembly. This arrangement provides a freedom for tilting the channel down to 2.5° from the horizontal.

The fluid tested is a modeled fluid which exhibits zero-yield pseudoplastic non-Newtonian fluid behaviour. The fluid consists of water, xanthan gum and potassium carbonate.

The Coriolis mass flow meter is still within its certified period of accuracy, and each of the level sensors was calibrated against a uniform solid block of known thickness.

The only challenge with the setup is ensuring accurate level measurement. Due to formation of foam and turbulences in the flow, there is significant irregularities on the fluid surface in the channel. This results in non-uniform fluctuations in the measurements given by each of the level sensors. The measurement results reported in this paper are average values at each location for a sensor reading taken over a period of 5 minutes.

4 Results and Discussions

The results of three cases considered are presented here. In Case 1, the simulated results based on the developed algorithm are compared with the experimental data. Case 2 compares the results of the proposed scheme with results from a literature, and Case 3 is used to demonstrate the capacity of the proposed scheme to handle unsteady state behaviours. In the first two cases, steady state flows are considered.

Because the flow properties need to be transported across a critical depth from upstream, the conservative form of the Saint Venant Equations is necessary. Any steady state model derived from SVE loses this conservativeness, and breaks at the critical points (that is, such a model does not give solutions across the critical depth) (Berg *et al*, 2015). The steady state solutions are obtained from solving the dynamic model described by Eqs. (5)-(13).

4.1 Case 1 - Venturi Channel

In the setup described in section 3, a flow at 300 kg/min was studied at its steady state in the channel. The flowing fluid has a density of 1109 kg/m³, and rheolo-

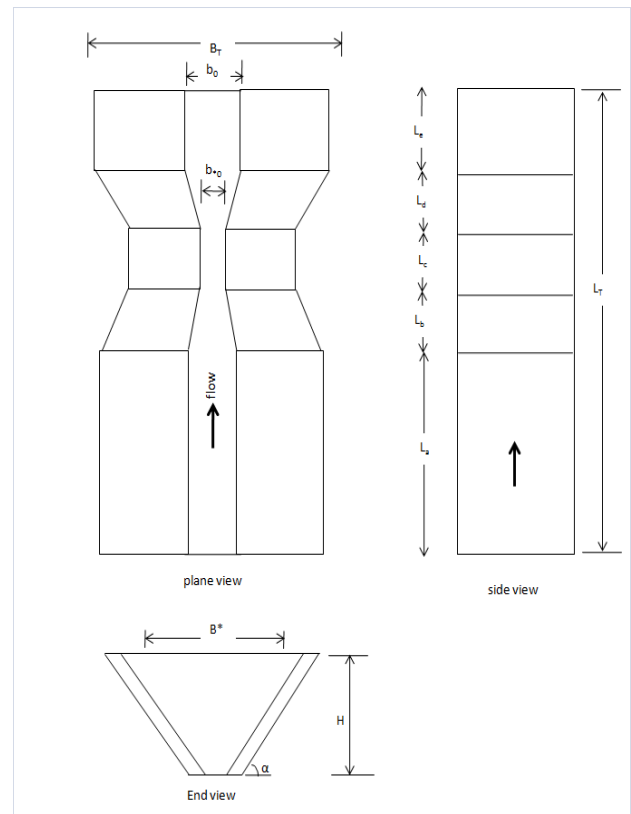


Figure 3. Geometry of a trapezoidal Venturi channel.

Table 1. Dimension of the Venturi flume in the rig³.

Symbol	Descriptions	Values
B_T	Top width of entrance to the converging section	0.455
B_*	Top width of exit from the converging section	0.355
b_0	Bottom width of entrance to the converging section	0.20
b_{*0}	Bottom width of exit from the converging section	0.10
H	Total height of the channel	0.35
α	Slope of the inclined sides of the channel	70
L_a	Length of the upstream section	2.95
L_b	Length of the converging section	0.15
L_c	Length of the throat section	0.20
L_d	Length of the diverging section	0.15
L_e	Length of the downstream section	0.25
L_T	Total length of the channel	3.70

³ In Table 1, the angle is in degree and side lengths in meters.

gical parameters of $\tau_y = 0$, $n = 0.5855$ and $K = 0.0631 \text{ Pa}\cdot\text{s}^n$. The channel was inclined at 0.08° .

The first measurement of the liquid level was taken at a position 2.18 m from the channel inlet, from where the liquid surface was somewhat stable. Subsequent level measurements to develop the profile of the flow, were taken at an interval of 10 cm before the throat, and at an interval of 5 cm from the throat to the last point (1.35 m from the first point).

The simulation of the model starts at a point 1.78 m from the leading end until the end of the channel. A total of 50 computational nodes was used, and the simulation was performed using MATLAB ode15s solver.

The dynamic model was simulated with initial conditions of 0.07 m for the level and 4.51 lit/s for flow rate until a steady state is reached. The results from the model simulation and the experimental data are shown in Figure 4.

Due to contraction of the channel before the throat, the liquid level decreases towards the throat. As can be seen in Figure 4, the flow passes through its critical depth within the throat. Since the flow is a free-flow (no imposed downstream boundary level), the flow remains supercritical after the critical point until the end. The figure shows that there is a good agreement between the simulated results and the experimental data. The simulated results deviate slightly from the experimental data after the flow reaches the critical depth and before the entrance to the downstream uncontracted section. This behaviour may be due to deviation of pressure distribution from the assumed hydrostatic distribution. The relative error associated with this scheme around this region is small as can be seen in the figure.

The flow profile given in Figure 4 is based on the average liquid level in the center line of the flow, assuming the flow occupies the full flow cross section at that level. The experimental study shows that the flow cross section remains full in the approaching section, and nearly full up to the entrance of the uncontracted section at the end. Within the uncontracted section, there is a strong effect of boundary layer, causing a drift of the fluid towards the channel walls. This effect reduces the centerline flow depth below its average value across every cross section in that region.

Figure 5 shows the profile of average velocity of the flow along the channel. Comparing with the critical velocity (wave celerity), which is about 0.673 m/s within the throat region, it can be seen that critical flow actually occurs within the throat, around 3.22 m from the leading end. Below this point, the flow is subcritical ($V < 0.673 \text{ m/s}$) and beyond it, the flow is supercritical ($V > 0.673 \text{ m/s}$).

4.2 Case 2 - Steep Chute Channel

This case considers a steep chute channel connecting a river to a reservoir. The channel has a rectangular cross-section of width 8 m, and length 1000 m. The channel is

divided into three regions with lengths 300 m, 300 m and 400 m, and bed slope 0.002, 0.009 and 0.001, respectively.

A steady state flow of water with flow rate of $20 \text{ m}^3/\text{s}$ through the channel is studied. The downstream imposed water level is 2.5 m, and Manning's roughness coefficient is chosen as 0.015. A similar example was published in (Meselhe *et al*, 1997).

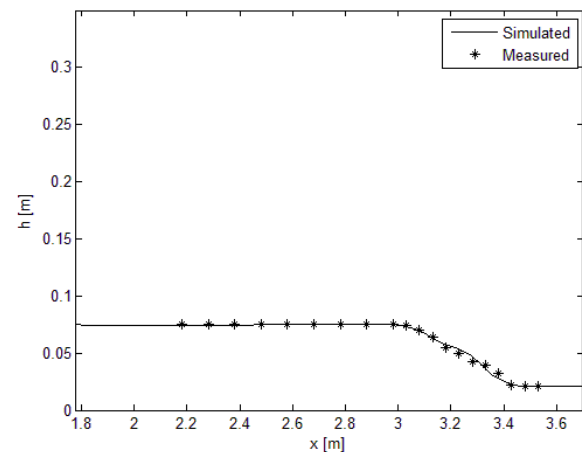


Figure 4. Level of the mudflow along the Venturi channel.

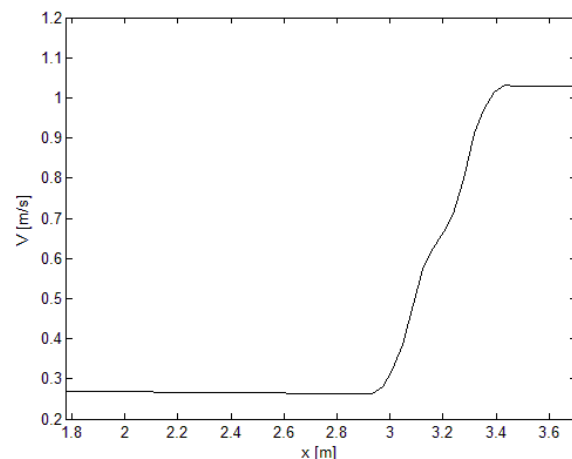


Figure 5. Velocity of the mudflow along the Venturi channel.

The model simulation was based on the dynamic model with initial conditions $20 \text{ m}^3/\text{s}$ for the flow rate, and 4.5 m for the water level for all computation points except the last node with imposed boundary condition of 2.5 m. Uniform grid of size 2 m was used compared to 20 m used in the literature. The simulation was performed using MATLAB ode15s solver.

The result obtained with the proposed scheme compared with a MESH scheme (Meselhe *et al*, 1997) is given in Figure 6. As can be seen in Figure 6, due to changes in the channel slope, the flow changes from subcritical flow in the first region to supercritical flow in the second region. There is an hydraulic jump before the end of the second region, returning the flow back to subcritical flow due to the imposed downstream water

level and due to the decrease in the channel slope at the last region. Critical depths are attained at the connecting point between the first two regions and somewhere during the shock propagation in the second region.

Figure 6 shows that the ODE scheme gives the same results as the MESH scheme except where the shock is located. The shock starts slightly later as given by the ODE scheme than as computed in the MESH scheme. The analytical result given in (Meselhe *et al*, 1997) shows that the shock location lies between the results given by MESH scheme and ODE scheme. Based on this, it can be inferred that the associated error with ODE scheme in predicting the shock is relatively small.

Figure 7 shows the evolutions of the upstream level and the level at midway of the channel. The result shows that the numerical scheme (ODE scheme) is stable, converging to steady state solution from the initial condition in about 10 minute without oscillations, and even appearance of shock as noted in midway of the channel does not influence its stability.

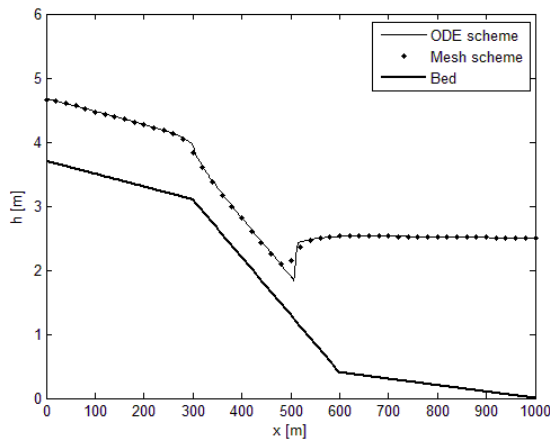


Figure 6. Profile of water flow in the steep chute channel.

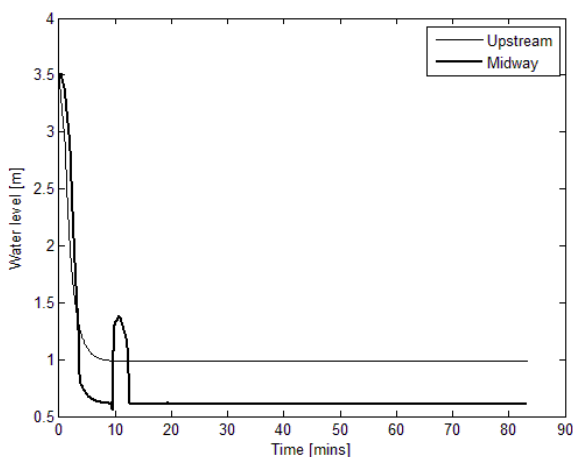


Figure 7. Evolution of water level with time in the steep chute channel.

4.3 Case 3 – Dynamic Flood Routing

To demonstrate the dynamic capability of the proposed scheme, consider its application to dynamic flood routing that is required for river planning and control.

Figure 8 shows a series of computed water level during a flood event in a 10 m wide rectangular channel comprising four reaches: ($S_1 = 0.006, L_1 = 500\text{ m}$), ($S_2 = 0.001, L_2 = 500\text{ m}$), ($S_3 = 0.006, L_3 = 500\text{ m}$) and ($S_4 = 0.001, L_4 = 500\text{ m}$). At the downstream boundary, a depth-discharge rating curve ($Q = 27.5h^{1.67}$) is imposed, and at the upstream boundary, the hydrograph, $Q(t)$ described in Eq. (14) is imposed (Tseng *et al.*, 2001). Manning's roughness coefficient is chosen as 0.02.

It can be seen in Figure 9 that the flowrate downstream attains the same peak value as the upstream flowrate. This shows that the volume of water in the channel is conserved during the flood event, despite the rise in the wave amplitude as depicted in Figure 10, where the peak level downstream is higher than the peak level upstream. Figure 8 also shows that the surge gradually moves upstream during the period the hydrograph rises, and downstream during the falling period of the hydrograph.

$$Q(t) = \begin{cases} 1.0\text{ m}^3/\text{s}; & 0 \leq t \leq 20\text{ mins} \\ 1.0 + 75 \left[1 - \cos\left(\frac{2\pi(t-20)}{120}\right) \right]; & 20 \leq t \leq 140\text{ mins} \\ 1.0\text{ m}^3/\text{s}; & 140 \leq t \leq 180\text{ mins} \end{cases} \quad (14)$$

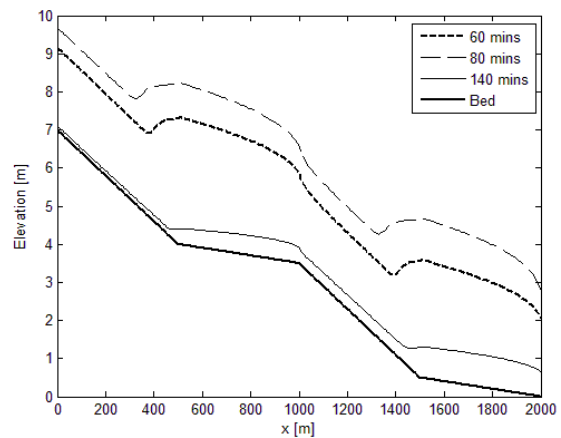


Figure 8. Profile of water level during hydrograph inflow.

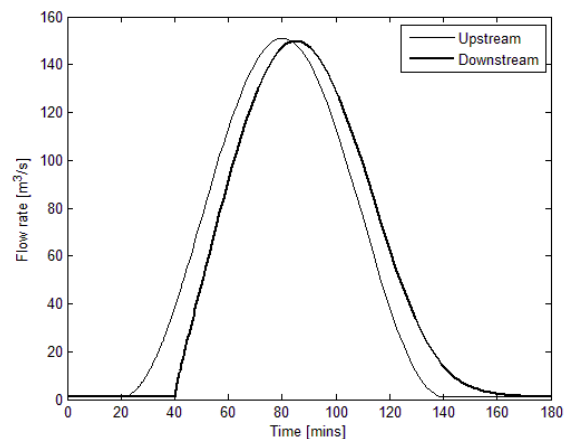


Figure 9. Evolution of hydrograph flow.

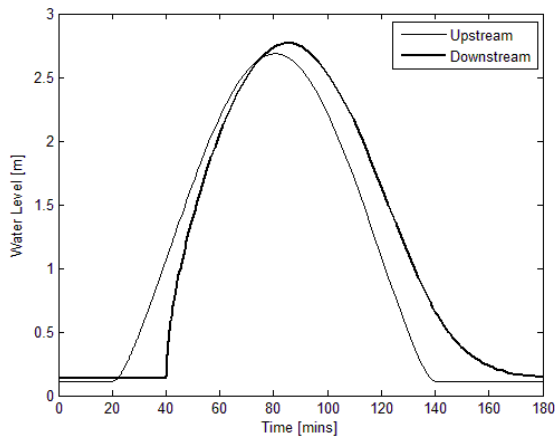


Figure 10. Evolution of upstream and downstream water levels.

5 Conclusions

In this paper, the Saint Venant Equations are discretized into a set of ordinary differential equations. A simple numerical algorithm (ODE scheme) based on these discrete equations is proposed for simulating transcritical flows in an open channel. The results show that by using an appropriate grid size and choosing the right ode solver, the scheme gives results which are in good agreement with some existing scheme.

The scheme is validated against experimental data obtained for a flow of mud in a Venturi channel, which confirms the applicability of the scheme to both Newtonian and non-Newtonian fluid behaviours.

Acknowledgements

The support from Statoil ASA, the Intelligent Drilling group is gratefully acknowledged.

References

- C. Berg, A. Malagalage, C.E. Agu, G.-O. Kaasa, K. Vaagsaether and B. Lie (2015): Model-Based Drilling Fluid Flow Rate Estimation Using Venturi Flume. *Proceedings, 2nd IFAC Workshop on Automatic Control in Offshore Oil and Gas Production*, Florianopolis, Brazil, May 27-29, 2015.
- C.E. Agu (2014): Model-Based Estimation of drilling mud Flow using a Venturi Channel. Master Thesis Report. Telemark University College, Porsgrunn, Norway, 2014.
- C.E. Agu and B. Lie. Numerical Solution of the Saint Venant Equation for Non-Newtonian Fluid. *Conference on Simulation and Modelling (SIMS 55)*, October 21-22, 2014. Aalborg, Denmark.

- C. Sart, J.-P. Baume, P.-O. Malaterre and V. Guinot (2010): Adaptation of Preissmann's Scheme for Transcritical Open Channel Flows. *Journal of Hydraulic Research*, 48(4): 428–440, 2010.
- E.A. Meselhe, F. Sotiropoulos and F.M. Holly-Jr. (1997): Numerical Simulation of Transcritical Flow in Open Channel. *Journal of Hydraulic Engineering*, 123(9): 0774–0783, 1997.
- H.K. Versteeg and W. Malalasekera (2007): An Introduction to Computational Fluid Dynamics: Finite Volume Method, 2nd ed. *England: Pearson Education Limited*, Edinburgh Gate Harlow Essex CM20 2JE, 2007.
- M.-H. Tseng, C.-A. Hsu and C.R. Chu (2001): Channel Routing in Open Channel Flows with Surges. *Journal of Hydraulic Engineering*, 127(2): 0115-0122, 2001.
- R. Sisson, P. Lacoste-Bouchet, M. Vera, M. Costello, E. Hedblom, B. Sheets and L. Sittoni (2012): An Analytical Model for Tailings Deposition from Pilot-Scale Testing. *In Proc. 3rd Int. Oil Sand Tailings Conference*, Edmonton, Canada, 2012.
- R. Szymkiewicz (2010): Numerical Modeling in Open Channel Hydraulics (Vol.83), *Springer*, ISBN 978-90-481-3673-5, 2010.
- T.Y. Zerihun and J.D. Fenton (2006): One-Dimensional Simulation Model for Steady Transcritical Free Surface Flows at Short Length Transitions. *Journal of Advances in Water Resources*, 29: 1598–1607, 2006. doi:10.1016/j.advwatres.2005.11.011.

Notation

A	Cross sectional area [m ²]
\bar{A}	Average cross sectional area [m ²]
g	Gravitational acceleration [m/s ²]
h	Free surface level [m]
K	Flow behaviour index [Pa.s ⁿ]
L	Length [m]
N	Spatial grid size
n	Fluid consistency index
P_{wet}	Wetted perimeter [m]
Q	Flow rate [m ³ /s]
R_h	Hydraulic radius [m]
S	Slope
x	Distance along a channel axis [m]
V	Average velocity [m/s]
Δx	The spacing of the grids along the channel [m]
β	Momentum correction coefficient
ρ	Density [kg/m ³]
θ	Inclination of the channel bottom [degree]

Optimal Control of an EMU Using Dynamic Programming and Tractive Effort as the Control Variable

Nima Ghaviha¹ Markus Bohlin² Fredrik Wallin¹ Erik Dahlquist¹

¹School of Business, Society and Engineering, Mälardalen University, Sweden, {nima.ghaviha, fredrik.wallin, erik.dahlquist}@mdh.se
²SICS Swedish ICT, Sweden, markus.bohlin@sics.se

Abstract

Problem of optimal train control with the aim of minimizing energy consumption is one of the old optimal control problems. During last decades different solutions have been suggested based on different optimization techniques, each including a certain number of constraints or different train configurations, one being the control on the tractive effort available from traction motor. The problem is previously solved using dynamic programming for trains with continuous tractive effort, in which velocity was assumed to be the control variable. The paper at hand presents a solution based on dynamic programming for solving the problem for trains with discrete tractive effort. In this approach, tractive effort is assumed to be the control variable. Moreover a short comparison is made between two approaches regarding accuracy and ease of application in a driver advisory system.

Keywords: train optimal control, dynamic programming

1. Introduction

The problem of optimal train control have been studied for decades (e.g. see (Ichikawa 1968)). Different mathematical solutions have been offered based on different optimization techniques. A common approach is coast control which is acceleration with full power until max speed and then driving the train with zero tractive effort until a certain speed (i.e. coasting speed) and then braking with full power. The problem is to find the best coasting speed. (Colak, Czarkowski et al. 2012) solves the coast control problem using Particle Swarm Optimization. (Chang and Sim 1997) and (Wong * and Ho 2004) solve the problem using a Genetic Algorithm and (Yang, Li et al. 2012) solves the problem for the network of trains. Heuristic searching methods have also been used to find the optimum coasting points (see (Wong and Ho 2004)). The coast control approach however is only suitable for short distance trips (e.g. subway trips) and other approaches are needed for long distance trips.

Different optimization techniques are suggested for solving the problem for the long distance trips: (Yasunobu, Miyamoto et al. 1983) solves the problem using fuzzy logic. (Liu and Golovitcher 2003) introduces an approach based on maximum principle, and (Howlett 2000) and (Shuai, Xiang et al. 2013) use Pontryagin Principle. The gradient method is used in (Miyatake and Ko 2007) and (Miyatake and Ko 2007). Sequential Quadratic Programming is used in (Miyatake and Matsuda 2008) and (Miyatake and Matsuda 2009) to solve the problem for trains with an on-board energy storage device. Dynamic Programming is used in (Ko, Koseki et al. 2004), (Miyatake, Haga et al. 2009), (Miyatake and Haga 2010) and (Franke, Terwiesch et al. 2000). A comparison is made in (Miyatake and Ko 2010) between three approaches of SQP, Gradient Method and dynamic programming. According to (Miyatake and Ko 2010) dynamic programming is the best approach when it comes to dealing with constraints on the state variables.

The final aim of developing algorithms for solving the optimal train control problem is to use them for giving instructions to driver on how to drive a train using a driver advisory systems (DAS). (Panou, Tzieropoulos et al. 2013) gives an overview on current DAS systems in the market and evaluates them based on different criteria.

In this paper an approach is presented based on dynamic programming for the optimal control of electric trains. The problem was previously solved in (Ghaviha, Bohlin et al. 2014) and (Ghaviha, Bohlin et al. 2015) for trains with continuous tractive effort with velocity as the control variable. However, in some trains tractive effort is discrete, meaning that driver has access to certain tractive efforts (notches) for acceleration and braking. The approach presented in (Ghaviha, Bohlin et al. 2014) is not suitable for such trains. In the approach presented here, tractive effort (i.e. notch number) is assumed to be the control variable which makes the approach suitable for such trains. Moreover a short comparison is made between

two approaches regarding accuracy and ease of application for a DAS system.

2. Train Model

The train is modeled according to equations of motion as presented in (Ghaviha, Bohlin et al. 2014). Forces affecting the train are the tractive effort (F_t), gravitational force (F_g) and running resistance (F_{rr}), which includes the aerodynamic resistance:

$$F_g = m * g * \frac{s}{1000} \tag{1}$$

$$F_{rr} = A + B * v + C * v^2 \tag{2}$$

$$F_a = m * a \tag{3}$$

$$F_a = F_t + F_{rr} + F_g, \tag{4}$$

where A , B and C are constants, m is mass of the train, g is the earth's gravitational constant, $\frac{s}{1000}$ is sinus estimation of slope, a is the acceleration and F_a is acceleration force. Energy consumption is also based on the equations of motion i.e. force time distance. The train is equipped with regenerative brakes which regenerates 80 percent of the energy of the tractive effort and the gradient force back to catenary system during the brake. Energy equations are as follows:

$$E = F_t * dx \quad ; \text{ during acceleration} \tag{5}$$

$$E = 0.8 * (F_a + F_g) * dx \quad ; \text{ during braking,} \tag{6}$$

where dx is the distance traveled.

3. Approach

The approach is based on discrete dynamic programming and Bellman's backward approach. States of the train are represented using three discretized variables of time (t), distance (x) and velocity (v), among which time is the independent variable and the rest are the state variables. In the approach previously presented in (Ghaviha, Bohlin et al. 2014), velocity in the next time step is assumed to be the control variable whereas in the approach presented here, the tractive effort is the control variable (i.e. u_i). Following terms are used in the approach presented here:

- Starting point: it's the start of the trip and therefore defined as $(0,0,0)$, which means time zero, distance zero and zero velocity.
- Destination point: It is the state in which the train is supposed to be at the end of the trip which is represented by $(T,X,0)$, where T is the last time

step and X is the last distance step and zero velocity.

- Minimum cost-to-go: minimum energy needed in order to get the train from a certain state to the destination point.
- First state: is the state in which the minimum cost-to-go is desirable.
- Second state: A state one time step ahead of the first state after applying the control u_i . It is presented as (t_{fi}, x_{fi}, v_{fi}) .

The optimization technique is based on the principle of optimality which can be presented as follows:

$$E(t_s, x_s, v_s) = \min_{u_i} (de(s, u_i) + E(t_{fi}, x_{fi}, v_{fi})) \quad ; \forall u_i, \tag{7}$$

where $E(t_s, x_s, v_s)$ is the minimum energy needed to get the train from the state (t_s, x_s, v_s) to the destination point (i.e. minimum cost-to-go). $de(s, u_i)$ is the energy needed to get the train from the first state to the second state, when applying the control u_i (i.e. the transition cost) and $E(t_{fi}, x_{fi}, v_{fi})$ is the minimum cost-to-go for the second state. Since $E(t_{fi}, x_{fi}, v_{fi})$ is only available for a certain number of states based on the control u_i and due to discretization of distance and velocity, x_{fi} and v_{fi} should be calculated based on other available variables and rounded to the closest distance and velocity step. The following equations represent the calculations:

$$F_a = F_t + F_{rr} + F_g \tag{8}$$

$$a = F_a/m \tag{9}$$

$$v_{fi} = a * dt + v_s \tag{10}$$

$$x_{fi} = x_s + \frac{(v_s + v_{fi})}{2} * dt, \tag{11}$$

where dt is the length of one time step. Assuming that the minimum cost-to-go at the destination point is known, by going backward in time the minimum cost-to-go for the starting point and the optimal sequence of the states to the destination point can be calculated.

4. Results

Figure 1 and 2 show optimum speed profile and control profile for a trip of 120 sec and 2 km. There are no speed limits nor elevations during the trip. The train in this example has the mass of 100 tons with nine notches for acceleration and nine notches for deceleration plus a coasting notch (i.e. no tractive effort) which means 10 control variables in total (Trip 1).

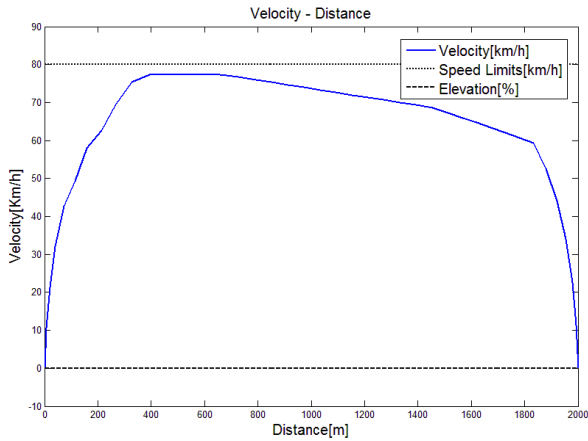


Figure 1. Optimum speed profile for a trip of 2km and 120 sec for a train with 9 notches for acceleration and 9 notches for brake (Trip 1)

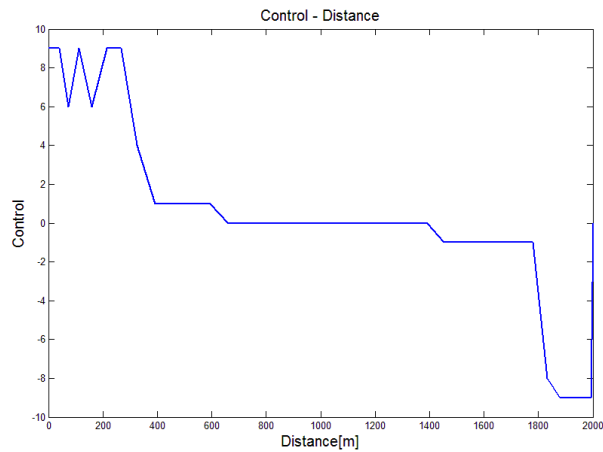


Figure 2. Optimum control profile for a trip of 2km and 120 sec for a train with 9 notches for acceleration and 9 notches for brake (Trip 2)

The same train is run on the same track with elevations and speed limits. Trip time in this case is 170 sec (Trip 2). The results are available in figure 3 and 4. The dotted line represents the speed limit and the dashed line represents the elevations.

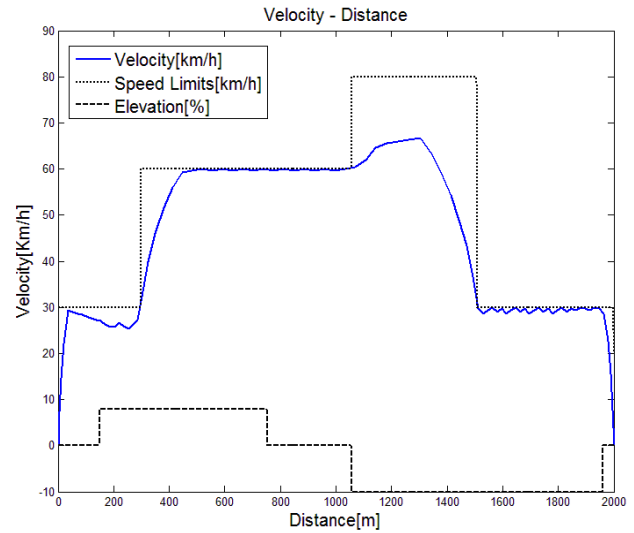


Figure 3. Optimum speed profile for a trip of 2km and 220 sec for a train with 9 notches for acceleration and 9 notches for brake (Trip 2)

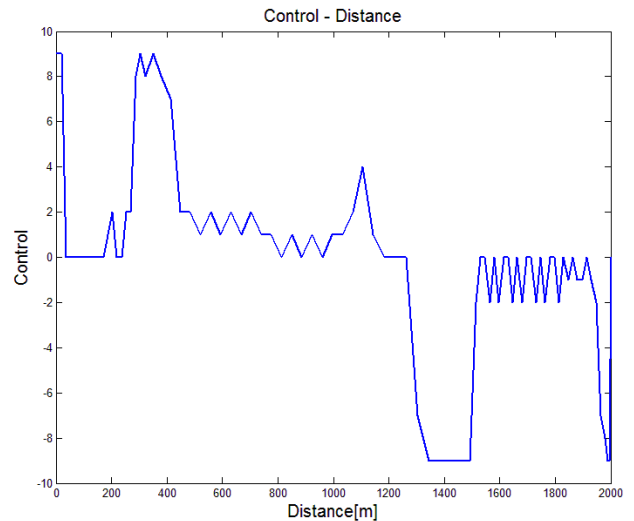


Figure 4. Optimum control profile for a trip of 2km and 220 sec for a train with 9 notches for acceleration and 9 notches for brake (Trip 2)

This approach can also be used for the trains with continuous tractive effort. In that case however, high discretization on the control variable is needed. Figures 5 and 6 show optimum speed profile and tractive effort profile for a train with continuous tractive effort on a level track with no elevation. Trip time is assumed to be 120 sec and track length is 2 km (Trip 3). The tractive effort is discretized in 120 steps.

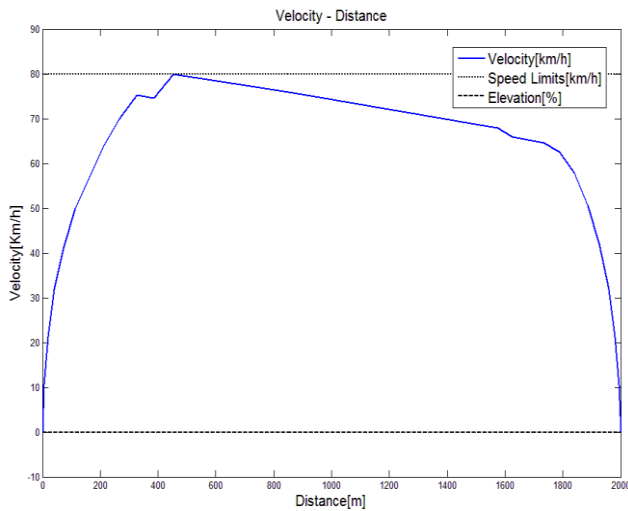


Figure 5. Optimum speed profile for a trip of 2km and 120 sec for a train with 60 notches for acceleration and 60 notches for brake (Trip 3)

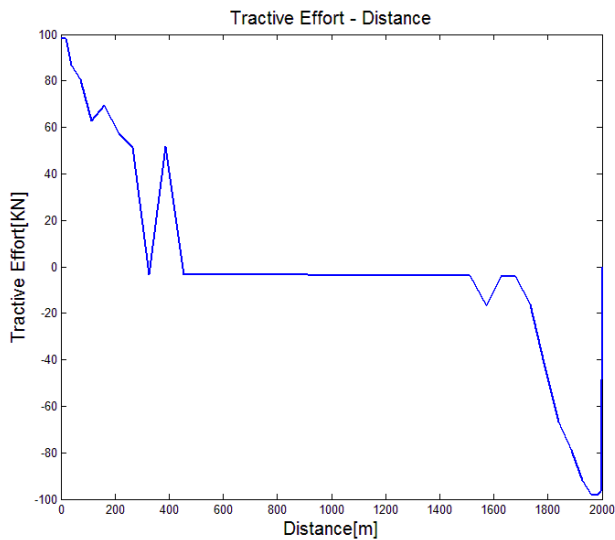


Figure 6. Optimum control profile for a trip of 2km and 120 sec for a train with 60 notches for acceleration and 60 notches for brake (Trip 3)

The same train is run on the same track with elevations and speed limits. The trip time in this case is 230 sec (Trip 4). The results are available in figure 7 and 8.

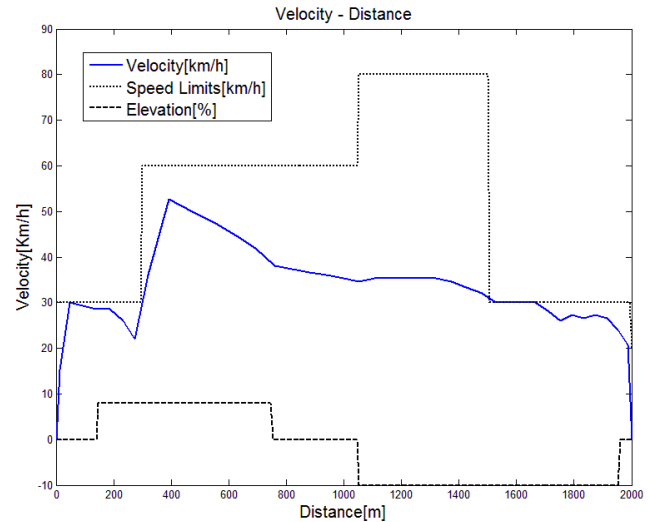


Figure 7. Optimum speed profile for a trip of 2km and 230 sec for a train with 60 notches for acceleration and 60 notches for brake (Trip 4)

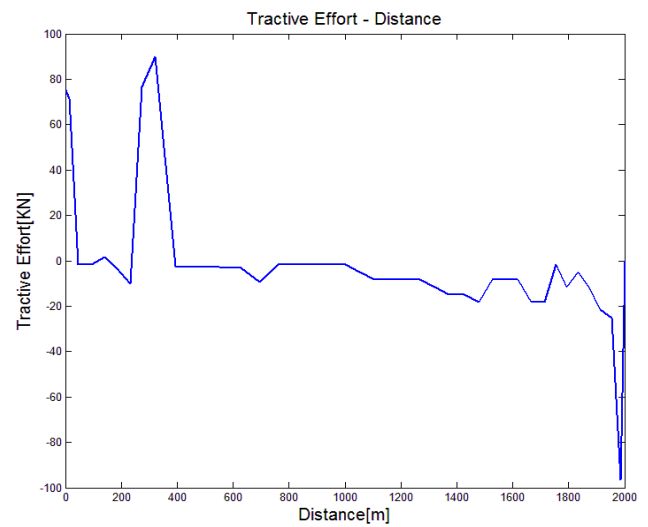


Figure 8. Optimum control profile for a trip of 2km and 230 sec for a train with 60 notches for acceleration and 60 notches for brake (Trip 4)

Table 1 shows the train configuration and the track data for each trip.

Table 1. Train data and track data for the 4 trips. Trip distance is 2 km for all trips

	<i>Number of control variables</i>	<i>Trip time [sec]</i>	<i>Speed limits</i>	<i>Elevations</i>
Trip 1	19	120	no	No
Trip 2	19	170	yes	Yes
Trip 3	120	120	no	No
Trip 4	120	230	yes	yes

5. Discussion

In this section the application and the accuracy of the approach is discussed and a short comparison is made between the two approaches (i.e. the one presented in (Ghaviha, Bohlin et al. 2014) and the approach presented here). The comparison is made with regard to two criteria of accuracy and ease of application.

5.1. Application

The approaches presented here and in (Ghaviha, Bohlin et al. 2014) are developed to be a base for a driver advisory system, which is a system that gives instructions to driver on how to drive a train with the aim of minimizing the energy consumption. Traction motor in some trains provide a certain number of notches for acceleration and braking, in other words the tractive effort is discrete, whereas in other trains the tractive effort is continuous which is like the gas pedal in cars. When it comes to controlling a train, driver has the direct control on the tractive effort of the train. Therefore the best way to design a driver advisory system is to give instructions in the form of optimal tractive effort. This would be easy in trains with different notches for the tractive effort and therefore the approach with the tractive effort as the control variable suits best for these kinds of trains. In the trains with the continuous tractive effort however, as the driver has access to continuous tractive effort, following the instructions in the form of the tractive effort would be problematic for the driver. In this case the optimum velocity sounds like a more suitable form of instruction. Although it is possible to give instruction in the form of the optimum velocity using the approach with the tractive effort as control variable, it is better to use the approach with the velocity as the control variable due to accuracy issues, which will be discussed in the next section, Accuracy.

5.2. Accuracy

As mentioned in the Approach section, x_{fi} and v_{fi} should be rounded to the closest distance and velocity step. As the result the model has an inaccuracy regarding the velocity and the distance calculations. To study these, two following errors are introduced:

$$e_{vi} = v_{ci} - v_{ri} \quad (12)$$

$$e_{xi} = x_{ci} - x_{ri} \quad (13)$$

Where e_{vi} is the difference between the real velocity (v_{ri}) and the rounded velocity (v_{ci}) in time step i and e_{xi} is the difference between the real distance (x_{ri}) and the rounded distance (x_{ci}) in time step i . Table 1 shows

the Root-Mean-Square error of the total errors for the 4 trips presented in the results section.

Table 2. RMSE of distance and velocity variables for the four trips

	<i>RMSE for $x[m]$</i>	<i>RMSE for $v[km/h]$</i>
Trip 1	1.988579	0.148767
Trip 2	1.008387	0.112893
Trip 3	1.994318	0.29593
Trip 4	2.157717	0.284606

As mentioned before, trip 3 and 4 are meant for the train with continuous tractive effort. A solution can also be generated using the previous approach presented in (Ghaviha, Bohlin et al. 2014). The same error is also calculated for that solution and can be seen in table 3. Note that since the velocity in the next time step is assumed to be the control variable in the previous approach, there would be no error for the velocity. This is because of the fact that in the previous approach, the velocity is selected, rather than being calculated and used as state variable (Ghaviha, Bohlin et al. 2014). Moreover for the sake of comparison, the same time, distance and velocity discretization is used for both approaches.

Table 3. RMSE of distance for the solution of trip 3 and 4 using the previous approach

	<i>RMSE for $x[m]$</i>
Trip 3	2.090435
Trip 4	2.480182

As it can be seen the errors are negligible considering the fact that the length of the track is 2 km and the maximum train speed is 80 km per hours. Both approaches also give almost the same RMSE for trip 3 and 4. However, when it comes to the comparison of the two approaches, the one presented in (Ghaviha, Bohlin et al. 2014) is more promising, as the distance is the only variable which is estimated in that approach.

6. Conclusion

A train model and an approach is presented in this paper for the optimal control of an electric train based on discrete dynamic programming. The problem was previously solved with the velocity as the control variable. In the approach presented here tractive effort is used as the control variable. This approach is most

suitable for the trains with different notches for the acceleration and braking (discrete tractive effort) as the control variable can be adjusted according to the number of notches available in the train. However for the trains with continuous control on the tractive effort, the approach presented in (Ghaviha, Bohlin et al. 2014) is more suitable as it has higher accuracy compared to the approach presented in this paper. It is to be mentioned that a more thorough study is needed to compare the two approaches regarding the application and instruction issues, as more data and information is needed regarding the drivers' behavior when using a driver advisory system.

Acknowledgements

This research is funded by VINNOVA, grant number 2014-04319. The authors would like to thank Christer Holmberg from Bombardier Transportation Västerås for the help and support with the data and information on electric trains and propulsion system.

References

- Chang, C. S. and S. S. Sim (1997). "Optimising train movements through coast control using genetic algorithms." *Electric Power Applications, IEE Proceedings - 144*(1): 65-73.
- Colak, K., D. Czarkowski, et al. (2012). *Energy minimization for catenary-free mass transit systems using Particle Swarm Optimization. Electrical Systems for Aircraft, Railway and Ship Propulsion (ESARS), 2012.*
- Franke, R., P. Terwiesch, et al. (2000). An algorithm for the optimal control of the driving of trains. *Decision and Control, 2000. Proceedings of the 39th IEEE Conference on.*
- Ghaviha, N., M. Bohlin, et al. (2014). An Algorithm For Optimal Control of an Electric Multiple Unit. *Proceedings from The 55th Conference on Simulation and Modelling (SIMS 55), 21-22 October, 2014. Aalborg, Denmark* ∴ Linköping, Linköping University Electronic Press.
- Ghaviha, N., M. Bohlin, et al. (2015). "Optimal Control of an EMU Using Dynamic Programming." *Energy Procedia* 75: 1913-1919.
- Howlett, P. (2000). "The Optimal Control of a Train." *Annals of Operations Research* 98(1-4): 65-87.
- Ichikawa, K. (1968). "Application of Optimization Theory for Bounded State Variable Problems to the Operation of Train." *Bulletin of JSME* 11(47): 857-865.
- Ko, H., T. Koseki, et al. (2004). "Application of dynamic programming to optimization of running profile of a train." *Computers in railways IX*: 103-112.
- Liu, R. and I. M. Golovitcher (2003). "Energy-efficient operation of rail vehicles." *Transportation Research Part A: Policy and Practice* 37(10): 917-932.
- Miyatake, M. and H. Haga (2010). *Optimization of speed profile and quick charging of a catenary free train with on-board energy storage. Electrical Systems for Aircraft, Railway and Ship Propulsion (ESARS), 2010.*
- Miyatake, M., H. Haga, et al. (2009). Optimal speed control of a train with On-board energy storage for minimum energy consumption in catenary free operation. *Power Electronics and Applications, 2009. EPE '09. 13th European Conference on.*
- Miyatake, M. and H. Ko (2007). Numerical analyses of minimum energy operation of multiple trains under DC power feeding circuit. *Power Electronics and Applications, 2007 European Conference on.*
- Miyatake, M. and H. Ko (2007). Numerical Optimization of Speed Profiles of Inverter Trains Considering DC Feeding Circuit. *Power Conversion Conference - Nagoya, 2007. PCC '07.*
- Miyatake, M. and H. Ko (2010). "Optimization of Train Speed Profile for Minimum Energy Consumption." *IEEJ Transactions on Electrical and Electronic Engineering* 5(3): 263-269.
- Miyatake, M. and K. Matsuda (2008). Optimal speed and charge/discharge control of a train with onboard energy storage devices for minimum energy operation. *Power Electronics, Electrical Drives, Automation and Motion, 2008. SPEEDAM 2008. International Symposium on.*
- Miyatake, M. and K. Matsuda (2009). "Energy Saving Speed and Charge/Discharge Control of a Railway Vehicle with On-board Energy Storage by Means of an Optimization Model." *IEEJ Transactions on Electrical and Electronic Engineering* 4(6): 771-778.
- Panou, K., P. Tzieropoulos, et al. (2013). "Railway driver advice systems: Evaluation of methods, tools and systems." *Journal of Rail Transport Planning & Management* 3(4): 150-162.
- Shuai, S., L. Xiang, et al. (2013). "A Subway Train Timetable Optimization Approach Based on Energy-Efficient Operation Strategy." *Intelligent Transportation Systems, IEEE Transactions on* 14(2): 883-893.
- Wong *, K. K. and T. K. Ho (2004). "Dynamic coast control of train movement with genetic algorithm." *International Journal of Systems Science* 35(13-14): 835-846.
- Wong, K. K. and T. K. Ho (2004). "Coast control for mass rapid transit railways with searching methods." *Electric Power Applications, IEE Proceedings - 151*(3): 365-376.
- Yang, L., K. Li, et al. (2012). "Optimizing trains movement on a railway network." *Omega* 40(5): 619-633.
- Yasunobu, S., S. Miyamoto, et al. (1983). "A Fuzzy Control for Train Automatic Stop Control." *Transactions of the Society of Instrument and Control Engineers* 19(11): 873-880.

Multiphysics Numerical Modeling of a Fin and Tube Heat Exchanger

Shobhana Singh Kim Sørensen Thomas Condra

Department of Energy Technology, Aalborg University, Denmark
ssi@et.aau.dk, kso@et.aau.dk, tc@et.aau.dk

Abstract

In the present research work, a modeling effort to predict the performance of a liquid-gas type fin and tube heat exchanger design is made. Three dimensional (3D) steady state numerical model is developed using commercial software COMSOL Multiphysics based on finite element method (FEM). For the purposes here, only gas flowing over the fin side is simulated assuming constant inner tube wall temperature. The study couples conjugate heat transfer mechanism with turbulent flow in order to describe the temperature and velocity profile. In addition, performance characteristics of the heat exchanger design in terms of heat transfer and pressure loss are determined by parameters such as overall heat transfer coefficient, Colburn j -factor, flow resistance factor, and efficiency index. The model provides useful insights necessary for optimization of heat exchanger design.

Keywords: Fin and tube heat exchanger, turbulent flow, conjugate heat transfer, numerical modeling, COMSOL

1 Introduction

Heat exchangers are commonly used thermal energy systems for a variety of applications. They are the key components in waste heat recovery technologies. Selection of suitable heat exchanger design is essential to achieve maximum efficiency of the system. However, the thermal performance of liquid-gas heat exchangers is greatly influenced by the high thermal resistance on gas-side which account for more than 80% of the total thermal resistance [Malapure et al., 2007; Kundu and Lee, 2011; Yaïci et al., 2014]. Over the past decade, fin and tube heat exchangers have been given a considerable attention among other available heat exchanger designs due to extended heat transfer surface area and ease of manufacturing [Rocha et al., 1997; Jang and Yang, 1998; Matos et al., 2004; Mon and Gross, 2004; Erek et al., 2005; Ibrahim and Gomma, 2009; Taler and Oclon, 2014; Hatami et al. 2014a; Łopata and Oclon, 2015].

Several numerical investigations of fin and tube heat exchangers for different applications including waste recovery systems are available in the literature. Chen et al. (2007) performed a numerical simulation of laminar flow with the finite-volume method in a finned

oval tube heat exchanger and studied conjugate heat transfer along with flow patterns and pressure distributions. Hatami et al. (2014b) numerically studied two cases for fin type heat exchangers in engines for exhaust waste heat recovery and concluded that recovered heat can be improved by increasing the fin numbers and length where maximum heat recovery occurs. Vortex generators of different types on the fin surface of the heat exchangers have also been studied extensively as an effective method to improve the air side heat transfer performance [Fiebig, 1995; Jacobi and Shah, 1995; Chang et al., 2009; Habchi et al. 2012; Gong et al., 2015; Li et al., 2015]. Chu et al. (2009) employed 3D numerical simulations to investigate the heat transfer characteristics and flow structure in full-scale fin-and-oval-tube heat exchangers with longitudinal vortex generators. Moreover, three dimensional simulations were accomplished by Borrajo-Peláez et al. (2010) to compare both air side and water side model and evaluate the performance through non-dimensional parameters: the air side Nusselt number and friction factor.

In most of the applications, various fin patterns (such as wavy, louver, slit, and convex-louver) are adopted in order to improve the performance of heat exchanger [Wang et al., 1999; Tao et al., 2007; Tang et al., 2009; Kundu and Lee, 2011]. Malapure et al. (2007) investigated fluid flow and heat transfer characteristics of louvered fins and flat tube with single and double row of tubes with in compact heat exchangers by 3D numerical simulations. Tao et al. (2007) also performed 3D numerical simulations for laminar flow of wavy fin-and-tube heat exchangers and reported that the fin efficiency at the inlet region of wavy fins is larger than that of plain plate fins. Most recently, Cobian- Iñiguez et al. (2015) introduced a methodology of analysis based on local and global energy balances to determine the hydrodynamic and heat transfer characteristics. The authors also emphasized on analyzing the parameters such as fin spacing, tube diameter and alignment, and flow velocity for designing efficient heat exchangers.

Innovative fin and tube heat exchanger designs always offer scope to explore possible opportunities for overall performance improvement. With this view in mind, present paper mainly focusses on predicting the performance of a fin and tube heat exchanger design by

utilizing multiphysics approach. 3D steady state numerical model using FEM is developed to predict the heat transfer characteristics as well as flow profile for a given fin and tube heat exchanger design. Heat exchanger performance characteristics, such as overall heat transfer coefficient, Colburn j-factor, flow resistance factor and efficiency index are estimated.

2 Fin and tube heat exchanger design

The heat exchanger design analyzed in the present work is of liquid-gas fin and tube type with plain fins and circular tubes. The typical configuration of the fin and tube exchanger is shown in Figure 1. The tubes are arranged in an in-line manner in a flow direction at fixed distance to each other, and fins are attached on a set of two tubes from both sides leaving a gap in between. It should be noted that the contact surface between the fins and tubes is assumed to be perfectly conducting (i.e. no gaps due to roughness). Figure 2 represents the schematic diagram of the single unit of heat exchanger design with specified dimensions as described in Table 1. The single unit design includes two circular tubes and two fins which on repetitive arrangement at fixed distance builds the complete fin and tube heat exchanger configuration for desired applications. The conjugate heat transfer phenomenon includes simultaneous convective heat transfer from the flowing fluid to the fin surface and tube outer wall surface, and conductive heat transfer from the outer wall to inner wall of the tube as well as through fin to tube.

3 Model development

3.1 Computational geometry

Numerical model in the present study entails a simple 3D computational geometry of the fin and tube heat exchanger design. Having symmetric geometry of the heat exchanger, we simulated only one half of the fin and tube heat exchanger unit. This keeps the simplicity of the model and reduces computational time as well as cost. In applications where evaporation or condensation of the fluid takes place inside the tubes, average temperature of inner tube wall temperature does not change or remains constant. For that purpose, only the fluid flowing over the fins outside the tubes is modeled in the present work. The 3D computational geometry consists of three distinct domains: gas domain, fin domain, and tube domain as shown in Figure 3. The dimensions of the heat exchanger geometry is chosen according to the given heat exchanger prototype design (Figure 1). To capture flow profile at the inlet, outlet and both sides of the heat exchanger geometry, gas domain is simulated with length 1.03 times of fin length (L_f) and width 1.18 times of fin width (W_f).

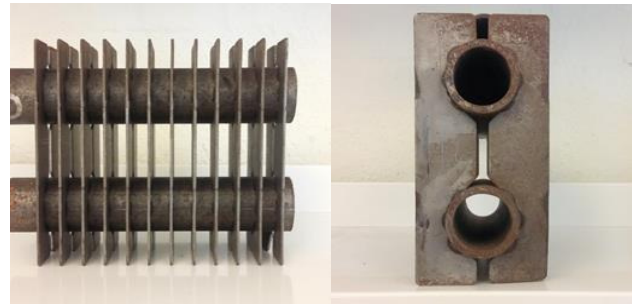


Figure 1. Pictorial view of the fin and tube heat exchanger prototype.

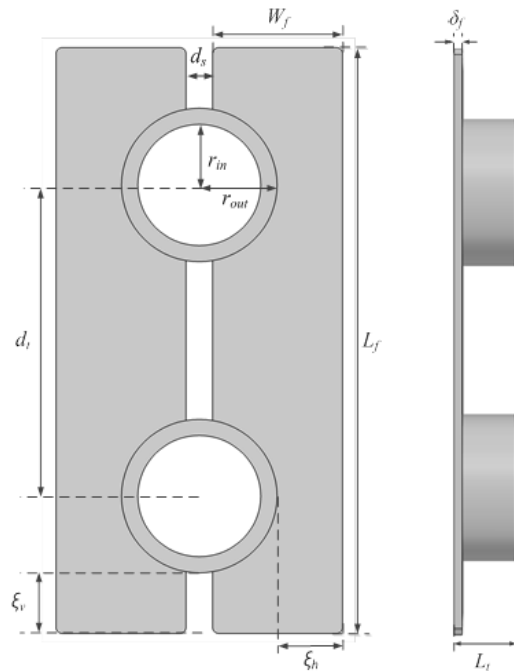


Figure 2. Schematic of the single unit of fin and tube heat exchanger.

Table 1. Design parameters used in numerical model

Description	Symbol	Value	Unit
Length of the gas domain	L_g	150.0	mm
Width of the gas domain	W_g	37.5	mm
Length of the fin	L_f	145.0	mm
Width of the fin	W_f	31.75	mm
Thickness of the fin	δ_f	2.0	mm
Distance between two fins (center to center)	d_f	13.0	mm
Thickness of the gap in fin	d_s	6.5	mm
Inner radius of the tube	r_{in}	15.0	mm
Outer radius of the tube	r_{out}	19.0	mm
Length of the tube	L_t	15.0	mm
Tube spacing (center to center)	d_t	77.0	mm
Tube pitch (vertical)	ζ_v	15.0	mm
Tube pitch (horizontal)	ζ_h	16.0	mm

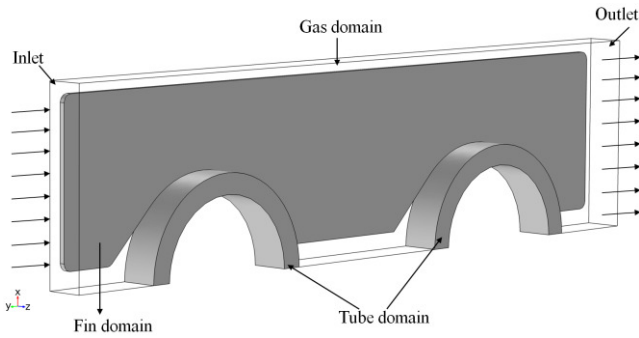


Figure 3. Domains and boundaries of computational geometry used in the numerical model.

Furthermore, gas domain represents the inlet and outlet boundary planes through which hot fluid enters and leaves the domain, respectively. The flow of gas in the gas domain is in negative y-direction. Fin and tube are solid domains that are assumed to be made of steel and the gas domain is simulated as ideal gas with constant air properties.

3.2 Governing Equations

The present 3D numerical model of a fin and tube heat exchanger design includes conjugate heat transfer that corresponds to the combination of heat transfer phenomenon in fin, tube and gas domains simultaneously. To simplify the model and computation, following assumptions are made:

- Steady state flow and heat transfer.
- Incompressible gas flow.
- Constant inner tube wall temperature.
- Thermal contact resistance is negligible.
- Constant material properties.
- No periodic boundary condition.

Considering the turbulent nature of the flow in the gas domain, k- ϵ turbulence model is used to solve the Reynolds-Averaged Navier-Stokes (RANS) equations for the averaged velocity and pressure fields in the gas flow domain. k- ϵ model is chosen as it performs well for most of the flow problems around complex geometries and can deliver an accurate enough result with good convergence rate and relatively low memory requirements.

The coupling of mass balance and the momentum balance for the flow in the gas domain is governed by RANS equations [Kuzmin et al., 2007; Hatami et al., 2014c] which are expressed as:

$$\nabla \cdot \mathbf{u} = 0 \quad (1)$$

$$\rho(\mathbf{u} \cdot \nabla)\mathbf{u} = \nabla \cdot [-p\mathbf{I} + \mu(\nabla\mathbf{u} + (\nabla\mathbf{u})^T)] + \mathbf{F} \quad (2)$$

where, \mathbf{u} [m/s] is the averaged velocity vector, ρ [kg/m³] and μ [Pa.s] are the density and dynamic viscosity of the gas, respectively.

p [Pa] is the averaged pressure, and \mathbf{F} [N/m³] is the body force vector.

The k- ϵ turbulence model also solves the turbulent kinetic energy, k [m²/s²] and turbulent dissipation rate, ϵ [m²/s³]. The differential transport equations describing the k and ϵ in the gas domain are:

$$\rho\mathbf{u} \cdot \nabla k = \nabla \cdot \left[\left(\mu + \frac{\mu_T}{\sigma_k} \right) \nabla k \right] + P_k - \rho\epsilon \quad (3)$$

$$\rho\mathbf{u} \cdot \nabla \epsilon = \nabla \cdot \left[\left(\mu + \frac{\mu_T}{\sigma_\epsilon} \right) \nabla \epsilon \right] + C_{\epsilon 1} \frac{\epsilon}{k} P_k - C_{\epsilon 2} \frac{\epsilon^2}{k} \quad (4)$$

where, P_k is the production term, which is defined as:

$$P_k = \mu_T [\nabla\mathbf{u} : (\nabla\mathbf{u} + (\nabla\mathbf{u})^T)] \quad (5)$$

The turbulent viscosity, μ_T is modeled as:

$$\mu_T = \rho C_\mu \frac{k^2}{\epsilon} \quad (6)$$

where, C_μ , $C_{\epsilon 1}$, $C_{\epsilon 2}$, σ_k , and σ_ϵ are model constants with values 0.09, 1.44, 1.92, 1.0 and 1.3, respectively which are used to numerically solve the model [Wilcox, 1998].

The energy transport in terms of heat transfer within gas domain is driven by both convection and conduction; however, based on the thermal properties of the fluid and the inlet velocity assumed in this study, it is mainly dominated by convection. The differential equation that describes the heat transfer in gas domain and solves for the temperature field is:

$$\rho C_p \mathbf{u} \cdot \nabla T + \nabla \cdot \mathbf{q} = Q \quad (7)$$

where, \mathbf{q} [W/m²] is the heat flux vector and is expressed as: $\mathbf{q} = -k\nabla T$. T [K] is the temperature, C_p [J/(kg.K)] is the heat capacity at constant pressure, k [W/(m.K)] is the thermal conductivity, and Q [W/m²] is the heat source or sink.

The heat transfer in the fin and tube domain is dominated by conduction and hence governs by Fourier's Law of heat conduction. It is to note that due to small temperature difference and lower emissivity, heat transfer through radiation is neglected. The heat transfer equation in the fin and tube domains also account for additional heat source or sink term and is expressed in the following form of energy conservation:

$$\rho C_p \mathbf{u} \cdot \nabla T + \nabla \cdot \mathbf{q} = Q \quad (8)$$

The first term represents contribution of translational motion to the heat transfer in solids, which is negligible in this case, hence neglected. Second term is the conductive heat flux vector, which is expressed as: $\mathbf{q} = -k_s \nabla T$ where, k_s [W/(m.K)] is the thermal conductivity of fin and tube material.

3.3 Boundary conditions

To pose a well-defined problem, we impose suitable boundary conditions to numerically solve the governing equations. Initial condition is simulated by assuming no gas flow in gas domain i.e. the velocity field is set to 0 m/s with pressure set to 0 Pa. Furthermore, the temperature of all three domains (fin, tube and gas domains) is set to room temperature at $T = 298.15$ K corresponding to no heat transfer at the initial stage of the simulation.

3.3.1 Inlet boundary condition

We set appropriate boundary conditions to define the conjugate heat transfer process in the considered geometry. At the inlet of the flow domain, the temperature boundary condition is set as:

$$T = T_{in} \quad (9)$$

The inlet velocity field boundary condition for the flow of fluid in the gas domain is:

$$\left. \begin{aligned} u &= 0 \\ v &= -u_{in} \\ w &= 0 \end{aligned} \right\} \quad (10)$$

3.3.2 Wall boundary condition

The contact surface between fin, tube and gas domains are the boundaries from where the heat flux is exchanged. In the present model, wall function boundary condition is applied which simulates the region near the contact surface where the flow variables have high gradients.

$$\left. \begin{aligned} \mathbf{u} \cdot \mathbf{n} &= 0 \\ \nabla k \cdot \mathbf{n} &= 0 \\ \nabla \varepsilon \cdot \mathbf{n} &= 0 \end{aligned} \right\} \quad (11)$$

For the purposes here, the inner tube wall temperature is assumed to be constant and the temperature boundary condition is set as:

$$T = T_w \quad (12)$$

3.3.3 Outlet boundary condition

In the present model, outlet boundary condition is set to represent the convection dominated heat transfer across the outlet of the gas domain. The temperature gradient in the normal direction is zero. Thus, the boundary condition at the outlet in terms of heat flux can be written as:

$$-\mathbf{n} \cdot \mathbf{q} = 0 \quad (13)$$

The pressure boundary is set to specify the negligible normal stress to the flow at the outlet. We note that there is no tangential stress to the flow of fluid at the outlet of the gas domain, and the backflow is also suppressed.

$$p = p_{out} \quad (14)$$

Homogeneous Neumann conditions are also applied for the turbulence variables at the outlet,

$$\left. \begin{aligned} \nabla k \cdot \mathbf{n} &= 0 \\ \nabla \varepsilon \cdot \mathbf{n} &= 0 \end{aligned} \right\} \quad (15)$$

3.3.4 Symmetry boundary condition

Symmetry boundary condition is used to account similar physical processes on the two sides of boundary. It imposes zero heat flux across a boundary which means temperature on both sides of the boundary is equal. In a fluid-flow simulation, it prescribes no penetration and shear stresses. The symmetry boundary condition used in the present model can be written as-

$$\left. \begin{aligned} -\mathbf{n} \cdot \mathbf{q} &= 0 \\ \mathbf{u} \cdot \mathbf{n} &= 0 \\ \nabla k \cdot \mathbf{n} &= 0 \\ \nabla \varepsilon \cdot \mathbf{n} &= 0 \end{aligned} \right\} \quad (16)$$

3.4 Performance of the heat exchanger

We calculate following parameters including dimensionless terms to characterize the overall performance of the analyzed fin and tube heat exchanger design.

3.4.1 Overall heat transfer coefficient

Overall heat transfer coefficient (U) is an important parameter to evaluate the performance of heat exchangers. It is defined as the total power exchanged between the geometric domains per unit heat transfer surface area per unit temperature difference [Cengel et al., 2012] and is expressed as:

$$U = \frac{Q_t}{A_t \cdot \Delta T_{lm}} \quad (17)$$

where, Q_t [W] is the total power exchanged between the inner tube wall to the fluid flowing in gas domain. A_t [m²] is the total heat transfer surface area of the fin and tube. ΔT_{lm} [K] is log mean temperature difference.

3.4.2 Colburn j -factor

The gas-side heat transfer characteristic is often presented by Colburn j -factor (j) [Taler and Oclon, 2014; Li et al., 2015] as:

$$j = \frac{Nu}{Re \cdot Pr^{1/3}} \quad (18)$$

where, Re is Reynolds number and Pr is the Prandtl number.

3.4.3 Flow resistance factor

The mechanical performance can be evaluated in terms of flow resistance factor (f) as a ratio of wall shear stress to kinetic energy of the flow.

$$f = \frac{\Delta p}{\frac{1}{2} \rho_g \cdot u_{in}^2 \cdot \left(\frac{L_g}{D_h} \right)} \quad (19)$$

where, Δp [Pa] is the pressure difference across the gas domain, ρ_g [kg/m³] and u_{in} [m/s] is the density and inlet velocity of the gas, respectively. L_g [m] is the length of the gas domain.

3.4.4 Efficiency index

The commonly used index for performance evaluation is the Efficiency index [Lu et al., 2013], which is a ratio of average Nusselt number to the pressure loss coefficient (K_g).

$$\text{Efficiency index} = \frac{Nu}{K_g} = \frac{Nu}{\left(\frac{\Delta p}{\frac{1}{2} \rho_g u_{in}^2} \right)} \quad (20)$$

4 Numerical procedure and solution

Procedure of numerical simulation of a fin and tube heat exchanger design is described in this section. We used commercial multiphysics simulation software, COMSOL 5.1 based on FEM to solve the governing equations described in Section 3.2. With defined computational geometry (Figure 3), we start by setting initial values and model parameters (Table 1). Along with appropriate boundary conditions, governing equations for conjugate heat transfer are defined in all three domains (fin, tube and gas) and equations for turbulent flow are defined in gas domain. Heat transfer and fluid flow equations are then coupled together by the non-isothermal flow multiphysics. Mesh independence study is performed and a mesh of total 437519 elements is selected which is fine enough to resolve important physical phenomena accurately in a reasonable amount of time. To minimize the discontinuities and to capture sharp temperature gradients especially at the interface finer boundary layer mesh near to the interfaces is created. Figure 4 shows the refined FEM mesh used in the present study. The simulation was then ran for a computational time of nearly 30 minutes, which is sufficient to achieve steady state. The results obtained from the numerical model including the performance parameters are post-processed for better understanding and visualization of fundamental phenomenological behavior. Table 2 lists the boundary condition values used to solve the model and achieve preliminary results.

Table 2. Boundary conditions values used to numerically solve the model.

Description	Symbol	Value	Unit
Inner tube wall temperature	T_w	453.15	K
Inlet gas temperature	T_{in}	573.15	K
Inlet gas velocity	u_{in}	9.60	m/s
Outlet gas pressure	p_{out}	0	Pa

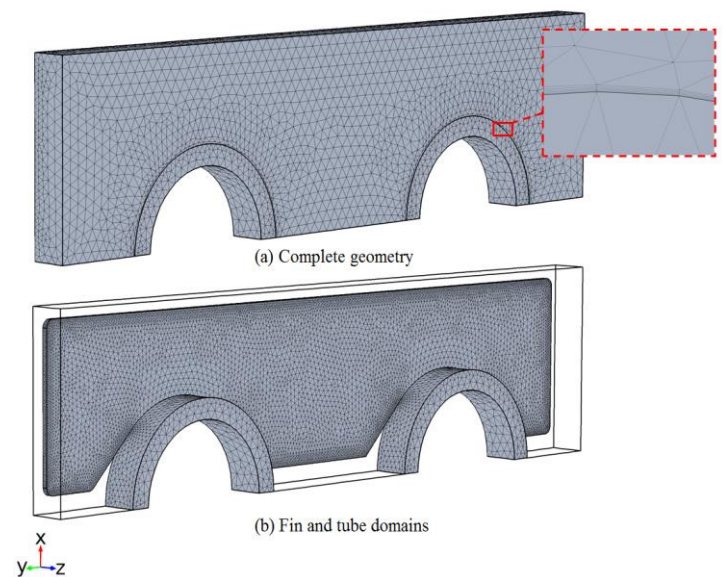


Figure 4. Mesh used in the numerical modeling.

5 Results and discussion

Since only half of the heat exchanger geometry is simulated in the present work, the results are represented for half of the geometry. Velocity profile influences the convective heat transfer to a great extent, hence it becomes important to analyze the velocity profile throughout the flow domain. Figure 5 represents the velocity profile of the flow in the gas domain. The inlet velocity profile can be clearly visualized where the gas enters the gas domain at a velocity of 9.6 m/s. It can be seen the gas flows with higher velocity near to the fin edges away from the tubes, while low velocity region generates between the tubes and at the bottom exit side of the tubes. Further velocity gradient across the length of gas domain can be clearly visualized using slice plot of the velocity profile as represented in Figure 6. The result is evident of frictional effect that develops along the length of the heat exchanger due to the tubes arrangement in an in-line manner.

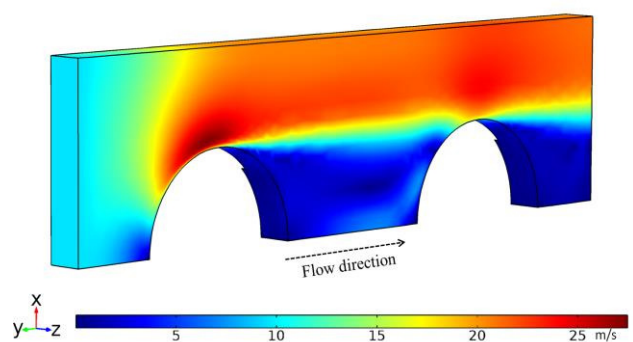


Figure 5. Velocity profile predicted in the gas domain

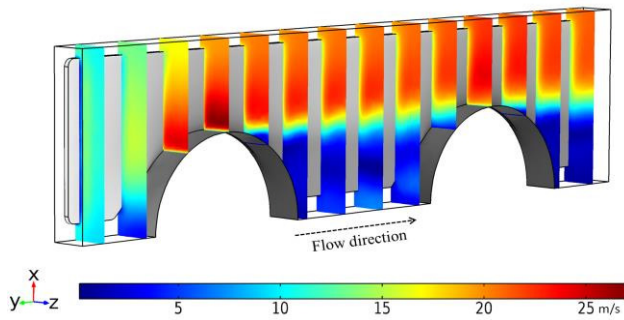


Figure 6. Slice plot for the velocity profile predicted in the gas domain

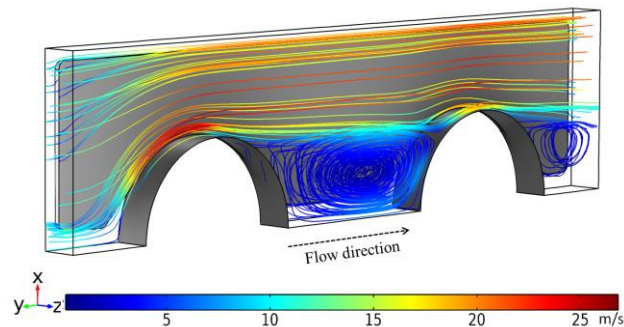


Figure 7. Streamline plot for the velocity profile predicted in the gas domain

The understanding of the flow passage within the domain is important to study the overall performance of the heat exchanger. Figure 7 depicts the velocity streamlines in the gas domain predicted by the model. Analysis of the velocity streamlines clearly shows the regions between the tubes and on the bottom exit side of the tube where the fluid recirculates to build a low or zero velocity zones. These zones prevent the effective heat transfer between the fluid and fin surface and thus degrades the overall performance of the heat exchanger.

Figure 8 shows the temperature distribution in the entire computational geometry predicted by the model. The gas enters into the gas domain at a temperature 573.15 K and is cooled down as it flows from the inlet to the outlet. The figure demonstrates the simultaneous process of conjugate heat transfer and turbulent flow. The heat is transferred from the flowing gas to fin and tube surface by convection and from outer surface fin and tube to the inner wall of the tube by conduction. The temperature gradients in Figure 8 clearly illustrate the strong influence of velocity profile on heat transfer in the heat exchanger design.

The temperature distribution in the gas domain is predicted by the model and is shown as slice plot in Figure 9. As observed, the gas has higher temperature at the inlet and on the fin edge side while lower temperature region exists between the tubes. The reason attributes to the developed low velocity region, which affects the heat transfer in the heat exchanger.

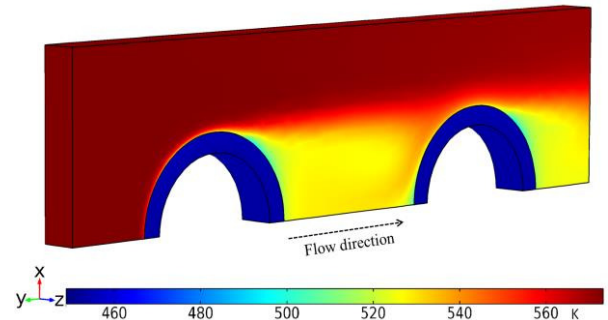


Figure 8. Temperature distribution predicted in the computational domain

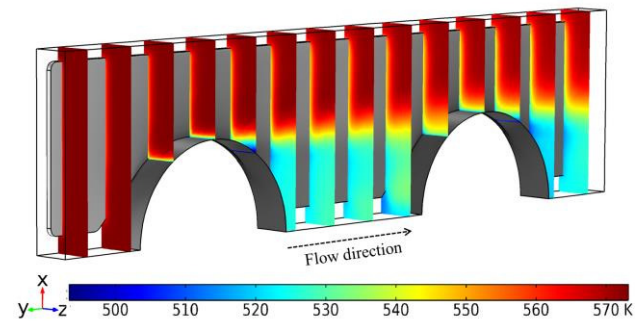


Figure 9. Slice plot for the temperature distribution predicted in the gas domain

Figure 10 depicts the predicted temperature distribution in the fin and tube domains. The high temperature can be seen at the inlet region from where hot gas enters into the gas domain. The temperature decreases along the length of the fin due to conjugate heat transfer. It is observed that the temperature gradients are high in the regions near to the fin base, where fin comes in contact with the tubes. These regions can be visualized as the regions of effective heat transfer. However, middle region of the fin length up to outer edge shows low temperature gradients and thus is not effective to contribute significantly in the overall heat transfer process. The reason attributes to the high velocity in this region that (Figure 6 and 7) does not allow the hot gas to stay for sufficient time for allowing better heat transfer.

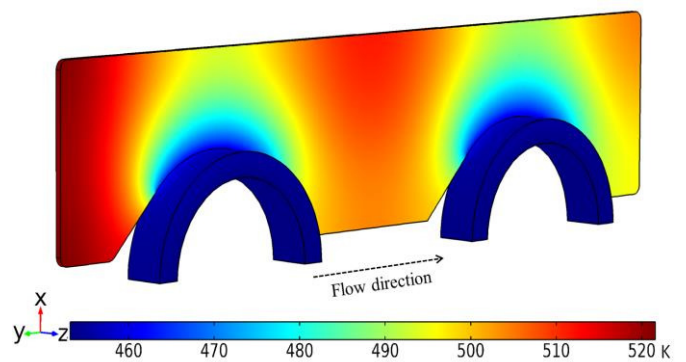


Figure 10. Temperature distribution predicted in the fin and tube domains

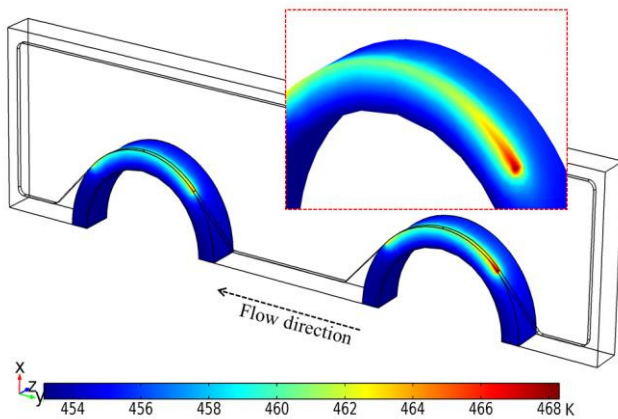


Figure 11. Contour plane plot of the conductive heat flux in fin and tube domain

The results are evident from the Figure 11, which shows temperature distribution in tube domain. It is clearly seen that the temperature gradients are high near to the contact interface of the fin and tubes. Higher temperature difference at the fin base leads to higher conductive heat flux transferred from the fin to the tube in this region. Temperature distribution in the first tube in the gas flow direction can be observed from the insert in Figure 11.

To help understand the results, vector plot for gas velocity field with temperature variations on fin and outer tube wall can be seen together in Figure 12. The direction of the arrows represents gas flow from the inlet to the outlet. The figure shows that how velocity vector moves around to create inefficient low heat transfer zone between the tubes and bottom exit side of the tube. In addition, temperature variations in the fin, tube and gas domain can also be seen simultaneously in the Figure 12.

The performance of the heat exchanger design is evaluated in terms of performance parameters defined in Section 3.4. Table 3 summarizes the values of performance parameters (Equations (17)-(20)) computed using the numerical model.

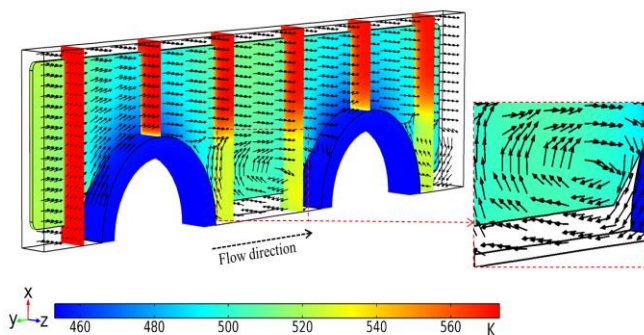


Figure 12. Vector plot for the velocity profile in gas domain with temperature distribution in fin and gas domain

Table 3. Performance parameters calculated from the numerical model

Performance parameter	Value	Unit
Overall heat transfer coefficient	41.499	W/m ² K
Colburn <i>j</i> -factor	0.0051	Dimensionless
Flow resistance factor	0.8146	Dimensionless
Efficiency index	3.474	Dimensionless

6 Conclusion

Multiphysics 3D numerical modeling of a fin and tube heat exchanger is performed. The model incorporates coupled heat transfer and turbulent flow to analyze the physical phenomenon in the heat exchanger operation. The model has a capability to predict the steady state temperature and velocity profiles, and thus predicts the overall performance of the heat exchanger design. The overall heat transfer coefficient for the heat exchanger design is calculated to be 41.499 W/m²K with an efficiency index of 3.474. The model predictions help to identify the areas where heat transfer is intensive and those where it is ineffective for waste heat recovery including bottlenecks to heat transfer within the heat exchanger which can be overcome by optimization of the design. Studies to optimize the weight of the heat exchanger will be conducted and a separate research article will be communicated in future. Moreover, developed model delivers vital guiding information to support its feasibility for large scale application in realistic conditions.

Acknowledgement

The work presented in this paper is a part of research project THERMCYC- *Advanced thermodynamic cycles utilising low-temperature heat sources* (No. 1305-0036B).

References

- A. Erek, B. O'zardem, L. Bilir and Z. Ilken. Effect of geometrical parameters on heat transfer and pressure drop characteristics of plate fin and tube heat exchangers. *Applied Thermal Engineering*, 25: 2421–2431, 2005.
- A. Jacobi and R. Shah. Heat transfer surface enhancement through the use of longitudinal vortices: a review of recent progress. *Experimental Thermal Fluid Science*, 11: 295–309, 1995.
- B. Gong, L. Wang and Z. Lin. Heat transfer characteristics of a circular tube bank fin heat exchanger with fins punched curve rectangular vortex generators in the wake regions of the tubes. *Applied Thermal Engineering*, 75: 224–238, 2015.
- B. Kundu and K. Lee. Thermal design of an orthotropic flat fin in fin-and-tube heat exchangers operating in dry and wet environments. *International Journal of Heat and Mass Transfer*, 54:5207–5215, 2011.
- C. C. Wang, W. H. Tao and C. J. Chang. An investigation of the airside performance of the slit fin-and-tube heat

- exchangers. *International Journal of Refrigeration*, 22: 595–603, 1999.
- C. Habchi, S. Russeil, D. Bougeard, J. Harion, T. Lemenand, D. D. Valle and H. Peerhossaini. Enhancing heat transfer in vortex generator-type multifunctional heat exchangers. *Applied Thermal Engineering*, 38:14–25, 2012.
- D. C. Wilcox. *Turbulence Modeling for CFD*. 2nd ed., DCW Industries, 1998.
- D. Kuzmin, O. Mierka and S. Turek. On the Implementation of the k - ϵ Turbulence Model in Incompressible Flow Solvers Based on a Finite Element Discretization. *International Journal of Computing Science and Mathematics*, 1(2–4): 193–206, 2007.
- D. Taler and P. Oclon. Thermal contact resistance in plate fin-and-tube heat exchangers determined by experimental data and CFD simulations. *International Journal of Thermal Science*, 84: 309–322, 2014.
- J. Cobian- Iñiguez, A. Wu, F. Dugast and A. Pacheco-Vega. Numerically-based parametric analysis of plain fin and tube compact heat exchangers. *Applied Thermal Engineering*, 86: 1–13, 2015.
- J. Y. Jang and J. Y. Yang. Experimental and numerical analysis of the thermal hydraulic characteristics of elliptic finned-tube heat exchangers. *Heat Transfer Engineering*, 19(4): 55–67, 1998.
- L. A. O. Rocha, F. E. M. Saboya and J. V. C. Vargas. A comparative study of elliptical and circular sections in one- and two-row tubes and plate fin heat exchangers, *International Journal of Heat and Fluid Flow*, 18(2): 247–252, 1997.
- L. H. Tang, Z. Min, G. N. Xie and Q. W. Wang. Fin Pattern Effects on Air-Side Heat Transfer and Friction Characteristics of Fin-and-Tube Heat Exchangers with Large Number of Large-Diameter Tube Rows. *Heat Transfer Engineering*, 30(3): 171–180, 2009.
- L. Li, X. Du, Y. Zhang, L. Yang and Y. Yang. Numerical simulation on flow and heat transfer of fin-and-tube heat exchanger with longitudinal vortex generators. *International Journal of Thermal Sciences*, 92: 85–96, 2015.
- L. M. Chang, L. B. Wang, K. W. Song and D. L. Sun. Numerical study of the relationship between heat transfer enhancement and absolute vorticity flux along main flow direction in a channel formed by a flat tube bank fin with vortex generators. *International Journal of Heat and Mass Transfer*, 52: 1794–1801, 2009.
- M. Fiebig. Embedded vortices in internal flow: heat transfer and pressure loss enhancement. *International Journal of Heat and Fluid Flow*, 16(5):376–388, 1995.
- M. Hatami, D. D. Ganji and M. Gorji-Bandpy. Numerical study of finned type heat exchangers for ICEs exhaust waste heat recovery. *Case Studies in Thermal Engineering* 4:53–64, 2014a.
- M. Hatami, D. D. Ganji and M. Gorji-Bandpy. A review of different heat exchangers designs for increasing the diesel exhaust waste heat recovery. *Renewable and Sustainable Energy Reviews*, 37:168–181, 2014b.
- M. Hatami, D. D. Ganji and M. Gorji-Bandpy. CFD simulation and optimization of ICEs exhaust heat recovery using different coolants and fin dimensions in heat exchanger. *Neural Computing and Applications*, 25: 2079–2090, 2014c.
- M. S. Mon and U. Gross. Numerical study of fin-spacing effects in annular-finned tube heat exchangers. *International Journal of Heat and Mass Transfer*, 47: 1953–1964, 2004.
- P. Chu, Y. L. He, Y. G. Lei, L. T. Tian and R. Li. Three-dimensional numerical study on fin-and-oval-tube heat exchanger with longitudinal vortex generators. *Applied Thermal Engineering*, 29: 859–876, 2009.
- R. Borrajo-Peláez, J. Ortega-Casanova and J. M. Cejudo-López. A three-dimensional numerical study and comparison between the air side model and the air/water side model of a plain fin-and-tube heat exchanger. *Applied Thermal Engineering*, 30: 1608–1615, 2010.
- R. S. Matos, J. V. C. Vargas, T. A. Laursen and T. A. Bejan. Optimally staggered finned circular and elliptic tubes in forced convection. *International Journal of Heat and Mass Transfer*, 47(13): 47–59, 2004.
- S. Łopata and P. Oclon. Numerical study of the effect of fouling on local heat transfer conditions in a high-temperature fin-and-tube heat exchanger. *Energy* doi:10.1016/j.energy.2015.03.048, 2015
- T. A. Ibrahim and A. Gomma. Thermal performance criteria of elliptic tube bundle in crossflow. *International Journal of Thermal Science*, 48(11): 2148–2158, 2009.
- T. J. Lu, F. Xu and T. Wen. *Thermo-fluid behaviour of periodic cellular metals*. Springer Heidelberg New York Dordrecht London (ISBN 978-3-642-33523-5), 2013.
- V. P. Malapure, S. K. Mitra and A. Bhattacharya. Numerical investigation of fluid flow and heat transfer over louvered fins in compact heat exchanger. *International Journal of Thermal Sciences*, 46:199–211, 2007.
- W. Yaïci, M. Ghorab and E. Entchev. 3D CFD analysis of the effect of inlet air flow maldistribution on the fluid flow and heat transfer performances of plate-fin-and-tube laminar heat exchangers. *International Journal of Heat and Mass Transfer*, 74:490–500, 2014.
- Y. A. Cengel, J. M. Cimbala and R. H. Turner. *Fundamentals of thermal-fluid sciences*, fourth edition in SI units. McGraw-Hill, 2012.
- Y. B. Tao, Y. L. He, J. Huang, Z. G. Wu and W.Q. Tao. Numerical study of local heat transfer coefficient and fin efficiency of wavy fin-and-tube heat exchangers. *International Journal of Thermal Sciences*, 46: 768–778, 2007.
- Y. Chen, M. Fiebig and N. K. Mitra. Conjugate heat transfer of a finned oval tube part a: flow patterns, Numerical Heat Transfer, Part A: Applications. *An International Journal of Computation and Methodology*, 33(4): 371–385, 2007.

Numerical Investigation of Single-phase Fully Developed Heat Transfer and Pressure Loss in Spirally Corrugated Tubes

Jakob Hærvig¹ Thomas Condra¹ Kim Sørensen¹

¹Department of Energy Technology, Aalborg University, 9220-Aalborg, Denmark, {jah,tc,kso}@et.aau.dk

Abstract

A numerical study is carried out to investigate heat transfer and friction argumentation in spirally corrugated tubes. 28 geometrically different tubes are investigated to cover a large set of different corrugation characteristics. The pipes investigated have pitch lengths l/D in the range 0.5 to 2.0 and pitch heights h/D in the range 0 to 0.16. Furthermore, the flow conditions defined by the Reynolds number are investigated for $Re = 5000$ and $Re = 10000$, resulting in a total of 56 Computational Fluid Dynamics (CFD) simulations. The performance of the heat exchangers are evaluated based on the Nusselt number, friction factor, and performance evaluation criterion coefficient combining the two into a single unique dimensionless parameter.

The results suggest corrugation to be an effective way to increase the performance of tube heat exchangers. If only heat transfer is considered without paying attention to pressure loss, the optimal tubes have high corrugation heights, where the Nusselt number can be increased by a factor of 2 compared to the non-corrugated tube. If the performance evaluation criterion is used, the optimal geometry has a moderate corrugation height h/D between 0.05 and 0.10 and a low corrugation length l/D around 1.0, which can be explained by a high increase in pressure loss due to severe corrugation.

Keywords: Stream-wise periodic boundaries, Heat transfer, Pressure loss, 3D CFD simulations, Parameter variation, Fully-developed flow

1 Introduction

Transferring heat through a straight tube is used in various applications. These applications include but are not limited to power generation, air-conditioning, petrochemical, and dairy applications. Two distinct different techniques for enhancing heat transfer are commonly used; namely a passive or active, where the active requires additional power input whereas the passive does not. Therefore, the passive technique is commonly used where the geometry is altered in a more or less sophisticated manner deforming the thermal boundary layer, creating recirculating local flow structures, or larger secondary flow structures flow-

ing perpendicular to the main flow. All these phenomena affect both the heat transfer and friction characteristics.

To enhance the forced convection inside a passive heat exchanger tube, two different methods are typically used. One method is to alter the flow by changing the inner geometry of the tube. Another method is to insert loose or fastened geometrical inserts filling the cross-section of the tube, thereby promoting mixing resulting in enhanced heat transfer. These techniques do in general increase the pressure loss as well, which results in the best geometry having a optimal combination of increased heat transfer at slightly higher pressure loss. As a result, numerous studies have already been carried out to investigate the effect of both spirally and transversally tube corrugation.

Even though all studies conclude that heat transfer and pressure drop is increased by corrugation, the literature overview by Vicente et al. (2004) points out that large disagreements between different studies exist. Ganeshan and Rao (1982) investigated seven different spirally corrugated tubes having different width and height of corrugation while suggesting the ratio between heat exchanger capacity to pumping power to be 100 to 150 % more efficient for $Pr = 4.3$ and $Pr = 109$ respectively. As a result, this study suggests the spirally corrugated tubes to be attractive especially for fairly viscous fluids with high Prandtl numbers. Zimparov et al. (1991) conducted experiments on 25 spirally corrugated tubes having pitch height h/D in the range 0.017 to 0.046 and pitch length in the range 0.25 to 0.65. The study found heat transfer enhancement factors ranging from 1.77 to 2.73 while the friction factor was increased from 100 to 400 %. The literature overview by Kareem et al. (2015) gives a great overview of all the studies published in the period 1977 to 2015. The study clearly shows that the number of publications on passive heat transfer enhancement has increased in recent years, which is attributed an increased awareness of energy savings. Furthermore, the study concludes that even though quite a number of studies already have been published, more parameters should be investigated to cover a larger design space. Therefore, the purpose of this study is to set up a numerical modelling framework that is able to predict both heat transfer and pressure loss in spirally corrugated tubes. Based on this validated framework, a parameter

variation can be carried out to investigate how different kinds of corrugation affect the performance in terms of heat transfer and pressure loss.

2 Geometry and Parameters of Interest

2.1 Terminology and Representation of the Geometry

The geometry of interest in this study can be described by the following two parameters:

- Corrugation length l : the corrugation length being the stream-wise distance between two successive points where the geometry repeats itself.
- Corrugation height h : the corrugation height being the constant distance between the surface of corrugated tube and the non-corrugated tube with same diameter.

Based on these two parameters, two dimensionless quantities are formed, namely Π_1 and Π_2 :

$$\Pi_1 = l/D, \quad (1)$$

$$\Pi_2 = h/D. \quad (2)$$

The pipe geometry investigated in this study has a constant diameter D and a centre line position which for each repeatable twisted pipe section is fully described by the following parametric trigonometric function for $t \in [0; 1]$:

$$\begin{aligned} x(t) &= h \cdot \sin(2\pi t), \\ y(t) &= h \cdot \cos(2\pi t), \\ z(t) &= l \cdot t. \end{aligned} \quad (3)$$

Based on the parametric representation in (3), the geometries will take the form shown in figure 1.

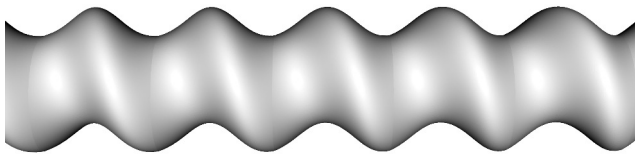


Figure 1. Heat exchanger geometry with $l/D = 0.8$ and $h/D = 0.2$.

2.2 Performance Parameters

To evaluate and compare the performance of the different heat exchangers, two dimensionless quantities describing the heat transfer and pressure loss are used. In the of corrugated tubes, two distinct different phenomena contributed to the pressure loss; wall shear stresses related to the local

velocity gradient normal to the tube surface, and pressure drag related to the local pressure distribution along the surface. By integrating the two along the surface and averaging yields a single friction factor parameter that takes both into account. This friction factor is used as a direct measure of the pressure loss in the tube. The Nusselt number and friction factor used to evaluate heat transfer and pressure loss respectively are defined as:

$$\text{Nu} = \frac{hD}{k}, \quad (4)$$

$$f = \frac{2\rho\Delta p D}{U^2 l}. \quad (5)$$

Instead of evaluating the performance of the corrugated tubes based on two parameters, the performance evaluation criterion η is commonly used. This criterion defines the ratio between heat transfer augmentation to friction factor augmentation compared to the non-corrugated straight tube having a Nusselt number Nu_0 and friction factor f_0 :

$$\eta = \frac{\text{Nu}/\text{Nu}_0}{(f/f_0)^{1/3}}. \quad (6)$$

That is, if the corrugated tubes have values above 1, the performance is superior to the non-corrugated tube. To evaluate the performance evaluation criterion, the well-validated and commonly used correlations by Gnielinski (1976) and Filonenko (1960) are used:

$$\text{Nu}_0 = \frac{(f_0/8)(\text{Re} - 1000)\text{Pr}}{1 + 12.7\sqrt{(f_0/8)}(\text{Pr}^2 - 1)} \left[1 + \left(\frac{D}{L}\right)^{2/3} \right] K, \quad (7)$$

$$f_0 = (1.8 \log_{10}\text{Re} - 1.5)^{-2}, \quad (8)$$

where the ratio D/L equals 0 in this study due to the stream-wise periodicity introduced by the boundary conditions described in the following section. The correction factor K used for this study is $(T_b/T_w)^n$ with n being 0.45 for air as discussed by Hufschmidt and Burck (1968) and Yakovlev (1960). In this study, air is used for all simulations. Therefore, the K correction term with the exponent 0.45 is used for all simulations in this study. Should simulations be carried out for different fluids, this exponent should be changed accordingly.

3 Numerical Modelling Framework

3.1 Governing equations

The basic equations governing the problem are the continuity (9), momentum (10), and energy (11) equations:

$$\frac{\partial \rho}{\partial t} + \frac{\partial (\rho u_i)}{\partial x_i} = 0, \quad (9)$$

$$\frac{\partial (\rho u_i)}{\partial t} + \frac{\partial (\rho u_i u_j)}{\partial x_j} = -\frac{\partial p}{\partial x_i} + \frac{\partial}{\partial x_j} \left(\mu \frac{\partial u_i}{\partial x_j} - \rho \overline{u_i u_j} \right), \quad (10)$$

$$\frac{\partial (\rho c_p T)}{\partial t} + \frac{\partial (\rho c_p u_j T)}{\partial x_j} = \frac{\partial}{\partial x_j} \left(k \frac{\partial T}{\partial x_j} - \rho c_p \overline{T u_j} \right). \quad (11)$$

As seen, the temperature is treated as a passive scalar instead of solving the full energy equation. That is, the transport properties do not vary with temperature but are constant. Using this approach, a fully periodic velocity and temperature profile can be obtained. Furthermore, to close the equations and predict the onset of separation accurately, the transition SST turbulence model combining transition modelling by Menter et al. (2006) and SST modelling by Menter (1992) is used.

3.2 Stream-wise Periodicity

As the flow in the majority of the heat exchanger tubes is both hydro-dynamically and thermally fully developed, focus will be on this part of the heat exchanger. Instead of simulating the whole heat exchanger starting with a non-developed flow and dealing with how the flow develops, periodic boundaries are utilised to couple the inlet and outlet. Using this approach, the inlet and outlet are two-way coupled and therefore a driving force is required to balance out the pressure loss to keep the fluid flowing. Using this approach, the mass flow is specified and the simulation converges towards the corresponding pressure loss. Likewise, modifications are required to keep the temperature from converging towards to wall temperature. The approach suggested by Patankar et al. (1977) is used to make both the temperature and pressure field repeat itself in a periodic manner.

Assuming a constant wall temperature, the fully-developed temperature field is obtained by solving for the scaled temperature field θ as suggested by Patankar et al. (1977):

$$\theta(x, y, z) = \frac{T(x, y, z) - T_w}{T_z^* - T_w}, \quad (12)$$

where $T(x, y, z)$ is the temperature field, T_w is the constant wall temperature, and T_z^* is a local reference temperature profile at the inlet. The reference temperature T_z^* is given by:

$$T_z^* = T_w \frac{\int_A (T - T_w) |\rho \vec{u} d\vec{A}|}{\int_A |\rho \vec{u} d\vec{A}|}. \quad (13)$$

That is, solving equation (12) yields the stream-wise periodic temperature profile, which is used directly to evaluate the local heat transfer coefficient and consequently the local and average Nusselt numbers.

3.3 Mesh Topology

A quarter of the cross-sectional mesh is shown in figure 2. The cross-sectional mesh is extruded along the path described by (3) resulting in a structured mesh having the same cross-sectional mesh along the length of the tube. To ensure the results reported in this study are reliable,

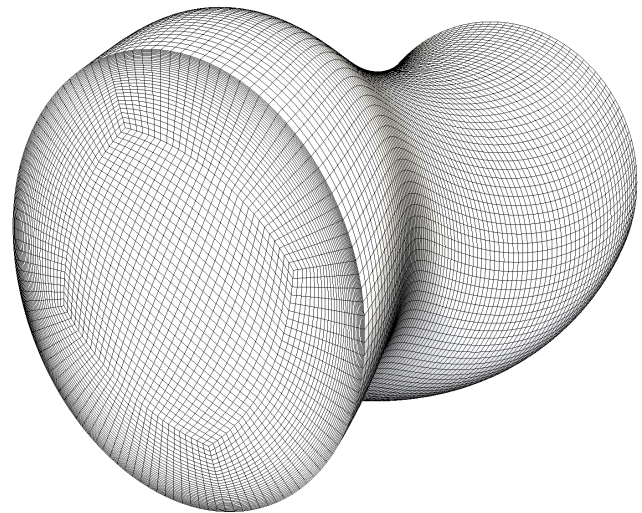


Figure 2. Overview of the structured computational mesh topology used for simulations

two measures are taken. First the number of cells are doubled for a corrugated tube until the results do not change anymore. Instead of simply doubling the number of cells without paying attention how the boundary layer is resolved, the first cell height is kept constant at $y^+ \approx 1$ for the transition SST turbulence model. This is done for the transition SST model to accurately be able to predict flow separation at higher corrugations.

3.4 Data Processing

As the solution converges, the periodic velocity and temperature profiles are obtained. For the converged solution, the bulk inlet temperature is constant at the specified value $T_{\text{bulk,in}}$. With the wall temperature held fixed at a specified value $T_{\text{wall}} < T_{\text{bulk,in}}$, the outlet bulk approaches a temperature between the inlet and wall temperature due to the periodic boundaries. With converged inlet and outlet temperatures, the average convective heat transfer coefficient h and consequently the Nusselt number Nu are calculated. To get dimensionless friction factor defined by (5), the pressure difference across the domain is calculated. The static pressure is fixed in a cell, and the pressure difference between inlet and outlet is evaluated based on the converged relative pressure field.

4 Validation of Results

Figure 3 shows how the number of cells affects the average Nusselt number. Based on figure 3, the mesh hav-

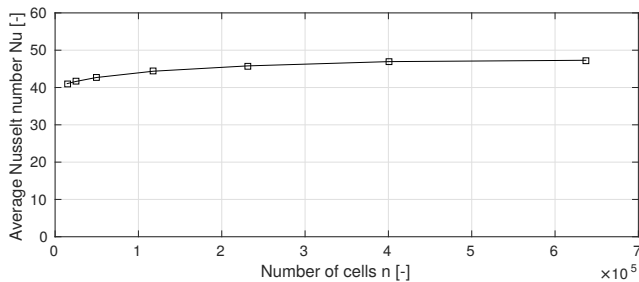


Figure 3. Grid independence study to investigate the importance of cell count for a corrugated pipe ($\Pi_1 = 1$ and $\Pi_2 = 0.1$).

ing 231,500 cells is chosen. Using this mesh, the results obtained for a straight tube ($\Pi_1 = 1$, $\Pi_2 = 0$) are in figure 4 and 5 compared to equation (7) and (8) by Gnielinski (1976) and Filonenko (1960) for various Reynolds and Prandtl numbers.

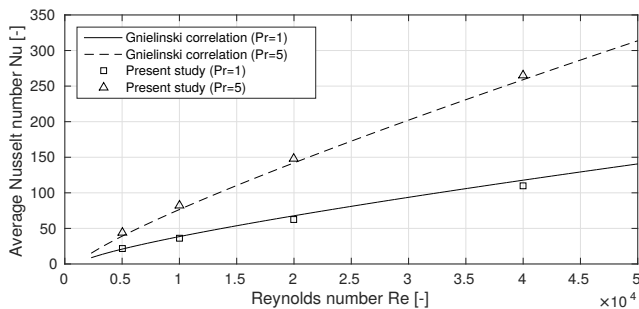


Figure 4. Comparison to the Gnielinski correlation ($\Pi_1 = 1$ and $\Pi_2 = 0$).

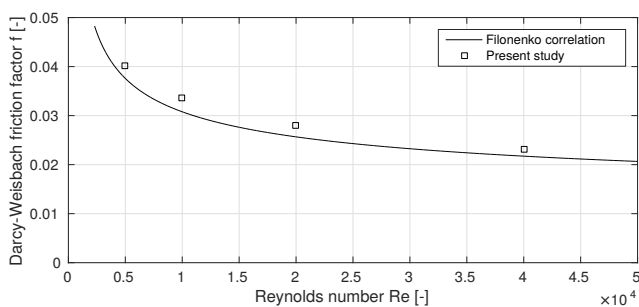


Figure 5. Comparison to the Filonenko correlation ($\Pi_1 = 1$ and $\Pi_2 = 0$).

The comparison suggests the CFD simulations to be able to predict smooth pipe performance. For the results in figure 4 and 5, the Nusselt numbers and friction factors numbers are within a maximum deviation of 6.9% and 9.4% respectively.

5 Results

In this study, results are reported for corrugations heights $h/D = [0.01, 0.03, 0.05, 0.07, 0.10, 0.13, 0.16]$, corrugations lengths $l/D = [0.5, 1.0, 1.5, 2.0]$ at Reynolds numbers $Re = [5000, 10000, 20000]$. The performance is evaluated based on the criteria defined in (4), (5), and (6).

5.1 Heat Transfer Characteristics

Figure 6 shows contours of constant Nusselt number as function of corrugation height and length at a Reynolds number of 5000. The results in the figure suggests the

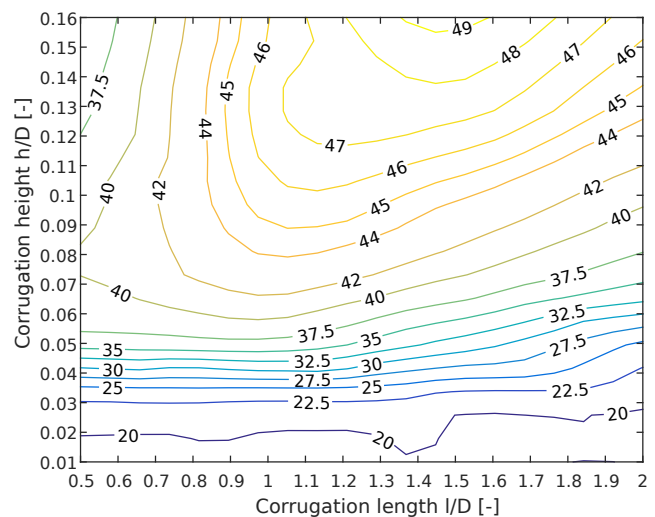


Figure 6. Contours showing the Nusselt number as function of dimensionless corrugation length l/D and height h/D at $Re = 5000$.

Nusselt number to be almost independent of corrugation length in the range $[0.5;2.0]$ at small corrugation heights. This can be explained by the fact that the corrugated tubes approaches the same non-corrugated tube as h/L approaches 0. At higher corrugation heights, the Nusselt number depends on the corrugation length. At small corrugation lengths $l/D \approx 0.5$, the maximum Nusselt number is obtained at corrugation heights in the range $[0.07;0.10]$. The decrease in Nusselt number at higher corrugation heights can be explained by the flow being mostly axial and unaffected by the corrugation while the surface area increases. At higher corrugation lengths, the maximum Nusselt number is obtained at higher corrugation heights. Figure 7 shows the results in terms of Nusselt number for $Re = 10000$. In general, higher Nusselt numbers are obtained as a result of higher Reynolds number. At low corrugation heights, the Nusselt number is again almost independent of the corrugation length, increasing slightly with corrugation length.

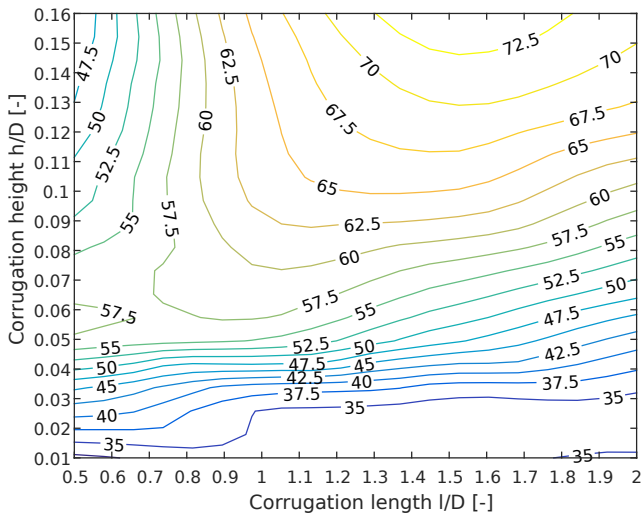


Figure 7. Contours showing the Nusselt number as function of dimensionless corrugation length l/D and height h/D at $Re = 10000$.

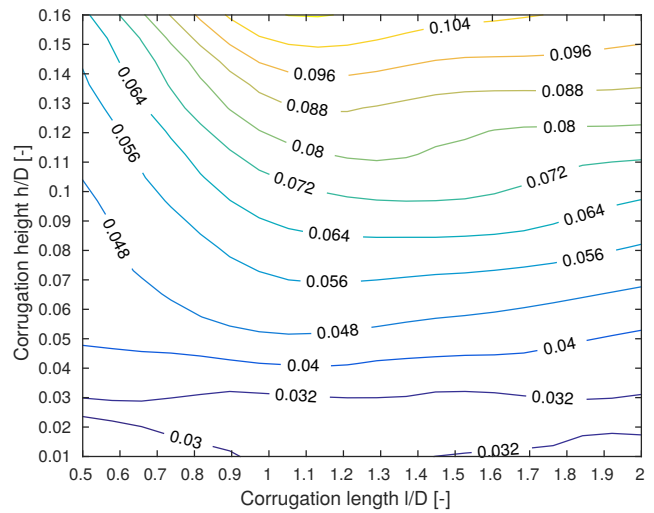


Figure 9. Contours showing the Darcy-Weisbach friction factor as function of dimensionless corrugation length l/D and height h/D at $Re = 10000$.

5.2 Friction Factor Characteristics

Figure 8 and 9 shows contours of the friction factor as function of corrugation height and length at a Reynolds numbers of 5000 and 10000 respectively. The figures

5.3 Optimal Combination of Heat Transfer and Pressure loss

To evaluate the optimal combination of heat transfer and pressure loss, the performance evaluation criterion defined by (6) is used. Figure 10 shows the criterion for the different corrugated tubes at $Re = 5000$. As the results in

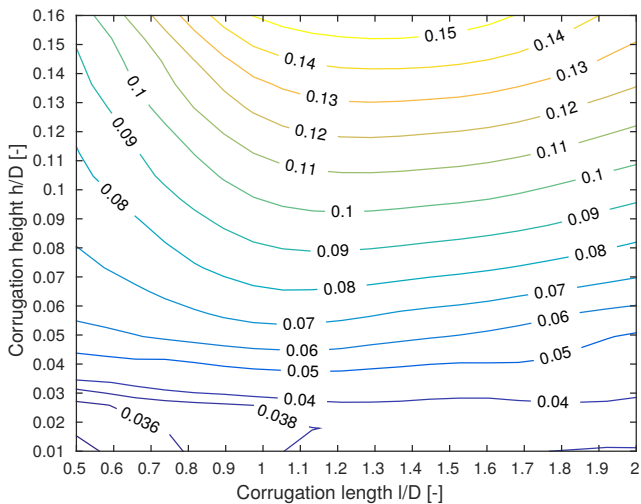


Figure 8. Contours showing the Darcy-Weisbach friction factor as function of dimensionless corrugation length l/D and height h/D at $Re = 5000$.

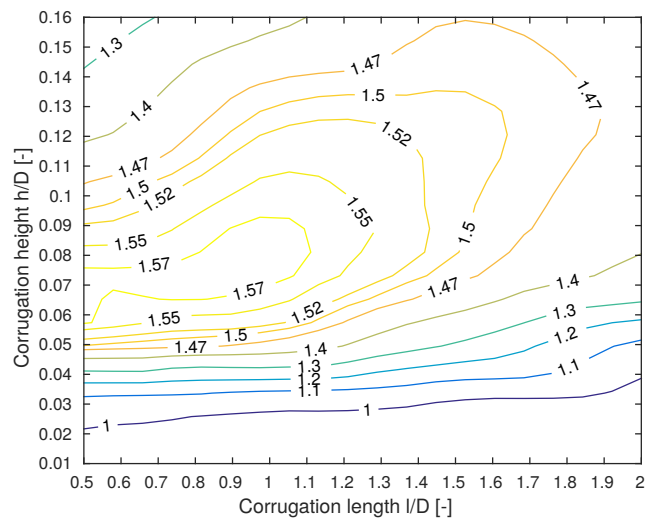


Figure 10. Contours showing the performance parameter $\eta = (Nu/Nu_0)/(f/f_0)^{1/3}$ as function of dimensionless corrugation length l/D and height h/D at $Re = 5000$.

shows that the friction factor in general increases with corrugation height starting at values close to the non-corrugated pipe at $h/D = 0.01$. Furthermore, the results suggest that there is a corrugation length l/D resulting in the highest friction coefficient. This value seems to be almost independent of the Reynolds number at a value between $l/D = 1$ and $l/D = 1.5$.

the figure suggest, the optimal combination of heat transfer and pressure loss is found at moderate corrugations heights opposed to when only heat transfer is considered. That is, to obtain the highest Nusselt number, a friction factor is obtained as well. The figure suggests lower corrugations lengths l/D in the range $[0.5;1.0]$ and corrugation heights h/D in the range $[0.05;0.10]$ to be optimal. In this region the performance evaluation criterion is 1.5. The results for a higher Reynolds number of 10000 are shown in

figure 11. The results for $Re = 10000$ suggest the max-

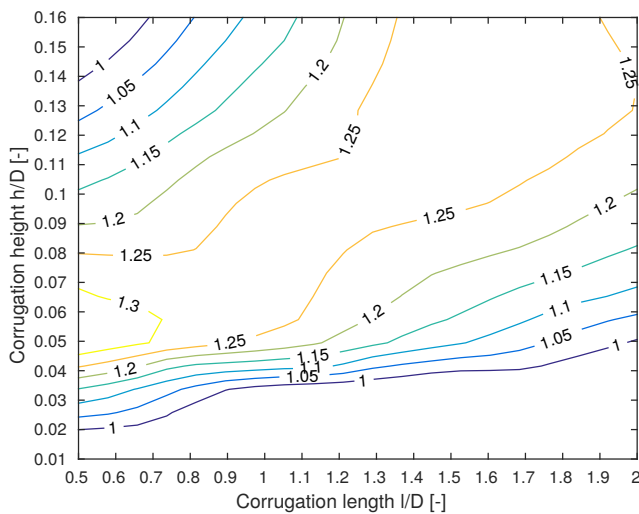


Figure 11. Contours showing the performance parameter $\eta = (\text{Nu}/\text{Nu}_0)/(f/f_0)^{1/3}$ as function of dimensionless corrugation length l/D and height h/D at $Re = 10000$.

imum performance evaluation criterion to be lower than for $Re = 5000$. At $Re = 10000$, the maximum performance evaluation criterion is again found for corrugated tubes having low corrugation lengths and moderate corrugation heights. For $Re = 10000$, a high criterion can, however, be maintained at higher corrugation heights if the corrugation length is increased accordingly.

6 Discussion and Conclusion

A CFD modelling framework to predict heat transfer and pressure loss in spirally corrugated tubes have been presented. The following sums up the findings of this study:

- (1) In general, both heat transfer and pressure loss are increased when corrugated is introduced. Without paying attention to additional pressure loss, the optimal corrugation is found at highly corrugated tubes having dimensionless corrugation heights h/D and lengths l/D at around $h/D = 0.16$ and $l/D = 1.5$ for both $Re = 5000$ and $Re = 10000$.
- (2) The pressure loss does in general increase with corrugation height h/D . The smallest increase is found at low corrugation lengths of $l/D = 0.5$. Furthermore, the pressure loss can increase by up to a factor of 4 when introducing a severe corrugation of $h/D = 0.16$.
- (3) When considering both heat transfer and pressure loss in the performance evaluation, the optimal corrugation is changed. At Reynolds numbers of 5000, the optimal combination corrugation is found at moderate corrugation heights ($h/D = [0.05; 0.10]$) and low corrugation lengths ($l/D = [0.5; 1.0]$). At these corrugations, performance can be increased by a factor of 1.57 compared to the non-corrugated tube. At $Re=10000$ the performance is only increased by a factor of 1.25 suggesting corrugation to be

more important for lower Reynolds numbers. Again the optimal corrugation is found by a combination of moderate corrugation height. At $Re = 10000$, the optimal corrugation height does however increase with corrugation length.

Acknowledgement

This work is sponsored by The Danish Council for Strategic Research and the program: *THERMCYC - Advanced thermodynamic cycles for low-temperature heat sources* (No. 1305-00036B).

References

- G.K. Filonenko. *Hydraulischer widerstand von rohrlösungen. Teploenergetika*, 1:1098–1099, 1960.
- S. Ganeshan and M. Rajo Rao. Studies on thermohydraulics of single- and multi-start spirally corrugated tubes for water and time-independent power law fluids. *International Journal of Heat and Mass Transfer*, 25:1013–1022, 1982. URL [http://dx.doi.org/10.1016/0017-9310\(82\)90076-X](http://dx.doi.org/10.1016/0017-9310(82)90076-X).
- V. Gnielinski. New equations for heat and mass transfer in turbulent pipe and channel flow. *Int. Chem. Eng.*, 16: 359–368, 1976. URL <http://dx.doi.org/10.1007/BF02559682>.
- W. Hufschmidt and E. Burck. Der einfluss temperaturabhängiger stoffwerte auf den wärmeübergang bei turbulenter strömung von flüssigkeiten in rohren bei hohen wärmestromdichten und prandtlzahlen. *Int. J. Heat Mass Transfer*, 11:1041–1104, 1968. URL [http://dx.doi.org/10.1016/0017-9310\(68\)90009-4](http://dx.doi.org/10.1016/0017-9310(68)90009-4).
- Zaid S. Kareem, M. N. Mohd Jaafar, Tholudin M. Lazim, Shahrir Abdullah, and Ammar F. Abdulwahid. Passive heat transfer enhancement review in corrugation. *Experimental Thermal and Fluid Science*, 68:22–38, 2015. URL <http://dx.doi.org/10.1016/j.expthermflusci.2015.04.012>.
- F. R. Menter. Improved two-equation k-omega turbulence models for aerodynamic flows. Technical report, National Aeronautics and Space Administration, 1992.
- F. R. Menter, R. Langtry, and S. Völker. Transition modelling for general purpose cfd codes. *Flow Turbulence Combust.*, 77: 277–303, 2006. URL <http://dx.doi.org/10.1007/s10494-006-9047-1>.
- S. V. Patankar, C. H. Liu, and E. M. Sparrow. Fully developed flow and heat transfer in ducts having streamwise-periodic variations of cross-sectional area. *Journal of Heat Transfer*, 99:180–186, 1977. URL <http://dx.doi.org/10.1115/1.3450666>.
- P. G. Vicente, A. García, and A. Viedma. Experimental investigation on heat transfer and frictional characteristics of spirally corrugated tubes in turbulent flow at different prandtl

numbers. *International Journal of Heat and Mass Transfer*, 47:671–681, 2004. URL <http://dx.doi.org/10.1016/j.ijheatmasstransfer.2003.08.005>.

V.V. Yakovlev. Ortliche und mittlere warmeubetragung bei turbulenter rohrstromung nichtsiedenden wassers und hohen warmebelastungen. *Kernenergie*, 3:1098–1099, 1960.

V. D. Zimparov, N. L. Vulchanov, and L. B. Delov. Heat transfer and friction characteristics of spirally corrugated tubes for power plant condensers — 1. experimental investigation and performance evaluation. *International Journal of Heat and Mass Transfer*, 34:2187–2197, 1991. URL [http://dx.doi.org/10.1016/0017-9310\(91\)90045-G](http://dx.doi.org/10.1016/0017-9310(91)90045-G).